Polymer 52 (2011) v–xii

Contents lists available at ScienceDirect

Polymer

journal homepage: www.elsevier.com/locate/polymer

Polymer Vol. 52, No. 1, 7 January 2011

Contents

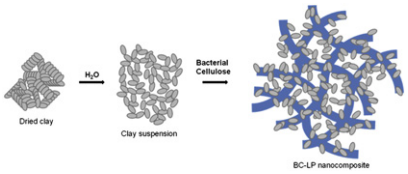

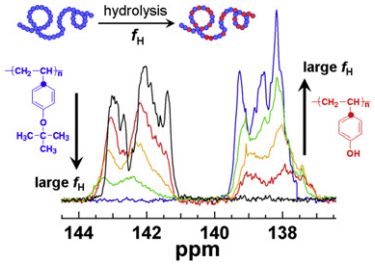

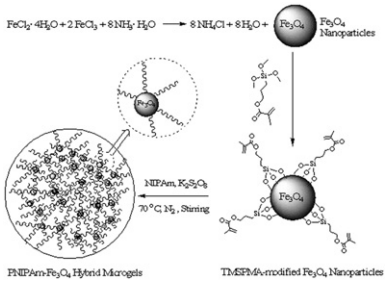

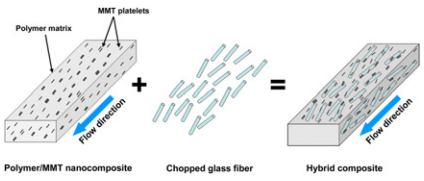

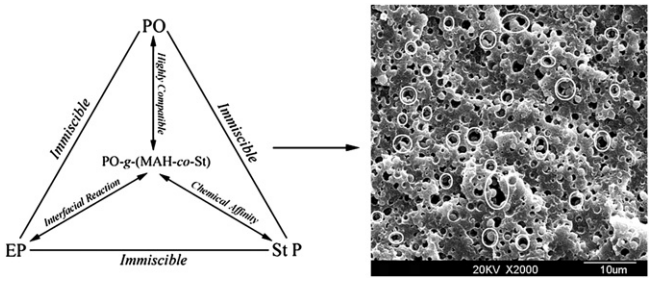

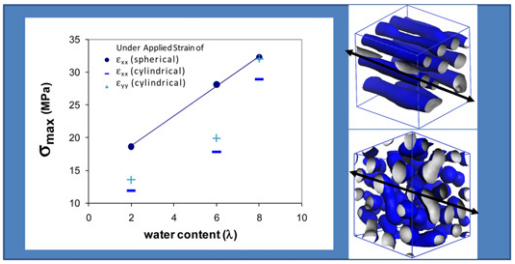

*Corresponding author

Abstracted/indexed in: AGRICOLA, Beilstein, BIOSIS Previews, CAB Abstracts, Chemical Abstracts. Current Contents: Life Sciences, Current Contents: Physical, Chemical and Earth Sciences, Current Contents Search, Derwent Drug File, Ei compendex, EMBASE/Excerpta Medica, Medline, PASCAL, Research Alert, Science Citation Index, SciSearch. Also covered in the abstract and citation database SCOPUS®. Full text available on ScienceDirect®

ELSEVIER

ISSN 0032-3861

Author Index

Polymer 52 (2011) 1–4

Contents lists available at ScienceDirect

Polymer

journal homepage: www.elsevier.com/locate/polymer

Publisher's note

Welcome to the first issue of *Polymer* for 2011!

The latest impact factor (for the year 2009, announced by Thomson Reuters in June 2010) is 3.573[1] which is 0.242 points above the previous (2008) impact factor of 3.331. The impact that *Polymer* makes in the community continues to grow consistently as Fig. 1 demonstrates.

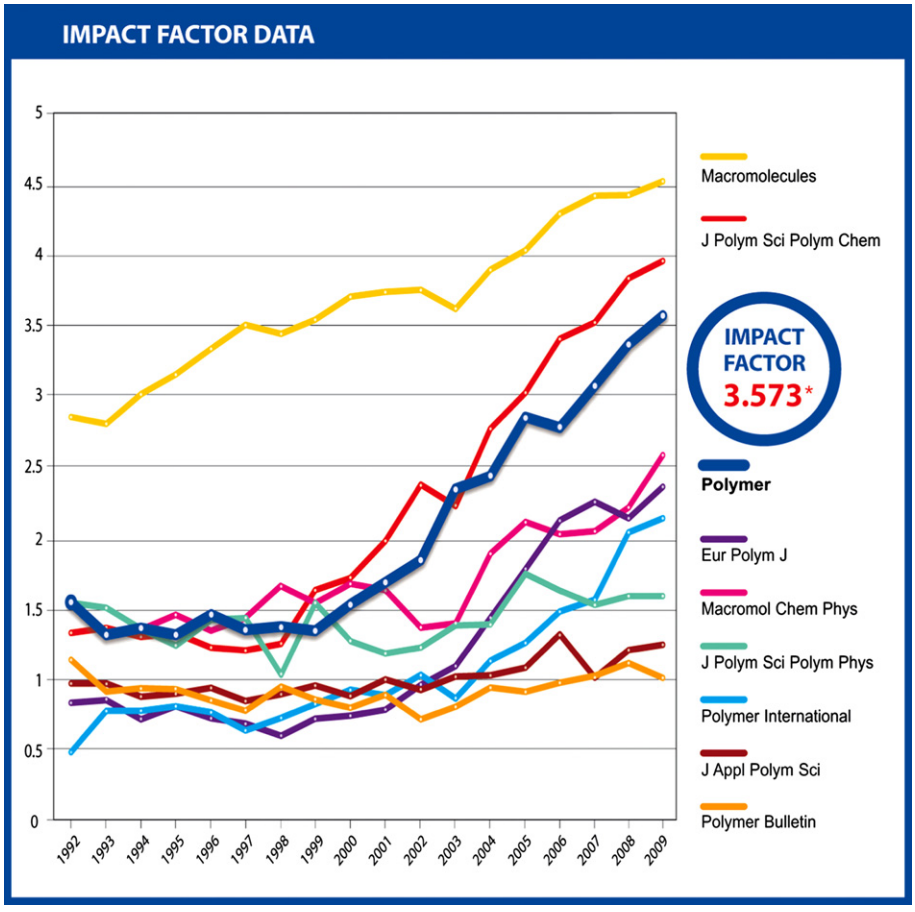

Fig. 1. Development of the impact factor of *Polymer* and other broad polymer journals publishing primarily regular papers. Journals publishing primarily reviews and/or rapid communications are not included since they show a very different citation pattern to regular journals.

[1] ©Journal Citation Reports, Thomson Reuters, 2010.

0032-3861/$ – see front matter
doi:10.1016/j.polymer.2010.11.043

During 2010 *Polymer* was very proud to be the sponsor of the following awards:

- The John H. Dillon Medal given by the American Physical Society and its Polymer Physics Division. The 2010 winner was Yueh-Lin Loo (Fig. 2).

Fig. 2. The 2010 John H. Dillon Medal Recipient Yueh-Lin Loo (Princeton University) receives her medal and certificate from the APS President Curtis Callan and the Elsevier Publisher Karien van Wetering.

- The newly established (in 2006) Feng Xinde Polymer Prize for Best Chinese Paper published in *Polymer*. The winners of the 4th Feng Xinde Polymer Prize for the Best Chinese Paper published in *Polymer* during 2009 were Yong-Quan Dong, Bo-Tao Dong, Fu-Sheng Du, Jian-Qiang Meng and Zi-Chen Li for their paper *An all ATRP route to PMMA–PEO–PS and PMAA–PEO–PS miktoarm ABC star terpolymer* published in *Polymer, vol. 50, 125-132 (2009)* (Fig. 3).

Fig. 3. Charles C. Han (Asian Editor for China for *Polymer*), Stephen Z.D. Cheng (Senior Editor of *Polymer*) and Erqiang Chen (Associate Asian Editor for China for *Polymer*) with the winner (Zi-Chen Li) and nominees for the 4th Feng Xinde Polymer Prize for Best Chinese Paper published in *Polymer* during 2009. The ceremony took place during the 9th International Symposium on Polymer Physics in Jinan, China. From left to right: student on behalf of Xiaogong Wang, student on behalf of Feng-Chih Chang, Zhen Tong, Wenbing Hu, Zi-Chen Li (the winner), associate on behalf of Lijia An, student on behalf of Yanhou Geng, student on behalf of Yanchun Han, Jiandong Ding, Erqiang Chen, Charles C. Han and Stephen Z.D. Cheng.

In 2010 *Polymer* announced its first ever Virtual Special Issue on Nanocomposites, an area of particular strength of the journal. We were proud to be able to dedicate the Virtual Special Issue to Professor Donald R. Paul on the occasion of his 70th birthday. Don is both the most prolific and most cited author in the 50-year history of the journal and has been publishing consistently some of his best work in *Polymer* through the years. More information about the special issue can be found in the Editorial [1] and Tribute [2] published in issue 22 of volume 51 (2010) of *Polymer* (Fig. 4).

Fig. 4. Donald R. Paul, the most prolific and the most cited author for the first 50 years of the existence of *Polymer*, to whom the first ever Virtual Special Issue of the journal was dedicated.

The full text of all 90 + Feature Articles ever published in *Polymer* is freely available through the dedicated 50th anniversary website (www.polymer50.com). I would encourage you to visit the website and get a feeling for which authors, papers and topics contributed most to the journal during its lifetime as well as in recent years.

I would like to announce the retirement of Professors Takeji Hashimoto and James E. Mark from the group of Editors of *Polymer*.

Takeji Hashimoto has been involved with the journal for almost two decades: first as Associate Editor for Polymer Communications from Asia, then as Polymer Physics Editor for Asia (until June 2004) and since then he has served two terms as Senior Editor of *Polymer*. As one of the world's top polymer physicists, Taki has applied consistently his extremely high standards to his editorial work for *Polymer* and has been a source of useful advice.

Jim Mark joined *Polymer* after the incorporation of the journal *Computational and Theoretical Polymer Science* (of which he was the founding Editor) into *Polymer* in January 2002. During the last eight years Jim has been responsible for the same topic within *Polymer* and has proved to be efficient and resourceful Editor, contributing many ideas about the improvement of the journal.

Both Taki and Jim have made a significant contribution to *Polymer* and I would like to express, on behalf of Elsevier and the other Editors, our great appreciation and good wishes for their retirement. We are very pleased that both of them will continue their association with the journal, as members of the Editorial Advisory Board.

Following the great success of the Symposium that we organised in 2009 in Mainz to celebrate the 50th anniversary of *Polymer*, we are organising a Second International Symposium Frontiers in Polymer Science from 29 to 31 May 2011 in Lyon, France. The meeting will follow the same pattern as in Mainz. More information is available on www.frontiersinpolymerscience.com.

I look forward to seeing many of you in end May 2011 in Lyon!

Rumen Duhlev
Publisher
Elsevier, Oxford, UK
Emil address: r.duhlev@elsevier.com

Available online 17 December 2010

References

[1] Krausch G, Han CC, Cheng SZD. Virtual special issue on nanocomposites dedicated to Donald R. Paul. Polymer 2010;51:5003–4.
[2] Freeman Benny D. Dedication of the virtual special issue of *Polymer* on nanocomposites in celebration of the 70th birthday of Professor Donald R. Paul. Polymer 2010;51:5005–6.

Polymer 52 (2011) 5–25

Contents lists available at ScienceDirect

Polymer

journal homepage: www.elsevier.com/locate/polymer

Feature Article

Graphene-based polymer nanocomposites

Jeffrey R. Potts [a], Daniel R. Dreyer [b], Christopher W. Bielawski [b,*], Rodney S. Ruoff [a,**]

[a] Department of Mechanical Engineering and the Texas Materials Institute, The University of Texas at Austin, 204 E. Dean Keeton St., Austin, TX 78712, USA
[b] Department of Chemistry and Biochemistry, The University of Texas at Austin, One University Station A5300, Austin, TX 78712, USA

ARTICLE INFO

Article history:
Received 15 September 2010
Received in revised form
22 November 2010
Accepted 24 November 2010
Available online 2 December 2010

Keywords:
Graphene
Polymer nanocomposites
Nanotechnology

ABSTRACT

Graphene-based materials are single- or few-layer platelets that can be produced in bulk quantities by chemical methods. Herein, we present a survey of the literature on polymer nanocomposites with graphene-based fillers including recent work using graphite nanoplatelet fillers. A variety of routes used to produce graphene-based materials are reviewed, along with methods for dispersing these materials in various polymer matrices. We also review the rheological, electrical, mechanical, thermal, and barrier properties of these composites, and how each of these composite properties is dependent upon the intrinsic properties of graphene-based materials and their state of dispersion in the matrix. An overview of potential applications for these composites and current challenges in the field are provided for perspective and to potentially guide future progress on the development of these promising materials.

1. Introduction

Graphene, a monolayer of sp^2-hybridized carbon atoms arranged in a two-dimensional lattice, has attracted tremendous attention in recent years owing to its exceptional thermal, mechanical, and electrical properties [1–3]. One of the most promising applications of this material is in polymer nanocomposites, polymer matrix composites which incorporate nanoscale filler materials. Nanocomposites with exfoliated layered silicate fillers have been investigated as early as 1950 [4], but significant academic and industrial interest in nanocomposites came nearly forty years later following a report from researchers at Toyota Motor Corporation that demonstrated large mechanical property enhancement using montmorillonite as filler in a Nylon-6 matrix [5]. Polymer nanocomposites show substantial property enhancements at much lower loadings than polymer composites with conventional micron-scale fillers (such as glass or carbon fibers), which ultimately results in lower component weight and can simplify processing [6]; moreover, the multifunctional property enhancements made possible with nanocomposites may create new applications of polymers [7].

On account of the recent emergence of using graphite oxide (GO) to prepare graphene-based materials for composites and other applications [8], this review will focus primarily on polymer nanocomposites utilizing GO-derived materials as fillers. Emphasis will be directed toward structure–property relationships as well as trends in property enhancements of these composites, and comparisons to other nanofillers will be made where appropriate. Some highlights from the literature on polymer composites with what have been referred to as graphite nanoplatelet (GNP) fillers, typically derived from graphite intercalation compounds (GICs), will also be presented and used to provide additional context. Although a review on GO-derived polymer nanocomposites has recently appeared [9], our review considers work with GNP fillers, and provides a historical perspective with more emphasis on preparative methods and processing.

2. Properties and production of graphene-based materials for composite filler

2.1. Overview and history of graphene-based materials

Graphene has a rich history which spans over forty years of experimental work [10]. 'Pristine' graphene (a single, purely sp^2-hybridized carbon layer free of heteroatomic defects) has been produced by several routes [1,11], including growth by chemical vapor deposition (both of discrete monolayers onto a substrate and agglomerated powders), micro-mechanical exfoliation of graphite, and growth on crystalline silicon carbide. While these approaches can yield a largely defect-free material with exceptional physical properties, current techniques of making powdered samples of graphene do not yield large enough quantities for use as composite filler [12].

* Corresponding author. Tel.: +1 512 232 3839; fax: +1 512 471 5884.
** Corresponding author. Tel.: +1 512 471 7681; fax: +1 512 471 4691.
E-mail addresses: bielawski@cm.utexas.edu (C.W. Bielawski), r.ruoff@mail.utexas.edu (R.S. Ruoff).

0032-3861/$ – see front matter © 2010 Elsevier Ltd. All rights reserved.
doi:10.1016/j.polymer.2010.11.042

Scalable approaches to GNPs and graphene-based materials (few-layer platelets or monolayer carbon sheets with heteroatoms and topological defects) primarily utilize GICs or GO as the precursor material, respectively. GO and GICs have been investigated as far back as the 1840s [13,14]. In the 1960s, Boehm and co-workers reported the reduction of dispersions of GO using a variety of chemical reductants [15,16], as well as thermal expansion and reduction [17], producing thin, lamellar carbon containing only small amounts of hydrogen and oxygen. By using transmission electron microscopy (TEM), the carbon material produced by chemical reduction was found to consist of "single carbon layers" [15]. The procedures currently used to produce these graphene-like materials have changed little since this early work [18,19]. Techniques for the exfoliation of GICs have also been developed, although most of these approaches do not yield single-layer sheets but rather platelets with thicknesses typically above approximately 5 nm. Liquid-phase exfoliation of graphite and chemical synthesis of graphene from polycyclic aromatic hydrocarbon precursors may also eventually provide scalable alternative routes for production of graphene [19], as could the further development of gas phase CVD methods [12]. Recently, graphene nanoribbons, produced by "unzipping" of multiwalled carbon nanotubes, have been investigated as composite filler [20].

A variety of uses have been envisioned or demonstrated for GNPs and graphene-based materials, and their use as a composite filler has attracted considerable interest [1]. While polymer nanocomposites incorporating GNP fillers continue to be a significant research focus, recent work has largely focused on use of graphene-based filler materials derived from GO. As will be described in the following sections, GO-derived fillers can exhibit high electrical conductivities (on the order of thousands of S/m) [8], high moduli (reported values ranging from 208 GPa [21] to over 650 GPa [22]), and can be easily functionalized to tailor their compatibility with the host polymer. The reported values of stiffness and electrical conductivity of GO-derived filler materials can be higher than those reported for nanoclays [23], but generally lower than those reported for single-walled carbon nanotubes (SWNTs) [24]. However, the intrinsic mechanical properties and electrical and thermal conductivities of SWNTs may be comparable to those of pristine graphene [24,25]. Moreover, the two-dimensional platelet geometry of graphene and graphene-based materials may offer certain property improvements that SWNTs cannot provide when dispersed in a polymer composite, such as improved gas permeation resistance of the composite [26].

2.2. Exfoliation of graphite

Most exfoliated graphite fillers are derived from GICs, which are compounds of graphite with atoms or molecules (such as alkali metals or mineral acids) intercalated between the carbon layers [27]. The intercalation of graphite increases its interlayer spacing, weakening the interlayer interactions and facilitating the exfoliation of the GIC by mechanical or thermal methods [28]. Varying structural arrangements of the intercalant are possible, such as alternating layers of graphene and intercalant (referred to as first-stage GICs), as well as multiple (two to five) adjacent graphene layers between intercalant layers (higher-stage GICs) [27]. It is the former arrangement, however, which is preferred for the complete exfoliation of these materials into monolayer platelets [29].

Intercalation of graphite by a mixture of sulfuric and nitric acid produces a higher-stage GIC that can be exfoliated by rapid heating or microwave treatment of the dried down powder, producing a material commonly referred to as expanded graphite (EG) [30]. EG retains a layered structure but has slightly increased interlayer spacing relative to graphite, consisting of thin platelets (30–80 nm) which are loosely stacked [30]. Notably, an acid treatment may also oxidize the platelets, albeit to a far lesser degree than GO [31]. EG itself has been investigated as a composite filler [32–34], although its effectiveness in enhancing properties compared with GO-derived fillers is limited by its layered structure and relatively low specific surface area (generally less than 40 m^2/g [35]). To produce a higher surface area material, EG can be further exfoliated by various techniques to yield GNPs down to 5 nm thickness [28,30].

The thickness and lateral dimensions of GNPs vary widely depending on the production method used, and several approaches have been reported. Sonication of EG in appropriate media can yield platelets with thicknesses of roughly 10 nm and with lateral dimensions as large as 15 μm [36]. Smaller platelet thicknesses have been reported by re-intercalation of EG or co-intercalation of GICs with organic molecules prior to exfoliation. For instance, mixing potassium with EG yielded a stoichiometric first-stage GIC (KC_8), which was reported to be exfoliated into GNPs with thicknesses as low as 2 nm upon reaction with water or alcohols, along with sonication [29]. It has also been reported that sulfuric acid-intercalated EG can be co-intercalated with tetrabutylammonium hydroxide (among many other molecules [37]). By sonicating this GIC in *N*,*N*-dimethylformamide (DMF) in the presence of a surfactant (a poly(ethylene glycol)-modified phospholipid), monolayer graphene-like sheets were obtained [31].

The isolation of pristine graphene by micro-mechanical exfoliation [38] has helped to motivate research towards a scalable procedure for liquid-phase exfoliation of graphite to afford high-quality graphene without the use of intercalants; as a result, several different approaches have now been reported [39–42]. Sonication of graphite flakes in water, for example, was reported to yield a mixture of monolayer and multi-layer graphene which was largely defect-free, but this approach required the use of surfactants which may negatively affect the electrical conductivity [41]. Direct exfoliation of graphite into solvents such as propylene carbonate (PC) or *N*-methylpyrrolidone (NMP) [40], and electrochemical exfoliation of graphite in ionic liquids [42] may eventually offer viable alternatives for production of solution-based graphene, although graphene made by these approaches has yet to be studied as composite filler.

2.3. Production and properties of GO

GO is generally produced by the treatment of graphite using strong mineral acids and oxidizing agents, typically via treatment with $KMnO_4$ and H_2SO_4, as in the Hummers method or its modified derivatives, or $KClO_3$ (or $NaClO_3$) and HNO_3 as in the Staudenmaier or Brodie methods [8]. These reactions achieve similar levels of oxidation (C:O ratios of approximately 2:1) [8] which ultimately disrupts the delocalized electronic structure of graphite and imparts a variety of oxygen-based chemical functionalities to the surface. While the precise structure of GO remains a matter of debate [8], it is thought that hydroxyl and epoxy groups are present in highest concentration on the basal plane, with carboxylic acid groups around the periphery of the sheets as shown in Fig. 1. GO has an expanded interlayer spacing relative to graphite which depends on humidity (for instance, 0.6 nm when subjected to high vacuum [43] to roughly 0.8 nm at 45% relative humidity [44]) due to intercalation of water molecules [43]. GO can be exfoliated using a variety of methods (most commonly by thermal shocking [45] or chemical reduction in appropriate media [11,46]), yielding a material reported to be structurally similar to that of pristine graphene on a local scale; these techniques will be discussed in more detail below.

2.4. Exfoliation of GO

With a few exceptions, production of well-dispersed polymer nanocomposites with GO-derived fillers hinges largely on the

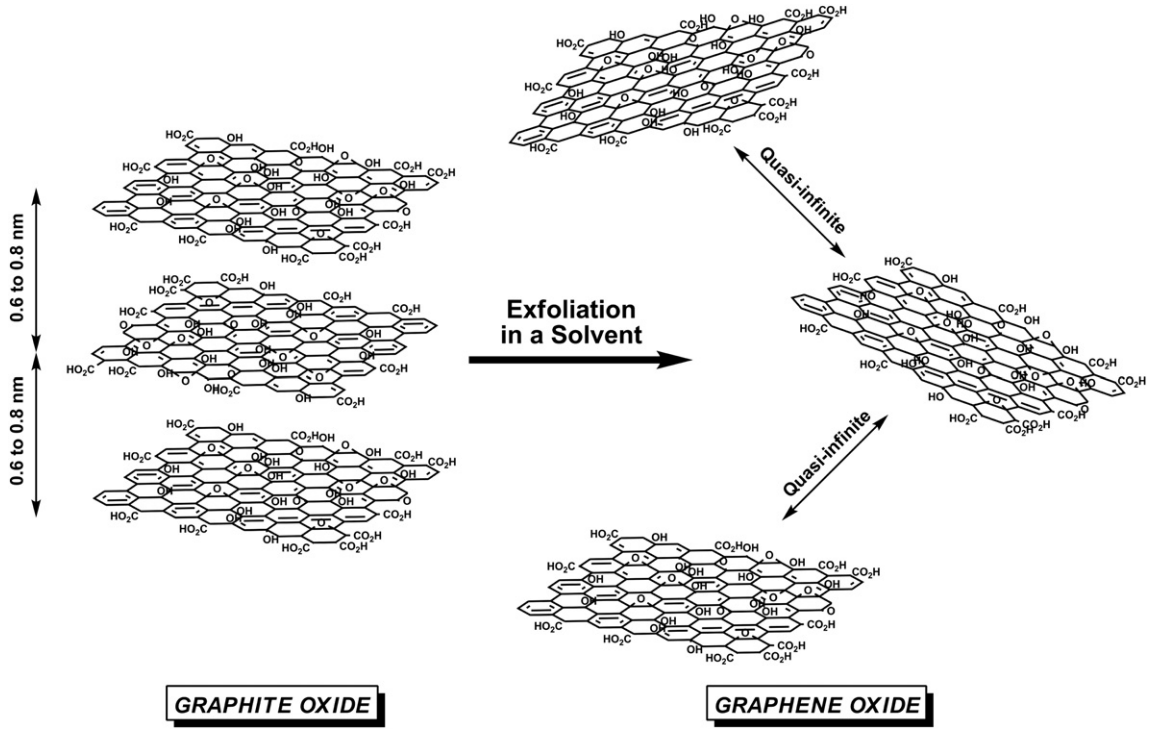

Fig. 1. Schematic illustrating the chemical structure of graphite oxide (GO) and the structural difference between layered GO and exfoliated graphene oxide (G–O) platelets.

exfoliation of GO prior to incorporation into a polymer matrix. Solvent-based exfoliation and thermal exfoliation techniques have emerged as two preferred routes for this step. In the former route, the hydrophilic nature and increased interlayer spacing of GO (relative to graphite) facilitates direct exfoliation into water assisted by mechanical exfoliation, such as ultrasonication and/or stirring, at concentrations up to 3 mg/ml, forming colloidal suspensions of 'graphene oxide' (that we define with the acronym 'G–O') [11]. Fig. 1 illustrates the structural difference between layered GO and exfoliated G–O platelets. Zeta potential measurements indicate that these suspensions are electrostatically stabilized by negative charges, possibly from the carboxylate groups that are believed to decorate the periphery of the lamellae [11]. Suspensions produced by sonication of GO are found, by atomic force microscopy (AFM) (when deposited onto various substrates), to consist primarily of single-layer G–O platelets [47,48] (Fig. 2); however, the sonication treatment fragments the platelets, reducing their lateral dimensions by over an order of magnitude down to a few hundred nanometers [8,49]. Mechanical stirring is an alternative route to produce single-layer G–O platelets of much larger lateral dimensions and aspect ratios when compared with G–O platelets produced by sonication. However, it has been reported that magnetic stirring exfoliates GO very slowly and in low yield [8]. GO can also be exfoliated to G–O platelets of similar aspect ratio to sonicated platelets (at lower concentrations below 0.5 mg/ml) via sonication in polar organic solvents such as DMF, PC, and NMP [50,51].

GO can also be exfoliated and reduced by rapid heating [45], yielding thermally expanded graphite oxide, or TEGO (also referred to commonly in the literature as functionalized graphene sheets, or FGS) [52,53]. In this exfoliation method, the dry powder is typically charged into a quartz tube (or other similar vessel) and subjected to thermal shock (i.e., exposure to a sudden jump in temperature), by heating to temperatures such as 400 °C [45] or higher [52] at high rates such as 2000 °C/min [52]. The rapid heating is believed to cause various small molecule species (e.g., CO, CO_2, water) to evolve and internal pressure to increase, forcing the sheets apart and yielding a dry, high-surface area material with a low bulk density (Fig. 2) [53]. Measurements of the surface area of TEGO by the Brunauer, Emmett, and Teller (BET) method [54] (which measures surface area based on isothermal gas adsorption/desorption) were found to range from 700 to 1500 m^2/g [52], compared with a theoretical limit of approximately 2600 m^2/g for graphene [55]. Also, GO can be exfoliated (and reduced) by microwave radiation, yielding a related material referred to as microwave-expanded graphite oxide, or MEGO [56]. Importantly, while G–O platelets are likely to maintain the chemical structure of GO, TEGO and MEGO are reduced (reported C:O ratios of 10:1 [52] and 3:1 [56], respectively), and are electrically conductive (reported values of roughly 2000 S/m [52] for TEGO [52] and 270 S/m for MEGO [56]). TEGO was reported to contain residual oxygen (in the form of carbonyl and ether groups) and adopted a crumpled accordion-like morphology, with lateral dimensions of a few hundred nanometers, similar to G–O platelets exfoliated by sonication [52,57].

2.5. Chemical reduction and functionalization of G–O platelets

The physical properties of G–O platelets are considerably different from that of graphene. G–O platelets can be chemically reduced to generate a material that resembles pristine graphene, using reducing agents such as hydrazine monohydrate or sodium borohydride [11]. Chemically reduced G–O platelets (henceforth, we will use the acronym RG–O) can exhibit C:O ratios of over 10:1 [8] and retain some of the functionality originally present on the G–O platelets [11,58]. Recently, it was reported that GO or G–O platelets may be used to catalyze the oxidation of a variety of benzylic and aliphatic alcohols [59], as well as various carbon–carbon bond forming reactions [60], while reducing GO as well as G–O platelets in the process. The products recovered after reduction by benzyl alcohol were reported to exhibit high C:O ratios (up to 29.9:1) and high electrical conductivities (up to 4600 S/m) [61]. Other reduction

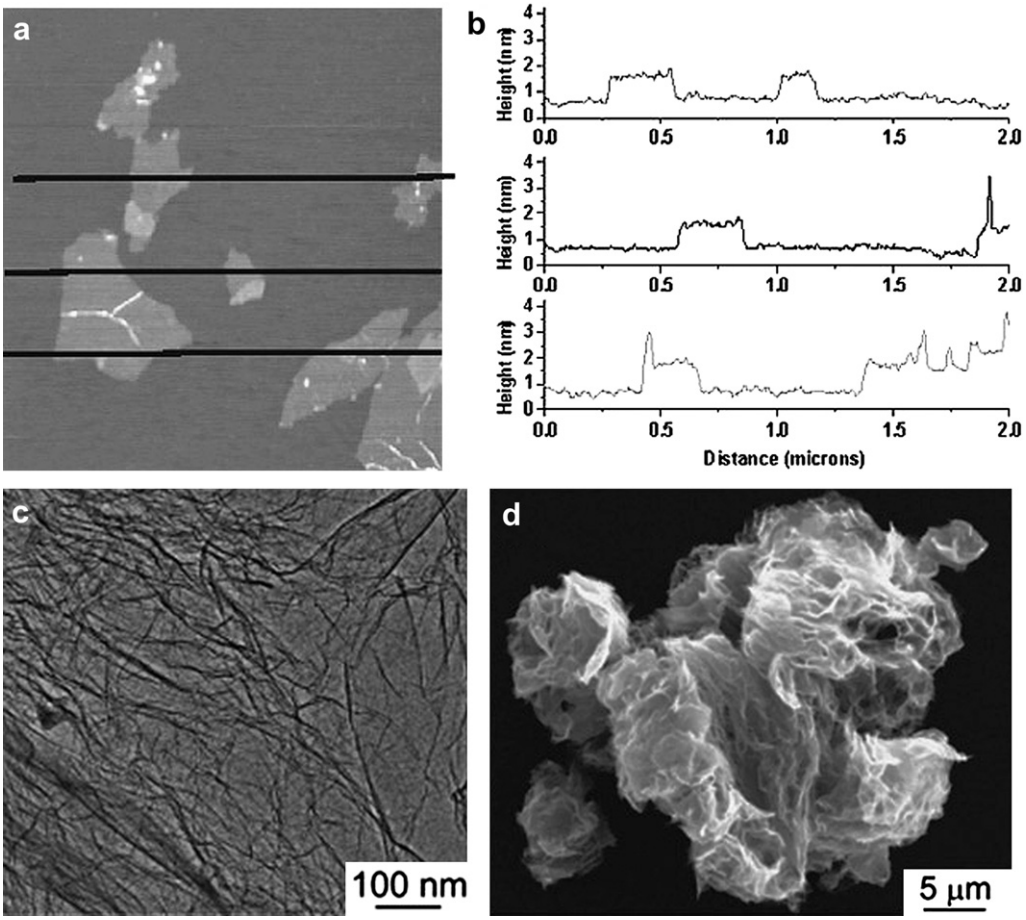

Fig. 2. (a, b) Non-contact AFM scans of graphene oxide (G–O) deposited on mica reveal the presence of single layers obtained from exfoliation in water via sonication. The wrinkled structure of thermally expanded GO (TEGO) is illustrated in this transmission electron micrograph (c) and scanning electron micrograph (d) ((a) and (b) were adapted from Ref. [64], (c) and (d) were adapted from Ref. [53]).

methods using environmentally friendly reductants, such as tryptophan and ascorbic acid, have been reported [62,63].

This reduction process can cause agglomeration of the platelets [64] (reducing accessible surface area) unless prior steps are taken to stabilize the suspension. Adjusting the pH of the suspension to increase the (negative) zeta potential of the sheets or the adsorption of polymers on the platelet surface are both effective routes to stabilizing aqueous suspensions of RG–O platelets [65,66]. Stable suspensions of RG–O platelets in organic solvents have also been achieved. One approach to these suspensions is progressive dilution of an aqueous suspension of G–O platelets with an organic solvent—with one possible route involving hydrazine in DMF:water (9:1 v/v) and further dilution in DMF to yield a stable suspension of RG–O platelets in 99% DMF [46]. Two-phase extraction of RG–O platelets from water into various organic solvents may be facilitated by end-functional polymers dissolved in the organic phase, which adsorb onto the platelets and help disperse the platelets in the solvent [67]. Freeze drying of aqueous RG–O dispersions has been reported to facilitate the re-dispersion of the RG–O platelets into organic solvents such as DMF [68]. Alternatively, one may avoid the use of water altogether, as stable dispersions of RG–O platelets in DMF and NMP have also been reported using dimethylhydrazine as the reductant [69]. For composites processed in solution, chemical reduction of G–O platelets in the polymer solution (provided the polymer is stable to the reaction conditions) may prevent the precipitation of the RG–O platelets from the solvent, as the polymer can maintain the dispersion of RG–O platelets [55].

While the most commonly employed reaction of G–O is its reduction to yield electrically conductive RG–O, a variety of other chemical transformations can be carried out at its oxygen-based functional groups, which are covered elsewhere [8]. Both covalent and non-covalent functionalization of G–O platelets has been reported to generate stable dispersions of chemically modified graphene (CMG) platelets in organic solvents and also to enhance their compatibility with various polymer matrices. Among others, reactions using amines [70–72] and isocyanates [73] have been reported for small molecule functionalization of G–O platelets because of the facility of the reactions, and the ability to react in multiple ways (e.g., amidations, nucleophilic epoxide ring-openings, carbamate formation, etc.) However, covalent functionalization of G–O platelets could adversely affect the electrical conductivity of the platelets as these functionalizations disrupt (or retain the disruption already present in) the sp^2-hybridized network required for good electron/hole conduction [74]. Non-covalent functionalization of RG–O platelets via, for example, π–π stacking could minimize disruption of the conductive, conjugated structure [75,76].

3. Preparation of graphene-based polymer nanocomposites

3.1. Overview and historical perspective

The earliest reports on polymer composites with exfoliated graphite fillers emerged from studies on the intercalation chemistry of GICs. In 1958, it was discovered that alkali metal-GICs could initiate the polymerization of ethylene [77], and subsequently, alkali

metal-GICs were found to initiate polymerization of other monomers such as styrene, methyl methacrylate, and isoprene [78,79]. Early reports focused on the characterization of the polymer produced from these reactions; it was decades later before the observation was reported that alkali metal-GIC-initiated polymerization could exfoliate the layers of the graphite host [37,80]. Building on his own work on the exfoliation of graphite, Bunnell proposed the production of polymer nanocomposites incorporating "as thin as possible" GNPs (derived from GICs exfoliated either by shear grinding or thermal treatment) as fillers in a 1991 patent [81], where he suggested that with "10 vol% inclusion of graphite flakes in…polyethylene or polypropylene, the stiffness of the finished product will approach that of aluminum." However, it was not until 2000 that a detailed study of the morphology and properties of an exfoliated graphite nanocomposite was published, which reported dispersed platelets of approximately 10 nm thickness, produced by exfoliation of EG due to the *in situ* polymerization of caprolactam [82]. This and subsequent studies have reported tremendous property improvements versus conventional polymer composites based on micron-scale fillers such as untreated flake graphite or carbon black (CB) [83–87]. For instance, much lower electrical percolation thresholds have been reported with GNP fillers versus CB: 8 wt% for CB/PMMA [88] and 9 wt% for CB/Nylon [89], compared with 1 wt% for GNP/PMMA [86] and 1.8 wt% for GNP/Nylon [82].

As with GICs, GO can be intercalated by various monomers, and subsequent polymerization has been reported to delaminate the layers [90]; however, it has also been reported that polymers can be directly intercalated into GO [91–93]. Hydrazine and electrochemical reduction of layered GO/polyelectrolyte films was used to generate electrically conductive polymer composites in 1996 [94], but it was nearly ten years later that an electrically conductive poly (styrene) composite was prepared by using well-dispersed, monolayer CMG fillers [55], stimulating an intense research effort on polymer composites with dispersed CMG platelets (and other GO-derived materials such as TEGO) as fillers.

In recent years, a variety of processing routes have been reported for dispersing both GNP and GO-derived fillers into polymer matrices. Many of these procedures are similar to those used for other nanocomposite systems [95], although some of these techniques have been applied uniquely to graphene-based composites. Among other factors, the nature of the bonding interaction at the interface between the filler and matrix has significant implications for the final composite properties, and most dispersion methods produce composites that are non-covalent assemblies where the polymer matrix and the filler interact through relatively weak dispersive forces. However, there is a growing research focus on introducing covalent linkages between graphene-based filler and the supporting polymer to promote stronger interfacial bonding, as will be illustrated in the following sections.

3.2. Non-covalent dispersion methods: solution and melt mixing

Solution-based methods generally involve the mixing of colloidal suspensions of G–O platelets or other graphene-based materials with the desired polymer, either itself already in solution or by dissolving in the polymer in the suspension of G–O platelets, by simple stirring or shear mixing. The resulting suspension can then be precipitated using a non-solvent for the polymer, causing the polymer chains to encapsulate the filler upon precipitation. The precipitated composite can then be extracted, dried, and further processed for testing and application. Alternatively, the suspension can be directly cast into a mold and the solvent removed. However, this latter technique can potentially lead to aggregation of the filler in the composite, which may be detrimental to composite properties [95].

Solution mixing has been widely reported in the literature, as CMG platelets can often be processed in either water or organic solvents. This approach has been used for incorporating GO-derived fillers into a variety of polymers, including: PS [55,96], polycarbonate [97], polyacrylamide [98], polyimides [99], and poly (methyl methacrylate) (PMMA) [7,100]. The facile production of aqueous G–O platelet suspensions via sonication makes this technique particularly appealing for water-soluble polymers such as poly(vinyl alcohol) (PVA) [100–105] and poly(allylamine), composites of which can be produced via simple filtration [104,106]. In addition, vacuum filtration of G–O/PVA and G–O/PMMA solutions has been used to make composite films across a broad range of loadings [107], which have a layered morphology similar to that of 'graphene oxide paper' [44].

While some restacking of the platelets may be possible, for solution mixing methods the dispersion of platelets in the composite is largely governed by the level of exfoliation of the platelets achieved prior to, or during, mixing. Thus, solution mixing offers a potentially simple route to dispersing single-layer CMG platelets into a polymer matrix. As previously mentioned, small molecule functionalization and grafting-to/from methods have been reported to achieve stable CMG platelet suspensions of highly exfoliated platelets prior to mixing with the polymer host. Lyophilization methods [68], phase transfer techniques [67,108], and surfactants [109] have all been employed to facilitate solution mixing of graphene-based composites. However, the use of surfactants may affect composite properties; for instance, surfactants have been reported to increase the matrix–filler interfacial thermal resistance in SWNT/polymer composites, attenuating the thermal conductivity enhancement relative to SWNTs that were processed without surfactants [110].

In melt mixing, a polymer melt and filler (in a dried powder form) are mixed under high shear conditions. Relative to solution mixing, melt mixing is often considered more economical (because no solvent is used) and is more compatible with many current industrial practices [111]; however, studies suggest that, to date, such methods do not provide the same level of dispersion of the filler as solvent mixing or *in situ* polymerization methods [26]. Notably, no means of dispersing single- or few-layer GO-derived fillers via melt mixing without prior exfoliation have been reported akin to layered silicate fillers (although, with a few exceptions, direct exfoliation of layered silicates in melt mixing requires prior treatment with a surfactant to increase miscibility with the polymer host [112]). Several studies report melt mixing using TEGO [113] and GNPs [114–117] as filler, where these materials could be fed directly into an extruder and dispersed into a polymer matrix without the use of any solvents or surfactants. Notably, the very low bulk density (approximately 0.004 g/cm^3 based on a volumetric expansion of 500 [52]) of TEGO makes handling of the dry powders difficult and poses a processing challenge (such as for feeding into processing equipment such as a melt extruder), and in one study a solution mixing process was used to disperse the TEGO in the polymer prior to compounding in order to circumvent this issue [118]. In a different approach to 'premix' the polymer and filler prior to mixing, GNPs were sonicated in a non-solvent, such that polymer particles were uniformly coated with GNPs prior to melt mixing, which was reported to lower the electrical percolation threshold of a GNP/polypropylene composite [119]. Notably, for composites incorporating G–O platelets as filler, melt processing and molding operations may cause substantial reduction of the platelets due to their thermal instability [120].

3.3. Non-covalent in situ polymerization

In situ polymerization methods for production of polymer composites generally involve mixing of filler in neat monomer

(or multiple monomers), or a solution of monomer, followed by polymerization in the presence of the dispersed filler. These efforts are often followed with precipitation/extraction or solution casting to generate samples for testing. Many reports using *in situ* polymerization methods have produced composites with covalent linkages between the matrix and filler, and many examples will be given in the following sections. However, *in situ* polymerization has also been used to produce non-covalent composites of a variety of polymers, such as poly(ethylene) [121], PMMA [122], and poly (pyrrole) [123,124].

Unlike what has been reported for solution mixing methods, a high level of dispersion of graphene-based filler has been achieved via *in situ* polymerization without a prior exfoliation step. In some reports, monomer is intercalated between the layers of graphite or GO, followed by polymerization to separate the layers. This technique, sometimes referred to as intercalation polymerization, has been widely investigated for nanoclay/polymer composites [112], and has been also applied to GNP and GO-derived polymer composites. For instance, *in situ* polymerization methods have been used to exfoliate GICs and EG to generate dispersions of GNPs in the matrix. Graphite can be intercalated by an alkali metal and a monomer (e.g., isoprene or styrene), followed by polymerization initiated by the negatively charged graphene sheets [37]. However, it is not known if the polymerization takes place on the surface of the GIC or between layers [37]. In any case, *in situ* polymerization in the presence of GICs has been reported to exfoliate the GIC into thin platelets [80], and this approach has also been reported to exfoliate EG [82,84,85], although exfoliation to afford isolated monolayers has yet to be achieved with this approach. In a recent study, metallocene-mediated polymerization of poly (ethylene) was conducted in the presence of dispersed GNPs, in an attempt to grow PE chains between the graphitic layers. Although the polymerization may have further exfoliated the GNPs, monolayer graphene platelets were not observed; TEM observations showed platelets down to 3.6 nm thickness (consistent with stacks of approximately 10 layers) with relatively low aspect ratios of about 30 dispersed in the PE matrix [121].

The larger interlayer spacing of GO (between about 0.6 and 0.8 nm depending on relative humidity) compared to graphite (0.34 nm) facilitates intercalation by both monomers and polymers [28]. Additionally, the polar functional groups of GO promote direct intercalation of hydrophilic molecules, with the interlayer spacing increasing with uptake of monomer or polymer (e.g., increasing up to 2.2 nm for the intercalation of PVA into GO) [93]. The interlayer spacing of vinyl acetate-intercalated GO was reported to decrease after polymerization [125], although the interlayer spacing still remains significantly higher than unmodified GO. *In situ* polymerization has been demonstrated for several GO composite systems, including poly(vinyl acetate) [125], and poly(aniline) (PANI) [90]. X-ray diffraction studies on these systems suggested an intercalated morphology where the individual graphene oxide sheets remain loosely stacked in the matrix with polymer intercalated between lamellae. However, the use of a macroinitiator to intercalate GO prior to *in situ* polymerization of methyl methacrylate was recently reported to improve the filler dispersion in a GO/PMMA composite. X-ray diffraction revealed an increased interlayer spacing of GO (from 0.64 nm to 0.8 nm) suggesting an intercalated morphology for GO/PMMA composites produced by conventional free radical polymerization. However, composites polymerized with the macroinitiator showed improved reinforcement and no diffraction peak from GO, suggesting a more exfoliated morphology [122].

3.4. Graphene-based composites with covalent bonds between matrix and filler

Given the relative sparseness of usable functionality on pure carbon materials, forming covalent linkages between the polymer matrix and such surfaces (when used as a composite filler) may be quite challenging. However, G–O platelets contain a surface rich in reactive functional groups, and a number of approaches for introducing covalent bonds between G–O platelets and polymers have been demonstrated. For instance, both grafting-from and grafting-to approaches have been used for the attachment of a broad range of polymers.

In one recent example of a grafting-from approach [126], atom transfer radical polymerization (ATRP) initiators were covalently attached via esterification with the alcohols present across the G–O platelet surface. Upon adding an ATRP-compatible monomer (e.g., styrene, butylacrylate, or methyl methacrylate) and a source of Cu^{I}, polymer brushes were grown in a controlled fashion from the surface (Fig. 3). The ester linkage between the polymer and the CMG platelet surface was then saponified using aqueous NaOH, allowing for characterization of the polymers independent of the carbon material. Similar studies using such ATRP-based methods have reported an increased scope of monomer reactivity [96,127], as well as the incorporation of these polymer-grafted CMG platelets

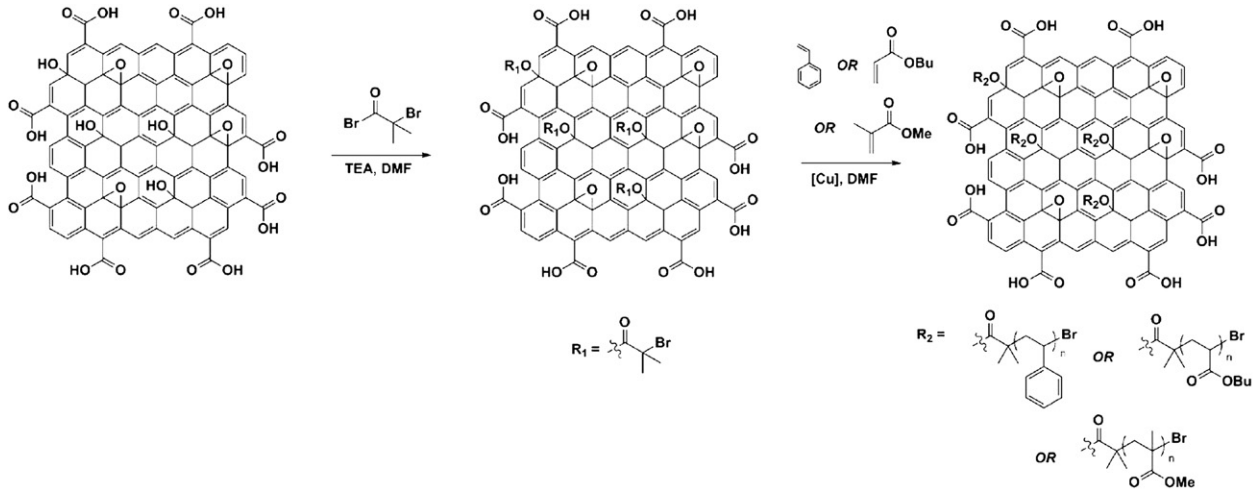

Fig. 3. Synthesis of surface-attached poly(styrene), poly(methyl methacrylate), or poly(butylacrylate) via ATRP following functionalization of G–O platelets with an ATRP initiator (α-bromoisobutyryl bromide) (adapted from Ref. [126]).

into a polymer matrix via solution mixing, reportedly leading to improvements in mechanical and thermal properties versus the neat matrix polymer [96,128,129]. Recent efforts have focused on correlation of thermal properties of these composites as a function of grafting density and polymer molecular weight [130].

These grafting-based approaches have also been used in conjunction with heterogeneous blending of polymer-functionalized G–O in matrices composed of conducting polymers [131], including poly(3-hexylthiophene) (P3HT) and a triphenylamine-based poly(azomethine) (see Fig. 4) [132,133]. Both polymers have been widely studied as conducting materials for use in photovoltaics and data storage devices, among other applications, and the incorporation of G–O platelets or other GO-derived materials into these devices may enhance the optoelectronic properties of the device, as well as enhance the device's mechanical and/or thermal properties. These two examples are good case studies for divergent pathways to polymer-functionalized G–O platelet composites: in the P3HT system, poly(*t*-butylacrylate) was grown via ATRP from the surface of G–O platelets (grafting-from, where a polymer is grown from a heterogeneous surface), and blended with pre-formed P3HT for the formation of organic electronic memory devices. Conversely, the poly(azomethine) was attached using the amino functional groups that were pendant to the end groups of the polymer (Fig. 4; grafting-to), possibly through amide formation with carboxylic acid groups present on the edges of G–O platelets. However, the presence of other reactive sites (e.g., epoxides) may make precise determination of the reactive site difficult [134]. Other reports of grafting-to approaches include reports of grafting of azide-terminated poly(styrene) (PS) chains to the surface of alkyne-functionalized G–O platelets via a Cu^{I}-catalyzed 1,3-dipolar cycloaddition in an example of click chemistry [135], and grafting of PVA to G–O platelets via carbodiimide-activated esterification [136]. The choice between using grafting-from or grafting-to methodologies will likely depend on the polymer being formed and which of the two approaches is more practical for the application under consideration. However, a grafting-to approach may lower the grafting density of chains to the platelet surface [137], which may in turn affect the dispersion of these polymer-grafted platelets if dispersed into a polymer matrix [138].

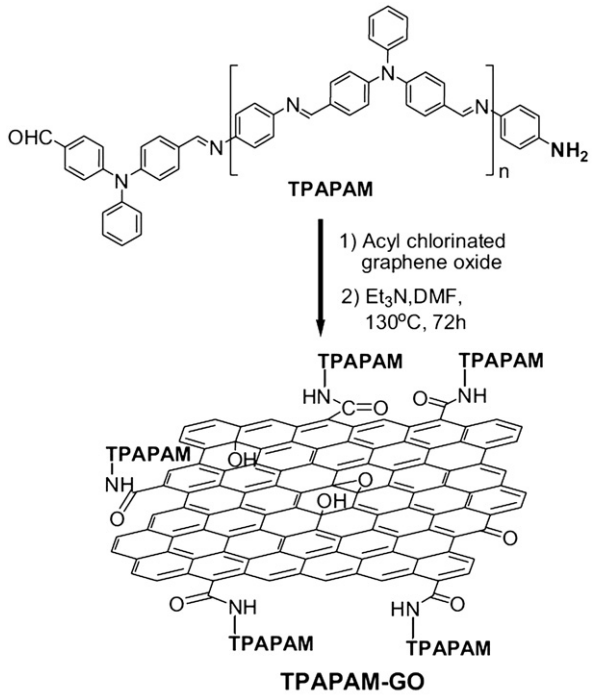

Fig. 4. Attachment of a triphenylamine-based poly(azomethine) (TPAPAM) to GO via amidation chemistry, embodying a grafting-to approach (adapted from Ref. [133]).

For certain polymers, covalent bonding between the matrix and G–O platelets may form during polymerization (on reaction with the functional groups of G–O) without the need for prior functionalization or controlled grafting methods. For an epoxy matrix composite, curing with an amine hardener may have resulted in the incorporation of G–O platelets directly into the crosslinked network [139], while for polyurethanes, TEGO was reported to function as a chain extender by reacting with the isocyanate groups of the monomer or prepolymer [26,140]. Ring-opening polymerization of caprolactam was reported to graft polyamide brushes to G–O platelets via condensation reactions between the amine-containing monomer and the carboxylic acid groups of the G–O platelets, though increased loadings of filler were found to lower the polymer molecular weight due to stoichiometric imbalance during polymerization [141].

G–O platelets have also been utilized as a Ziegler–Natta catalyst support for the heterogeneous *in situ* polymerization of propylene. Functionalization of G–O platelets with a Grignard reagent (BuMgCl) served to immobilize $TiCl_4$ on the G–O platelet surface (as evidenced by IR spectroscopy, X-ray photoelectron (XPS) spectroscopy, and energy-dispersive X-ray (EDX) spectroscopy). Subsequent initiation with $AlEt_3$ was reported to afford high molecular weight, isotactic poly(propylene) (Fig. 5). The resulting composites showed a homogeneous dispersion of few-layer CMG platelets, and exhibited moderate electrical conductivity (0.3 S/m at 4.9 wt%), with the authors noting that the G–O platelets were not intentionally reduced [142].

3.5. Other methods for composite preparation

In addition to those described above, several other methods have been reported for producing graphene-based composites. Although most of these procedures have been demonstrated on just one composite system, many could potentially find use as general approaches to composite fabrication. One such approach is the non-covalent grafting of well-defined polymers to RG–O platelets via π–π interactions. For instance, the attachment of pyrene-terminated poly(*N*-isopropylacrylamide) to RG–O was recently reported; the composite was stated to retain the thermoresponsive properties of the neat polymer [143]. This technique has since been extended to various other polymers [144], suggesting that non-covalent grafting of polymers to the surface of CMG platelets may provide a versatile approach to producing graphene-based composites. Moreover, such non-covalent composites may better preserve the conjugated structure of graphene-based materials as compared with covalent functionalization or grafting approaches, which may benefit composite properties such as electrical conductivity.

Variants of typical *in situ* polymerization and solution mixing methods may provide useful methods of dispersing graphene-based fillers in a polymer matrix. For instance, emulsion polymerizations can be carried out in aqueous suspensions of G–O platelets [145,146], suggesting a general approach for dispersion of CMG platelets with latex-based polymers [147]. As previously mentioned, lyophilization methods [68] or phase transfer techniques [67,108] may offer general approaches to dispersing RG–O platelets as filler in a polymer matrix. In one report, reduction of an aqueous suspension of G–O platelets with hydrazine resulted in the extraction of the hydrophobic RG–O platelets into an organic layer (containing the dissolved polymer) and formation of a homogeneously dispersed nanocomposite [108].

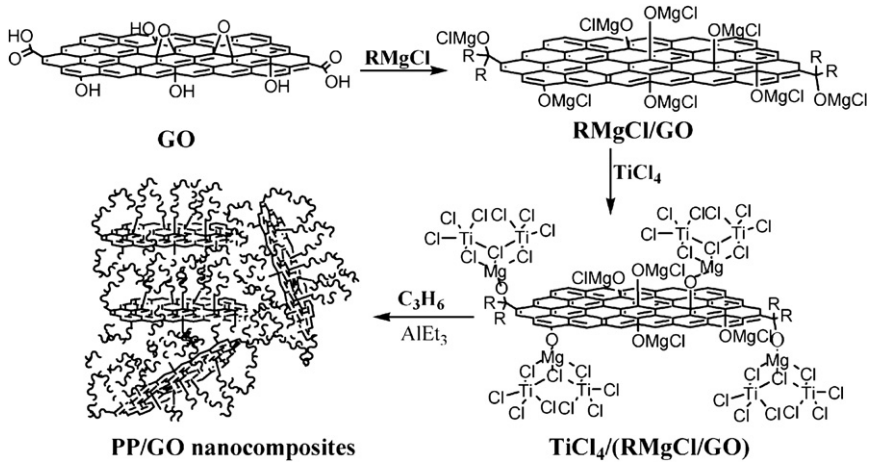

Fig. 5. Ziegler–Natta polymerization of propylene from the surface of G–O, which acts as a support for the growing polymer chains (adapted from Ref. [142]).

A variety of other methods for composite production have been reported. Attempts to exfoliate graphite directly via conventional melt mixing techniques have not been successful to date [148]. However, solid state shear pulverization, which uses a twin screw extruder to blend solid materials using shear, was reported to exfoliate and disperse unmodified graphite directly into polypropylene, yielding nanocomposites with platelets having thicknesses of approximately 10 nm or less [149]. Other production methods, such as layer-by-layer assembly of polymer composite films [150] and backfilling of G–O platelet aerogel structures (produced by freeze drying aqueous G–O suspensions) with polymer may provide means to produce nanocomposites with defined morphologies [151]. In one study, directional freeze drying of an aqueous G–O platelets/PVA platelets mixture was reported to yield nanocomposites with a three-dimensional macroporous structure and a surface area of approximately 37 m^2/g [152].

4. Morphology and crystallization behavior

As property enhancements correlate strongly with nanocomposite microstructure, effective characterization of morphology is important to establishing structure–property relationships for these materials. For instance, TEM of microtomed thin sections of the composite can provide direct observation of dispersed multilayer GNPs and graphene-based platelets; such thicker platelets typically show adequate contrast against the polymer matrix to be imaged without staining, whereas single-layer platelets may be difficult to directly observe by TEM [26]. Compared with TEM, wide-angle X-ray scattering (WAXS) can more rapidly provide insight into the state of dispersion over a larger volume of composite; however, since the scattering intensity varies with the concentration of the scattering feature, some morphological information may be missed [148].

Both graphite and GO, as the precursors to many graphene-based materials, have a layered structure as do certain silicates (e.g., montmorillonite) which have been widely investigated as composite fillers [111]. Indeed, when dispersed into a polymer matrix, both nanoclays and graphene-based platelets exhibit similar states of dispersion depending upon factors such as the processing technique and the affinity between the phases. Moreover, nanoclay fillers often exhibit comparable aspect ratios to graphene-based fillers (up to 1000) [112], although fillers such as TEGO often appear more crumpled on a local scale relative to nanoclays [7]. Earlier studies on nanoclay-based composites have suggested the existence of three general states of platelet dispersion on short length scales: stacked, intercalated, or exfoliated, as shown in Fig. 6. As similar morphologies have been observed in the literature on both GO-derived and GNP/polymer nanocomposites, we thus suggest extension of this terminology to these systems.

TEM and WAXS studies are perhaps the two most common means by which the state of dispersion can be assessed. Immiscibility of the phases and/or insufficient exfoliation of the graphite or GO-derived filler prior to mixing with polymer can result in large agglomerates consisting of stacked platelets when observed by TEM, which may also be suggested by the presence of a diffraction peak corresponding to the interlayer spacing of GO or graphite

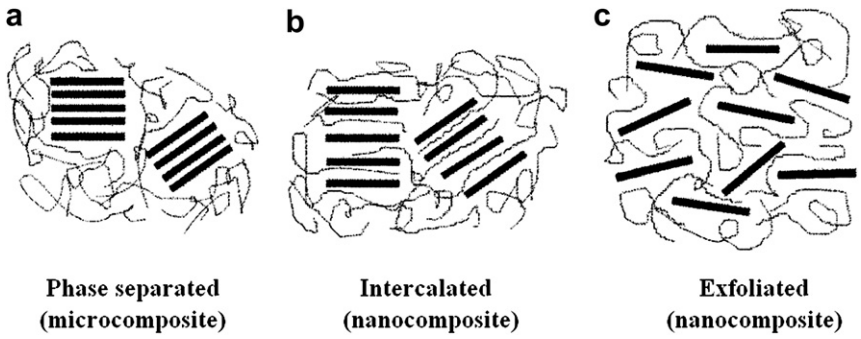

Fig. 6. Schematic showing three morphological states, as originally suggested for layered silicate fillers, that are also possible with graphene-based nanocomposites: (a) phase separated, (b) intercalated, (c) exfoliated (adapted from Ref. [23]).

[26,148,153]. Intercalated platelets retain a stacked structure but with increased interlayer spacing (on the order of a few nanometers), as evidenced by a shifted diffraction peak from that of unmodified graphite or GO [154]. As will be discussed in the following sections, high aspect ratio platelets are generally found to be beneficial to the mechanical, electrical, and thermal properties of a composite material. An exfoliated morphology of GO or GICs is thus usually desired as it provides higher aspect ratio platelets relative to stacked or intercalated platelets [155]. This state of dispersion may be suggested by a scattering profile corresponding to that of the neat matrix polymer; however, multi-layer intercalated platelets could actually be dispersed (as observed by TEM) despite the absence of a diffraction peak. Conversely, quantitative evaluation of platelet exfoliation and geometry via TEM poses its own set of challenges (such as sampling sufficient number of filler particles at such high magnification and the possible influence of TEM sample preparation on apparent level of dispersion).

While WAXS or TEM can be used to assess dispersion of individual platelets, neither can detect larger-scale morphological features [111,156]. Small-angle X-ray scattering (SAXS) and ultra-small-angle X-ray scattering (USAXS) measurements have been used on a variety of nanocomposite systems to detect the presence of fractal-like aggregates of filler at length scales beyond that of individual particles, although only limited information of this nature exists on GO-derived polymer composites [148], perhaps due in part to the limited accessibility of such techniques [111]. However, TEGO/polycarbonate nanocomposites were recently examined by small-angle neutron scattering. These measurements were used to quantify dispersion of the platelets (based on an idealized platelet model developed for montmorillonite), which suggested a decreasing effective aspect ratio with increased loading of TEGO and increased aggregation of filler at higher loadings [157]. Finally, cross-sectional analysis with scanning electron microscopy (SEM) has been used to evaluate dispersion of graphene-based filler [55] as well as to examine the surface for filler pull-out, possibly giving insight into the strength of interfacial adhesion [7,158]. However, care must be exercised when identifying the dispersed filler; moreover, SEM generally cannot resolve the degree of exfoliation of the platelets and is therefore best utilized as a complementary technique.

Exfoliated graphene-based materials are often compliant, and when dispersed in a polymer matrix are typically not observed as rigid disks, but rather as bent or crumpled platelets. Moreover, graphene has been shown to 'scroll up' irreversibly when its polymer host is heated above its glass transition temperature (T_g) [159]. Compatibility between the polymer matrix and the CMG platelets also can reportedly affect the platelets' conformation [160]. If the platelets' affinity for the matrix is high, then the particles may adopt a more extended conformation. However, the platelets may gradually adopt a more crumpled conformation as the affinity between the components decreases [160]. The technique used to process the composites can affect the microstructure, as shown in Fig. 7: randomly oriented, exfoliated platelets may be favored when composites are processed by solution mixing or *in situ* polymerization, compared with a more oriented and intercalated/stacked structure for composites produced by melt mixing, possibly due to restacking of the platelets [26]. The processing technique can also induce orientation of the dispersed platelets, which can be beneficial for reinforcement [161] but may raise the percolation threshold [153]. For composites processed by injection molding, platelets may be more randomly oriented near the interior of the specimen, with platelets aligned parallel to the surface [153]. By comparison, sufficiently thin, compression molded specimens [153] or solution-cast films [99] may have aligned platelets along the entire cross section. The filler type may also affect the orientation of the dispersed platelets. As shown in Fig. 8, solution-cast TEGO/Nafion composites exhibited a randomly oriented dispersion of TEGO platelets, whereas solution mixing of Nafion with G–O platelets, followed by hydrazine reduction, produced a highly oriented, uniform dispersion of RG–O platelets (it was stated that the reduction did not affect the orientation) [162]. The consequences of platelet conformations and orientations on composite properties will be discussed in more detail below.

For semicrystalline polymers, incorporation of a nanofiller can lead to an altered degree of crystallinity, crystallite size, spherulite structure, and may even induce crystallization of otherwise amorphous polymers [163,164]. Depending on the identity of the polymer, incorporation of graphene-based filler has been reported to cause increases [101,103,165,166], decreases [167], or no change [162] in the degree of crystallinity of a semicrystalline polymer matrix; changes in the polymer melting temperature have also been reported [168]. The presence of graphene-based nanofillers may also affect the rate of crystallization, by serving as a heterogeneous nucleation site for crystal growth [163]. Additionally, GNPs have been reported to accelerate the crystallite growth kinetics of poly (L-lactide), though the effect was found to be less pronounced than with carbon nanotubes (CNTs) [164].

Aside from crystallization, incorporation of graphene-based filler can impart other changes in the morphology of the polymer matrix or composite structure. The morphology of a self-assembling triblock copolymer, poly(styrene-*block*-isoprene-*block*-styrene), was stated to be affected by the presence of TEGO filler: AFM and electrostatic force microscopy (EFM) studies on approximately 300 nm-thick films prepared by spin coating revealed loss of long range order in the domains, with the TEGO preferentially dispersed in the PS blocks where they adopted a folded conformation [169]. Highly aligned G–O platelets dispersed in Nafion may have directed the orientation of the ionic domains of Nafion parallel to the surfaces of solution-cast films of the composites [162]. For electrospun graphene-based composites, a poor dispersion of CMG platelets has been reported to induce formation of bead-like structures in the fibers [170].

5. Rheological and viscoelastic properties

Study of nanocomposite rheology is important for the understanding of processing operations but it may also be used to examine nanocomposite microstructure [171–173]. In linear viscoelastic rheology measurements, the low-frequency moduli may provide information on the platelet dispersion; for instance, the presence of a low-frequency storage modulus (G') plateau is indicative of rheological percolation due to formation of a 'solid-like' elastic network of filler [174]; an example is illustrated in Fig. 9 for a TEGO/polycarbonate composite. The onset of a frequency-independent G' may also coincide with other phenomena, such as the loading at which a large decrease in the linear viscoelastic strain limit is observed [153]. The percolation threshold determined from such measurements can be used to roughly quantify dispersion in terms of an equivalent aspect ratio of idealized platelets [148,153]. Generally, G' has been found to increase across all frequencies with dispersion of rigid nanoplatelets, consistent with reinforcement. In addition to melt rheology, changes in the dynamic moduli have been studied in several composite systems with GNP and GO-derived fillers using dynamic mechanical analysis (DMA) temperature scans [175–178].

As previously mentioned, orientation of CMG platelets has been stated to affect the onset of rheological percolation, as randomly oriented, well-dispersed platelets would be expected to percolate at lower concentrations than aligned, well-dispersed platelets. One route to promoting the randomization of filler orientation is thermal annealing above the T_g of the polymer. As Fig. 9 shows, the

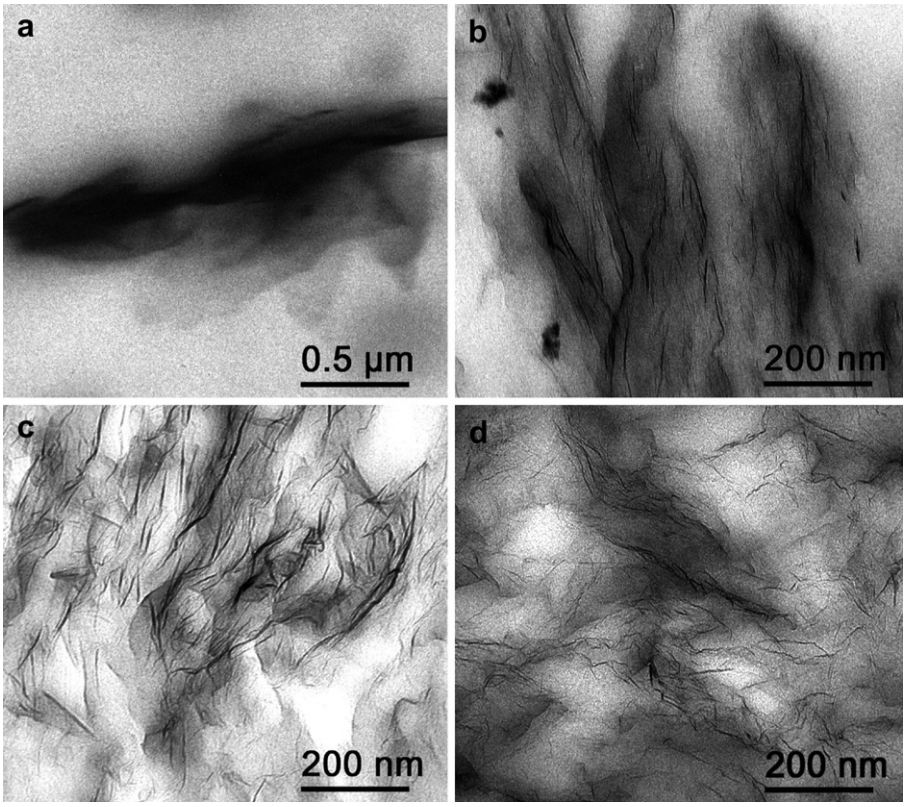

Fig. 7. TEM images illustrating the morphological differences in composites with a thermoplastic poly(urethane) matrix filled with (a) unexfoliated graphite in a stacked morphology, and (b) TEGO, processed by melt mixing. Images (c) and (d) show TEGO/polyurethane composites produced by solution blending and *in situ* polymerization, respectively, illustrating a more exfoliated state of dispersion (adapted from Ref. [26]).

rheological percolation threshold of a TEGO/polycarbonate composite was lowered from 1.5 vol% to 0.5 vol% by annealing for several hours [153]. Moreover, orientation of the platelets (induced by high strain) lowered the melt elasticity, while subsequent annealing steps were reported to restore the solid-like behavior of the composite melt. Hence, annealing of the composites following molding operations may provide a route to improve properties that benefit from randomly oriented (rather than aligned) platelets, such as the percolation threshold for electrical conductivity.

Lower composite solution viscosities have been reported with GNP fillers compared to CNTs [179], which may be advantageous for solution-based processing techniques, such as commercial molding processes for epoxy composite thermal interface materials. It has been suggested that at sufficiently high loadings, entanglement of CNTs in the matrix could result in undesirably large viscosity increases, whereas platelets can more easily slide past one another, thus moderating the viscosity increase [28]. Nonetheless, the solution viscosities of CMG/epoxy composites have been found to increase substantially with loading of filler, which could inhibit the formation of the crosslinked epoxy network [180]. It has been reported that functionalization to enhance compatibility of the filler with the polymer matrix may help to moderate the composite solution viscosity with increased loading [175]. Notably, GO composite solutions may exhibit electro-rheological properties, a characteristic of insulating colloidal particles in insulating media where increases in solution viscosity due to morphological changes can be observed upon application of an electric field [181].

6. Changes in the glass transition temperature

Low loadings of CMG fillers have been reported to cause large shifts in the T_g of the host polymer. This behavior has been explained,

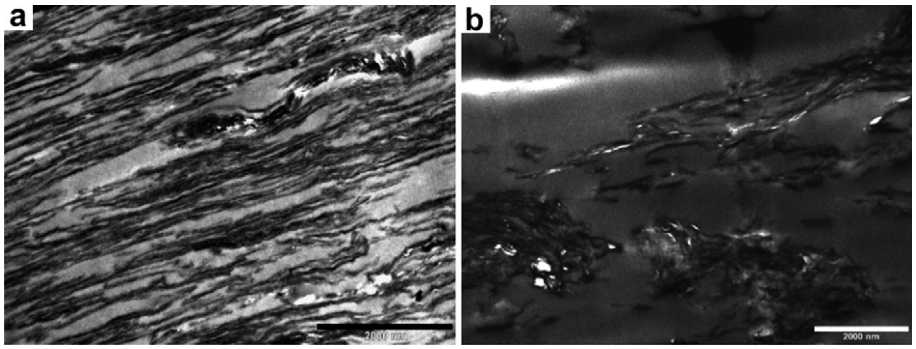

Fig. 8. TEM images contrasting (a) the preferential orientation of RG–O platelets parallel to the surface of a solution-cast RG–O/Nafion and (b) the randomly oriented dispersion of TEGO platelets in Nafion (scale bars = 2 μm; adapted from Ref. [162]).

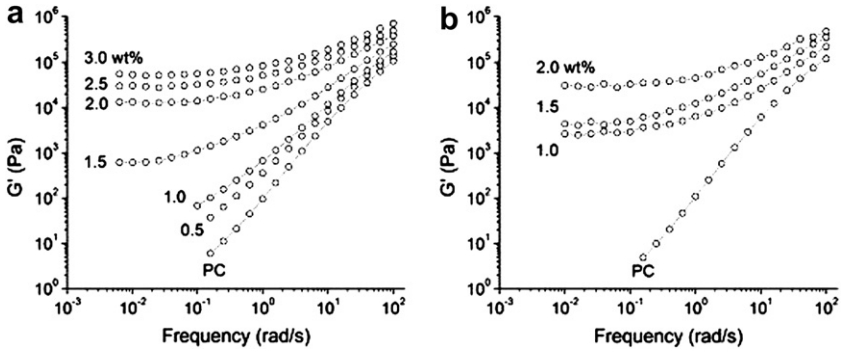

Fig. 9. Dynamic frequency sweeps of melt-blended TEGO/polycarbonate composite melts, illustrating the changes in low-frequency moduli of the composites after annealing times of (a) 10,000 s and (b) 20,000 s (adapted from Ref. [153]).

in general, by the altered mobility of polymer chains at an interface [163,182,183]. Fundamentally, an attractive polymer–matrix interface could restrict the chain mobility and thus tend to raise the T_g, whereas free surfaces and repulsive interfaces enhance chain mobility and lower the T_g; these mobility effects have been found to propagate away from the interface and gradually taper off with distance [184]. Depending on the strength of the interaction between the polymer and filler, this 'interphase' region of polymer chains with altered mobility may extend tens or even hundreds of nanometers away from the interface [185], potentially creating an enormous volume of polymer with significantly altered viscoelastic behavior. Formation of a network of interphase polymer may thus manifest large increases in the nanocomposite T_g at low loadings [186].

A striking example of this behavior was reported in nanocomposites of TEGO and poly(acrylonitrile) (PAN), where a shift in T_g of 40 °C at only 0.05 wt% loading of TEGO was observed [7]. In addition to the residual hydroxyl groups present on the TEGO surfaces promoting a positive T_g shift due to favorable non-covalent interactions with the polymer, the nanoscale roughness of the TEGO sheets was suggested to accentuate the effect [7]. T_g shifts have also been observed for CMG/polymer nanocomposites where the polymer is covalently bound to the platelet surface. In one report, G–O with PVA chains grafted to the surface via esterification was incorporated into a bulk PVA matrix, and the resulting composites showed a 35 °C shift in T_g [187]. Other reports on CMG composites with covalent matrix–filler interfaces have shown smaller but significant T_g shifts [96,188]; for such composites, it has been reported that higher grafting densities and lower molecular weight of grafted chains correlated with higher T_g values [130]. In general, T_g shifts over 20 °C are unusual—some studies have reported maximum T_g shifts between 10 and 20 °C [165,175,189], but many are lower still. Decreases in T_g have also been noted in composites which otherwise showed improvements in stiffness and electrical conductivity [157].

7. Electrical percolation and conductivity

One of the most promising aspects of graphene-based materials is their potential for use in device and other electronics applications, owing to their high electrical conductivity. 'Paper' materials made of stacked RG–O platelets have been reported to exhibit conductivities as high as 35,100 S/m [190], and such highly conductive materials, when used as fillers, may increase the bulk conductivity of an otherwise insulating polymer (e.g., poly(styrene) [55], poly(ethylene terephthalate) [113], etc.) by several orders of magnitude. In order for a nanocomposite with an insulating matrix to be electrically conductive, the concentration of the conducting filler must be above the electrical percolation threshold, where a conductive network of filler particles is formed [191]. As shown in Fig. 10, once electrical percolation has been achieved, the increase in conductivity as a function of filler loading can be modeled by a simple power-law expression

$$\sigma_c = \sigma_f(\phi - \phi_c)^t$$

where ϕ is the filler volume fraction, ϕ_c is the percolation threshold, σ_f is the filler conductivity, σ is the composite conductivity, and t is a scaling exponent. The filler need not be in direct contact for current flow; rather, conduction can take place via tunneling between thin polymer layers surrounding the filler particles, and this tunneling resistance is said to be the limiting factor in the composite conductivity [192,193]. Interestingly, recent work on TEGO/poly(vinylidene fluoride) (PVDF) nanocomposites showed a decrease in composite resistivity with increasing temperature (a negative temperature coefficient, or NTC, effect), which may suggest that for this system that the interplatelet contact resistance dominates over the tunneling resistance [177].

The electrical percolation thresholds achieved with graphene-based nanocomposites are often compared with those reported for CNT/polymer composites. Comparison of the sampling of percolation thresholds shown in Table 1 (representing the lowest threshold values reported to date) with comprehensive data

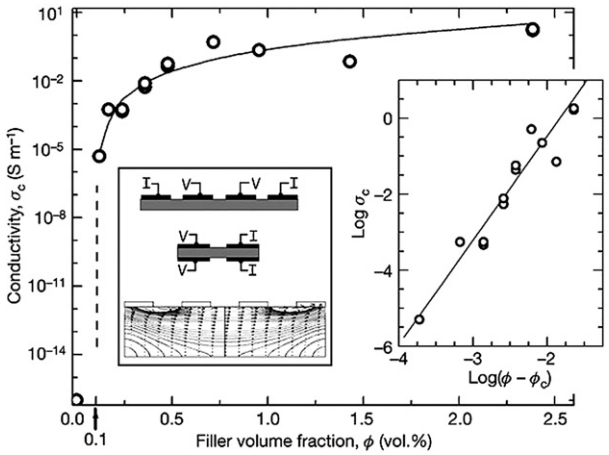

Fig. 10. Conductivity of composites of PS filled with phenyl isocyanate-functionalized RG-O versus filler volume fraction, illustrating the power-law dependence of conductivity above the percolation threshold ϕ_c (adapted from Ref. [55]).

Table 1
Values of the lowest electrical percolation thresholds and maximum electrical conductivities which have been reported in the literature for GNP and graphene-based nanocomposites for selected polymer matrices.

Matrix polymer	Filler type	Lowest percolation threshold reported (wt%)	Ref.	Filler type	Maximum conductivity (S/cm)[a]	Ref.
Epoxy	Funct. EG	1.0	[74]	RG–O	~0.05 (19 wt%)	[208]
Nylon-6	GO	0.5	[168]	GO	8.4×10^{-3} (1.8 wt%)	[168]
Poly(aniline) (doped)	GNP	0.7	[298]	GNP	522 (10 wt%)	[298]
Polycarbonate	TEGO	0.3	[157]	TEGO	0.5 (4.8 wt%)	[157]
Poly(ethylene)	RG–O	0.2	[198]	RG–O	0.1 (1.3 wt%)	[198]
Poly(ethylene terephthalate)	TEGO	1.0	[113]	TEGO	0.02 (6.5 wt%)	[113]
Poly(methyl methacrylate)	GNP	0.7	[84]	GNP	~1 (10 wt%)	[84]
Poly(propylene)	GNP	0.7	[119]	GNP	5×10^{-3} (10 wt%)	[119]
Poly(styrene)	Funct. G–O	0.2	[55]	RG–O	0.15 (2 wt%)	[147]
Poly(vinyl alcohol)	RG–O	0.5	[165]	RG–O	0.1 (7.5 wt%)	[165]
Poly(vinyl chloride)	GNP	1.4	[299]	GNP	0.06 (14.8 wt%)	[299]
Poly(vinylidene fluoride)	TEGO	2.0	[177]	TEGO	3×10^{-4} (4 wt%)	[177]
Polyurethane[b]	TEGO	0.6	[26]	TEGO	N/A (3.6 wt%)	[26]

[a] When loading was reported in volume percent, the density of bulk graphite (2.2 g/cm^3) was used to convert to a weight percent loading.
[b] Minimum resistance reported: ~200 Ω.

compiled on CNT-based nanocomposites [194] reveals that the lowest values reported for GNP- and graphene-based nanocomposites are, in general, somewhat higher than those reported for CNT-based composites. In particular, CNT/epoxy nanocomposites have been reported with electrical percolation thresholds as low as approximately 0.0025 wt% [195,196], far lower than has been reported for any graphene-based nanocomposite. These exceptional results have been ascribed to 'kinetic percolation' that most notably arises in composites with a low viscosity during processing (e.g., pre-cured epoxy), which can induce formation of a flocculated network of CNTs that electrically percolates at a much lower loading than possible with well-dispersed, randomly oriented fillers [156,197]. While comparison of the electrical percolation thresholds of composites is often valid, one must consider the influence of the sample geometry used for the conductivity measurements. For instance, a sufficiently long nanotube may be able to bridge between the electrodes for a sufficiently small test specimen, potentially suggesting a low percolation threshold which would otherwise not exist in a bulk composite specimen of much larger size.

It has been said that a high degree of dispersion may not necessarily yield the lowest onset of electrical percolation [156], as a sheath of polymer may coat the surfaces of well-dispersed filler and prevent direct interparticle contact. Indeed, the lowest percolation threshold achieved thus far for a graphene-based polymer nanocomposite (approximately 0.15 wt%; see Table 1) was observed when the filler was not homogeneously dispersed in the polymer matrix, but rather segregated from the matrix to form a conductive network [198]. In this study, poly(ethylene) particles were mixed with G–O in a water/ethanol mixture and were reduced using hydrazine, causing agglomeration of the RG–O and subsequent deposition onto the poly(ethylene) particles. This heterogeneous system was then hot pressed to generate a composite with a segregated, highly conducting network of RG–O filler [198]; however, such a morphology could compromise the composite's mechanical properties due to the agglomeration of filler [24]. In a related approach, an emulsion mixing method was used to coat polycarbonate microspheres with TEGO prior to compression molding which lowered the percolation threshold by over 50% versus a standard solution mixing method (to approximately 0.31 wt%, from 0.84 wt%) [157]. TEM observations showed a uniform dispersion of TEGO in the solution-mixed composites, compared with a segregated conductive network of TEGO in the emulsion-mixed composites, perhaps due to the exclusion of TEGO from the microspheres. Moreover, these composites (made by both dispersion methods) showed improved mechanical properties [157].

Alignment of the filler also plays a major role in the onset of electrical percolation: when the platelets are aligned in the matrix, there are, at least at relatively low concentrations, fewer contacts between them, and thus the percolation threshold would be expected to increase [199]. Compression molded polycarbonate and TEGO/polyester composites with aligned platelets were reported to show an electrical percolation threshold roughly twice that of annealed samples with randomly oriented platelets [148,153], while in another study, injection molding was reported to raise the percolation threshold over an order of magnitude versus compression molding for a GNP/poly(propylene) composite [119]. In general, the percolation threshold for electrical conductivity is often slightly higher than for rheological percolation, due to the requirement for closer proximity between platelets for particle tunneling (approximately 5 nm) for electrical percolation versus bridging by the interphase, which may extend over tens of nanometers [32,185,200]. In addition to lowering the percolation threshold, slight aggregation of the conductive filler may also improve the maximum electrical conductivities of these composites [194,201]. A combination of conductive carbon fillers may also be beneficial for lowering the electrical percolation threshold of graphene-based nanocomposites [202].

The electrical percolation threshold also depends on the intrinsic filler properties, and both theoretical models [203,204] and experiments [205] suggest that the electrical conductivity of a CMG/polymer nanocomposite depends strongly on the aspect ratio of the platelets, with a higher aspect ratio translating to a higher conductivity. Transistors produced using a phenyl isocyanate-functionalized RG–O/PS composite as the active layer reportedly exhibited an increased carrier mobility for composites containing larger-area platelets, suggesting that sheet–sheet junctions limit the composite conductivity [205] (Fig. 11). Wrinkled, folded, or otherwise non-ideal platelet conformations may also raise the electrical percolation threshold [206].

Aside from being used to impart electrical conductivity to an insulating polymer host, graphene-based fillers can also endow other unique electrical properties to composites. The positive temperature coefficient of resistivity of an RG–O/poly(ethylene) composite was stated to be tunable by varying the time of an isothermal heat treatment of the composite (at 180 °C), which was thought to randomize the RG–O network and raise the resistivity, thus raising the PTC [207]. Graphene-based composites are being explored for their dielectric properties [208], and in one study a large increase in the dielectric constant (up to 4.5×10^7 at 1000 Hz) was reported in a GNP/poly(vinylidene fluoride) composite near the percolation threshold of the composite [209].

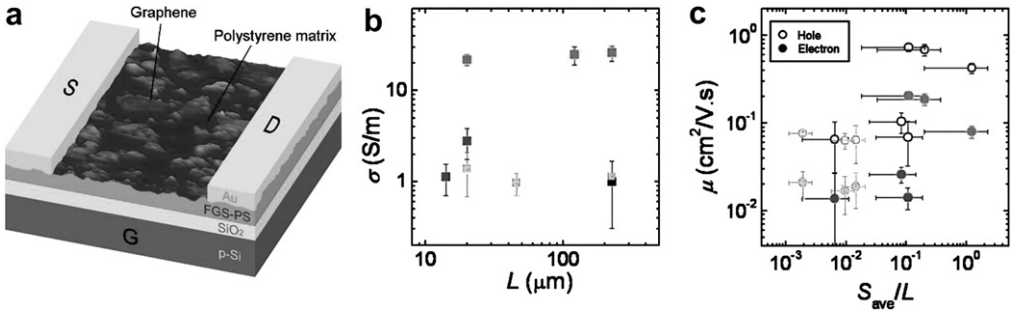

Fig. 11. (a) A transistor based off a phenyl isocyanate-functionalized RG–O/poly(styrene) composite shows different levels of (b) electrical conductivity and (c) carrier mobility depending on the aspect ratio of the platelets. The average lateral dimensions for the three platelet sizes studied were 0.44 μm, 1.5 μm, and 22.4 μm for the light grey, black, and medium grey points, respectively (adapted from Ref. [205]).

Notably, a variety of device applications have also been explored for graphene-based composites and these will be discussed in a following section.

8. Reinforcement and mechanical properties

The in-plane elastic modulus of pristine, defect-free graphene is approximately 1.1 TPa and is the strongest material that has ever been measured on a micron length scale [210]. CMG platelets exhibit an appreciably lower in-plane stiffness which calculations suggest may scale inversely with an increasing level of oxidation of the platelets [211]. A study using AFM nanoindentation on suspended CMG platelets reported the opposite, with the elastic modulus of the platelets evidently increasing with increasing oxidation level (decreasing conductivity), ranging from 250 GPa for RG–O platelets up to approximately 650 GPa for G–O platelets [22]. In another study, AFM tip-induced deformation on suspended platelets yielded an elastic modulus of monolayer G–O platelets of approximately 208 GPa. Moreover, the measurements revealed similar modulus values for two- and three-layer G–O platelets, at low strain [21]. These relatively large modulus values (compared to most polymeric materials), coupled with the large surface areas of the platelets, allow GO-derived fillers to be the primary load-bearing component of a polymer nanocomposite [161]. Fig. 12 provides an example of the reinforcing effect reported for RG–O/PVA composites.

Once dispersed in a polymer matrix, these compliant sheets or thin platelets commonly adopt wavy or wrinkled structures which may effectively reduce these modulus values [149], as crumpled platelets would tend to unfold rather than stretch in-plane under an applied tensile stress. Moreover, platelet restacking or incomplete exfoliation to single platelets could also lead to lower effective modulus values due to the decreased aspect ratios [161]. Highly crumpled conformations are often reported in composites using TEGO as filler, which along with structural defects generated during the high-temperature exfoliation processes [15], may significantly reduce the effective stiffness of the platelets and thus diminish their reinforcing capability. For instance, polycarbonate and poly (ethylene-2,6-naphthalate) (PEN) composites filled with TEGO showed only slightly larger modulus gains than composites reinforced with graphite at equivalent loadings, and calculations based on this experimental data suggested an effective modulus of around 70 GPa for TEGO—less than one-third of the measured value for single-layer RG–O [148,153]. Conversely, other studies have reported significant reinforcement from TEGO, attributed to strong interfacial bonding augmented by mechanical interlocking with the matrix due to the nanoscale roughness of the platelets [7,212]. Notably, the composites showing weaker reinforcement from TEGO were processed with melt mixing, which could possibly reduce the platelet aspect ratio (and thus reinforcement) due to particle attrition [32].

Aside from these issues with the intrinsic structure of GO-derived fillers, the reinforcing effectiveness observed from these materials thus far may be limited by problems with interfacial adhesion and spatial distribution of filler. Mechanical property enhancements have been found to correlate with improved nanofiller dispersion [23], and alignment of the filler in the matrix may increase reinforcement [161]. However, there is evidence that nanofillers (including CNTs and organoclays) which appear

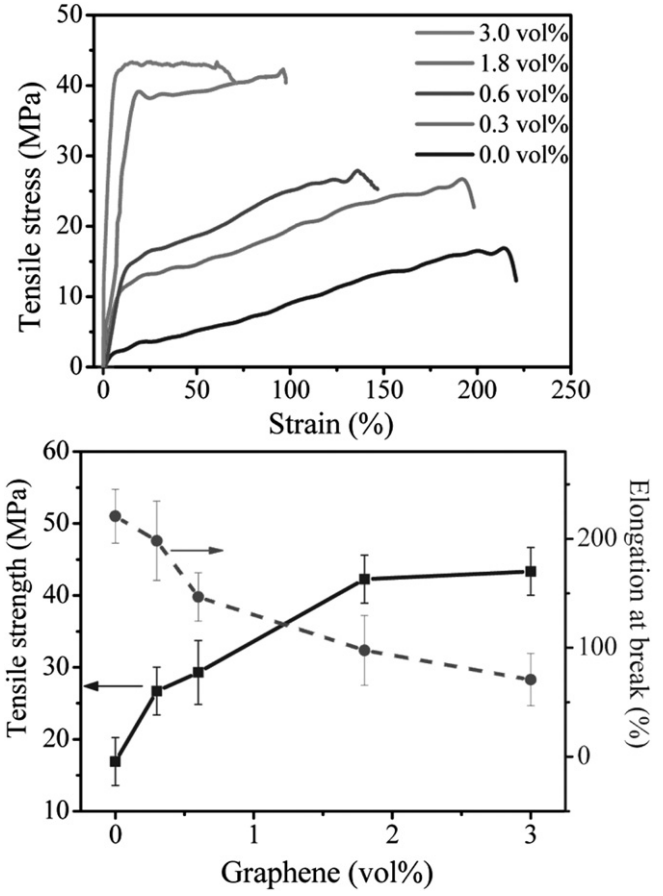

Fig. 12. Stress–strain plots of RG–O/poly(vinyl alcohol) composites as a function of filler loading, showing the pronounced reinforcing effect of RG–O. Tensile strength and elongation at break show opposing trends with increasing volume fraction of RG–O (adapted from Ref. [102]).

uniformly dispersed on short length scales may actually be aggregated into micron-scale fractal-like structures [156,213,214]. It has been suggested that such aggregates may be highly compliant and could reduce the effective aspect ratio of the filler, with both factors diminishing the reinforcing effect [156]. On the other hand, some have suggested that the presence of large-scale aggregates of filler is beneficial for reinforcement [138,215]. In any case, consideration of higher levels of nanocomposite structural hierarchy (as characterized by SAXS and USAXS, for example) may ultimately be necessary for extracting the full reinforcement potential of graphene-based fillers, and polymer-grafted platelets could potentially provide one route to tailoring the spatial distribution of filler [138,215].

Strong interfacial adhesion between the platelets and polymer matrix is also crucial for effective reinforcement [111,214,216–218]. Aside from making dispersion difficult, incompatibility between the phases may lower stress transfer due to low interfacial adhesion, resulting in a lower composite modulus [219]. Measurements of graphene-polymer interfacial adhesion have been carried out using AFM and Raman spectroscopy [220,221]. Evaluation of Raman spectra measured under strain revealed an interfacial shear stress of approximately 2.3 MPa in a graphene/PMMA composite (where the graphene was produced by micro-mechanical exfoliation) [220]. This value is similar to the value (2.7 MPa) of interfacial shear stress predicted by simulations of a poly(ethylene)/CNT nanocomposite with only van der Waals interactions between the matrix and filler [222], suggesting that the interaction between PMMA and the monolayer graphene platelets was also mediated by weak dispersive forces. By comparison, interfacial shear stresses up to 47 MPa have been measured for CNT/polymer composites [223] and values up to 500 MPa have been predicted for CNT-filled composites with covalent bonding at the matrix–filler interface [224]. These measurements thus suggest low levels of reinforcement for graphene-based polymer nanocomposites in the absence of covalent or stronger non-covalent bonding between the phases, emphasizing the importance of 'engineering' the filler–matrix interface in these systems.

Small molecule functionalization of graphene-based materials, either covalent or non-covalent, is a route to tailor the interface to promote stronger non-covalent interactions between the matrix and platelets [26]. Hydrogen bonding between GO-derived fillers and their polymer hosts has been cited as a major factor in large modulus and strength improvements observed in several polymers that can serve as hydrogen bond acceptors and/or donors [7,101,105,225]. Formation of a crystalline layer around the platelets by an isothermal treatment may also enhance stress transfer, as has been reported for a G–O/poly(caprolactone) composite [167]. Covalent bonding between the filler and matrix may provide the most effective means to increase the interfacial shear stress for improving stress transfer [218]. Monomers or chain extenders containing functional groups that can react directly with G–O in an *in situ* step-growth polymerization may thus covalently link G–O to the matrix; as recently reported for a G–O/Nylon-6 nanocomposite, this approach resulted in an unprecedented doubling of modulus and strength versus neat Nylon-6 at just 0.1 wt% loading [141]. The formation of covalent bonds between matrix and filler has also been reported to improve mechanical properties in epoxy and polyurethane composites with GNP and GO-derived fillers [26,74,140,226–228]. In addition, incorporation of polymer-grafted CMG fillers has been reported to greatly enhance the mechanical properties of PS [96], PMMA [129,188], and PVDF [128]. For such polymer-grafted fillers incorporated into a chemically identical polymer matrix, improvements in reinforcement may be strongly influenced by the relative molecular weights of the grafted polymer and matrix polymer [229].

Particularly large modulus gains have been reported in elastomeric matrices, most notably polyurethanes [26,140,226,227,230–232]. It has been pointed out that the pronounced modulus increases of elastomers may arise from the large difference in modulus between the filler and matrix—which also makes elastomers less sensitive to filler defects and non-ideal conformations than rigid thermoplastics—indeed, for graphene-based polyurethane composites the reinforcement effect was reported to be significantly attenuated above the soft segment T_g (approximately −30 °C) [26]. Increases in modulus of over two orders of magnitude (from approximately 10 MPa to 1.5 GPa at 55 wt% GNP [230]) have been reported in polyurethanes. In one study, moderate ductility was said to be retained despite the high loading, affording a composite with modulus and strength comparable to many rigid thermoplastics (e.g., polycarbonate) but with a much higher toughness and strain at break (15%) [230]. As shown in Fig. 13, TEGO/polyurethane composites made via *in situ* polymerization showed less improvement in modulus as compared with solution-mixed composites despite good dispersion, possibly due to chain extension by TEGO which may have inhibited formation of ordered, hydrogen-bonded hard segments [26]. In the case of a TEGO/silicone foam nanocomposite, densification of the composite relative to the neat foam may have complemented the effect of particle reinforcement, leading to the observed 200% increase in the normalized compressive modulus at just 0.25 wt% [233]. While the reported modulus increases are often significant, generally the remarkable ductility of elastomers is significantly compromised by incorporation of rigid filler; furthermore, graphene-filled elastomers often show a decline in tensile strength.

Beyond simple reinforcing effects, improvements in fracture toughness, fatigue strength, and buckling resistance have been noted in graphene-based composites [158,180,212,234–236]. At equivalent loadings, *in situ* polymerized TEGO/epoxy composites reportedly show a much higher buckling strength, fracture strength, and fracture energy than single- or multi-walled nanotubes-filled composites. In one study, a 94% increase in the fracture toughness of an CMG/epoxy composite versus neat epoxy was reported at 0.6 wt % loading. The toughness increase was attributed to the presence of pendant amine functionality on the CMG platelets potentially

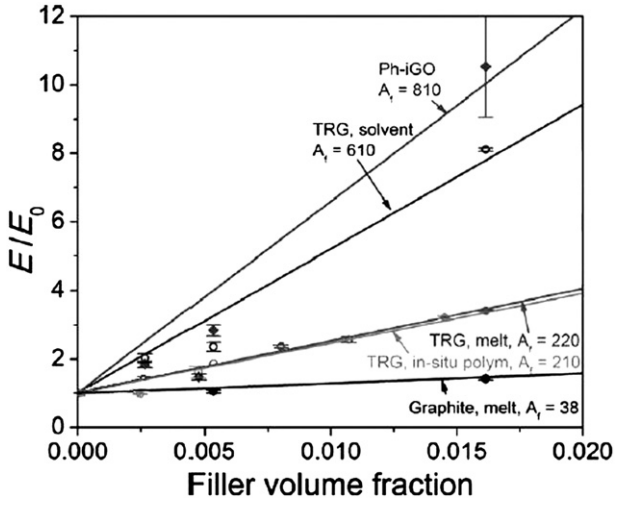

Fig. 13. Elastic moduli of polyurethane composites with flake graphite, TEGO ('TRG'), and phenyl isocyanate-functionalized G–O platelets (Ph–iGO) as filler, processed by either melt mixing, solvent mixing, or *in situ* polymerization (Ph–iGO composites were made by solution mixing). Fitting of the data to micro-mechanical models (solid lines) allows for calculations of effective aspect ratios (A_f) to quantify dispersion (adapted from Ref. [26]).

creating a "flexible interphase," although cross-linking between the CMG platelets may have also played a role [180]. Both increases [236] and decreases [237] in the impact strength of graphene-based composites have been reported.

As suggested above, GO-derived fillers could show superior reinforcement to layered clays due to their higher intrinsic stiffness. Calculations have suggested that randomly oriented graphene platelets may also produce nanocomposites with higher stiffness and strength than randomly oriented nanotubes, although calculations suggest that aligned CNTs may provide better reinforcement than aligned platelets at equivalent loading, aspect ratio, and dispersion [238]. Comparisons with GNP-filled composites [36,116,117,119,176,239] reveal that, generally, better mechanical properties are evidently achieved using well-exfoliated, GO-derived fillers at equivalent loadings. This may be primarily due to the relatively large platelet thicknesses (with a stacked structure) of GNP fillers, resulting in a lower aspect ratio and lower effective platelet modulus, thus decreasing their reinforcing effect. Notably, filler combinations such as SWNTs and TEGO [240] as well as TEGO and GO [241] may provide synergistic reinforcement, although the benefit (or lack of benefit) of these systems versus a single CMG filler at the same loading has not been fully established.

Comparisons of micro-mechanical predictions (e.g., Mori-Tanaka and Halpin-Tsai models) with experimental results on nanocomposites seem to indicate that reinforcement arises predominately from the native properties of the filler [111,161]. On the other hand, it has been suggested that the interphase concepts used to explain viscoelastic behavior may play a significant role in reinforcement owing to the modification of the properties of a large volume fraction of the matrix [163,216,242–244]. While these micro-mechanical models have been applied to some graphene-based composites in some reports [102,148,153], other results using GO-derived fillers have reportedly shown reinforcement at low loadings that exceed the upper-bound modulus predictions of these micro-mechanical models, perhaps suggesting a non-negligible contribution from the modified interphase matrix for such 'strongly bonded' systems [7,158]. Regardless, the apparent discrepancy between these results and theory highlights the need to develop further understanding of the relative contributions of native filler properties and changes in the polymer matrix in regards to the reinforcement of these systems.

9. Thermal conductivity, thermal stability, and dimensional stability

The exceptional thermal properties of GNPs and graphene-based materials have been harnessed as fillers to improve the thermal conductivity, thermal stability, and dimensional stability of polymers. Pristine graphene is highly thermally conductive; at room temperature, the thermal conductivity has been measured to be exceed 3000 W/m K when suspended [245,246] and approximately 600 W/m K when supported on a SiO_2 substrate [247]. CNTs show similar intrinsic thermal conductivities, but the sheet-like geometry of graphene-based materials may provide lower interfacial thermal resistance and thus produce larger conductivity improvements in polymer composites [248,249]. The geometry of graphite and graphene filler can also impart significant anisotropy to the thermal conductivity of the polymer composite [36], with the measured in-plane thermal conductivity as much as ten times higher than the cross-plane conductivity [250,251].

Many of the same considerations discussed for reinforcement and electrical conductivity apply for improving thermal conductivity. Close interparticle contact reduces thermal resistance and thermal conductivity in nanocomposites has been rationalized with percolation theory [252,253]. Since phonons are the primary mode of thermal conduction in polymers, covalent bonding between the matrix and filler can reduce phonon scattering at the matrix–filler interface, promoting higher composite thermal conductivity [175]. However, just as with electrical conduction, thermal conduction in nanocomposites can be compromised to some degree by platelet functionalization to enhance interfacial bonding [254].

Thermal conductivity studies of GNP and graphene-based composites have largely focused on epoxy matrix composites [175,179,248,250,255–257]. Significant improvements in thermal conductivity have been achieved in these systems (with composite conductivities ranging from 3 to 6 W/m K, up from approximately 0.2 W/m K for neat epoxy), but such large gains require relatively high carbon loadings (20 wt% and higher). Conductivities as high 80 W/m K at 64 wt% have been reported for GNP/epoxy composites, based on measurements of the thermal diffusivity [250]. The much smaller thermal conductivity contrast between polymer matrices and carbon nanofillers (as compared with electrical conductivity) may be the reason for the lower increases in thermal conductivity observed versus electrical conductivity at a given loading [95]. Different techniques have been utilized to lower the filler loading necessary to achieve large thermal conductivity gains. For instance, functionalization of EG with amine silyl groups improved the thermal conductivity by up to 20% over unmodified EG at the same loading [175]. A synergistic effect of combining SWNTs and GNPs (maximizing at a ratio of approximately 3:1 of GNPs:SWNTs) was reported, with TEM observations by the authors used to attribute the effect to the morphology of the filler blend in which the SWNTs bridged across adjacent GNP platelets, forming an extended network of filler in direct contact (Fig. 14) [248]. For G–O platelets with surface-initiated polymer brushes, higher composite thermal conductivities were reported to correlate with lower molecular weights of polymer and lower initiator grafting densities, perhaps illustrating the negative effect of excessive functionalization on thermal conduction [130].

A significant number of reports have reported increased thermal stability (as typically defined by the maximum mass loss rate measured by thermogravimetric methods) of polymers using GNPs and various CMGs as filler [114,116,170,177]; even GO can enhance the overall composite thermal stability versus the neat polymer [141,181], despite being thermally unstable itself. Studies on nanoclay-filled composites have suggested improved thermal stability trends with increased levels of exfoliation and interfacial

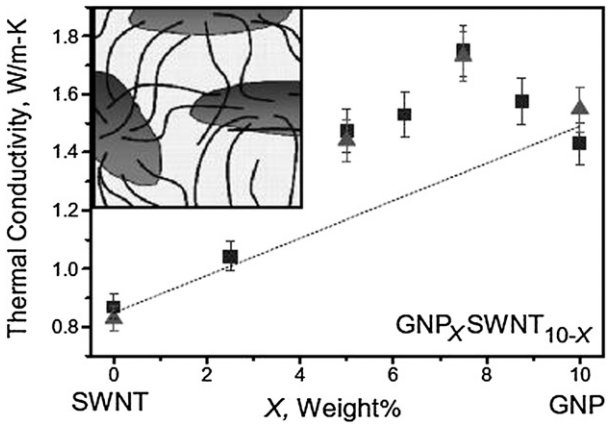

Fig. 14. Combination of graphite nanoplatelets (GNP) and single-walled carbon nanotubes (SWNTs) synergistically improve the thermal conductivity of epoxy. TEM studies established the presence of SWNTs bridging between dispersed GNPs (as shown in the schematic, inset) which may be responsible for the effect (adapted from Ref. [248]).

adhesion [258]. Most of these studies have focused on non-oxidative stability (heating under inert gas such as nitrogen or argon) and comparatively little data exists on the oxidative stability of GO composites. Increases in the onset of (non-oxidative) degradation of 20–30 °C and higher have been reported with GO-derived fillers [7,103,104,177]. However, GO is not always observed to confer thermal stability—in one case the presence of GO filler was found to accelerate the decomposition kinetics [259].

The negative coefficient of thermal expansion (CTE) of graphene [260,261], along with its high specific surface area and high stiffness, can significantly lower the coefficient of thermal expansion (CTE) of a polymer matrix [111]. In one study, the CTE of a G–O/epoxy composite was lowered by nearly 32% for temperatures below the T_g of the matrix at 5 wt% loading, although at 1 wt%, SWNTs produced a larger decrease in CTE than G–O platelets also loaded at 1 wt% (the two fillers were not compared at 5 wt%) [255]. Compared with CNTs, GNPs were reported to decrease the CTE of PP in two directions instead of one when aligned in the matrix [36].

10. Gas barrier properties

The incorporation of GNPs and GO-derived fillers can significantly reduce gas permeation through a polymer composite relative to the neat matrix polymer. A percolating network of platelets can provide a 'tortuous path' which inhibits molecular diffusion through the matrix, thus resulting in significantly reduced permeability (Fig. 15) [111]. Permeability studies on CMG/PS nanocomposites, however, suggest that at low loadings (e.g., below 0.05 vol%), the reduction in permeability of the composite is largely driven by a reduction in gas solubility in the composite, with diffusion effects becoming more important at higher loadings [262]. Orientation of the platelets may further enhance barrier properties perpendicular to their alignment, while higher platelet aspect ratios correlate with increased barrier resistance [111]. Notably, the one-dimensional geometry of CNTs may limit their effectiveness in improving the barrier properties of a composite relative to the neat polymer [26].

Both GNP and GO-derived fillers have been investigated in various permeation studies [26,36,114,115,153,262]; for thermoplastics, results include a 20% reduction in oxygen permeability for PP with 6.5 wt% GNP [36], and a 39% reduction in the nitrogen permeability of a polycarbonate/TEGO composite at approximately 3.5 wt% loading [153]. As shown in Fig. 15, CMG/PS composites were reported to show a lower oxygen permeability than exfoliated montmorillonite/PS composites at equivalent loadings [262]. In a comparative study of GO-derived fillers in thermoplastic polyurethanes, phenyl isocyanate-functionalized G–O platelets were reported to confer superior barrier properties relative to TEGO, with up to a 99% reduction in nitrogen permeability observed at approximately 3.7 wt% loading compared with an 81% reduction for TEGO at the same loading. Notably, the barrier properties in this study correlated with modulus improvements suggesting better filler alignment or higher aspect ratio for the functionalized G–O composites [26].

11. Applications of graphene-based polymer nanocomposites

Though numerous challenges remain in developing a fundamental understanding of GO-derived materials and their polymer composites, these materials have already been explored for a range of applications. Reflective of G–O's close relationship to graphene, many of the applications have focused on harnessing its electronic properties, particularly for devices. However, this is somewhat counterintuitive given that G–O is essentially an insulating material. For device applications, typically the G–O platelets and polymer are mixed and then the G–O platelets are reduced using hydrazine (or other strong chemical reductants) or thermal annealing, as discussed in the examples above.

One notable exception to this paradigm can be found in the development of an electronic memory device. Using the previously described surface-initiated polymerization methods, poly(*t*-butylacrylate) was reportedly grown from the surface of a thin film of G–O platelets [132]. The functionalized sheets were blended with P3HT and spun cast onto a surface of indium tin oxide (ITO), and then coated with a layer of aluminum. This device made use of the low conductivity of stacked and overlapped G–O platelets as a means of creating a barrier for inter-lamellar electron-hole recombination after excitons were formed. This created a clearly defined OFF state for the memory device. At the switching potential (found to be relatively high; −1.6 V), electrons were said to be excited from the HOMO of the P3HT portion of the mixture into the LUMO of the G–O platelet film/poly(*t*-butylacrylate) portion via intermolecular charge transfer. As the oxygen-containing functional groups of G–O platelets are believed to be inhomogeneously distributed across the lamellae [3], the excited electrons were able to travel relatively freely within the highly delocalized π-domains. Notably, the low bulk conductivity prevented recombination, resulting in a non-volatile memory storage system. This unique example took advantage of what is often perceived as a negative trait of G–O platelet material: its low conductivity. In contrast,

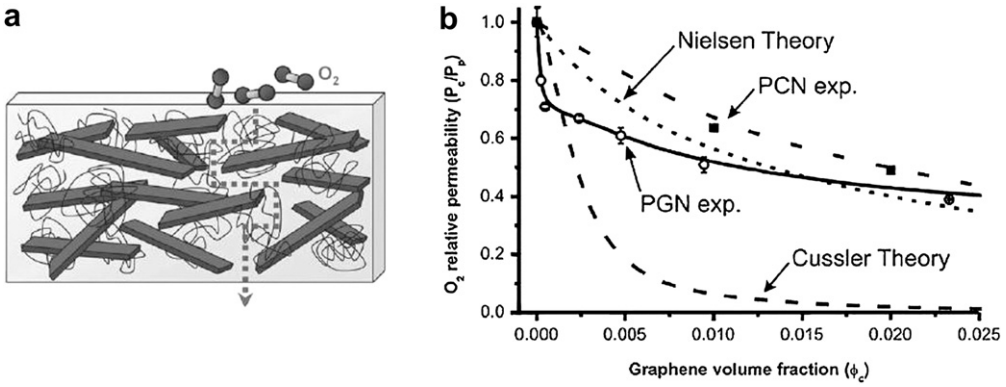

Fig. 15. (a) Illustration of formation of a 'tortuous path' of platelets inhibiting diffusion of gases through a polymer composite (Nielsen model). (b) Measurements of oxygen permeability of CMG/PS ('PGN') and montmorillonite/PS ('PCN') composites as a function of filler loading, compared with two theoretical models of composite permeability (adapted from Ref. [262]).

metal- and dopant-free conductive composites can be prepared from electrically conductive CMGs. These studies typically utilize the high degree of surface functionalization present on G–O platelets to attach polymers or polymerization initiators (grafting-to or grafting-from approaches, as previously discussed), followed by reduction of the oxidized surface to render the composite electrically conductive.

Field effect transistors (FETs) [205], solar cells (and other opto-electronic applications) [263], and energy storage devices [264] are three areas where such conductive composites may be particularly applicable. All of these applications capitalize upon the high conductivity inherent to many CMG composites. Photovoltaics and optoelectronics, in particular, rely on the fact that monolayers of graphene are about 98% transparent but still have high electrical conductivity. This feature makes graphene-based materials potentially well-suited to address issues related to photoexcitation and exciton mobility/diffusion as transparent conducting electrodes [265–268]. Overall efficiencies for these devices are still relatively low to date (typically less than 1% power conversion efficiency) when applied as organic photovoltaics, but this remains an area of interest particularly since the testing of these materials started so recently.

In addition to conductive polymers such as P3HT, graphene-based composites incorporating PANI have been studied as energy storage materials. Specific capacitances reported from 210 F/g to over 1000 F/g have been reported for these composites [269–274]. The precise reasons for this enhancement in energy storage capacity are still under investigation, but the authors state that this likely involves Faradaic transitions between the three different oxidation states of PANI (leucoemeraldine, emeraldine salt, and pernigraniline), in addition to the electrochemical double-layer capacitance (EDLC; general schematic shown in Fig. 16) provided by the carbon material [275]. It has been reported that PANI can intercalate into the layers of unexfoliated GO, increasing compatibility between the phases [181,276–278]. Even when GO was not reduced, the composite was rendered conductive by the PANI [276,277], though to a lesser extent than when RG–O platelets were incorporated [269].

Aside from devices, a host of diverse applications have been envisioned for graphene-based nanocomposites, all harnessing the property improvements discussed in the previous sections. For instance, the electrical conductivity of these composites may find use in electromagnetic wave interference shielding and anti-static coatings [208], while potentially maintaining properties of the host polymer such as transparency by virtue of the low percolation thresholds of these composite systems [55]. The combination of the improved barrier properties and increased light absorption of a CMG/PS composite versus neat PS suggests wider application as a packaging material [262]. The mechanical reinforcement achieved at low loadings of GO-derived filler offers potential uses in weight-sensitive aerospace and automotive applications such as tires, which could also benefit from the conductivity of RG–O platelets. Electrically conductive and robust GO-derived composite membranes could find use as capacitive pressure sensors in MEMS applications [279]. One less conventional application for these composites may be in self-healing materials [280,281]: very small loadings of multi-layer graphene in a shape memory epoxy matrix was reported to improve the composite's resistance to crack formation, thus enhancing scratch recovery upon heating above its T_g [282]. Interestingly, the filler used in this study was grown via microwave plasma-enhanced chemical vapor deposition, representing the first report of graphene composite filler generated from a 'bottom-up' synthesis route.

Nanofillers can also be used to reduce or overcome the intrinsic flammability of thermoplastics [111], and such applications have been explored for GO, despite the high flammability of GO when contaminated by synthetic byproducts such as potassium salts [283]. However, the thermal expansion of GO coupled with its evolution of gaseous byproducts (e.g., CO_2) at high temperatures may confer flame retardancy [284]. A recent study compared the fire retardancy of a GO/Nylon-6 composite to a nanoclay/Nylon-6 composite, and concluded that the volumetric expansion of GO particles conferred good short-term fire resistance, but the low structural integrity of the resulting material and release of oxidants on heating was a major disadvantage relative to nanoclays [285].

An emerging research direction for graphene-based composites is focused on biomedical applications. Graphene has been investigated for biosensor applications [286] and efforts have been directed at graphene-based composite biosensors as well [287–289]. Composite films of DNA and RG–O platelets have been prepared via solution mixing, and incorporation of other biological macromolecules along with DNA may provide a general approach to multifunctional, biocompatible composites [290]. A biocompatible hydrogel composite produced via physical cross-linking of PVA chains between G–O platelets showed a controlled release of Vitamin B12 depending on solution pH, and the authors stated this could find use in drug delivery [291]. Moreover, biocompatible free-standing composite films of poly(oxyethylene sorbitan laurate) (TWEEN) and RG–O could find use in transplant devices and implants [292]. Other biocompatible and biodegradable polymer composites have also been investigated, and incorporation of G–O

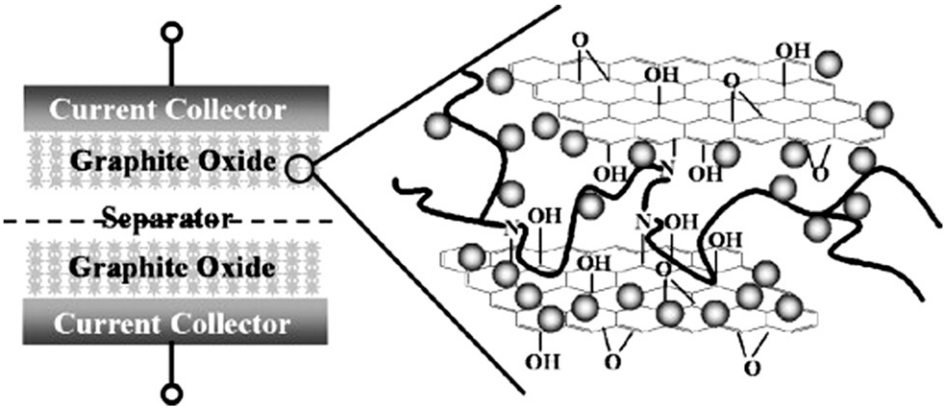

Fig. 16. Schematic of test electrochemical double-layer capacitor (EDLC) assembly and structural model of a GO/polymer composite assembled in the EDLC. The spheres in represent the electrolyte ions, which can be conveyed via diffusion and the segmental motion of the polymer chains (adapted from Ref. [264]).

platelets into chitosan [189,225] and poly(lactide) [114,164], in particular, may greatly expand the utility of these polymers that are otherwise limited by their mechanical properties.

12. Conclusions

Graphene-based polymer nanocomposites represent one of the most technologically promising developments to emerge from the interface of graphene-based materials and polymer materials. However, there are still many challenges that must be addressed for these nanocomposites to reach their full potential. For example, the sonication and thermal shock techniques commonly used to exfoliate GO also reduce the aspect ratio of the exfoliated platelets, which may negatively affect reinforcement as well as electrical and thermal properties [8,52]. Results suggesting poor interfacial adhesion in graphene/polymer composites in the absence of covalent bonding or additional non-covalent binding interactions such as $\pi-\pi$ interactions or hydrogen bonding underscore the importance of the platelet surface chemistry in reinforcement and the need for continued progress in this direction [220]. Moreover, the defects introduced into G–O platelets by either the oxidation to convert graphite to GO or the processing to generate G–O platelets, might ultimately limit the electrical conductivity and mechanical properties achievable with RG–O platelets relative to pristine and defect-free graphene platelets. Thus, methods of graphene platelet production which preserve its extended, conjugated structure may find favor for certain demanding applications of graphene-based composites [12].

Further property improvements in graphene-based composites will be influenced by improved morphological control. Defects and wrinkles in platelets are likely to influence their reinforcing capabilities, and so exfoliation and/or dispersion techniques that promote a more elongated morphology could conceivably further improve mechanical properties of these composites. Also, increased control over alignment and spatial organization of graphene-based fillers could be beneficial to nearly all types of composite properties. Thermal annealing of graphene-based composites to randomize GNP and graphene-based platelets may benefit the composite's electrical conductivity [153], whereas improved alignment of the platelets may improve reinforcement [161]. A variety of techniques for alignment of CNTs in polymer composites have been reported [293], and some of these techniques may find use for graphene-based composites. While the end application of graphene-based composites may dictate their specific morphological characteristics, the use of 'top-down' patterning or 'bottom-up' mesophase self-assembly approaches that have better morphological control could help to guide future studies of these systems, which may reveal new applications for these composites [213].

Despite these challenges, some of which are not unique to graphene-based nanocomposites, polymer nanocomposites have already found use in industry and their commercial impact is expected by many to rise significantly in the future [294]. As further improvements are made in the chemical production of graphene-based materials [295], composites using this class of filler could become a commercial reality. Notably, there is already significant effort and industrial interest in scaling up GO production [296]; GNP fillers have attracted similar attention [297]. Particularly relevant to large-scale production and transport of GO, flammability issues with this material have been identified and methods to alleviate these problems have been demonstrated [283]. Graphite, the precursor to GO and GO-derived fillers, is relatively cheap and abundant [296], and this cost factor will likely remain one of the primary advantages for using graphene-based fillers over CNTs in nanocomposites particularly as work on scale-up progresses. Furthermore, while CNTs and graphene reportedly offer comparable mechanical and electrical property enhancements, graphene-based materials appear to provide larger thermal conductivity enhancement as well as the advantage of improving barrier properties. The multifunctional property enhancements already demonstrated with graphene-based fillers, coupled with their potential for low cost and large-scale production, may expedite the applications of these nanocomposites as well as their transition to the marketplace.

Acknowledgements

This work was supported (in part) by the Laboratory Directed Research and Development (LDRD) program and the National Institute for Nano-Engineering at Sandia National Laboratories. Sandia is a multiprogram laboratory operated by Sandia Corporation, a Lockheed Martin Company, for the United States Department of Energy's National Nuclear Security Administration under Contract DE-AC04-94AL85000. CWB is grateful to the Robert A. Welch Foundation (F-1621) for support.

References

[1] Zhu Y, Murali S, Cai W, Li X, Suk JW, Potts JR, et al. Adv Mater 2010; 22:3906–24.
[2] Geim AK, Novoselov KS. Nat Mater 2007;6:183–91.
[3] Compton OC, Nguyen SBT. Small 2010;6:711–23.
[4] Carter LW, Hendricks JG, Bolley DS. 2531396, National Lead Company; 1950.
[5] Usuki A, Kojima Y, Kawasumi M, Okada A, Fukushima Y, Kurauchi T, et al. J Mater Res 1993;8:1179–84.
[6] Winey KI, Vaia RA. MRS Bull 2007;32:314–9.
[7] Ramanathan T, Abdala AA, Stankovich S, Dikin DA, Herrera-Alonso M, Piner RD, et al. Nat Nanotechnol 2008;3:327–31.
[8] Dreyer DR, Park S, Bielawski CW, Ruoff RS. Chem Soc Rev 2010;39:228–40.
[9] Kim H, Abdala AA, Macosko CW. Macromolecules 2010;43:6515–30.
[10] Dreyer DR, Ruoff RS, Bielawski CW. Angew Chem Int Ed 2010;49:9336–44.
[11] Park S, Ruoff RS. Nat Nanotechnol 2009;5:217–24.
[12] Dato A, Radmilovic V, Lee Z, Phillips J, Frenklach M. Nano Lett 2008;8:2012–6.
[13] Schafhaeutl C. J Prakt Chem 1840;21:129.
[14] Schafhaeutl C. Philos Mag 1840;16:570.
[15] Boehm HP, Clauss A, Fischer G, Hofmann U. Proceedings of the fifth conference on carbon; 1962.
[16] Boehm HP, Clauss A, Fischer GO, Hofmann U. Z Naturforsch 1962;17b:150–3.
[17] Boehm HP, Clauss A, Fischer GO, Hofmann U. Z Anorg Allg Chem 1962; 316:119–27.
[18] Allen MJ, Tung VC, Kaner RB. Chem Rev 2010;110:132–45.
[19] Loh KP, Bao Q, Ang PK, Yang J. J Mater Chem 2010;20:2277–89.
[20] Rafiee MA, Liu W, Thomas AV, Zandiatashbar A, Rafiee J, Tour JM, et al. ACS Nano; 2010. doi:10.1021/nn102529n.
[21] Suk JW, Piner RD, An J, Ruoff RS. ACS Nano; 2010. doi:10.1021/nl101902k.
[22] Gómez-Navarro C, Burghard M, Kern K. Nano Lett 2008;8:2045–9.
[23] Alexandre M, Dubois P. Mater Sci Eng R Rep 2000;28:1–63.
[24] Thostenson ET, Li CY, Chou TW. Compos Sci Technol 2005;65:491–516.
[25] Li D, Kaner RB. Science 2008;320:1170–1.
[26] Kim H, Miura Y, Macosko CW. Chem Mater 2010;22:3441–50.
[27] Dresselhaus MS, Dresselhaus G. Adv Phys 1981;30:139–326.
[28] Jang BZ, Zhamu A. J Mater Sci 2008;43:5092–101.
[29] Viculis LM, Mack JJ, Mayer OM, Hahn HT, Kaner RB. J Mater Chem 2005; 15:974–8.
[30] Chen G, Wu D, Weng W, Cuiling W. Carbon 2003;41:619–25.
[31] Li X, Zhang G, Bai X, Sun X, Wang X, Wang E, et al. Nat Nanotechnol 2008;3:538–42.
[32] Potschke P, Abdel-Goad M, Pegel S, Jehnichen D, Mark JE, Zhou DH, et al. J Macromol Sci Part A Pure Appl Chem 2010;47:12–9.
[33] Yasmin A, Luo J-J, Daniel IM. Compos Sci Technol 2006;66:1182–9.
[34] Zheng W, Lu X, Wong S-C. J Appl Polym Sci 2004;91:2781–8.
[35] Celzard A, Mareche JF, Furdin G, Puricelli S. J Phys D Appl Phys 2000; 33:3094–101.
[36] Kalaitzidou K, Fukushima H, Drzal LT. Carbon 2007;45:1446–52.
[37] Shioyama H. Synth Met 2000;114:1–15.
[38] Novoselov KS, Geim AK, Morozov SV, Jiang D, Zhang Y, Dubonos SV, et al. Science 2004;306:666–9.
[39] Zhang M, Parajuli RR, Mastrogiovanni D, Dai B, Lo P, Cheung W, et al. Small 2010;6:1100–7.
[40] Hernandez Y, Nicolosi V, Lotya M, Blighe FM, Sun Z, De S, et al. Nat Nanotechnol 2008;3:563–8.
[41] Lotya M, Hernandez Y, King PJ, Smith RJ, Nicolosi V, Karlsson LS, et al. J Am Chem Soc 2009;131:3611–20.
[42] Lu J, Yang J-X, Wang J, Lim A, Wang S, Loh KP. ACS Nano 2009;3:2367–75.

[43] Buchsteiner A, Lerf A, Pieper Jr A. J Phys Chem B 2006;110:22328–38.
[44] Dikin DA, Stankovich S, Zimney EJ, Piner RD, Dommett GHB, Evmenenko G, et al. Nature 2007;448:457–60.
[45] Ruess VG, Vogt F. Monatsh Chem 1948;78:222–42.
[46] Park S, An JH, Jung IW, Piner RD, An SJ, Li XS, et al. Nano Lett 2009;9:1593–7.
[47] Becerril HA, Mao J, Liu Z, Stoltenberg RM, Bao Z, Chen Y. ACS Nano 2008; 2:463–70.
[48] Gómez-Navarro C, Weitz RT, Bittner AM, Scolari M, Mews A, Burghard M, et al. Nano Lett 2007;7:3499–503.
[49] Li Z, Zhang W, Luo Y, Yang J, Hou JG. J Am Chem Soc 2009;131:6320–1.
[50] Paredes JI, Villar-Rodil S, Martinez-Alonso A, Tascon JMD. Langmuir 2008;24:10560–4.
[51] Zhu Y, Stoller MD, Cai W, Velamakanni A, Piner RD, Chen D, et al. ACS Nano 2010;4:1227–33.
[52] Schniepp HC, Li JL, McAllister MJ, Sai H, Herrera-Alonso M, Adamson DH, et al. J Phys Chem B 2006;110:8535–9.
[53] McAllister MJ, Li JL, Adamson DH, Schniepp HC, Abdala AA, Liu J, et al. Chem Mater 2007;19:4396–404.
[54] Brunauer S, Emmett PH, Teller E. J Am Chem Soc 1938;60:309–19.
[55] Stankovich S, Dikin DA, Dommett GHB, Kohlhaas KM, Zimney EJ, Stach EA, et al. Nature 2006;442:282–6.
[56] Zhu YW, Murali S, Stoller MD, Velamakanni A, Piner RD, Ruoff RS. Carbon 2010;48:2118–22.
[57] Bagri A, Mattevi C, Acik M, Chabal YJ, Chhowalla M, Shenoy VB. Nat Chem 2010;2:581–7.
[58] Boukhvalov DW, Katsnelson MI. J Am Chem Soc 2008;130:10697–701.
[59] Dreyer DR, Jia HP, Bielawski CW. Angew Chem Int Ed 2010;49:6813–6.
[60] Jia HP, Dreyer DR, Bielawski CW. Adv Synth Catal; 2011. doi:10.1039/adsc.201000748.
[61] Murali S, Dreyer DR, Zhu Y, Ruoff RS, Bielawski CW. J Mater Chem; 2011. doi:10.1039/C0JM02704A.
[62] Gao J, Liu F, Liu Y, Ma N, Wang Z, Zhang X. Chem Mater 2010;22:2213–8.
[63] Zhang J, Yang H, Shen G, Cheng P, Zhang J, Guo S. Chem Commun 2010; 46:1112–4.
[64] Stankovich S, Dikin DA, Piner RD, Kohlhaas KA, Kleinhammes A, Jia Y, et al. Carbon 2007;45:1558–65.
[65] Li D, Muller MB, Gilje S, Kaner RB, Wallace GG. Nat Nanotechnol 2008;3:101–5.
[66] Stankovich S, Piner RD, Chen X, Wu N, Nguyen SBT, Ruoff RS. J Mater Chem 2006;16:155–8.
[67] Choi EY, Han TH, Hong J, Kim JE, Lee SH, Kim HW, et al. J Mater Chem 2010; 20:1907–12.
[68] Cao Y, Feng J, Wu P. Carbon 2010;48:3834–9.
[69] Villar-Rodil S, Paredes JI, Martinez-Alonso A, Tascon JMD. J Mater Chem 2009;19:3591–3.
[70] Niyogi S, Bekyarova E, Itkis ME, McWilliams JL, Hamon MA, Haddon RC. J Am Chem Soc 2006;128:7720–1.
[71] Xu Y, Liu Z, Zhang X, Wang Y, Tian J, Huang Y, et al. Adv Mater 2009;21:1275–9.
[72] Liu Y, Zhou J, Zhang X, Liu Z, Wan X, Tian J, et al. Carbon 2009;47:3113–21.
[73] Stankovich S, Piner RD, Nguyen ST, Ruoff RS. Carbon 2006;44:3342–7.
[74] Miller SG, Bauer JL, Maryanski MJ, Heimann PJ, Barlow JP, Gosau JM, et al. Compos Sci Technol; 2010:1120–5.
[75] Su Q, Pang S, Alijani V, Li C, Feng X, Müllen K. Adv Mater 2009;21:3191–5.
[76] Xu Y, Bai H, Lu G, Li C, Shi G. J Am Chem Soc 2008;130:5856–7.
[77] Podall H, Foster WE, Giraitis AP. J Org Chem 1958;30:82–5.
[78] Panayotov IM, Rashkov IB. J Polym Sci Part A Polym Chem 1973;11:2615–22.
[79] Parrod J, Beinert G. J Polym Sci 1961;53:99.
[80] Shioyama H. Carbon 1997;35:1664–5.
[81] Bunnell LR. 5186919, Battelle Memorial Institute; 1993.
[82] Pan YX, Yu ZZ, Ou YC, Hu GH. J Polym Sci Part B Polym Phys 2000;38:1626–33.
[83] Chen G, Zhao W, editors. Nano- and biocomposites. CRC Press; 2009. p. 79–106.
[84] Chen G, Weng W, Wu D, Wu C. Eur Polym J 2003;39:2329–35.
[85] Chen G, Wu C, Weng W, Wu D, Yan W. Polymer 2003;44:1781–4.
[86] Zheng W, Wong S-C. Compos Sci Technol 2003;63:225–35.
[87] Zheng W, Wong S-C, Sue H-J. Polymer 2002;43:6767–73.
[88] Zois H, Apekis L, Omastova M. Proceedings – international symposium on electrets, 10th international symposium on electrets; 1999: pp. 529–532.
[89] Gabriel P, Cipriano LG, Ana JM. Polym Compos 1999;20:804–8.
[90] Liu P, Gong K. Carbon 1999;37:701–11.
[91] Kyotani T, Moriyama H, Tomita A. Carbon 1997;35:1185–7.
[92] Matsuo Y, Tahara K, Sugie Y. Carbon 1997;35:113–20.
[93] Matsuo Y, Hatase K, Sugie Y. Chem Mater 1998;10:2266–9.
[94] Kotov NA, Dékány I, Fendler JH. Adv Mater 1996;8:637–41.
[95] Moniruzzaman M, Winey KI. Macromolecules 2006;39:5194–205.
[96] Fang M, Wang KG, Lu HB, Yang YL, Nutt S. J Mater Chem 2009;19:7098–105.
[97] Higginbotham AL, Lomeda JR, Morgan AB, Tour JM. ACS Appl Mater Interfaces 2009;1:2256–61.
[98] Pandey R, Awasthi K, Tiwari RS, Srivastava ON. 2010; arXiv:1004.4281 [cond-mat.mes-hall].
[99] Chen D, Zhu H, Liu T. ACS Appl Mater Interfaces; 2010. doi:10.1021/am1008437.
[100] Das B, Prasad KE, Ramamurty U, Rao CNR. Nanotechnology 2009;20:125705.
[101] Liang JJ, Huang Y, Zhang L, Wang Y, Ma YF, Guo TY, et al. Adv Funct Mater 2009;19:2297–302.
[102] Zhao X, Zhang QH, Chen DJ, Lu P. Macromolecules 2010;43:2357–63.
[103] Yang X, Li L, Shang S, Tao X. Polymer 2010;51:3431–5.
[104] Xu YX, Hong WJ, Bai H, Li C, Shi GQ. Carbon 2009;47:3538–43.
[105] Jiang L, Shen XP, Wu JL, Shen KC. J Appl Polym Sci 2010;118:275–9.
[106] Satti A, Larpent P, Gun'ko Y. Carbon 2010;48:3376–81.
[107] Putz KW, Compton OC, Palmeri MJ, Nguyen SBT, Brinson LC. Adv Funct Mater 2010;20:3322–9.
[108] Wei T, Luo GL, Fan ZJ, Zheng C, Yan J, Yao CZ, et al. Carbon 2009;47:2296–9.
[109] Lee HB, Raghu AV, Yoon KS, Jeong HM. J Macromol Sci Part B Phys 2010;49:802–9.
[110] Bryning MB, Milkie DE, Islam MF, Kikkawa JM, Yodh AG. Appl Phys Lett 2005; 87:161909.
[111] Paul DR, Robeson LM. Polymer 2008;49:3187–204.
[112] Sinha Ray S, Okamoto M. Prog Polym Sci 2003;28:1539–641.
[113] Zhang HB, Zheng WG, Yan Q, Yang Y, Wang JW, Lu ZH, et al. Polymer 2010; 51:1191–6.
[114] Kim IH, Jeong YG. J Polym Sci Part B Polym Phys 2010;48:850–8.
[115] Jiang X, Drzal LT. Polym Compos; 2009:1091–8.
[116] Kim S, Do I, Drzal LT. Polym Compos 2010;31:755–61.
[117] Kalaitzidou K, Fukushima H, Drzal LT. Compos Part A Appl Sci Manuf 2007; 38:1675–82.
[118] Steurer P, Wissert R, Thomann R, Mulhaupt R. Macromol Rapid Commun 2009;30:316–27.
[119] Kalaitzidou K, Fukushima H, Drzal LT. Compos Sci Technol 2007; 67:2045–51.
[120] Jeong H-K, Lee YP, Jin MH, Kim ES, Bae JJ, Lee YH. Chem Phys Lett 2009;470:255–8.
[121] Fim FC, Guterres JM, Basso NRS, Galland GB. J Polym Sci Part A Polym Chem 2010;48:692–8.
[122] Jang JY, Kim MS, Jeong HM, Shin CM. Compos Sci Technol 2009;69:186–91.
[123] Gu Z, Zhang L, Li C. J Macromol Sci Part B Phys 2009;48:1093–102.
[124] Gu ZM, Li CZ, Wang GC, Zhang L, Li XH, Wang WD, et al. J Polym Sci Part B Polym Phys 2010;48:1329–35.
[125] Liu P, Gong K, Xiao P, Xiao M. J Mater Chem 2000;10:933–5.
[126] Lee SH, Dreyer DR, An JH, Velamakanni A, Piner RD, Park S, et al. Macromol Rapid Commun 2010;31:281–8.
[127] Yang YF, Wang J, Zhang J, Liu JC, Yang XL, Zhao HY. Langmuir 2009;25:11808–14.
[128] Layek RK, Samanta S, Chatterjee DP, Nandi AK. Polymer 2010;51:5846–56.
[129] Goncalves G, Marques PAAP, Barros-Timmons A, Bdkin I, Singh MK, Emami N, et al. J Mater Chem 2010;20:9927–34.
[130] Fang M, Wang KG, Lu HB, Yang YL, Nutt S. J Mater Chem 2010;20:1982–92.
[131] Zhang B, Chen Y, Zhuang XD, Liu G, Yu B, Kang ET, et al. J Polym Sci Part A Polym Chem 2010;48:2642–9.
[132] Li GL, Liu G, Li M, Wan D, Neoh KG, Kang ET. J Phys Chem C 2010;114:12742–8.
[133] Zhuang XD, Chen Y, Liu G, Li PP, Zhu CX, Kang ET, et al. Adv Mater 2010;22:1731–5.
[134] Park S, Dikin DA, Nguyen ST, Ruoff RS. J Phys Chem C 2009;113:15801–4.
[135] Sun ST, Cao YW, Feng JC, Wu PY. J Mater Chem 2010;20:5605–7.
[136] Veca LM, Lu FS, Meziani MJ, Cao L, Zhang PY, Qi G, et al. Chem Commun; 2009:2565–7.
[137] Coleman J, Khan U, Gun'ko Y. Adv Mater 2006;18:689–706.
[138] Akcora P, Kumar SK, Moll J, Lewis S, Schadler LS, Li Y, et al. Macromolecules 2010;43:1003–10.
[139] Yang H, Shan C, Li F, Zhang Q, Han D, Niu L. J Mater Chem 2009;19:8856–60.
[140] Lee YR, Raghu AV, Jeong HM, Kim BK. Macromol Chem Phys 2009; 210:1247–54.
[141] Xu Z, Gao C. Macromolecules 2010;43:6716–23.
[142] Huang YJ, Qin YW, Zhou Y, Niu H, Yu ZZ, Dong JY. Chem Mater 2010; 22:4096–102.
[143] Liu JQ, Yang WR, Tao L, Li D, Boyer C, Davis TP. J Polym Sci Part A Polym Chem 2010;48:425–33.
[144] Liu JQ, Tao L, Yang WR, Li D, Boyer C, Wuhrer R, et al. Langmuir 2010; 26:10068–75.
[145] Hu HT, Wang XB, Wang JC, Wan L, Liu FM, Zheng H, et al. Chem Phys Lett 2010;484:247–53.
[146] Zheming G, Ling Z, Chunzhong L. J Macromol Sci Part B Phys 2009; 48:226–37.
[147] Tkalya E, Ghislandi M, Alekseev A, Koning C, Loos J. J Mater Chem 2010; 20:3035–9.
[148] Kim H, Macosko CW. Macromolecules 2008;41:3317–27.
[149] Wakabayashi K, Pierre C, Dikin DA, Ruoff RS, Ramanathan T, Brinson LC, et al. Macromolecules 2008;41:1905–8.
[150] Wu JH, Tang QW, Sun H, Lin JM, Ao HY, Huang ML, et al. Langmuir 2008; 24:4800–5.
[151] Wang J, Ellsworth MW. ECS Trans 2009;19:241–7.
[152] Vickery JL, Patil AJ, Mann S. Adv Mater 2009;21:2180–4.
[153] Kim H, Macosko CW. Polymer 2009;50:3797–809.
[154] Kai W, Hirota Y, Hua L, Inoue Y. J Appl Polym Sci 2008;107:1395–400.
[155] Fu X, Qutubuddin S. Polymer 2001;42:807–13.
[156] Schaefer DW, Justice RS. Macromolecules 2007;40:8501–17.
[157] Yoonessi M, Gaier JR. ACS Nano; 2010. doi:10.1021/nn1019626.
[158] Rafiee MA, Rafiee J, Wang Z, Song HH, Yu ZZ, Koratkar N. ACS Nano 2009; 3:3884–90.
[159] Li Q, Li ZJ, Chen MR, Fang Y. Nano Lett 2009;9:2129–32.
[160] Hirata M, Gotou T, Horiuchi S, Fujiwara M, Ohba M. Carbon 2004;42:2929–37.
[161] Fornes TD, Paul DR. Polymer 2003;44:4993–5013.
[162] Ansari S, Kelarakis A, Estevez L, Giannelis EP. Small 2010;6:205–9.

[163] Schadler LS, Brinson LC, Sawyer WG. J Miner Met Mater Soc 2007;59:53–60.
[164] Xu JZ, Chen T, Yang CL, Li ZM, Mao YM, Zeng BQ, et al. Macromolecules 2010;43:5000–8.
[165] Salavagione HJ, Martinez G, Gomez MA. J Mater Chem 2009;19:5027–32.
[166] Cerezo FT, Preston CML, Shanks RA. Compos Sci Technol 2007;67:79–91.
[167] Cai DY, Song M. Nanotechnology 2009;20:315708.
[168] Du N, Zhao CY, Chen Q, Wu G, Lu R. Mater Chem Phys 2010;120:167–71.
[169] Peponi L, Tercjak A, Verdejo R, Lopez-Manchado MA, Mondragon I, Kenny JM. J Phys Chem C 2009;113:17973–8.
[170] Bao QL, Zhang H, Yang JX, Wang S, Tong DY, Jose R, et al. Adv Funct Mater 2010;20:782–91.
[171] Solomon MJ, Almusallam AS, Seefeldt KF, Somwangthanaroj A, Varadan P. Macromolecules 2001;34:1864–72.
[172] Wagener R, Reisinger TJG. Polymer 2003;44:7513–8.
[173] Zhang Q, Fang F, Zhao X, Li Y, Zhu M, Chen D. J Phys Chem B 2008; 112:12606–11.
[174] Vermant J, Ceccia S, Dolgovskij MK, Maffettone PL, Macosko CW. J Rheol 2007;51:429–50.
[175] Ganguli S, Roy AK, Anderson DP. Carbon 2008;46:806–17.
[176] Ramanathan T, Stankovich S, Dikin DA, Liu H, Shen H, Nguyen ST, et al. J Polym Sci Part B Polym Phys 2007;45:2097–112.
[177] Ansari S, Giannelis EP. J Polym Sci Part B Polym Phys 2009;47:888–97.
[178] Pramoda KP, Linh NTT, Tang PS, Tjiu WC, Goh SH, He CB. Compos Sci Technol; 2009:578–83.
[179] Yu A, Ramesh P, Itkis ME, Bekyarova E, Haddon RC. J Phys Chem C 2007; 111:7565–9.
[180] Fang M, Zhang Z, Li J, Zhang H, Lu H, Yang Y. J Mater Chem 2010;20:9635–43.
[181] Zhang WL, Park BJ, Choi HJ. Chem Commun 2010;46:5596–8.
[182] Bansal A, Yang H, Li C, Cho K, Benicewicz BC, Kumar SK, et al. Nat Mater 2005;4:693–8.
[183] Priestley RD, Ellison CJ, Broadbelt LJ, Torkelson JM. Science 2005;309:456.
[184] Ellison CJ, Torkelson JM. Nat Mater 2003;2:695–700.
[185] Rittigstein P, Priestley RD, Broadbelt LJ, Torkelson JM. Nat Mater 2007; 6:278–82.
[186] Qiao R, Catherine Brinson L. Compos Sci Technol 2009;69:491–9.
[187] Salavagione HJ, Gomez MA, Martinez G. Macromolecules 2009;42:6331–4.
[188] Pramoda KP, Hussain H, Koh HM, Tan HR, He CB. J Polym Sci Part A Polym Chem 2010;48:4262–7.
[189] Fan H, Wang L, Zhao K, Li N, Shi Z, Ge Z, et al. Biomacromolecules 2010; 11:2345–51.
[190] Chen H, Müller MB, Gilmore KJ, Wallace GG, Li D. Adv Mater 2008; 20:3557–61.
[191] Balogun YA, Buchanan RC. Compos Sci Technol; 2010:892–900.
[192] Roldughin VI, Vysotskii VV. Prog Org Coat 2000;39:81–100.
[193] Toker D, Azulay D, Shimoni N, Balberg I, Millo O. Phys Rev B Condens Matter Mater Phys 2003;68:41403.
[194] Bauhofer W, Kovacs JZ. Compos Sci Technol 2009;69:1486–98.
[195] Martin CA, Sandler JKW, Shaffer MSP, Schwarz MK, Bauhofer W, Schulte K, et al. Compos Sci Technol 2004;64:2309–16.
[196] Sandler JKW, Kirk JE, Kinloch IA, Shaffer MSP, Windle AH. Polymer 2003; 44:5893–9.
[197] Kovacs JZ, Velagala BS, Schulte K, Bauhofer W. Compos Sci Technol 2007; 67:922–8.
[198] Pang H, Chen T, Zhang G, Zeng B, Li ZM. Mater Lett 2010;64:2226–9.
[199] Haggenmueller R, Gommans HH, Rinzler AG, Fischer JE, Winey KI. Chem Phys Lett 2000;330:219–25.
[200] Du F, Scogna RC, Zhou W, Brand S, Fischer JE, Winey KI. Macromolecules 2004;37:9048–55.
[201] Hernández JJ, García-Gutiérrez MC, Nogales A, Rueda DR, Kwiatkowska M, Szymczyk A, et al. Compos Sci Technol 2009;69:1867–72.
[202] Wei T, Song L, Zheng C, Wang K, Yan J, Shao B, et al. Mater Lett 2010; 64:2376–9.
[203] Hicks J, Behnam A, Ural A. Appl Phys Lett 2009;95:213103.
[204] Li J, Kim JK. Compos Sci Technol 2007;67:2114–20.
[205] Eda G, Chhowalla M. Nano Lett 2009;9:814–8.
[206] Yi YB, Tawerghi E. Phys Rev E Stat Nonlin Soft Matter Phys 2009;79: 041134.
[207] Pang HA, Zhang YC, Chen T, Zeng BQ, Li ZM. Appl Phys Lett 2010;96:251907.
[208] Liang JJ, Wang Y, Huang Y, Ma YF, Liu ZF, Cai FM, et al. Carbon 2009; 47:922–5.
[209] He F, Lau S, Chan HL, Fan JT. Adv Mater 2009;21:710–5.
[210] Lee C, Wei X, Kysar JW, Hone J. Science 2008;321:385–8.
[211] Paci JT, Belytschko T, Schatz GC. J Phys Chem C 2007;111:18099–111.
[212] Rafiee MA, Rafiee J, Srivastava I, Wang Z, Song HH, Yu ZZ, et al. Small 2010;6:179–83.
[213] Vaia RA, Maguire JF. Chem Mater 2007;19:2736–51.
[214] Kluppel M, editor. The role of disorder in filler reinforcement of elastomers on various length scales, vol. 164. Springer; 2003. p. 86.
[215] Akcora P, Liu H, Kumar SK, Moll J, Li Y, Benicewicz BC, et al. Nat Mater 2009;8:354–9.
[216] Pukánszky B, Fekete E, editors. Adhesion and surface modification, vol. 139. Springer; 1999. p. 109–53.
[217] Lv C, Xue Q, Xia D, Ma M, Xie J, Chen H. J Phys Chem C 2010;114:6588–94.
[218] Wagner HD, Vaia RA. Mater Today 2004;7:38–42.
[219] Schadler LS, Giannaris SC, Ajayan PM. Appl Phys Lett 1998;73:3842–4.
[220] Gong L, Kinloch IA, Young RJ, Riaz I, Jalil R, Novoselov KS. Adv Mater 2010;22:2694–7.
[221] Cai M, Glover AJ, Wallin TJ, Kranbuehl DE, Schniepp HC. AIP Conf Proc 2010; 1255:95–7.
[222] Frankland SJV, Caglar A, Brenner DW, Griebel M. J Phys Chem B 2002; 106:3046–8.
[223] Barber AH, Cohen SR, Wagner HD. Appl Phys Lett 2003;82:4140–2.
[224] Wagner HD, Lourie O, Feldman Y, Tenne R. Appl Phys Lett 1998;72:188–90.
[225] Yang XM, Tu YF, Li LA, Shang SM, Tao XM. ACS Appl Mater Interfaces 2010;2:1707–13.
[226] Cai DY, Yusoh K, Song M. Nanotechnology 2009;20:085712.
[227] Nguyen DA, Lee YR, Raghu AV, Jeong HM, Shin CM, Kim BK. Polym Int 2009;58:412–7.
[228] Raghu AV, Lee YR, Jeong HM, Shin CM. Macromol Chem Phys 2008; 209:2487–93.
[229] Bansal A, Yang H, Li C, Benicewicz BC, Kumar SK, Schadler LS. J Polym Sci Part B Polym Phys 2006;44:2944–50.
[230] Khan U, May P, O'Neill A, Coleman JN. Carbon 2010;48:4035–41.
[231] Quan H, Zhang B-Q, Zhao Q, Yuen RKK, Li RKY. Compos Part A Appl Sci Manuf 2009;40:1506–13.
[232] Nguyen DA, Raghu AV, Choi JT, Jeong HM. Polym Polym Compos 2010;18:351–8.
[233] Verdejo R, Barroso-Bujans F, Rodriguez-Perez MA, de Saja JA, Lopez-Manchado MA. J Mater Chem 2008;18:2221–6.
[234] Rafiee MA, Rafiee J, Yu ZZ, Koratkar N. Appl Phys Lett 2009;95:223103.
[235] Yavari F, Rafiee MA, Rafiee J, Yu ZZ, Koratkar N. ACS Appl Mater Interfaces 2010;2:2738–43.
[236] Rafiq R, Cai D, Jin J, Song M. Carbon 2010;48:4309–14.
[237] Jiang X, Drzal LT. Polym Compos 2010;31:1091–8.
[238] Liu H, Brinson LC. Compos Sci Technol 2008;68:1502–12.
[239] Kim S, Drzal LT. J Adhes Sci Technol 2009;23:1623–38.
[240] Prasad KE, Das B, Maitra U, Ramamurty U, Rao CNR. Proc Natl Acad Sci USA 2009;106:13186–9.
[241] Jang JY, Jeong HM, Kim BK. Macromol Res 2009;17:626–8.
[242] Ciprari D, Jacob K, Tannenbaum R. Macromolecules 2006;39:6565–73.
[243] Putz KW, Palmeri MJ, Cohn RB, Andrews R, Brinson LC. Macromolecules 2008;41:6752–6.
[244] Jancar J, Douglas JF, Starr FW, Kumar S, Cassagnau P, Lesser AJ, et al. Polymer; 2010:3321–43.
[245] Balandin AA, Ghosh S, Bao W, Calizo I, Teweldebrhan D, Miao F, et al. Nano Lett 2008;8:902–7.
[246] Ghosh S, Calizo I, Teweldebrhan D, Pokatilov EP, Nika DL, Balandin AA, et al. Appl Phys Lett 2008;92:151911.
[247] Seol JH, Jo I, Moore AL, Lindsay L, Aitken ZH, Pettes MT, et al. Science 2010;328:213–6.
[248] Yu A, Ramesh P, Sun X, Bekyarova E, Itkis ME, Haddon RC. Adv Mater 2008;20:4740–4.
[249] Lin W, Zhang R, Wong CP. J Electron Mater 2010;39:268–72.
[250] Veca LM, Meziani MJ, Wang W, Wang X, Lu F, Zhang P, et al. Adv Mater 2009;21:2088–92.
[251] Ghose S, Watson KA, Working DC, Connell JW, Smith Jr JG, Sun YP. Compos Sci Technol 2008;68:1843–53.
[252] Zhong H, Lukes JR. Phys Rev B 2006;74:125403.
[253] Zhang G, Xia Y, Wang H, Tao Y, Tao G, Tu S, et al. J Compos Mater 2010; 44:963–70.
[254] Shenogin S, Bodapati A, Xue L, Ozisik R, Keblinski P. Appl Phys Lett 2004; 85:2229–31.
[255] Wang SR, Tambraparni M, Qiu JJ, Tipton J, Dean D. Macromolecules 2009; 42:5251–5.
[256] Debelak B, Lafdi K. Carbon 2007;45:1727–34.
[257] Hung MT, Choi O, Ju YS, Hahn HT. Appl Phys Lett 2006;89:023117.
[258] Leszczynska A, Njuguna J, Pielichowski K, Banerjee JR. Thermochim Acta 2007;453:75–96.
[259] Kaczmarek H, Podgórski A. Polym Degrad Stab 2007;92:939–46.
[260] Mounet N, Marzari N. Phys Rev B Condens Matter Mater Phys 2005;71:205214.
[261] Fasolino A, Los JH, Katsnelson MI. Nat Mater 2007;6:858–61.
[262] Compton OC, Kim S, Pierre C, Torkelson JM, Nguyen SBT. Adv Mater 2010;22:4759–63.
[263] Spitsina NG, Lobach AS, Kaplunov MG. High Energy Chem 2009;43:552–6.
[264] Tien CP, Teng HS. J Power Sources 2010;195:2414–8.
[265] Liu Z, He D, Wang Y, Wu H, Wang J. Sol Energy Mater Sol Cells; 2010:1196–200.
[266] Tung VC, Chen LM, Allen MJ, Wassei JK, Nelson K, Kaner RB, et al. Nano Lett 2009;9:1949–55.
[267] Valentini L, Cardinali M, Bon SB, Bagnis D, Verdejo R, Lopez-Manchado MA, et al. J Mater Chem 2010;20:995–1000.
[268] Geng X, Niu L, Xing Z, Song R, Liu G, Sun M, et al. Adv Mater 2010;22:638–42.
[269] Wu Q, Xu YX, Yao ZY, Liu AR, Shi GQ. ACS Nano 2010;4:1963–70.
[270] Wang D-W, Li F, Zhao J, Ren W, Chen Z-G, Tan J, et al. ACS Nano 2009; 3:1745–52.
[271] Wang H, Hao Q, Yang X, Lu L, Wang X. Electrochem Commun 2009; 11:1158–61.
[272] Yan J, Wei T, Shao B, Fan Z, Qian W, Zhang M, et al. Carbon 2010;48:487–93.
[273] Murugan AV, Muraliganth T, Manthiram A. Chem Mater 2009;21:5004–6.
[274] Bai H, Xu Y, Zhao L, Li C, Shi G. Chem Commun 2009;45:1667–9.
[275] Stejskal J, Gilbert J. Pure Appl Chem 2002;74:857–67.
[276] Higashkia S, Kimura K, Matsuo Y, Sugie Y. Carbon 1999;37:351–8.

[277] Wang H, Hao Q, Yang X, Lu L, Wang X. ACS Appl Mater Interfaces 2010; 2:821–8.
[278] Zhou X, Wu T, Hu B, Yang G, Han B. Chem Commun 2010;46:3663–5.
[279] Kulkarni DD, Choi I, Singamaneni SS, Tsukruk VV. ACS Nano 2010;4:4667–76.
[280] Williams KA, Boydston AJ, Bielawski CW. J R Soc Interface 2007;4:359–62.
[281] Williams KA, Dreyer DR, Bielawski CW. MRS Bull 2008;33:759–65.
[282] Xiao X, Xie T, Cheng YT. J Mater Chem 2010;20:3508–14.
[283] Kim F, Luo J, Cruz-Silva R, Cote LJ, Sohn K, Huang J. Adv Funct Mater; 2010. doi:10.1002/adfm.201000736.
[284] Rothon RN. In: Jancar J, editor. Mineral fillers in thermoplastics: filler manufacture and characterisation, vol. 139. Springer; 1999. p. 67–108.
[285] Dasari A, Yu ZZ, Mai YW, Cai GP, Song HH. Polymer 2009;50:1577–87.
[286] Wenrong Y, Kyle RR, Simon PR, Pall T, Gooding JJ, Filip B. Angew Chem Int Ed 2010;49:2114–38.
[287] Lu J, Do I, Drzal LT, Worden RM, Lee I. ACS Nano 2008;2:1825–32.
[288] Lu J, Drzal LT, Worden RM, Lee I. Chem Mater 2007;19:6240–6.
[289] Zhou KF, Zhu YH, Yang XL, Luo J, Li CZ, Luan SR. Electrochim Acta 2010; 55:3055–60.
[290] Patil AJ, Vickery JL, Scott TB, Mann S. Adv Mater 2009;21:3159–64.
[291] Bai H, Li C, Wang X, Shi G. Chem Commun 2010;46:2376–8.
[292] Park S, Mohanty N, Suk JW, Nagaraja A, An J, Piner RD, et al. Adv Mater 2010; 22:1736–40.
[293] Xie XL, Mai YW, Zhou XP. Mater Sci Eng R Rep 2005;49:89–112.
[294] Hussain F, Hojjati M, Okamoto M, Gorga RE. J Compos Mater 2006;40:1511–75.
[295] Marcano DC, Kosynkin DV, Berlin JM, Sinitskii A, Sun Z, Slesarev A, et al. ACS Nano 2010;4:4806–14.
[296] Segal M. Nat Nanotechnol 2009;4:611–3.
[297] University MS http://research.msu.edu/techtransfer/1-mil-support-msu-spinoff-xg-sciences. [accessed 30.07.10].
[298] Wu X, Qi S, He J, Duan G. J Mater Sci 2010;45:483–9.
[299] Vadukumpully S, Paul J, Mahanta N, Valiyaveettil S. Carbon 2011;49:198–205.

Jeffrey R. Potts is a Ph.D. student in materials science at the University of Texas at Austin working with Prof. Rodney S. Ruoff. He received his B.S. from Oklahoma State University in 2008 where he conducted research in Raman and photoluminescence spectroscopy with Prof. Don A. Lucca. He is a part of the National Institute for Nano-Engineering (NINE) program at Sandia National Laboratories (NM), where he works on chemically modified graphene materials for stimuli-responsive nanocomposites. His current research focus is on the synthesis and characterization of graphene-based materials and their incorporation into polymers to form nanocomposites.

Daniel R. Dreyer is a Ph.D. candidate in the chemistry program at the University of Texas at Austin studying under Prof. Christopher W. Bielawski. He received his B.S. in chemistry from Wheaton College (IL) in 2007 where he conducted research in confocal microscopy under Prof. Daniel L. Burden. During his undergraduate career he also studied X-ray reflectometry and plasma polymerization under Prof. Mark D. Foster at the University of Akron as part of an NSF-sponsored REU. His current research interests include applications of ionic liquids in synthetic polymer chemistry, structurally dynamic/self-healing materials, and carbon materials for use in catalysis and energy storage devices.

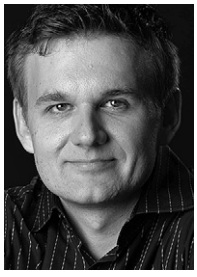

Christopher W. Bielawski received a B.S. degree in chemistry from the University of Illinois at Urbana-Champaign (1996) and a Ph.D. in chemistry from the California Institute of Technology (2003). After postdoctoral studies (also at Caltech), he became an assistant professor of chemistry at The University of Texas at Austin in 2004 and was promoted to associate professor in 2009, and professor in 2010. Prof. Bielawski's research program focuses primarily on synthetic problems at the interface of polymer, organic, and materials chemistry.

Rodney S. Ruoff is a Cockrell Family Regents Chair at The University of Texas at Austin, after having been Director of the Biologically Inspired Materials Institute and John Evans Chair at Northwestern University. He received his BS in Chemistry from UT-Austin and Ph.D. in Chemical Physics from the UI-Urbana (advisor H.S. Gutowsky). Prior to Northwestern he was a Staff Scientist at the Molecular Physics Laboratory of SRI International and Associate Professor of Physics at Washington University at St. Louis. He has 238 refereed journal articles in the fields of chemistry, physics, mechanics, and materials science, and is a co-founder of Graphene Energy Inc., and founder of Graphene Materials, LLC and Nanode, Inc.

Polymer 52 (2011) 26–32

Contents lists available at ScienceDirect

Polymer

journal homepage: www.elsevier.com/locate/polymer

Synthesis and spectroscopic analysis of cellulose sulfates with regulable total degrees of substitution and sulfation patterns via ^{13}C NMR and FT Raman spectroscopy

Kai Zhang [a,*], Erica Brendler [b], Andreas Geissler [a], Steffen Fischer [a]

[a] Institute of Plant and Wood Chemistry, Dresden University of Technology, Pienner Str. 19, D-01737 Tharandt, Germany
[b] Institute of Analytical Chemistry, Freiberg University of Mining and Technology, Leipziger Str. 29, D-09599 Freiberg, Germany

ARTICLE INFO

Article history:
Received 18 August 2010
Received in revised form
3 November 2010
Accepted 9 November 2010
Available online 18 November 2010

Keywords:
Cellulose sulfate (CS)
^{13}C NMR spectroscopy
FT Raman spectroscopy

ABSTRACT

Synthesis and spectroscopic characterisation of cellulose sulfate (CS) were reported. Various CS exhibiting diverse degrees of sulfation (DS_S) were prepared through acetosulfation or direct sulfation of cellulose. During the acetosulfation, intermediate product – cellulose acetate sulfate (CAS) – was formed after the comparative esterification and subsequent deacetylation of CAS led to CS. The direct sulfation proceeded quasi-homogeneously and heterogeneously in N,N-dimethylformamide (DMF) or homogeneously in N,N-dimethylacetamide (DMAc)/LiCl mixture. The total DS_S between 0.21–2.59 and partial DS_{S6} as well as DS_{S2} of up to 1 were determined via elemental analysis and ^{13}C NMR spectroscopy. Besides, solid-state CP/MAS ^{13}C NMR could characterise CS regarding the sulfation. Subsequently, FT Raman investigation of obtained CS was conducted with the aim to establish analysis methods quantifying the total DS_S. The intensities of Raman bands ascribed to the vibrations of O═S═O and C–O–S groups were used as analysis parameters, yielding calibration curves with high correlation coefficients of more than 0.96.

1. Introduction

Sulfate groups are found to be important for the biological activities of natural glycosaminoglycans, such as heparin and heparan sulfate [1,2], but these glycosaminoglycans exhibit various molecular compositions and therefore distinct biological activities [2,3]. In order to overcome the limitations of naturally occurring glycosaminoglycans, diverse glycosaminoglycan–analogues have been prepared by sulfating other renewable polysaccharides including cellulose [4–7].

After the sulfation of cellulose, the product CS showed highly improved water-solubility and enzymatic degradability [8]. With these advantageous properties, CS found a wide use in biotechnology and pharmaceutics, e.g. as polyelectrolyte for the encapsulation of enzymes and cells [9–11]. Moreover, CS exhibited diverse biological effects, such as antivirus and anticoagulant activity [4,12]. CS with high total DS_S could bind FGF2 and strongly promote FGF-induced proliferation [13].

CS can be synthesized non-homogeneously in pyridine or homogeneously in ionic liquid starting from cellulose or cellulose derivatives [8,14–16]. Various sulfating agents including SO_3, chlorosulfuric acid and SO_3·DMF complex have been applied for the sulfation of cellulose [16–18]. The total DS_S of prepared CS could be analysed via elemental analysis or FT Raman spectroscopy [8,15,18]. For the quantification based on Raman spectroscopy, the peak area of the Raman band attributed to stretching vibrations of C–O–S groups was applied. Because of the beneficial properties of Raman spectroscopy including ultra-sensitive and non-destructive analysis, other Raman analysis parameters may also be considered for quantifying the total DS_S.

In addition to the total DS_S, the distribution of sulfate groups within the sulfated polysaccharides is proposed essential for their properties. The sulfate groups at 6-*O*-position of heparin were found to be important for its interaction with fibroblast growth factor (FGF) [19]. FGF2-induced proliferation increased with rising total DS_S and especially with elevating partial DS_{S6}, as described for heparin oligosaccharides [20,21]. The molecular structure of chondroitin sulfate oligosaccharide was proposed to be critical for its function and the distribution of sulfate groups could affect its interaction with growth factors [22]. The sulfate groups at 6-*O*-position were assumed as necessary for the anticoagulant activities of sulfated chitosan and cellulose [16,23], while only 3,6-disulfated

* Corresponding author. Tel.: +49 (0) 35203 38 31239; fax: +49 (0) 35203 38 31201.
E-mail address: kzhang@forst.tu-dresden.de (K. Zhang).

0032-3861/$ – see front matter © 2010 Elsevier Ltd. All rights reserved.
doi:10.1016/j.polymer.2010.11.017

chitin demonstrated improved anticoagulant activity compared to 6-*O*-sulfated chitin [24]. Besides, the chitosan sulfate-enhanced bioactivity of BMP-2 was suggested to be primarily ascribed to the sulfate groups at 6-*O*-position [25]. Thus, in order to elucidate the structure–property relationship of sulfated polysaccharides, it is of importance to determine not only the total DS_S but also the exact distribution of sulfate groups and therefore the partial DS_S. However, the distribution of sulfate groups within the repeating units of CS prepared under homogeneous or non-homogeneous conditions has rarely been investigated.

In this report, CS with diverse total DS_S were prepared at first through acetosulfation and direct sulfation of cellulose using distinct sulfating agents. The partial DS_S at 2- and 6-*O*-position of prepared CS were determined via ^{13}C NMR spectroscopy. The reaction parameters influencing the sulfation progresses regarding the total and partial DS_S of CS were evaluated. Finally, the feasibility of using the intensities of Raman bands ascribed to the vibrations of O═S═O and C–O–S groups for quantifying the total DS_S of CS was examined and thus, novel methods for determining the total DS_S can be established.

2. Experimental section

2.1. Materials

Microcrystalline cellulose (MCC) with an average Cuen-DP of 276 was received from J. Rettenmaier & Söhne GmbH (Rosenberg, Germany). Pulp V-81 (AC, with 97.0% alpha cellulose) with a viscosity (in 0.5% cupri-diethylenediamine) of 7.2 cP and an average DP of 1180 was purchased from Buckeye Technologies Inc. (Memphis, USA). Irradiated cellulose (IC) with an average DP of 113 was attained through treating cellulose (DP ~ 500) with electron-beam (100 kGy). DMF was freshly distilled and water was demineralised before use in all experiments. Other chemicals were all of analysis grade and used as received. Dialysis membrane from Spectrum Laboratories Inc. (Rancho Dominquez, USA) has an approximate molecular weight cut off of 500 Da.

2.2. Sulfation of cellulose

The sulfation of cellulose was carried out either as acetosulfation or as non-homogeneous direct sulfation and 1 g cellulose was suspended in 50 ml anhydrous DMF at RT for over 14 h [8,15,17]. For the homogeneous direct sulfation, cellulose (1 g) was dissolved in DMAc/LiCl (16 ml/1.5 g) mixture [26].

2.2.1. Acetosulfation

For a typical acetosulfation, the reaction agent consisting of 0.35 ml chlorosulfuric acid and 4.7 ml acetic anhydride in DMF was dropped into the cellulose suspension under vigorous stirring. After being kept at 50 °C for 5 h, the solution was cooled down to RT and poured into the saturated ethanolic solution of anhydrous sodium acetate. The precipitate was collected through centrifugation and deacetylated with 1 M ethanolic solution of NaOH for over 15 h after washing with 4% sodium acetate solution in ethanol. Then, the pH value of the mixture was adjusted to 8.0 with acetic acid/ethanol (50/50, w/w) and the product was dissolved in water after washing with ethanol. Finally, the solution was filtered, dialysed against demineralised water and lyophilised.

To prepare the intermediate product – cellulose acetate sulfate (CAS) – before the deacetylation, the solution was precipitated in ethanol after the acetosulfation and the pH value of the mixture was adjusted to 7.5. After washing with ethanol/water-mixture (8:2, v/v), the product was dissolved in water and the solution was filtered, dialysed and lyophilised. CAS1 was prepared with 3 mol chlorosulfuric acid and 8 mol acetic anhydride per mol AGU (anhydro glucose units) at 50 °C for 5 h.

During the acetosulfation, cellulose was converted totally into water-soluble CS or CAS except for the preparation of CS10. The yield of water-soluble CS10 was 71.9%.

2.2.2. Direct sulfation

For a typical non-homogeneous direct sulfation in DMF, chlorosulfuric acid (1.85 ml) or sulfamidic acid (9 g) in DMF was added into the suspension under vigorous stirring and the temperature of the mixture was raised to 50 °C. After 5 h, the solution was cooled down to RT and poured into a saturated ethanolic solution of anhydrous sodium acetate. After being collected and washed, the product was dissolved in water and the pH value of the solution was adjusted to 8.0 with acetic acid/ethanol (50/50, w/w). The solution was finally filtered, dialysed against demineralised water and lyophilised.

For a homogeneous direct sulfation, chlorosulfuric acid (1.85 ml) in DMF was added slowly into the cellulose solution in DMAc/LiCl mixture under stirring. After 5 h reaction at RT, the solution was poured into saturated ethanolic solution of anhydrous sodium acetate. Then the product was treated and purified as described above.

During the quasi-homogeneous and homogeneous sulfation, cellulose was converted completely into water-soluble CS. The yields of heterogeneously prepared CS29 and CS30 were 145.9% and 143%, respectively.

2.3. Measurements

The contents of carbon, hydrogen and nitrogen were determined with Elemental Analyser vario El from Elementar (Hanau, Germany). The content of sulphur was measured with Elemental Analyser Eltra CS 500 (Neuss, Germany). Total DS_S of CS were calculated according to the equation: Total $DS_S = (S\%/32)/(C\%/72)$.

The ^{13}C NMR spectra of CS in D_2O were recorded at RT on Bruker DFX 400 spectrometer (Bruker, Etlingen, Germany) with a frequency of 100.13 MHz, 30° pulse length, 0.35 acq. time and a relaxation delay of 3 s. Scans of up to 20,000 were accumulated.

The solid-state CP/MAS ^{13}C NMR was carried out using Bruker Avance 400 WB spectrometer at RT with a frequency of 100.65 MHz, 35 ms acquisition time and a relaxation delay of 3 s. Scans between 5000 and 7000 were accumulated.

FT Raman spectra of the samples in small aluminium discs were recorded on a Bruker MultiRam spectrometer Ge diode as detector that is cooled with liquid-nitrogen. A cw-Nd:YAG-laser with an exciting line of 1064 nm was applied as light source for the excitation of Raman scattering. The spectra were recorded over a range of 3500–150 cm^{-1} using an operating spectral resolution of 3 cm^{-1} and a laser power output of 100 mW. A double analysis per 400 scans was carried out for each sample. An average Raman spectrum was formed afterwards and the spectrum was vector-normalised in the range of 1600–720 or 3150–2650 cm^{-1} using the operating spectroscopy software OPUS Ver. 6.5 (Bruker).

The analysis of the data was executed with OriginPro 7.0 (OriginLab Corporation, MA, USA).

3. Results and discussion

3.1. Acetosulfation of cellulose

Cellulose could be sulfated through acetosulfation, i.e. simultaneous sulfation and acetylation of cellulose, by chlorosulfuric acid or sulphuric acid and acetic anhydride as sulfating and acetylating agent with subsequent saponification (Scheme 1). The reaction was

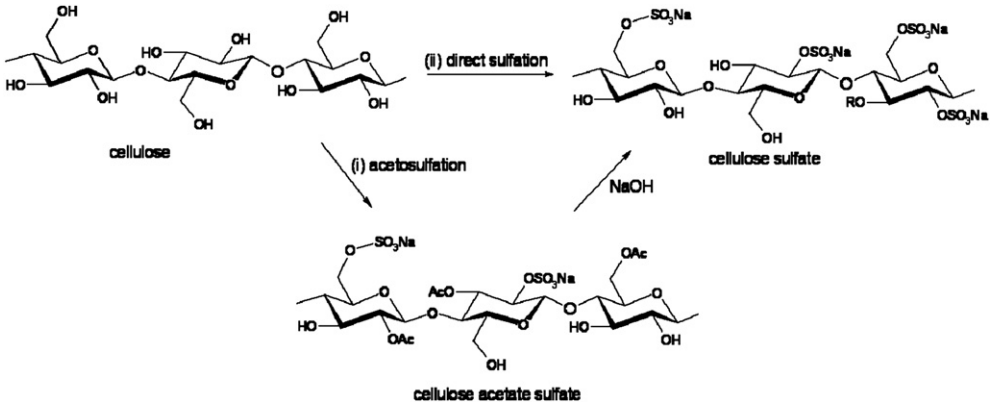

Scheme 1. Simplified reaction equation for the sulfation of cellulose. R = H or SO_3Na according to the total DS_S.

quasi-homogeneous because cellulose suspended in DMF was dissolved gradually in the reaction mixture during the acetosulfation, resulting in a homogeneous and optically transparent solution.

3.1.1. Preparation of CAS

The simultaneous competitive esterification of cellulose during the acetosulfation resulted in a water-soluble intermediate product – CAS. As described in experimental section, purified CAS1 could be obtained. According to solid-state CP/MAS ^{13}C NMR and FT Raman spectrum in Fig. 1, CAS1 contains both sulfate and acetyl groups.

Within the solid-state CP/MAS ^{13}C NMR spectrum of CAS1, the peaks at 174.8 and 21.8 ppm are visible and they are ascribed to carbonyl and methyl groups within the acetyl groups [27]. Using the peak of methyl groups, the DS attributed to acetyl groups (DS_{Ac}) of CAS1 were determined to be 1.2. After deacetylation of CAS1, CS13 was obtained and 73% of primary hydroxyl groups are sulfated, implying that the acetyl groups were located primarily at 2/3-*O*-position and 6-*O*-position was only partly acetylated.

Moreover, comparing the spectrum of CAS1 and cellulose, the signals derived from C1 and C6 shift upfield and downfield, respectively. These shifts are resulted from the substitution at 2- and 6-*O*-position by the sulfate and acetyl groups. The signals between 80 and 90 ppm ascribed to C4 are not observable within the spectrum of CAS1. Additionally, within the spectrum of CAS1 only a large peak lies between 70 and 80 ppm in contrast to two peaks attributed to C2, 3 and 5 of the AGU within the spectrum of cellulose. The mergence of the signals ascribed to C2, 3, 4 and 5 should be due to the change in the structure of cellulose. Before the acetosulfation, cellulose has a well-ordered structure which can be measured by solid-state ^{13}C NMR with good resolution [28]. After the substitution of the hydroxyl groups and the regeneration of CAS, the crystalline structure was destroyed and the product should be amorphous. Besides, the substitution by acetyl and sulfate groups results in the shifts of some NMR signals. As a total, the signals attributed to C2–5 are all under the signal between 70 and 80 ppm.

FT Raman spectroscopy delivers also the information about the substitution of the hydroxyl groups. As depicted in Fig. 1, new peaks at 1735, 1070 and 834 cm^{-1} immerge within the Raman spectrum of CAS1 compared to cellulose. The band at 1735 cm^{-1} is attributed to the stretching vibrations of carbonyl groups [29,30]. The other two bands at 1070 and 834 cm^{-1} are attributed to stretching vibrations of O=S=O and C–O–S groups [15,31]. In addition, the peak of the band attributed to vibrations of CH groups shifted from 2896 cm^{-1} to 2944 cm^{-1}. This shift possibly arises from the substitution of the hydroxyl groups and especially by acetyl groups which bring more CH groups into the cellulose backbone, leading to the shift of this peak and the increase of its intensity as well.

Apart from the chlorosulfuric acid, sulphuric acid has also been used for the preparation of CAS [32,33]. Moreover, CAS could be obtained after a homogeneous sulfation of cellulose acetate, leading to products with regioselectively distributed acetyl and sulfate groups [17,34].

3.1.2. Synthesis of CS

The synthesis of CS through the acetosulfation was completed after the cleavage of the acetyl groups using NaOH. The sulfation progress was investigated by evaluating a few important parameters

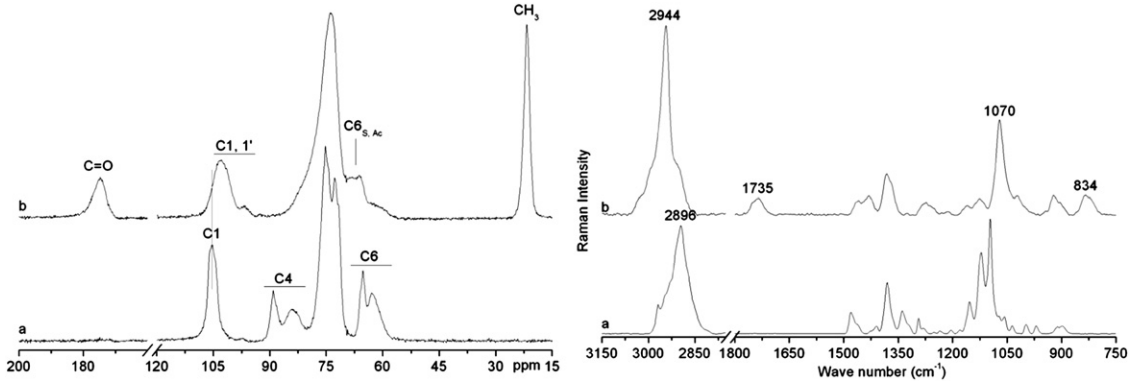

Fig. 1. Left: Solid-state CP/MAS ^{13}C NMR spectrum (200–15 ppm) of (a) MCC and (b) CAS1 at RT. Right: FT Raman spectrum (3150–750 cm^{-1}) of (a) MCC and (b) CAS1 at RT.

Table 1
Acetosulfation of cellulose with chlorosulfuric acid or sulphuric acid as sulfating agent and 8 mol acetic anhydride per mol AGU as acetylating agent.

Samples[a]	Starting materials	Molar ratios[b]	Reaction temperature (°C)	DS_S[c]		Total DS_S
				DS_{S6}	DS_{S2}	
CS1	AC	0.85	40	0.6	0.06	0.66
CS2	AC	0.55	50	0.35	0.03	0.38
CS3	AC	0.85	50	0.48	0.05	0.53
CS4	AC	3	50	0.77	0.15	0.92
CS5	AC	0.55	70	0.31	0.04	0.35
CS6	AC	0.85	70	0.34	0.02	0.36
CS7	AC	1.5	70	0.45	0.03	0.48
CS8	IC	0.85	50	0.52	0.06	0.58
CS9	IC	0.85	70	0.36	0.03	0.39
CS10	MCC	0.3	50	0.20	0.04	0.24
CS11	MCC	0.55	50	0.39	0.03	0.42
CS12	MCC	0.85	50	0.43	0.04	0.47
CS13	MCC	3	50	0.73	0.24	0.97
CS14	MCC	6	40	1	0.57	1.61[c]
CS15	MCC	0.3	70	0.18	0.035	0.21
CS16	MCC	0.4	70	0.21	0.025	0.23
CS17	MCC	0.7	70	0.30	0.04	0.34
CS18	MCC	0.85	70	0.38	0.03	0.41
CS19[a]	MCC	3	50	1	0.69	1.71[c]
CS20[a]	MCC	3	50	0.91	0.55	1.57[c]
CS21[a]	MCC	6	50	–	–	0.85[c]

[a] reaction duration for CS1 to 19 was 5 h and that for CS20 and 21 was 6 h.
[b] molar ratio in mol chlorosulfuric acid per mol AGU for CS1–18 and in mol sulphuric acid per mol AGU for CS19–21. Acetic anhydride of 4 and 2 mol per mol AGU was used for the preparation of CS14 and CS21, respectively.
[c] DS_{S6} and DS_{S2} were analysed with ^{13}C NMR spectroscopy. The total DS_S of CS1–13 and 15–18 are equal to the sum of DS_{S6} and DS_{S2}. The total DS_S of CS14, 19, 20 and 21 were determined via elemental analysis.

that can affect the total DS_S and sulfation patterns, such as starting materials, the amount of sulfating agent, reaction temperature and duration. The total DS_S of CS were determined via elemental analysis or ^{13}C NMR and are listed in Table 1. According to the data, various CS with diverse total DS_S were obtained.

Characteristic ^{13}C NMR spectra of CS in D_2O are displayed in Fig. 2. A new signal at 66.3 ppm beside the signal at 60 ppm is visible. Because both signals are derived from C6 of AGU, the DS_{S6} can be calculated based on the integrals of both signals [13,35]. Moreover, the signal of C1 shifts from 102.5 ppm to 100.5 ppm as shown in Fig. 1b–d, which is due to the influence of the sulfation at 2-*O*-position. Based on the integrals of the two peaks ascribed to C1, the DS_{S2} can be estimated. Without the signal at 60 and 100.5 ppm, the partial DS_{S6} and DS_{S2} can be regarded as 1 (Fig. 2d). In addition, new peaks between 80 and 82 ppm are notable which are ascribed

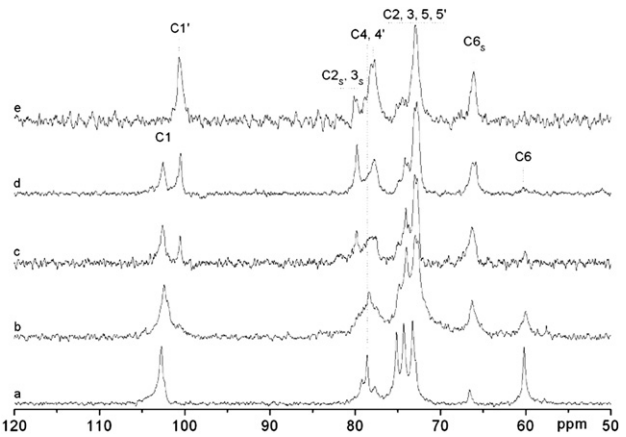

Fig. 2. ^{13}C NMR spectra (120–50 ppm) of (a) CS24 (total $DS_S = 0.2$), (b) CS1 (total $DS_S = 0.66$), (c) CS32 (total $DS_S = 1.09$), (d) CS20 (total $DS_S = 1.57$) and (e) CS28 (total $DS_S = 2.59$) in D_2O at RT.

to C2 and C3 with sulfate groups at 2 and 3-*O*-positon [13,15,35]. Other signals attributed to C2, 3, 4 and 5 lie between 70 and 80 ppm within the spectra of CS (Table 2).

Exhibiting distinct partial DS_S as listed in Table 1, CS with diverse sulfation patterns were synthesized. The 6-*O*-position was primarily sulfated in comparison to 2- and 3-*O*-position. Using low amount of chlorosulfuric acid, the sulfate groups are mostly located at 6-*O*-position. Appling high amount of chlorosulfuric acid (6 mol per mol AGU) or sulphuric acid (3 mol per mol AGU), complete sulfation at 6-*O*-position and intensive sulfation at 2-*O*-position were achieved. These results indicate the high reactivity of primary hydroxyl groups towards sulfation during the acetosulfation, while the secondary hydroxyl groups may be preferably acetylated. After the deacetylation, CS with intensely sulfated 6-*O*-position were obtained in comparison to the other two positions.

In this report, three celluloses were used for the acetosulfation and they have different crystallinities in the order of MCC (67.1%) > AC (50.4%) > IC (48.8%) which were determined with the method as described in Ref. [36]. As presented in Table 1, starting material seems to affect the total DS_S at 70 °C only very slightly, because CS with similar total DS_S were prepared from three different celluloses under other equal reaction conditions. However, at 50 °C with the application of 0.85 mol chlorosulfuric acid and 8 mol acetic anhydride per mol AGU, the CS from IC exhibits the highest total DS_S and the CS from MCC the lowest. Thus, the crystallinity of cellulose may be important for the sulfation at 50 °C and can affect the total DS_S of prepared CS. On the other hand, no correlation between the total DS_S of CS and the DP value of cellulose is notable.

Moreover, the amount of sulfating agent is another important parameter for regulating the total DS_S, because the total and partial DS_S of CS increase with elevating amount of sulfating agent as shown in Table 1. Varying the amount of chlorosulfuric acid between 0.3 and 6 mol per mol AGU, the total DS_S between 0.21 and 1.61 with the DS_{S6} between 0.18 and 1 were determined. Simultaneously, partial DS_{S6} rise from 0.18 to 1 and partial DS_{S2} of up to 0.57 was achieved. In addition, the sulphuric acid can be used as sulfating agent and it demonstrated higher capacity towards sulfating cellulose in comparison to chlorosulfuric acid regarding the total and partial DS_S of prepared CS using both sulfating agents under other equal reaction conditions, e.g. CS4, 13 and CS19, 20. Normally, sulphuric acid acts as an activator during the acetylation of cellulose with acetic anhydride [17], but according to CS19–21, also CS with high total DS_S could be prepared after deacetylation of the intermediate products.

Furthermore, high reaction temperature reduced the total DS_S and DS_{S6}, comparing the DS_S of CS prepared at 50 and 70 °C [13]. Similarly, the sulfation duration could influence the total and partial DS_S of CS and they sink with longer reaction duration at 70 °C. According to Table 3, total DS_S and DS_{S6} of 0.68 and 0.55 were observed for CS22 which was prepared after the reaction temperature of 70 °C was reached. With longer sulfation durations through 0.5, 5–24 h, the total DS_S drop to 0.51, 0.41 and 0.2. After 24 h reaction, the DS_{S6} sink significantly to 0.2 and no sulfation at 2-*O*-

Table 2
Assignment of the signals within ^{13}C NMR of CS in D_2O.

Signals (in ppm)	Carbons within repeating units
102.5	C1
100.5	C1′
80–82	$C2_S$, $C3_S$
78.6	C4
78.4–77.7	C4′
70–75	C2, 3, 5, 5′
66.3	$C6_S$
60	C6

Table 3
Acetosulfation of MCC with 0.85 mol chlorosulfuric acid and 8 mol acetic acid per mol AGU at 70 °C.

Samples	Reaction duration (h)	DS_S[a]		Total DS_S
		DS_{S6}	DS_{S2}	
CS22	(only heating to 70 °C)[b]	0.55	0.13	0.68
CS23	0.5	0.45	0.06	0.51
CS18	5	0.38	0.03	0.41
CS24	24	0.20	0	0.20

[a] The DS_S were determined via ^{13}C NMR and the total DS_S are equal the sum of the DS_{S6} and DS_{S2}.
[b] For CS22 the reaction was stopped after the reaction temperature of 70 °C was reached and no further heating was executed.

position is visible. It can be assumed that the sulfation of cellulose with high sulfation temperature and long sulfation duration proceeds with severe side-reactions, such as a degradation of cellulose by the acid or a displacement of sulfate groups by acetyl groups [32]. Subsequently, both the total and partial DS_S are reduced remarkably.

As a result, CS with distinct total and partial DS_S, i.e. diverse sulfation patterns, were prepared. The total DS_S and the sulfation patterns can be regulated by varying the reaction parameters as discussed above.

3.2. Direct sulfation of cellulose

Direct sulfation of cellulose could proceed quasi-homogeneously in DMF using chlorosulfuric acid, heterogeneously in DMF using sulfamidic acid or homogeneously in DMAc/LiCl mixture (Fig. 2c–e, Table 4) [15,17,37,38]. During the homogeneous sulfation of cellulose, cellulose remained dissolved in the reaction medium throughout the sulfation, while cellulose stayed non-dissolved during the heterogeneous sulfation. The quasi-homogeneous sulfation of cellulose stands for the sulfation starting with heterogeneously dispersed cellulose and ending with a homogeneous solution. In order to prepare water-soluble CS, high amounts of sulfating agents were required during the non-homogeneous direct sulfation, while homogeneous direct sulfation could be conducted also with low amount of chlorosulfuric acid.

After quasi-homogeneous direct sulfation using chlorosulfuric acid, CS with high total DS_S could be obtained. The DS_{S6} were determined always to be 1 after sulfation at RT and 2-*O*-position was intensively or completely sulfated. Using 13 mol chlorosulfuric acid per mol AGU after 2.5 h sulfation, a high total DS_S of 2.59 could be reached.

Table 4
Direct sulfation of cellulose and characterisation of CS.

Samples[a]	Starting materials	Molar ratios[b]	Reaction temperature (°C) /duration (h)	Partial DS_S[c]		Total DS_S[c]
				DS_{S6}	DS_{S2}	
CS25	MCC	4.5	RT/6	1	0.80	2.15
CS26	MCC	6	RT/3	1	0.79	1.99
CS27	MCC	13	RT/3	1	0.94	2.28
CS28	MCC	13	RT/2.5	1	1	2.59
CS29[c]	MCC	6	80/5	1	0.81	1.89
CS30[c]	MCC	15	70/24	0.83	0.59	1.78
CS31	MCC	2	RT/5	0.55	0	0.57
CS32	MCC	3	RT/5	0.8	0.22	1.09
CS33	MCC	4.5	RT/5	1	0.84	1.85

[a] Quasi-homogeneous sulfation for CS25–28, heterogeneous sulfation for CS29-30 and homogeneous sulfation for CS31–33.
[b] Molar ratio in mol chlorosulfuric acid (CS25–28, 31–33) or sulfamidic acid (CS29, 30) per mol AGU.
[c] The partial DS_S were estimated with ^{13}C NMR spectroscopy and the total DS_S were determined via elemental analysis.

In comparison to chlorosulfuric acid, sulfamidic acid could only sulfate cellulose heterogeneously at high reaction temperature of 70 or 80 °C and high total DS_S were obtained (Table 4). Both 2- and 6-*O*-position could be intensely or totally sulfated. High sulfation temperature seems to be important for complete sulfation of primary hydroxyl groups comparing CS29 and 30, although much lower amount of sulfamidic acid was used for preparation of CS29.

Through the homogeneous direct sulfation at RT, water-soluble CS with diverse total DS_S were prepared, which is different from the previous statement [38]. This difference may lie in the celluloses used in both reports. MCC used in this report should have a much lower DP value than the spruce sulfite pulp (normally having a DP value of 750) in [38], which facilitated the dissolution and then the derivatisation of cellulose. The total DS_S increase with rising amount of applied chlorosulfuric acid. Similar to non-homogeneous direct sulfation, the homogeneous direct sulfation resulted in CS with the sulfate groups located mainly at 6/2-*O*-position and the 6-*O*-position was more preferably sulfated (Table 4).

Compared to 2- and 6-*O*-position, the 3-*O*-position was much lower sulfated, which should be due to the sterically hampered accessibility of the hydroxyl groups at this position [17,39]. This selective substitution of 2- and 6-*O*-position has also been detected during other derivatisations of cellulose [17,39–42]. Consequently, the 2- and 6-*O*-position show higher reactivity during the direct sulfation. Even though cellulose was dissolved in DMAc/LiCl mixture before the sulfation, no significant enhancement of the reactivity of the hydroxyl groups at 3-*O*-position was notable.

3.3. Solid-state CP/MAS ^{13}C NMR of CS

Besides the ^{13}C NMR in D_2O, solid-state CP/MAS ^{13}C NMR can be used to characterise CS. Within the spectrum of cellulose as shown in Fig. 3a, the signals between 80 and 90 ppm are attributed to the C4 and the signals between 60 and 66 ppm are ascribed to C6. The peaks at 89.1 and 65.2 ppm are due to C4 and C6 of the crystalline parts within cellulose, while the peaks at 83.8 and 62.8 ppm are derived from the amorphous parts [28]. The signal at 105 ppm is attributed to C1, as the signals of C2, 3 and 5 are notable between 70 and 80 ppm. After the sulfation (Fig. 3b–d), the signal of C1 is broader and shifts upfield. The signal with peak maximum between 70 and 75 ppm becomes the dominant one within the spectrum. A shoulder between 65 and 70 ppm is visible which is because of the sulfation at 6-*O*-position. The peaks ascribed to C4 and C6 of the crystalline parts of cellulose are strongly decreased (CS29) or

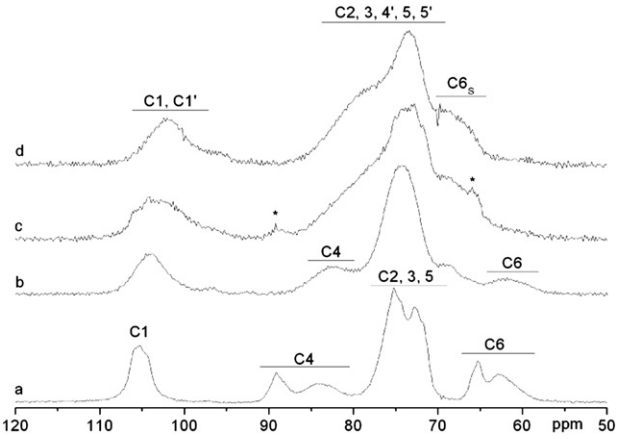

Fig. 3. Solid-state CP/MAS ^{13}C NMR spectra (120–50 ppm) of (a) MCC, (b) CS3 (total $DS_S = 0.53$), (c) CS29 (total $DS_S = 1.89$) and (d) CS28 (total $DS_S = 2.59$) at RT. * for the peaks at 89.2 and 65.9 ppm.

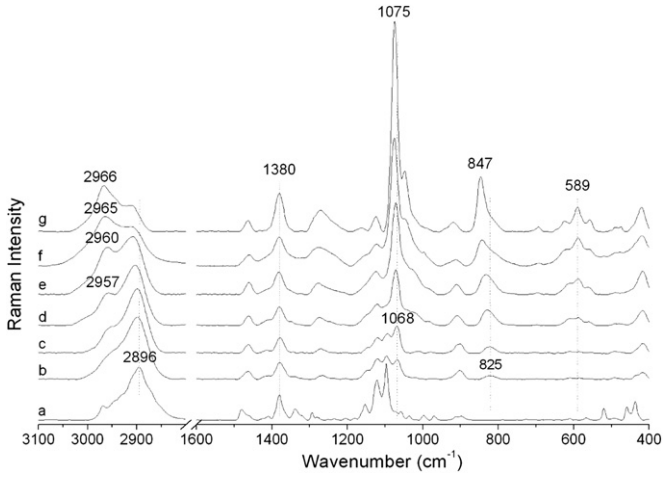

Fig. 4. FT Raman spectra (3100–400 cm^{-1}) of (a) cellulose, (b) CS10 (total $DS_S = 0.24$), (c) CS12 (total $DS_S = 0.47$), (d) CS4 (total $DS_S = 0.92$), (e) CS20 (total $DS_S = 1.57$), (f) CS29 (total $DS_S = 1.89$) and (g) CS28 (total $DS_S = 2.59$) at RT.

disappeared (CS3 and 28), suggesting the destruction of the crystalline parts during the sulfation of cellulose. Within the spectrum of CS 28, no signal between 60 and 66 ppm is observable, indicating the sulfation of all primary hydroxyl groups.

However, within the spectrum of CS29, small peaks at 89.2 and 65.9 ppm ascribed to the crystalline regions are still notable. Thus, very small parts of crystalline region may be maintained during the heterogeneous sulfation for preparation of CS29.

3.4. FT Raman spectroscopic analysis

FT Raman spectroscopy is a promising method in characterising cellulose derivatives including CS and carboxymethyl cellulose [15,43]. As shown in Fig. 4, new signals emerge at 589, 825–847 and 1068–1075 cm^{-1} comparing the Raman spectra of CS and cellulose. The band between 825 and 847 cm^{-1} is attributed to stretching vibrations of C–O–S groups. The other two bands are derived from deformation and symmetric stretching vibrations of O=S=O groups within sulfate groups [15,31]. Regarding the peaks in the range of 825–847 cm^{-1} and 1068–1075 cm^{-1}, both peaks shifted to higher wave numbers with rising total DS_S. On the other hand, the band at 589 cm^{-1} remains constant despite increasing total DS_S. This difference of these peaks could be due to the diverse types of the vibrations.

Moreover, the change of the signals ascribed to stretching vibrations of CH and CH_2 groups in the range of 2800–3050 cm^{-1} is visible. After the sulfation of cellulose, the band at 2896 cm^{-1} becomes weaker and a new band between 2950 and 2966 cm^{-1} is notable. With increasing total DS_S, this new band shifts to higher wave numbers and becomes more intensive. Within the spectra of CS with low total DS_S (e.g. below 0.47), this signal at 2950–2955 cm^{-1} appears only as a shoulder of the peak at 2896 cm^{-1}. However, within the spectra of CS exhibiting high total DS_S, especially the total DS_S of more than 1, this signal has a strong intensity. Finally, within the spectrum of CS showing total DS_S of more than 1.5, this new band is the dominant one, while the signal at 2896 cm^{-1} turns into a shoulder of this new band.

Table 5
Linear regression parameters for the calibration curves in Fig. 5.[a]

Normalization ranges	Ratios of band intensities	*a*	*b*	*r*	SD	*p*	*n*
1600–720 cm^{-1}	I_{830}/I_{1380}	0.1383	0.5039	0.9669	0.1030	<0.0001	26
	I_{1070}/I_{1380}	0.7875	2.0573	0.9800	0.3232	<0.0001	26
3150–2650 cm^{-1}	I_{830}/I_{1380}	0.1460	0.4984	0.9658	0.1037	<0.0001	26
	I_{1070}/I_{1380}	0.8072	2.0529	0.9793	0.3283	<0.0001	26

[a] $Y = a + bX$; where Y is the Raman band intensity ratios between the peaks at 1070 or 830 cm^{-1} and the internal standard at 1380 cm^{-1}. X is the total DS_S, a is the Y-intercept, b is the slope, r is the correlation coefficient, SD is the standard deviation, p is the significance level and n is sample volume.

For the purpose of quantifying the total DS_S, proper Raman analysis parameters should be applied. Besides the area of the band between 825 and 847 cm^{-1} that has been used for the quantification of the total DS_S [15], the bands arisen from the sulfate groups can also be considered, e.g. the band between 1068 and 1075 cm^{-1}. In addition, the band intensity instead of the band area can be applied for the quantification. Hence, Raman band intensities of the bands at 1068–1075, 825–847 cm^{-1} and 1380 cm^{-1} were acquired from the spectra of CS. The band at 1380 cm^{-1} is attributed to the vibrations of cellulose backbone. It should be stable towards the introduction of sulfate groups and can therefore be used as internal standard. The band intensity ratios between the marker bands and the internal standard (i.e. I_{830}/I_{1380} and I_{1070}/I_{1380}) were calculated and used as analysis parameters. Besides, two distinct normalization ranges were chosen for the acquirements of the band intensities, namely 3150–2650 and 1600–720 cm^{-1}, in order to find out if the normalization range could affect the quantification.

After plotting Raman band intensity ratios against the total DS_S, calibration curves with high correlation coefficients of more than 0.96 were generated (Fig. 5 and Table 5). As demonstrated, the calibration with the intensity ratio I_{1070}/I_{1380} as analysis parameter provides slightly higher correlation coefficients than the calibration with I_{830}/I_{1380} as analysis parameter. Moreover, the normalization ranges do not have a significant effect on the quantification

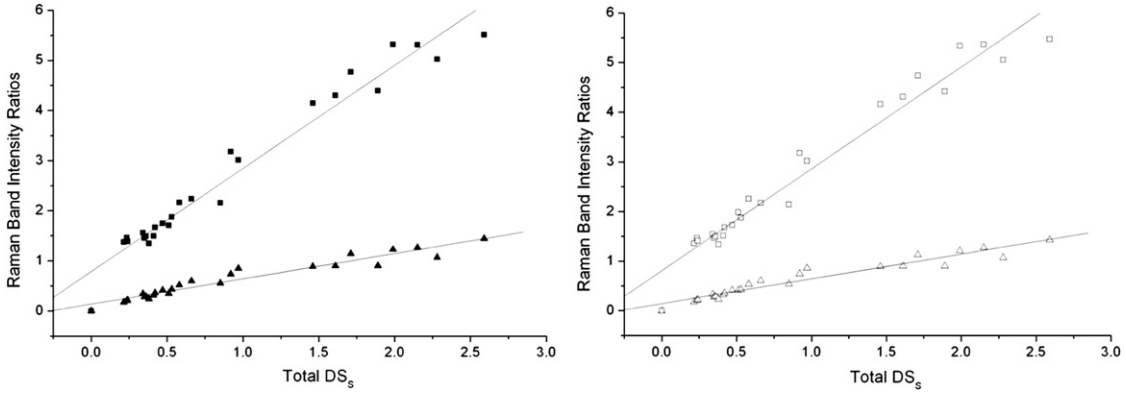

Fig. 5. Calibration curves with the normalization in the range of 1600-720 (left) and 3150–2650 (right) after plotting the total DS_S against Raman band intensity ratios in ▲ and △ for I_{830}/I_{1380} or in ■ and □ for I_{1070}/I_{1380}.

according to Table 5 and both can be applied for the establishment of quantifying method via Raman spectroscopy.

4. Conclusion

Various CS showing diverse total and partial DS_S were prepared through direct sulfation and acetosulfation of cellulose with chlorosulfuric acid, sulphuric acid or sulfamidic acid. During the acetosulfation of cellulose, CAS was formed as intermediate product and could be converted into CS after following deacetylation. Acetosulfation of cellulose could be realised with low or high amount of sulfating agent, while high amount of sulfating agents were necessary for the non-homogeneous direct sulfation of cellulose, in order to prepare water-soluble CS. Homogeneous direct sulfation was conducted on cellulose dissolved in DMAc/LiCl, yielding water-soluble CS with low or high total DS_S.

The total DS_S of 0.21–2.59 and partial DS_{S6} as well as DS_{S2} of maximal 1 were determined for obtained CS. The total and partial DS_S of CS can be regulated by varying the reaction parameters including starting materials, the amount of the sulfating agents, reaction temperature and duration. Compared to previous studies, all CS exhibiting total DS_S in a wide range were prepared after one-step synthesis and these CS are well water-soluble. Moreover, almost all CS obtained in this report were synthesized under quasi-homogeneous or homogeneous conditions. These sulfation progresses may result in uniform distributions of sulfate groups along the cellulose chains.

The sulfation of cellulose under diverse reaction states could be analysed via solid-state CP/MAS ^{13}C NMR spectroscopy.

FT Raman spectroscopic analysis of CS confirms the introduction of sulfation groups into cellulose chains. The characteristic bands ascribed to the vibrations of O═S═O groups at 1070 cm^{-1} and C–O–S groups around 830 cm^{-1} can be used for the quantification of the total DS_S. Plotting the intensity ratios between the Raman bands at 1070 or 830 cm^{-1} and 1380 cm^{-1} against the total DS_S, calibration curves with high correlation coefficients of more than 0.96 were obtained.

Acknowledgement

The financial support from German Research Foundation (Deutsche Forschungsgemeinschaft, grants: FI755/4-1 and FI755/4-2, GR1290/7-1 and GR1290/7-2) is gratefully acknowledged.

References

[1] Ai X, Do AT, Lozynska O, Kusche-Gullberg MK, Lindahl U, Emerson CPJ. J Cell Biol 2003;162:341–51.
[2] Rabenstein DL. Nat Prod Rep 2002;19:312–31.
[3] Mulloy B, Mourão PAS, Gray E. J Biotechnol 2000;77:123–35.
[4] Groth T, Wagenknecht W. Biomaterials 2001;22:2719–29.
[5] Leali D, Belleri M, Urbinati C, Coltrini D, Oreste P, Zoppetti G, et al. J Biol Chem 2001;276:37900–8.
[6] Liekens S, Leali D, Neyts J, Esnouf R, Rusnati M, Dell'Era P, et al. Mol Pharmacol 1999;56:204–13.
[7] Parish CR, Freemann CF, Brown KJ, Francis DJ, Cowden WB. Cancer Res 1999;59:3433–41.
[8] Saake B, Puls J, Wagenknecht W. Carbohydr Polym 2002;48:7–14.
[9] Dautzenberg H, Schuldt U, Lerche D, Woehlecke H, Ehwald R. J Membr Sci 1999;162:165–71.
[10] Stadlbauer V, Stiegler PB, Schaffellner S, Hauser O, Halwachs G, Iberer F, et al. Xenotransplantation 2006;13:337–43.
[11] Zhang J, Yao S, Guan Y. J Membr Sci 2005;255:89–98.
[12] Yamamoto I, Takayama K, Matsuzaki K, Hatanaka K, Uryu T, Yamamoto N, et al. Carbohydr Polym 1991;14:53–63.
[13] Peschel D, Zhang K, Aggarwal N, Brendler E, Fischer S, Groth T. Acta Biomater 2010;6:2116–25.
[14] Wang ZM, Li L, Xiao KJ, Wu JY. Bioresour Technol 2009;100:1687–90.
[15] Zhang K, Brendler E, Fischer S. Cellulose 2010;17:427–35.
[16] Baumann H, Richter A, Klemm D, Faust V. Macromol Chem Phys 2000;201:1950–62.
[17] Klemm D, Philipp B, Heinze T, Heinze U, Wagenknecht W. Comprehensive cellulose chemistry. 1st ed., vol. 2. Weinheim: Wiley; 1998.
[18] Wang ZM, Li L, Zheng BS, Normakhamatov N, Guo SY. Int J Biol Macromol 2007;41:376–82.
[19] Schlessinger J, Plotnikov A, Ibrahimi OA, Eliseenkova AV, Yeh BK, Yayon A, et al. Mol Cell 2000;6:743–50.
[20] Pye DA, Vivès RR, Turnball JE, Callagher JT. J Biol Chem 1998;273:22936–46.
[21] Pye DA, Vivès RR, Hyde P, Gallagher JT. Glycobiology 2000;10:1183–92.
[22] Gama CI, Tully SE, Sotogaku N, Clark PM, Rawat M, Vaidehi N, et al. Nat Chem Biol 2006;2:467–73.
[23] Nishimura S, Kai H, Shinada K, Yoshida T, Tokura S, Kurita K, et al. Carbohyd Res 1998;306:427–33.
[24] Zou Y, Khor E. Carbohyd Polym 2009;77:516–25.
[25] Zhou H, Qian J, Wang J, Yao W, Liu C, Chen J, et al. Biomaterials 2009;30:1715–24.
[26] Erler U, Klemm D, Nehls I. Makromol Chem Rapid Commun 1992;13:195–201.
[27] Kono H, Erata T, Takai M. J Am Chem Soc 2002;124:7512–8.
[28] Larsson PT, Wickholm K, Iversen T. Carbohydr Res 1997;302:19–25.
[29] VanderHart DL, Hyatt JA, Atalla RH, Tirumalai VC. Macromolecules 1996;29:730–9.
[30] Guo Y, Wu P. Carbohydr Polym 2008;74:509–13.
[31] Cabassi F, Casu B, Perlin AS. Carbohydr Res 1978;63:1–11.
[32] Chauvelon G, Buléon A, Thibault J, Saulnier L. Carbohydr Res 2003;338:743–50.
[33] Thomas M, Chauvelon G, Lahaye M, Saulnier L. Carbohydr Res 2003;338:761–70.
[34] Wagenknecht W. Das Papier 1996;50:712–20.
[35] Nehls I, Wagenknecht W, Philipp B, Stscherbina D. Prog Polym Sci 1994;19:29–78.
[36] Schenzel K, Fischer S, Brendler E. Cellulose 2005;12:223–31.
[37] Schweiger RG. Carbohydr Res 1972;21:219–28.
[38] Wagenknecht W, Philipp B, Keck M. Acta Polym 1985;36:697–8.
[39] Klemm D, Heublein B, Fink HP, Bohn A. Angew Chem 2005;117:3422–58.
[40] Heinze T. Macromol Chem Phys 1998;199:2341–64.
[41] Klemm D, Heinze T, Philipp B, Wagenknecht W. Acta Polym 1997;48:277–97.
[42] Zhou J, Zhang L, Deng Q, Wu X. J Polym Sci Polym Chem 2004;42:5911–20.
[43] Yuen S, Choi S, Phillips DL, Ma C. Food Chem 2009;114:1091–8.

Polymer 52 (2011) 33–39

Contents lists available at ScienceDirect

Polymer

journal homepage: www.elsevier.com/locate/polymer

Microwave synthesis: An alternative approach to synthesize conducting end-capped polymers

Pierre Marcasuzaa [a], Stéphanie Reynaud [a,*], Bruno Grassl [a], Hugues Preud'homme [b], Jacques Desbrières [a], Miroslava Trchová [c], Olivier F.X. Donard [b]

[a] IPREM-EPCP, Hélioparc, 2 avenue du président Angot, 64053 Pau cedex 9, France
[b] IPREM-LCABIE, UMR 5254 (CNRS/UPPA), Hélioparc, 2 avenue du président Angot, 64053 Pau cedex 9, France
[c] Institute of Macromolecular Chemistry, Academy of Sciences of the Czech Republic, 162 06 Prague 6, Czech Republic

ARTICLE INFO

Article history:
Received 6 July 2010
Received in revised form
8 November 2010
Accepted 9 November 2010
Available online 18 November 2010

Keywords:
Tetra-aniline
Microwave synthesis
Intrinsically conducting polymers

ABSTRACT

Within this study microwave assisted syntheses of functionalized polystyrene (PS), via ATRP, and tetra-aniline (TANI) end-capped polymers are demonstrated. Compared to conventional heating, microwave irradiation process in pulsed mode shows the feasibility of conducting end-capped polymers synthesis with no degradation, strong acceleration of polymerization rate and coupling reaction, controlled size and chemical formulation. Conducting polymers with controlled architectures in terms of molecular size of both the insulating (PS) and the conducting (TANI) moieties show a conductivity above 10^{-1} S cm^{-1} when containing 2 wt% TANI while composites of PS and TANI exhibited a conductivity of *ca* 10^{-5} S cm^{-1} when containing more than 7 wt% TANI.

1. Introduction

Microwave heating represents a major breakthrough in synthetic chemistry as it can be considered considerably more efficient than conventional heating methods. While microwave energy was developed from the middle of the 20th century onwards, its application to organic chemistry was not explored until the mid-1980s [1,2]. In current polymer science, the use of microwave-assisted polymer synthesis has been widely investigated and reviews have appeared in recent years [3–7]. Few are dedicated to controlled radical polymerizations [3,5–7] such as nitroxide mediated polymerization, atom transfer radical polymerization (ATRP) and reversible addition fragmentation chain-transfer polymerization (RAFT). Multi-mode domestic microwave ovens, as used until recently, were not designed for the requirements of the laboratory and most of the problems arise due to concerns around experimental accuracy (temperature and pressure monitoring). A brief overview of the results of microwave-assisted ATRP, as example, reveals contradictory conclusions. If we consider the most studied monomer, methyl methacrylate (MMA), its copper catalyzed ATRP has been reported in bulk with a good control and a greatly increased propagation rate by Li et al. [8] while other authors [9] did not find any improvement of the reaction rate when performed this polymerization in *p*-xylene. Same controversies have been revealed in polar solvent [10] or on the ruthenium-catalyzed [11]. Up to know, only one article has been published on ATRP and reverse-ATRP of styrene under microwave irradiation [12]. The polymerizations were conducted under pulsed microwave irradiation in DMF and better polymerization control has been observed via reverse-ATRP as shown by a chain extension experiment.

On the other hand, in the field of intrinsically conducting polymers (ICPs) composite, conducting properties are known to be difficult to obtain at low percolation threshold because of the incompatibility of the ICPs, and among them polyaniline (PANI), with common polymer matrix. By considering PANI itself, efforts have been made to avoid this drawback; this includes the blending methods or chemical process. Blends may be obtained via thermal processing, however the chemical formulation usually requires the use of additives and low percolation threshold remains difficult to reach [13,14]. A chemical approach may be used to favour the dispersion of the ICP within a polymer matrix as PANI functionalization either on PANI backbone [15,16] or dopant [17–19]. This method, however, suffers from multi-step synthesis and/or the use of toxic and corrosive solvents [20–24] and has to be systematically optimized to the matrix. An alternative method has been developed

* Corresponding author.
E-mail address: stephanie.reynaud@univ-pau.fr (S. Reynaud).

0032-3861/$ – see front matter © 2010 Elsevier Ltd. All rights reserved.
doi:10.1016/j.polymer.2010.11.016

avoiding as much as possible the use of any organic solvent *i.e.* the synthesis in aqueous dispersed phase [25–28]. Again this strategy often needs the help of additives to reach an acceptable conductivity (above 10^{-3} S cm^{-1}) at low PANI content (below 5 wt%). Other authors studied the synthesis of block copolymer insulating polymer-PANI. Nevertheless, the architecture is not easy to control when using PANI since the molar mass of this polymer is difficult to predict or tailor [29,30] thus affecting the percolation threshold. In this context, it is easy to understand that attention has been paid to oligomers of aniline. Phenyl/phenyl or phenyl/amine end-capped octa-aniline [31] and tetra-aniline [32–34] have been already described as models of polyaniline exhibiting good conductivity values and enhanced solubility in common solvents. Nevertheless, most of the synthetic routes require complicated steps, or leads to a mixture of oligomers. Good conductivity results have been reported on copolymers obtained from multi-step synthesis of composites made of polymer matrix and oligo-aniline [35,36]. Another article deals with the synthesis of polymers containing a tetra-aniline block [37] even though there is no report on tetra-aniline characterization nor conductivity measurements. Nevertheless, the efficiency of the coupling route was demonstrated to obtain well defined arm-capped star polymers.

Previous study has been made in our group demonstrated that controlled NMP of acrylamide in water is achievable under microwave irradiation along with a strong acceleration of the polymerization process (>50 times). Encouraged by the above results, as a part of our research to prepare conducting materials with architecture control [14,38], we here report the synthesis of conducting end-capped polymer *i.e.* (insulating polymer)-TANI by using another way of controlled radical polymerization both under conventional heating and microwave irradiation. Based on our knowledge, study on the irradiated microwave synthesis of conducting end-capped polymers having well defined tetra-aniline end-group has not been reported. Thus we focussed on microwave synthesis for both polymer synthesis and end-chain modification as described within Fig. 1 and made a comparison with polymers obtained under conventional heating.

The telechelic TANI end-capped polystyrene (PS) were synthesized using ATRP in bulk. The precursor succinimide-terminated polymers were subsequently functionalized with oligo-aniline to obtain the conducting polymer. Special attention was given to the comparison between conventional (oil bath) and microwave (MW) heating in terms of reaction time, molar mass control and the properties of the final product.

2. Experimental section

2.1. Microwave irradiation method

A discover single-mode microwave synthesizer (from CEM Corp.) was used, this apparatus allows controlling many parameters as temperature, power, cooling and stirring. Standard microwave-transparent Pyrex microwave process vials (obtained from CEM) have been employed for all the experiments under microwave irradiation. The experimental conditions (temperature and irradiation power) used for the polymerization are reported within the figure legends.

2.2. Materials

Styrene was purified by passing through a basic alumina column. Copper (I) bromide (CuBr) was purified as previously described [39]. All other reagents were from commercial sources and used as received unless noted.

2.3. Procedures

Initiator (NHSBr) [37]: 500 mL round-bottom flask equipped with a magnetic stirrer and a reflux condenser was charged with 2-bromoisobutyric acid (1.670 g, 0.010 mol) and *N*-hydroxysuccinimide (1.380 g, 0.012 mol) in 200 mL dichloromethane. The reaction mixture is then heated up at 60 °C under stirring to a complete solubilisation, dicyclohexylcarbodiimide (2.060 g, 0.010 mol, in 10 mL of dichloromethane) was slowly added via syringe. The reaction mixture was stirred at 60 °C for 24 h. A white insoluble by-product was obtained and separated by filtration. The organic layer was washed three times with 150 mL of distilled water and dried over sodium sulfate. The solution was concentrated under vacuum and the crude product purified by recrystallization in heptane. Yield: 90% as white crystals. ^{1}H NMR (DMSO-d_6): 2.06 (s, 6H, Br–C(CH_3)$_2$–CO–), 2.80 (s, 4H, –OCH_2–CH_2–CO–).

ATRP under microwave irradiation: 10 mL Glass tube (CEM Corporation) equipped with a magnetic stirrer was charged with CuBr, initiator and 5 mL of styrene. The tube was deoxygenated by nitrogen bubbling for 5 min before adding *N*,*N*,*N*′,*N*″,*N*″-pentamethyldiethylenetriamine (PMDETA) via syringe. The vessel was then carefully end-capped under nitrogen before being introduced inside the microwave reactor. Pressure, temperature and irradiation power were monitored via SPS mode throughout the polymerization. At the end of the reaction, the monomer conversion was measured by ^{1}H NMR based on residual monomer to the polymer peaks. Withdrawn samples were diluted with THF; the copper complex was removed by passing the solution through an alumina column before filtering it through a 0.45 μm membrane. The number-average molar mass (M_n) and polydispersity (M_w/M_n) was then determined by size exclusion chromatography (SEC) in tetrahydrofuran (THF), using a Waters Styragel HR 05, HR2, HR4 and HR6 and polystyrene standard calibration.

ATRP under conventional heating: 25 mL round-bottom flask equipped with a magnetic stirrer was charged with CuBr, initiator and 5 mL of styrene. The flask was deoxygenated by nitrogen bubbling during 5 min before adding PMDETA via syringe. The flask is then carefully end-capped under nitrogen before to be placed into an oilbath at the polymerization temperature. The characterization of the product is then conducted as detailed above.

Tetra-aniline [40] (TANI): 250 mL round-bottom flask equipped with a magnetic stirrer was charged with diphenylamine (2.700 g, 0.016 mol) and 4-4′diaminodiphenylamine (5.600 g, 0.016 mol) in a mixture of 100 mL of DMF, 20 mL of distilled water, and 15 mL of HCl (1 M). After complete dissolution, an aqueous solution of ammonium persulfate (3.648 g, 0.016 mol) (APS) in 10 mL of

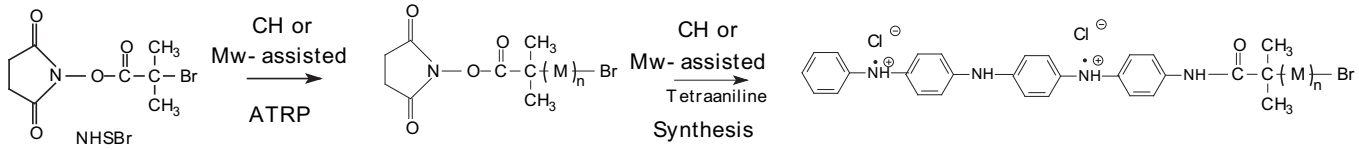

Fig. 1. Synthesis routes of HCl-doped TANI end-capped polymers either by conventional heating (CH) or under microwave irradiation (MW).

distilled water was added dropwise at 5 °C under stirring and the reaction mixture was stirred for 1 h at 5 °C. The final product was purified by precipitation in distilled water and washed with HCl 1 M. 7.0 g of dark green powder (HCl-doped TANI) is obtained (yield = 80%). The conductivity of compressed pellets (under 5000 kg cm^{-2}) was determined using the standard four-point probe technique at room temperature. The sample exhibits a conductivity of 5 S cm^{-1}. TANI UV characterization *versus* pH is close to those of PANI and reveals the transition from the doped to the undoped state. In acidic condition, the UV spectra show three characteristic absorption bands, 280–285, 420–430, and 765–770 nm. The first absorption is due to the excitation of the nitrogen in the benzenoid segments ($\pi-\pi^*$ transition) while the second and the third ones are ascribed to polaron/bipolaron transition. As the pH increases from 4 to 8, the initial 765–770 nm peak shifts to lower wavelength region (down to 580–590 nm), and is related to the exciton transition of the quinoid ring. The 420–430 nm peak disappears whereas the absorption band at 280–285 nm is not affected. The FTIR analysis was performed on a Bruker IFS 55 EQUINOX and exhibited a spectrum of doped TANI close to the spectrum of protonated (or doped) polyaniline [41] (see Supporting information, S1). Mass spectrometry characterizations were performed using a oMALDI-qQqTOF (QSTAR XL, Applied Biosystems (USA) by Sciex (Canada)) instrument, with a nitrogen UV-laser at 337 nm with an energy of 15 μJ. An accelerating voltage of 20 kV was applied following a 10 kHz pulser frequency for an acquisition range of 250–1000 amu. The molecular TANI ion was confirmed at $m/z = 366.1902$, with a mass accuracy of 17 ppm and an MSMS experiment on parent ion revealed daughter ions every 91 amu (oligo-aniline), see Supporting information (Figure S2). The experimental procedure leads to the exclusive formation of oligo-aniline containing 4 units.

End-capped polymer synthesis: The insulating polymer part (PS) was added to DMF (10 wt%) and left under stirring till complete solubilisation. The TANI was then added to the reactive medium with a molar ratio of [TANI]/[PS] = 10. The reactive medium was then left at 70 °C with continuous stirring for five days in conventional oil bath or 12 h under microwave heating with set irradiation power of 30 W (SPS mode). The final end-capped polymer was precipitated in methanol several times to obtain a colorless filtrate. The conversion was calculated from ^{1}H NMR spectroscopy and the succinimide peak at 2.8 ppm (Bruker AVANCE 400 MHz in $CDCl_3$). A suspension of PS end-capped TANI in HCl 0.1 M is let under stirring overnight and filtered to obtain the conducting polymer.

3. Results and discussion

A microwave is a form of electromagnetic energy defined in the range where only molecular rotation is affected (and the most commonly used frequency is 2450 MHz). Microwave heating is a very different process compared to conventional heating (mainly in oil bath) in organic or macromolecular synthesis. The microwave process in not dependent upon the thermal conductivity of the vessel materials, and leads to a rapid rise in temperature directly related to the rotational motion of the molecules as induced by microwave irradiation. As a result, the heating rate and efficiency of MW heating strongly depend on the dielectric properties of the reactant and/or solvent. Indeed, under such frequency irradiation, the dipole re-orientates by generating a phase difference between the orientation of the field and that of the dipole. This feature causes energy to be lost from the dipole by molecular friction and collisions, giving rise to dielectric heating. The abilities of styrene to generate heat from microwave irradiation are reported in Fig. 2 and compared to polar and apolar solvents such as water and toluene,

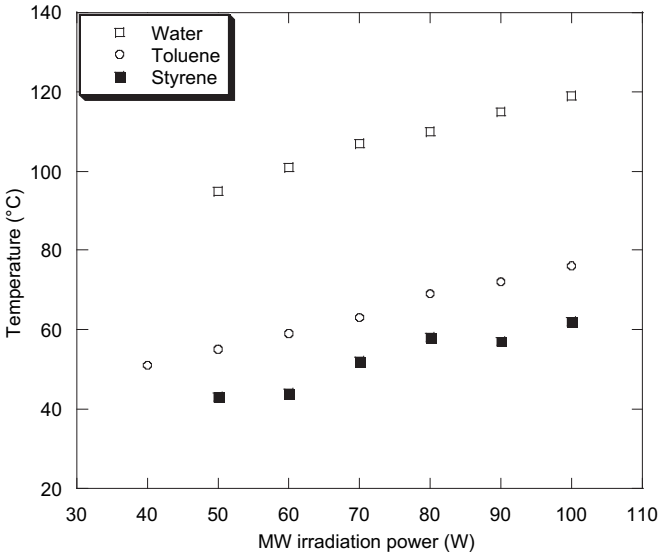

Fig. 2. Maximum temperature against microwave irradiation power (SPS mode).

the maximum temperature that could be reached at the set power value is reported *versus* irradiation power. It appears that the heating efficiency follows the dielectric constants [42] equals to 80; 2.4 and 2.3 for pure water, toluene and styrene respectively.

In order to be as reliable as possible, the irradiation mode was scrupulously studied to enhance the microwave effect during the polymerization. Pulsed power mode (SPS) and dynamic mode (DYN) are irradiation modes used within the articles dealing with the microwave-assisted syntheses. The DYN mode [12,43–45] is defined by only one set parameter which is the reaction temperature with no constraint on the microwave irradiation power. Previous work [46] showed that DYN mode did not exhibit any microwave effect and the kinetics overlapped those obtained under conventional heating. Within the current study, SPS mode [8,47–49] has been preferred. It is worth mentioning that the use of air cooling during the process is suspected to lead to an underestimation of the temperature readout of the IR sensor since the air cools mainly the exterior of the reaction vessel. However, previous article [46] did not record significant increase in pressure that would have been due to this misreading of the temperature. We thus assume that the reaction temperature did not increase excessively during the polymerization process. SPS mode is defined by two set parameters which are the reaction temperature and the microwave irradiation power, moreover, the vessel cavity is air-cooled throughout the reaction. At the beginning of the reaction the power is on at the set value till the target temperature is reached, then the power is on at the set power or off for the remainder of the run time as the reaction temperature (measured via infrared sensor) varies between the set value and a deviation of 2 °C. Both modes have been compared and the results are reported in Fig. 3, on polymerization medium. The same experimental conditions as used for the kinetic studies have been employed: styrene/CuBr/PMDETA/EBP = 200/1/1/1, target temperature: 110 °C, mixture volume: 5 mL.

During the last years, the use of commercial monomodal microwave synthesizers with excellent temperature and power control has significantly improved the reliability of the microwave-assisted reactions. SPS mode was chosen and the polymerization temperature as well as the microwave input was simultaneous accurately monitored and controlled at constant values. Moreover, power and set temperature have been adjusted to irradiate the

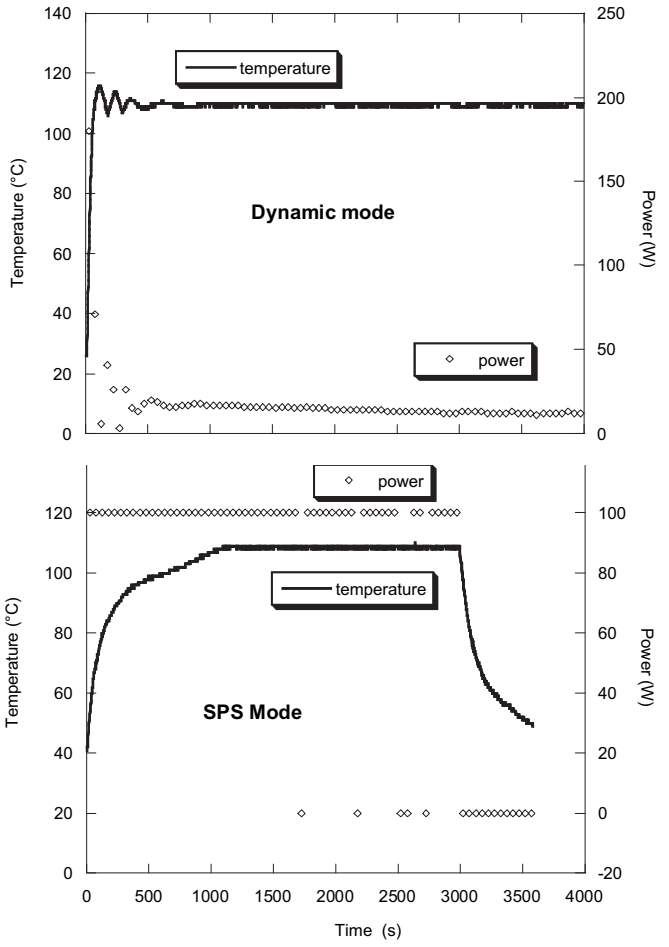

Fig. 3. Microwave irradiation modes: comparison between dynamic and pulsed (SPS) modes.

reactive medium over 90% of the reaction time. The experimental conditions of ATRP of styrene in microwave irradiation were investigated and compared with the conventional oil bath heating (CH) method. To exclude the influence of temperature difference between conventional and MW heating, the reaction mixture was kept as close as possible in both conditions. All the experimental conditions and characterizations are reported in Table 1.

The logarithmic conversion of styrene using the following ATRP experimental conditions [50], $[styrene]_0/[CuBr]_0/[PMDETA]_0/[EBP]_0 = 200/1/1/1$ is reported in Fig. 4.

As expected the kinetic plots of ATRP under conventional heating exhibit a first-order kinetic with respect to the monomer concentration, indicating that the propagating radical concentration was constant and no significant termination occurred during the polymerization (only styr2 conducted at the lowest irradiation power showed sort of induction period). The polymerization rate under MW followed the CH kinetic until a critical point is reached. Beyond this point, the kinetics exhibited a spectacular increase of the polymerization rate, as recently observed elsewhere [45,46]. It is worth noticing that the present results show similar interesting rate acceleration as compared to the previous results [46] even though it is a completely different system in terms of the kind of the controlled radical polymerization (NMP *vs*. ATRP), the monomer (acrylamide *vs*. styrene) and the chemical nature of the medium (water solution *vs*. bulk polymerization).

This MW effect on the kinetics of the polymerization was observed whatever the microwave input was (see Fig. 5).

Table 1
Experimental conditions and results of ATRP of styrene under microwave irradiation and conventional heating conditions with $[styrene]_0/[EBP]_0/[CuBr]_0/[PMDETA]_0 = 200/1/1/1$ but styr 6: 400/1/1/1. EBP is ethyl 2-bromopropionate and is used as initiator. Conversion was obtained by NMR analysis with $M_{n,th} = 181 + Conv.*[styrene]_0/[EBP]_0*MM$, with MM, the monomer molar mass.

Styrene Series #	Time (min)	Power (W)	T (°C)	Conv. %	$M_{n,th}$ (g mol^{-1})	$M_{n,SEC}$ (g mol^{-1})	M_w/M_n
Styr1	30	0	95	15	3300	3810	1.15
	60			28	6000	6640	1.10
	90			38	8080	8790	1.10
	120			51	10790	10860	1.10
Styr2	60	60	85	5	1220	1130	1.20
	90			23	4960	4700	1.10
	120			28	6000	5370	1.10
	150			43	9120	7920	1.10
	180			60	12660	12160	1.10
Styr3	30	80	98	15	3300	2760	1.10
	45			19	4132	4250	1.10
	60			25	5380	6200	1.10
	75			31	6630	6680	1.10
	90			55	11620	11660	1.15
	120			94	19730	20350	1.20
Styr4	20	100	110	5	1220	730	1.20
	30			23	4960	5050	1.10
	40			27	5800	5960	1.10
	60			30	6420	6040	1.10
	75			74	15570	16250	1.15
	90			93	19520	19220	1.30
Styr5	30	80	80	10	2260	1710	1.15
	90			29	6210	5470	1.10
	150			48	10160	10330	1.15
	180			51	10790	10190	1.15
	195			72	15150	15750	1.25
	210			76	15990	17700	1.20
	240			93	19520	19250	1.25
Styr6	60	80	80	3	1430	1170	1.10
	120			14	6000	3580	1.10
	150			17	7250	4090	1.10
	210			28	11830	6420	1.15
	240			63	26390	22000	1.20

All the kinetic plots for reactions that were carried out under microwave irradiation clearly show a drastic slope change above $\ln([M]_0/[M]) = 0.5$ that correspond to a polymer conversion above 0.4. This effect was magnified by an increase of the microwave

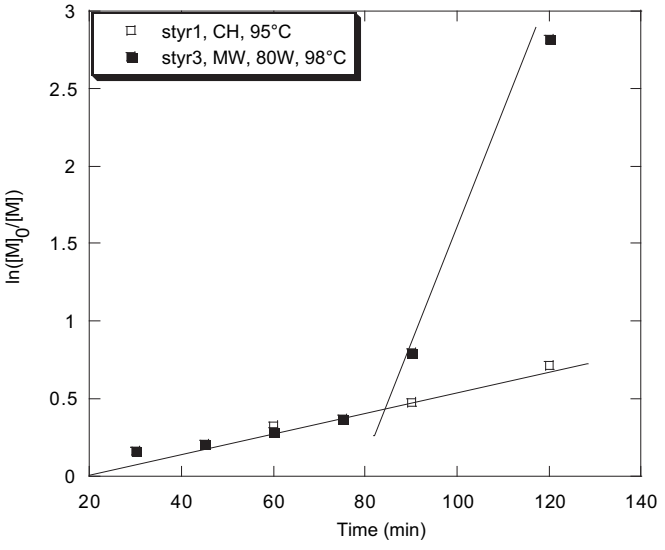

Fig. 4. Logarithmic styrene conversion from microwave irradiation (MW) and conventional heating (CH) conditions (see Table 1).

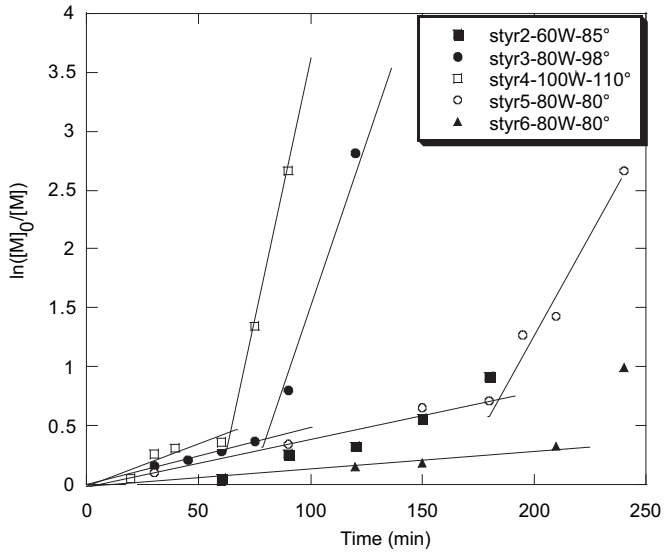

Fig. 5. Kinetic plots of $\ln([M]_0/[M])$ *vs.* reaction time for bulk polymerization of styrene using the following ratios $[styrene]_0/[CuBr]_0/[PMDETA]_0/[EBP]_0 = 200/1/1/1$ (■ ● □ ○) and 400/1/1/1 (▲) under microwave irradiation (see Table 1). The lines are guides for the eyes.

irradiation power and/or temperature. Nevertheless, this particular behaviour did surprisingly not affect the control of the polymerization as shown by the plots of M_n against conversion (see Fig. 6). The molar masses did not only increase linearly with the conversion but they all fit on one single straight line along with the data

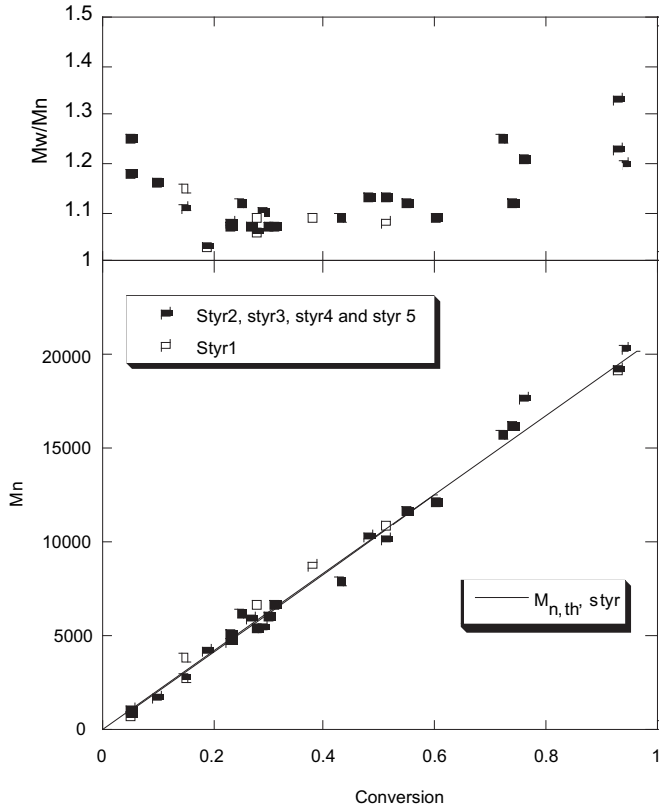

Fig. 6. Dependence of M_n and M_w/M_n on monomer conversion under microwave irradiation (MW) and conventional heating (CH) conditions (see Table 1). All the polymerizations were carried out using the following ratios $[styrene]_0/[CuBr]_0/[PMDETA]_0/[EBP]_0 = 200/1/1/1$.

obtained by conventional heating following the theoretical calculations. Moreover, the control of the molar masses is obtained whatever the $[monomer]_0/[initiator]_0$ ratio is. In the same manner, even if higher M_w/M_n values are observed above 40% conversions, the polydispersity index stays below 1.35 for all the polymerization experiments.

Applying microwave irradiation to ATRP of styrene, with EBP/CuBr/PMDETA as initiating system, can significantly increase the polymerization rate while keeping the perfect control of the molar masses in shorter reaction times. Further experiments are currently under progress to better understand the cause of the sudden increase of the conversion shown in Fig. 5. Several hypotheses should be investigated and especially the occurrence of a gel effect [46] or local superheating effects [51,52]. In the present study, we focussed on the synthesis of conducting end-capped polymers using a microwave-assisted synthesis. Those results were then used to synthesize and control the size of the insulating part. The second step of the reaction was again carried out under conventional heating and microwave irradiation, and both methods were compared (Fig. 1).

The second part is an oligomer of polyaniline α,ω-end-capped. During the course of the present research, the synthesis of the phenyl/amine end-capped tetra-aniline (TANI) in the emeraldine oxidation state has been developed (see Experimental part). As compared to previous tetra-aniline syntheses [53], the present method is convenient since the starting materials are commercially available, and the reaction time and steps are reduced as compared to previous articles [31–34]. This synthesis is also advantageous because the synthesized TANI is pure as revealed by the mass spectrum analysis. Moreover, the conducting properties are maintained since TANI already exhibits conductivity as high as a typical PANI [54].

The insulating end-capped precursor polymer was then obtained via ATRP and the experimental conditions (temperature, [styrene]/[initiator] ratio and reaction time) are based on the above results. A specific initiator denoted NHSBr was employed; it bears an alkyl halide group able to initiate the ATRP in a first step and a succinimide group able to react with the amino-group of the TANI to obtain the end-capped polymer in a second step. Target molar masses are in the range of 5000–25000 g mol^{-1} in order to obtain final polymers containing from 2 to 7 wt% of HCl-doped TANI at the end of the process.

Due to the relative low targeted molar masses, both end-chain groups of the NHS-polystyrene-Br are identified by NMR spectroscopy in $CDCl_3$. The four protons of the succinimide group ($CO-CH_2-CH_2-CO$) appear at 2.8 ppm, while the proton of the second end-chain functionality ($CH-Br$) is detected at 5.1 ppm, and the theoretical number of 4:1 is verified. Moreover, if we assume that ATRP was controlled under microwave irradiation, $M_{n,NMR}$ could be calculated with ^1H NMR data according to Equation (1) with I_M, I_{succ} and I_{CHBr} the normalized integral values of the peaks belonging to polymer backbone, succinimide moiety and bromine group respectively, and M_M, the molar mass of styrene unit.

$$M_{n,NMR} = \frac{I_M}{I_{succ}} M_M + 264 = \frac{I_M}{I_{CHBr}} M_M + 264 \quad (1)$$

The results are listed in Table 2. The agreement of theoretical M_n, $M_{n,SEC}$ and $M_{n,NMR}$ indicates that all polymers are telechelic, *i.e.* they are α,ω-difunctionalized. The second step of the reaction as described in Fig. 1 was carried out under conventional heating and the results are reported in Table 2.

The PS-TANI were analyzed by FTIR spectroscopy (Fig. 7). The spectrum of precursor PS is very close to the spectrum of standard atactic PS. Some small differences in the peak ratios and the shape of the peaks are observed mainly due to the chain-end functionality

Table 2
Bulk Polymerization of styrene (Styr) ATRP under conventional heating with $[styrene]_0/[NHSBr]_0/[CuBr]_0/[PMDETA]_0 = 200/1/1/1$ but (1): 450/1/1/1. The conversion is calculated via ^1H NMR characterization. $M_{n,th} = 264+[styrene]_0*M_M*conversion/[NHSBr]_0$ the theoretical number-average molar mass with M_M the molar mass of the monomer. $M_{n,SEC}$ and $M_{n,NMR}$ the molecular weights obtained by SEC and NMR analyses respectively. PS-TANI are obtained at 70 °C under conventional heating. *wt.%* TANI is the content of TANI within the final polymer obtained from wt% TANI $= M_{TANI}/[M_{TANI} + M_{n,\ SEC,PS\ precursor}]$ with M_{TANI} the molar mass of HCl-doped TANI, *i.e.* 436 g mol^{-1}. All the experimental conditions are done for quantitative yield as measured by NMR spectroscopy.

PS precursor polymer							Conducting PS-TANI		
Name	Reaction time *(min.)*	Conv. %	$M_{n,th}$ *(g mol^{-1})*	$M_{n,SEC}$ *(g mol^{-1})*	M_w/M_n	$M_{n,NMR}$ *(g mol^{-1})*	Name	Doped TANI *%wt*	Conductivity S cm^{-1}
Styr11	45	10	5100(1)	5380	1.15	4800	Styr11-TANI	7.0	5.0
Styr12	75	47	10040	10560	1.10	11130	Styr12-TANI	4.0	2.3
Styr13	100	51	21480	N/A	N/A	19760	Styr13-TANI	2.0	0.2

of the PS as obtained via ATRP (at about 1743 cm^{-1}). The spectra of PS-doped-TANI and PS-undoped-TANI contain the peaks of PS. After subtraction of the spectrum of precursor PS they are very close to the spectra of doped and undoped polyaniline, especially below 2000 cm^{-1}.

FTIR characterization confirmed that both parts (PS and TANI) are present within the sample however there is no proof of the efficiency of the coupling reaction between the PS precursor polymer and the TANI. The coupling efficiency is revealed with the ^1H NMR analysis of the end-capped PS and the complete disappearance of the succinimide group (CO–CH_2–CH_2–CO) at 2.8 ppm in $CDCl_3$.

As reported in Table 2, all PS-HCl-doped TANI were conducting even at the lowest TANI content. Moreover, the conductivity increases with the TANI content up to the conductivity result of pure TANI indicating that the percolation threshold is reached before 7 wt% of TANI. It is worth noticing that a PS/TANI composite obtained by the blending method is insulating in this TANI content range, a value of 2.10^{-5} S cm^{-1} has been measured for a PS/TANI blend containing 7.5 wt% doped TANI. The synthesis of block copolymer or end-capped polymers allows lowering the percolation threshold to obtain high conductivity at low and controlled TANI content. Previous articles already reported that conjugated rod-coil copolymers show self assembly characters. The conjugated rod is assimilated to a crystalline domain that can be sterically separated by coils and thus provides nanoscale supramolecular architectures. Moreover, strong intermolecular interactions among the conjugated rods favour the formation of conducting network [55–57]. This phenomenon may help to decrease the percolation threshold as noticed within the present results. Further experiments are under progress and will be the aim of a future article dedicated to the study of the phase separation and the film structure.

In the last stage, it was interesting to know whether the PS-TANI could be obtained following a microwave approach for both steps *i.e.* the precursor block synthesis and the coupling reaction with TANI. The optimized experimental conditions described above been carried out to obtain a PS block i.e. a microwave irradiation power of 80 W, for 90 min using the SPS mode. The characterization confirmed the synthesis of a α,ω-functionalized PS (NHS-PS-Br) with $M_{n,th} = 7960$ g mol^{-1}, $M_{n,SEC} = 7710$ g mol^{-1}, $M_{n,NMR} = 6300$ g mol^{-1} and $M_w/M_n = 1.10$. The coupling reaction was then again carried out under microwave irradiation: SPS mode, set irradiation power of 30 W and at a temperature of 70 °C. Under these experimental conditions, microwave process has considerable effect on the rate of the reaction and the coupling reaction is quantitative within 12 h instead of several days using conventional heating as revealed by the disappearance of the peak of the succinimide group at 2.8 ppm by NMR spectroscopy. This new PS-HCl-doped TANI contains 4.7 wt% HCl-doped TANI and exhibits a conductivity of 2.0 S cm^{-1}; this result is in accordance with those reported in Table 2. Due to the use of oligomer of TANI, the polymers were all soluble in THF. SEC based data of both the precursor PS and the end-capped PS obtained via obtained under MW irradiation are reported in Fig. 8.

The differential number fraction distribution, represented by the ratio of the differential refractive index to the molar mass (DRI/M) *vs.* the logarithmic molar mass, allows an evaluation of the molar fraction of samples [58] and enhances any trace of residual precursor polymer. No un-reactive precursor polymer seems to appear in Fig. 8; moreover a slight increase of the final end-capped

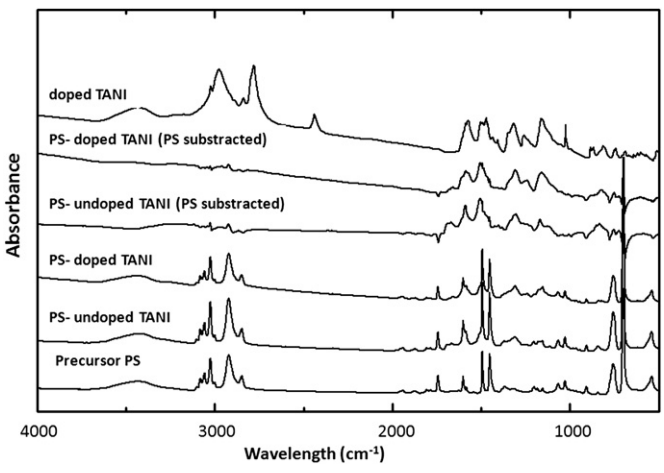

Fig. 7. FTIR characterization of conducting end-capped PS and precursors. Precursor PS was obtained via ATRP with NHSBr/CuBr/PMDETA and TANI was obtained via oxidative method as described within the experimental part. The PS-doped TANI is obtained under conventional heating and is alkali treated to obtain the PS-undoped TANI.

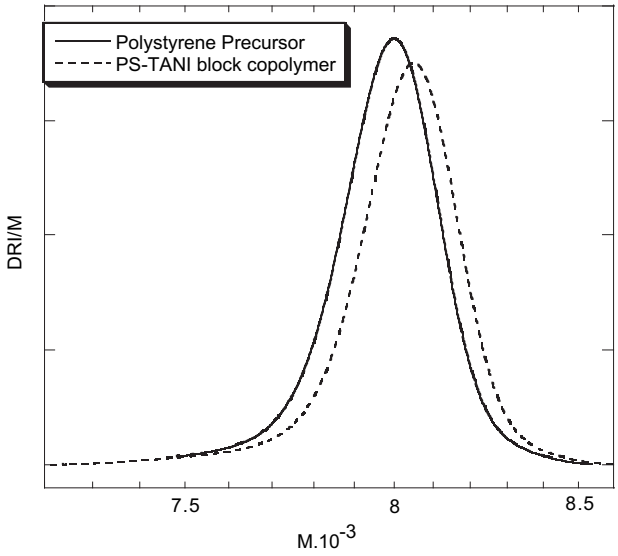

Fig. 8. Number molar mass distribution of the precursor PS obtained via ATRP and the PS-TANI. Both are obtained under MW irradiation.

polymer molar mass *versus* precursor polymer is noticed as expected due to the small size of the TANI end-group. Furthermore, this is in good agreement with the NMR analysis and let think that all the precursor polymer chains have been end-modified. It is also worth noticing that no low molar mass materials are detected which indicates that the microwave irradiation as used within this synthesis (polymerization and coupling reaction) is a non-destructive method. This result shows the feasibility of conducting end-capped polymers with strong acceleration of both polymerization rate and coupling reaction, controlled size and chemical formulation under MW irradiation.

4. Conclusion

The synthesis of a conducting material made of an insulating moiety and an intrinsically conducting part requires a homogeneous dispersion of the conducting moiety. Within this study, microwave assisted synthesis has been tested both in polymer synthesis and polymer functionalization. Conducting end-capped polymers with controlled architectures in terms of molecular size of both the insulating and the conducting parts as well as the chemical formulation have been obtained. The synthesis has been performed under conventional heating and microwave irradiation to highlight the effect of MW heating. Characterization of the resulting polymers demonstrates that the synthesis using microwaves results in materials with properties equivalent to those obtained when using conventional heating routes. Beneficially, microwave-assisted polymerization allows a reduction in the reaction time and energy saving. Similar interesting rate acceleration as already mentioned within previous article [46] has been observed even though it is a completely different system in terms of way of polymerization, monomer and reactive medium chemical natures. Conducting polymers containing an optimized HCl-doped TANI content (from 2 to 7 wt%) and reasonable conductivity (0.2–5 S cm^{-1}) have been obtained. Further experiments are currently under progress to first better understand the microwave effect on the kinetics of controlled radical polymerization and second to apply the microwave-assisted synthesis to larger range of conducting materials in terms of chemical formulation (insulating polymer, PANI content) and macromolecular architectures.

Appendix. Supplementary information

Supplementary data related to this article can be found online at doi:10.1016/j.polymer.2010.11.016.

Acknowledgements

The authors thank the French Ministry of Education and Eco-net project (16256SA) for financial support and CEM for the loan of the Discover unit. Authors gratefully acknowledge Dr R. C. Hiorns for editing the manuscript prior to submission.

References

[1] Giguere RJ, Bray TL, Duncan SM, Majetich G. Tetrahedron Lett 1986;27(41):4945–8.
[2] Gedye R, Smith F, Westaway K, Ali H, Baldisera L, Laberge L, et al. Tetrahedron Lett 1986;27(3):279–82.
[3] Bardts M, Gonsior N, Ritter H. Macromol Chem Phys 2008;209(1):25–31.
[4] Hoogenboom R, Schubert US. Aust J Chem 2009;62(3):181–3.
[5] Hoogenboom R, Schubert US. Macromol Rapid Commun 2007;28(4):368–86.
[6] Sinnwell S, Ritter H. Aust J Chem 2007;60(10):729–43.
[7] Wiesbrock F, Hoogenboom R, Schubert US. Macromol Rapid Commun 2004;25(20):1739–64.
[8] Li X, Zhu X, Cheng Z, Xu W, Chen G. J Appl Polym Sci 2004;92(4):2189–95.
[9] Zhang H, Schubert US. Macromol Rapid Commun 2004;25(13):1225–30.
[10] Cheng Z, Zhu X, Chen M, Chen J, Zhang L. Polymer 2003;44(8):2243–7.
[11] Delfosse S, Borguet Y, Delaude L, Demonceau A. Macromol Rapid Commun 2007;28(4):492–503.
[12] Cheng Z, Zhu X, Zhou N, Zhu J, Zhang Z. Radiat Phys Chem 2005;72(6):695–701.
[13] Shacklette LW, Han CC, Luly MH. Synth Met 1993;57(1):3532–7.
[14] Kohut-Svelko N, Dinant F, Magana S, Clisson G, François J, Dagron-Lartigau C, et al. Polym Int 2006;55(10):1184–90.
[15] Leclercs M, Guay J, Dao LH. Macromolecules 1989;22:649–53.
[16] Chevalier JW, Bergeron J-Y, Dao LH. Macromolecules 1992;25:3325–31.
[17] Cao Y, Smith P, Heeger AJ. Synth Met 1992;48(1):91–7.
[18] Paul RK, Vijayanathan V, Pillai CKS. Synth Met 1999;104(3):189–95.
[19] Pron A, Laska J, Österholm J-E, Smith P. Polymer 1993;34(20):4235–40.
[20] Andreatta A, Yong C, Chiang JC, Heeger AJ, Smith P. ACS Polym Preprints 1989;30(1):149.
[21] Abraham D, Bharathi A, Subramanyam SV. Polym Commun 1996;37(23):5295.
[22] Ananda J, Palaniappan S, Sathyanarayana DN. Eur Polym J 2000;36(1):157.
[23] Fu Y, Weiss RA. Macromol Rapid Commun 1996;17(7):487–92.
[24] Hu H, Cadenas JL, Saniger JM, Nair PK. Polym Int 1998;45(3):262–70.
[25] Armes SP, Aldissi M. J Chem Soc Chem Commun 1989;288–9.
[26] Kim BJ, Oh SG, Han MG, Im SS. Polymer 2002;43(1):111–6.
[27] Gospodinova N, Mokreva P, Tsanov T, Terlemezyan L. Polymer 1997;38(3):743–6.
[28] Cairns DB, Armes SP, Bremer LGB. Langmuir 1999;15(23):8052–8.
[29] Li S, Dong H, Cao Y. Synth Met 1989;29(1):329–36.
[30] Kinlen PJ, Frushour BG, Ding Y, Menon V. Synth Met 1999;101(1–3):758–61.
[31] Honzl J, Ulbert K, Hádek V, Tlustáková M. Chem Commun 1965;440.
[32] Rebourt E, Joule JA, Monkman AP. Synth Met 1997;84(1–3):65–6.
[33] Wang W, MacDiarmid AG. Synth Met 2002;129(2):199–205.
[34] Gao J, Li K, Wanjin Z, Ce W, Zhongwen W, Yiping J, et al. Macromol Rapid Commun 1999;20(10):560–3.
[35] Hanfu W, Yanchun H. Macromol Rapid Commun 2009;30(7):521–7.
[36] Hu J, Huang L, Lang L, Liu Y, Zhuang X, Chen X, et al. J Polym Sci A Polym Chem 2009;47(5):1298–307.
[37] Han D-H, Pan C-Y. Polymer 2006;47(20):6956–62.
[38] Kohut-Svelko N, Reynaud S, Martinez H, Dedryvère R, Gonbeau D, François J. Langmuir 2005;21:1575–83.
[39] Keller RN, Wrcoff HD, Marchi LE. Inorg Synth; 1946:21–4.
[40] Chen L, Yu Y, Mao H, Lu X, Zhang W, Wei Y. Mater Lett 2005;59(19–20):2446–50.
[41] Blinova NV, Stejskal J, Trchová M, Prokes J, Omastová M. Eur Polym J 2007;43(6):2331–41.
[42] Handbook of chemistry and physics. NY: CRC Press; 1996.
[43] Cheng Z, Zhu X, Chen G, Xu W, Lu J. J Polym Sci A Polym Chem 2002;40(21):3823–34.
[44] Steven LB, Christopher MR, Sébastien P. Macromol Rapid Commun 2007;28(4):478–83.
[45] Costa C, Santos AF, Fortuny M, Araújo PHH, Sayer C. Mater Sci Eng C 2009;29(2):415–9.
[46] Rigolini J, Grassl B, Billon L, Reynaud S, Donard OFX. J Polym Sci A Polym Chem 2009;47(24):6919–31.
[47] Li J, Zhu X, Zhu J, Cheng Z. Radiat Phys Chem 2006;75(2):253–8.
[48] Lascelles SF, Armes SP, Zhdan PA, Greaves SJ, Brown AM, Watts JF, et al. J Mater Chem 1997;7(8):1349–55.
[49] Li N, Lu J, Xu Q, Xia X, Wang L. Eur Polym J 2007;43(10):4486–92.
[50] Davis KA, Matyjaszewski K. Macromolecules 2000;33(11):4039–47.
[51] Obermayer D, Gutmann B, Kappe CO. Angew Chem Int Ed 2009;48(44):8321–4.
[52] Obermayer D, Kappe CO. Org Biomol Chem 2010;8:114–21.
[53] Ochi M, Furusho H, Tanaka J. Bull Chem Soc Jpn 1994;67(6):1749–52.
[54] MacDiarmid AG, Chiang JC, Richter AF, Somarisi NLD. In: Alcacer L, editor. Conducting polymers: special applications. Dordrecht: Reidel; 1984. p. 105.
[55] Jenekhe SA, Chen XL. Science 1998;279:1903–7.
[56] Jenekhe SA, Chen XL. Science 1999;283:372–5.
[57] Klok H-A, Lecommandoux S. Adv Mater 2001;13(16):1217–29.
[58] Matyjaszewski K, Shipp DA, McMurtry GP, Gaynor SG, Pakula T. J Polym Sci A Polym Chem 2000;38(11):2023–31.

Polymer 52 (2011) 40–45

Contents lists available at ScienceDirect

Polymer

journal homepage: www.elsevier.com/locate/polymer

Chromatographic separation of polylactides by stereochemical composition

Tiantian Li [a], Sandra Strunz [a], Wolfgang Radke [a,*], Roland Klein [a], Thorsten Hofe [b]

[a] Deutsches Kunststoff-Institut (German Institute for Polymers), Schlossgartenstrasse 6, D-64289 Darmstadt, Germany
[b] PSS Polymer Standards Service GmbH, POB 3368, D-55023 Mainz, Germany

ARTICLE INFO

Article history:
Received 28 August 2010
Received in revised form
24 October 2010
Accepted 28 October 2010
Available online 3 November 2010

Keywords:
Polymer separations
Stereochemistry
Polylactide

ABSTRACT

Polylactides exist in different stereochemical compositions, as pure L-(PLLA), pure D-(PDLA), or mixtures containing the two enantiomeric forms in varying amounts. Polylactides of different stereochemical compositions differ in their solubility in THF. Based on the difference in solubility a gradient chromatographic method was developed allowing separation of polylactides differing in their stereochemical compositions (excess of enantiomers, *e.e.*). Moreover, blends composed of polylactides having different stereochemical purity could be separated into their individual components. However, for mixtures of PDLA with PLLA an additional peak was observed at higher elution volume. Since this peak cannot be attributed to any of the individual components, this peak might result from the formation of the stereocomplex described in literature.

1. Introduction

Polylactic acid (Polylactide, PLA), a biodegradable, thermoplastic polymer derived from renewable sources, is attracting much attention due to its bio-based synthesis and biodegradability [1,2]. The properties of PLA can be adjusted by controlling process conditions, molecular weight distribution, stereochemical compositions etc [3]. Thus, PLA can be used in a broad range of applications e.g biomedical materials for surgical sutures [4–6], drug delivery systems [7,8] and internal bone fixation [9]. PLA attracts also much attention as packaging materials for food, agricultural mulch films, fibers etc [10].

In spite of the unique characteristics and versatile applications of PLA, the commercial viability has been limited so far. Beside cost factors this is due to the lack of knowledge on the relationship between PLAs molecular structure and the macroscopic properties.

The monomer of PLA, lactic acid, contains a stereocenter, resulting in the two enantiomers L- and D-lactic acid. The incorporation of these monomers into the polymer results in polylactides of different stereochemical compositions and distributions. The amount and distribution of the D- and L-lactic acid units have a significant influence on the chemical, physical, mechanical, and degradation properties [11,12,13,14]. For example, pure PLLA and PDLA are semicrystalline, while Poly(D,L-lactide) (PDLLA) is known to be amorphous. Furthermore, the melting point decreases with decreasing enantiomeric purity [15]. Therefore determination of the stereochemical composition and distribution is very important in studying the relationship between molecular structure and application properties, as well as to control the properties of PLA during synthesis.

The average stereochemical compositions can be determined based on the specific optical rotation [16,17], but no information can be obtained on the distribution of the enantiomers among the polymer chains by this method. Such information requires the application of a suitable separation technique.

In the present work, we present a study on the separation of polylactides according to differences in stereochemical composition using gradient chromatography.

2. Experimental

2.1. Samples and solvents

PLA-Samples of different stereochemical composition were obtained from Boehringer Ingelheim Pharma GmbH & Co.KG (Ingelheim, Germany) and Purac Biochem (Gorinchem, the Netherlands).

Chloroform ($CHCl_3$) and n-hexane were purchased from VWR (Darmstadt, Germany) and used as received. Technical tetrahydrofuran (THF, BASF Ludwigshafen, Germany), was dried over calcium hydride and distilled. 1,1,1,3,3,3-hexafluoro-2-propanol (HFiP) was purchased from Chempur (Karlsruhe, Germany) and used after distillation.

* Corresponding author. Deutsches Kunststoff-Institut (German Institute for Polymers), Schlossgartenstrasse, D-64289 Darmstadt, Germany. Tel.: +49 6151 162804; fax: +49 6151 292855.
E-mail address: wradke@dki.tu-darmstadt.de (W. Radke).

0032-3861/$ – see front matter © 2010 Elsevier Ltd. All rights reserved.
doi:10.1016/j.polymer.2010.10.056

2.2. DSC

Differential scanning calorimetry (DSC) measurements were performed on a Mettler Toledo DSC 822e instrument. Temperature calibration was performed using indium and zinc. Melting endotherms were determined by heating the samples from 0 °C to 250 °C at a heating rate of 10 °C min^{-1}. The samples were then cooled to 0 °C at a cooling rate of 10 °C min^{-1} and after 5 min *a* second heating run to 250 °C was performed.

2.3. SEC

The average molecular weight was determined by size exclusion chromatography in chloroform using a Micro-SEC-System EcoSEC with RI-detection produced by TOSOH Bioscience (Tokyo, Japan). The SEC-column set was composed of SDV 1000 Å and SDV 10^5 Å (PSS Polymer Standards Service GmbH, Mainz, Germany). A flow rate of 1 mL/min was applied. The sample concentration was 2 g/L with an injection volume of 20 µL. The solvent contained small amount of toluene as flow marker to correct for flow rate variations. The SEC was calibrated with polystyrene standards with molar masses ranging from 580 to 7 450 000 g/mol (PSS Polymer Standards Service GmbH, Mainz, Germany). The calibration data were fitted by a third order polynomial. For data acquisition and evaluation PSS WINGPC Unity Software (PSS Polymer Standards Service GmbH, Mainz, Germany) was used.

2.4. HPLC

The HPLC measurements were performed using an Agilent Series 1100 (Agilent Technologies, Santa Clara, USA) chromatography system, consisting of a degasser (G1379A), a quaternary pump (G1311A) and an autosampler (G1313A). The temperature of the column was controlled to 35 °C using a column thermostat "Jetstream II Plus" (Techlab, Erkerode, Germany). For detection an evaporative light scattering detector (ELSD), ELS 1000, (Polymer Laboratories, Church Stretton, England) was used. Data acquisition and evaluation was performed using PSS WINGPC Unity Software (PSS Polymer Standards Service GmbH, Mainz, Germany). Separations were carried out using a Nucleosil 1000 Å silica column (7 µm particles, 250 mm length and 4.6 mm ID), produced by Macherey&Nagel GmbH & Co. KG (Dühren, Germany).

2.5. Determination of the specific optical rotation

The specific optical rotations of the samples used were determined using a polarimetric detector "Chiralyser" produced by IBZ Messtechnik GmbH (Hannover, Germany). The samples were dissolved in $CHCl_3$ at a concentration of 1 g/L and injected with an injection volume of 20 µl into an SEC system Agilent Series 1200 (Agilent Technologies, Santa Clara, USA), consisting of a binary pump (G1312A) and an autosampler (G1329A). A SEC-column PSS PFG 100 Å (300 mm length and 8 mm ID, PSS Polymer Standards Service GmbH, Mainz, Germany) was used.

3. Results and discussion

The samples used in this study, the information of the suppliers on their stereochemical composition, the determined weight average molar masses and determined specific optical rotations are listed in Table 1. The presented weight average molar masses are given relative to a PS-calibration. Assuming validity of the universal calibration principle and using the Mark-Houwink-parameters (a = 0,73 and $K = 5{,}45 \times 10^{-4}$) for PLA [18] and for PS (a = 0,78 and $K = 5{,}2 \times 10^{-3}$)[19] in chloroform the use of a polystyrene calibration curve is expected to overestimate the true molar masses by approximately 60%.

Table 1
PLAs with different stereochemical compositions and specific rotations.

Sample	L/D-ratio	Spec. opt. Rotation	M_w [10^3 g/mol][a]	Crystallinity[b]	Solubility in THF[c]
1	100/0	278 ± 5	87	sc	i
2	100/0	278 ± 8	191	sc	i
3	100/0	298 ± 4	338	sc	i
4	100/0	280 ± 4	599	sc	i
5	100/0	286 ± 1	691	sc	i
6	100/0	310 ± 7	1340	sc	i
7	100/0	285 ± 1	1440	sc	i
8	96/4	272 ± 4	600	sc	i
9	96/4	271 ± 5	680	sc	i
10	90/10	227 ± 4	1600	a	2.5 h at RT
11	85/15	211 ± 6	383	a	1 h at RT
12	85/15	202 ± 1	896	a	1 h at RT
13	85/15	208 ± 4	1250	a	1.5 h at RT
14	50/50	0	13	a	1.5 h at RT
15	50/50	0	20	a	1 h at RT
16	50/50	0	29	a	1 h at RT
17	50/50	0	320	a	2.5 h at RT
18	0/100	282 ± 7	455	a	i

[a] M_w = weight-average molecular weight, determined by size exclusion chromatography in $CHCl_3$, calibrated with polystyrene standards.
[b] sc: semicrystalline, a: amorphous.
[c] i: insoluble in THF.

To determine the crystallinity of the samples, DSC experiments were conducted. Fig. 1 shows the thermal behaviour of five PLA-samples of different stereochemical compositions in the first heating cycle. It can be seen that the pure PLLA and pure PDLA exhibit an endothermic melting peak at 193 °C. As the optical purity is reduced to 92% (L/D 96/4), the melting peak appears at a lower temperature at 159 °C. The samples of lower optical purities (L/D 85/15 and 50/50) don't show melting peaks at all. This indicates that samples of higher optical purity, pure D or L or 96/4, are crystalline or semicrystalline, while samples of lower optical purity are amorphous, which corresponds to literature [20]

The solubility of the samples in THF was also investigated. Fig. 2 shows the melting points of the PLAs as black bars. Solubility in THF is indicated by a shaded area. It can be observed that samples showing a melting behaviour (black bar) do not show a shaded area and vice versa. Therefore all semicrystalline PLAs are insoluble in THF, while the amorphous PLAs can be dissolved in THF, indicating

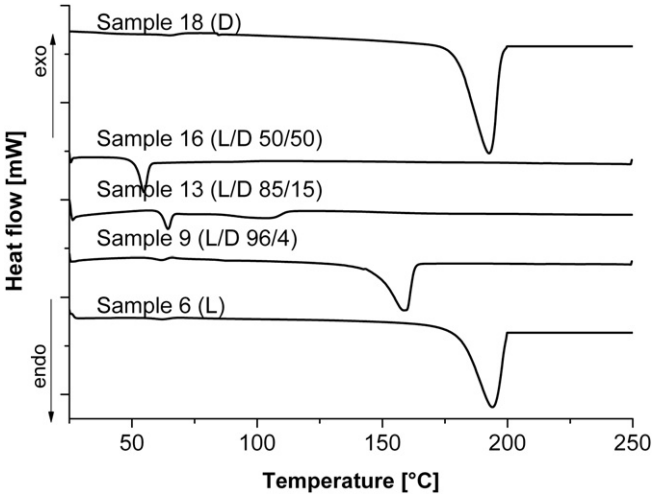

Fig. 1. DSC curves (2nd heating) of polylactides having different optical purities.

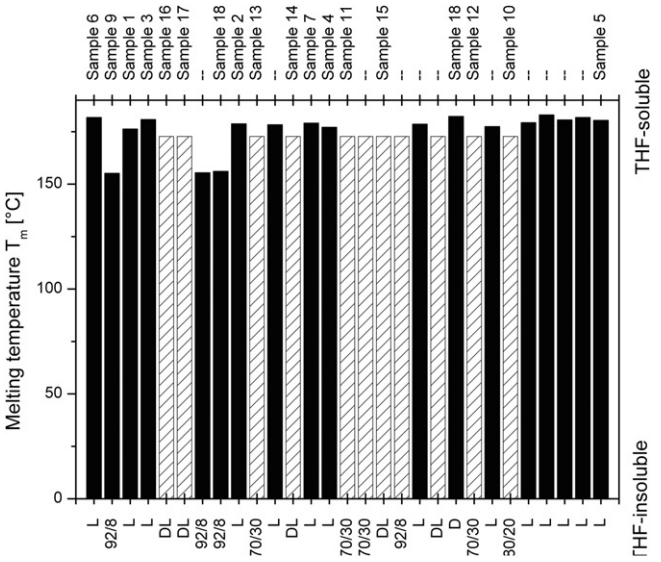

Fig. 2. Melting points (determined from the second heating run) and THF-solubility of PLA-samples. Black columns: Melting temperature of the samples. Shaded columns indicate solubility of the samples in THF. The figure contains samples which have not been listed in Table 1. However, these samples have not been used for the chromatographic investigations.

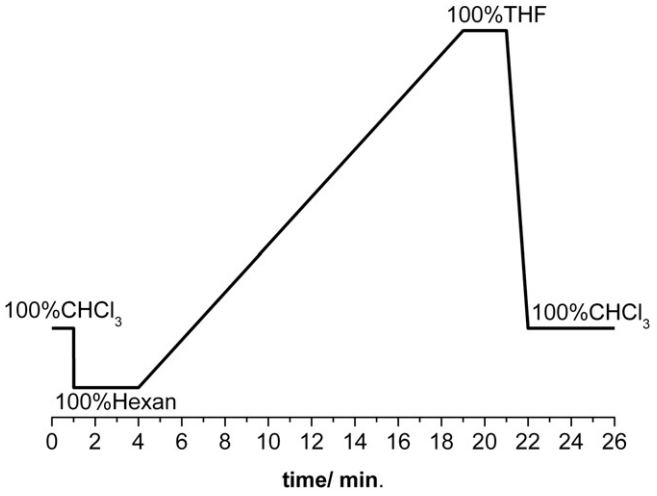

Fig. 3. Gradient $CHCl_3$-Hexane-THF-$CHCl_3$.

that the solubility in THF depends on crystallinity. Since the crystallinity correlates with the stereochemical composition, it can be concluded that PLAs of different stereochemical compositions can be distinguished by their solubility in THF.

As a result of the correlation between stereochemical composition and solubility in THF, it might be possible to achieve a separation according to stereochemical composition based on the differences in solubility. Chloroform was found to be a solvent for all samples irrespective of the stereochemical composition, while n-hexane was identified as a precipitant.

If PLAs are injected in 100% $CHCl_3$ onto a polar stationary phase they become adsorbed due to the low polarity of $CHCl_3$. THF desorbes the samples resulting in elution from the column. However, our attempts to separate PLAs by stereochemical composition using a simple gradient from $CHCl_3$ to THF, thus using a gradient based on desorption/adsorption effects were not successful. This was most probably due to the additional adsorption effects of polar end-groups of the PLAs.

Therefore the gradient in Fig. 3 was developed based on following considerations: The samples dissolved in $CHCl_3$ were injected into the column using $CHCl_3$ as the mobile phase, resulting in adsorption. The adsorbed samples were precipitated within the column by changing the mobile phase from the good solvent but weak eluent $CHCl_3$ to the non-solvent hexane. After precipitation a gradient from hexane to THF was applied. Thus, samples soluble in THF, i.e. amorphous PLAs of lower stereochemical purity, should be dissolved. At the same time, the dissolved samples are supposed to be eluted, since THF has a higher polarity than $CHCl_3$ resulting in desorption [21]. In contrast, samples of higher stereochemical purity (pure PLLAs and PDLAs), are expected to remain in the column, since they are insoluble in THF. Upon application of a gradient from THF to $CHCl_3$ the samples will be redissolved at a specific amount of $CHCl_3$. Because the simple gradient from $CHCl_3$ to THF has shown that all PLAs can be eluted, the application of the gradient step from THF to $CHCl_3$ should result in elution of those samples that cannot be eluted in pure THF. Based on these considerations the pure enantiomers should separate from samples of lower stereochemical purity.

The chromatograms of selected samples of different stereochemical composition obtained applying the described gradient, are shown in Fig. 4. As expected, with increasing enantiomeric excess the samples indeed elute at higher elution volumes. Since an achiral column was applied pure PDLAs and PLLAs elute latest, at identical elution volume. The amorphous PLAs elute within the gradient step from hexane to THF. Contrary to our expectations, however, pure PDLAs and PLLAs do not elute in the gradient step from THF to $CHCl_3$, but earlier, also in the gradient step from hexane to THF. However, they elute later than the amorphous samples at higher THF contents. This unexpected result may be explained, by the fact that the PLLAs and PDLAs might precipitate onto the stationary phase as isolated chains due to the low concentration. This might alter the solubility in comparison to PLA pellets. The dependence of the retention volume on the stereochemical composition for all samples is more clearly visualized in Fig. 5.

It can be seen in Fig. 5 that the elution volume does not decrease linearly with decreasing *e.e.*, but approaches a limiting value when the enantiomeric excess is lower than about 80%. This means the described gradient should be applicable to study the stereochemical composition distribution of samples having high L- or D-content. This might at first glimpse be a drawback. However,

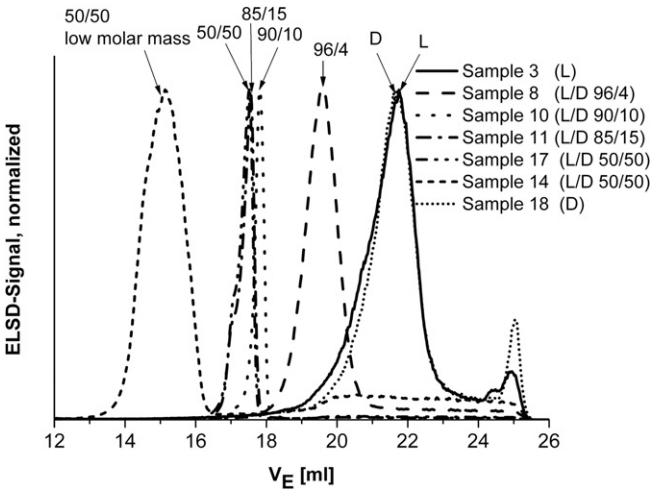

Fig. 4. Overlay of normalized chromatograms of PLAs having different stereochemical compositions. Gradient described in Fig. 3.

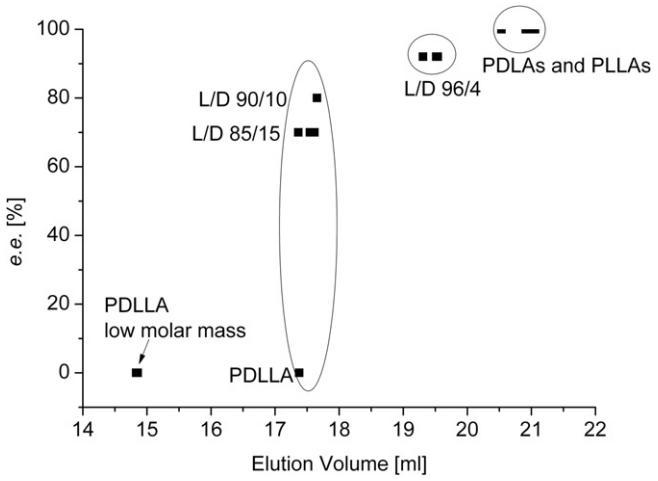

Fig. 5. Dependence of elution volume on enantiomeric excess.

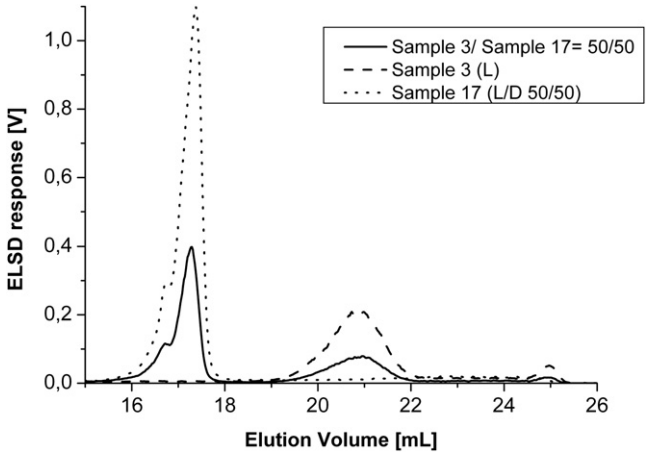

Fig. 7. Chromatograms of sample 3, sample 17 and a 50/50-mixture (wt/wt) of them.

since the change in crystallinity and thus influence on the mechanical properties of the material happens at rather low contents of the second enantiomer, the developed gradient might be suitable to distinguish samples close to the ones having a critical enantiomeric excess.

It can also be seen in Fig. 5 that sample 14, the PDLLA with molecular weight of 8000 g/mol elutes significantly earlier than sample 17, the PDLLA-sample having a high molecular weight of 170 000 g/mol, indicating that the elution volume is influenced by molecular weight as well.

To clarify the effect of molecular weight on elution volume the chromatograms of samples having identical stereochemical composition but differing in molecular weights are compared in Fig. 6A–C. In Fig. 6D the dependence of elution volume on molecular weight is plotted for the six PLLA-samples.

In the first three plots in Fig. 6 a shift of the chromatogram to higher elution volume with increasing molecular weight can be observed, indicating an effect of molecular weight on elution volume. However, as demonstrated in Fig. 6D, the elution volume varies significantly for lower molar masses but approaches a limiting value at high molar mass. Thus, for PLAs with molar masses above 10 000 g/mol the stereochemical composition is the main factor influencing the elution volume, while for lower molar masses the molecular mass has to be taken into account as well.

So far it has been shown that samples of different enantiomeric excess elute at different retention times in the developed gradient.

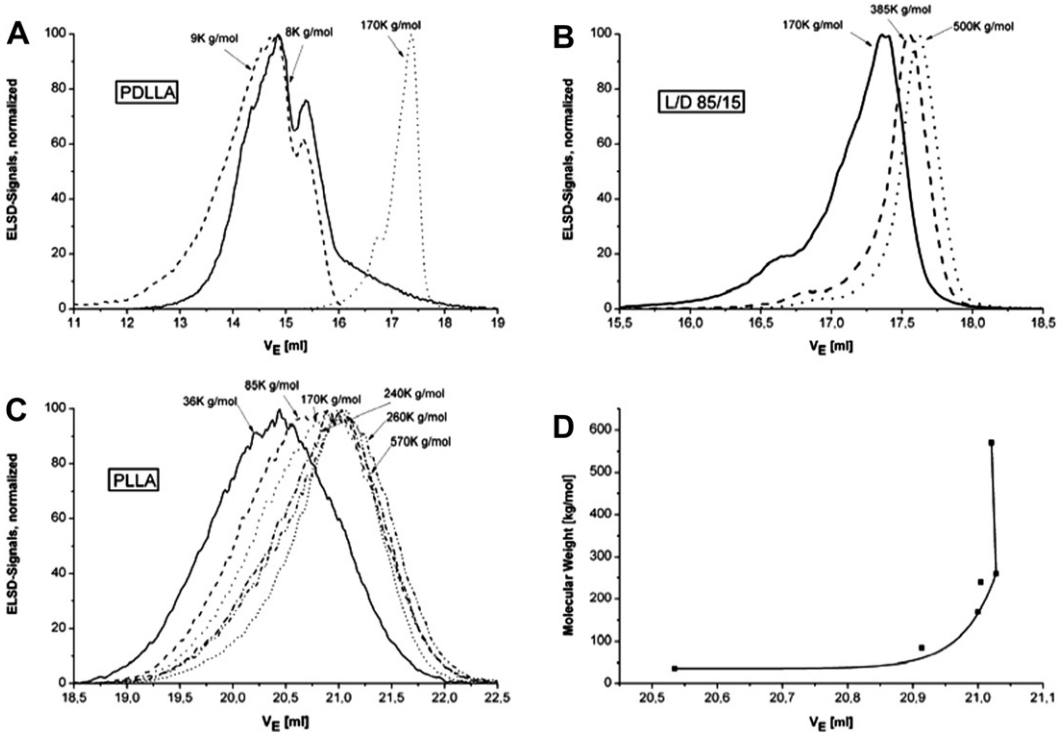

Fig. 6. Normalized chromatograms of (A) three PDLLA, (B) three PLA with an L/D-ratio of 85/15, (C) six PLLA-samples in gradient chromatography, (D) Dependence of elution volume on molecular weight for the PLLA-samples (The line just serves as a guide for the eye). Note the different scales on the volume axis.

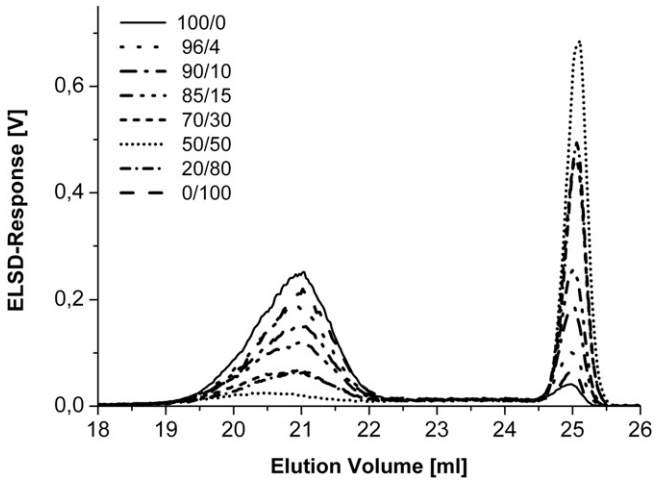

Fig. 8. Chromatograms of mixtures of sample 3 (PLLA) and sample 18 (PDLA) at different blend compositions.

The question arises, whether blends of samples of different stereochemical compositions can be separated into their components as well. To answer this question sample 3 (PLLA) and sample 17 (PDLLA) were mixed in a 1:1 ratio (wt/wt) and injected into the gradient chromatography. Fig. 7 shows the chromatograms of the blend in comparison to the chromatograms of the individual components of the same concentration.

In Fig. 7 two peaks are observed for the mixture, whose peak positions correspond to those of the individual components. Therefore it is proven that samples differing in their stereochemical compositions can actually be separated.

Since the two enantiomerically pure PLAs, PDLA and PLLA, elute at the same elution volume of about 21 mL, a mixture of PDLA and PLLA is expected to give rise to a single peak at the same retention volume. To verify this statement sample 3 (PLLA, 170K g/mol) and sample 18 (PDLA, 160K g/mol) were blended in various ratios and analyzed using the above developed gradient. Fig. 8 shows the chromatograms of such mixtures of different composition. As expected, in all chromatograms a peak at 21 mL is observed. Unexpectedly, however, an additional peak is observed for each mixture at an elution volume of 25 mL. This elution volume corresponds to the gradient step from THF to $CHCl_3$. The relative peak areas of both peaks vary with the blend composition. For the pure sample 3 or 18, the peaks at 25 mL are of negligible intensity, while for the mixture of 50% sample 3 and 50% sample 18 the second peak is much larger than the first one which has almost disappeared.

To illustrate this interesting effect the relative peak area of the peak at 25 mL is plotted in Fig. 9 against the percentage of sample 18 in the blends.

Fig. 9 clearly shows an increase of the relative peak area of the peak at 25 mL with increasing fraction of sample 18 until a maximum is reached at a composition of 50% sample 18 and 50% sample 3. A further increase in the amount of sample 18 decreases the peak area of the second peak. This effect is probably a consequence of the formation of stereocomplexes, which are formed by mixing of PLLA and PDLA. The stereocomplex is known to exhibit a higher melting temperature than the pure PLLAs or PDLAs. Stereocomplexation of polylactides was first described by Ikada et al. [22] and has been intensively investigated by many research groups [12,23–32].

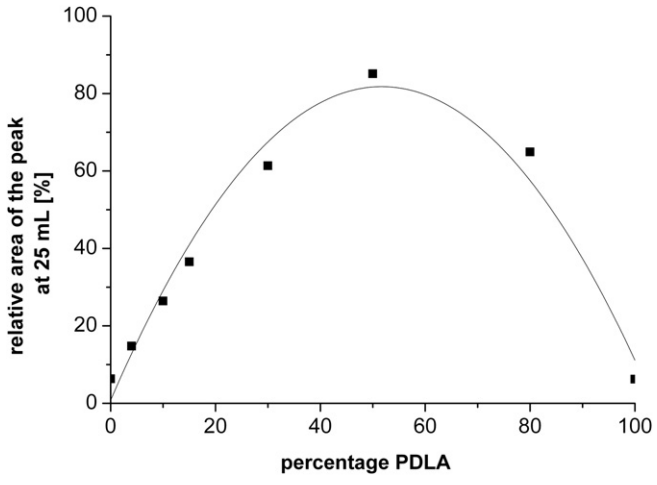

Fig. 9. Relative peak area of the peak at 25 mL in Fig. 8 versus mass fractions of sample 18 (PDLA) in the mixtures of PLLA and PDLA (The line just serves as a guide for the eye).

4. Conclusions

In this work a chromatographic method was developed, in which the retention volume of PLA varies with the excess of enantiomers. The pure PDLAs and PLLAs elute later than samples of lower stereochemical purity. However, PLAs having an enantiomeric excess of less than about 80% elute at almost identical elution volume and therefore cannot be separated. The application of the developed gradient to blends of PLAs of different stereopurity allowed separation into the individual components. Finally, mixtures of pure PDLA and pure PLLA, which were expected to show a single peak, revealed a second peak at significantly higher elution volume, whose relative peak area depends on the PLLA/PDLA-ratio of the blend. This effect is assumed to be a consequence of the formation of stereocomplexes.

Acknowledgments

The financial support of the Cornet project by EU via the Federal Ministry of Economics and Technology [Bundesministerium für Wirtschaft und Technologie (BMWi)] through the Federation of Industrial Cooperative Research Associations “Otto von Guericke” [Arbeitsgemeinschaft industrieller Forschungsvereinigungen “Otto von Guericke” e.V. (AiF)] (AiF-No. 8 EN) is gratefully acknowledged. The authors like to thank Boehringer Ingelheim GmbH and Purac Biochem for providing samples.

References

[1] Brochu S, Prud'homme RE, Barakat I, Jerome R. Macromolecules 1995;28:5230.
[2] Karuta M, Hirata M, Kimura Y. J Macromolecular Sci Part C: Polym Rev 2009;49:107.
[3] Ikada Y, Tsuji H. Macromol Rapid Commun 2000;21:117.
[4] Henton DE, Gruber P, Lunt J, Randall J. Polylactid Acid Technology. In: Natural fibers, biopolymers and biocomposites; 2005. p. 538. Chapter 16.
[5] Goddard H, Kenneth KM, Sosely OS. Eur. Pat. Appl. 830866 A2 25; 1998.
[6] Hartmann MH. High molecular weight polylactic acid polymers. In: Biopolymers from renewable resources. Berlin: Springer; 1998.
[7] Lipinsky ES, Sinclair RG. Chem Eng Prog 1986;82:26.
[8] Bhardwaj R, Blanchard J. Int J Pharm 1998;170:109.
[9] Chasin M, Langer R. Biodegradable polymers as drug delivery systems. New York: Marcel Dekker; 1990.
[10] Winet H, Bao J. Biomed Mater Res 1998;40:567.
[11] Haque R, Saxena M, Yadav B, Ahmed M. J Environ Res Dev 2008;3:257.
[12] Perego G, Cella GD, Bastioli CJ. Appl Polym Sci 1996;59:37.
[13] Spinu M, Jackson C, Keating MY, Gardner KH. J Macromol Sci Pure Appl Chem 1996;33:1497.
[14] Kolstad JJ. J Appl Polym Sci 1996;62:1079.

[15] Thakur KAM, Kean RT, Zupfer J, Buehler N, Doscotch MA, Munson EJ. Macromolecules 1996;29:8844.
[16] Baratian S, Hall ES, Lin JS, Xu R, Runt J. Macromolecules 2001;34:4857.
[17] Matsuo S, Iwakura Y. Makromolekulare Chem 1972;152:203.
[18] Schindler A, Harper D. J Polym Sci 1979;17:2593.
[19] Dondos A, Skordilis V. J Polym Sci 1985;23:615.
[20] Zhao P, Wang QF, Zhong Q, Zhang NW, Ren J. J Appl Polym Sci 2010;115:2955.
[21] Vert M, Chabot F, LeRay J, Chabot P. Macromol Chem 1981;5(Suppl.):30.
[22] Kromidas S. HPLC made to measure. Weinheim: Wiley VCH; 2006.
[23] Ikada Y, Jamshidi K, Tsuji H, Hyon SH. Macromolecules 1987;20:904.
[24] Brizzolara D, Cantow HJ, Diederichs K, Keller E, Domb AJ. Macromolecules 1996;29:191.
[25] Tsuji H, Hyon SH, Ikada Y. Macromolecules 1991;24:5657.
[26] Tsuji H, Hyon SH, Ikada Y. Macromolecules 1992;25:2940.
[27] Tsuji H, Ikada Y. Macromolecules 1993;26:6918.
[28] Tsuji H, Ikada Y. Macromolecules 1996;197:3483.
[29] Tsuji H. Macromol Biosci 2005;5:569.
[30] Biela T, Duda A, Penczek S. Macromolecules 2006;39:3710.
[31] Maillard D, Prud'homme RE. Macromolecules 2010;43:4006.
[32] Quynh TM, Mitomo H, Yoneyama M, Hien NQ. Polym Eng Sci 2009;49:970.

Polymer 52 (2011) 46–54

Contents lists available at ScienceDirect

Polymer

journal homepage: www.elsevier.com/locate/polymer

Synthesis and characterization of polyaniline derivatives and related carbon nanotubes nanocomposites – Study of optical properties and band gap calculation

Valter Bavastrello [a], Tercio Bezerra Correia Terencio [a], Claudio Nicolini [a,b,*]

[a] CIRSDNNOB, Inter-University Centre for Research and Educational Services on Organic and Biological Nanoscience and Nanotechnology, University of Genoa, Corso Europa 30, 16132 Genoa, Italy
[b] Fondazione EL.B.A. Piazza SS Apostoli 66, 00100 Rome, Italy

ARTICLE INFO

Article history:
Received 13 August 2010
Received in revised form
7 October 2010
Accepted 12 October 2010
Available online 20 October 2010

Keywords:
Nanocomposites
Polyanilines
UV–vis Spectroscopy

ABSTRACT

Poly(o-methylaniline) (POTO), poly(o-methoxyaniline) (POAS), poly(2,5-dimethylaniline) (PDMA), poly-(2,5-dimethoxyaniline) (PDOA), and nanocomposite based on multi-walled carbon nanotubes (MWNTs) and single-walled carbon nanotubes (SWNTs) embedded in these conducting polymers, were synthesized by oxidative polymerization. We used the Langmuir–Schaefer (LS) technique to fabricate films at the air–water interface and performed the doping process on the undoped films by dipping the substrates in 1 M hydrochloric acid (HCl) aqueous solution. We recorded UV–vis spectra for both the undoped and doped forms and calculated the related band gaps by using the Tauc equation. Experimental data showed the substituents affected the final oxidation ratio of the polymer chains and the presence of carbon nanotubes (CNTs) in the medium of reaction changed the properties in relation of the kind and number of substituents along the aromatic ring. The study of UV–vis spectra of the undoped nanocomposites and the calculated band gaps highlighted that the conducting polymer chains simply wrapped up around CNTs with no strong interaction. Both the kind and number of substituents along the aromatic rings strongly affected the protonation process, since their capability of "tuning" the formation of the polaronic state. The presence of CNTs in the polymer matrix showed no appreciable influence in the chemical properties of the doped nanocomposites with respect to the pure conducting polymers.

1. Introduction

In recent years, two classes of organic materials like conducting polymers and carbon nanotubes (CNTs) have gained great interest for their unique physical chemistry properties [1–4]. An interesting application can be the embedding of little quantity of CNTs, either single-walled carbon nanotubes (SWNTs) or multi-walled carbon nanotubes (MWNTs), inside the polymer matrix of conducting polymers for the fabrication of nanocomposites [5,6]. This method of synthesis, carried on by polymerizing the monomer in the presence of a dispersion of CNTs, is very simple. Polyaniline derivatives have been deeply studied among conducting polymers in the last decades for their good electrical properties, easy methods of synthesis and high environmental stability [7–10]. The chemistry of polyanilines is generally more complex with respect to other conducting polymers, due to their dependence on both the pH value and the oxidation states, described by three different forms known as leucoemeraldine base (fully reduced form), emeraldine base (EB) (50% oxidized form), and pernigraniline base (fully oxidized form). The most important is the EB form and its protonation by means of H^+ ions, generated from protic acids, gives the emeraldine salt form, responsible of the strong increment of the conducting properties [11]. This process is reversible and it is possible for the presence of imine group basic sites located along the conducting polymer backbone [12,13]. The doping process of polyanilines is always associated to conformational modifications of the polymer chains, due to the local distortions created by the addition of H^+ ions to the basic sites [14]. These distortions are even able to affect the morphology of the deposited films by varying their organization and play an important role in the electrical properties of the conducting polymer [15]. The number and kind of substituents along the aromatic rings of the polymer backbone seems to affect the molecular rearrangement occurring during the doping process and in some cases, the sterical hindrance generated by "too close" substituents to the aromatic ring is responsible of the

* Corresponding author. CIRSDNNOB, Inter-University Centre for Research and Educational Services on Organic and Biological Nanoscience and Nanotechnology, University of Genoa, Corso Europa 30, 16132 Genoa, Italy. Tel.: +39 010 35338217; fax: +39 010 35338215.
E-mail address: manuscript@ibf.unige.it (C. Nicolini).

0032-3861/$ – see front matter © 2010 Elsevier Ltd. All rights reserved.
doi:10.1016/j.polymer.2010.10.022

spontaneous undoping process [16]. Taking into account these considerations, the aim of the present study was to investigate the possible variations on polyaniline derivatives physical chemistry properties by performing standardized oxidative polymerizations on monomers with different kind and number of substituents along the aromatic rings. We carried out further investigations by polymerizing in the presence of dispersions of either MWNTs or SWNTs, in order to study the influence of these materials in the medium of reaction on the chemical properties of the synthesized conducting polymers, as well as the properties of the related nanocomposites with respect to the pure conducting polymers.

2. Experimental section

2.1. Materials

Monomers of *ortho*-methylaniline, *ortho*-methoxyaniline, 2,5-dimethylaniline, 2,5-dimethoxyaniline, ammonium persulfate [$(NH_4)_2S_2O_8$] as oxidizing agents and other reagents were obtained from Sigma. We purchased High purity MWNTs and SWNTs from NANOCS Inc, New York, USA. MWNTs had a diameter ranging between 30 ÷ 40 nm and length between 40 ÷ 50 micron. SWNTs had a diameter of ~2 nm for individual tubes and length of ~500 nm. Fig. 1 shows the chemical structure of monomers used in the syntheses.

2.2. Syntheses of pure conducting polymers and related nanocomposite materials

The standardized synthesis of both nanocomposite materials and pure conducting polymers was carried out by oxidative polymerization under controlled conditions, maintaining the temperature at 0 ÷ 4 °C by means of an ice bath for 24 h. The medium of reaction was 200 ml of 1 M HCl solution of the monomers. For the synthesis of the nanocomposites, we dispersed 100 mg CNTs in the medium of reaction by sonication. We performed the sonication by means of SONIC 300 VT equipment, setting a 10% power for 1 min in order to only disperse CNTs without braking processes. We used a monomer/MWNTs weight ratio of 100/1 and a monomer/oxidant molar ratio of 4/1, following methods of polymerization previously performed [17]. We utilized the same ratios on using SWNTs for the synthesis of the related nanocomposites. Table 1 resumes the amounts of reagents used for the synthesis.

Particular care was taken on adding the oxidizing agent to have the most reproducible conditions at the very begin of the polymerization. In order to obtain the solvent processable undoped form, we filtered and subsequently treated the crude materials in the doped form (emeraldine salt form) with ammonium hydroxide for 2 h. We finally filtered the undoped materials (EB form) and performed a treatment with methanol and diethyl ether in order to eliminate the oligomers, followed by the evaporation of the residue solvents by vacuum. We synthesized the pure polymers by following the same steps carried out for the nanocomposites, save for the presence of either MWNTs or SWNTs in the medium of reaction. The final products, in the EB forms, were completely soluble in chloroform. Fig. 2 illustrates the scheme of synthesis.

Table 1
Amounts of reagents used for the synthesis of the materials carried out in 200 ml of 1M HCl aqueous solution.

Synthesized Material	MWNTs (mg)	SWNTs (mg)	Monomer (g)	Oxidant (g)
POTO	–	–	9.97	5.26
POTO-MWNTs	100.8	–	10.08	5.32
POTO-SWNTs	–	100.5	10.05	5.30
POAS	–	–	10.03	4.61
POAS-MWNTs	99.2	–	9.92	4.56
POAS-SWNTs	–	100.7	10.07	4.63
PDMA	–	–	9.89	4.62
PDMA-MWNTs	99.5	–	9.95	4.65
PDMA-SWNTs	–	100.9	10.09	4.71
PDOA	–	–	10.04	3.70
PDOA-MWNTs	100.2	–	10.02	3.71
PDOA-SWNTs	–	99.7	9.97	3.69

2.3. Fabrication of LS films

We fabricated the Langmuir monolayers in a Langmuir–Blodgett trough (MDT corp., Russia), 240 mm × 100 mm in size and 300 mL in volume, having a compression speed of 1.67 mm/s (100 cm^2/min). The spreading solutions of pure conducting polymers and nanocomposites materials were prepared by dissolving 5 mg of materials in 20 ml of chloroform. The Langmuir–Schaefer (LS) films were deposited at air–water interface, maintaining the surface pressure at 25 mN/m [6,15–17]. We used distilled water as subphase for the deposition to obtain films of the materials in the undoped form. We subsequently performed the doping process on the deposited films in the undoped form by dipping the substrate in 1 M HCl aqueous solution for 1 h. Experimental observations highlighted that the doping process reached the top just after 30 min of dipping. Anyway, as will be discussed in the next section of the paper, the presence of

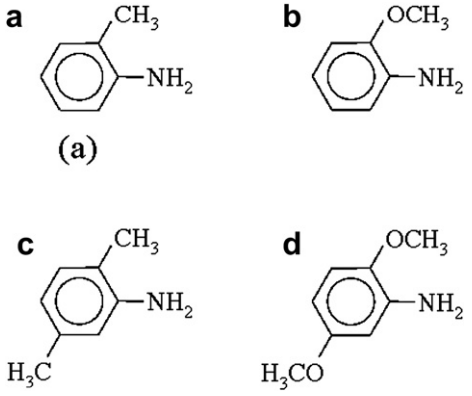

Fig. 1. Chemical structure of the monomer used for the synthesized materials. a) ortho-methylaniline; b) ortho-methoxyaniline; c) 2,5-dimethylaniline; d) 2,5-dimethoxyaniline.

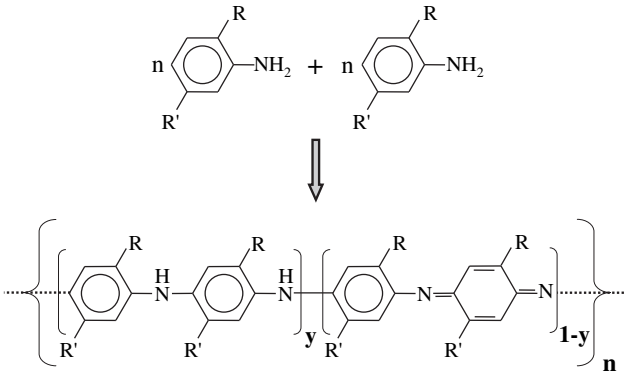

Fig. 2. Scheme of the synthesis leading to the formation of a repeat unit starting from monomers. Basing on the fraction of imine nitrogen groups per repeat unit it is possible to obtain different reduced/oxidized polymer chains as following: Fully reduced form (leucoemeraldine base) for $y = 1$; Fully oxidized form (pernigraniline base) for $y = 0$; Half oxidized form (emeraldine base) for $y = 0.5$.

specific substituents along the aromatic rings represented a barrier to the complete protonation of the imine group basic sites during the doping process.

2.4. Optical measurements and band gap calculation

We recorded the UV–vis spectra of the nanocomposite materials and the corresponding pure conducting polymers, deposited in thin films on quartz substrates, in both the undoped and doped forms by using a UV–vis spectrophotometer Jasco V530 with software. We recorded UV–vis spectra by ranging between 250 ÷ 1000 nm, setting 100 nm/min scanning speed and 1.0 nm data pitch. We thus utilized the spectra for the calculation of the band gap by means of the Tauc equation:

$$\alpha = B\frac{(h\nu - Eg)^n}{h\nu} \quad (1)$$

where α is the absorption coefficient, B is a fitting parameter, h is the Planck constant, ν is the photon frequency, E_g is the band gap, and n takes into account different possible electronic transitions responsible for the light absorption [18]. On considering polyaniline and its derivatives, $n = 1/2$ [19]. All calculations were subsequently obtained from UV–vis spectra plotted as $(\alpha h\nu)^2$ vs. $h\nu$, and the energy gap was obtained by the intercept on the abscissa of the best fitting of Equation (1).

3. Results and discussion

3.1. Syntheses of pure conducting polymers and related nanocomposite materials

We studied the standardized oxidative polymerization, carried out for the synthesis of both pure conducting polymers and related nanocomposite materials, to investigate whether the presence of dispersed CNTs into the medium of reaction could affect the polymer chains oxidation ratio in the final products of synthesis. In Fig. 3 is proposed the monomers oxidation stoichiometry, by means of $(NH_4)_2S_2O_8$, to polyaniline derivatives chlorides in acidic medium for HCl.

For this purpose, we studied the UV–vis spectra to verify the amount of quinone-like structure per repeat unit, as illustrated in Fig. 2. McCall and co-workers gave proof that the peak related to the π–π^* transition can give an estimation of the oxidation ratio

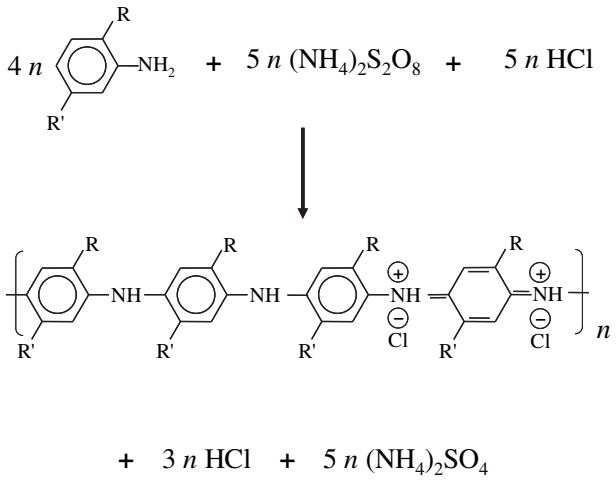

Fig. 3. Stoichiometry of monomers oxidation by means of $(NH_4)_2S_2O_8$ in acidic medium for HCl. The synthesis leads to polyaniline derivatives chlorides.

comparing the related absorbance to that of n–π^* one [20], which will be fully discussed in the next section. We thus took into consideration the peaks absorbance ratio, express as Abs(π–$\pi^*_{Undoped}$)/Abs(n–$\pi^*_{Undoped}$), to calculate the reduced/oxidized ratio of the synthesized materials. In Figs. 4 and 5 are reported the UV–vis spectra of all materials in the undoped form.

On taking into account monosubstituted aromatic rings conducting polymers, POTO and POAS, the oxidative polymerization issued polymer chains with a more predominant reduced form (see Fig. 4). This predominance was much more evident for POTO and related nanocomposites than POAS based materials. Anyway, the presence of CNTs dispersed in the medium of reaction showed to increase the oxidation grade of the polymer chains in both cases, as summarized in Table 2.

The study of the disubstituted aromatic rings polymer chains highlighted a reduced/oxidized ratio close to 1 for all the materials based on PDMA and PDOA (see Fig. 5). Interestingly, the presence of CNTs in the medium of reaction had a minor influence than previously illustrated for monosubstituted ones. Furthermore, we observed an opposite trend for the related nanocomposites (see Table 2). In fact, while polymer chains containing electron donor substituents along the aromatic rings, such as the methoxy group (CH_3O–) in PDOA, showed a slight decrement of the reduced form per repeat unit, an opposite effect was obtained in the presence of non-electron donor substituents, such as the methyl group (CH_3–) in PDMA. Suparina and co-workers gave a full view of the mechanism of reaction involving the oxidative polymerization of aniline monomers by means of $(NH_4)_2S_2O_8$ as oxidizing agent in an acidic medium [21]. When the acidic medium has a pH <2.5 the oxidative polymerization proceeds, as a chain reaction, by adding further monomers to the active chain ends [22]. In the case of polyaniline, the 95% of macromolecules follow a growing chains head-to-tail *para* position, while the remnant 5% is oriented to the *ortho* position [23–25]. Taking into account the monomers used for our polymerizations, the occupied *ortho* position for all of them enhanced the growing chains head-to-tail *para* position. Anyway, the *meta* position was free for *ortho*-methylaniline and *ortho*-methoxyaniline monomers, thus leading to the formation of instable intermediates capable to stop the polymerization. In fact, the rate of monomers oxidation is affected by the presence of small amount of phenilenediamines reaction intermediates, such as 1,2-phenylenediamine, 1,3-phenylenediamine, and 1,4-phenylenediamine, respectively [26,27]. Specifically, while 1,4-phenylenediamine intermediate shortens the induction period and "pave the way" for the successive chains growing process, 1,3-phenylenediamine extends this period, and 1,2-phenylenediamine has practically no effect on the oxidation process. Furthermore, 1,3-phenylenediamine intermediate (*meta* position) tends to disrupt the formation of pernigraniline-like structure during the growing process. The polymerization then proceeds as illustrated in the schematic of Fig. 6, where protonated pernigraniline chains grow by adding anilinium cations in *para* position and the possible delocalization of the positive charges along the polymer backbone strictly rules their stability, also increased by the best reachable alignment ("*in a plane*" zigzag configuration) of the benzene/quinoid-like rings.

The growing process ends after depletion of either the oxidizing agent or the monomers and the final structure of the macromolecules strictly depends on the reagent in excess. For exceeding oxidant (oxidant/monomer molar ratio over 1.5) the resulting polymers remain in the pernigraniline form [28]. Either a monomer/oxidant molar ratio equals to 1.25 or more than this limit leads to a reduction of pernigraniline to emeraldine form [29]. Protonated pernigraniline chains thus reduce to the emeraldine form, at the end of the oxidation process, by the aniline excess in the

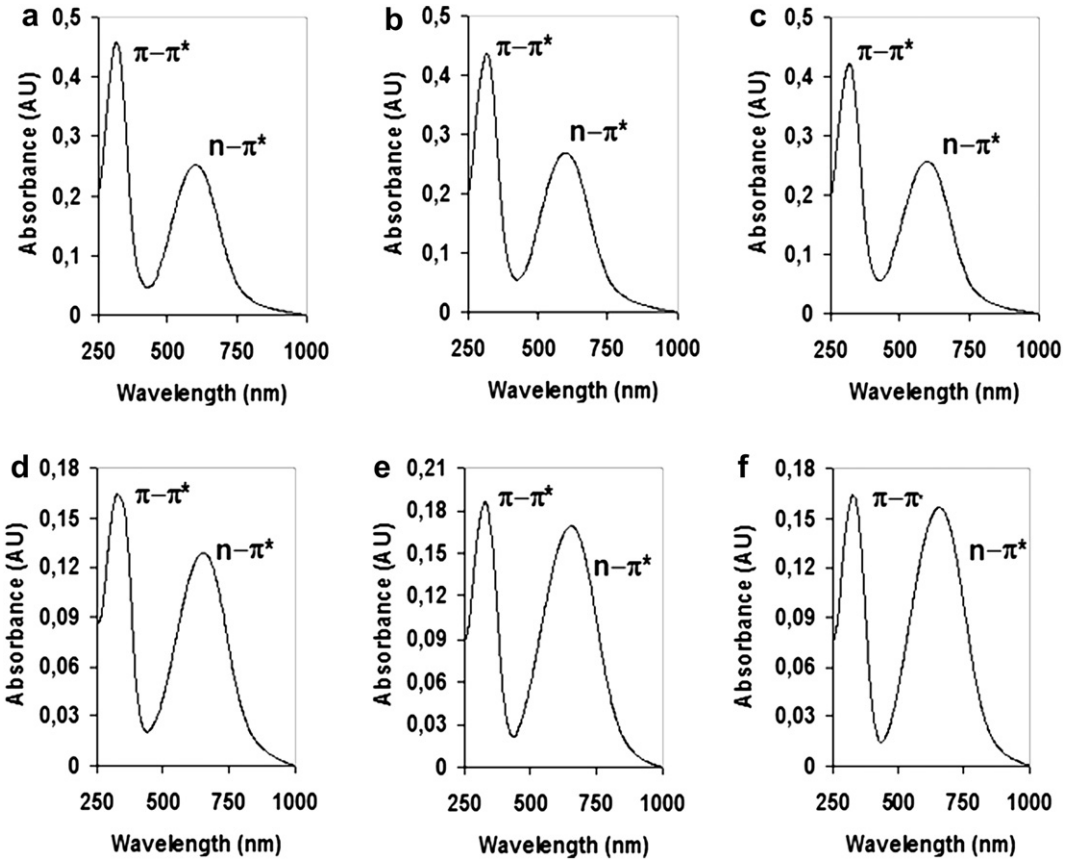

Fig. 4. UV–vis spectra of materials in the undoped form based on monosubstituted aromatic ring conducting polymer (POTO and POAS): a) POTO pure conducting polymer; b) POTO-MWNTs nanocomposite material; c) POTO-SWNTs nanocomposite material. d) POAS pure conducting polymer; e) POAS-MWNTs nanocomposite material; f) POAS-SWNTs nanocomposite material.

medium of reaction [30]. Taking into account all considerations so far discussed, the equal to 4 monomer/oxidant molar ratio used in our syntheses allowed the formation of polymers in the EB form, even though in different reduced/oxidized segments ratio. For the pure conducting polymers, the presence of substituents along the aromatic rings produced a "tuning" effect on the final structure. The explanation takes into account the monomer consumption in relation of the growing positive charged pernigraniline-like polymer chains. Since both the intermediates formation and the positive charges delocalization along the polymer backbone deeply affect the stability of the growing chains, the sterical hindrance and the electron donor effect played an important role in this process. In order to have a clear vision of the following considerations, it is important to underline that the CH_3– group is "closer" to the aromatic ring than the CH_3O– group, since the latter bears an oxygen atom [31]. Furthermore, the CH_3O– can "supply" the electron donor effect to the stability of the positive charges during the polymerization. On considering the pure polymers, the presence of either CH_3– or CH_3O– groups along the aromatic rings was in fact responsible of a worse alignment due to a major sterical hindrance with respect to polyaniline, since the substituents did not allow a full "*in a plane*" configuration. The worse alignment decreased the positive charge delocalization during the growing process, and this gain in free energy resulted in an earlier stop of the polymerization. The consequence was a decreased consumption of monomers and the corresponding higher concentration in the final medium of reaction corresponded to a major reduction of the polymer-oxidized segments. It is very important to highlight that disubstituted aromatic rings polymers showed a decreased reduced/oxidized ratio with respect to monosubstituted ones. The increased number of substituents would correspond to a major sterical hindrance, thus to an increased reduced/oxidized ratio as so far discussed. On the contrary, POTO and POAS did not show this behavior, since for monosubstituted aromatic rings polymers we have to take into account a third parameter. In fact, for these materials the free *meta* position allowed the 1,3-phenylenediamine derivatives intermediate formation, which deeply affected the propagation of pernigraniline-like structure during the growing process as fully discussed above in this section [26,27]. The consequence was an increased concentration of non-reacted monomers in the final medium of reaction, responsible of an increased reduction of the pernigraniline-like form. Therefore, the sterical hindrance and the electron donor effect strictly ruled the mechanism of reaction of pure conducting polymers in the case of disubstituted aromatic rings. It mostly affects the "*in a plane*" alignment of the aromatic rings responsible of the positive charges delocalization, while the 1,3-phenylenediamine derivatives intermediate formation took place since the very begin of the polymerization overruling the sterical hindrance and the electron donor effect. This fact can also explain the little difference obtained between PDMA and PDOA reduced/oxidized ratios, where a doubled donor effect was not able to make the same difference highlighted for POTO and POAS. The presence of CNTs dispersion into the acidic medium of reaction affected all the synthesized materials. Jimenez and co-workers recently carried out the polymerization of polyaniline into dispersions of MWNTs [32]. They observed an acceleration of the polymerization when CNTs were dispersed in the medium of reaction, since the induction period at

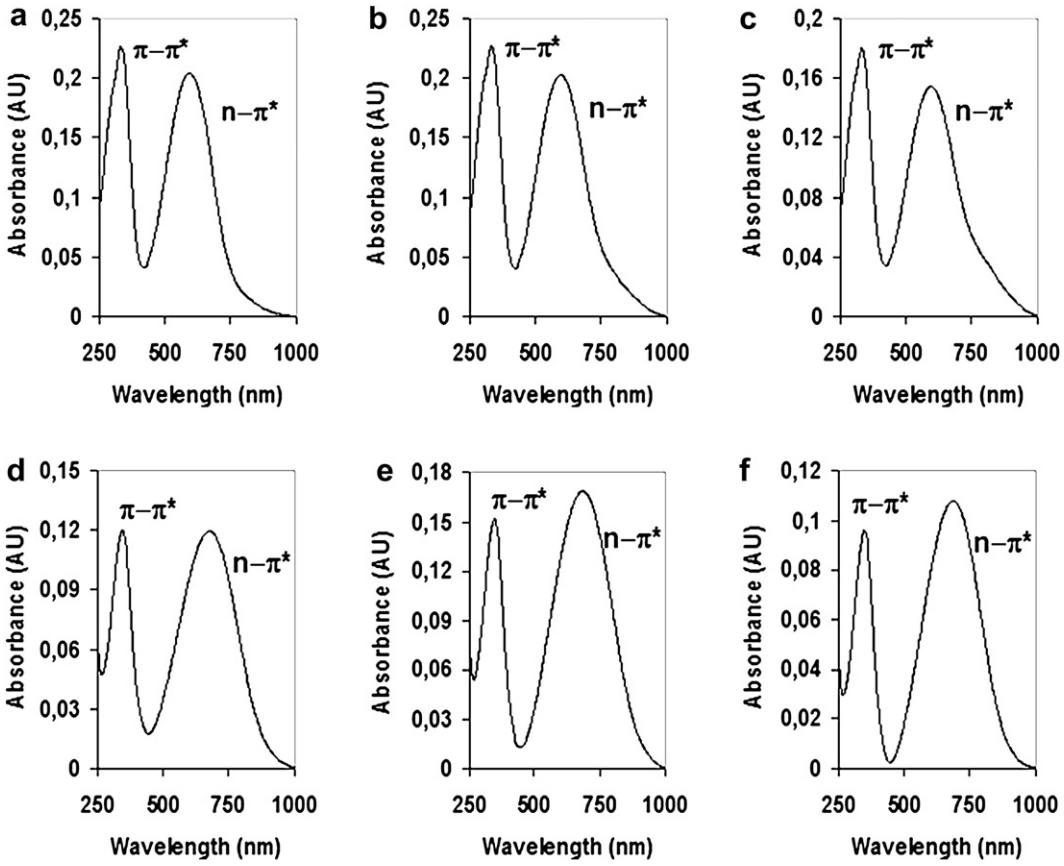

Fig. 5. UV–vis spectra of materials in the undoped form based on disubstituted aromatic ring conducting polymer (PDMA and PDOA): a) PDMA pure conducting polymer; b) PDMA-MWNTs nanocomposite material; c) PDMA-SWNTs nanocomposite material; d) PDOA pure conducting polymer; e) PDOA-MWNTs nanocomposite material; f) PDOA-SWNTs nanocomposite material.

the very begin of the synthesis decreased from 4 min for pure polyaniline to approximately 90 s for all the nanocomposites. They gave a possible explanation because of a catalytic effect of the CNTs surface during the first stage of aniline oxidation. The catalytic effect was due to the fact CNTs worked as nucleation points where the polymer chains grew up. As previously described, the trend was an extra decrement in the reduced/oxidized ratio for all the polymers save for PDMA based nanocomposites, where the same ratio showed a slight increment. This behavior can find an explanation in the support given by the peculiar chemical structure of CNTs to the electron donor effect and in the partial negative counterbalance given to positive charges delocalized along the growing polymers. This "contact" among polymers and the surface of CNTs took place since CNTs worked as nucleation point where the polymer chains grew up by tangling around the surface without the formation of

Table 2
Calculation of the reduced/oxidized ratio of the synthesized materials by taking into account the peaks absorbance, expressed as Abs($\pi-\pi^*_{Undoped}$)/Abs($n-\pi^*_{Undoped}$). Abs($\pi-\pi^*_{Undoped}$) = Absorbance of peak related to $\pi-\pi^*$ transition of materials in the undoped form. Abs($n-\pi^*_{Undoped}$) = Absorbance of peak related to $n-\pi^*$ transition of materials in the undoped form.

Material	Abs ($\pi-\pi^*_{Undoped}$)	Abs ($n-\pi^*_{Undoped}$)	Oxidation ratio Abs($\pi-\pi^*_{Undoped}$)/ Abs($n-\pi^*_{Undoped}$)
POTO	0.460 ± 0.001	0.252 ± 0.001	1.82 ± 0.01
POTO-MWNTs	0.439 ± 0.001	0.270 ± 0.001	1.63 ± 0.01
POTO-SWNTs	0.422 ± 0.001	0.257 ± 0.001	1.64 ± 0.01
POAS	0.165 ± 0.001	0.129 ± 0.001	1.28 ± 0.01
POAS-MWNTs	0.125 ± 0.001	0.119 ± 0.001	1.05 ± 0.01
POAS-SWNTs	0.160 ± 0.001	0.153 ± 0.001	1.05 ± 0.01
PDMA	0.228 ± 0.001	0.204 ± 0.001	1.11 ± 0.01
PDMA-MWNTs	0.228 ± 0.001	0.203 ± 0.001	1.12 ± 0.01
PDMA-SWNTs	0.180 ± 0.001	0.155 ± 0.001	1.16 ± 0.01
PDOA	0.120 ± 0.001	0.120 ± 0.001	1.01 ± 0.01
PDOA-MWNTs	0.152 ± 0.001	0.169 ± 0.001	0.90 ± 0.01
PDOA-SWNTs	0.096 ± 0.001	0.108 ± 0.001	0.89 ± 0.01

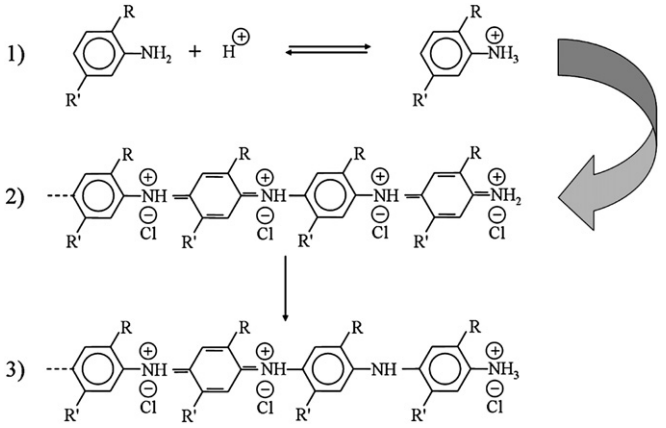

Fig. 6. Scheme of the protonated pernigraniline chains growing process by addition of anilinium cations in *para* position. Their stability is strictly ruled by the possible delocalization of the positive charges along the polymer backbone, which is increased by the best reachable alignment ("*in a plane*" zigzag configuration) of the benzene/quinoid-like rings.

strong interaction. The fact either using MWNTs or SWNTs equally affected the final reduced/oxidized segments ratio is a further support for the experimental results so far discussed. The contribute of electron donor substituent seemed to be more relevant than the partial positive charge counterbalance, and this can explain the anomalous behavior found for PDMA based nanocomposite materials. The study of the optical properties, illustrated in the next section, also supported all the considerations so far discussed.

3.2. Optical measurements and band gap calculation

As widely discussed in the previous section, the study of the UV–vis spectra collected for all the synthesized materials in the undoped form (see Figs. 3 and 4) showed that the oxidative polymerization led to the formation of polymer chains EB form, due to the presence of two bands. The first was assigned to the $\pi-\pi^*$ interband transition in the benzoid/quinoid ring structure, ranging between 331 ÷ 348 nm, and the second assigned to the $n-\pi^*$ transition from the nonbonding nitrogen lone pair to the conduction band π^*, ranging between 594 ÷ 688 nm, respectively [33]. In Table 3 are reported the wavelengths of each band for all the synthesized undoped materials.

The optical characterizations highlighted that the presence of CNTs inside the polymer matrix produced no change in the $\pi-\pi^*$ transition. This result suggests that the polymer chains simply wrapped up around CNTs with no strong interaction, as illustrated in the representation proposed in Fig. 7, thus supporting the considerations related to the polymer chains growing process around the surface of CNTs previously highlighted.

On the contrary, the nanocomposites $n-\pi^*$ transitions showed a perceptible red shift with respect to the corresponding pure conducting polymers, depending on the kind and number of substituents along the aromatic ring (see Table 3). Specifically, the presence of electron donor substituents, corresponded to a lower energy in the $n-\pi^*$ transitions, and subsequently to a major availability of the imine group basic sites lone pairs, responsible of the proton doping process illustrated in the schematic of Fig. 8.

The same effect did not take place when the substituents were not electron donor. The presence of CNTs inside the polymer matrix thus affected the properties of the CH_3O- group by enhancing the electron donor effect and thus the availability of the lone pairs of imine groups. We observed this change in the optical properties for both the materials based on POAS and PDOA. We obtained for POAS pure conducting polymer a wavelength of 654 nm for the $n-\pi^*$ interband transition, and 661 nm for both the related nanocomposite materials. PDOA pure conducting polymer showed the $n-\pi^*$ interband transitions at 677 nm, while the interband was at 685 nm in the case of MWNTs and at 688 nm in the case of SWNTs

Table 3
Wavelength of the peaks related to the $\pi-\pi^*$ and $n-\pi^*$ transitions for all materials in the undoped forms.

Material	$\pi-\pi^*_{(Undoped)}$ (nm)	$n-\pi^*_{(Undoped)}$ (nm)
PDMA	331 ± 1	594 ± 1
PDMA-MWNTs	332 ± 1	597 ± 1
PDMA-SWNTs	331 ± 1	597 ± 1
PDOA	345 ± 1	677 ± 1
PDOA-MWNTs	345 ± 1	685 ± 1
PDOA-SWNTs	348 ± 1	688 ± 1
POTO	314 ± 1	601 ± 1
POTO-MWNTs	316 ± 1	600 ± 1
POTO-SWNTs	316 ± 1	599 ± 1
POAS	328 ± 1	654 ± 1
POAS-MWNTs	328 ± 1	661 ± 1
POAS-SWNTs	327 ± 1	661 ± 1

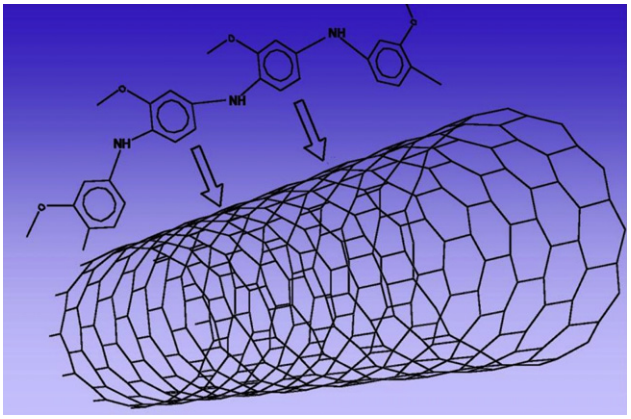

Fig. 7. Representation of nanocomposite materials based on wrapped up polymer chains around CNTs without the formation of strong interactions.

inside the polymer matrix, respectively. On the contrary, the materials based on POTO and PDMA, where the aromatic rings of the polymer chains have CH_3- group as substituent, showed no evident change since the $n-\pi^*$ transition among pure conducting polymers and the related nanocomposites ranged only 2 nm (see Table 3). The calculation of the band gaps was performed taking into account the $\pi-\pi^*$ interband transition that is considered a good estimation of the material band gap [34], by applying the Equation (1) previously described, as shown in the graphics of Fig. 9.

The experimental data, summarized in Table 4, showed no differences between band gap values of mono and disubstituted aromatic rings either considering the same or different groups.

A possible explanation can be the more stretched conformation of the polymer chains due to the presence of substituents, which are responsible of a "range-reduced" torsion angle among benzene/quinoid-like rings, so generating a similar alignment for the electron delocalization along the conducting polymers. This result is supported by the band gap calculated for polyaniline [30,35–37], where the absence of substituents along the aromatic rings was responsible of a major "tangling rate" of the polymer chains, which turned into a worse alignment of the benzene rings and a decreased electron delocalization [38,39]. The analysis of the UV–vis spectra

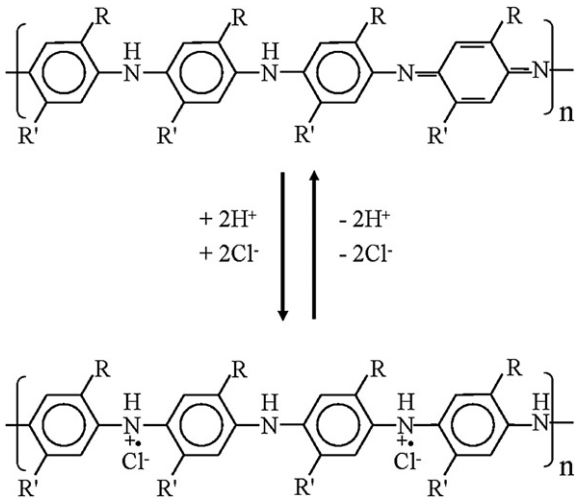

Fig. 8. Scheme of the doping process by addition of H^+ ions to the imine basic sites with formation of the polaronic state.

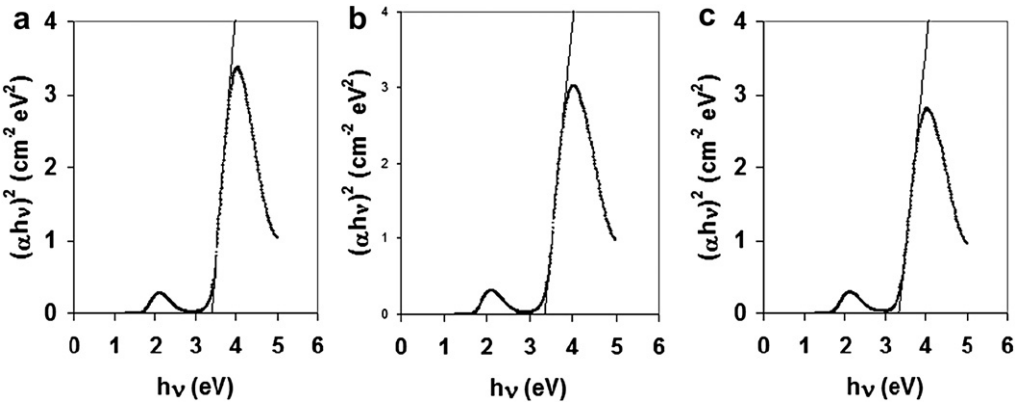

Fig. 9. Calculation of the undoped form band gaps for POTO (a), POTO-MWNTs (b), and POTO-SWNTs (c), obtained from UV–vis spectra by plotting $(\alpha h\nu)^2$ vs. $h\nu$. The energy gap was obtained by the intercept on the abscissa of the best fitting of Equation (1).

Table 4
Values of the band gaps ($E_{g\text{Undoped}}$) calculated for the $\pi-\pi^*$ interband transitions of all materials in the undoped form.

Material	$E_{g(\text{Undoped})}$ (eV)
PDMA	3.3 ± 0.1
PDMA-MWNTs	3.3 ± 0.1
PDMA-SWNTs	3.3 ± 0.1
PDOA	3.2 ± 0.1
PDOA-MWNTs	3.2 ± 0.1
PDOA-SWNTs	3.2 ± 0.1
POTO	3.4 ± 0.1
POTO-MWNTs	3.4 ± 0.1
POTO-SWNTs	3.4 ± 0.1
POAS	3.1 ± 0.1
POAS-MWNTs	3.2 ± 0.1
POAS-SWNTs	3.2 ± 0.1

showed a very interesting behavior on doping with 1 M HCl protic acid. The formation of the polaronic state and the presence of the relative bands due to the polaron–π^* and π–polaron transitions were obtained for materials based on POTO, POAS, and PDOA respectively (see Figs. 10, 11 and 13), while these bands were missing in the PDMA spectra (see Fig. 12).

The presence of the CH_3- group along the aromatic rings of the polymer chains seemed to have stronger effect than CH_3O- group on the doped macromolecules. Since the doping process takes place on the imine groups basic sites nitrogen atoms, characterized by a planar configuration (sp^2 hybridization), and the protonation issues tetrahedral configuration (sp^3 hybridization), this change in the atoms spatial disposition was likely to be mostly affected by the sterical hindrance for non-electron donor substituents. Moreover, the doping process took place on solid-state films, with consequent diminished degrees of freedom of the polymer chains. Taking into account the major hindrance of CH_3- substituents than CH_3O- ones and the strong impediment generated to the modification of the torsion angles on doping, it is thus possible to have an explanation of the incomplete doping process occurring for PDMA and related nanocomposites. More specifically, for PDMA based materials the $\pi-\pi^*$ interband transition moved to shorter wavelengths while a band centered at about 810 nm was formed. This behavior was consistent with a very low protonation of the polymer chains even using highly concentrated protic acids as doping agent. The scarce protonation was anyway responsible for the reduced conjugation among interchain aromatic rings which turned into a $\pi-\pi^*$ interband higher energy transition (hypsochromic shift).

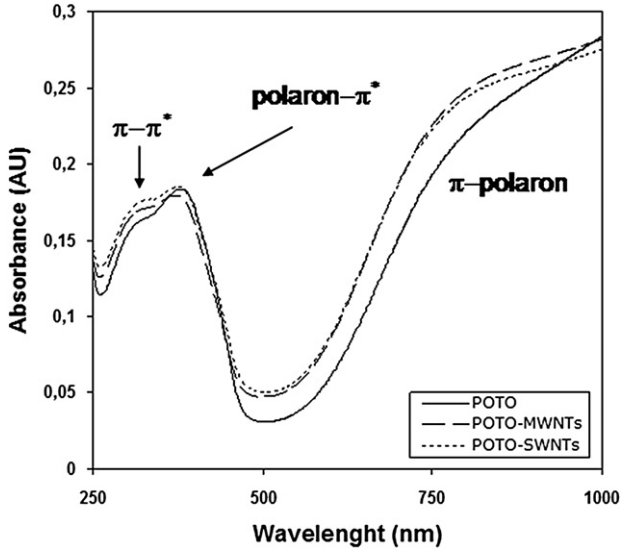

Fig. 10. UV–vis spectra of materials in the doped form based on POTO conducting polymer: Solid line = POTO pure conducting polymer; Semisolid line = POTO-MWNTs nanocomposite material; Dotted line = POTO-SWNTs nanocomposite material.

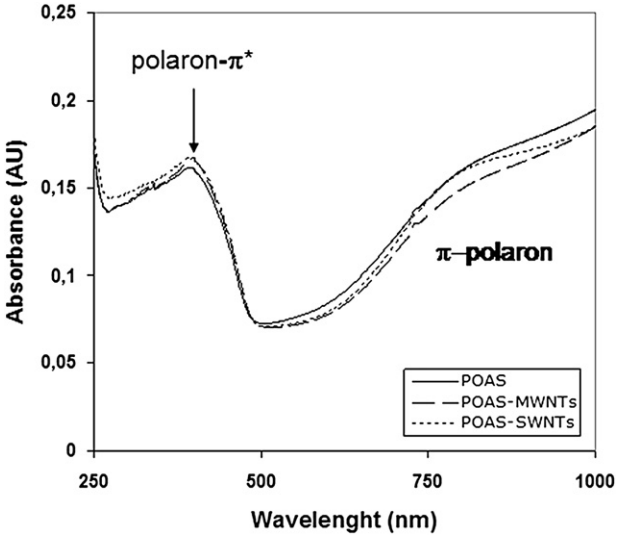

Fig. 11. UV–vis spectra of materials in the doped form based on POAS conducting polymer: Solid line = POAS pure conducting polymer; Semisolid line = POAS-MWNTs nanocomposite material; Dotted line = POAS-SWNTs nanocomposite material.

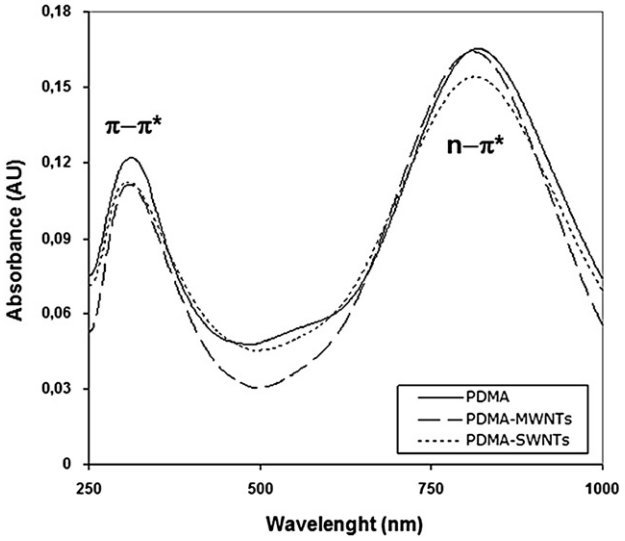

Fig. 12. UV–vis spectra of materials in the doped form based on PDMA conducting polymer: Solid line = PDMA pure conducting polymer; Semisolid line = PDMA-MWNTs nanocomposite material; Dotted line = PDMA-SWNTs nanocomposite material.

The reduced conjugation was also responsible of the red shift occurring to the n–π^* interband, since the diminished "engagement" of imine group lone pairs in this process (see Fig. 12). For the monosubstituted aromatic ring polymer chains containing the CH_3– group (POTO and related nanocomposites), besides the presence of the two bands mention above there was another one related to the π–π^* transition, typical of the udoped form, centered at about 310 nm and appearing as a shoulder of the polaron–π^* transition band (see Fig. 10). Thus the sterical hindrance generated by the CH_3– groups strongly affected the doping process for the double-substituted aromatic ring polymer chains (PDMA and related nanocomposites), since the formation of the polaronic states was impeded, while for monosubstituted aromatic rings (POTO and related nanocomposites) was responsible of an uncompleted doped material. The presence of CH_3O– group reduced the sterical hindrance and allowed a very high protonation

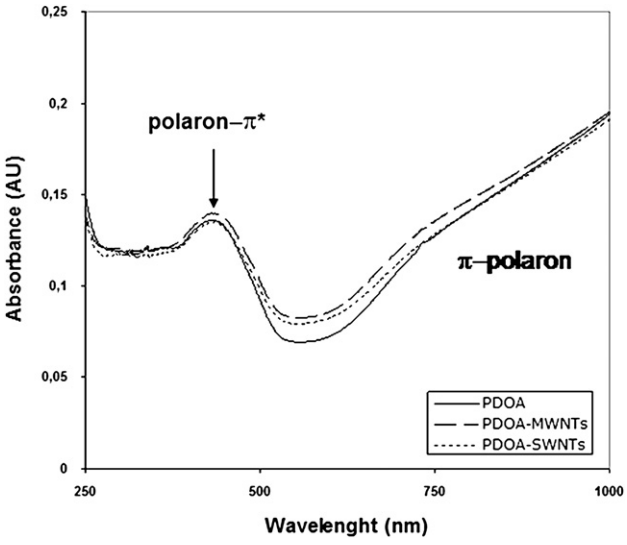

Fig. 13. UV–vis spectra of materials in the doped form based on PDOA conducting polymer: Solid line = PDOA pure conducting polymer; Semisolid line = PDOA-MWNTs nanocomposite material; Dotted line = PDOA-SWNTs nanocomposite material.

Table 5
Values of the band gaps (E_{gDoped}) calculated for the polaron–π^* transitions of POTO, POAS, PDOA and related nanocomposites in the doped form. The calculation for PDMA and related nanocomposites was obtained by considering the π–π^* transition since for these materials the formation of the polaronic state was impeded.

Material	$E_{g(Doped)}$ (eV)
PDMA	3.1 ± 0.1
PDMA-MWNTs	3.1 ± 0.1
PDMA-SWNTs	3.0 ± 0.1
PDOA	2.3 ± 0.1
PDOA-MWNTs	2.3 ± 0.1
PDOA-SWNTs	2.3 ± 0.1
POTO	2.7 ± 0.1
POTO-MWNTs	2.7 ± 0.1
POTO-SWNTs	2.7 ± 0.1
POAS	2.5 ± 0.1
POAS-MWNTs	2.5 ± 0.1
POAS-SWNTs	2.5 ± 0.1

of the polymer chains even when two substituents were present. The UV–vis spectra of both the materials based on POAS and PDOA showed in fact the presence of the polaron–π^* transition band centered at about 390 nm for the former and 420 nm for the latter, while the π–π^* interband transition was absent (see Figs. 11 and 13). Moreover, the CH_3O– groups, acting as electron donor substituents, were able to favor and enhance the doping process. This was consistent with the experimental data, since the polaron–π^* transition band of PDOA based materials found at higher wavelength than PDMA ones, indicating a higher grade of protonation. Hence, for the CH_3O– group the electron donor effect is more relevant than the sterical hindrance. These considerations, found support by the calculation of the related band gaps (Figures not shown), summarized in Table 5.

The presence of both MWNTs and SWNTs inside the polymer matrix showed no modification in the chemical properties of the doped materials save for a little increment of the π–π^* interband transition of the POTO nanocomposites with respect to the pure conducting polymer. It is possible that the only CH_3– substituent is not enough to compromise the formation of the polaronic state as in the case of PDMA and related nanocomposites, but the presence of CNTs in the polymer matrix seemed to reduce the degrees of freedom with consequent reduced protonation. This result was not consistent with those recently obtained in water dispersible composites [32], and the explanation can be find in the reduced degrees of freedom in the solid-state.

4. Conclusions

We synthesized chloroform processable pure conducting polymers and related nanocomposites by oxidative polymerization. Thin solid films were prepared for all materials in the undoped form by means of LS technique, and subsequently doped by dipping the substrates in 1 M HCl aqueous solution. The oxidative polymerization issued EB form polymer chains with different oxidized segments along the polymer backbone and the reduced/oxidized ratio, depended on the kind and number of substituents along the aromatic rings as well as on the presence of dispersion of CNTs in the medium of reaction. We found for POTO and POAS a predominant reduced form, more evident for POTO than POAS, and a reduced/oxidized ratio close to 1 for PDMA and PDOA. Furthermore, PDOA showed a slight decrement of the reduced form per repeat unit, while we obtained an opposite effect for PDMA. The experimental results found an explanation for the syntheses of POTO and POAS in the 1,3-phenylenediamine intermediate

formation at the very begin of the polymerization, overruling both the sterical hindrance and the electron donor effect and responsible of an earlier stop of the polymerization. On the contrary, in the syntheses of PDMA and PDOA, since the lack the of 1,3-phenylenediamine intermediate formation, both the sterical hindrance and the electron donor effect strictly ruled the mechanism of reaction and allowed a major consumption of monomers. The presence of CNTs dispersion during the syntheses affected all the synthesized materials, by acting as nucleation points for the growing polymer chains. They also enhanced the electron donor effect of the CH_3O- group and gave partial negative counterbalance to the positive charges delocalized along the growing polymers. The contribution of electron donor substituent was more relevant than the partial positive charge counterbalance, and this explained the anomalous behavior found for PDMA based nanocomposite materials. The calculation of the undoped material band gaps showed no differences among mono and disubstituted aromatic rings, either considering the same or different groups. The doped materials UV–vis spectra showed the presence of the relative bands due to the polaron–π^* and π–polaron transitions for POTO, POAS, PDOA and related nanocomposites respectively, while these bands were missing for PDMA based materials. The presence of the CH_3- group along the aromatic rings had more influence than CH_3O- one in the atoms spatial configuration during the doping process. The strong impediment to the modification of the torsion angles upon doping generated by two CH_3- groups along the aromatic rings was in fact responsible of the incomplete doping process occurring for PDMA and related nanocomposites, while for POTO and related nanocomposites, the sterical hindrance generated by only one CH_3- group was only responsible of an uncompleted doped material. The reduced sterical hindrance of CH_3O- group allowed a very high protonation of the polymer chains even when two substituents were present. The CH_3O- groups, acting as electron donor, were also able to favor and enhance the doping process. The presence of both MWNTs and SWNTs inside the polymer matrix showed no modification in the chemical properties of the doped materials save for a little increment of the π–π^* interband of POTO nanocomposites with respect to the pure conducting polymer. It is possible that the only CH_3- substituent was not enough to compromise the formation of the polaronic state as in the case of PDMA and related nanocomposites, but the presence of CNTs in the polymer matrix seemed to reduce the degrees of freedom with consequent reduced protonation. In the light of the results discussed in this paper, the possibility of "tuning" the physical chemistry properties of polyaniline derivatives-CNTs nanocomposites in relation of the kind and number of substituents along the aromatic rings of the monomers used in the synthesis can be useful for the fabrication of materials with specific characteristic. Different concentration of CNTs inside the polymer matrix and their correlation to different substituents is under consideration and will be the future task of our research.

Acknowledgements

This project was supported by grants to Fondazione EL.B.A., by MIUR (Italian Ministry of Education, University and Research) for "Funzionamento" and by a FIRB Research National Network on Nanosciences – ItalNanoNet (RBPR05JH2P) from MIUR to CIRSDNNOB of the University of Genoa.

References

[1] MacDiarmid AG, Yang LS, Huang WS, Humphrey BD. Synth Met 1987;18:393.
[2] Iijima S. Nature 1991;56:354.
[3] Dresselhaus MS, Dresselhaus G, Eklund PC. Science of fullerenes and carbon nanotubes. New York: Academic Press; 1996.
[4] Iijima S, Brabec C, Maiti A, Bernholc JJ. Chem Phys 1996;5:2089.
[5] Coleman JN, Curran S, Dalton AB, Davey AP, McCarthy B, Blau W, et al. Phys Rev B 1998;58:7492.
[6] Bavastrello V, Ram MK, Nicolini C. Langmuir 2002;20:1535.
[7] MacDiarmid AG, Chiang JC, Halpen M, Huang WS, Mu SL, Somasiri NLD, et al. Mol Cryst Liq Cryst 1985;121:173.
[8] Paul EW, Ricco AJ, Wrighton MSJ. Phys Chem 1985;89:1441.
[9] Epstein AJ, MacDiarmid AG. In: Kuzmany H, Mehring M, Roth S, editors. Electronic properties of conjugated polymer. Berlin: Springer-Verlag; 1989.
[10] Kobayashi T, Yoneyama H, Tamura HJ. Electroanal Chem 1984;177:281.
[11] Chiang JC, MacDiarmid AG. Synth Met 1986;13:193.
[12] Epstein AJ, Ginder JM, Zuo F, Bigelow RW, Woo HS, Tanner DB, et al. Synth Met 1987;18:303.
[13] Genies EM, Labkowski MJ. Electroanal Chem 1987;236:199.
[14] de Oliveira Jr ZT, dos Santos MC. Solid State Commun 2000;114:49.
[15] Bavastrello V, Erokhin V, Carrara S, Sbrana F, Ricci D, Nicolini C. Thin Solid Films 2004;468:17.
[16] Bavastrello V, Stura E, Carrara S, Erokhin V, Nicolini C. Sensors Actuators B 2004;98:247.
[17] Bavastrello V, Carrara S, Ram MK, Nicolini C. Langmuir 2004;20:969.
[18] Tauc J. In: Abeles A, editor. Optical properties of solids. Amsterdam: North Holland; 1970. p. 227.
[19] Huang LM, Wen TC, Gopalan A, Ren F. Mater Sci Eng B 2003;104:88.
[20] McCall RP, Ginder JM, Leng JM, Ye HJ, Manohar SK, Masters JG, et al. Phys Rev B 1990;41:5202.
[21] Sapurina I, Stejskal J. Polym Int 2008;57:1295.
[22] Stejskal J, Kratochvíl P, Jenkins AD. Polymer 1996;37:367.
[23] Bacon J, Adams RN. J Am Chem Soc 1968;90:6596.
[24] Hand RL, Nelson RF. J Electrochem Soc 1978;125:1059.
[25] Hagiwara T, Depura T, Iwata K. Synth Met 1987;18:317.
[26] Duíc L, Kralíc M, Grigíc S. J Polym Sci A Polym Chem 2004;42:1599.
[27] Stejskal J, Kratochvíl P, Špírková M. Polymer 1995;36:4135.
[28] Manohar SK, MacDiarmid AG, Epstein AJ. Synth Met 1991;41:711.
[29] Kolla HS, Surwade SP, Zhang X, MacDiarmid AG, Manohar SK. J Am Chem Soc 2005;127:16770.
[30] Madathil R, Ponrathman S, Byrne HJ. Polymer 2004;45:5465.
[31] D'Aprano G, Leclerc M, Zotti G. J Electroanal Chem 1993;351:145.
[32] Jiménez P, Castell P, Sainz R, Ansón A, Martínez MT, Benito AM, et al. Phys Chem B 2010;4:114.
[33] Bredas JL. In: Salaneck WR, Lundström I, Ranby B, editors. Conjugated polymers and related materials. New York: Oxford University Press; 1993. p. 187.
[34] Osaheni JA, Jenekhe SA, Vanherzeele H, Meth JS, Sun Y, MacDiarmid AG. J Phys Chem 1992;96:2830.
[35] Cao Y, Smith P, Heeger AJ. Synth Met 1989;32:263.
[36] Scully M, Petty MC, Monkman AP. Synth Met 1993;55:183.
[37] D'Aprano G, Leclerc M, Zotti G. Synth Met 1996;82:59.
[38] Travain SA, de Souza NC, Balogh DT, Giacometti JA. J Colloid Interface Sci 2007;316:292.
[39] Libert J, Cornil J, dos Santos DA, Brédas JL. Phys Rev B 1997;56:8638.

Polymer 52 (2011) 55–62

Contents lists available at ScienceDirect

Polymer

journal homepage: www.elsevier.com/locate/polymer

Effect of π–π stacking on the atom transfer radical polymerization of styrene

Phillip D. Pickett, Eric S. Tillman*, Andrew F. Voter

Department of Chemistry, Bucknell University, Lewisburg, PA 17837, USA

ARTICLE INFO

Article history:
Received 29 September 2010
Received in revised form
3 November 2010
Accepted 6 November 2010
Available online 13 November 2010

Keywords:
ATRP
Controlled free radical polymerization
NMR

ABSTRACT

The atom transfer radical polymerization (ATRP) of styrene (St) was carried out in the presence of varying equivalents (eq) of hexafluorobenzene (HFB) to probe the effect of pi–pi stacking on the rate of the polymerization and the resulting tacticity of polystyrene (PSt) formed. The extent of interaction between the electron deficient face of the HFB and the electron rich face of the styrenic or polystyrenic phenyl ring was also examined as a function of reaction solvent, incorporating both non-aromatics (hexanes and THF) and aromatics (benzene and toluene). It was found that in all cases the rate of the ATRP of St was slowed by the addition of HFB to the reaction mixture, with increasing amounts of HFB (1 full eq. compared to St) retarding the rate to a relatively greater extent compared to smaller amounts (0.5 eq). Additionally, when aromatic solvents were used instead of hydrocarbons the effect of HFB on the rate of the ATRP was minimized, consistent with the solvent itself competing with the styrenic phenyl groups for pi–pi stacking interactions with HFB. The decreased rate in the presence of HFB is consistent with a reduced ability of the terminal phenyl group on the PSt chain to stabilize the active polymer radical, pushing the equilibrium further to the dormant alkyl halide. This interaction between the dormant alkyl bromide and HFB was verified by ^{1}H NMR, with 1-bromoethylbenzene used as the alkyl bromide. When the ATRP of non-aromatic vinyl monomers was studied (butyl acrylate and methyl methacrylate), the effect of HFB on the system was almost unnoticeable as expected due to their inability to participate in pi–pi stacking interactions. The tacticity of the PSt formed in the presence of HFB was compared to PSt formed in its absence by observing the C1 resonance on ^{13}C NMR, but no change in the shape or chemical shift of the signal was observed.

1. Introduction

Controlled radical polymerization (CRP) has allowed for precise synthesis of vinyl polymers to an extent historically unattainable using radical-based methods. The hallmark of all CRP systems, notably atom transfer radical polymerizations (ATRP) [1–7], nitroxide mediated polymerizations (NMP) [6,8], and reverse addition fragmentation chain transfer (RAFT) [6,9,10], is the reversible trapping of polymer radicals and the drastic suppression of bimolecular termination pathways [2–7]. Of these methods, ATRP is the most widespread owing to its ability to incorporate a plethora of initiators and monomers and the robust nature of the reaction system [1–7,11–14]. The position of the equilibrium (K_{ATRP} or k_{act}/k_{deact}) dictates the concentration of the active radical ($P_n^{\bullet}$), and is primarily determined by the redox potential of the ligand–metal complex, the choice of halogen, and the stability of the resulting carbon-based radical [1,6]. As shown in the below equations, the position of this equilibrium is directly tied to the rate of the polymerization:

$$\text{Rate} = k_p[P_n^{\bullet}][M]$$
$$\text{Rate} = K_{ATRP}k_p\frac{[Cu(I)-L][R-X][M]}{[X-Cu(II)-L]}$$

It is well known that the pi system in benzene creates a quadrupole moment; conversely the fluorine atoms on the perimeter of hexafluorobenzene (HFB) pull electron density from the center of the ring and create a quadrupole moment of the opposite signs compared to benzene (Scheme 1, A) [15,16]. When benzene and hexafluorobenzene (HFB) are mixed in 1:1 M amounts, they participate in a face-to-face, alternating interaction known as pi–pi stacking (Scheme 1, B) [17–19]. These pi–pi interactions have found utility in synthetic chemistry, for example, by controlling the stereochemistry of certain organic reactions and organometallic complexes [20–22].

The ATRP of styrene (St) or other vinyl arenes represents a system with a large quantity of aromatic faces capable of pi–pi stacking with HFB. In terms of the application of pi–pi stacking to

* Corresponding author. Tel.: +1 5705773265; fax: +1 5705771739.
E-mail address: etillman@bucknell.edu (E.S. Tillman).

0032-3861/$ – see front matter © 2010 Elsevier Ltd. All rights reserved.
doi:10.1016/j.polymer.2010.11.005

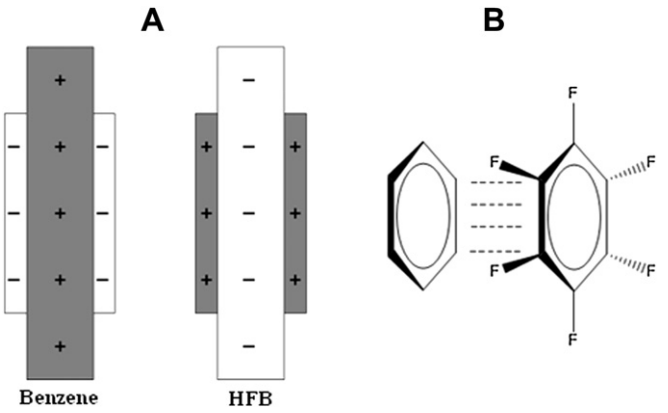

Scheme 1. (A) Quadrupole moments for benzene and hexafluorobenzene. (B) Pi–pi stacking interaction between benzene and hexafluorobenzene in the sandwich configuration.

polymer synthesis, the ATRP of St and pentafluorostyrene (PFS) has been reported to produce an alternating copolymer in some cases [18], speculated to be due to pi–pi stacking between the two different monomer units. The same group has also reported that copolymers consisting of PFS and vinylnaphthalene possess the same alternating configurations of monomer units, likely for the same reason [19]. The tacticity of the copolymers in the above examples was not reported, and it is not known if pi–pi stacking can impart stereocontrol on the polymerization of vinyl monomers. While the synthesis of highly isotactic or syndiotactic polymers is traditionally accomplished by coordination-insertion polymerizations, such as Ziegler-Natta [23,24], stereoregulation in ATRP has been shown possible by Lewis-acid-mediation, producing isotactic polymers, and solvent-mediation, producing syndiotactic polymers. These methods are only compatible with polar monomers, such as acrylamide, that can either coordinate with a Lewis-acid, or participate in hydrogen-bonding with a polar solvent [25]. Additionally, the effect of pi–pi stacking interactions on the rate of the ATRP of styrene or other vinyl monomers is not known.

In this study, the impact of HFB on the ATRP of St is studied in non-aromatic and aromatic solvents. Specifically, the effect of HFB on the rate of the ATRP of St, as observed by monomer consumption, as well as the tacticity of the polystyrene (PSt) polymer produced was studied over a range of solvents. The polymerization under investigation, shown in Scheme 2, employed well established initiator, catalyst, ligand, and solvents to better extract the effects of HFB on the ATRP of St.

2. Experimental

2.1. Materials

Hexafluorobenzene (HFB) (Aldrich, 99%), (1-bromoethyl)benzene (BEB) (Aldrich, 97%), N,N,N′,N′,N″-pentamethyldiethylenetriamine (PMDETA) (Aldrich, 99%), copper(I)bromide (Aldrich, 98%) were used as received. Styrene (Aldrich, Reagent Plus, ≥99%) and toluene (Aldrich, for HPLC, ≥99%) were purified by distillation from calcium hydride and stored in sealed glass ampoules under an atmosphere of argon at −15 °C. Methyl methacrylate (99%, Aldrich) and butyl acrylate (99%, Aldrich) were passed through an alumina column prior to use. THF, hexanes, and benzene were obtained from a Grubb's type solvent purification system. Chloroform-d (Aldrich, "100%", 99.6 atom % D, contains 0.03% (v/v) TMS) and cyclohexane-d_{12} (Aldrich, 99.6 atom % D) were used as NMR solvents as received.

2.2. Typical ATRP of styrene with 1 M eq. of HFB present in THF

All reaction vessels were flame dried and all syringes were flushed with argon prior to use. In addition, all reactions were performed under reduced atmosphere using Schlenk line techniques and all trials were conducted with 1 mL of St in 3 mL of reaction solution to maintain a constant concentration of St (exceptions are trials 1A–1C, Table 1). The ATRP of St in THF with 1 M eq. of HFB was conducted as follows: styrene (1.0 mL, 8.73 mmol), HFB (1.0 mL, 8.71 mmol), BEB (0.0240 mL, 0.176 mmol), CuBr (0.0254 g, 0.177 mmol), and a micro stir bar were added to the reaction vessel along with 1 mL THF. The vessel was sealed and evacuated of air through three freeze/pump/thaw cycles, placed into an oil bath at 86 °C, and PMDETA (0.0370 mL, 0.177 mmol) was added to the vessel by syringe after 5 min to commence the polymerization. The reagents were allowed to stir at the indicated temperature for 24 h, after which the vessel was removed from the oil bath and immediately placed into an ice bath and opened to atmospheric pressure. The product was then dissolved in a minimum amount of THF (~1 mL) and $CDCl_3$ (~1 mL) and analyzed by ^{1}H NMR to determine the percent conversion followed by characterization by GPC. Other trials were conducted in an identical manner using various solvents and HFB ratios as listed in Table 1 and Table 2.

2.3. Typical ATRP of butyl acrylate with 1 M eq. of HFB present in THF

All reaction vessels were flame dried and all syringes were flushed with argon prior to use. In addition, all reactions were

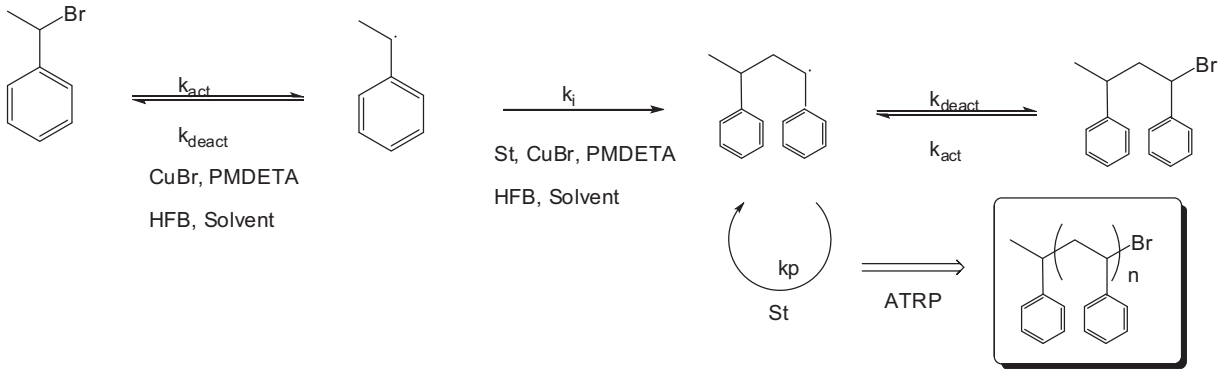

Scheme 2. ATRP of styrene in the presence of HFB.

Table 1
Results for the ATRP of St with or without HFB in non-aromatic organic solvents.

Run	[HFB]:[St][a]	Solvent[b]	% Conversion[c]	Theoretical Mn/daltons[d]	Experimental Mn/daltons[e]	PDI
1A	0	bulk	92	4950	2560	1.23
1B	0.5	bulk	94	5080	4850	1.16
1C	1	bulk	54	3000	3890	1.08
2A	0	THF	95	5140	4950	1.07
2B	0.5	THF	91	4930	3980	1.07
2C	1	THF	51	2860	3120	1.09
3A	0	Hexanes	87	4720	5130	1.18
3B	0.5	Hexanes	80	4340	5850	1.10
3C	1	Hexanes	52	2880	3330	1.16

Reactions were run with 50:1:1:1 $[\text{styrene}]_o$:$[\text{BEB}]_o$:$[\text{PMDETA}]_o$:$[\text{Cu(I)Br}]_o$ at 84 ± 4 °C for 24 h. See experimental section for more details.
[a] initial molar ratios of HFB:styrene in reaction mixture.
[b] solvents, if any, were added to adjust the total reaction volume to 3 mL. See experimental section for more details.
[c] monomer conversion as determined by ^{1}H NMR of raw reaction mixture after termination of reaction.
[d] theoretical number average molecular weight as calculated by conversion.
[e] apparent number average molecular weight as determined by GPC.

performed under reduced atmosphere using Schlenk line techniques and all runs were conducted with 1 mL of butyl acrylate in 3 mL of reaction solution to maintain a constant concentration of butyl acrylate (also true for methyl methacrylate trials). The ATRP of butyl acrylate with 1 M eq. of HFB in THF was conducted as follows: butyl acrylate (1.0 mL, 7.00 mmol), HFB (0.80 mL, 7.00 mmol), methyl-2-butylpropionate (0.0161 mL, 0.140 mmol), CuBr (0.0201 g, 0.140 mmol), and a micro stir bar was added to the reaction vessel along with 1.2 mL of purified THF. The vessel was then sealed and evacuated of air through three freeze/pump/thaw cycles. The vessel was then placed into an oil bath at 60 °C and PMDETA (0.0292 mL, 0.140 mmol) was added to the vessel by syringe. The reagents were allowed to stir at 60 °C for 8 h, after which the vessel was removed from the oil bath and immediately placed into an ice bath and opened to atmospheric pressure. The product was then dissolved in a minimum amount of THF ($\sim$1 mL) and $CDCl_3$ ($\sim$1 mL) and analyzed by ^{1}H NMR and GPC for percent conversion and molecular weight data, respectively. Other polymerizations were performed with varying monomers and initiators as listed in Table 3.

2.4. Characterization

The polymers were analyzed on a Waters Gel Permeation Chromatography (GPC) system connected to a PC running Waters Breeze software. The system consists of a Waters 1515 isocratic pump, a Waters 717 auto sampler, two Pl-gel 5 mm Mixed C columns (Polymer Labs), a Waters 2487 dual wavelength detector and a Waters 2414 RI detector. A 10 point calibration using polystyrene standards (Polymer Laboratories, Mp range: 5.0×10^2–3.05×10^6 Da) was used to obtain number average molecular weight (M_n) values and polydispersity index (PDI) values, with THF as the mobile phase. Percent monomer conversion values for ATRP reactions were determined by ^{1}H NMR on the raw reaction mixture in $CDCl_3$. Tacticity studies were done using ^{13}C NMR on isolated polymer samples in $CDCl_3$. ^{1}H NMR studies on observing the pi–pi interactions between HFB and St were conducted in cyclohexanes-d_{12} with an HFB:St ratio of 10:1. ^{1}H NMR studies on observing the pi–pi interactions between HFB and BEB were conducted in cyclohexane-d_{12} with an HFB:BEB ratio of 50:1. ^{1}H NMR measurements were taken on a Varian 400 MHz FT-NMR at room temperature while ^{13}C NMR measurements were taken on a Varian 600 MHz FT-NMR at room temperature.

Table 2
Results for the ATRP of St with or without HFB in aromatic organic solvents.

Run	[HFB]:[St][a]	Solvent[b]	% Conversion[c]	Theoretical Mn/daltons[d]	Experimental Mn/daltons[e]	PDI
4A	0	Benzene	97	5230	5580	1.10
4B	0.5	Benzene	96	5160	5850	1.10
4C	1	Benzene	74	4040	3470	1.11
5A	0	Toluene	97	5240	5060	1.10
5B	0.5	Toluene	80	4370	3380	1.09
5C	1	Toluene	69	3800	2670	1.09

Reactions were run with 50:1:1:1 $[\text{styrene}]_o$:$[\text{BEB}]_o$:$[\text{PMDETA}]_o$:$[\text{Cu(I)Br}]_o$ at 84 ± 4 °C for 24 h. See experimental section for more details.
[a] initial molar ratios of HFB:styrene in reaction mixture.
[b] solvents, if any, were added to adjust the total reaction volume to 3 mL. See experimental section for more details.
[c] monomer conversion as determined by ^{1}H NMR of raw reaction mixture after termination of reaction.
[d] theoretical number average molecular weight as calculated by conversion.
[e] apparent number average molecular weight as determined by GPC.

3. Results and discussion

3.1. Effect of HFB on the ATRP of styrene in non-aromatic solvents or bulk

The effect of HFB on the ATRP of St was initially studied by comparing results of a typical bulk ATRP reaction (Table 1, *run 1A*) to analogous trials with varying equivalents (eq) of HFB added to the reaction (Table 1, *runs 2B, 2C*). The well-known pi–pi stacking interaction between HFB and the monomeric or polymeric phenyl group would be expected to effect the K_{ATRP} (k_{act}/k_{deact}, Scheme 2), altering the rate at which the ATRP reaction occurs. It is important to note that in these initial trials (Table 1, *runs 1A-1C*), the addition of HFB to the reaction mixture decreases the concentration of St monomer while in all other trials in co-solvent systems the concentration of St is held constant. Given that the rate of an ATRP reaction is tied to the concentration of St, it would be expected that even with no interaction the addition of HFB would reduce the rate of the polymerization, leading to lower conversions at time *t*. Interestingly, with 0.5 eq. of HFB present (compared to St) the rate at which the ATRP reaction occurred modestly increased compared to the bulk trial (Table 1, *1A vs. 1B*). The further addition of a full eq. of HFB reduced the rate substantially as judged by monomer conversion, while the PDI of the system remained low throughout and generally decreased as HFB was added to the system. GPC traces of the polymers formed in each case are shown in Fig. 1.

Carrying out the ATRP in THF, with no HFB, produced PSt with low PDI and predictable molecular weights, as expected (Table 1, *run 2A*). The addition of 0.5 eq. of HFB lowered the conversion but to a very small extent (95%–91% after 24 h), while not affecting the control over the polymerization with PDI values low. With 1 full eq. of HFB in the reaction mixture, the rate of the polymerization was substantially lowered, as evidenced by a large decrease in monomer conversion (Table 1, *run 2C*) while PDI values remained low. Performing ATRP reactions in hexanes with or without HFB showed a slight increase in PDI values of the resulting polymers compared to analogous trials with THF (Table 1, *runs 3A – 3C*), but otherwise the trend mirrored that seen in THF. All ATRP reactions performed in hexanes and THF were done at a constant St concentration to allow for the effect of HFB to be extracted.

3.2. Effect of HFB on the ATRP of styrene in aromatic solvents

The effect of HFB on the ATRP of St was studied in the aromatic solvents benzene and toluene, as these solvents themselves will interact with HFB and should suppress its effect on the ATRP

Table 3
Results for the ATRP of BA and MMA with or without HFB in THF.

Run	[HFB]:[M][a]	Monomer[b]	Initiator[c]	% Conversion[d]	Theoretical Mn/daltons[e]	Experimental Mn/daltons[f]	PDI
6A	0	BA	MBP	98	6420	1700	1.13
6B	1	BA	MBP	99	6550	1850	1.16
7A	0	MMA	EBIB	97	5050	3120	1.30
7B	1	MMA	EBIB	98	5120	3190	1.31
8A[g]	0	MMA	EBIB	84	4400	8240	1.34
8B[g]	1	MMA	EBIB	86	4500	10200	1.33

Reactions were run with 50:1:1:1 $[Monomer]_o$:$[Initiator]_o$:$[PMDETA]_o$:$[Cu(I)Br]_o$. See experimental section for more details.
[a] initial molar ratios of HFB: monomer in reaction mixture.
[b] butyl acrylate (BA); methyl methacrylate (MMA).
[c] methyl-2-bromopropionate (MBP); ethyl-α-bromoisobutyrate (EBIB).
[d] monomer conversion as determined by ^{1}H NMR of raw reaction mixture after termination of reaction.
[e] theoretical number average molecular weight as calculated by conversion.
[f] apparent number average molecular weight as determined by GPC.
[g] runs were performed at 84 °C for 5.5 h in a total of 4 mL of reaction solution.

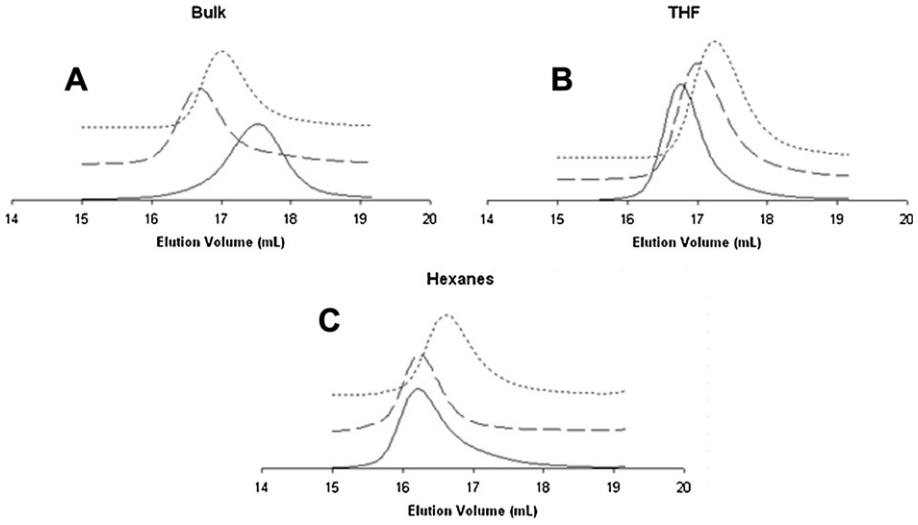

Fig. 1. GPC traces of PSt produced by ATRP in non-aromatic organic solvents in the presence or absence of HFB. (A) bulk, (B)THF, (C) hexanes. (Solid line: No HFB; Dashed line: 0.5 eq. HFB; Dotted line: full eq. HFB).

reaction [26]. In benzene with no HFB, the ATRP of St was well controlled and produced PSt of predictable molecular weight and of low PDI (Table 2, *Run 4A*). The addition of 0.5 eq. of HFB to the polymerization showed almost no effect, while the addition of a full eq. of HFB lead to substantially lower conversion of monomer in an analogous ATRP reaction (Table 2, *runs 4B vs 4B*, respectively). In the case of toluene as the solvent, the ATRP of St in the absence of HFB lead, as expected, to PSt of low PDI and predictable molecular weight values (Table 2, *run 5A*). The addition of 0.5 and 1.0 eq. of HFB lessened the conversion of St, but in this case the effect of 0.5 eq. of HFB was greater than when performed in benzene (Table 2, *runs 5B and 4C*). Shown in Fig. 2 are GPC-RI traces of the polymers formed in the ATRP of St in benzene and toluene. Regardless of the amount of HFB in the solution, the polymerizations consistently produced polymers with low PDI values.

3.3. Mechanistic account of the effect of HFB on the ATRP of styrene

To impact the ATRP of St, the HFB must interact with one or more of the constituents involved in k_{act}/k_{deact} or k_p. The electropositive face of the HFB would be expected to interact most strongly with aromatic groups having electronegative faces. When both monomeric St and polymeric phenyl groups are present, the HFB has multiple phenyl groups to interact with. However, unless

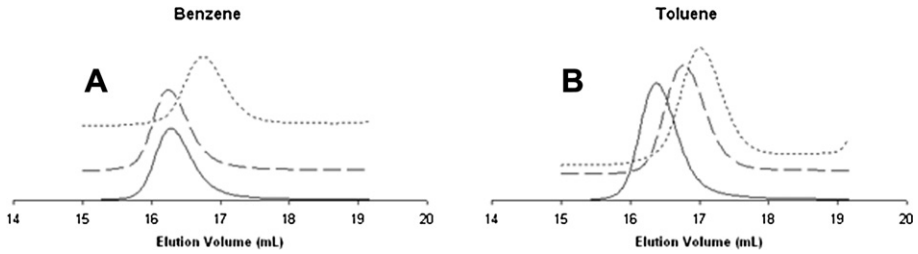

Fig. 2. GPC traces of PSt produced by ATRP in aromatic solvents in the presence or absence of HFB. (A) benzene, (B) toluene. (Solid line: No HFB; Dashed line: 0.5 eq. HFB; Dotted line: full eq. HFB).

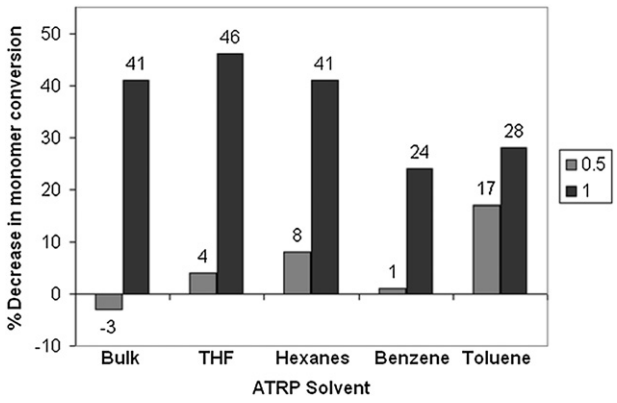

Fig. 3. Reduction in percent conversion of styrene in ATRP reactions as a function of HFB eq. in various solvents as compared to ATRP w/no HFB (Tables 1 & 2).

the HFB is interacting with the polymeric aromatic group at the chain end, which is responsible for stabilizing the active polymer radical, its effect on K_{ATRP} (k_{act}/k_{deact} in Scheme 2) and thus the rate of the polymerization should be negligible. However, HFB interactions with monomeric styrene, especially the vinylic group, may directly alter k_p (Scheme 2) and still impact the observed rate of the polymerization.

As shown in Fig. 3, the change in monomer conversion without HFB or with 0.5 eq. is 8% or less, suggesting that K_{ATRP} is only slightly altered in these reactions. This is likely due to the HFB in the system selectively interacting with aromatic groups besides that on the chain end, minimizing the effect of its presence on the rate of the ATRP of St.

When a full eq. of HFB was added to the system in non-aromatic solvents, a substantial altering of the rate of the ATRP reaction was observed. As shown in Fig. 3, this increased amount of HFB in the reaction mixture (essentially a second 0.5 eq) affected the conversion of monomer to a much larger extent than the initial 0.5 eq. In all, whether in bulk, hexanes, or THF, a 40+% decrease was observed overall in monomer conversion when a full eq. of HFB in respect to St was present compared to identical ATRP reactions performed without HFB. In the case of the ATRP with no other solvent (only St and HFB, Table 1), this could be partially due to a decrease in monomer concentration with increasing HFB addition, but in the cases of hexanes and THF the concentration of St was held constant (by adjusting hexanes or THF volumes) and the effect can be directly attributed to HFB. This trend suggests that the pi–pi interaction between the chain end aromatic group and HFB is not occurring to an appreciable extent until other phenyl moieties are already preferentially interacting with other aromatic units (i.e., only at equimolar HFB amounts).

In the case of aromatic solvents, it is expected that the solvent itself will interact with the HFB in the reaction mixture, minimizing its impact on the polymerization. Consistent with this, in benzene solvent the addition of 0.5 eq. of HFB showed a negligible impact on the rate of the ATRP of St. As shown in Fig. 3, the addition of a full eq. of HFB to the benzene ATRP system impacted the rate of the polymerization but to a much lesser extent than analogous reactions performed in non-aromatic systems. For example, a 24% reduction in monomer conversion was observed with a full eq. of HFB present in an ATRP reaction performed in benzene, while an otherwise identical trial in THF produced a 46% drop in conversion. This result implies that the aromatic rings of the solvent compete with the monomeric and polymer aromatic rings for interacting with the HFB. Toluene is also expected to associate with HFB by

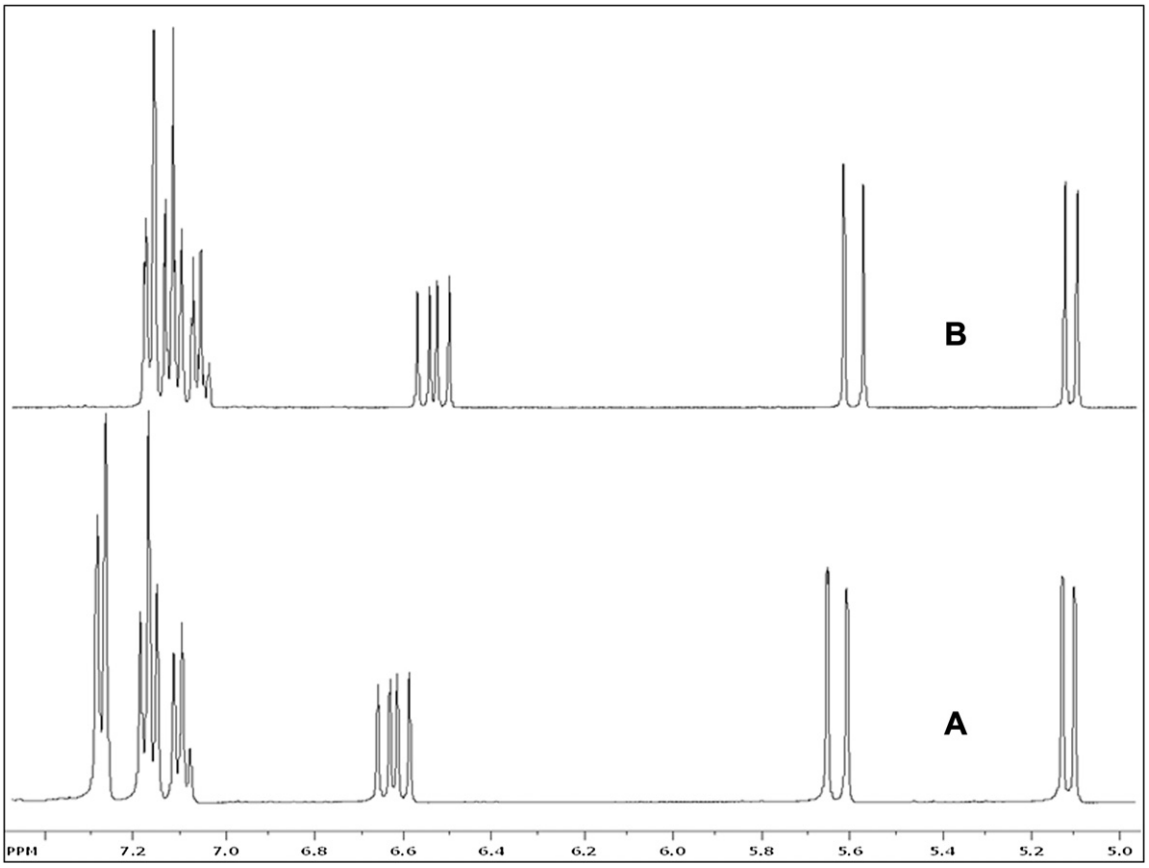

Fig. 4. ^{1}H NMR of styrene in cyclohexane-d_{12} in absence of HFB (A) and with 10 M excess HFB (B).

pi–pi stacking interactions, but does so to a greater extent than benzene [26]. As shown in Fig. 3, toluene ATRP systems showed more sensitivity to the addition of 0.5 eq. of HFB than any other system. The explanation for this reproducible result is unknown. Altogether, the addition of a full eq. of HFB to the ATRP performed in toluene showed a similar impact to ATRP reactions performed in benzene (28% compared to 24% reduction in monomer conversion).

While the rate data indirectly points to pi–pi stacking interactions altering the system of investigation, NMR spectroscopy was used to directly probe the interaction between HFB and the constituents of the ATRP reaction. Shown in Fig. 4 are the ^{1}H NMR spectra of styrene in both the presence and absence of 10 M eq. of HFB, obtained in cyclohexane-d_{12} (chosen as a non-aromatic solvent). A downfield shift of both the aromatic and vinylic protons is apparent in the spectrum with HFB (B), consistent with pi–pi stacking interactions reported by others [27]. That the chemical shift of the vinyl signals is affected by HFB (especially C1 on the vinyl group) suggests that the monomer's reactivity may be altered in the presence of HFB.

Shown in Fig. 5 are the ^{1}H NMR spectra of 1-bromoethylbenzene both in the presence and absence of 50 M excess HFB, also obtained in cyclohexane-d_{12}, to simulate the conditions of a non-aromatic reaction solvent and ATRP reactions performed with 1 eq. of HFB. (This is because the monomer-to-initiator ratio is 50:1, and the HFB:St ratio is 1:1). An upfield shift, accompanied by tightening of the aromatic region as a whole, was observed in the spectrum of 1-BEB when HFB was present. Because this also models the chain end of the dormant PStBr in the ATRP reaction, this would be an indication of an interaction between not only the initiating alkyl bromide species, but also the chain end directly involved in the k_{act}/k_{deact}. This interaction is expected to decrease the ability of the chain end to stabilize a radical, as electron density of the aromatic system is tied up in pi–pi stacking and less available to stabilize a radical via resonance. This is consistent with reduced rate observed in the presence of HFB compared to analogous runs in its absence.

3.4. Effect of HFB on the ATRP of non-aromatic vinyl monomers

If pi–pi stacking interactions are responsible for the reduction of rate in the ATRP of St with increasing HFB eq, it would follow that HFB should have only a negligible impact on the ATRP of non-aromatic vinyl monomers. To probe this, ATRP reactions of butyl acrylate (BA) and methyl methacrylate (MMA) were performed in the absence of and with one full eq. of HFB. As shown in Table 3, when the concentration of BA was held constant and ATRP was performed with or without one eq. of HFB, the polymerization rate was unchanged as determined by the monomer conversion after 8 h. In the case of MMA, when the identical study was done, the rate again held relatively constant in the presence or absence of HFB. These results support the assertion that the rate changes in the ATRP of St in the presence of HFB is a result of pi–pi stacking interactions.

3.5. Effect of HFB on the tacticity of polystyrene

The interaction between the polymeric pendant groups and an additive has been shown to impart stereocontrol in ATRP reactions of certain monomers. For example, stereoregular poly(vinyl acrylamide) has been produced by performing the ATRP with eq. of Lewis acids such at $Y(OTf)_2$ [28,29]. The chain end pendant group must be involved in this interaction, because it is only at this location that stereocontrol can be effected since it has already been

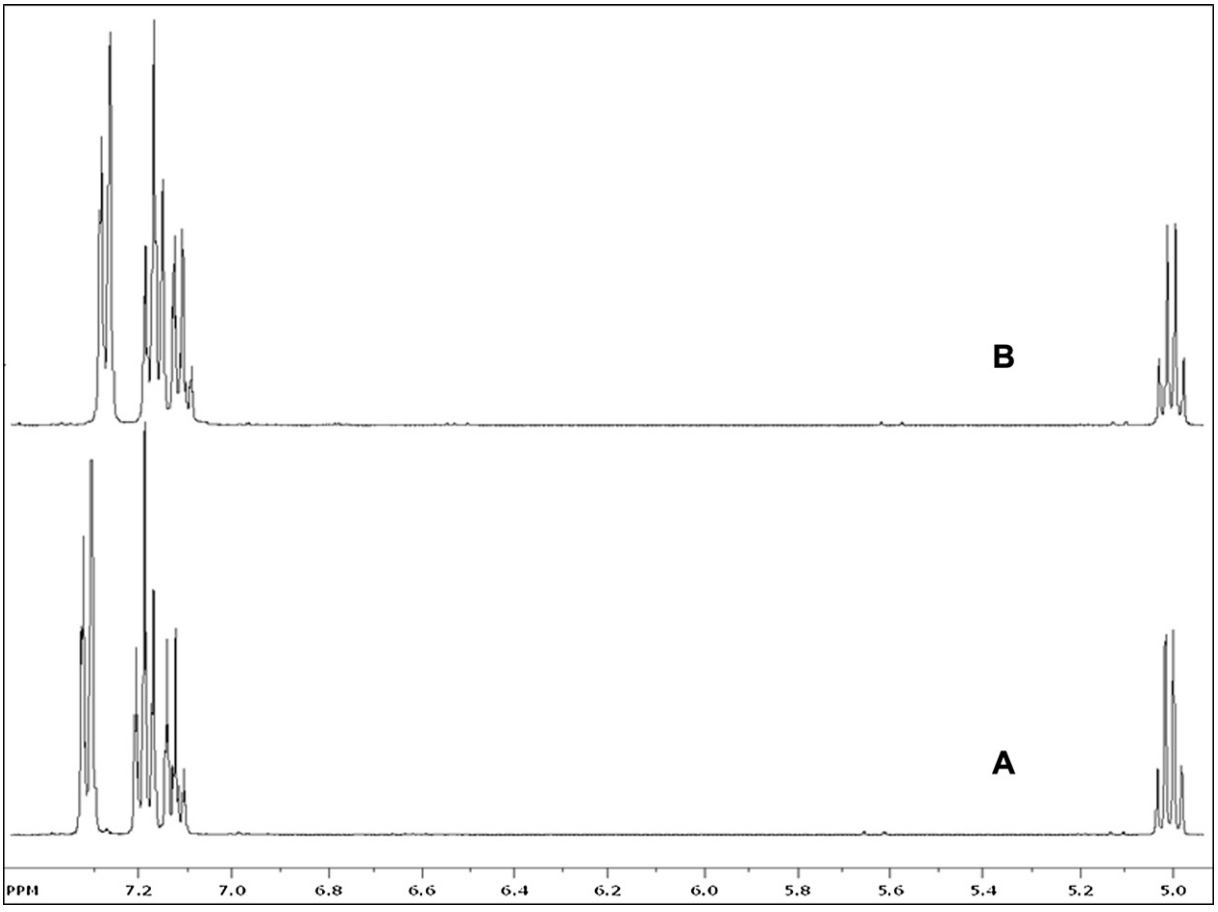

Fig. 5. ^{1}H NMR of 1-bromoethylbenzene in cyclohexane-d_{12} in absence of HFB (A) and with 50 M excess HFB (B).

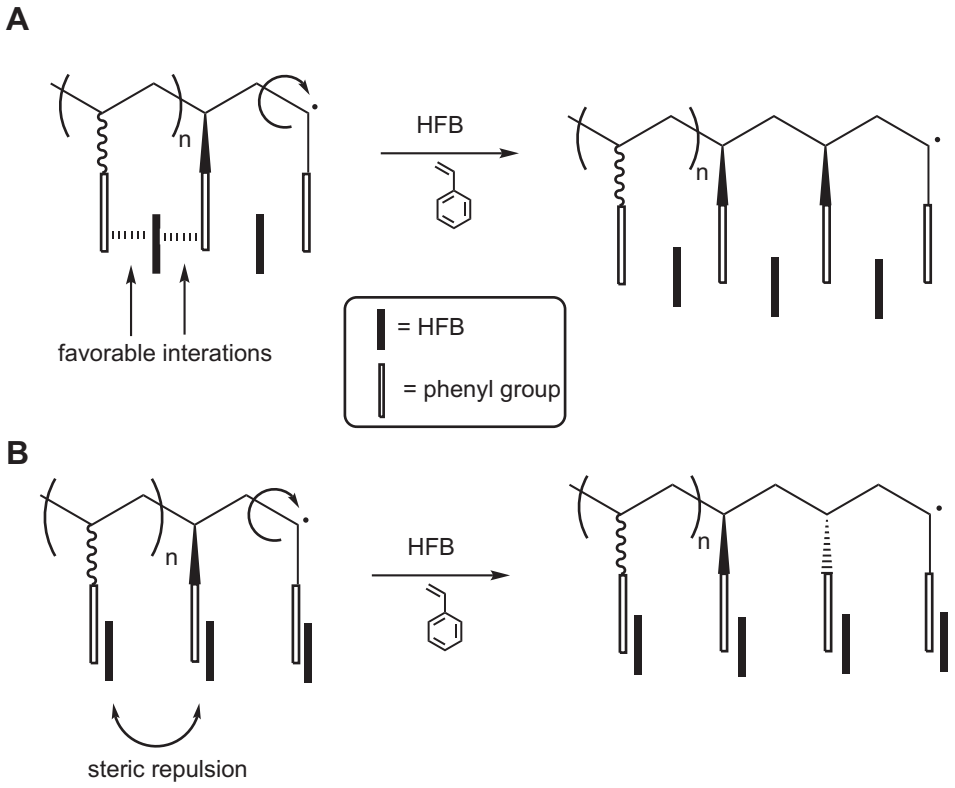

Scheme 3. Proposed interactions of HFB in the ATRP of styrene leading to: (A) isotactic PSt, and (B) syndiotactic PSt.

determined at other stereogenic centers along the polymer backbone. Similarly, if a solvent of additive interacts with each pendant group separately, increased sterics now dictate that syndiotactic vinyl polymer will be preferred [30–32].

Pi–pi stacking interactions between a fluorinated aromatic species and St have been exploited to produce alternating copolymers by using a monomer system of fluorinated and non-fluorinated St units, but the stereochemistry of the system is unknown

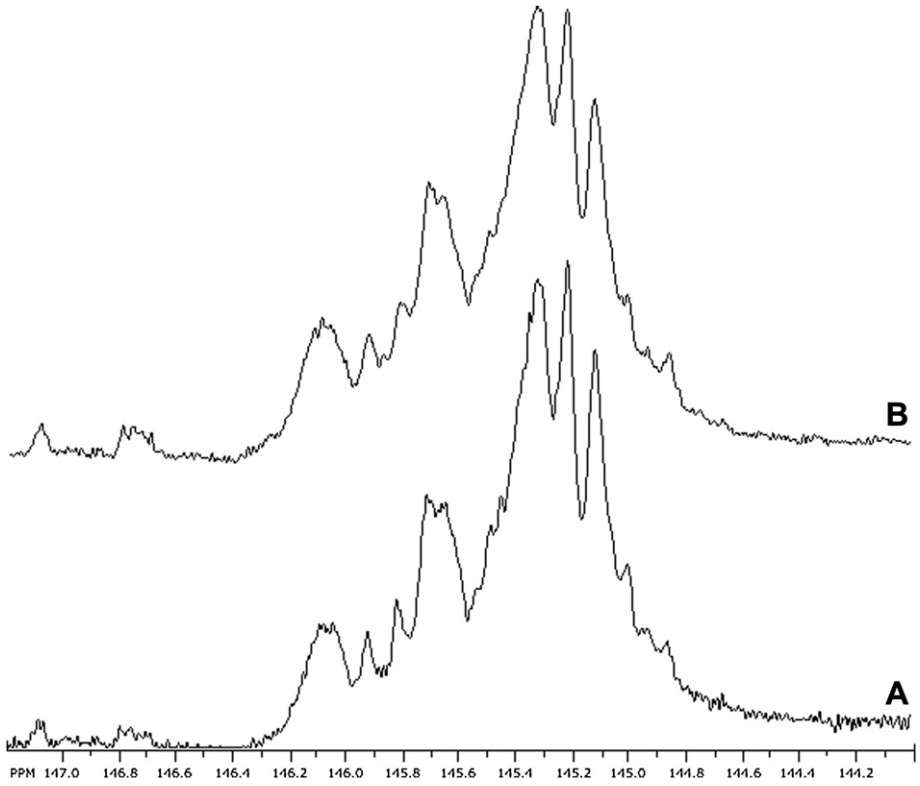

Fig. 6. ^{13}C NMR spectra of the C1 of PSt formed by ATRP in THF: (A) with no HFB; (B) with full eq. of HFB.

[18,19]. Because the HFB has been demonstrated above to affect the rate of the ATRP of St and NMR has verified an interaction with an alkyl bromide modeling the chain end, it may also alter the tacticity of the resulting polymer. As shown in Scheme 3A, it can be envisioned that the HFB may interact with two pendant groups, resulting in isotactic PSt if one unit is at the chain end. If, instead, each pendant group coordinates separately with an HFB unit there is potential for predominantly syndiotactic PSt due to effectively increasing the bulkiness of the pendant group (Scheme 3B). This would be much like the solvent-mediated syndiotactic preference.

Examination of the tacticity of the PSt was done using ^{13}C NMR, by evaluating the resonance due to the C1 carbon of the aromatic group. It has been shown that the chemical shift of this signal is dependent on the tacticity, with isotactic PSt (higher mm triad content) demonstrating a shift in the C1 signal further downfield [33–36]. Fig. 6 compares the ^{13}C NMR spectra of isolated and purified PSt formed in THF in the absence of HFB (Table 1, *run 2A*) to that formed in THF with 1 full eq. of HFB (Table 1, *run 2C*). The signals are nearly identical in each case in both shape and chemical shift, indicating that there is little to no stereochemical differences between the PSt formed with or without HFB.

The HFB must be interacting with the chain end phenyl group to the extent that it is able to reduce its ability to stabilize a benzylic radical, yet not interact strongly enough to impart stereocontrol by either mechanism shown in Scheme 3. It is unlikely, then, that a single HFB unit is interacting simultaneously with the penultimate and ultimate phenyl group on the chain as shown in Scheme 3A. This interaction would almost certainly produce PSt with increased isotactic content. If the interaction in Scheme 3B is dominant, there remains the possibility that the planar nature of the groups are not effectively bulky enough to impart syndiotactic control over the polymerization. There also remains the possibility that the interaction between HFB and the polymeric phenyl groups is too fleeting to lead to stereoregular structures in the polymer chain. Work in our lab studying the effect of bulkier fluorinated aromatics on the ATRP of styrene is underway.

4. Conclusion

The ATRP of St was affected by the presence of HFB in the reaction, resulting in decreased monomer conversions compared to analogous reactions in its absence. The effect was amplified in non-aromatic co-solvents with HFB concentrations equal to the initial concentration of St. In aromatic solvents, the effect of HFB on the ATRP of St was minimized due to competition for pi–pi stacking interactions between the solvent and the styrenic phenyl groups. As expected, the ATRP of non-aromatic vinyl monomers BA and MMA was not sensitive to the presence of HFB due to their inability to participate in pi–pi stacking interactions. The tacticity of PSt formed in the presence of HFB was identical to that formed in its absence.

Acknowledgements

The National Science Foundation (award no. 0717949) and Gebhart Fellowship provided financial support of this work. The authors are also grateful to Prof. Robert Stockland and Prof. David Rovnyak for their assistance with obtaining NMR spectra.

References

[1] Matyjaszewski K, Braunecker WA. J Mol Catal A Chem 2006;254:155–64.
[2] Seeleger F, Matyjaszewski K. Macromolecules 2009;42:6050–5.
[3] Coca S, Paik H, Matyjaszewski K. Macromolecules 1997;30:6513–6.
[4] Coca S, Matyjaszewski K. Macromolecules 1997;30:2808–10.
[5] Xia J, Matyjaszewski K. Chem Rev 2001;101:2921–90.
[6] Goto A, Fukuda T. Prog Polym Sci 2004;29:329–85.
[7] Roof AC, Tillman ES, Malik RE, Roland AM, Miller DJ, Sarry LR. Polymer 2006;47:3325–35.
[8] Thakur S, Cohen NA, Tillman ES. Polymer 2008;49:1483–9.
[9] Whittaker MR, Goh Y, Gemici H, Legge TM, Perrier S, Monteiro MJ. Macromolecules 2006;39:9028–34.
[10] Ray B, Isobe Y, Matsumoto K, Habaue S, Okamoto Y, Kamigaito M, et al. Macromolecules 2004;37:1702–10.
[11] Tsarevsky NV, Braunecker WA, Brooks SJ, Matyjaszewski K. Macromolecules 2006;39:6817–24.
[12] Patten TE, Matyjaszewski K. Acc Chem Res 1999;32:895–903.
[13] Hawker CJ. Acc Chem Res 1997;39:373–82.
[14] Ng Y, Hong H, Wong S, Lim K, Chai CLL. Macromolecules 2010;43:592–4.
[15] William JH. Acc Chem Res 1993;26:593–8.
[16] Ngola SM, Dougherty AD. J Org Chem 1998;63:4566–7.
[17] Tsuzuki S, Uchimaru T, Mikami M. J Phys Chem 2006;110:2027–33.
[18] Pugh C, Tang CN, Paz-Pazos M, Samtani O, Dao AH. Macromolecules 2007;40:8178–88.
[19] Pugh C, Paz-Pazos M, Tang CN. J Polym Sci A Polym Chem 2009;47:331–45.
[20] Jones GB. Tetrahedron 2001;57(38):7999–8016.
[21] Blanchard MD, Hughes RP, Concolino TE, Rheingold AL. Chem Mater 2000;12:1604–10.
[22] Corey EJ, Loh TP, Roper TD, Azimioara MD, Noe MC. J Am Chem Soc 1992;114:8290–2.
[23] Yang X, Stern CL, Marks TJ. J Am Chem Soc 1994;116:10015–31.
[24] Pastorino R, Capacchione C, Ferro R, Milione S, Grassi A. Macromolecules 2009;42:2480–7.
[25] Kamigaito M, Satoh K. Macromolecules 2008;41:269–76.
[26] Gung BW, Amicangelo JC. J Org Chem 2006;71:9261–70.
[27] Sun H, Ye K, Wang C, Qi H, Li F. J Phys Chem A 2006;110:10750–6.
[28] Isobe Y, Fujioka D, Habaue S, Okamoto Y. J Am Chem Soc 2001;123:7180–1.
[29] Lutz J, Neugebauer D, Matyjaszewski K. J Am Chem Soc 2003;125:6986–93.
[30] Yamada K, Nakano T, Okamoto Y. Macromolecules 1998;31:7598–605.
[31] Miura Y, Satoh T, Narumi A, Nishizawa O, Okamoto Y, Kakuchi T. Macromolecules 2005;38:1041–3.
[32] Isobe Y, Yamada K, Nakano T, Okamoto Y. Macromolecules 1999;32:5979–81.
[33] Tonelli AE. Macromolecules 1979;12:252–5.
[34] Cazzaniga L, Cohen RE. Macromolecules 1989;22:4125–8.
[35] Matsuzaki K, Uryu T, Osada K, Kawamura T. Macromolecules 1972;5:816–8.
[36] Makino T, Hogen-Esch TE. Macromolecules 1999;32:5712–4.

Polymer 52 (2011) 63–67

Contents lists available at ScienceDirect

Polymer

journal homepage: www.elsevier.com/locate/polymer

Synthesis and nucleation mechanism of inverse emulsion polymerization of acrylamide by RAFT polymerization: A comparative study

Liu Ouyang [a], Lianshi Wang [a], F. Joseph Schork [b,*]

[a] College of Materials Science and Engineering, South China University of Technology, Guangzhou, 510640, China
[b] School of Chemical and Biomolecular Engineering, Georgia Institute of Technology, 311 Ferst Drive, Atlanta, GA 30332-0100, USA

ARTICLE INFO

Article history:
Received 1 September 2010
Received in revised form
28 October 2010
Accepted 30 October 2010
Available online 5 November 2010

This paper is dedicated to the late Professor John Vanderhoff who advocated some of the ideas in this paper over thirty years ago.

Keywords:
Inverse emulsion
Reversible addition fragmentation chain transfer (RAFT)
Acrylamide

ABSTRACT

Well-defined poly (acrylamide) is synthesized by RAFT inverse emulsion polymerization using hydrophilic and lipophilic initiators. The kinetic behavior observed for RAFT inverse emulsion polymerization is similar to that for RAFT inverse *miniemulsion* polymerization. The nucleation mechanism of inverse emulsion polymerization of acrylamide is firstly investigated by RAFT polymerization and verified by GPC and SEM measurements. Droplet nucleation is found to be the primary mechanism in the inverse emulsion polymerization of acrylamide. However, polymerization occurring in the continuous phase is not negligible when lipophilic initiator is used.

1. Introduction

Water-soluble polymers are an important class of materials because of their numerous applications. Polymers based on poly (acrylamide) (PAM) and its derivatives are widely used commercial polymers, particularly in wastewater treatment applications, as drag reduction agents and drilling fluids in enhanced oil recovery, as additives in paper making, and as drug-delivery agents [1–9]. Water-in-oil (inverse) emulsion polymerization is one of the ideal methods for obtaining such polymers with high molecular weight and low viscosity. An inverse emulsion, however, cannot be simply considered as an analogy to conventional emulsion in which the water is replaced by the oil and the hydrophobic monomer by the hydrophilic monomer. The kinetic mechanism of inverse emulsion polymerization can be affected by many factors such as initiators, surfactants, and oils [10]. Studies have been made to investigate the mechanism and kinetics of the inverse emulsion polymerization since 1960s. Vanderhoff et al. [11] suggested that the principal locus of particle nucleation was the monomer droplets in the inverse emulsion polymerization of p-sodium styrene sulfonate. Some later studies [12–15] on inverse emulsion polymerization of acrylamide also showed the existence of droplet nucleation, although some of to the systems studied would now be called miniemulsions. Until now, a fully comprehensive description of the nucleation mechanism of inverse emulsion polymerization has not been made.

As one of three major approaches to controlled (living) radical polymerization, reversible addition fragmentation chain transfer (RAFT) polymerization has been successfully implemented in heterogeneous systems [16–20]. Some studies have been made in RAFT inverse miniemulsion polymerization to obtain well-defined controlled water-soluble (co)polymers [21–23]. However, RAFT polymerization in inverse emulsion, has not been investigated. In this paper, well-defined PAM was synthesized by RAFT inverse emulsion polymerization, and the nucleation mechanism is discussed.

2. Experimental

2.1. Materials

All chemicals were purchased from Aldrich except as otherwise stated. Acrylamide (AM, 99.5%) was recrystallized from chloroform. Azobisisobutyronitrile (AIBN, >98%), 2, 2′-Azobis [2-(2-imidazolin-2-yl) propane] dihydrochloride (VA-044, Wako, >98%) were

* Corresponding author. Tel.: +1 678 642 5366; fax: +815 301 9729.
E-mail address: Joseph.Schork@chbe.gatech.edu (F.J. Schork).

0032-3861/$ – see front matter © 2010 Elsevier Ltd. All rights reserved.
doi:10.1016/j.polymer.2010.10.063

purified by recrystallization from methanol. Span 80, B246SF (Uniqema) were used as received.

2.2. RAFT inverse emulsion polymerization

The inverse emulsion was prepared by mixing a solution of nonionic surfactant (i.e. Span 80 or B246SF) in cyclohexane with a water solution of AM. Two types of initiators were used: the hydrophilic initiator VA-044 was dissolved in the water solution or, the lipophilic initiator AIBN was dissolved in cyclohexane. The AM water solution was degassed for 5 min under vacuum prior to use. The reaction mixture prepared above was stirred under nitrogen at approx. 400 rpm for 5 min at room temperature. The resulting emulsion was charged into a 250 ml flask equipped with a nitrogen sweep and a magnetic stirrer, and then polymerized in an oil bath preheated to 60 °C. All the experiments in this study are shown in Table 1. The ratio of monomer and RAFT agent was fixed at 100:1. For comparison purposes, RAFT inverse miniemulsion polymerization was also carried out. The preparation procedure for inverse miniemulsion was the same as for inverse emulsion except that the 5 min stirring process was replaced by sonicating with an Omni-Ruptor 250 ultrasonic homogenizer operated at 30% power output for 5 min. The emulsion was cooled in the ice bath during sonication.

The CMC was measured by a Du Nouy Ring Surface Tensiometer (Fisher) equipped with a platinum-iridium ring. The surface tension was measured three times for each sample then the surfactant concentration in cyclohexane was increased. Measurements were made at room temperature and a constant solution volume of 50 ml.

Molecular weights of the polymers were determined by aqueous size exclusion chromatography (ASEC) at 35 °C. The ASEC system was comprised of a Waters 1525 Binary HPLC pump, a Waters 2414 refractive index detector (RI), a Waters 2487 dual λ absorbance UV detector, an Ultrahydrogel Guard column, and Ultrahydrogel 2000A, 250A, 120A columns mounted in series. The mobile phase was 0.05 M Na_2SO4 in water and the flow rate was maintained at 0.6 ml/min. PAM narrow standards were used to calibrate the ASEC by the universal calibration method. The conversion of the monomer was determined with ASEC using a known method by comparing the area of the RI signals that corresponded to the monomer and the polymer [24].

Morphology of polymer particles was investigated by scanning electron microscopy (SEM) with a JEOL JSPM-4500A (JEOL, Tokyo, Japan) instrument. For SEM analysis, a drop of latex obtained after 24 h of polymerization was placed on the glass and freeze-dried. This was then placed under vacuum, flushed with argon, and then sputter-coated with gold.

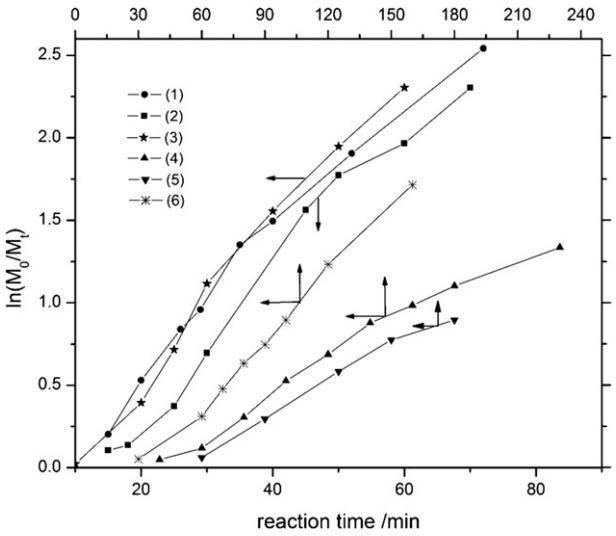

Fig. 1. Evolution of the conversion as a function of reaction time: (1) RAFT inverse emulsion polymerization with B246SF and VA-044 (Expt.1). (2) RAFT inverse miniemulsion polymerization with B246SF and VA-044 (Expt.2). (3) RAFT inverse emulsion polymerization with Span 80 and VA-044 (Expt.3). (4) RAFT inverse emulsion polymerization with B246SF and AIBN (Expt. 4). (5) RAFT inverse emulsion polymerization with B246SF and AIBN (Expt. 5). (6) RAFT inverse emulsion polymerization with B246SF and AIBN (Expt. 6).

3. Results and discussion

The results of RAFT inverse emulsion polymerization of acrylamide with different initiators and surfactants are shown in Fig. 1. The kinetic data (curves 1, 3) are close to inverse miniemulsion polymerization (curve 2), and follow pseudo- first order kinetics. The induction time for inverse miniemulsion polymerization is a bit longer, most likely caused by the oxygen or other impurities which are introduced during sonication. Although different surfactants were used, curve 1 and curve 3 are almost identical. When the initiator was changed from water-soluble (VA-044) to oil-soluble (AIBN), as shown in curve 1 and curve 4, the polymerization rate decreased significantly and a much longer induction time was observed. This can be attributed to the long time interval that the oligoradicals take to enter droplets and initiate polymerization. This is discussed later in more detail. It is worth noting that for Expt. 4 and Expt. 5, the polymerization rate decreased with a higher surfactant concentration. This may be because of the steric stabilization employed in these inverse emulsions: the increased interfacial barrier caused by a higher surfactant concentration makes it more difficult for oligoradicals to enter droplets, resulting in a lower enter rate of the initiator.

For the RAFT inverse emulsion system, the RAFT agent is water-soluble and mainly located in the droplets; hence, polymerization occurring in the continuous phase is uncontrolled due to the

Table 1
Experimental set up for the RAFT inverse emulsion polymerizations of acrylamide.

Expt	Type	Disperse phase/g				Continuous phase/g		
		AM	CTA	VA-044	water	AIBN	Cyclohexane	Surfactant
1	RAFT inverse emulsion	2.5	0.089	0.028	7.5	–	20	B246SF, 150% CMC
2	RAFT inverse miniemulsion	2.5	0.089	0.028	7.5	–	20	B246SF, 150% CMC
3	RAFT inverse emulsion	2.5	0.089	0.028	7.5	–	20	Span 80, 150% CMC
4	RAFT inverse emulsion	2.5	0.089	–	7.5	0.014	20	B246SF, 150% CMC
5	RAFT inverse emulsion	2.5	0.089	–	7.5	0.014	20	B246SF, 300% CMC
6	RAFT inverse emulsion	2.5	0.089	–	7.5	0.028	20	B246SF, 150% CMC
7	RAFT inverse emulsion	2.5	0.089	–	7.5	0.014	20	B246SF, 60% CMC

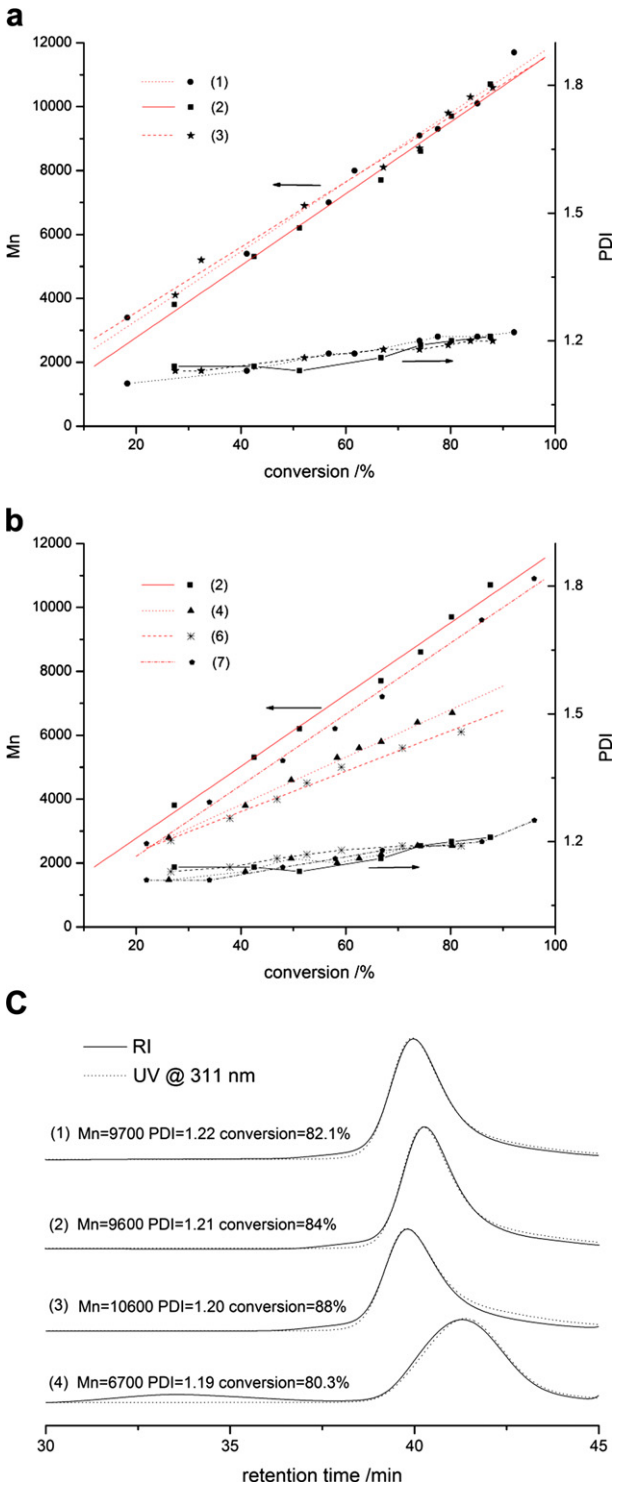

Fig. 2. RAFT polymerization of acrylamide: a) Evolution of Mn and PDI as a function of conversion. b) Evolution of Mn and PDI for controlled PAM as a function of conversion. c) ASEC chromatogram (RI and UV traces at 311 nm) evolution during the polymerization.

absence of the RAFT agent. Considering the fact that the GPC RI trace accounts for the polymer species, and the UV trace at 311 nm reflects the presence of the C═S double bond in the RAFT agent [22], the fraction of polymer formed in the dispersed phase and continuous phase can be determined respectively, by comparing and calculating the areas of the RI and UV curves. In other words,

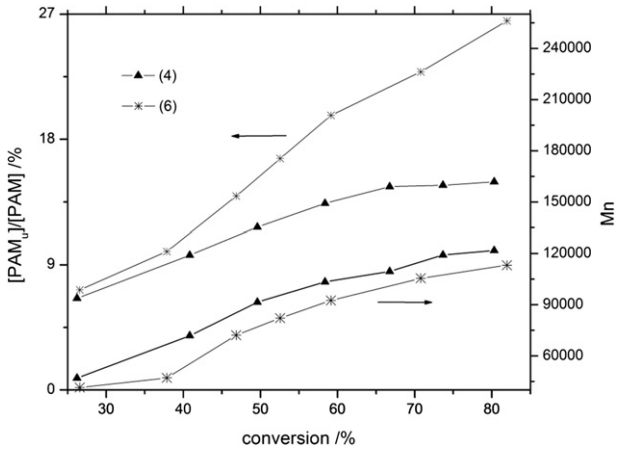

Fig. 3. Mn and mole fraction of the PAM_u as a function of conversion in Expt. 4 and Expt. 6

the kinetic mechanism of RAFT inverse emulsion polymerization can be analyzed by monitoring the RI and UV signals.

The molecular weights of PAM are shown in Fig. 2a with the same number designation as in Fig. 1. Again, like the kinetic curves in Fig. 1, the molecular weights of Expt. 1, Expt. 2 and Expt. 3 are quite close and the GPC curves of Expt. 1 and Expt. 3, as shown in Fig. 2c, are unimodal and exhibit narrow molecular weight distribution. The RI curves have good overlay with the UV curves, indicating good control throughout the polymerization [10] and the same polymerization mechanism as inverse miniemulsion.

Oil-soluble initiator AIBN (Expt. 3) was used to compare with the water-soluble initiator VA-044. From Fig. 2b, it is clear that the molecular weight evolutions of Expt. 4 and Expt. 6 show a downward deviation from Expt. 2 which was polymerized with the hydrophilic initiator VA-044. The decrease in molecular weight in Expt. 3 is most likely due to the lower concentration of living chains. The small wide peak that appears at shorter retention time in RI curve (3) (Fig. 2c), reflects the polymer fraction polymerized under uncontrolled conditions.

When Qi [22] and coworkers used AIBN as the initiator in RAFT inverse miniemulsion polymerization, similarly bimodality in RI curves were observed, and the RI curves showed a poor overlay with the UV curves.

Fig. 3 shows the molecular weight and mole fraction of the uncontrolled polymers (PAM_u) in Expt. 4 and Expt. 6. The mole fraction of PAM_u increased with monomer conversion, as did the molecular weight. For Expt. 4, the ratio $[PAM_u]/[PAM]$ remains low until high degree of conversion, indicating a dominant droplets nucleation. However, when the initiator concentration is increased by 200%, the fraction of PAM_u grows extensively, especially in the late stage of polymerization, suggesting that polymerization in continuous phase is enhanced by the increased initiator concentration.

Thus, the proposed nucleation mechanism (see Fig. 4) can be described as follows: For inverse emulsion polymerization with water-soluble initiators, the nucleation mechanism is similar to that of inverse miniemulsion polymerization. For inverse emulsion with oil-soluble initiators, the nucleation mechanism can be regarded as a mix of droplet nucleation and continuous phase (micellar or homogeneous) nucleation. Primary free radicals are formed by decomposition of initiator and grow by adding monomer units dissolved in the continuous phase. After the oligoradicals grow to a certain length, they become hydrophilic enough to enter droplets and initiate the RAFT polymerization. Meanwhile, a certain fraction of the oligoradicals are captured by monomer-swollen micelles, and form new particles by micellar nucleation. Alternatively, they may

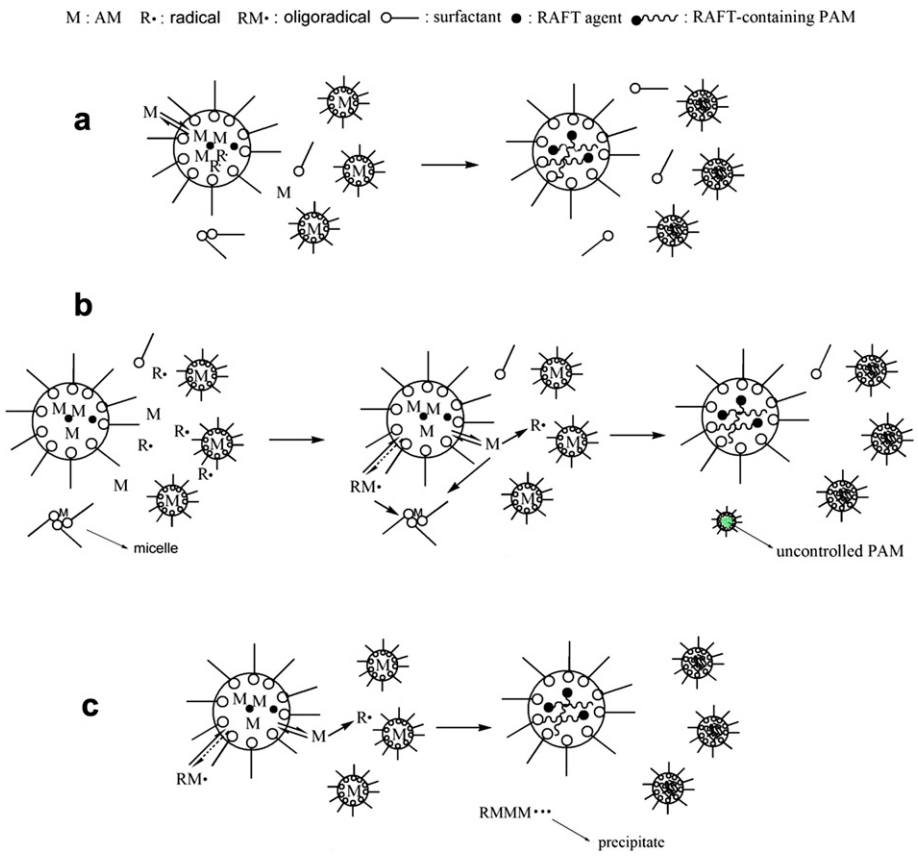

Fig. 4. Proposed nucleation mechanisms of RAFT inverse emulsion polymerization with a) water-soluble initiator b) oil-soluble initiator c) oil-soluble initiator, surfactant concentration below CMC.

continue to propagate until they reach the limit of their solubility in the continuous phase and precipitate out (homogeneous nucleation). Both of these two possibilities will lead to the uncontrolled polymerization to high molecular weight. Based on the above, at the beginning of the polymerization, the polymerization rate in particles is mainly determined by the entry rate of oligoradicals; when most of the free oligoradicals have entered the droplets, they become the main polymerization locus. Therefore, the polymerization rate increases and the polymerization progresses by living polymerization kinetics. Increased initiator concentration will enhance the micelle nucleation due to the accelerated formation of new particles, and lead to a higher fraction of uncontrolled polymers.

Inverse emulsion polymerization with low surfactant concentration (<CMC, Expt. 7) was conducted to gain an in depth understanding of the nucleation happening in the continuous phase when initiated by AIBN. Fig. 5 shows the GPC curves of the polymer obtained by RAFT inverse emulsion polymerization with different surfactant concentrations. When the surfactant concentration was higher than the CMC, the uncontrolled polymer peak was observed and kept growing with increasing reaction time, following the nucleation mechanism described above. It is worth noting that when the surfactant concentration was below the CMC (Expt. 4 - See Fig. 5 for details.), there was also a peak at the early stage of polymerization; however it almost completely disappeared when the monomer conversion reached 34%, and the corresponding molecular weight is much lower than the one in Expt. 4. This phenomenon can be explained based on the presence of micelles. When the surfactant concentration is low, propagation in the continuous phase occurs without the stabilization of surfactant from micelles, therefore, the propagating polymer precipitates out after it reaches the limit of solubility, and contributes to the disappearance of the uncontrolled polymer peak. The rest of the monomer in the dispersed phase polymerizes via a living mechanism. A schematic representation for this case is shown in Fig. 4c.The fitted line 7 shown in Fig. 2b is the molecular weight of controlled PAM in Expt. 7 as a function of conversion, which is parallel to the one in Expt. 2. That is because of the decreased ratio

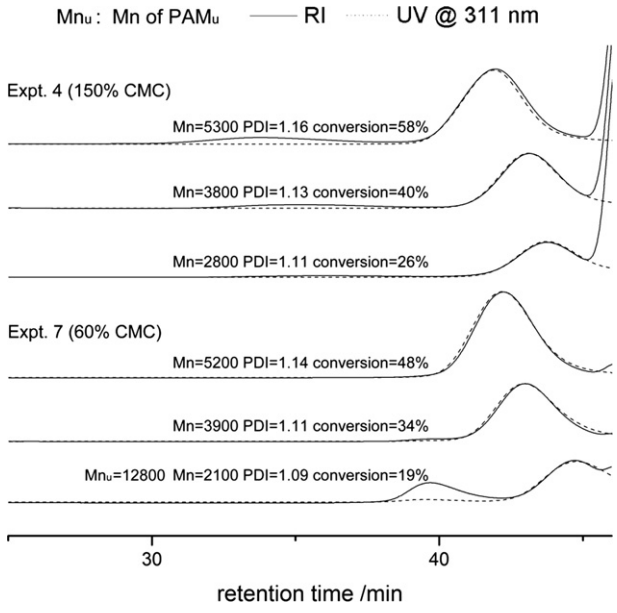

Fig. 5. ASEC chromatogram (RI and UV traces at 311 nm) evolution of Expt. 4 and Expt. 7

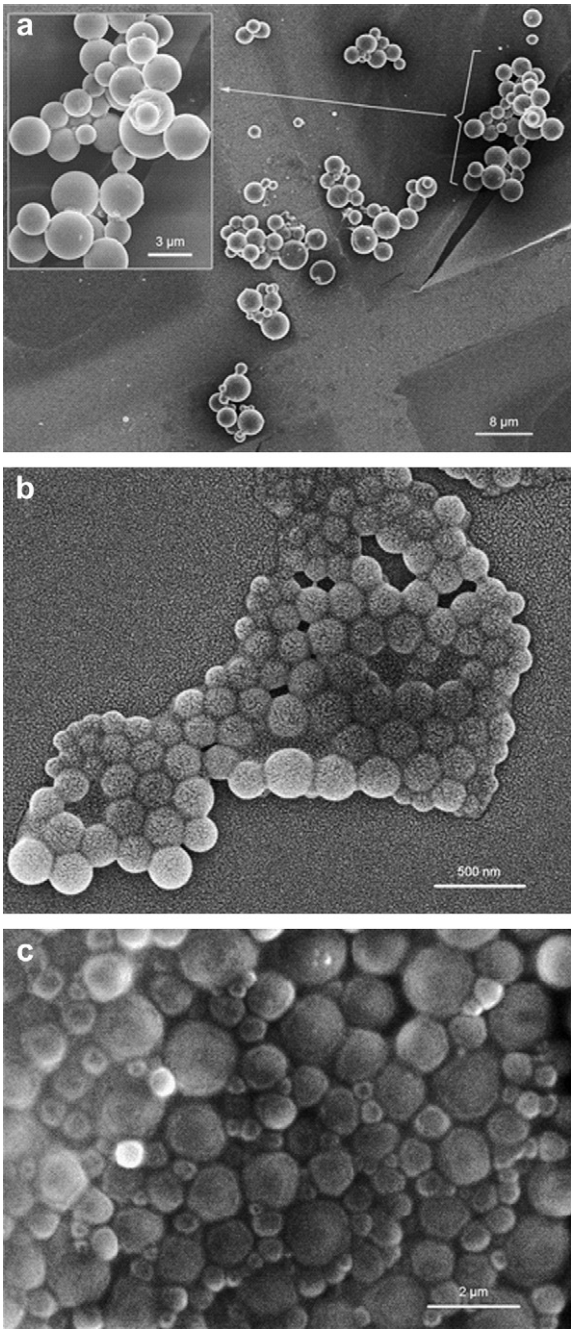

Fig. 6. SEM micrographs of the latex particles obtained from a) RAFT inverse emulsion polymerization, conversion: 95%, Expt. 1. b) RAFT inverse miniemulsion polymerization, conversion: 94%, Expt. 2. c) RAFT inverse emulsion polymerization with AIBN, 150% CMC, conversion: 80%, Expt. 6.

of monomer to RAFT agent due to the loss of uncontrolled polymer formed in continuous phase.

To confirm the mechanism presented above, SEM was used to determine the size and morphology of final particles. The particle size of RAFT inverse emulsion polymerization (Expt. 1), as shown in Fig. 6a, is above 1 μm and has a wide distribution from 1 μm to 4 μm. Latex particles obtained from RAFT inverse miniemulsion polymerization (Expt. 2), shown in Fig. 6b for comparison, exhibit a much narrower distribution with a smaller average size. The wide range particle sizes of RAFT inverse emulsion can be related to the absence of costabilizers, which are used to retard Ostwald ripening [25]. Fig. 6c is the SEM micrograph of the latex from inverse emulsion polymerization with AIBN as the initiator. Two populations of particles are observed. The submicron particles are thought to be derived from the uncontrolled PAM formed by continuous phase nucleation, while the larger particles come from droplet nucleation. The large particles, compared to Fig. 6a, exhibit a more uniform distribution and smaller particle size, which should result from the monomer diffusion from large droplets to newly-formed particles.

4. Conclusion

RAFT inverse emulsion polymerization is a viable method to prepare controlled water-soluble polymers. It was found that when the water-soluble initiator VA-044 was used, the kinetics of inverse emulsion polymerization and inverse miniemulsion polymerization were similar and they have a same (droplet) nucleation mechanism. When the oil-soluble initiator AIBN was used to replace VA-044, a certain amount of uncontrolled polymer was observed and appeared as a wide peak in the GPC RI trace, which resulted from micellar or homogeneous nucleation. RAFT polymerization can be used as a universal technique in investigating the kinetic mechanism of inverse emulsion polymerizations of various monomers.

Acknowledgements

The authors would like to acknowledge the support of the US National Science Foundation (CTS-0553516) and China Scholarship Council (CSC) for this work.

References

[1] Wada T, Sekiya H, Machi S. J Appl Polym Sci 1976;20:3233.
[2] Virk PS. J Fluid Mech 1971;45:225.
[3] Enright DP, Perricone AC. Pet Eng Int 1988;60:55.
[4] Date JL, Shute JM. Tappi 1959;42:824.
[5] Buck S, Pennefather PS, Xue HY, Grant J, Cheng Y-L, Allen CJ. Biomacromolecules 2004;5:2230.
[6] Singh B, Chauhan GS, Kumar S, Chauhan N. Carbohydr Polym 2007;67:190.
[7] Chaw C-S, Chooi K-W, Liu X-M, Tan C-W, Wang L, Yang Y-Y. Biomaterials 2004;25:4297.
[8] Al-Karawi A, Ahemed Jasim M, Al-Daraji AHR. Carbohydr Polym 2010;79:769.
[9] Salehi R, Davaran S, Rashidi MR, Entezami AA. J Appl Polym Sci 2009;111:1905.
[10] Lovell PA, EL-Aasser MS. "Emulsion polymerization and emulsion polymers". Wiley; 1997.
[11] Vanderhoff JW, Tarkowski HL, Shaffer JB, Brad-ford EB, Wiley RM. Adv Chem Ser 1962;34:32.
[12] Vanderhoff JW, Visioli DL, El-Aasser MS. Polym Mater Sci Eng 1986;54:375.
[13] Benda D, Snuparek J, Cermak V. Eur Polym J 1997;33:1345.
[14] Graillat C, Pichot C, Guyot A, El Aasser MS. J Polym Sci Part A: Polym Chem 1986;24:427.
[15] Hernandez-Barajas J, Hunkeler DJ. Polymer 1997;38:437.
[16] Jun A, Masamichi N, Kiyotaka S, Teruo O. J Polym Sci Part A: Polym Chem 2008;21:7127–37.
[17] PerB Z, Fawaz A, Masayoshi O. J Polym Sci Part A: Polym Chem 2009;47:3711–28.
[18] Oh JK. J Polym Sci Part A: Polym Chem 2008;46:6983–7001.
[19] An Z, Shi QH, Tang W, Tsung CK, Hawker CJ, Stucky GD. J Am Chem Soc 2007;129:14493–9.
[20] Lu FJ, Luo YW, Li BG, Schork FJ. Macromolecules 2010;43:568–71.
[21] Qi GG, Bennett E, Jones CW, Schork FJ. Macromolecules 2009;42:3906–16.
[22] Qi GG, Jones CW, Schork FJ. Macromol Rapid Commun 2007;28:1010.
[23] L. Ouyang, L.S. Wang, F.J. Schork, Macromol Chem Phys, in press.
[24] Albertin L, Stenzel M, Barner-Kowollik C, Foster LJR, Davis TP. Macromolecules 2004;37:7530–7.
[25] Ostwald W. Z Phys Chem 1901;37:495.

Polymer 52 (2011) 68–76

Contents lists available at ScienceDirect

Polymer

journal homepage: www.elsevier.com/locate/polymer

Effects of molten poly(3-hydroxybutyrate) on crystalline morphology in stereocomplex of poly(L-lactic acid) with poly(D-lactic acid)

Ling Chang, E.M. Woo*

Department of Chemical Engineering, National Cheng Kung University, Tainan 701-01, Taiwan

ARTICLE INFO

Article history:
Received 21 August 2010
Received in revised form
13 November 2010
Accepted 18 November 2010
Available online 26 November 2010

Keywords:
Stereocomplex
Poly(L-lactic acid)
Morphology

ABSTRACT

Effects of poly(3-hydroxybutyrate) (PHB) on crystalline morphology of stereocomplexing capacity of poly (L- and D-lactic acid) (PLLA and PDLA) were studied by differential scanning calorimetry (DSC), polarizing-light optical microscopy (POM), atomic-force microscopy (AFM) and wide-angle X-ray diffraction (WAXD). When crystallized at high T_c (130 °C or above), morphology transition of stereocomplexed PLA (sc-PLA) occurs from original well-rounded Maltese-cross spherulites to dendritic form in blends of high PHB contents (50 wt.% or higher), where PHB acts as an amorphous species. Microscopy characterizations show that morphology of sc-PLA in PHB/sc-PLA blends crystallized at $T_c = 170$ °C no longer retain original complexed Maltese-cross well-rounded spherulites; instead, the spherulites are disintegrated and restructured into two types of dendrites: (1) edge-on feather-like dendrites (early growth) and (2) flat-on wedge-like crystal plates (later growth) by growing along different directions and exhibiting different optical brightness. The concentration and/or distribution of amorphous PHB at the crystal growth front, corresponding to variation of the slopes of spherulitic growth rates, is a factor resulting in alteration and restructuring of the sc-PLA spherulites in the blends. Despite of spherulite disintegration, WAXD result shows that these two PHB-induced dendrites still retain the original unit cells of complexes, and thus these two new dendrites are sc-PLA.

1. Introduction

The crystallization and crystalline morphologies of miscible blends of amorphous/crystalline systems have been extensively studied [1–3]. However, less attention has been paid to miscible blends composed of two crystalline polymers. Semicrystalline polymers may exhibit a wide variety of superamolecular structures and phase morphologies in crystalline/crystalline systems, such as poly(L-lactic acid)/poly(3-hydroxybutyrate) (PLLA/PHB) [4], poly (vinylidene fluoride)/poly(butylene adipate) (PVDF/PBA) [5], and poly(ethylene oxide)/poly(butylene succinate) (PEO/PBSU) [6]. Semicrystalline polylactides (PLA's) has attracted much attention for their potential applications in medical devices due to its biodegradability, biocompatibility, excellent optical and good mechanical properties [7–10]. PLA exists in typical three isomeric forms, such as L-lactic acid (PLLA), D-lactic acid (PDLA), and racemic-lactic acid (PDLLA), which display a wide variety of properties. Stereocomplexation can occur between some polymers, which is based on interactions of stereoselective van der Waals forces, such as isotactic with sydiotactic poly(methacrylate) (iPMMA and sPMMA) [11–22], or L-configured with D-configured PLA [23–30]. For examples, iPMMA and sPMMA upon mixing in some solvents or melt-mixing in bulk can lead to formation of aggregates of complexes [14–16]. Furthermore, influence of stereocomplex PMMA formation, such as polymer concentration [17,18], mixing ratio [15,16,19], molecular-weight [14,21] and thermal treatments [14], have been well investigated. Recently, stereocomplex of tactic PMMAs (isotactic and syndotactic) of high-molecular weights are enhanced by adding a third polymer which decreases T_g of the more rigid PMMA chain segments [22]. On the other hand, equimolar mixtures of PLLA and PDLA are able to form a stereocomplexed PLA (sc-PLA), which shows a melting temperature (T_m) of 50 °C higher than that of PLLA or PDLA and has higher mechanical properties than PLLA [27,28].

The typical morphology of sc-PLA spherulite is of a Maltese-cross pattern for melt-crystallized polymer, whereas the sc-PLA spherulites may become disordered and less distinct under non-equimolar conditions [26–29]. When crystallized at any T_c's, the spherulites of stereocomplexes are distinctly of a Maltese-cross pattern, in contrast with ring-banded patterns in the constituent. As a sc-PLA complex is being packed by cooling from a mixture in

* Corresponding author. Tel.: +886 6 275 7575x62670; fax: +886 6 234 4496.
E-mail address: emwoo@mail.ncku.edu.tw (E.M. Woo).

0032-3861/$ – see front matter © 2010 Elsevier Ltd. All rights reserved.
doi:10.1016/j.polymer.2010.11.028

the melt state, properties of PLA complexes may be influenced by various parameters, such as molecular-weight, mixing ratios, and temperature and time. There have been some previous studies on some of influencing factors on the formation and properties of sc-PLA have been reported [24–26,29–30]. As PLLA/PDLA mixtures are further blended with diluents, effects of above parameters and additionally interaction strength of PLAs with the diluents, on final complex morphology of PLA complexes have yet to be fully understood.

The miscibility and phase behavior of blends of PHB with PLLA is strongly dependent on the molecular weights of either of constituents [4,31–35]. It is known that PHB can be miscible with low-molecular-weight PLLA (M_w < 18,000) in the melt at 200 °C over the entire compositions, whereas PHB blends with high-molecular-weight PLLA (M_w > 18,000) show phase separation [4,31–35]. Two types of spherulitic morphologies, respectively related to the crystal forms of PHB and PLLA, are observed when PLA/PHB blends are cooled from the melt [4].

Although blends of PHB with PLLA have been widely investigated; however, studies have yet to be directed to investigation of influence of miscible diluents co-crystallizing with the complexes on the crystalline morphology of the sc-PLA structures. It was of great interest to probe whether the stably complexed Maltese-cross spherulites in sc-PLA might be altered or disrupted when sc-PLA crystallized in presence of miscible diluents or polymers, such as PHB. In blends kept at T_c of PLAs, PHB is molten and remains non-crystallizable in a melt state, and thus PHB acts as an amorphous/molten diluent throughout crystallization of sc-PLA being packed into complexes from the liquid PHB/sc-PLA mixtures. It was of interest to investigate effects of PHB contents on morphology and thermal behavior of isothermally crystallized complex PLA system. Influencing factors of the crystallization conditions including PHB compositions and crystallization temperature, on thermal behavior of sc-PLA in blends were discussed. To understand the progress of influence of PHB molecules on sc-PLA spherulite transformation, in-situ monitoring of sc-PLA crystallization in blends was investigated.

2. Experimental

2.1. Materials and preparation procedures

Poly(L-lactic acid) (PLLA) of a low-molecular-weight (M_w = 11,000 g mol^{-1}) and poly(D-lactic acid) (PDLA) (M_w = 124,000 g mol^{-1} and M_w/M_n = 1.3) were purchased from Polysciences, Inc. (USA) and Fluka, Inc. (Switzerland), respectively, and used as received. Poly[(R)-3-hydroxybutyrate] (PHB) (M_w = 500,000 g mol^{-1}) was purchased from Polysciences, Inc. (USA) and used as received. Binary blends with PLLA and PDLA and ternary blends comprising PLLA, PDLA, and PHB were first separately prepared, then stereocomplexing sc-PLA and PHB mixtures were prepared using solvent-mixing, followed with film-casting. PHB was first dissolved in hot chloroform ($CHCl_3$) solution, and then further blended with solutions of PLLA and PDLA with proper ratios. Ratios of PLLA to PDLA in blends were maintained at 1/1 by weight in either binary or ternary blends. In ternary blends, PLLA/PDLA was fixed at 1/1, with the PHB contents ranging from 90/10 to 10/90 in weight ratios, the first number referring to the weight percentage of PHB. Before thermal treatment, the solution was subsequently cast on a glass plate at 45 °C, and blend films were obtained after evaporating most of the solvent on a hot plate at ca. 50 °C for 2 days. In the first step of ambient drying at 45 °C because it was the temperature of preliminary film cast. Polymer mixing and film uniformity was balanced with solvent drying at the most appropriate temperature of 45 °C, which was chosen by trials. Then, trace residual solvent in polymer samples was further driven off at a slightly higher 50 °C for fast degassing under vacuum. Solution-coating was used for preparation of PHB/sc-PLA samples of thickness around 6–7 μm. Samples were not used for second time in thermal analysis to avoid thermal degradation.

2.2. Apparatus

Thermal analysis was carried out with a differential scanning calorimetry (DSC) (Diamond, Perkin–Elmer Corp.), under a dry/inert nitrogen atmosphere. The melted samples were kept at 230 °C for 1 min for completely removing prior thermal history of blends, and immediately placed in liquid nitrogen to quench into an amorphous state for T_g measurements. For analysis of blends, the procedure for isothermal crystallization experiments was as follows: all samples were heated to 230 °C for 1 min and immediately quenched to the desired crystallization temperature, T_c. For T_g measurements, the PHB/sc-PLA blends were heated to 230 °C for 1 min (above T_m's of either sc-PLA or PHB), immediately immersed in liquid nitrogen to an amorphous state. In such rapid quenching condition, sc-PLA or PHB crystallites could not form during rapid cooling, and their glassy states were preserved for T_g characterization. Gaussian curve-fitting of PHB/sc-PLA (50/50) blend at 130–170 °C from DSC measurements was the preformed, using Peakfit software (web trial version-Jandel Scientific).

The spherulitic morphologies were observed on a Nikon Optiphot-2 polarizing-light optical microscope (POM) equipped with a Nikon CCD digital camera. Non-polarizing-light optical microscopy (OM) was also used for better discerning the topographic shapes of spherulites. Samples were first melted on a hot stage at 230 °C for 1 min, and then quickly transferred to hot stage (Linkam THMS-6000) equilibrated at the desired crystallization temperature. To further investigate the morphologies of blends, samples were also examined using atomic-force microscopy (AFM) (Caliber, Veeco-DI Corp., USA) with a tapping mode. Silicon tips with a resonance frequency of ~280 kHz were used, and the scan rate was 0.3 Hz. All samples were deposited on substrates of glass slides with an open face up, and were characterized using a set-point amplitude ratio of 0.8.

Wide-angle X-ray diffraction (WAXD) patterns for neat PHB, neat sc-PLA and blends were characterized with X-ray instrument (Shimadzu/XRD-6000) with a CuK_α radiation (30 kV and 40 mA). The scanning angle (2θ) covered a range between 10 and 30° at a rate of 2°/min.

3. Results and discussion

3.1. Thermal behavior of PHB/sc-PLA blends

To examine the influence of PHB content on thermal behavior of sc-PLA formation, a low-molecular-weight PLLA was chosen for probing miscibility between PHB and PLLA. Fig. 1 shows the DSC thermograms of melt-quenched sc-PLA blend with various PHB contents. It has been found that neat sc-PLA exhibits a glass temperature (T_g) around 40 °C, and a melting temperature (T_m) at about 221 °C with ΔH_f of 84.9 J/g, which agree with literature [23,26,27]. The glass temperature transition of neat PHB is −6.3 °C, which is lower than that of neat sc-PLA. Fig. 1 (A) shows that a single and composition-dependent T_g (onset position indicated with arrow marks), and this provides that the sc-PLA and PHB are miscible in the melt. Dependence of T_g on composition relationship for PHB/sc-PLA blend was fitted with the Gordon–Taylor equation [36]: $T_{g,blend} = (w_1T_{g,1} + w_2kT_{g,2})/(w_1 + kw_2)$, with $k = 0.43$ as shown in Fig. 1 (B).

Furthermore, the depression in the crystallization temperature of sc-PLA (indicated with solid lines) in blends with the increase of

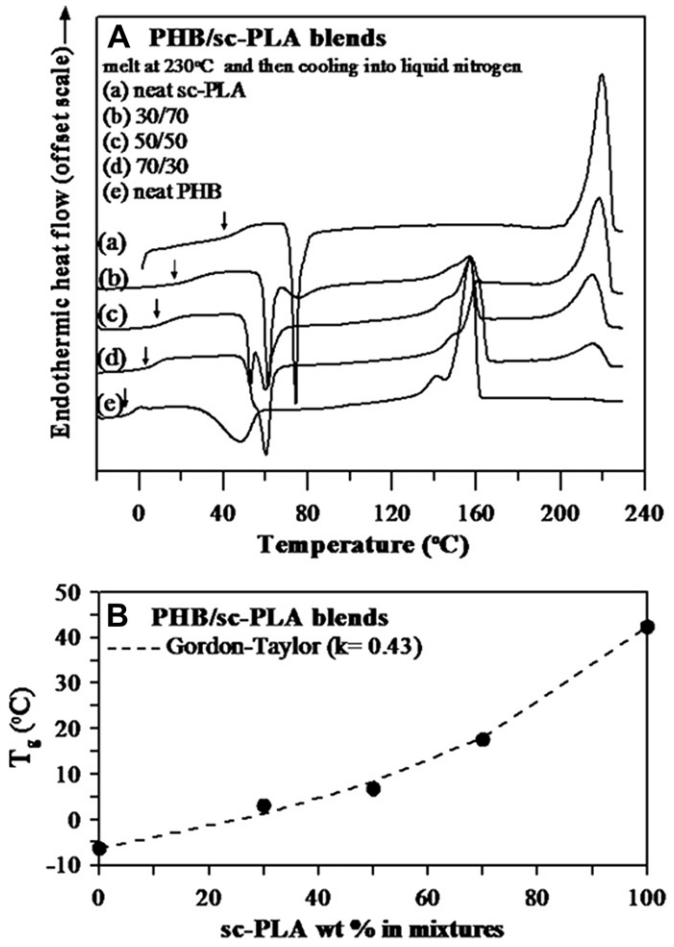

Fig. 1. (A) DSC thermograms of PHB/sc-PLA blends; (B) plot of blend's single T_g's vs. composition.

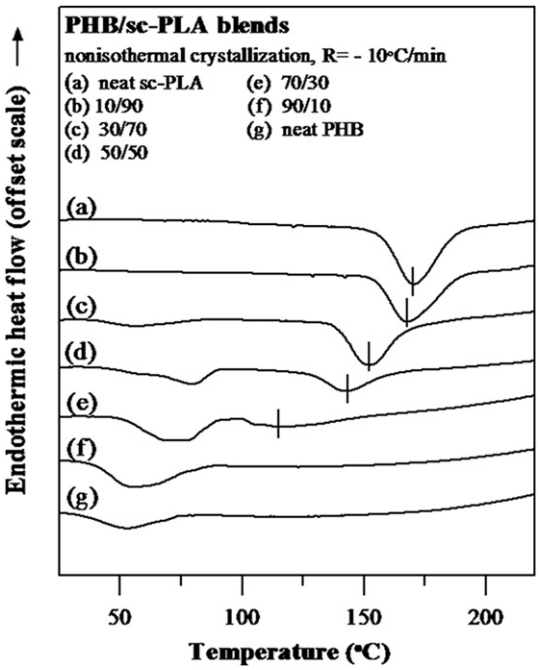

Fig. 2. DSC thermograms of PHB/sc-PLA blends of seven compositions at cooling rate of −10 °C/min.

PHB content can be observed in Fig. 2. The result indicates that the crystallization of sc-PLA in blends is significantly hindered, leading to that imperfect crystals are formed with increasing PHB contents. In addition, DSC thermograms of melt-crystallized at 130 °C for PHB/sc-PLA blends with various compositions are shown in Fig. 3. Two endothermic peaks of sc-PLA in blends can be observed, labeled as P_1 and P_2 for low- and high-temperature melting endotherms, respectively. Note that PHB in the sc-PLA complex acts as an amorphous component in blends for the blends held and crystallized at 130 °C or above. When held and crystallized at 130 °C, sc-PLA could crystallize but PHB was molten and non-crystallizable at all. PHB can crystallize only when cooled to 100 °C or lower including ambient temperature. Thus, the DSC curves by isothermally holding and scanning from 130 °C reveal no melting of PHB as PHB has never been given chance to crystallize at all. For neat sc-PLA, a single melting peak P_2 is observed, corresponding to the fusion of the crystallites formed during cooling or subsequent isothermal crystallization. In addition, a small exothermic peak, labeled as P_{exo}, appears with PHB weight fraction changing from 30 to 70 wt.%. According to Fig. 3 (A), the subsequent melting DSC curves of PHB/sc-PLA blends show a broader melting peak P_2 compared with those of neat sc-PLA. Besides, the melting peak P_2 of sc-PLA in blend shifts to lower temperature with increase in PHB contents. Fig. 3 (B) presents that the ΔH_f values of melting peak P_2 in blends decrease with increase of PHB weight fraction, indicating that less stable (or less perfect) crystals of sc-PLA in blends are augmented with increase of PHB content.

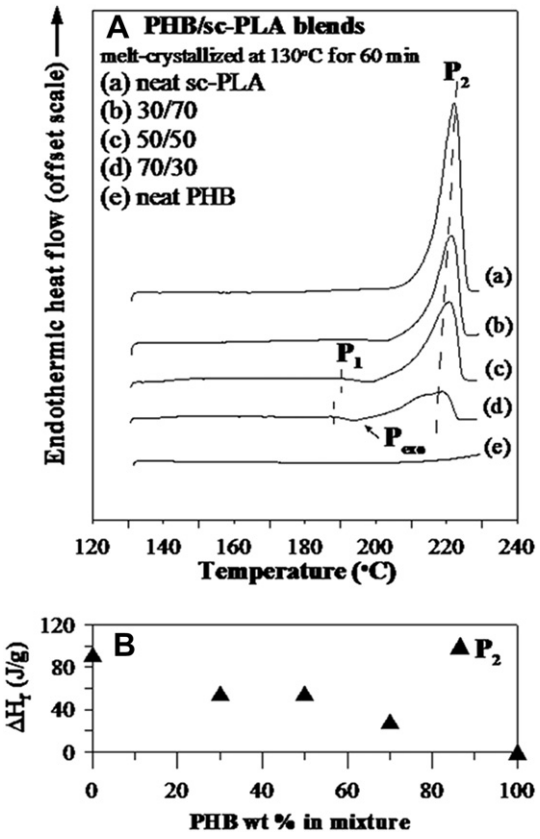

Fig. 3. (A) DSC thermograms of PHB/sc-PLA blends of various compositions melt-crystallized at 130 °C; (B) ΔH_f values of melting peak P_2 as a function of PHB content in blends.

3.2. Dendritic morphology in PHB/sc-PLA blend

In addition to PHB composition, effects of crystallization temperature (T_c) on sc-PLA formation were also analyzed. Fig. 4 shows DSC curves of PHB/sc-PLA blend = 50/50 isothermally crystallized at temperatures from 130 to 170 °C. According to Fig. 4 (A), the DSC curves indicate that the position of melting peak P_1 shifts from 185 to 197 °C with increasing T_c; P_{exo} can not be distinctly seen with increasing T_c. Note that melting peak P_2 remains almost constant around 218 °C for the blends crystallized at various temperatures. As shown in Fig. 4 (B), the ΔH_f values of melting peak P_1 increase with increasing T_c due to enhanced crystal perfection or thickening of the lamellae, while those of peak P_2 decrease with increasing T_c. From the observation that the position and ΔH_f values of melting peak P_1 is dependent on the T_c, it is suggested that less stable (or less perfect) crystallites of P_1 increases in crystal perfection or thickening with increasing T_c.

It was of interest to investigate influence of PHB content and T_c on sc-PLA spherultic formation. Fig. 5 shows the morphologies of neat and blended sc-PLA with various weight fractions of PHB (70/30–30/70) crystallized at 130 °C. In blends held at these T_c's, PHB is in an amorphous molten state and acts as a diluent throughout crystallization of sc-PLA. The spherulites of neat sc-PLA crystallized at 130 °C are typical Maltese-cross patterns as shown in Fig. 5-(a), whereas those of sc-PLA in blend tend to formation of highly dendritic crystals. For the PHB-rich compositions (i.e., 50/50–70/30 blends), Fig. 5-(c) and (d) shows dendritic sc-PLA spherulitic textures with disruption of Maltese-cross patterns.

In addition to PHB composition, others factors, such as crystallization temperature (T_c), may also influences the morphologic formation of stereocomplexes PLA in blends. Fig. 6 shows POM and OM images of sc-PLA with PHB (i.e., 50/50) melt-crystallized at various temperatures (T_c = (a) 150 °C and (b) 170 °C). The POM images of sc-PLA in blends with PHB crystallized at 150 °C (Fig. 6-a) show dendritic textures with disruption of Maltese-cross patterns, whereas those of sc-PLA in blends melt-crystallized at 170 °C, show coexistence of feather-like and wedge-like spherulites (Fig. 6-b). At an even higher T_c = 170 °C, the dendrites can be classified into two types, indicated with dotted and solid-line arrows, respectively. The detailed structures of these dual-type crystallites will be discussed later. Upon crystallization of the 50/50 blend at 150 °C or above, original circular Maltese-cross spherulites no longer exist. Instead, the Maltese-cross pattern typical of the sc-PLA spherulites disappears, and is now replaced with dendritic bundles, which may be ascribed to presence of PHB molecules dissolving and reorienting the stereocomplexed spherulites into dendrites. These facts reveal that spherulitic morphologies of sc-PLA in blends generated by melt-crystallization are not only affected by PHB compositions but also crystallization temperature. In Fig. 6-(c) and (d), POM micrographs for the enlarged areas of sc-PLA in blends crystallized at T_c = 170 °C show feather-like patterns with higher brightness and wedge-like patterns with lower brightness, respectively. In Fig. 6-(c) and (d), non-polarizing OM micrographs for the enlarged areas of feather-like and wedge-like crystals, respectively, are shown jointly for comparison with the interested areas as illustrated in POM photos. The OM image (Fig. 6-d) further reveals that the wedge-like dendrites display a coarser texture than the feather-like ones. The POM and DSC results suggest that sc-PLA spherulites with dendritic textures contain less stable (or less perfect) lamellae in crystalline structure.

To explain the nature of morphologic changes and melting behavior of sc-PLA in blends, the wide-angle X-ray measurements on blends isothermally crystallized at various temperatures were analyzed. Fig. 7 shows WAXD profiles of (a) neat sc-PLA, (b) PHB/sc-PLA blends = 50/50 and (c) neat PHB, isothermally crystallized at indicated T_c's. Neat sc-PLA shows diffraction peaks at 2θ = 11.5°, 20.5°, and 23.5°, which are characteristic of sc-PLA crystallized with a trigonal unit cell of dimension: a = b = 1.50 nm, c = 0.823 nm, $\alpha = \beta = 90°$, $\gamma = 120°$ [37]. Two main characteristic diffraction peaks located at 2θ = 12.9°, and 16.4° are assigned to the neat PHB crystal, which is in agreement with the literature results [38,39]. The blended sc-PLA exhibits the same diffraction peaks as the neat sc-PLA, indicating that the unit cells of sc-PLA in blends are not altered by addition of PHB. Although the melting behavior and morphology of sc-PLA in blend are different from those of neat sc-PLA, the same crystalline cell structures are revealed in the WAXD pattern. To clarify the original structures of melting peaks P_1 and P_2, the WAXD profile for the blends which are erasing the melting peak P_1 is the same with that consisting of melting peaks P_1 and P_2 (not shown here).

As discussed earlier, POM graphs in Fig. 6 for the PHB/sc-PLA blends (50/50) crystallized at 170 °C show coexisting feather-like and wedge-like dendrites/spherulites with bright and dark-brightness, respectively. These two different morphologies grown from the complexes of the PHB/sc-PLA blend only occurs at high T_c temperatures, suggesting that mobility of molten PHB chains in contacting with sc-PLA is the main factor for the morphology transition from sc-PLA complex spherulites to dendrites. The lamellar patterns of these two different dendrites were further analyzed in details using AFM. Fig. 8 shows AFM height images for PHB/sc-PLA blends (50/50) crystallized at 170 °C, revealing height profiles for two different structures in the PHB-disintegrated sc-PLA spherulites. The height image of Fig. 8 (A) shows that feather-like and wedge-like dendrites are different in heights. The height profile of the wedge-like dendrite is much higher than that of the

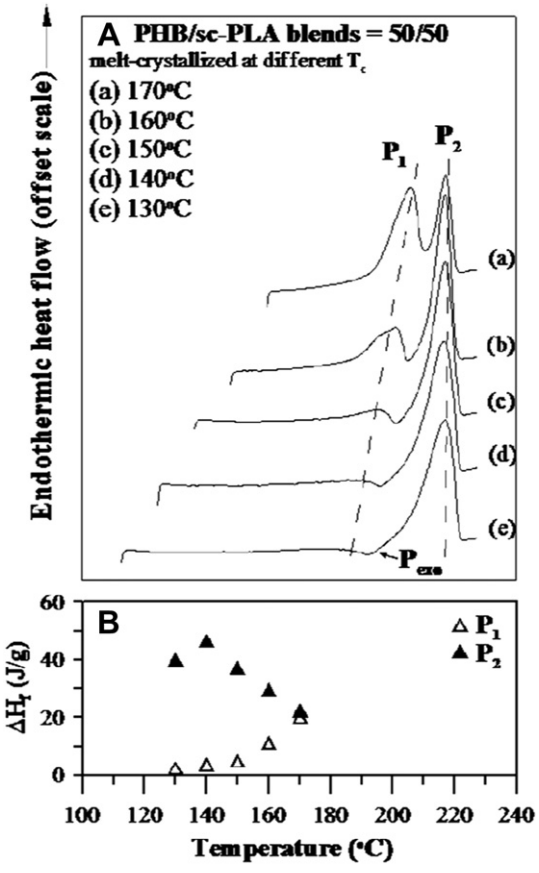

Fig. 4. (A) DSC thermograms of PHB/sc-PLA blends = 50/50 melt-crystallized at T_c; (B) ΔH_f values of melting peaks P_1 and P_2 as a function of crystallization temperature.

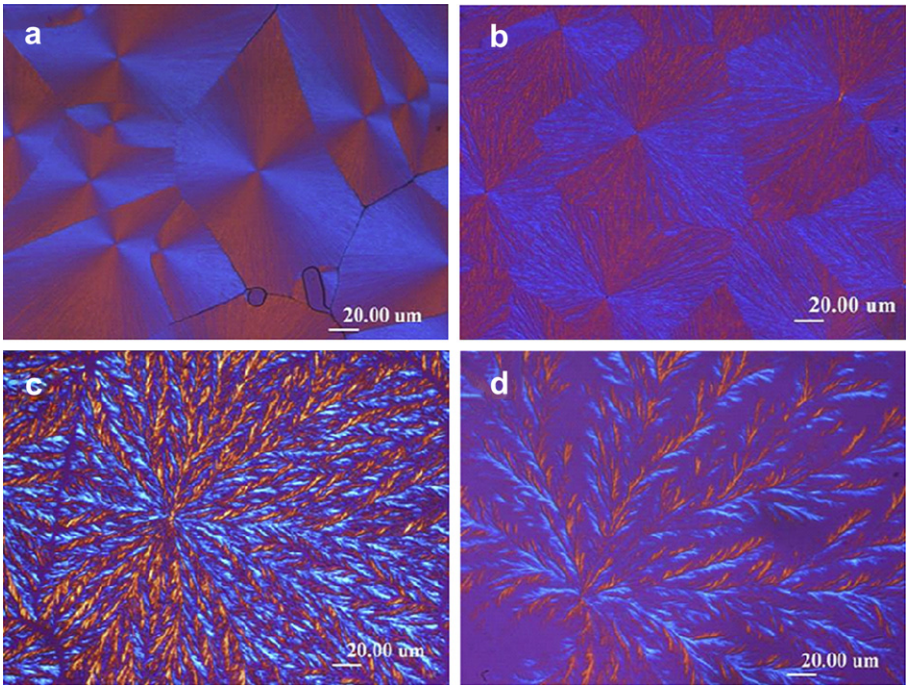

Fig. 5. POM graphs of PHB/sc-PLA blends melt-crystallized at 130 °C: (a) neat sc-PLA, (b) 70/30, (c) 50/50, and (d) 30/70.

feather-like one as shown in the bottom plot of Fig. 8 (A). The enlarged areas of the square-boxed regions (b) and (c) of Fig. 8 (A) are shown in Fig. 8 (B) and (C), corresponding to the wedge-like and feather-like dendrites, respectively. The arrow mark in Fig. 8 (B) and (C) indicates the radial direction of spherulite growth. Obviously, the wedge-like and feather-like dendrites are of two distinctly different crystal types: platelet and long-stripe morphologies, respectively. Fig. 8 (B) shows that the wedge-like dendrite of sc-PLA is composed of platelet crystals; however, the feather-like dendrite is made up of long-stripe lamellae.

Fig. 9 shows AFM phase images of the enlarged area of the wedge-like and feather-like dendrites (see Fig. 8 (B) and (C)) in the PHB/sc-PLA blend (50/50) crystallized at 170 °C. Fig. 9 (A) shows the phase image of wedge-like dendrites, revealing wedge-like dendrites with multi-layered platelet morphology. The inset in Fig. 9 (A) shows the enlarged area of the square-boxed region of

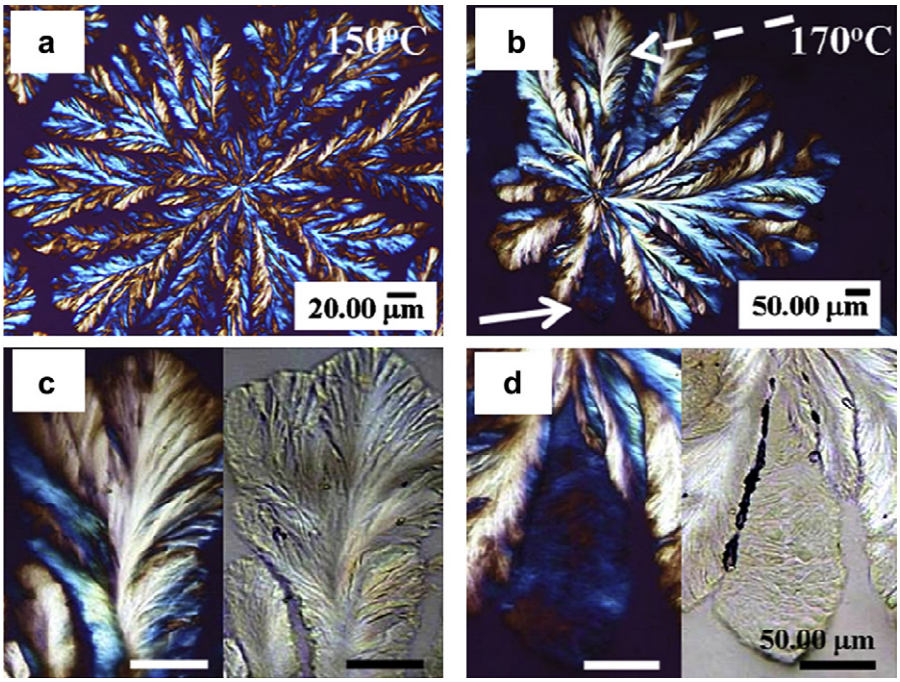

Fig. 6. POM and OM graphs of PHB/sc-PLA blends (1:1) melt-crystallized at various temperatures: (a) 150 °C, (b) 170 °C; enlarged micrographs showing (c) feather-like, and (d) wedge-like lamella (indicated with dotted and solid-line arrows, respectively).

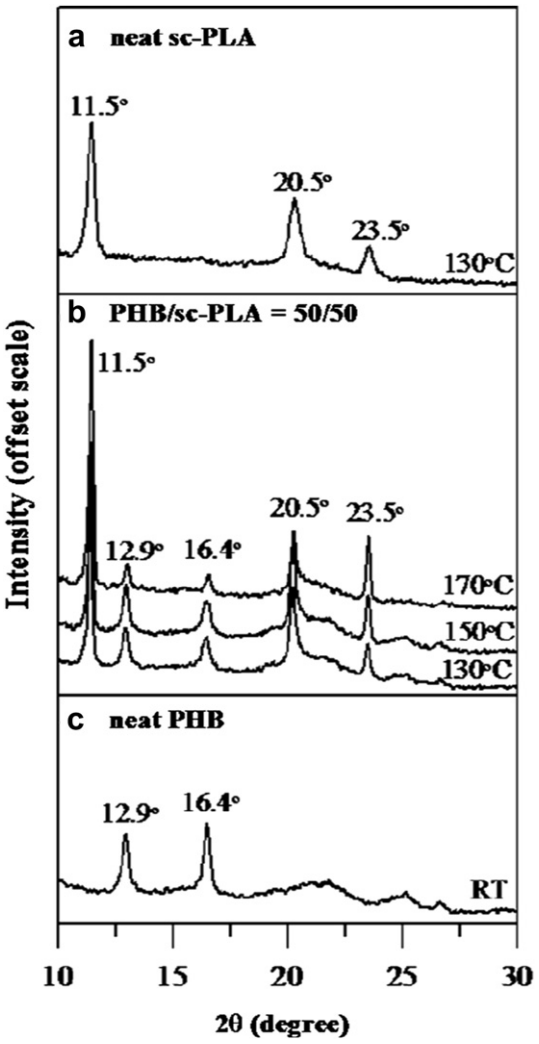

Fig. 7. WAXD profiles of (a) neat sc-PLA, (b) PHB/sc-PLA blend = 50/50 at three T_c's, and (c) neat PHB, isothermally crystallized at T_c's.

Fig. 9 (A), indicating that the lamellar thickness of the wedge-like dendrite, measured from the cross-sectional phase image, is ca. 16 nm and the direction of platelet crystal growth is almost perpendicular to the radial direction of spherulites growth. For the feather-like dendrite, the inset in Fig. 9 (B) shows that the lamellar thickness of the feather-like dendrite is ca. ~13 nm and the growth direction of long stripes of lamellae is almost parallel to the radial direction of spherulites growth. The results of AFM characterization show that the feather-like (bright area) and wedge-like (dark area) dendrites mainly consist of edge-on long-stripe lamellae and flat-on platelet lamellae, respectively.

Note that the AFM morphology for the platelet lamella in the wedge-like dendrites of the PHB/sc-PLA blend is quite similar to the flat-on lamella in the dark bands of ring-banded spherulites of PLLA crystallized between 125 and 130 °C [40,41]. More strikingly, the AFM morphology for the long stripes of lamella in the feather-like dendrites of the PHB/sc-PLA blend is quite similar to the edge-on lamella in the bright bands of ring-banded spherulites of PLLA crystallized between 125 and 130 °C [40,41]. The fact demonstrates that the crystal species of flat-on and edge-on lamellae can exist side-by-side and not only as concentric alternating rings. Note also the crystal species in the feather-like and wedge-like dendrites grow simultaneously from a common center, and they are not inter-related by continuous spiraling from one to another. The feather-like dendrite is filled with thin stripes of lamellar bundles, while the wedge-like dendrite is composed of discrete crystal platelet intersected by amorphous interfaces. The crystal species in two dendrites are not continuous inter-related but grow side-by-side. The morphologies of crystal species in these two dendrites demonstrate that edge-on and flat-on lamellae can exist by simultaneous or alternating growth, and not necessarily are created by spiraling from one lamella orientation to another. Therefore, edge-on and flat-on lamellae, discrete and not inter-related, can also be aligned in concentric fashion. This postulation can be an alternative mechanism to the conventional assumption that the lamellae continuously and rhythmically from flat-on to edge-on orientation to create alternating dark/bright bands, respectively.

3.3. Morphology evolution of sc-PLA in contact with molten PHB

Fig. 10 shows the growth rates in terms of spherulitic radius versus time for dual types dendritic structures in PHB/sc-PLA blend (50/50) crystallized at T_c of 170 °C. Insets in Fig. 10 show OM graphs for dual types of spherulites of feather-like and wedge-like patterns, respectively. The spherulitic growth rate of wedge-like pattern (indicated with solid crosses) is much slower than feather-like pattern (indicated with solid triangles); however, a nonlinear relationship to time exists in the growth of both types of spherulites. Various explanations for the nonlinear spherulitic growth rate have been proposed [42–44]. Most notably, Keith and Padden [42] have reported that the diffusion rates of impurities (i.e., non-crystallizable components) are higher than the crystal growth rates of crystallizable components, the concentration of the impurities will increase at the crystal growth front and result in the nonlinear growth. In the case of sc-PLA in blends (50/50) crystallized at T_c = 170 °C, the differences between diffusion rates of impurities (i.e., amorphous PHB chains) and crystal growth rates of the crystallizable component (i.e., sc-PLA crystals) in the dual-type morphologies is a factor resulting in variation of the slopes of spherulitic growth rates. Hence, the concentration and/or distribution of the impurities at the crystal growth front, corresponding to variation of the slopes of spherulitic growth rates, is one of factors resulting in different orientations of sc-PLA lamellae in blends.

Result in Fig. 10 leads to useful correlation and analogy between the constituent crystal plates in dendrites in complex PLLA/PDLA and those in the extinction-banded spherulites in PLLA or other polymers. Many insights into complex morphology can be investigated by disintegrating the well-rounded Maltese-cross spherulites into dark-bright lamellae dendrites with radial direction straight wedge (dark) plate sandwiched between radial direction feather-like (bright) dendrites. There seems to be an interesting correlation between the growth kinetics of the dual-type dendrites in PHB/sc-PLA complex spherulites and that of the alternating bright-dark bands in extinction-band spherulites in other polymers. Result in Fig. 10 clearly points out that growth rate of the dark dendrite (wedge-like plate) is lower than that of the bright dendrite (feather-like crystal).

By comparisons between the growth rates for the dendrites and ring-banded spherulites, an interesting analogy can be drawn for the bright-dark dendrites and dark-bright rings in banded spherulites. Prior studies reported in the literature on the ring-banded spherulites in polymers have indicated that two distinct growth rates are alternately different in the dark and bright band regions in the ring-banded spherulites. Examples are seen in ring-banded polymers, such as poly(trimethylene terephthalate) (PTT) [45], poly (ε-caprolactone)/poly(styrene-co-acrylonitrile) (PCL/SAN) [46], and poly(ester urethane) copolymers [47]. The growth rate of edge-on

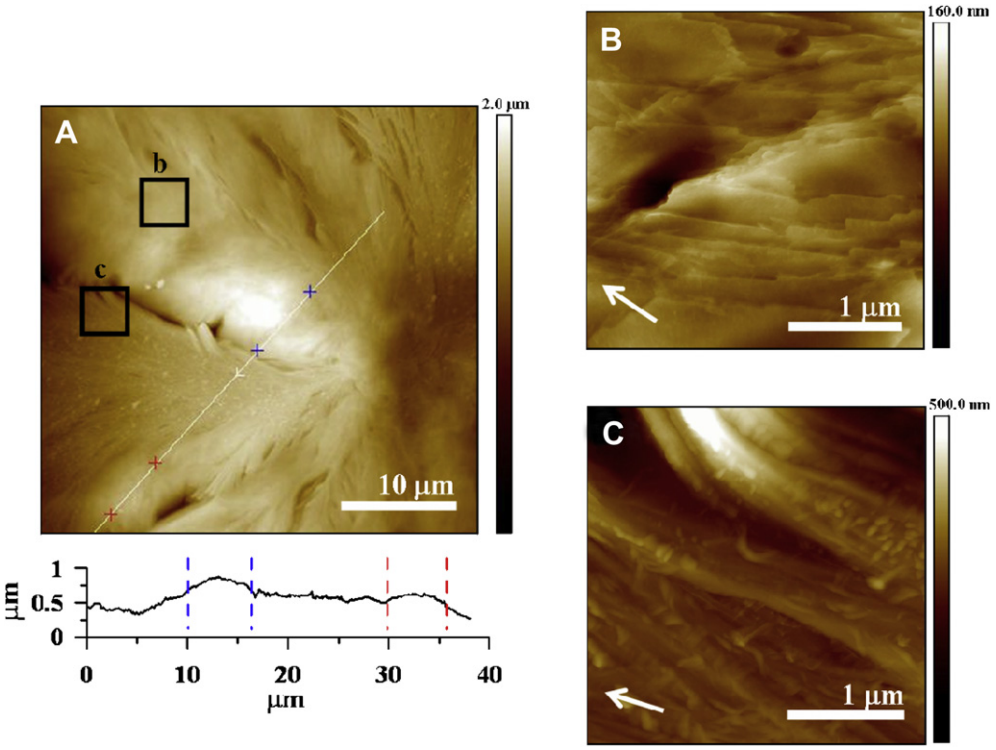

Fig. 8. AFM height images for 170 °C-crystallized PHB/sc-PLA blend (50/50). Graphs-(B) and (C) are the enlarged areas of the square-boxed regions (b) and (c) in Fig. 8 (A).

lamellae of dark band of PTT is decelerated in forming a valley (or dark) band; meanwhile, the growth rate of flat-on lamellae is slightly accelerated in forming a ridge (or bright) band [45]. By contrast, the growth rates of flat-on and edge-on lamellae of sc-PLA spherulites in blends are growth alternately from circumferential direction for forming the wedge-like (dark) plate and feather-like (bright) dendrites, respectively. The result in Fig. 8 (A) also shows that a wavy height profile is seen in going across the alternating wedge-like and feather-like dendrites. These AFM image and height profile results indicate that alternating growth of edge-on and flat-on lamellae spherulites can be seen not only in concentric ring-banded spherulites, but also in the alternating wedge-like and feather-like straight dendrites as demonstrated in this study on the PHB/sc-PLA blend. Interestingly, these two straight dendrites (wedge-like and feather-like) are of dark and bright crystals as viewed in POM characterizations, respectively, just like the alternating dark/bright bands in most conventional ring-banded spherulites. Thus, alternating height up-and-down can occur not only in the radial direction (in ring-banded spherulites) but also in the circumferential direction (in wedge-like and feather-like dendrites). Certainly, this result also points out that the periodic height up-and-down is not necessarily created only by spiraling of one lamella along the radial direction in forming ring-banded spherulites; furthermore, significant height difference can also occur in distinctly straight lamellae of different textures, without any spiraling or twisting, such as the feather-like and wedge-like dendrites demonstrated in this case.

In-situ dynamic observation of process from sc-PLA complex of Maltese-cross spherulites transforming to dendrites in the PHB/sc-PLA blend may provide hints for mechanisms of dendrite

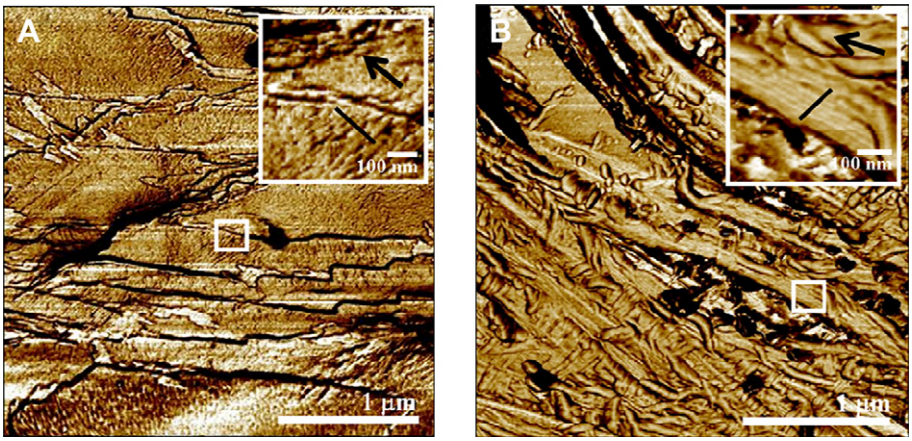

Fig. 9. AFM phase images for (A) wedge-like and (B) feather-like dendrites in 170 °C-crystallized PHB/sc-PLA blend (50/50). Insets: enlarged images of square-boxed region in (A) and (B).

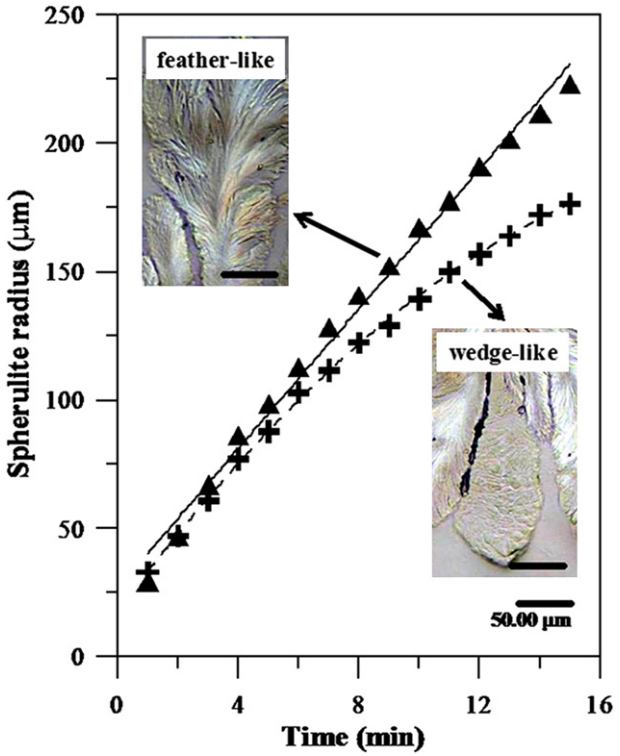

Fig. 10. Plots of spherulitic radius versus time for feather-like (solid triangles) and wedge-like (solid crosses) patterns of dendritic structures in PHB/sc-PLA blend crystallized at T_c = 170 °C. Insets: OM graphs for feather-like and wedge-like patterns, respectively.

formation. Neat sc-PLA (PLLA/PDLA = 50/50) was first cast on a glass plate, melted at 230 °C for 1 min, and immediately quenched to T_c = 170 °C for the observation of neat sc-PLA spherulites. After an early-stage crystallization of neat sc-PLA, the neat sc-PLA film initially cast on glass substrate was further covered with a molten neat PHB film, which had been prepared by solvent-cast of neat PHB on another substrate. That is, PHB/sc-PLA dual-layer samples were prepared by pressing the PHB film on top of a sc-PLA complex film at T_c = 170 °C, where molten PHB was fused into sc-PLA pre-melted at 230 °C then quenched to, held and crystallized at T_c = 170 °C. On the PHB/sc-PLA dual-layer sample, POM dynamic monitoring was started from time t = 0–35 min with various intervals. Fig. 11 shows in-situ monitoring of morphology evolution for neat sc-PLA covered with a thin PHB film isothermally crystallized at 170 °C. The figure shows monitoring on only a single spherulite. Note here that growth may appear to be unbalanced in circumferential regions (right vs. left) of the single spherulite, but statistically, the differences should be weighed on several spherulites. Two reasons are responsible for the different growth rates in two sides of a single spherulite. Concentration distributions in local areas may differ; in addition, film thickness may differ slightly across the single spherulite. In the entire polymer film sample, there are many, i.e., more than one spherulite, and for some other spherulites, growth patterns of upper vs. lower or right vs. left are reversed. Statistically, the differences are averaged out. At 170 °C, PHB remained in a molten amorphous state interacting with the sc-PLA crystallizing species. Obviously, in the early-stage of neat sc-PLA crystallized at 170 °C, the crystal morphology in Fig. 11-(a) shows a typical Maltese-cross pattern for sc-PLA before disintegration of complex spherulites, as also shown earlier in Fig. 5-(a). Fig. 11-(b) shows a disordered Maltese-cross pattern (indicated with dotted-line circle area) in spherulites of the preformed sc-PLA

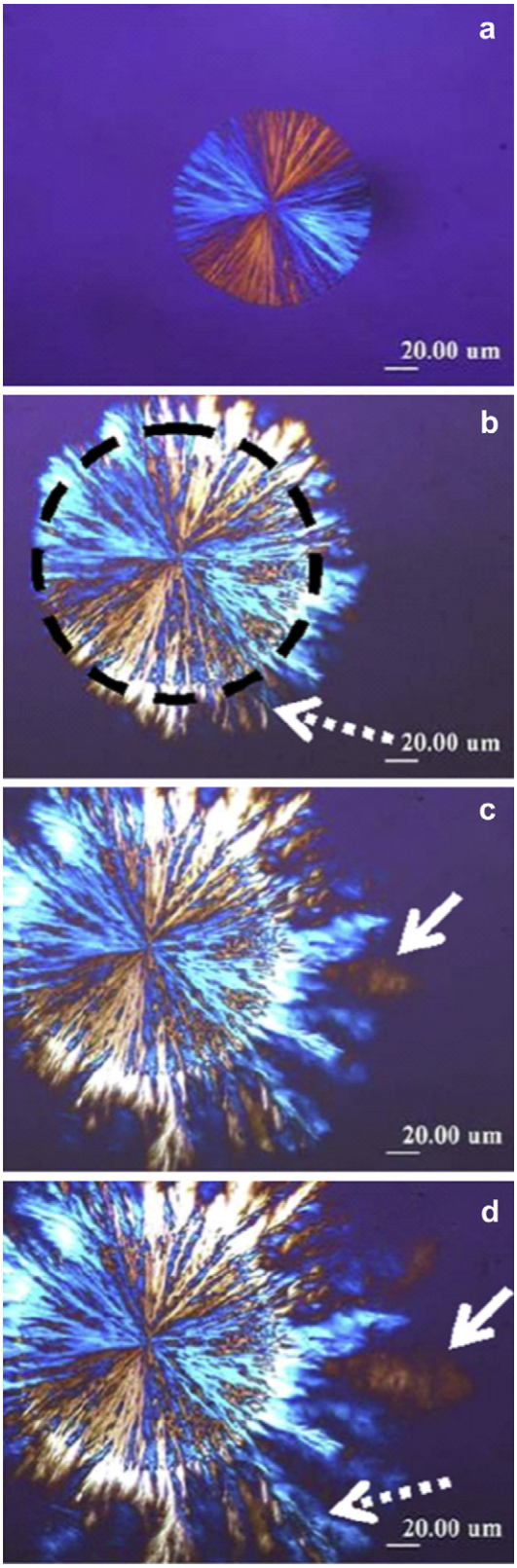

Fig. 11. POM graphs for the blends isothermally crystallized at 170 °C: (a) neat sc-PLA, (b) sc-PLA covered with molten PHB film at 170 °C for 8 min, (c) 25 min, and (d) 35 min.

spherulites, pressed with a PHB film, then isothermally crystallized at 170 °C for 8 min. For the PHB-pressed sc-PLA sample, feather-like patterns of sc-PLA spherulite develop first and appear to be less compact than those in neat sc-PLA. This observation indicates that at 170 °C, the amorphous PHB polymer chains dissolved and reoriented in the sc-PLA spherulite leads to the increase of brightness. Fig. 11-(*c*) shows the formation of new secondary crystallites (indicated with a solid-line arrow mark) at the later-stage crystallization ($t = 25$ min). Wedge-like pattern of sc-PLA spherulite with a lower brightness develops later, indicating low crystallinity in the constituent crystals within the sc-PLA spherulites. Fig. 11-(d) presents growth of sc-PLA spherulite crystallized at 170 °C for 35 min. As the crystallization proceeds further ($t = 35$ min), feather-like and wedge-like patterns of sc-PLA spherulites (indicated with dotted and solid-line arrows, respectively) grow simultaneously. These also agree with the previous POM results (Fig. 6-b), showing that the feather-like dendrites (bright area) are brighter than and different contrast from the wedge-like ones (dark area). AFM results have revealed that the different brightness/birefringence in these two crystals in disintegrated sc-PLA spherulites can be attributed to predominantly edge-on and flat-on orientations of the feather-like dendrites and wedge-like plates, respectively. These results reveal that the morphology of sc-PLA spherulites in the blend transforms apparently from a stable Maltese-cross spherulite, to disordered Maltese-cross one in early-stage crystallization, then to feather-like pattern; further in final stage, it transforms into coexistence of feather-like and wedge-like patterns in later-stage crystallization upon introducing molten PHB into sc-PLA at 170 °C.

4. Conclusion

The PHB/sc-PLA blend system shows a single composition-dependent T_g in all composition, indicating miscibility and interactions between PHB and sc-PLA, which leads to that crystallization growth of sc-PLA in blends is hindered by presence of PHB and final morphology of the sc-PLA complexes is altered. The less perfect lamellae of sc-PLA formed in blends induced by the increase of PHB content in blends or higher T_c, suggesting that the sc-PLA dendritic textures contain less stable (or less perfect) lamellae than those in the well-rounded Maltese-cross type spherulites. Effects of PHB on complexed PLA patterns are apparently associated with crystallization temperature and PHB contents in the PHB/sc-PLA mixtures, which both influence growth rates, leading to unbalanced lamellar extension that no longer sustain a well-round spherulites. PHB, via intimate miscibility interactions with both PLLA and PDLA, also acts as an amorphous diluent component to disintegrate the originally well-rounded sc-PLA spherulites into dendrites of two distinctly different types. PHB/sc-PLA blend crystallized at $T_c = 170$ °C exhibits two distinct crystals appearing at two different stages: (1) earlier-stage feather-like and (2) later-stage wedge-like dendrites. Interestingly, growth of the flat-on wedge-like dendrites is much shower than edge-on feather-like dendrites. These results indicate that the concentration and/or distribution of the PHB (amorphous diluents) at the crystal growth front corresponding to variation of the slopes of spherulitic growth rates is a factor which results in the different orientation of sc-PLA lamellae in blends. This fact also provides interesting and useful clues that the flat-on and edge-on lamellar orientation in PLLA/PDLA complexes can be independently and discretely packed into separate crystal entities, and are not necessarily inter-connected in an alternating twisting pattern. Despite of alteration of spherulites into dendrites by PHB, the WAXD result indicates that the unit cells of sc-PLA in PHB/sc-PLA blends are not altered by addition of PHB.

Acknowledgments

This work has been financially supported by basic research grants (NSC-95 2221 E006 183 and NSC-97-2221-E006-034-MY3) in three consecutive years from Taiwan's National Science Council (NSC), to which the authors express their gratitude.

References

[1] Okabe Y, Kyu T, Saito H, Inoue T. Macromolecules 1998;31:5823–9.
[2] Crevecoeur G, Groeninckx G. Macromolecules 1991;24:1190–5.
[3] Woo EM, Chang CS, Wu MC. Mater Lett 2007;61:3542–6.
[4] Blümm E, Owen AJ. Polymer 1995;36:4077–81.
[5] Penning JP, John Manley RSJ. Macromolecules 1996;29:84–90.
[6] Qiu Z, Ikehara T, Nishi T. Polymer 2003;44:2799–806.
[7] Vert M, Li SM, Spenlehauer G, Guerin P. J Mater Sci Mater Med 1992;3:432–46.
[8] Drumright RE, Gruber PR, Henton DE. Adv Mater 2000;12:1841–6.
[9] Miyata T, Masuko T. Polymer 1998;39:5515–21.
[10] Tsuji H, Ikada Y. Polymer 1995;36:2709–16.
[11] Fox TG, Garrett BS, Goode WE, Gratch S, Kincaid JF, Spell A, et al. J Am Chem Soc 1958;80:1768–9.
[12] Lohmeyer JHGM, Tan YY, Lako P, Challa G. Polymer 1978;19:1171–5.
[13] Schomaker E, Challa G. Macromolecules 1988;21:3506–10.
[14] Watanabe WH, Ryan CF, Fleischer Jr PC, Garrett BS. J Phys Chem 1961;65:896.
[15] Schomaker E, Challa G. Macromolecules 1988;21:2195–203.
[16] Schomaker E, Hoppen H, Challa G. Macromolecules 1988;21:2203–9.
[17] Pyrlik M, Rehage G. Colloid Polym Sci 1976;254:329–41.
[18] Rehage G, Wanger D. Polym Prepr 1982;23:29–30.
[19] Spěváček J, Schneider B. Makromol Chem 1974;175:2939–65.
[20] Biroš J, Máša Z, Pouchlý J. Eur Polym J 1974;10:629–32.
[21] Bosscher F, Ten Brinke G, Challa G. Macromolecules 1982;15:1442–4.
[22] Chang L, Woo EM. Ind Eng Chem Res 2009;48:3432–40.
[23] Tsuji H. Macromol Biosci 2005;5:569–97.
[24] Tsuji H, Hyon SH, Ikada Y. Macromolecules 1991;24:5651–6.
[25] Tsuji H, Hyon SH, Ikada Y. Macromolecules 1991;24:5657–62.
[26] Tsuji H, Ikada Y. Macromolecules 1993;26:6918–26.
[27] Ikada Y, Jamshidi K, Tsuji H, Hyon SH. Macromolecules 1987;20:904–6.
[28] Tsuji H, Ikada Y, Hyon SH, Kimura Y, Kitao T. J Appl Polym Sci 1994;51:337–44.
[29] Brochu S, Prudhomme RE, Barakat I, Jerome R. Macromolecules 1995;28:5230–9.
[30] Sarasua JR, López Arraiza A, Balerdi P, Maiza I. J Mater Sci 2005;40:1855–62.
[31] Koyama N, Doi Y. Polymer 1997;38:1589–93.
[32] Yoon JS, Lee WS, Kim KS, Chin IJ, Kim MN, Kim C. Eur Polym J 2000;36:435–42.
[33] Park JW, Doi Y, Iwata T. Biomacromolecules 2004;5:1557–66.
[34] Furukawa T, Sato H, Murakami R, Zhang JM, Duan YX, Noda I, et al. Macromolecules 2005;38:6445–54.
[35] Gazzano M, Focarete ML, Riekel C, Scandola M. Biomacromolecules 2004;5:553–8.
[36] Gordon M, Taylor JS. J Appl Chem 1952;2:493.
[37] Sawai D, Tsugane Y, Tamada M, Kanamoto T, Sungil M, Hyon SH. J Polym Sci Part B Polym Phys 2007;45:2632–9.
[38] Škrbić Ž, Divjaković V. Polymer 1996;37:505–7.
[39] Gazzano M, Tomasi G, Scandola M. Macromol Chem Phys 1997;198:71–80.
[40] Xu J, Guo BH, Zhou JJ, Li L, Wu J, Kowalczuk M. Polymer 2005;46:9176–85.
[41] Nurkhamidah S. thesis MS: Dept. Chem. Eng., National Cheng Kung University. Tainan, Taiwan; 2009.
[42] Keith Jr HD, Padden FJ. J Appl Phys 1964;35:1270–85.
[43] Keith Jr HD, Padden FJ. J Appl Phys 1964;35:1286–96.
[44] Kit KM. Polymer 1998;39:4969–71.
[45] Chuang WT, Hong PD, Chuah HH. Polymer 2004;45:2413–25.
[46] Wang ZG, An LJ, Jiang BZ, Wangh XH. Macromol Rapid Comm 1998;19:131–3.
[47] Wang W, Jin Y, Yang XN, Su ZH. J Polym Sci Part B Polym Phys 2010;48:541–7.

Polymer 52 (2011) 77–85

Contents lists available at ScienceDirect

Polymer

journal homepage: www.elsevier.com/locate/polymer

Synthesis and optoelectronic properties of thermally cross-linkable hole-transporting poly(fluorene-*co*-triphenylamine)

Wen-Fen Su, Yun Chen*

Department of Chemical Engineering, National Cheng Kung University, Tainan, Taiwan

ARTICLE INFO

Article history:
Received 14 September 2010
Received in revised form
26 October 2010
Accepted 31 October 2010
Available online 18 November 2010

Keywords:
Thermally cross-linkable
Hole-transporting
Triphenylamine

ABSTRACT

This paper describes the synthesis of a new thermally cross-linkable hole-transporting poly(fluorene-*co*-triphenylamine) (**PFTV**) by Suzuki coupling reaction and its application in polymer light-emitting diodes (PLEDs). The characteristics of **PFTV** were analyzed by ^{1}H NMR, differential scanning calorimetry, optical spectroscopy, cyclic voltammetry, and atomic force microscopy. Its HOMO level lies between those of PEDOT:PSS and poly(9,9-dioctylfluorene), forming a stepwise energy ladder to facilitate hole-injection. Multilayer device with thermally cross-linked **PFTV** as hole-transporting layer (ITO/PEDOT:PSS/HTL/**PFO**/LiF/Ca/Al) was readily fabricated by successive spin-coating processes, its maximum luminance efficiency (2.27 cd/A) was significantly higher than that without **PFTV** layer (0.50 cd/A). In addition, the **PFTV** was successfully applied as host for red-emitting Ir(piq)$_2$acac to obtain a device with moderate performance (5300 cd/m^2 and 2.64 cd/A). The **PFTV** is a promising hole-transporting material for the fabrication of multilayer PLEDs by wet processes as well as a potential host for phosphorescent PLEDs.

1. Introduction

Polymer light-emitting diodes (PLEDs) have attracted much attention, since the first discovery of electroluminescene of poly (*p*-phenylenevinylene) (PPV) in 1990, due to their potential applications in large area flat panel displays and solid-state lighting [1–5]. Organic materials in PLEDs have some advantages such as potentially low cost, facile processing by spin-coating and ink-jet printing methods. A lot of conjugated polymers have been extensively investigated, such as poly(*p*-phenylenevinylene) (PPV) [1], polyfluorene (PF) [6] and their derivatives. PF and its derivatives are promising blue-light-emitting materials widely used in PLEDs because of its excellent thermal and chemical stability and high photoluminescence (PL) quantum yield [7–9]. However, the lower highest occupied molecular orbital (HOMO) level of PF ($E_{HOMO} = -5.8$ eV) creates a high hole-injection barrier, which lead to imbalance in charges injection [10,11]. This characteristic ultimately results in low efficiency obtainable for its polymeric light-emitting diodes.

To solve this problem, in general two strategies have been adopted, one is through appropriate design of chemical structure and the other is via adequate modification of device structure. For the first strategy, the incorporation of hole-transporting moieties on a main or side chain, such as carbazole or triphenylamine, is usually adopted to improve hole-injection from anode [12–18]. For the second strategy, multilayer devices are required and fabricated by adding an extra hole-transporting layer (HTL) to reduce the hole-injection barrier from anode [19–24]. Several polymers have been reported as suitable materials for HTL between poly(styrenesulphonate):poly(3,4-ethylenedioxythiophene) (PEDOT:PSS) and emitting layer (EML), such as poly(*N*-vinylcarbazole) (PVK) and poly[(9,9-dioctylfluorenyl-2,7-diyl)-co-(4,4′-(*N*-(4-*sec*-butylphenyl))diphenylamine)] (TFB) [23–26]. The hole-transporting layer (HTL) effectively improves the device efficiency of multilayer PLEDs. However, for multilayer polymer devices the HTL layer may be dissolved or destroyed by the solution of emitting layer during subsequent spin-coating. Therefore, the homogeneity and actual thickness of the HTL cannot be controlled at will. This will lead to poor reproducibility in the fabrication of multilayer devices by solution processes. Accordingly, solvent resistance of the HTL layer should be high enough to prevent the dissolution during subsequent coating. An effective way to increase the solvent resistance of a polymer is forming as a three dimensional network structure, which can be attained by thermal or photo-initiated cross-linking reaction [27–36]. Moreover, the solvent resistance increases with the increase of cross-linking density. Therefore, the HTL applicable in multilayer PLEDs fabricated by solution-processes should possess not only a proper energy level lying between anode and emitting layer to facilitate hole-injection but also high solvent resistance to avoid being dissolved during subsequent spin-coating of the emitting layer.

* Corresponding author. Tel.: +886 6 2085843; fax: +886 6 2344496.
E-mail address: yunchen@mail.ncku.edu.tw (Y. Chen).

0032-3861/$ – see front matter © 2010 Elsevier Ltd. All rights reserved.
doi:10.1016/j.polymer.2010.10.065

In the present study we synthesized a new thermally cross-linkable hole-transporting poly(fluorene-*co*-triphenylamine) (**PFTV**) by Suzuki coupling reaction, incorporated with pendent styryl groups which is thermally reactive. The **PFTV** is composed of hole-transporting triphenylamine groups and fluorenes substituted with nonsymmetric and bulky aromatic groups at C-9 position. This molecular design is expected to enhance thermal and chemically stability, good film-forming properties and device efficiency. Moreover, fabricating multilayer PLEDs with **PFTV** as hole-transporting layer will be highly reproducible due to its thermally cross-linking ability. The multilayer device with cross-linked **PFTV** as HTL shows significantly enhanced emission efficiency than those with uncross-linked **PFTV** as HTL or without the **PFTV** layer. Furthermore, the **PFTV** was effectively applied as host for red-emitting Ir $(piq)_2$acac, indicating that it acts both as hole-transporting and host materials in PLEDs. These results demonstrate that the new **PFTV** is a promising hole-transporting and host material for optoelectronic devices.

2. Materials and methods

2.1. Materials and characterization

Tri(4-bromophenyl)amine (**2**) [37] and 4-(3-methylpropyl)-*N*,*N*-bis(4-bromophenyl)aniline (**5**) [38,39] were synthesized according to the procedures reported previously. 9,9-diarylfluorene-2,7-diboronic acid bispinacol ester (**4**) and poly(9,9-dioctylfluorene) (**PFO**) were prepared according to our previously reported procedures [40]. All reagents and solvents were purchased from Acros, TCI, Aldrich, Lancaster Chemicals Co. and used without further purification. All the solvents such THF and acetonitrile were dried with appropriate drying agents (Na or $CaCl_2$), then distilled under reduced pressure and stored over 4 Å molecular sieves before use. The polymerization catalyst was tetrakis(triphenylphosphine) palladium [$Pd(PPh_3)_4$] procured from Strem. Newly synthesized compounds were identified by ^{1}H NMR, ^{13}C NMR spectroscopy, mass spectrometry, and elemental analysis (EA). ^{1}H NMR and ^{13}C NMR spectra were recorded with Bruker AVANCE-400 and 500 NMR spectrometers respectively, and the chemical shifts are reported in ppm using tetramethylsilane (TMS) as an internal standard. Mass and elemental analysis were carried out on a JEOL JMS-700 spectrometer and Heraus CHN-Rapid elemental analyzer, respectively. The FT-IR spectra were measured as KBr disk using a Fourier transform infrared spectrometer, model 7850 from Jasco. Molecular weight and molecular weight distribution of the polymer were determined by a gel permeation chromatograph (GPC) using THF as an eluent at a flow rate of 1 mL/min at 40 °C. Monodisperse polystyrene standards were used for molecular weight calibration. Thermogravimetric analysis (TGA) was performed under nitrogen atmosphere at a heating rate of 20 °C/min, using a PerkinElmer TGA-7 thermal analyzer. Thermal curing behaviors and thermal transitional properties of the polymer were investigated using a differential scanning calorimeter (DSC), Mettler DSC 1, at a heating rate of 10 °C/min. Absorption spectra and photoluminescence (PL) spectra were measured with a Jasco V-550 spectrophotometer and a Hitachi F-4500 fluorescence spectrophotometer, respectively. Cyclic voltammograms were recorded using a voltammetric analyzer (model CV-50W from Bioanalytical Systems, Inc.) under nitrogen atmosphere. The measuring cell was consisted of a polymer-coated ITO glass as the working electrode, an Ag/AgCl electrode as the reference electrode and a platinum wire as the auxiliary electrode. The electrodes were immersed in acetonitrile containing 0.1 M $(n\text{-Bu})_4NClO_4$ as electrolyte. The energy levels were calculated using ferrocene (FOC) as standard (−4.8 eV with respect to vacuum level which is defined as zero) [41,42]. An atomic force microscope (AFM), equipped with a Veeco/Digital Instrument Scanning Probe Microscope (tapping mode) and a Nanoscope IIIa controller, was used to examine surface morphology and to estimate thickness and root-mean-square (rms) roughness of deposited films. The film thickness of hole-transporting and emitting layers was measured by surface profiler, α-step 500.

2.2. Synthesis of monomer (*3*) and copolymer (*PFTV*)

2.2.1. Synthesis of N,N-bis(4-bromophenyl)-p-(4-vinylphenyl) aniline (*3*)

Tri(4-bromophenyl)amine (**2**, 4.82 g, 10 mmol), *p*-vinylphenylboronic acid (1.15 g, 5 mmol) and $(PPh_3)_4Pd(0)$ (0.144 g, 0.13 mmol) were dissolved in a mixture consisting of tetrahydrofuran (THF: 20 mL), aqueous solution of 2 M K_3PO_4 (11 mL). The mixture was first purged with Argon and stirred at 100 °C for 48 h under vigorous stirring. It was poured into water (50 mL) and extracted twice with dichloromethane (250 mL). The combined organic extracts were dried ($MgSO_4$) and concentrated by rotary evaporation. Further purification by column chromatography on silica gel (ethyl acetate/*n*-hexane) afforded product **3** as white solids (yield: 65%, melting point: 160–161 °C). FT-IR (KBr pellet, cm^{-1}): ν 719, 815, 898, 1068, 1286, 1317, 1484, 1521, 1579, 1602, 1621, 3033, 3054, 3081. ^{1}H NMR (400 MHz, $CDCl_3$, ppm): δ 7.54–7.45 (m, 6H, Ar-H), 7.37–7.35 (d, 4H, Ar-H, J = 8 Hz), 7.11–7.09 (d, 2H, Ar-H, J = 8 Hz), 6.99–6.97 (d, 4H, Ar-H, J = 8 Hz), 6.78–6.71 (dd, 1H, =CH-, J_1 = 16 Hz, J_2 = 16 Hz), 5.80–5.76 (d, 1H, =CH_2, J = 16 Hz), 5.30–5.26 (d, 1H, =CH_2, J = 16 Hz). ^{13}C NMR (500 MHz, $CDCl_3$, ppm): δ 146.38, 146.24, 139.68, 136.45, 136.39, 135.82, 132.43, 127.88, 126.74, 126.69, 126.02, 125.63, 124.45, 115.74, 113.8. E_{LEM} $A_{NAL.}$ Calcd. for $C_{26}H_{19}Br_2N$ (%): C, 61.81; H, 3.79; N, 2.77. Found: C, 61.70; H, 3.85; N, 2.71. EI-MS (*m*/*z*): calcd: 504.99; found: 505.00.

2.2.2. Synthesis of poly(fluorene-co-triphenylamine) (*PFTV*)

The synthesis of poly(9,9-dioctylfluorene) (**PFO**) and copolymer **PFTV** was carried out using a palladium-catalyzed Suzuki coupling reaction. For instance, purified *N*,*N*-bis(4-bromophenyl)-*p*-(4-vinylphenyl)aniline (**3**: 0.304 g, 0.6 mmol), 9,9-diarylfluorene-2,7-diboronic acid bispinacol ester (**4**: 3.843 g, 5 mmol), 4-(3-methylpropyl)-*N*,*N*-bis(4-bromophenyl)aniline (**5**: 2.02 g, 4.4 mmol) and $(PPh_3)_4Pd(0)$ (0.104 g, 0.09 mmol) were dissolved in a mixture consisting of THF (30 mL) and aqueous solution of 2 M K_3PO_4 (16 mL). The mixture was first purged with Argon and then stirred at 100 °C for 72 h under vigorous stirring. Finally, monomer **4** and 1-bromo-4-*tert*-butylbenzene were added to the mixture to end-cap the polymer chain. The mixture was poured into a large amount of methanol; the appeared solid was collected by filtration and washed successively with methanol, 2-propanol and hexane, followed by Soxhlet extraction with acetone to remove trace oligomers. The residual palladium catalyst was removed by stirring together with a silica gel (Silicycle, Si-Thiol) in toluene. Then the solution was further extracted with de-ionized water three times to reduce the concentration of metal ions. It was then poured into a large amount of methanol to afford light-yellow fiber of **PFTV** (yield: 75%). The **PFTV** was soluble in conventional organic solvents such as toluene, xylene, THF and chloroform. ^{1}H NMR (400 MHz, $CDCl_3$, ppm): δ 7.78–7.76 (d, Ar-H, J = 8 Hz), 7.58–7.56 (d, Ar-H, J = 8 Hz), 7.49–7.44 (m, Ar-H), 7.26–7.04 (m, Ar-H), 6.94–6.87 (m, Ar-H), 6.64–6.62 (m,=CH–), 5.80–5.76 (d,=CH_2, J = 16 Hz), 5.27–5.24 (m,=CH_2, J = 12 Hz), 3.94–3.91 (t, $-OCH_2-$, J = 12 Hz), 2.58–2.56 (m, 1H, –CH–), 2.20 (s, 3H, $-CH_3$), 2.10 (s, 3H, $-CH_3$), 1.80–0.83 (m, $-CH_2-$ and $-CH_3$). ^{13}C NMR (500 MHz, $CDCl_3$, TMS, 25 °C): δ 155.86, 152.83, 147.04, 142.79, 139.60, 138.83, 136.63, 134.63, 134.42, 132.36, 131.31,

130.58, 127.47, 126.62, 126.25, 125.93, 125.08, 124.20, 120.34, 110.32, 66.17, 65.28, 40.98, 39.19, 37.26, 36.32, 31.34, 29.91, 27.93, 24.65, 22.67, 22.58, 21.81, 21.24, 19.73, 16.58, 12.27. ELEM. ANAL. Calcd. for **PFTV** (%): C, 88.43; H, 7.67; N, 1.71. Found (%): C, 87.64; H, 7.71; N, 1.28.

2.3. Fabrication and characterization of light-emitting devices

Multilayer light-emitting diodes [ITO/PEDOT:PSS/HTL/**PFO**/LiF/Ca/Al] or phosphorescent light-emitting diodes [ITO/PEDOT:PSS/**PFTV**:Ir(piq)$_2$acac/Ca/Al] were fabricated to investigate their optoelectronic characteristics. The ITO-coated glass substrate was washed successively in ultrasonic baths of neutraler reiniger/de-ionized water (1:3 v/v) mixture, de-ionized water, acetone and 2-propanol, followed with treatment in a UV–Ozone chamber. A thick PEDOT:PSS layer was spin-coated on top of the freshly cleaned ITO glass and annealed at 150 °C for 15 min in a dust-free atmosphere. The **PFTV** solutions were filtered through a syringe filter (0.2 μm) before the spin-coating. The hole-transporting layer (HTL) was formed by spin-coating a solution of **PFTV** in toluene (10 mg/mL, 2000 rpm) on top of the PEDOT:PSS layer and thermally treated at 230 °C for 30 min under nitrogen atmosphere. Then the emitting layer (EML) was spin-coated onto the HTL. The actual thickness of HTL and EML is 40 and 70 nm, respective. Finally, a thick layer of cathode was deposited by successive thermal evaporation of LiF (1 nm), Ca (50 nm) and Al (100 nm) under 110^{-6} Torr. The luminance versus bias, current density versus bias, and emission spectra of the PLEDs were recorded using a combination of Keithley power source (model 2400) and Ocean Optics usb2000 fluorescence spectrophotometer. The fabrication of the devices was done in ambient conditions, with the following performance tests conducted in a glove-box filled with nitrogen.

3. Results and discussion

3.1. Synthesis and characterization

The hole-transporting poly(fluorene-*co*-triphenylamine) (**PFTV**) was synthesized by the palladium-catalyzed Suzuki coupling of 9,9-diarylfluorene-2,7-diboronic acid bispinacol ester (**4**) and dibromotriphenylamine derivatives (**3**, **5**) as shown in Scheme 1. The emitting poly(9,9-dioctylfluorene) (**PFO**) was also synthesized by the Suzuki coupling reaction. Tri(4-bromophenyl)amine (**2**) and 4-(3-methylpropyl)-*N*,*N*-bis(4-bromophenyl)aniline (**5**) were synthesized according to the procedures reported previously [37–39]. 9,9-diarylfluorene-2,7-diboronic acid bispinacol ester (**4**) and poly(9,9-dioctylfluorene) (**PFO**) were prepared according to our previously reported procedures [40]. Monomer **3** was synthesized by the Suzuki coupling of *p*-vinylphenylboronic acid with stoichiometric amount of tri(4-bromophenyl)amine (**2**), which was obtained by complete bromination of triphenylamine with *N*-bromosuccinimide (NBS). Chemical structure of monomer **3** was satisfactorily confirmed by ^{1}H NMR, ^{13}C NMR spectra, elemental analysis, and mass spectrometry. ^{1}H NMR spectrum of **3** verifies the characteristic chemical shifts at 6.78–6.71 ppm and 5.26–5.80 ppm assigned to protons of the vinyl substituents (=CH$_2$ and =CH–). The structure of **PFTV** was satisfactorily characterized by its ^{1}H NMR, ^{13}C NMR spectra (Fig. S1 in Supporting Information) and elemental analysis. The actual composition of pendent styryl group is *ca.* 5 mol%, as estimated from the areas of the peaks at 5.24–5.80 ppm

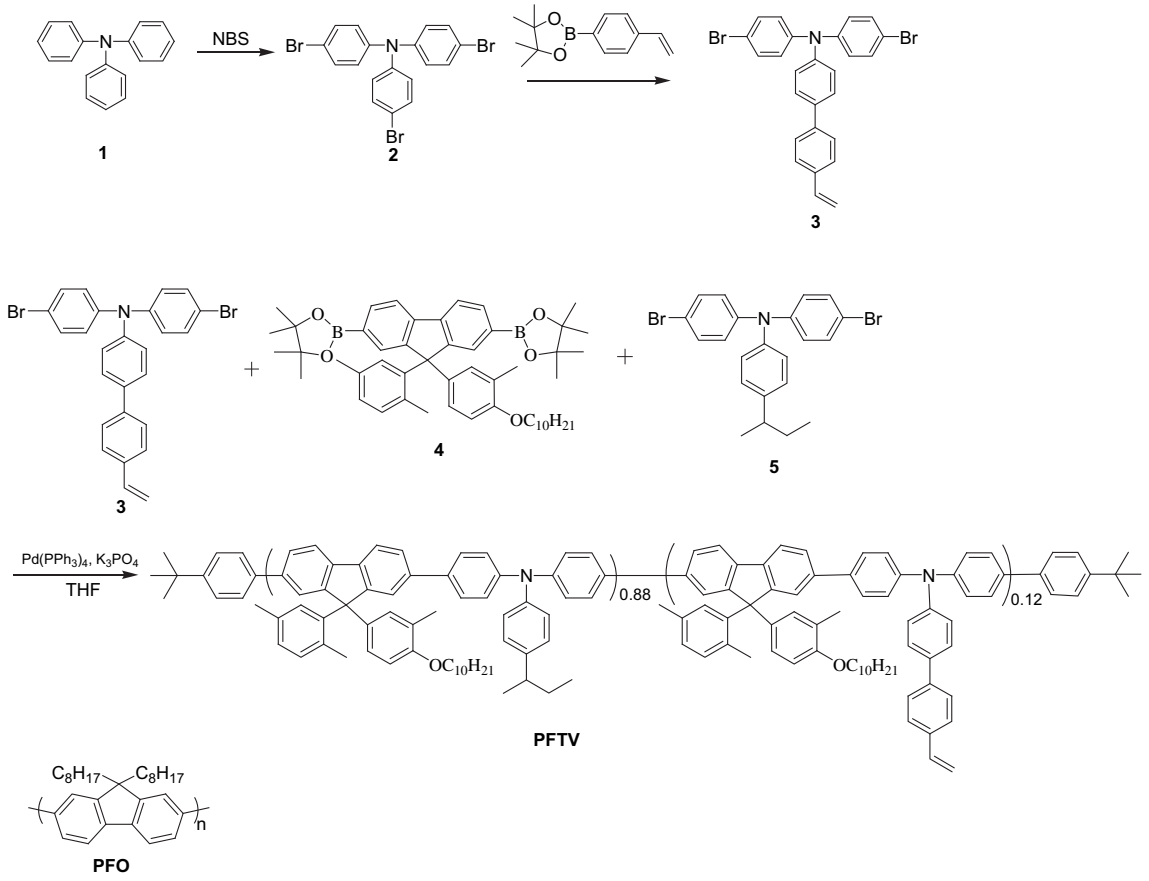

Scheme 1. Synthesis of monomer **3** and copolymer **PFTV**, and chemical structure of poly(9,9-dioctylfluorene (**PFO**).

Table 1
Thermal and electrochemical properties of **PFTV** and **PFO**.

	T_g (°C)[a]	T_d (°C)[b]	E_{ox} vs. FOC (V)[c]	E_{HOMO} (eV)[d]	E_{LUMO} (eV)[e]	E_g^{opt} (eV)[f]
PFTV	225	419	0.47	−5.27	−2.41	2.86
PFO	68	432	0.90	−5.70	−2.77	2.93

[a] Determined by differential scanning calorimetry (DSC) at a heating rate of 10 °C/min.
[b] The temperature at 5 wt% loss in nitrogen atmosphere, measured by TGA.
[c] $E_{FOC} = 0.47$ V vs. Ag/AgCl.
[d] $E_{HOMO} = -(E_{ox,\ FOC} + 4.8)$ eV.
[e] $E_{LUMO} = E_g + E_{HOMO}$.
[f] Band gaps obtained from onset absorption (λ_{onset}): $E_g = 1240/\lambda_{onset}$.

(=C$\underline{H}_2$) and 3.91 ppm (−OC$\underline{H}_2$−). The characteristic chemical shifts at 5.24–5.80 ppm confirm the existence of pendent styryl groups, from which thermally cross-linkable character can be expected. The **PFTV** and **PFO** are soluble in common organic solvents such as toluene, THF, and chloroform. The weight-average molecular weight (M_w) of **PFTV** and **PFO** was 6.9 × 10^4 and 14.4 × 10^4, respectively, with the polydispersity indexes (PDIs) being 1.8, as determined by gel permeation chromatography using monodisperse polystyrenes as calibration standards.

3.2. Thermal cross-linking properties and surface morphology of *PFTV*

Since the copolyfluorene (**PFTV**) contains reactive pendent styryl groups which will give rise to networks structure (cross-linking) under proper thermal treatment. Thermal cross-linking and thermal stability characteristics of **PFTV** were studied by differential scanning calorimetry (DSC) and thermogravimetric analysis (TGA), respectively. The thermal decomposition temperature (T_d, 5% weight loss) of **PFTV** is 419 °C under nitrogen atmosphere, indicating that the **PFTV** is highly thermal stable (Table 1). As shown in Fig. 1 (inset), during the first DSC heating scan of monomer **3** a clear-cut melting point at about 161 °C is observed, followed closely by an exothermic peak around 163 °C. The exothermic peak is attributed to the reaction of styryl groups which is induced by the melt of **3**. Thermal cross-linking conditions of **PFTV** were first determined by a similar DSC heating scan to 300 °C (Fig. 1). During the first heating scan, **PFTV** showed broad an exothermic peak around 230 °C, in which the exotherm starts at about 210 °C. This exothermic peak (230 °C) of **PFTV** is much higher than that of monomer **3** (163 °C), which is ascribed to high

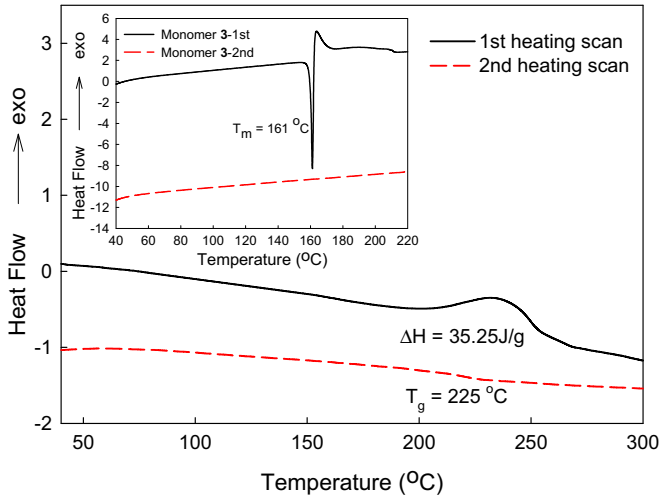

Fig. 1. DSC traces of **PFTV** at a heating rate of 10 °C/min. The first scan was used to observe the reaction heat of styryl groups. The inset shows the DSC trace of monomer **3** at a heating rate of 10 °C/min.

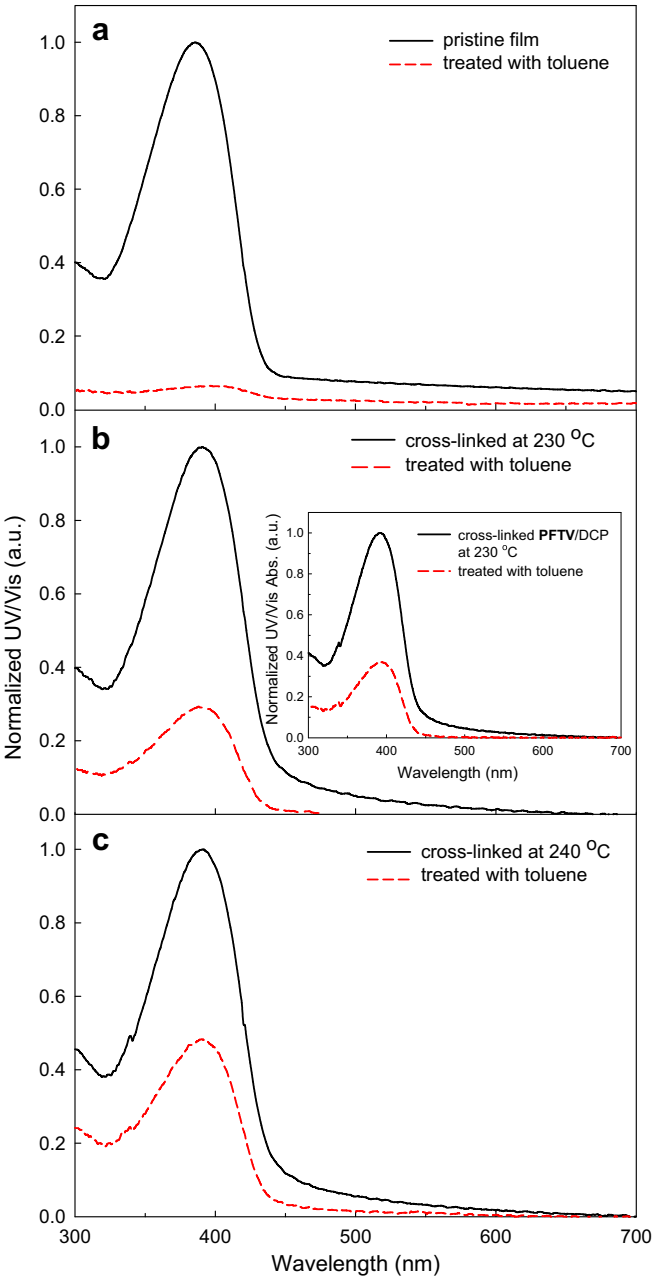

Fig. 2. Absorption spectra of pristine and cross-linked **PFTV** films: (–) before and (---) after spin-coated with pure toluene. The cross-linking was conducted at 230 °C or 240 °C for 30 min under nitrogen atmosphere. The inset in (b) shows the absorption spectra of **PFTV** film containing 1 wt% of dicumyl peroxide (DCP).

glass transition temperature of **PFTV** comprising rigid aromatic main chain structure and bulky aromatic substituents at the C-9 position. The exothermic heat (35.25 J/g) is attributable to the thermal cross-linking reaction of the pendent styryl groups. No obvious exotherm is observed in the second heating scan, indicating the cross-linking has been completed during the first scan. Furthermore, the glass transition temperature (T_g) of the cured **PFTV** is about 225 °C with no detectable crystallization and melting transitions, suggesting that it is basically an amorphous material. The high T_g is a highly desirable property for polymers used in PLEDs, since it prevents the detrimental crystallization process during device operation or thermal annealing which deteriorates long-term morphological stability.

Solvent resistance of the cured **PFTV** film was investigated by the absorption variations (300–700 nm) before and after washing

with a good solvent (toluene). As shown in Fig. 2, the absorption spectrum of the pristine **PFTV** film disappears almost completely after rinsing with toluene, meaning that the **PFTV** film is dissolved out during spin-coating process. However, the solvent resistance of **PFTV** was enhanced by the thermal curing processes. For instance, the remaining absorption intensity of the thermally cross-linked **PFTV** film (at 230 °C for 30 min) was about 27% after rinsing with toluene. Moreover, its solvent resistance is further promoted when cured at higher temperature (240 °C for 30 min), i.e., more than 48% of absorption intensity was remained after rinsing with toluene. In addition, the degree of cross-linking could be increased by adding dicumyl peroxide (DCP) as cross-linking agents. The remaining absorption intensity of thermally cross-linked **PFTV** film, added with DCP (1 wt%) and cured at 230 °C for 30 min, was about 37% after rinsing with toluene. These results indicate that both higher curing temperature and cross-linking agent are effective in increasing cross-linking density, which can be evidenced by elevated glass transition temperatures [32]. Therefore, the solution-processable and thermally cross-linkable characteristics of **PFTV** are useful to fabricate multilayer PLEDs by spin-coating processes.

To achieve high performance in multilayer PLEDs, it is imperative to obtain highly homogeneous film for each layer. Homogeneous film is a prerequisite to obtain PLEDs with high device performance and long lifetime. The morphology of **PFTV** spin-coated onto ITO substrate, before and after thermal curing, was investigated using an atomic force microscope (AFM). As shown in Fig. 3, the **PFTV** film exhibits a uniform surface morphology with no observable pinhole or aggregate after thermal cross-linking at 230 °C for 30 min. Moreover, the average root-mean-square (rms) roughness of the cross-linked **PFTV** film surface is 0.85 nm (0.88 nm, 0.82 nm, 0.85 nm), which is slightly lower than 0.94 nm of pristine film (0.92 nm, 0.99 nm, 0.90 nm). According, the thermal treatment not only promotes solvent resistance but also smoothes out the film surface of **PFTV**. Most of the reported thermally curable HTLs are low molecular weight compounds [28,31–33], although polymers with trifluorovinyl ether pendent groups were also investigated [29,33]. The film-forming property and thermal stability of low molecular weight HTLs are usually inferior to polymeric counterparts. Moreover, thermal cross-linking of the polymers containing trifluorovinyl ether pendent groups required both high temperatures (>225 °C) and long times (1–2 h). Therefore, the thermally cross-linkable **PFTV** should be a potential candidate for hole-transporting materials from the viewpoint of thermal property and processing feasibility.

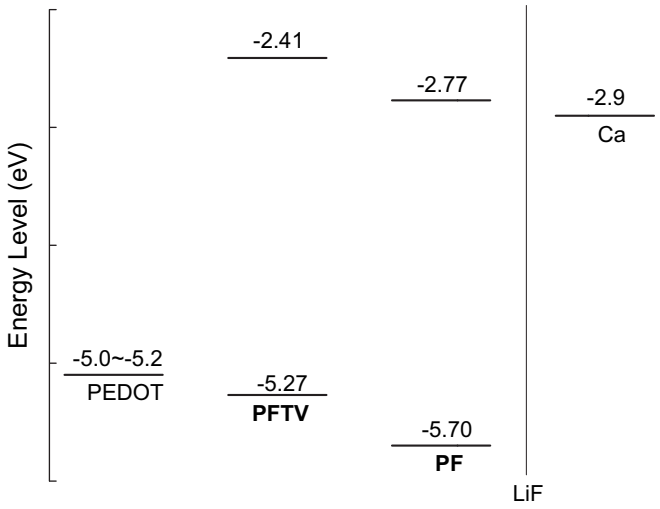

Fig. 4. The energy level diagrams of **PFTV**, **PFO**, PEDOT:PSS and Calcium electrode.

3.3. Electrochemical properties

Cyclic voltammetry (CV) is a commonly used technique to investigate electrochemical properties of conjugated polymers [43,44]. An ITO glass coated with **PFTV** was used as the working electrode, supporting in anhydrous acetonitrile containing 0.1 M tetra-*n*-butylammonium perchlorate [$(n\text{-Bu})_4NClO_4$], to measure its CV. The highest occupied molecular orbital (HOMO) which corresponds to ionization potential (IP) can be estimated from the onset oxidation potential (E_{ox}) revealed in CV by the equation $E_{HOMO} = -(E_{ox} + 4.8)$ eV. The lowest unoccupied molecular orbital (LUMO) level is calculated by $E_{LUMO} = -e(E_{HOMO} + E_g^{opt})$, where the optical band gap (E_g^{opt}) is estimated from onset absorption. The HOMO and LUMO levels of **PFTV** are estimated to be −5.27 eV and −2.41 eV, respectively (Table 1). Fig. 4 depicts the energy levels of **PFTV**, **PFO**, and PEDOT:PSS. Clearly the HOMO level of **PFTV** (−5.27 eV) situates between those of PEDOT:PSS (−5.0 ~ −5.2 eV) [45] and **PFO** (−5.70 eV) [40], forming a stepwise energy ladder of HOMO levels to facilitate hole-injection. This means that the hole-injection from PEDOT:PSS to **PFTV** then transport to **PFO** is much easier than direct injection from PEDOT:PSS to **PFO**. Therefore, the improvement in hole-injection and transport are expected to enhance device efficiency.

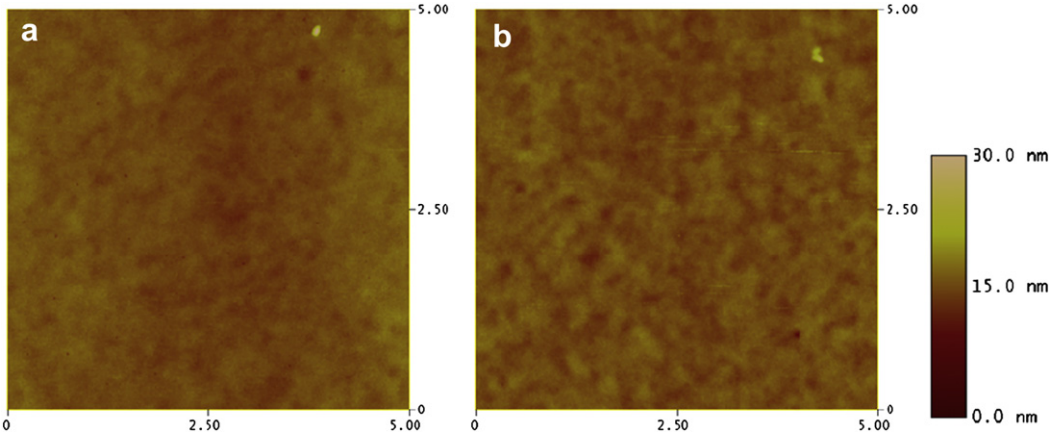

Fig. 3. The AFM images of **PFTV** films coated on ITO glass: (a) pristine film, average rms roughness = 0.94 nm; (b) film thermally treated at 230 °C for 30 min, average rms roughness = 0.85 nm.

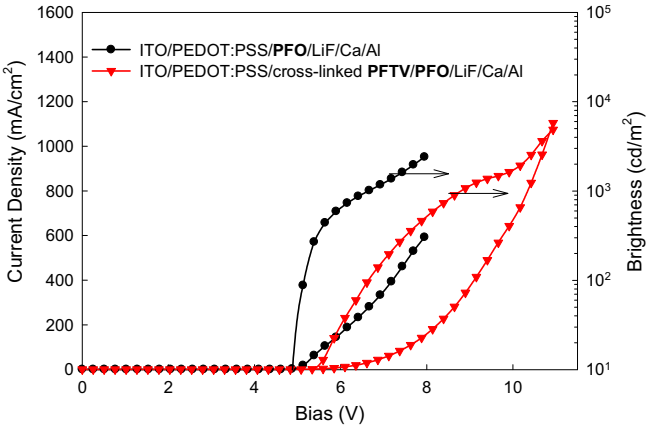

Fig. 5. Brightness versus bias and current density versus bias characteristics of multilayer PLEDs. Device structure: ITO/PEDOT:PSS/(**PFTV**)/**PFO**/LiF/Ca/Al. The **PFTV** film was cross-linked at 230 °C for 30 min.

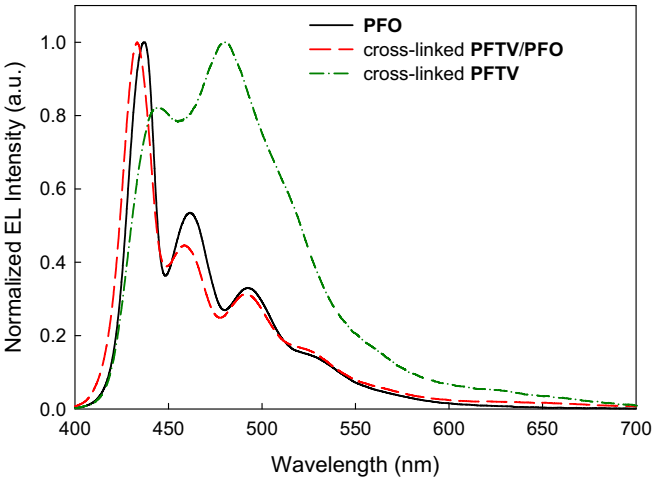

Fig. 6. Emission spectra of light-emitting diodes using **PFO** or cross-linked **PFTV** as emitting layer. Device structures: (–) ITO/PEDOT:PSS/**PFO**/LiF/Ca/Al; (––) ITO/PEDOT:PSS/cross-linked **PFTV**(HTL)/**PFO**/LiF/Ca/Al; (–•–•) ITO/PEDOT:PSS/cross-linked **PFTV**/LiF/Ca/Al.

3.4. Optoelectronic properties of multilayer PLEDs using *PFTV* as hole-transport layer

To evaluate the applicability of **PFTV** as hole-transporting layer for multilayer devices, a polymer light-emitting diode [ITO/PEDOT:PSS/**PFTV**/**PFO**/LiF(1 nm)/Ca(50 nm)/Al(100 nm)] was fabricated by successive spin-coating process. The **PFTV** was spin-coated on top of the PEDOT:PSS layer and treated at 230 °C for 30 min under nitrogen atmosphere, followed by the spin-coating of **PFO** solution. The **PFO** and LiF were used as emitting layer and electron-injection layer, respectively. The device without hole-transporting layer (ITO/PEDOT:PSS/**PFO**/LiF/Ca/Al) was also fabricated simultaneously for comparative study. Fig. 5 shows the current density versus bias and brightness versus bias curves (*J*–*V*–*B*) of the devices, with the characteristic data summarized in Table 2. The maximum brightness and maximum current efficiency of the device with cured **PFTV** as HTL are 4870 cd/m^2 and 1.15 cd/A, respectively. These performances are much better than those of the devices using pristine **PFTV** as HTL (2560 cd/m^2, 0.49 cd/A) or without **PFTV** layer (2410 cd/m^2, 0.50 cd/A). The result indicates that uncross-linked **PFTV** (pristine) contributes little in promoting the performance when compared with the device without **PFTV** as HTL. This is due to substantial dissolution of **PFTV** film during spin-coating of the emitting **PFO** layer. However, when thermally cross-linked **PFTV** is used as hole-transporting layer, both current efficiency and brightness are greatly enhanced (about 2 times). The enhancement is attributable to improved hole-injection from PEDOT:PSS to **PFTV** layers, which is much easier than direct injection from PEDOT:PSS to **PFO** layers. As mentioned above, the HOMO level of **PFTV** forms a stepwise energy ladder with those of PEDOT:PSS and **PFO** to facilitate hole-injection. To confirm hole-injection property of the cross-linked **PFTV**, hole-only devices [ITO/PEDOT:PSS/with or without **PFTV**/**PFO**/Au(50 nm)/Al(100 nm)] were fabricated to investigate their current density versus electric field characteristics. Inserting a cross-linked **PFTV** layer shifts the curve to the left greatly, indicating that the cross-linked **PFTV** layer effectively increases the device's current density under the same external field (Fig. S2).

The EL spectra of the multilayer devices reveal similar emission peaks at 437 nm corresponding to $S_{10} \rightarrow S_{00}$ vibronic transition of fluorene segments (Fig. 6). To verify the EL emission is mainly contributed from emitting **PFO** layer, the device [ITO/PEDOT:PSS/**PFTV**/LiF/Ca/Al] using cross-linked **PFTV** as emitting layer was fabricated to investigate its EL spectrum. The EL spectrum of using **PFTV** as emitting layer device shows a main peak at 479 nm and a shoulder at 444 nm, which are very different from that of multilayer devices. This indicates that the electrons and holes recombine mainly in the emitting **PFO** layer.

As mentioned previously, the degree of cross-linking can be increased by adding suitable cross-linking agents. The hole-transporting **PFTV** was thermally cured in the presence of dicumyl peroxide (DCP: 1 wt%) during the fabrication of a multilayer device [ITO/PDEOT:PSS/**PFTV**+DCP/**PFO**/LiF(1 nm)/Ca(50 nm)/Al (100 nm)]. The maximum brightness and maximum current efficiency are 5560 cd/m^2 and 2.27 cd/A (Table 2), respectively, which are higher than those without adding DCP (4870 cd/m^2, 1.15 cd/A). The results demonstrate that increasing cross-linking density in **PFTV** layer gives rise to improved device performance. To conclude, the performance enhancement of the EL devices using **PFTV** as hole-transporting layer is attributed to promoted hole-injection ability. However, the **PFTV** layer should be thermally cross-linked during the fabrication processes to fully display its hole-transporting function. The **PFTV** is a promising hole-transporting material which can be employed in the fabrication of multilayer devices by successive spin-coating processes.

Table 2
Optoelectronic properties of the multilayer PLEDs.[a]

HTL	V_{on}[b] (V)	L_{max}[c] (cd/m^2)	LE_{max} (cd/A)[d]	CIE 1931 (x, y)[e]
None	5.1	2410	0.50	(0.16, 0.08)
PFTV (cured)[f]	5.6	4870	1.15	(0.17, 0.08)
PFTV (uncured)	5.7	2560	0.49	(0.17, 0.10)
PFTV + DCP (cured)[f]	6.1	5560	2.27	(0.17, 0.10)

[a] Device structure: ITO/PEDOT:PSS/HTL/**PFO**/LiF/Ca/Al; HTL: hole-transporting layer.
[b] Turn-on voltage defined as the bias at a luminance of 10 cd/m^2.
[c] Maximum luminance.
[d] Maximum luminance efficiency.
[e] The 1931 CIE coordinates at *ca.* 1000 cd/m^2.
[f] Treated at 230 °C for 30 min.

3.5. Optoelectronic properties of electrophosphorescent devices using *PFTV* as host

The efficacy of **PFTV** as an efficient hole-transporting material has been verified in multilayer PLEDs mentioned above. The **PFTV** seems applicable as host for electrophosphorescent devices because it contains triphenylamine moieties in main chain. However, the triplet energy (E_T) of the host should be larger than

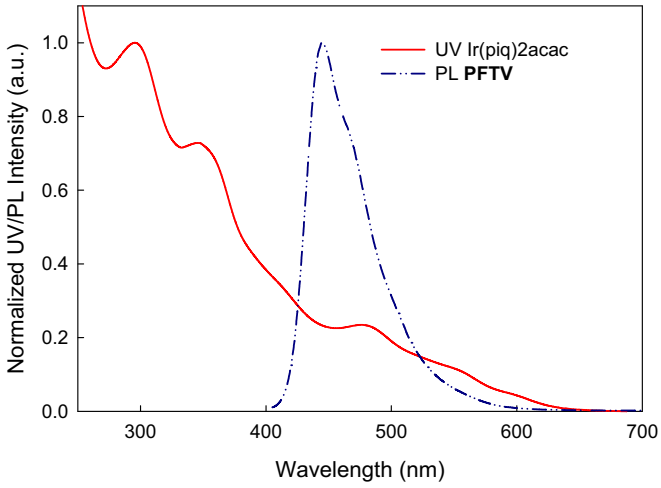

Fig. 7. Absorption spectrum of Ir(piq)$_2$acac and PL spectrum of **PFTV** film coated on quartz plate (with λ_{ex} = 385 nm).

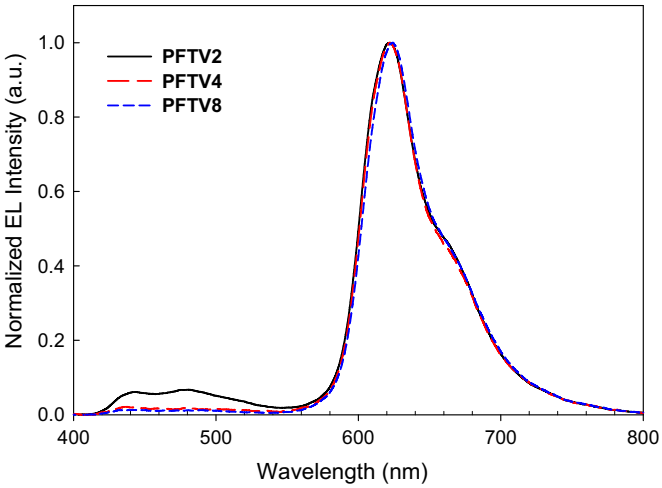

Fig. 9. EL spectra of the **PFTV** films doped with different amounts of Ir(piq)$_2$acac. The number represents weight percent of the Ir(piq)$_2$acac in the film.

that of phosphorescent emitter to improve the efficiency of triplet–triplet energy transfer [46–48]. Therefore, phosphorescent emission spectrum of **PFTV** at 77 K in a frozen solution of toluene was measured to estimate its triplet energy. The phosphorescent emission maximum of **PFTV** is 559 nm, which corresponds to a triplet energy gap of 2.21 eV. This E_T of **PFTV** is higher than that of red-emitting dopant Ir(piq)$_2$acac (2.0 eV) [49], ensuring that the back energy transfer from Ir(piq)$_2$acac to **PFTV** can be effectively suppressed. Moreover, the PL spectrum of **PFTV** overlaps with that of Ir(piq)$_2$acac (Fig. 7), suggesting that efficient energy transfer from **PFTV** to Ir(piq)$_2$acac can be expected. As shown in Fig. 8, the PL intensity of **PFTV** doped with Ir(piq)$_2$acac decreases gradually with increasing weight percent of the dopant (from 2 wt% to 8 wt%). The emission spectra show two peaks at 442 and 620 nm, which originate respectively from **PFTV** host (PL) and Ir(piq)$_2$acac dopant (radiative decay from triplet state to ground state) [14]. The efficient energy transfer from host to dopant and suppressed back energy transfer are prerequisites for attaining high performance in host-guest electrophosphorescent devices.

Therefore, a series of EL devices, ITO/PEDOT:PSS/**PFTV**:Ir(piq)$_2$acac(110 nm)/Ca(50 nm)/Al (100 nm), using blends of **PFTV** and Ir(piq)$_2$acac (2–8 wt%) as emitting layer were fabricated to investigate their optoelectronic characteristics. The main EL emission peak is around 620 nm with degenerated **PFTV** emission (400–530 nm). The EL emission of **PFTV** is almost completely

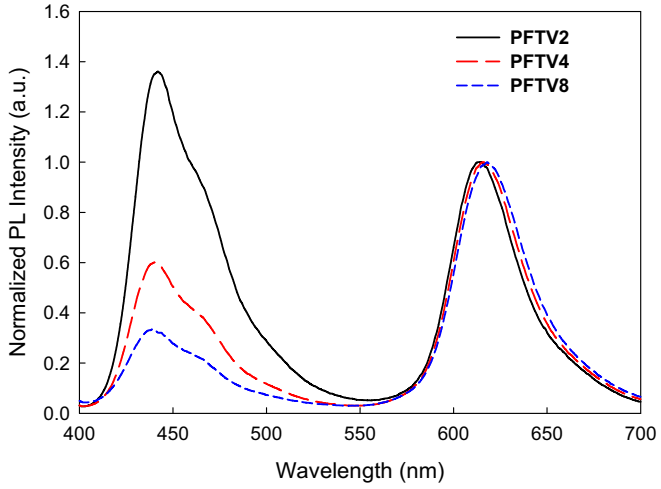

Fig. 8. PL spectra of the **PFTV** films doped with different amounts of Ir(piq)$_2$acac (with λ_{ex} = 385 nm). The number represents weight percent of the Ir(piq)$_2$acac in the film.

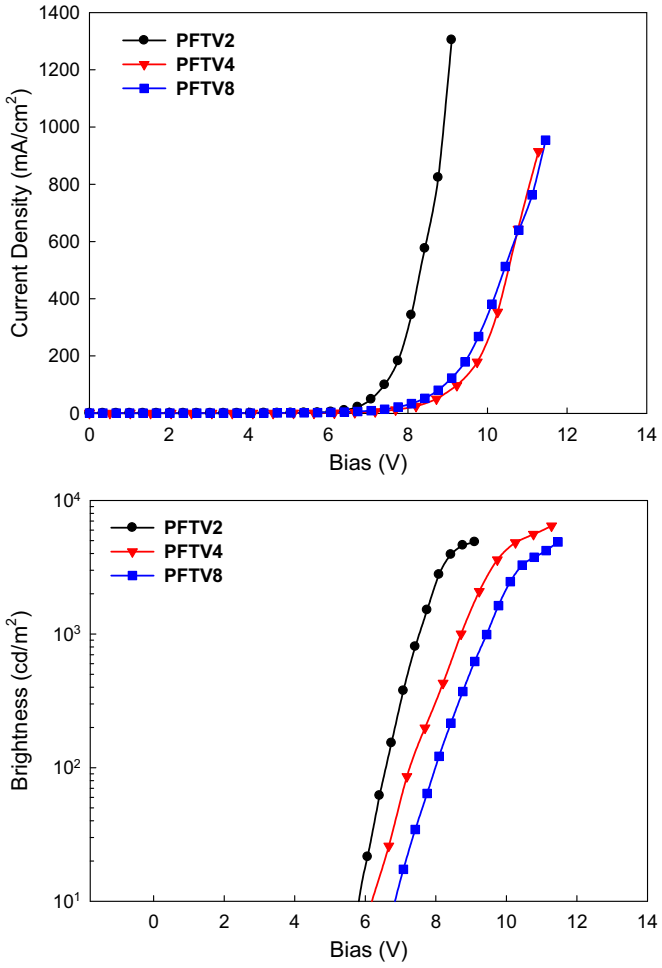

Fig. 10. Current density versus bias and brightness versus bias characteristics of PLEDs using Ir(piq)$_2$acac-doped **PFTV** as emitting layer. The number represents weight percent of the Ir(piq)$_2$acac in the film; devices structure: ITO/PEDOT:PSS/**PFTV**:Ir(piq)$_2$acac/Ca(50 nm)/Al(100 nm).

Table 3
Optoelectronic properties of the electrophodphorescent devices using **PFTV** as a host polymer doped with Ir(piq)$_2$acac.

Host[a]	V_{on}[c] (V)	L_{max}[d] (cd/m^2)	LE_{max} (cd/A)[e]	CIE 1931 (x, y)[f]
PFTV2[b]	6.1	4880	0.83	(0.58, 0.30)
PFTV4	6.7	5580	2.15	(0.64, 0.32)
PFTV8	7.1	4890	0.65	(0.66, 0.32)
PFTV4[g]	6.7	5300	2.64	(0.65, 0.32)

[a] Device structure: ITO/PEDOT:PSS/**PFTV**:Ir(piq)$_2$acac/Ca/Al.
[b] The number presents weight percent of Ir(piq)$_2$acac in the film.
[c] Turn-on voltage defined as the bias at a luminance of 10 cd/m^2.
[d] Maximum luminance.
[e] Maximum luminance efficiency.
[f] The 1931 CIE coordinates at *ca.* 1000 cd/m^2.
[g] Device with additional LiF as electron-injection layer: ITO/PEDOT:PSS/**PFTV**:Ir(piq)$_2$acac/LiF/Ca/Al.

quenched at 4 wt% and 8 wt% Ir(piq)$_2$acac. The EL spectra peaked at 622 nm are similar to the PL spectrum of Ir(piq)$_2$acac (Fig. 8), indicating that the same emitting species are involved in both conditions. However, the EL emission spectra (Fig. 9) are very different from corresponding PL spectra (Fig. 8). This is presumably attributed to different underlying energy transfer mechanisms occurred under photo- and electro-excitation. The energy transfer from **PFTV** to Ir(piq)$_2$acac is more complete under electro-excitation which usually results in about 75% triplet excitons. Moreover, the Ir(piq)$_2$acac may act as carriers trapping sites due to its low band gap. Fig. 10 shows the current density versus bias and brightness versus bias curves (*J*–*V*–*B*), with the characteristic data summarized in Table 3. The maximum brightness and maximum current efficiency of the devices are 4880–5580 cd/m^2 and 0.65–2.15 cd/A, respectively. The turn-on voltage is increases from 6.1 V to 7.1 V with the increase of Ir(piq)$_2$acac concentration (2 wt% to 8 wt%), confirming that the Ir(piq)$_2$acac acts as charges trapping sites under electro-excitation. Because the HOMO (−5.17 eV) and LUMO (−3.23 eV) levels of Ir(piq)$_2$acac [33,49] lie between those of **PFTV** (−5.27 eV, −2.41 eV), both holes and electrons are readily trapped and recombined in Ir(piq)$_2$acac (Fig. 10).

The **PFTV4**-based device exhibits the best performance, with the maximum brightness and maximum current efficiency being 5580 cd/m^2 and 2.15 cd/A, respectively. With increasing Ir(piq)$_2$acac concentration the maximum current efficiency is first enhanced from 0.83 cd/A (2 wt%) to 2.15 cd/A (4 wt%) and then dropped abruptly to 0.65 cd/A (8 wt%). The abrupt reduction in efficiency at 8 wt% Ir(piq)$_2$acac is probably due to concentration quenching. In order to improve the EL performance, a device with extra lithium fluoride (LiF) layer was fabricated to balance charges injection and transport; the device structure was ITO/PEDOT:PSS/**PFTV4** (110 nm)/LiF(1 nm)/Ca(50 nm)/Al(100 nm). Its maximum brightness and maximum current efficiency were 5300 cd/m^2 and 2.64 cd/A, respectively (Table 3). This efficiency enhancement (from 2.15 to 2.64 cd/A) is attributed to improved electron-injection by LiF layer that results in more balanced charges injection and transport. Current results demonstrate that **PFTV** is not only an efficient hole-transporting polymer for electroluminescent devices but also applicable as host for electrophosphorescent devices.

4. Conclusions

We have successfully synthesized and characterized a thermally cross-linkable poly(fluorene-*co*-triphenylamine) (**PFTV**) containing pendent styryl groups by the Suzuki coupling reaction, which was applied as hole-transporting layer or as host in the fabrication of PLEDs. The **PFTV** demonstrated high thermal stability, with thermal decomposition (T_d) and glass transition (T_g) temperatures being above 419 and 225 °C, respectively. Thermal curing of **PFTV** at 230 °C for 30 min led to homogeneous surface morphology with the root-mean-square (rms) roughness being 0.88 nm. The HOMO level of **PFTV** (−5.27 eV) lies between those of PEDOT:PSS (−5.0 ~ −5.2 eV) and **PFO** (−5.8 eV), forming a stepwise energy ladder to facilitate hole-injection. The multilayer devices using cross-linked **PFTV** as hole-transporting layer [ITO/PEDOT:PSS/**PFTV**/**PFO**/Ca/Al] were readily fabricated by successive spin-coating processes. The device performances were significantly enhanced, by using the cured **PFTV** as hole-transporting layer. The best maximum current efficiency and brightness were 5560 cd/m^2 and 2.27 cd/A, respectively. Moreover, the **PFTV** was confirmed as effective host for electrophosphorescent devices with Ir(piq)$_2$acac as red emitter. The maximum brightness and maximum current efficiency reached 5300 cd/m^2 and 2.64 cd/A, respectively. Current results reveal that the **PFTV** is a promising optoelectronic material which is applicable not only as hole-transporting polymer in multilayer PLEDs but also as host polymer for electro-phosphorescent LEDs.

Acknowledgment

The authors thank the National Science Council of Taiwan for financial aid through project NSC 98-2221-E-006-002-MY3.

Appendix. Supporting information

Supporting information associated with this article can be found, in the online version, at doi:10.1016/j.polymer.2010.10.065.

References

[1] Burroughes JH, Bradley DDC, Brown AR, Marks RN, Mackay K, Friend RH, et al. Nature 1990;347(6293):539–41.
[2] Friend RH, Gymer RW, Holmes AB, Burroughes JH, Marks RN, Taliani C, et al. Nature 1999;397(6715):121–8.
[3] Tang CW, VanSlyke SA. Appl Phys Lett 1987;51(12):913–5.
[4] Kraft A, Grimsdale AC, Holmes AB. Angew Chem Int Ed 1998;37(4):402–28.
[5] Forrest SR. Nature 2004;428(6986):911–8.
[6] Pei Q, Yang Y. J Am Chem Soc 1996;118(31):7416–7.
[7] Bernius MT, Inbasekaran M, O'Brien J, Wu W. Adv Mater 2000;12 (23):1737–50.
[8] Scherf U, List EJW. Adv Mater 2002;14(7):477–87.
[9] Neher D. Macromol Rapid Commun 2001;22(17):1365–85.
[10] Janietz S, Bradley DDC, Grell M, Giebeler C, Inbasekaran M, Woo EP. Appl Phys Lett 1998;73(17):2453–5.
[11] Redecker M, Bradley DDC, Inbasekaran M, Woo EP. Appl Phys Lett 1998;73 (11):1565–7.
[12] Huang F, Zhang Y, Liu MS, Cheng Y-J, Jen AK- Y. Adv Funct Mater 2007;17 (18):3808–15.
[13] Huang C-W, Peng K-Y, Liu C-Y, Jen T-H, Yang N-J, Chen S-A. Adv Mater 2008;20(19):3709–16.
[14] Wu F-I, Shih P-I, Shu C-F, Tung Y-L, Chi Y. Macromolecules 2005;38 (22):9028–36.
[15] Yuan M-C, Shih P-I, Chien C-H, Shu C- F. J Polym Sci A Polym Chem 2007;45 (14):2925–37.
[16] Shu C-F, Dodda R, Wu F-I, Liu MS, Jen AK-Y. Macromolecules 2003;36 (18):6698–703.
[17] Wong W-Y, Liu L, Cui D, Leung LM, Kwong C-F, Lee T-H, et al. Macromolecules 2005;38(12):4970–6.
[18] Peng Q, Xu J, Li M, Zheng W. Macromolecules 2009;42(15):5478–85.
[19] Yan H, Lee P, Armstrong NR, Graham A, Evmenenko GA, Dutta P, et al. J Am Chem Soc 2005;127(9):3172–83.
[20] Shi W, Fan S, Huang F, Yang W, Liu R, Cao Y. J Mater Chem 2006;16 (24):2387–94.
[21] Gong X, Moses D, Heeger AJ, Liu S, Jen AKY. Appl Phys Lett 2003;83(1):183–5.
[22] Grice AW, Bradley DDC, Bernius MT, Inbasekaran M, Wu WW, Woo EP. Appl Phys Lett 1998;73(5):629–31.
[23] Kim J-S, Friend R,H, Grizzi I, Burroughes JH. Appl Phys Lett 2005;87 (2):023506.
[24] Choulis SA, Choong V-E, Patwardhan A, Mathai MK, So F. Adv Funct Mater 2006;16(8):1075–80.
[25] Ego C, Grimsdale AC, Uckert F, Yu G, Srdanov G, Müllen K. Adv Mater 2002;14 (11):809–11.

[26] Stelios AC, Vi-En C, Mathew KM, Franky S. Appl Phys Lett 2005;87 (11):113503.
[27] Chen JP, Klaerner G, Lee JI, Markiewicz D, Lee VY, Miller RD, et al. Synth Met 1999;107(2):129–35.
[28] Jiang XZ, Liu S, Liu MS, Herguth P, Jen AKY, Fong H, et al. Adv Funct Mater 2002;12(11–12):745–51.
[29] Niu Y-H, Liu MS, Ka J-W, Jen AKY. Appl Phys Lett 2006;88(9):093505.
[30] Paul GK, Mwaura J, Argun AA, Taranekar P, Reynolds JR. Macromolecules 2006;39(23):7789–92.
[31] Niu Y-H, Liu MS, Ka J-W, Bardeker J, Zin MT, Schofield R, et al. Adv Mater 2007;19(2):300–4.
[32] Cheng Y-J, Liu MS, Zhang Y, Niu Y, Huang F, Ka J-W, et al. Chem Mater 2008;20 (2):413–22.
[33] Liu MS, Niu Y-H, Ka J-W, Yip H-L, Huang F, Luo J, et al. Macromolecules 2008;41(24):9570–80.
[34] Zhang Y-D, Hreha RD, Jabbour GE, Kippelen B, Peyghambarian N, Marder SR. J Mater Chem 2002;12(6):1703–8.
[35] Park M-J, Lee J-I, Chu H-Y, Kim S-H, Zyung T, Eom J-H, et al. Synth Met 2009;159(14):1393–7.
[36] Wang PH, Ho M-S, Yang S-H, Chen K-B, Hsu C- S. J Polym Sci A Polym Chem 2010;48(3):516–24.
[37] Lee HJ, Sohn J, Hwang J, Park SY, Choi H, Cha M. Chem Mater 2004;16 (3):456–65.
[38] Wenseleers W, Stellacci F, Meyer-Friedrichsen T, Mangel T, Bauer CA, Pond SJK, et al. J Phys Chem B 2002;106(27):6853–63.
[39] Changkun L, Amanda R, Bing Z. J Polym Sci A Polym Chem 2008;46 (21):7268–72.
[40] Chen R-T, Chen S-H, Hsieh B-Y, Chen Y. J Polym Sci A Polym Chem 2009;47 (11):2821–34.
[41] Rusling JF, Suib SL. Adv Mater 1994;6(12):922–30.
[42] Liu Y, Liu MS, Jen AK-Y. Acta Polymerica 1999;50(2–3):105–8.
[43] Tang CW, VanSlyke SA, Chen CH. J Appl Phys 1989;65(9):3610–6.
[44] Morgado J, Cacialli F, Friend RH, Iqbal R, Yahioglu G, Milgrom LR, et al. Chem Phys Lett 2000;325(5–6):552–8.
[45] Liao JL, Chen X, Liu CY, Chen SA, Su CH, Su AC. J Phys Chem B 2007;111 (35):10379–85.
[46] Avilov I, Marsal P, Brédas JL, Beljonne D. Adv Mater 2004;16(18):1624–9.
[47] Wong K-T, Chen Y-M, Lin Y-T, Su H-C, Wu C-C. Org Lett 2005;7(24):5361–4.
[48] Liu Q-D, Lu J, Ding J, Day M, Tao Y, Barrios P, et al. Adv Funct Mater 2007;17 (6):1028–36.
[49] Lyu Y-Y, Kwak J, Jeon WS, Byun Y, Lee HS, Kim D, et al. Adv Funct Mater 2009;19(3):420–7.

Polymer 52 (2011) 86–90

Contents lists available at ScienceDirect

Polymer

journal homepage: www.elsevier.com/locate/polymer

Nanoporous hard etch masks using silicon-containing block copolymer thin films

Se Jin Ku, Su Min Kim, Chang Hong Bak, Jin-Baek Kim*

Department of Chemistry, Korea Advanced Institute of Science and Technology (KAIST), 373-1, Guseong-Dong, Yuseong-Gu, Daejeon 305-701, Republic of Korea

ARTICLE INFO

Article history:
Received 2 September 2010
Received in revised form
28 October 2010
Accepted 6 November 2010
Available online 13 November 2010

Keywords:
Block copolymer lithography
Hard etch mask
Nanotemplate

ABSTRACT

Nanoporous hard etch masks with various pore sizes were fabricated using a new type of silicon-containing block copolymers, polystyrene-*block*-poly(4-(*tert*-butyldimethylsilyl)oxystyrene) with different molecular weights. Since organic–inorganic block copolymers have a large difference in etch resistance between the organic and inorganic blocks, a hard etch mask of silicon oxide can be directly produced upon oxygen plasma treatment. Orientation and hexagonal arrays of cylindrical nanodomains were manipulated simply by adjusting the relative composition of selective and non-selective solvents in the annealing solvent. When the cylindrical nanostructures aligned perpendicular to the substrate surface were exposed to an oxygen plasma, hexagonally arranged nanopore arrays of silicon oxide with controlled pore sizes were fabricated. These nanoporous hard etch masks can be applied to the nanopatterning processes that require high aspect ratio structures.

1. Introduction

The self-assembly of block copolymers is a promising technique for making nanometer-sized structures with regularly sized and spaced features, such as spheres, cylinders, and lamellae [1]. To obtain long range ordering and positional registration of self-assembled nanostructures, several techniques have been applied, such as strong external fields, solvent evaporation, and thermal treatments [2,3]. Among them, solvent vapor annealing has attracted much attention as a prominent approach to manipulate the orientation and long range order of well-defined nanostructures in a short period of time without the need of surface modification [4,5]. Self-assembled nanostructures of block copolymers have been extensively studied for applications in many fields, such as semiconductor, magnetic storage media, and optical devices, which require nanoscale functional features [6–8]. However, several issues still need to be addressed such as multistep processes and long processing times for the practical applications. In particular, selective etching of one of the blocks is a key requirement for subsequent pattern transfer to the substrate in device fabrication; the removal of one polymer block leaves the other to be used as a mask. However, the remaining block, which is typically polystyrene, has a relatively low etch resistance, making it undesirable for nanolithographic applications. The integration of organic–organic block copolymers in nanolithography has therefore involved additional processes such as formation of an intermediate SiN layer, selective ozonolysis, and staining with heavy metals for successful pattern transfer [9].

The introduction of a silicon moiety into a block copolymer allows a soft organic template to be converted to a hard etch mask of silicon oxide after oxygen plasma treatment. This hard etch mask also has the enhanced properties of the thermal stability, dielectricity, and mechanical strength [10]. Several methods have been reported the use of a sol–gel reaction to functionalize or co-assemble silicon precursors with block copolymers [11]. However, these methods result in a limited long range order of self-assembled nanostructures. Recently, few silicon-containing block copolymers have been reported for the etch-resistant nanotemplates. Parallel cylinder arrays of polystyrene-*block*-poly(dimethylsiloxane) (PS-*b*-PDMS) were developed using solvent-vapor-induced self-assembly on a PDMS brush-treated silica substrate. In this case, PDMS surface and bottom layers were formed. Therefore, CF_4 plasma treatment was required to remove the PDMS surface layer before the oxygen plasma processing [12]. Hirai et al. reported the self-assembly of polyhedral oligomeric silsesquioxane (POSS)-containing block copolymer thin films by solvent annealing on unmodified substrates to obtain both vertically oriented lamellae and cylinders [13].

Here, we demonstrate a novel method to fabricate nanoporous hard etch masks using a new type of silicon-containing block copolymer, polystyrene-*block*-poly(4-(*tert*-butyldimethylsilyl)oxystyrene) (PS-*b*-PSSi). Organic–inorganic block copolymers are expected to have a large difference in etch resistance between the organic and inorganic blocks, which

* Corresponding author. Tel.: +82 42 350 2837; fax: +82 42 350 2810.
E-mail address: kjb@kaist.ac.kr (J.-B. Kim).

0032-3861/$ – see front matter © 2010 Elsevier Ltd. All rights reserved.
doi:10.1016/j.polymer.2010.11.012

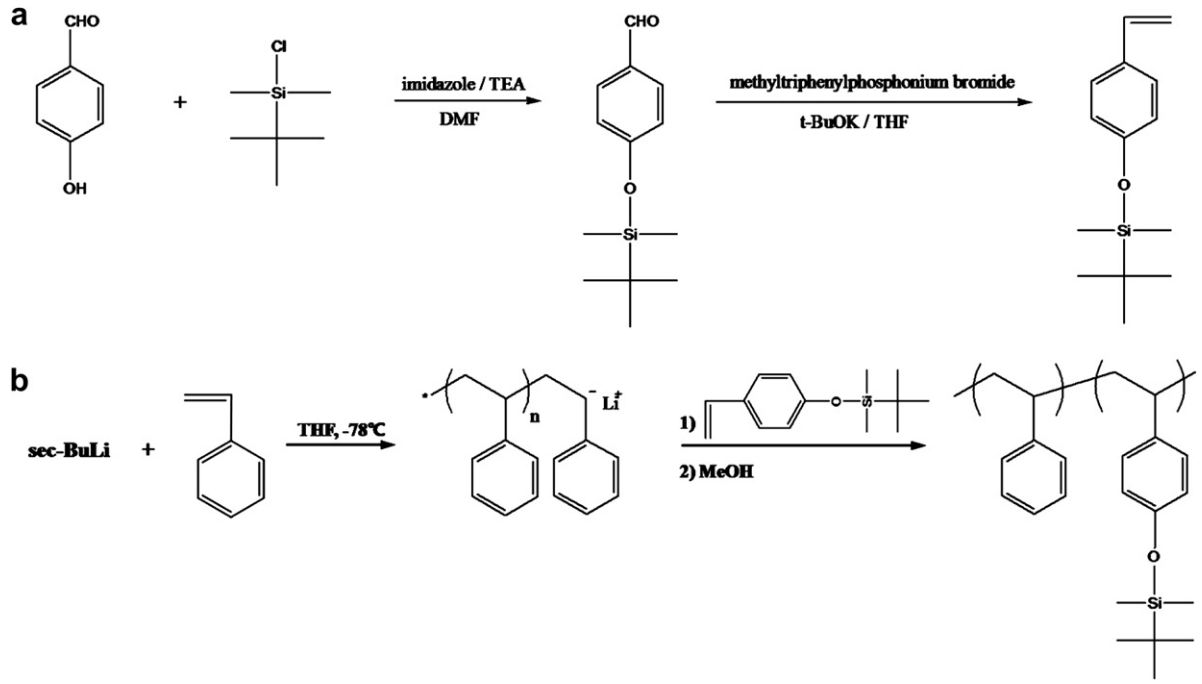

Fig. 1. Schematic of synthesis steps: (a) synthesis of silicon-containing monomer; (b) synthesis of PS-*b*-PSSi block copolymer by living anionic polymerization.

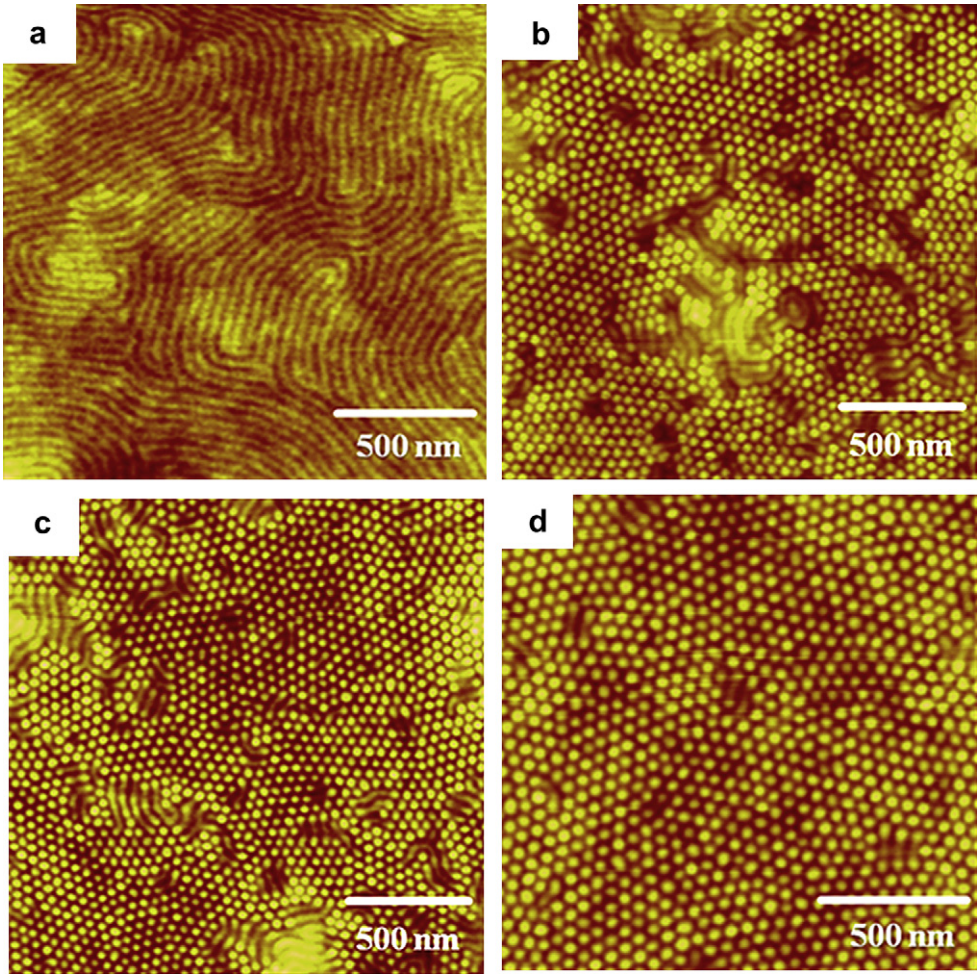

Fig. 2. AFM images of $PS_{22.1k}$-*b*-$PSSi_{49.7k}$ thin films solvent annealed for 4 h at room temperature (a) in toluene vapor, (b) in a mixed solvent vapor of $V_{hep}/V_{tol} = 0.5$, (c) $V_{hep}/V_{tol} = 1$ and (d) $V_{hep}/V_{tol} = 4$.

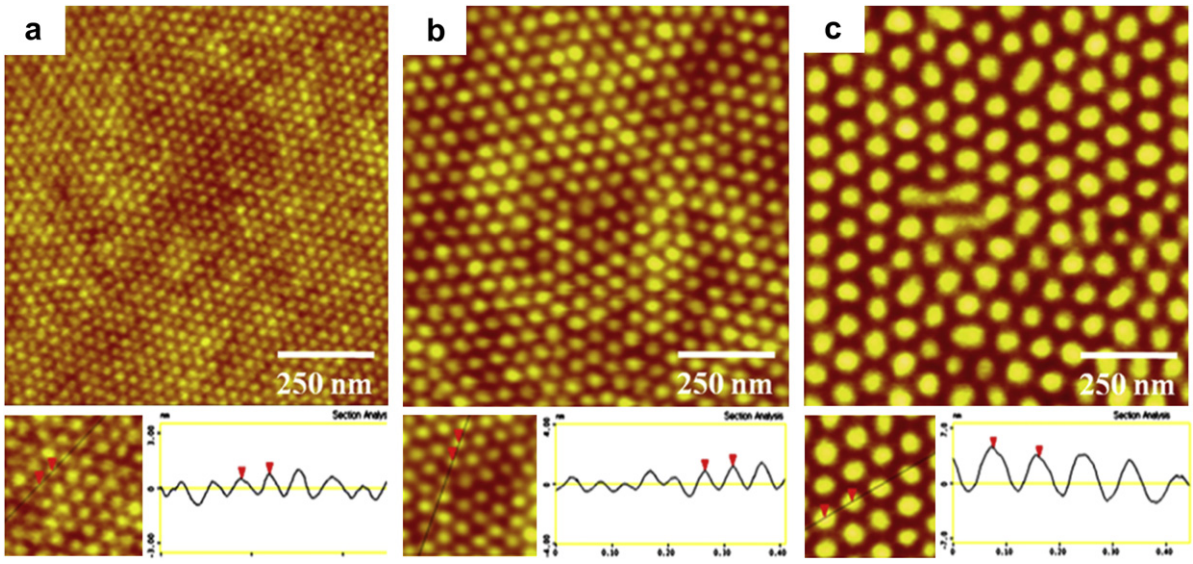

Fig. 3. AFM images of PS-*b*-PSSi thin films with different molecular weights, (a) $PS_{12.5k}$-*b*-$PSSi_{28.1k}$, (b) $PS_{22.1k}$-*b*-$PSSi_{49.7k}$ and (c) $PS_{31.0k}$-*b*-$PSSi_{69.7k}$, after solvent annealing in a mixed solvent vapor of $V_{hep}/V_{tol} = 4$ for 4 h at room temperature.

allows a direct formation of a hard etch mask of silicon oxide after oxygen plasma treatment. PS-*b*-PSSi block copolymers with three different molecular weights are synthesized by living anionic polymerization to control domain sizes of self-assembled nanostructures from 20 nm to 50 nm in diameter. The cylinder orientation can be manipulated simply by changing the solvent for annealing without any substrate modification within a short period of time. To fabricate highly ordered nanoporous masks of silicon oxide, the cylindrical nanostructures aligned perpendicular to the substrate surface are directly exposed to an oxygen plasma. This nanoporous hard etch masks can be applied to the nanofabrication processes by subsequent pattern transfer to underlying substrates. This new approach reduces the complexity and time of the process.

2. Experimental part

2.1. Materials and instrumentation

All chemicals were purchased from Aldrich Chemical Company. Tetrahydrofuran (THF) was freshly distilled from sodium/benzophenone (deep purple color) after refluxing for at least 12 h. Styrene and 4-(*tert*-butyldimethylsilyl)oxystyrene were purified by stirring with calcium hydride for 24 h at room temperature and then distilled under vacuum. The purified monomers were stored under nitrogen atmosphere in the refrigerator. ^{1}H spectra were recorded on a Bruker AM-300 MHz FT-NMR spectrometer in $CDCl_3$ at room temperature. ^{13}C spectrum was recorded on a Bruker AVANCE 400 (inverse gated decoupling mode) in $CDCl_3$ at room temperature. GPC was performed in THF on a Viscotek T60A GPC system equipped with two PLgel 10 μm MIXED-B columns and a PLgel 10 μm 500 A at 35 °C, calibrated with polystyrene standards. Film thickness was measured with a Rudolph Research ellipsometer using a helium–neon laser ($\lambda = 633$ nm). Atomic force microscope (AFM) images were obtained with a Nanoscope IIIa multimode scanning probe microscope (Veeco, USA) in tapping mode. Scanning electron microscope (SEM) images were obtained with a Hitachi model S-2280N SEM. Oxygen reactive ion etching was carried out in a Vacuum Science reactive ion etching system, model VSRIE-600T.

2.2. Synthesis of PS-b-PSSi by living anionic polymerization

Silicon-containing monomer, 4-(*tert*-butyldimethylsilyl)oxystyrene, was synthesized in high yield (see Supplementary material) [14]. PS-*b*-PSSi was synthesized by living anionic polymerization. 40 ml of THF was transferred to a flame-dried round-bottom flask, and then the glass reactor was cooled to −78 °C using an acetone/dry ice cooling bath. *sec*-Butyllithium as an initiator was added by means of syringe until the persistent yellowish color appeared, followed by the addition of the prescribed amount of *sec*-butyllithium. A few minutes later styrene was added to the reactor. The color rapidly changed from yellow to red. After 30 min, a small amount of aliquot was pulled out of the reactor for GPC analysis of the PS segment, and then the silicon-containing monomer was transferred to the polymerization flask without any color change. After 60 min, excess of degassed methanol was added to the reactor. The resulting colorless mixture was concentrated on a rotary evaporator, dissolved in THF, and precipitated in methanol. PS-*b*-PSSi block copolymers with different molecular weights were successfully obtained at the PS mass fraction 31% (Details are described in Supplementary material). The number average molecular weight (M_n) and polydispersity index of each PS-*b*-PSSi block copolymer were 40,600 g mol^{-1} and 1.09 for $PS_{12.5k}$-*b*-$PSSi_{28.1k}$ (12,500 g mol^{-1} for PS and 28,100 g mol^{-1} for PSSi), 71,800 g mol^{-1} and 1.14 for $PS_{22.1k}$-*b*-$PSSi_{49.7k}$ (22,100 g mol^{-1} for PS and 49,700 g mol^{-1} for PSSi), 100,700 g mol^{-1} and 1.13 for $PS_{31.0k}$-*b*-$PSSi_{69.7k}$ (31,000 g mol^{-1} for PS and 69,700 g mol^{-1} for PSSi), determined by gel permeation chromatography and ^{13}C NMR spectra (inverse gate decoupling mode).

2.3. Control of solvent annealed morphologies and formation of hard etch masks with different pore sizes

A 1.5 wt% solution of $PS_{22.1k}$-*b*-$PSSi_{49.7k}$ in xylene was spin-coated onto a silicon wafer at 3000 rpm for 60 s. To control the orientation of PS cylinder, the resulting 40-nm-thick film was exposed to either toluene vapor or mixed solvent vapor of toluene and heptane with different volume ratios of heptane to toluene ($V_{hep}/V_{tol} = 0.5–4$) at room temperature for 4 h. Perpendicular cylinders of PS were observed embedded in the PSSi matrix after

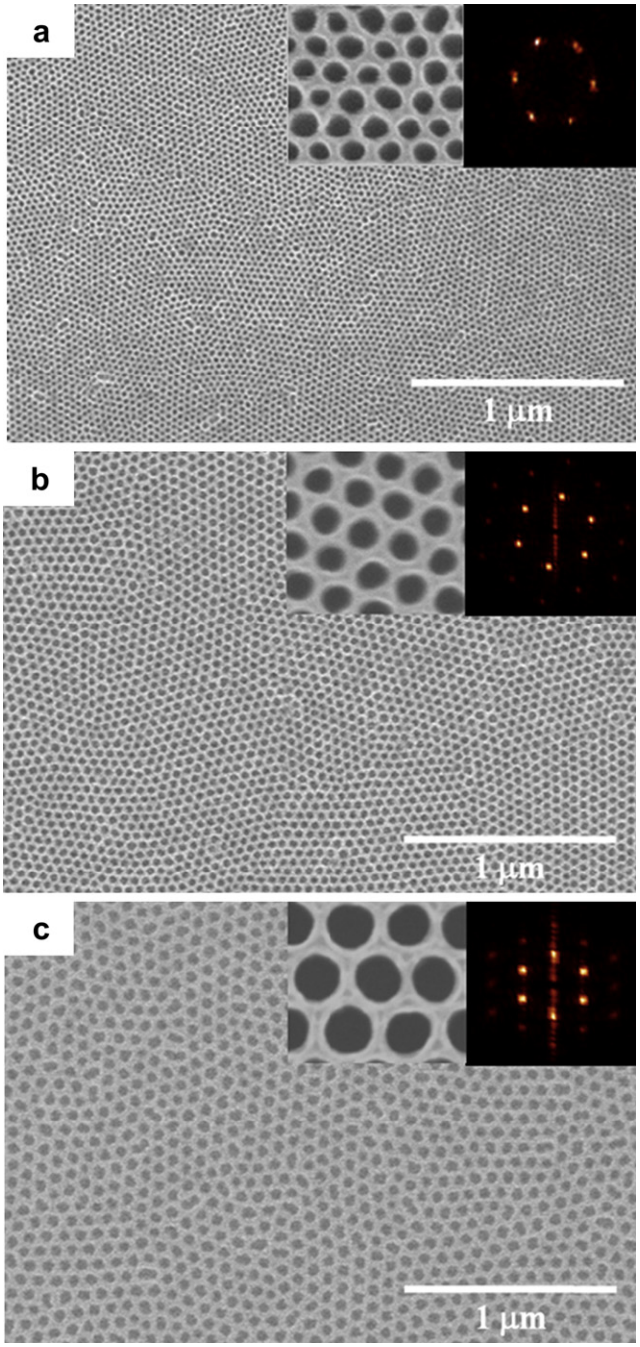

Fig. 4. SEM images of hexagonal nanopore arrays with different pore sizes after solvent annealing in a mixed solvent vapor of $V_{hep}/V_{tol} = 4$, followed by oxygen reactive ion etching (a) ~20 nm for $PS_{12.5k}$-*b*-$PSSi_{28.1k}$, (b) ~30 nm for $PS_{22.1k}$-*b*-$PSSi_{49.7k}$ and (c) ~50 nm for $PS_{31.0k}$-*b*-$PSSi_{69.7k}$. The inset image is a 2-D fast Fourier transformation pattern from each image.

solvent annealing in mixed vapor with volume ratio of $V_{hep}/V_{tol} = 4$, while parallel PS cylinders after annealing in toluene vapor.

PS-*b*-PSSi block copolymer films with different molecular weights were prepared to control the domain sizes of self-assembled nanostructures: $PS_{12.5k}$-*b*-$PSSi_{28.1k}$, $PS_{22.1k}$-*b*-$PSSi_{49.7k}$ and $PS_{31.0k}$-*b*-$PSSi_{69.7k}$. After spin-coating each block copolymer solution on Si wafers, the samples with the thickness of 40 nm were annealed in mixed solvent vapor with volume ratio of $V_{hep}/V_{tol} = 4$ to obtain the self-assembled structures of perpendicular PS cylinders embedded in the PSSi matrix. Then, thin films were subjected to an anisotropic oxygen reactive ion etching to remove the organic block. The oxygen pressure in the plasma was 6 mTorr with a flow rate of 30 sccm, a radio-frequency power of 300 W, and platen power of 50 W, respectively. Image analysis software was used to obtain 2-D fast Fourier transformation patterns.

3. Results and discussion

Schematic for synthesis of PS-*b*-PSSi block copolymers is illustrated in Fig. 1. Styrene was first polymerized by a *sec*-butyllithium initiator, followed by the sequential addition of the silicon-containing monomer, and the polymerization was quenched with degassed methanol. Block copolymers with different molecular weights were synthesized and denoted as $PS_{12.5k}$-*b*-$PSSi_{28.1k}$, $PS_{22.1k}$-*b*-$PSSi_{49.7k}$ and $PS_{31.0k}$-*b*-$PSSi_{69.7k}$. Each block copolymer has the PS mass fraction of 31%. Styrenic monomers used in both blocks are readily polymerized and are suitable for living anionic polymerization [15]. The polymerization was carried out without any additives such as diphenylethylene and LiCl because there were no functional groups that could participate in side reactions such as chain termination [16]. Therefore, polymerization of the PS-*b*-PSSi block copolymer is highly producible, scalable, and easy to control the molecular weight in living anionic polymerization.

To manipulate the orientation and hexagonal order of cylindrical morphology, 40-nm-thick block copolymer films of $PS_{22.1k}$-*b*-$PSSi_{49.7k}$ were first annealed in saturated solvent vapor with various compositions of selective and non-selective solvents. It is well known that treatments with selective or non-selective solvent vapor can make a significant difference in the resulting morphologies in block copolymer thin films. Furthermore, adjusting the fraction of selective and non-selective solvents in the annealing solvent allowed the manipulation of PS cylinder orientation [5c]. In this study, two solvents, toluene and heptane, were used for annealing. Toluene is a non-selective solvent for both polymer blocks, while heptane is a good solvent for the PSSi block, but a poor solvent for the PS block, and thus behaves as a selective solvent. In toluene vapor, parallel PS cylinders embedded in the PSSi matrix were observed after annealing for 4 h at room temperature, as shown in Fig. 2a. An average center-to-center distance was about 50 nm. On the contrary, in mixed solvent vapor of heptane and toluene, PS cylinders aligned perpendicular to the substrate surface were observed. To fabricate well-ordered arrays of perpendicular PS cylinders, the volume ratio of the solvents for annealing was changed from 0.5 to 4. After 4 h of solvent annealing in a mixed solvent vapor of $V_{hep}/V_{tol} = 0.5–1$, a mixed morphology of both parallel and perpendicular PS cylinders was observed, as shown in Fig. 2b and c. However, annealing in a mixed solvent vapor of $V_{hep}/V_{tol} = 4$ for 4 h at room temperature resulted in highly ordered arrays of PS cylindrical patterns oriented perpendicular to the substrate surface and embedded in the PSSi matrix over a large area, as shown in Fig. 2d. The average cylinder diameter was about 30 nm. Thus, the orientation of the cylinders can be adjusted by altering the solvent composition without any substrate modification within a short period of time. To fabricate nanoporous hard etch masks of silicon oxide with high degree of order, we employed the self-assembled nanostructures of cylindrical morphology aligned perpendicular to the substrate.

PS-*b*-PSSi block copolymers with different molecular weights were prepared to fabricate different pore sizes of self-assembled nanostructures. 40-nm-thick films were exposed to a mixed solvent vapor with the volume ratio of $V_{hep}/V_{tol} = 4$ at room temperature. After 4 h of solvent annealing, well-defined hexagonal arrays of perpendicular cylinders with different diameters and center-to-center distances were observed for three different molecular weights, as shown in Fig. 3. Average cylinder diameters and center-

to-center distances were 20 nm and 35 nm for $PS_{12.5k}$-*b*-$PSSi_{28.1k}$, 30 nm and 50 nm for $PS_{22.1k}$-*b*-$PSSi_{49.7k}$, and 50 nm and 85 nm for $PS_{31.0k}$-*b*-$PSSi_{69.7k}$, respectively. It is noted that the $PS_{31.0k}$-*b*-$PSSi_{69.7k}$ block copolymer exhibited cylindrical morphology with high degree of order, despite its high molecular weight of 100,700 g mol^{-1}. The results show that solvent annealing can produce an ordered surface morphology over a large area, especially for high molecular weight block copolymers in which thermal treatment is not a feasible route to achieve thermal equilibrium.

To directly fabricate hard etch masks of nano-sized hole patterns, the solvent-annealed nanostructures of silicon-containing block copolymers with different cylinder diameters were subjected to an oxygen plasma under controlled conditions. The upper and the lateral surfaces of the inorganic PSSi block were converted to silicon oxide, while the organic PS block was sufficiently removed, after 20 s of oxygen reactive ion etching (see Supplementary material, Fig. S4). Then, highly ordered nanopore arrays with uniform pore sizes of 20 nm, 30 nm and 50 nm for different molecular weights are observed in Fig. 4. The nanopores were completely etched down to the substrate surface and confirmed by cross-sectional SEM image in Fig. S5a. The nanoporous silicon oxide film with thickness of about 13 nm is shown in Fig. S5b. We also studied the effect of film thickness on the morphology of perpendicular cylinders with 50 nm of center-to-center distance. After oxygen reactive ion etching, the same results were obtained in thin films with different thicknesses from 20 nm to 60 nm in both AFM and SEM images, which indicated the cylindrical nanostructure aligned perpendicular to the substrate. We also studied the effect of film thickness on the morphology of perpendicular cylinders with 50 nm of center-to-center distance. After oxygen reactive ion etching, the same results were obtained in thin films with different thicknesses from 20 nm to 60 nm in both AFM and SEM images, which indicated the cylindrical nanostructure aligned perpendicular to the substrate. Furthermore, as in the inset images of fast Fourier transformation patterns, the six sharp first-order peaks equidistant from the center indicate the presence of hexagonally ordered nanostructures. These nanoporous structures of silicon oxide can be fabricated on various substrates, such as polymer, metal, or metal oxide, and also exhibit high thermal stability, high etch resistance, and high degree of order, which indicated the possibilities of these hard etch masks for the further applications. Consequently, the high etch contrast between the organic and silicon-containing polymer blocks ultimately resulted in direct formation of a silicon oxide nanotemplate with uniformity over a large surface area.

4. Conclusion

In conclusion, the direct formation of a hard etch mask by using the high etch contrast between the two polymer blocks in a new type of silicon-containing block copolymer, PS-*b*-PSSi, was demonstrated. PS-*b*-PSSi block copolymers with different molecular weights were easily synthesized by living anionic polymerization without any additives. The orientation of cylindrical domains was controlled by adjusting the relative composition of selective and non-selective solvents during solvent annealing. The use of toluene in solvent annealing resulted in cylinders of PS aligned parallel to the substrate, while a mixed solvent vapor with $V_{hep}/V_{tol} = 4$ resulted in PS cylinders oriented perpendicular to the substrate over a large area. Self-assembled nanostructures with perpendicular PS cylinders were directly converted to nanoporous hard etch masks of silicon oxide with hexagonally arranged hole patterns with average 20 nm, 30 nm and 50 nm pore sizes, after a single exposure to an oxygen plasma. These well-controlled nanoporous patterns having high etch resistance and a high degree of order can make them potentially useful in nanopatterning processes that require high aspect ratio structures by subsequent pattern transfer. Currently, we are investigating the use of nanoporous hard etch masks in the fabrication process of high aspect ratio nanopore arrays using a lithographic bilayer system.

Acknowledgements

This research was supported by a grant from the Fundamental R&D Program for Core Technology of Materials funded by the Ministry of Knowledge Economy, Republic of Korea. This research was supported by the National Research Foundation of Korea (NRF) grant by the Korea government (MEST) (2010-0014312).

Appendix. Supplementary material

Supplementary material related to this article can be found online at doi:10.1016/j.polymer.2010.11.012.

References

[1] (a) Darling SB. Prog Polym Sci 2007;32:1152;
(b) Segalman RA. Mater Sci Eng R 2005;48:191;
(c) Mansky P, Liu Y, Huang E, Russell TP, Hawker CJ. Science 1997;275:1458.
[2] (a) Turturro A, Gattiglia E, Vacca P, Viola GT. Polymer 1995;36:3987;
(b) Fukunaga K, Elbs H, Magerle R, Krausch G. Macromolecules 2000;33:947.
[3] (a) Bal M, Ursache A, Tuominen MT, Goldbach JT, Russell TP. Appl Phys Lett 2002;81:3479;
(b) Li M, Christopher AC, Ober CK. Adv Polym Sci 2005;190:183.
[4] (a) Zhang J, Yu X, Yang P, Peng J, Luo C, Huang W, et al. Macromol Rapid Commun 2010;31:591;
(b) Kim G, Libera M. Macromolecules 1998;31:2569.
[5] (a) Peng J, Han Y, Knoll W, Kim DH. Macromol Rapid Commun 2007;28:1422;
(b) Wang Y, Hong X, Liu B, Ma C, Zhang C. Macomolecules 2008;41:5799;
(c) Jung YS, Ross CA. Adv Mater 2009;21:2540;
(d) Nandan B, Gowd EB, Bigall NC, Eychmuller A, Formanek P, Simon P, et al. Adv Funct Mater 2009;19:2805.
[6] Park M, Harrison C, Chaikin PM, Register RA, Adamson DH. Science 1997;276:1401.
[7] (a) Cheng JY, Ross CA, Thomas EL, Smith HI, Vancso GJ. Adv Mater 2003;15:1599;
(b) Park HJ, Kang MG, Guo LJ. ACS Nano 2009;3:2601;
(c) Popa AM, Niedermann P, Heinzelmann H, Hubbell JA, Pugin R. Nanotechnology 2009;20:485303.
[8] (a) Cheng JY, Ross CA, Chan VZH, Thomas EL, Lammertink RGH, Vancso GJ. Adv Mater 2001;13:1174;
(b) Chai J, Wang D, Fan X, Buriak JM. Nat Nanotechnol 2007;2:500;
(c) Kim DH, Kim SH, Lavery K, Russell TP. Nano Lett 2004;4:1841;
(d) Ross CA. Annu Rev Mater Res 2001;31:203.
[9] (a) Harrison C, Park M, Chaikin PM, Register RA, Adamson DH. J Vac Sci Technol B 1998;16:544;
(b) Chang SW, Chuang VP, Boles ST, Ross CA, Thompson CV. Adv Funct Mater 2009;19:2495;
(c) Guarini KW, Black CT, Zhang Y, Kim H, Sikorski EM, Babich IV. J Vac Sci Technol B 2002;20:2788.
[10] Fukukawa K, Zhu L, Gopalan P, Ueda M, Yang S. Macromolecules 2005;38:263.
[11] (a) Freer EM, Krupp LE, Hinsberg WD, Rice PM, Hedrick JL, Cha JN, et al. Nano Lett 2005;5:2014;
(b) Park OH, Cheng JY, Hart MW, Topuria T, Rice PM, Krupp LE, et al. Adv Mater 2008;20:738.
[12] Jung YS, Ross CA. Nano Lett 2007;7:2046.
[13] (a) Hirai T, Leolukman M, Hayakawa T, Kakimoto M, Gopalan P. Macromolecules 2008;41:4558;
(b) Hirai T, Leolukman M, Liu CC, Han E, Kim YJ, Ishida Y, et al. Adv Mater 2009;21:4334.
[14] Ito H, Knebelkamp A, Landmark SB, Nguyen CV, Hinsberg WD. J Polym Sci A Polym Chem 2000;38:2415.
[15] Hadjichristidis N, Iatrou H, Pispas S, Pitsikalis M. J Polym Sci A Polym Chem 2000;38:3211.
[16] Pitsikalis M, Siakali-Kioulafa E, Hadjichristidis E. J Polym Sci A Polym Chem 2004;42:4177.

Polymer 52 (2011) 91–97

Contents lists available at ScienceDirect

Polymer

journal homepage: www.elsevier.com/locate/polymer

A novel route for the preparation of thermally sensitive core-shell magnetic nanoparticles

Muhammad Omer [a], Sajjad Haider [a,b], Soo-Young Park [a,*]

[a] Department of Polymer Science, Kyungpook National University, #1370 Sankyuk-Dong, Buk-gu, Daegu 702-701, Republic of Korea
[b] Department of Chemical Engineering, College of Engineering, King Saud University, P.O. Box 800, Riyadh 11421, Saudi Arabia

ARTICLE INFO

Article history:
Received 26 August 2010
Received in revised form
29 October 2010
Accepted 6 November 2010
Available online 13 November 2010

Keywords:
MNPs
OA/MAH-β-CD coating
Poly(NIPAAm)

ABSTRACT

This study has developed a novel route for the synthesis of the thermoresponsive core-shell nanoparticles that consist of the magnetite core and the poly(N-isopropylacrylamide) (poly(NIPAAm) shell in aqueous medium. Magnetic nanoparticles (MNPs) were coated first with oleic acid (OA) and then vinyl carboxylic acid-β-cyclodextrin (MAH-β-CD). The OA-MNPs and the MAH-β-CD-MNPs showed monodispersion in n-hexane and aqueous medium, respectively. NIPAAms were successfully polymerized from the vinyl double bonds of the MAH-β-CD MNPs and cross-linked with N, N-methylenebisacrylamide (MBA) to make the stable thermoresponsive core-shell morphology with the MNP core and the poly (NIPAAm) shell (poly(NIPAAm)-MNP). The aqueous solutions dispersed with poly(NIPAAm)-MNPs showed magnetic heating due to a superparamagnetic property, and the poly(NIPAAm) shell shrank above its LCST temperature. The combination of these properties are potentially important in the targeted delivery of therapeutic agents *in vivo*, hyperthermic treatment of tumors, magnetic resonance imaging (MRI) as a contrasting agents, tissue repair, immunoassay, cell separation, biomagnetic separation of biomolecules, etc.

1. Introduction

In the past few years, considerable interest has been devoted toward the design of new drug delivery systems [1] with an aim to release drug at a controlled rate and desired time [2]. MNPs have shown great potential for use in biomedicine due to their ability to get close to biological entities such as cells, viruses, proteins, and genes with heating ability when exposed to a time-varying magnetic field [3]. Superparamagnetic MNPs with proved biocompatibility [4], have attracted significant attention as drug carriers in hyperthermia therapy [5], magnetic resonance imaging (MRI) as a contrasting agent, tissue repair, immunoassay, and cell separation procedures [6]. A wide range of methods were proposed for the synthesis of iron and iron-based MNPs. To produce MNPs in an aqueous medium considerable research has been done so far. Co-precipitation is a simple and suitable way to produce iron oxides from aqueous salt solutions of Fe^{+2}/Fe^{+3} by the addition of a base under inert atmosphere at room temperature or at elevated temperature. The size, shape, and composition of the magnetic nanoparticles much depend on the type of salts used (e.g. chlorides, nitrates, sulfates) the Fe^{+2}/Fe^{+3} ratio, the reaction temperature, the pH value and ionic strength of the media. With this synthesis, once the synthetic conditions are fixed, the quality of the magnetite nanoparticles is fully reproducible [7,8]. Barick et al. synthesized aqueous stable amine functionalized Fe_3O_4 magnetic nanoparticle nanoassemblies (MNNAs) by a single step process [9]. Park et al. synthesized MNPs by modified high temperature thermal decomposition method [10]. Popovici et al. used a laser pyrolysis technique to produce iron-based nanomaterials [11]. Choi et al. synthesized MNPs by chemical vapor condensation and pyrolysis of organometallic precursors of $Fe(CO)_5$ [12]. Xiaomin et al. developed a one-step route for the preparation of MNPs by reduction of iron salts with hydrazine hydrate in a strong alkaline solution [13]. Mera et al. synthesized MNPs by a colloidal method at room temperature without the use of surfactants [14].

MNPs generates heat *via* magnetic hysteresis loss, Neel-relaxation, and Brown-relaxation when exposed to a varying magnetic field [7] whereas thermally-responsive polymers can collapse or expand on heating [15]. Combining MNPs with thermally-responsive polymers represents an important class of composite responsive material with potential applications in biomedical fields, such as micro fluidic devices [16], pulsatile drug release systems [17–20], bioadhesion mediators [21,22] and motors/actuators and hyperthermia, etc.,

* Corresponding author. Tel.: +82 53 950 5630; fax: +82 53 950 6623.
E-mail address: psy@knu.ac.kr (S.-Y. Park).

0032-3861/$ – see front matter © 2010 Elsevier Ltd. All rights reserved.
doi:10.1016/j.polymer.2010.11.011

[23–25]. Poly(NIPAAm) collapses when the temperature increases above its LCST temperature. The phase transition in poly(NIPAAm) is due to the amphiphilic nature of the monomer unit itself. The balance between the hydrogen bonding interactions (between the hydrophilic −C═O and −NH groups) and the hydrophobic interactions (between pendant isopropyl groups) is instrumental in stabilizing poly(NIPAAm) [26]. The major problem associated with MNPs is that they are usually dispersed in organic media. Not many studies have been reported in the literature on the synthesis of MNPs dispersible in aqueous medium. To potentially use MNPs in biomedical fields and to understand their implications, it is essential to develop a generic synthetic route which can transfer MNPs from an organic phase to an aqueous-phase.

The present work has developed a novel route for the synthesis of the aqueous-phase dispersible MNPs coated with the thermoresponsive polymer poly(NIPAAm). It is believed that this novel route for the synthesis of the thermoresponsive core-shell MNPs in aqueous medium (Scheme 1) will prove a potential step forward in the use of these core-shell MNPs in robust controlled drug delivery [27], tissue repair, immunoassay, cell separation, biomagnetic separation of biomolecules, etc.

2. Experimental

2.1. Preparation of poly(NIPAAm)-MNPs

Ferric chloride hexahydrate ($FeCl_3 \cdot 6H_2O$), ferrous chloride tetrahydrate ($FeCl_2 \cdot 4H_2O$), sodium hydroxide (NaOH), oleic acid (OA), maleic anhydride (MAH), benzene, n-hexane, N, N-dimethyl formamide (DMF), acetone (C_3H_6O), trichloromethane ($CHCl_3$) potassium persulfate (KPS) were purchased from Duksan©. β-cyclodextrin (β-CD), N-isopropylacrylamide (NIPAAm) and N, N-methylenebisacrylamide (MBA) were purchased from Sigma Aldrich©. KPS and NIPAAm were recrystallized from water and a benzene/n-hexane (3:6 v/v) mixture, respectively. All the other chemicals were of analytical-reagent grade and were used as received. Magnetites were synthesized using the chemical co-precipitation method. Calculated amounts of $FeCl_2 \cdot 4H_2O$ and $FeCl_3 \cdot 6H_2O$ in grams were dissolved into deionized water. A three-necked flask was charged with 100 mL of 2 mol L^{-1} NaOH solution. The solution of Fe^{+2}/Fe^{+3} was added dropwise to the NaOH solution and the mixture solution was vigorously stirred over a period of 2 h. The resulting MNPs were washed repeatedly with deionized water, dried in a vacuum oven at 50 °C for 12 h, and stored in glass vials.

To obtain the OA-modified MNPs (OA-MNPs), calculated amounts of MNPs were sonicated in deionized water for 1 h. 13 mL of OA per gram of MNPs were added dropwise into the MNP-dispersed in water at 80 °C over the course of 2 h under vigorous mechanical stirring and nitrogen atmosphere. After modification, the MNPs were extracted into n-hexane and washed repeatedly with first water and then ethanol to remove the unreacted OAs [28]. The introduction of MAH in β-CD was performed according to the reported method as follows [29]. A 5.68 g of β-CD (0.005 mol) was dissolved in 30 mL DMF, and then 4.90 g of MAH (0.05 mol) was added to it. The solution was heated at 80 °C under vigorous stirring for 10 h. When the reaction was completed, the solution was cooled at room temperature and 30 mL of trichloromethane were added to it. White precipitates of MAH-β-CD were filtered, washed three times with acetone, dried in a vacuum oven at 40 °C for 24 h, and stored in a glass vial. For the coating of the OA-MNPs with MAH-β-CD (MAH-β-CD-MNPs), equal volumes of the OA-MNPs n-hexane solution (2 wt %) and the MAH-β-CD aqueous solution (2 wt %) were mechanically stirred at room temperature for 48 h. The OA-MNPs were transferred into the MAH-β-CD aqueous solution to make the MAH-β-CD-MNPs (the details will be discussed in the Results and discussion section) [30]. The MAH-β-CD-MNP powders were obtained by drying the aqueous part of the phase-separated n-hexane/water solution. The MAH-β-CD-MNPs were used to make the thermoresponsive core-shell MNPs that consist of the magnetite core and the poly(NIPAAm) shell (poly(NIPAAm)-MNPs) [31] by using a precipitation polymerization method in the presence of KPS (as an initiator) and MBA (as a cross-linker) under nitrogen atmosphere at 70 °C [32]. The mixture was cooled to room temperature and diluted with distilled water. The poly(NIPAAm)-MNPs were isolated from the solution by placing a magnet below the reaction vial. This process was repeated several times to remove the unreacted NIPAAm monomers and the separated poly(NIPAAm) chains from the MNPs.

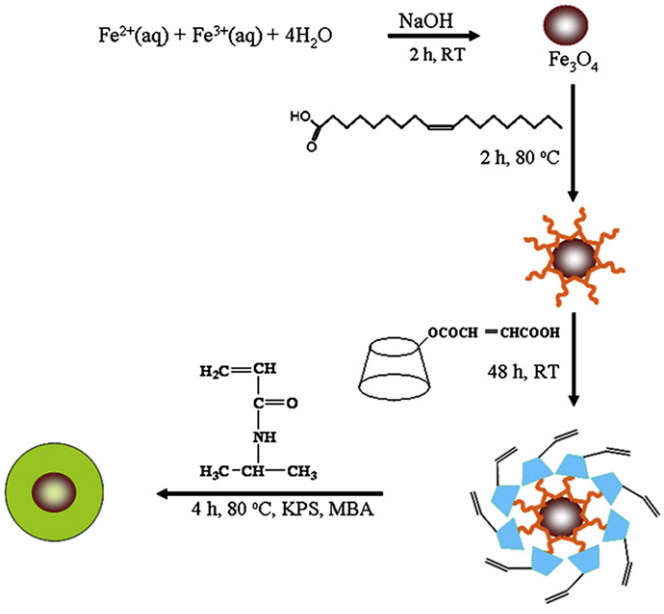

Scheme 1. Schematic for the preparation of the thermoresponsive MNPs coated with OA, MAH-β-CD and poly(NIPAAm) in sequence.

2.2. Characterization

FT-IR spectra were obtained with a Nicolet-560 spectrometer on KBr pellets. X-ray diffraction (XRD) patterns of the MNPs were recorded using an X-ray diffractometer (D/max-Ra, Rigaku, Japan) with Cu-Kα radiation at 42 kV and 109 mA. The crystal size of MNPs was calculated using a Scherrer's equation (Eq.(1)) where β is the width of the peak at half maximum intensity of a specific (hkl) diffraction peak in radians, K is a constant of 0.9, λ is the wavelength of the incident X-ray, θ is the half angle between the incident and diffracted beams (2θ), and L is the crystallite size.

$$L = \frac{K\lambda}{\beta \cos\theta} \quad (1)$$

Different sizes (diameter) of magnetic nanoparticles i.e., 8.6, 10.7, and 14.9 nm were obtained as mentioned in the Table 1 by using the Scherrer's equation along with their saturation magnetization (Ms) and coercivity (Hc). The magnetic properties of the synthesized MNPs were measured by using a lakeshore 7400 vibrating-sample magnetometer (VSM) at room temperature. The morphologies of the as-synthesized MNPs, the OA-MNPs, the MAH-β-CD-MNPs, and the poly(NIPAAm)-MNPs were studied using transmission electron microscopy (TEM, JEM-1OOCX, JEOL, Japan) with an accelerating voltage of 80 kV. Samples for TEM were

Table 1
Crystal size and magnetic properties of S1, S2, and S3 determined from X-ray and VSM. Particle size along with their standard deviation of OA coated, MAH-Beta-CD and PNIPAAm coated MNPS is given. M_s is saturation magnetization, the values for coercivity (Hc) (unit is Oersted (Oe) in cgs system and Amperes per meter (A/m) in SI system) are given.

Sample	Fe^{+2} (M)	Fe^{+3} (M)	Particle size (nm)	Standard deviation (sd)	Ms ($emu.g^{-1}$)	Hc (Oe)
S1	0.05	0.1	8.6	–	67.0	53.57
S2	0.1	0.2	10.7	–	67.0	57.40
S3	0.5	1.0	14.9	–	80.0	74.69
OA coated MNPs	–		36.0	16	–	
MAH-Beta-CD MNPs	–		66.0	18	–	
PNIPAAm-MNPs	–		87.0	33	–	

prepared by dispersing the MNPs in acetone at a very dilute concentration, dropping the dispersed solution on the carbon-coated copper grid, and then evaporating it. Poly(NIPAAm) was negatively stained with phosphotungstic acid in order to make the polymer part visible (Negative staining solution was prepared by dissolving 0.1 g (1 wt%) of sodium phosphotungstate (PTA) powder to 10 mL of distilled water in a shell vial). The pH of the solution was adjusted to 7.2–7.4 with the 0.1 N NaOH. The particle size of the OA-MNPs, MAH-β-CD-MNPs, and poly(NIPAAm)-MNPs were measured by taking into consideration upto two hundred (200) particles each from OA-MNPs, MAH-β-CD-MNPs, and poly (NIPAAm)-MNPs, determined their diameters and then find out their mean value (diameter) in nm along with the standard deviation as presented in Table 1. TGA thermograms were obtained in a nitrogen atmosphere at a heating rate of 10 °C/min between 25 °C and 600 °C using a TA 4000/Auto DSC 2910 System. The induction heating was measured with HF Induction Heater at 293 kHz and 2.5 kW with 4 mL and 2 g/L solutions in which the weight of the MNPs from TGA results were considered for calculating the concentration of the solutions in the case of the organic material coated MNPs such as the OA-MNP and the poly (NIPAAm)-MNP. The hydrodynamic radius (R_h) of the poly(NIPAAm)-MNPs was measured with a dynamic light scattering (DLS) method (ELS-8000, Photal Otsuka electronics) at a wavelength of 632.8 nm (helium neon laser) from 22 °C to 68 °C with an increment of 2 °C. The concentration of the poly(NIPAAm)-MNP solution was 0.06 wt%, and the sample was sonicated before DLS measurement.

3. Results and discussion

3.1. Preparation of MNPs

The MNPs were synthesized with different Fe^{+2}/Fe^{+3} ratios as given in Table 1. The Fe^{+2}/Fe^{+3} ratios of S1, S2, and S3 in mol L^{-1} (M) are 0.05/0.1, 0.1/0.2, and 0.5/1, respectively (As Fe_3O_4 can be synthesized by a molar ratio of 1:2 of ferrous and ferric salts, therefore, same ratio (1:2) has been kept for the concentration of

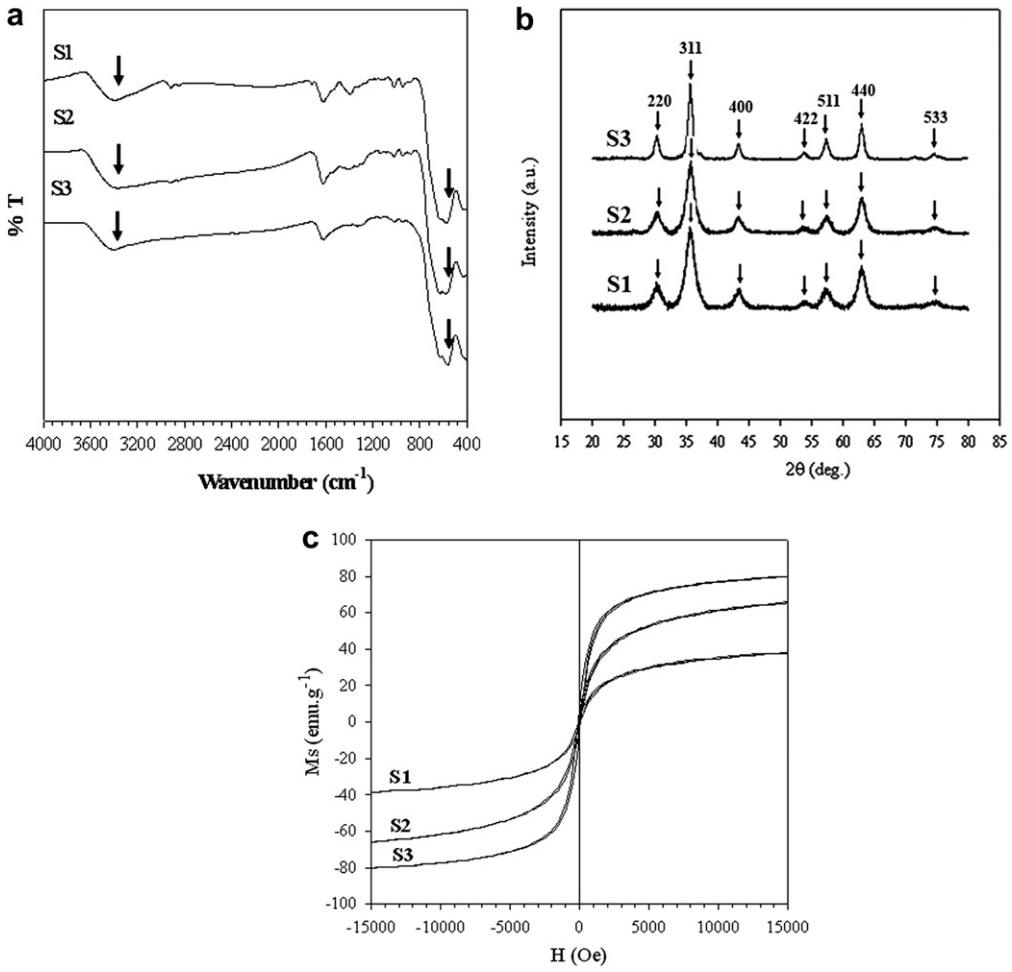

Fig. 1. (a) FT-IR spectra, (b) X-ray diffraction patterns, and (c) magnetization curves of the S1, S2 and S3 MNPs at room temperature where M_s is the saturation magnetization and H is the magnetic field strength.

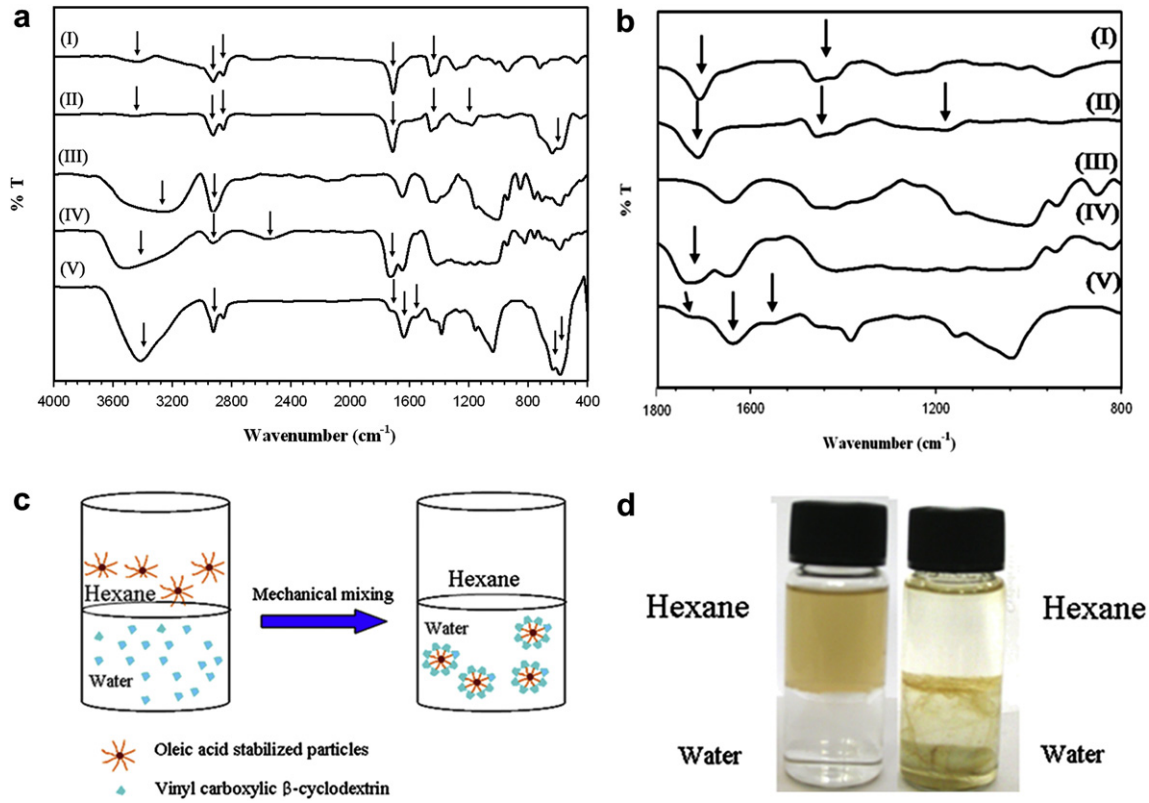

Fig. 2. (a) FT-IR spectra of the (I) OA, (II) the OA-MNPs, (III) the β-CD, (IV) the MAH-β-CD, and (V) the poly(NIPAAm)-MNPs, (b) FT-IR spectra of coated particles zoomed from 800 to 1800 cm^{-1} (c) the schematic, and (d) the digital image of the phase transfer of S3 MNPs from an organic phase to an aqueous-phase.

Fe^{+2} and Fe^{+3}). Fig. 1a shows the FT-IR spectra of the synthesized MNPs. As-synthesized MNPs showed bands at 570 and 630 cm^{-1} corresponding to the absorption bands of the Fe—O bond in the crystalline lattice, indicating that MNPs were successfully synthesized [33]. Fig. 1b represents the XRD patterns of the S1, S2, and S3 with seven strong Bragg diffraction peaks, which can be indexed as (220), (311), (400), (422), (511), (440), and (533) of magnetite (Fe_3O_4) in a cubic phase [34]. The crystal size of MNPs calculated from the most intense (311) peak increased with an increase in the Fe^{+2}/Fe^{+3} M ratio (Table 1). Due to concentration effects the particle size has increased, also the same concentration ratio (1:2) has been kept throughout the synthesis of MNPs as Molar ratio for Fe^{+2} and Fe^{+3} is also same as 1:2. Fig. 1c illustrates the magnetization curves of the S1, S2, and S3. The saturation magnetization (M_s) increased with an increase in the crystal size of the particles. The undetectable hysteresis and coercivity suggests that the synthesized MNPs have superparamagnetic properties. The S3 MNPs showed higher M_s compared to S1 and S2, therefore, S3 MNPs were used in this article.

3.2. Structure of MNPs

Fig. 2a shows the FT-IR spectra of the OA, the OA-MNPs, the β-CD, the MAH-β-CD, and the Poly(NIPAAm)-MNPs. The FT-IR spectrum of the OA showed bands at2924, 2854, 3500, 1708, 1453 and 1285 cm^{-1}, which were attributed to the asymmetric CH_2 and symmetric CH_2 stretching, O—H in plan bending, and C=O and C—O stretch [35]. The OA-MNPs spectrum showed bands at 2922, 2852, 1187 cm^{-1} and reduced band at 3500 cm^{-1} as well as the MNP bands (the absorption bands of the Fe—O bond, Fig. 1a) at 570 and

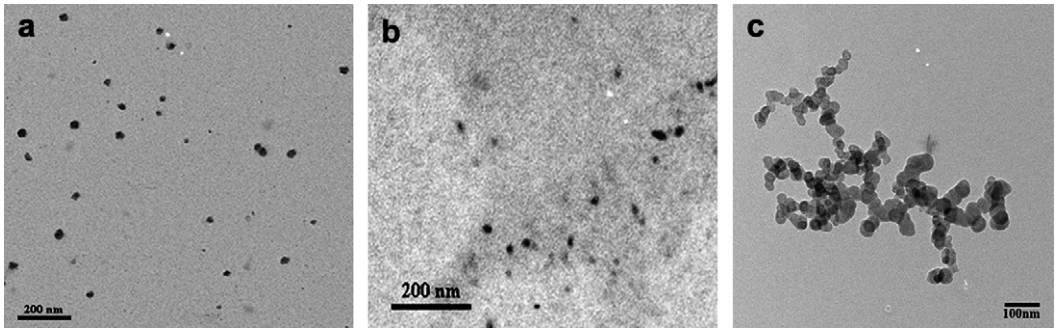

Fig. 3. TEM micrographs of (a) OA-MNPs, (b) MAH-β-CD-MNPs, and (c) poly(NIPAAm)-MNPs. The samples were prepared by dispersing OA-MNPs in n-hexane and MAH-β-CD-MNPs and poly(NIPAAm)-MNPs in distilled water. The dispersed samples were dropped on to a graphite coated copper grid and the solvent was allowed to evaporate. Poly (NIPAAm)-MNPs were stained with phosphotungstic acid.

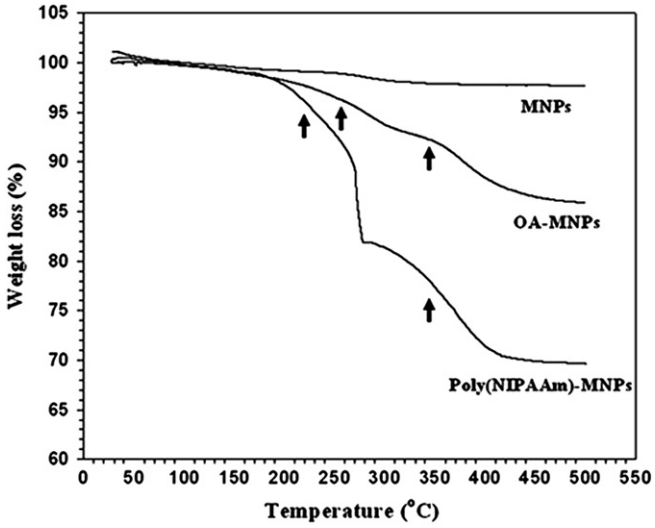

Fig. 4. TGA thermograms of the MNPs, the OA-MNPs and the poly(NIPAAm)-MNPs.

630 cm^{-1}. The shift in the bands to the lower wave numbers 2922, 2852 and 1187 cm^{-1}, the reduction of 3500 cm^{-1} and broadening of 1453 cm^{-1} bands might be attributed to the fact that OA molecules in the adsorbed state were subject to the field of solid surface and that hydrocarbon chains in the monolayer surrounding the MNPS were in closed-packed crystalline state [35]. The results confirm that OA chemisorbed onto the surface of the MNPs, although the consistent C═O stretching band at 1712 cm^{-1} might be due to some uncoated OA molecules [36]. In the spectra of β-CD and MAH-β-CD, the −OH band at 3200 cm^{-1} in β-CD was shifted to 3500 cm^{-1} in MAH-β-CD as a result of the introduction of MAH [29]. The intensity of the $-CH_2O-H$ vibration band around 2900 cm^{-1} in β-CD was reduced in MAH-β-CD due to the nucleophilic reaction of the hydroxyl oxyen in $-CH_2O-H$ groups with the carbonyl carbon of MAH [37]. New −COOH and C═O stretching bands at 2560 and 1720 cm^{-1}, respectively, also appeared in MAH-β-CD. The shift of −OH band, the reduction in intensity of the $-CH_2-OH$ stretching bands, and the appearance of new −COOH and C═O bands in the spectrum of MAH-β-CD confirmed the successful synthesis of MAH-β-CD. The FT-IR spectrum of the poly(NIPAAm)-MNP showed the characteristic poly(NIPAAm) bands (at 3300 cm^{-1} (broad secondary NH amide), 2971-2861 cm^{-1} (CH group in isopropyl group), 1649 cm^{-1} (strong C═O amide), 1541 cm^{-1} (strong NH amide II), 1458 cm^{-1} ($-CH_2$ scissoring vibration), 1385 cm^{-1} ($-CH_3$ bending vibration), 1365 cm^{-1} (C−H bending vibration), and 1170 cm^{-1} (bending vibration)) as well as the characteristic hydrolyzed MAH (~1707 cm^{-1}) and the Fe−O bands (570 cm^{-1}). All these bands confirmed the successful synthesis of poly(NIPAAm)-MNP. Fig. 2 shows the schematic (Fig. 2b) and the digital image (Fig. 2c) of the MNPs in the n-hexane/water mixture solution before and after mechanical stirring during which the yellowish color gradually disappeared from the top n-hexane layer, then the aqueous layer became yellowish, and finally the bottom layer ended up as a translucent suspension. This phase transfer did not

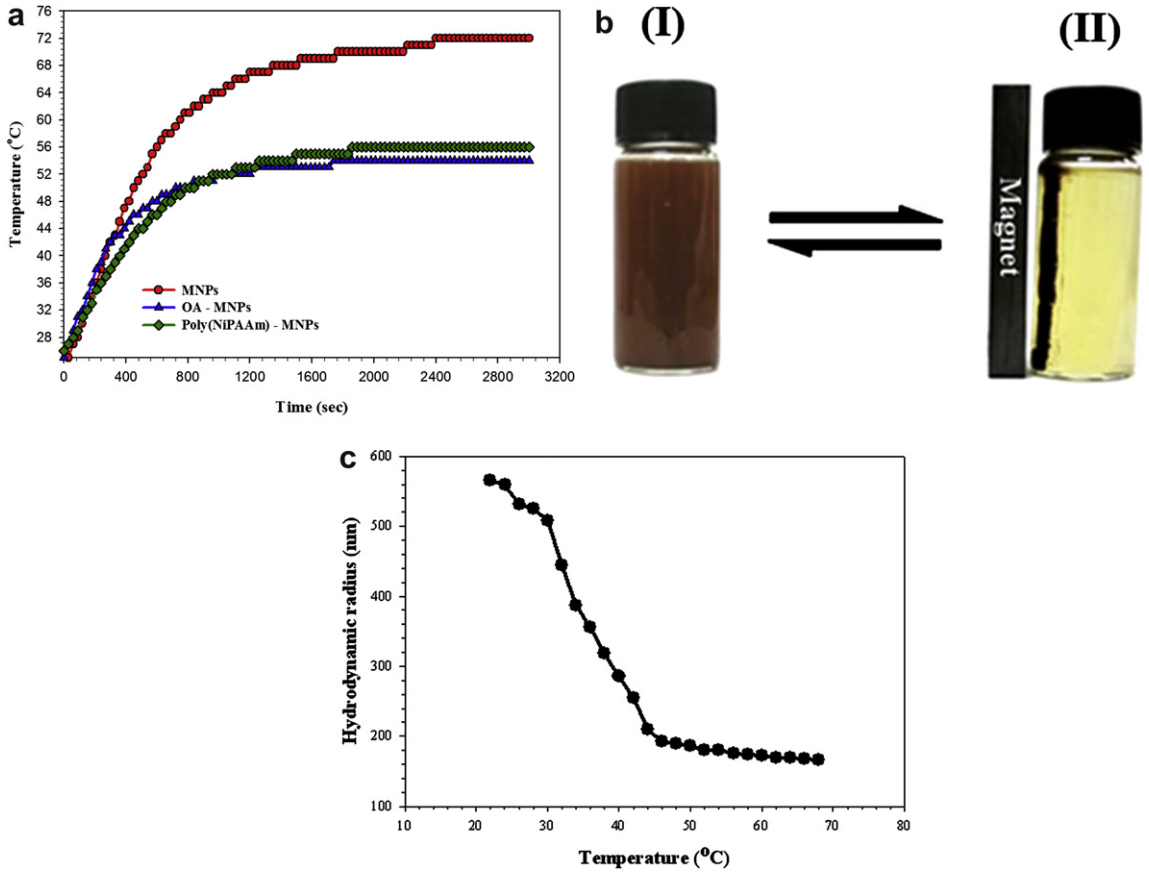

Fig. 5. (a) The temperature changes of the MNP (in 1 M HNO_3), the OA-MNP (in hexane), and the poly(NIPAAm)-MNP (in water) in the oscillating magnetic field as a function of time, (b) digital images of poly (NIPAAm)-MNPs in aqueous solution (I) without and (II) with magnet, and (c) hydrodynamic radii of the poly (NIPAAm)-MNPs dispersed in distilled water.

occur in a control experiment without MAH-β-CD, indicating that the MAH-β-CD formed an inclusion complex with the OA, and the hydrophilic groups in the β-CD made the β-CD-MNPs hydrophilic and dispersible in aqueous medium [30].

Fig. 3 shows the TEM micrographs of the dispersed OA-MNPs in n-hexane, β-CD-MNPs and poly(NIPAAm)-MNPs in distilled water. The narrowly distributed mean diameters and standard deviation values of OA-MNPs, β-CD-MNPs and poly(NIPAAm)-MNPs calculated from TEM are tabulated in Table 1. OA-MNPs (Fig. 3a) and β-CD-MNPs (Fig. 3b) showed mono-dispersion in n-hexane and distilled water, respectively although some aggregations between synthesized poly(NIPAAm)-MNPs were observed. This aggregation could happen during the evaporation of the solvent on the TEM grids although there were also possibilities of the aggregated form during the synthesis. A similar morphology for the polymer-coated MNPs was reported by Wang et al. [38].

Fig. 4 shows the TGA thermograms of the MNPs, the OA-MNPs, and the poly (NIPAAm)-MNPs. The MNPs did not show any weight loss whereas the OA-MNPs and the poly(NIPAAm)-MNPs showed step-wise weight loss as temperature increased. The weight losses of the OA-MNPs at ~250 and ~350 °C might be due to the thermal degradations of the free (1.35 mg) and coated OAs (2.86 mg), respectively and those of the poly(NIPAAm)-MNPs at ~220 and ~350 °C might be due to the thermal degradations of the MAH-β-CD inclusion complex (0.71 mg) and the poly (NIPAAm) (1.59 mg), respectively [39,40]. These results also indicate the successful polymerization of poly(NIPAAm) onto the MNP surface.

3.3. Properties of MNPs

Fig. 5a shows the temperature changes of the MNP (in 1 M HNO_3), the OA-MNP (in hexane), and the poly(NIPAAm)-MNP (in water) in the oscillating magnetic field as a function of time. The temperature linearly increased initially and then saturated as time increased further. The temperature increase in the solutions indicates that the MNP particles have an ability of magnetic heating when exposed to an alternating magnetic field [7,41]. The saturated temperatures of the MNPs, the OA-MNPs, and the poly(NIPAAm)-MNPs solutions were 65, 49, and 52 °C, respectively. The decrease of the saturation temperatures of the OA-MNPs and the poly (NIPAAm)-MNPs solutions as compared to that of the MNP might be due to low electrical conductivity of the organic shell (OA and poly(NIPAAm)) [42]. Fig. 5b shows the reversible attraction of the poly(NIPAAm)-MNPs toward a magnet. The poly(NIPAAm)-MNPs were homogeneous dark brown without magnet (Fig. 5b(I)). However, the poly(NIPAAm)-MNPs were attracted toward the magnet when it was close to the wall of the vial (Fig. 5b(II)) indicating a superparamagnetic property for the poly(NIPAAm)-MNPs. Superparamagnetic and magnetic heating properties of the poly (NIPAAm)-MNPs are critical for their applications in biomedical [43] and bioengineering fields, because they prevent MNPs from aggregation and enables them to redisperse when the magnetic field is removed [44]. Fig. 5c shows the thermoresponsive behavior of the poly(NIPAAm)-MNPs. The decrease in the hydrodynamic radii (R_h) happened at ~34 °C (LCST temperature of poly(NIPAAm)) [45]. The decrease in radius at elevated temperature was due to the increased hydrophobicity of the poly(NIPAAm) segments, which led to the collapse of polymer chains and shrinkage of the gel network. Thus, this result indicates that the method developed in this article might be one of the novel ways of synthesizing a thermoresponsive poly(NIPAAm)-MNPs which shows magnetic heating by MNPs in the core causing the shrinkage of the poly(NIPAAm) chains in the shell.

4. Conclusion

This study has successfully prepared MNPs *via* a co-precipitation method in order to attach the poly(NIPAAm) chains on the MNPs to make the thermoresponsive core-shell MNPs. The MAH-modified β-CD where β-CD made an inclusion complex with OA which was first coated on MNP was introduced. The double bonds of the MAH in (MAH-β-CD) initiated the polymerization of NIPAAm and the poly (NIPAAm) chains in the shell were cross-linked with MBA. It is theorized that this novel approach for the preparation of the aqueous-dispersible thermoresponsive MNPs could be a step forward in their use in the fields of biomedical and bioengineering.

Acknowledgements

This work was supported by the National Research Foundation of Korea Grant (2010-0014822) funded by the South Korean Government.

References

[1] Kim JH, Lee TR. Drug Dev Res 2006;67(1):61–9.
[2] Zhang J, Misra RDK. Acta Biomater 2007;3(6):838–50.
[3] Pankhurst QA, Connolly J, Jones SK, Dobson J. J Phys D Appl Phys 2003;36 (13):R167–81.
[4] Schwertmann U, Cornell RM. Iron oxides in the laboratory preparation and characterization. 2nd ed. Weinheim, Cambridge: VCH; 1991.
[5] Meyer DE, Shin BC, Kong GA, Dewhirst MW, Chilkoti A. J Controlled Release 2001;74(1–3):213–24.
[6] Kim DH, Lee SH, Im KH, Kim KN, Kim KM, Shim IB, Lee MH, Lee YK. Curr Appl Phys 2006;6(S1):e242–6.
[7] Lu AH, Salabas EL, Schuth F. Angew Chem Int Ed 2007;46(8):1222–44.
[8] Ana CA, Roque ACA, Bicho A, Batalha IL, Cardoso AS, Hussain A. J Biotechnol 2009;144(4):313–20.
[9] Barick KC, Aslam M, Lin YP, Bahadur D, Pottumarthi V, Prasadd PV, et al. J Mater Chem 2009;19(38):7023–9.
[10] Park J, An K, Hwang Y, Park JG, Noh HJ, Kim JY, et al. Nat Mater 2004;3(12):891–5.
[11] Popovici E, Dumitrache F, Morjan I, Alexandrescu R, Ciupina V, Prodan G, et al. Appl Surf Sci 2007;254(4):1048–52.
[12] Choi CJ, Tolochko O, Kim BK. Mater Lett 2002;56(3):289–94.
[13] Xiaomin N, Xiaobo S, Huagui Z, Dongen Z, Dandan Y, Qingbiao Z. J Crystal Growth 2005;275(3–4):548–53.
[14] Mera IM, Pesqueira MEE, Hernández RP, Alatorre JA. Mater Lett 2007;61 (23–24):4447–51.
[15] Owens III DE, Jian Y, Fang JE, Slaughter BV, Chen YH, Peppas NA. Macromolecules 2007;40(20):7306–10.
[16] Barker SLR, Ross D, Tarlov MJ, Gaitan M, Locascio LE. Anal Chem 2000;72 (24):5925–9.
[17] Kikuchi A, Okano T. Adv Drug Deliv Rev 2002;54(1):53–77.
[18] Li SK, D'Emanuele A. J Controlled Release 2001;75(1–2):55–67.
[19] Kost J, Langer R. Adv Drug Deliv Rev 2001;46(1–3):125–48.
[20] Peppas N. Curr Opin Colloid Interface Sci 1997;2(5):531–7.
[21] Ista LK, Lopez GP. J Ind Microbiol Biotechnol 1998;20(2):121–5.
[22] Yamato M, Konno C, Utsumi M, Kikuchi A, Okano T. Biomaterials 2002;23 (2):561–7.
[23] Hoffmann J, Plotner M, Kuckling D, Fischer WJ. Sens Actuators A 1999;77 (2):139–44.
[24] Urry DW. Biopolymers 1998;47(2):167–78.
[25] Tabatabaei SN, Lapointe J, Sylvain Martel J, Martel S. International Conference on Intelligent Robots and Systems, art. no. 5354162; 2009: 546–551.
[26] Sun T, Wang G, Feng L, Liu B, Ma Y, Jiang L, et al. Angew Chem Int Ed 2004;43 (3):357–60.
[27] Munish C, Zhengwei M, Dayang W. J Biomed Nanotechnol 2009;5(6):652–68.
[28] Hong MK, Park BJ, Choi HJ. J Phys Conf Ser 2009;149:012055.
[29] Liu YY, Fan XD. Polymer 2002;43(18):4997–5003.
[30] Wang Y, Wong JF, Lin XZ, Yang H. Nano Lett 2003;3(11):1555–9.
[31] Chakraborty S, Bishnoi SW, Pérez-Luna VH. J Phys Chem C 2010;114 (13):5947–55.
[32] Deng Y, Yang W, Wang C, Fu S. Adv Mater 2003;15(20):1729–32.
[33] Liu X, Kaminski MD, Guan Y, Chen H, Liu H, Rosengart AJ. J Magn Magn Mater 2006;306(2):248–53.
[34] Han L, Li S, Yang Y, Zhao F, Huang J, Chang J. J Magn Magn Mater 2007;313 (1):236–42.
[35] Zhang L, He R, Gu HC. Appl Surf Sci 2006;253(5):2611–7.
[36] Zhao SY, Lee DK, Kim CW, Cha HG, Kim YH, Kang YS. Bull Korean Chem Soc 2006;27(2):237–42.
[37] Muller G, Schopper C, Vos H, Kharazipour A, Polle A. BioResources 2009; 4(1):49–71.

[38] Wang Y, Li B, Zhou Y, Jia D. Nanoscale Res Lett 2009;4(9):1041–6.
[39] Song LX, Teng CF, Xu P, Wang HM, Zhang ZQ, Liu Q. J Incl Phenom Macrocycl Chem 2008;60:223–33.
[40] Schild HG. J Polym Sci Part A Polym Chem 1996;34(11):2259–62.
[41] Kneller E. Theory of the magnetization curve of small crystals. In: Wijn HPJ, editor. Encyclopedia of physics, ferromagnetism, vol. XVIII/2. New York: Springer; 1966. p. 438–544.
[42] Hergt R, Andr W, D'Ambly CG, Hilger I, Kaiser WA, Richter U, et al. IEEE Trans Magn 1998;34:3745–54.
[43] Yu F, Yang VC. J Biomed Mater Res A 2010;92A(4):1468–75.
[44] Mary M. In: Hafeli U, Schutt W, Zborowski M, editors. Scientific and clinical applications of magnetic carriers. New York: Plenum Press; 1997. p. 303.
[45] Jie JX, Liu L, Xie R, Hui N, Yin CL. Polymer 2009;50(3):922–9.

Polymer 52 (2011) 98–106

Contents lists available at ScienceDirect

Polymer

journal homepage: www.elsevier.com/locate/polymer

Radiation-induced graft polymerization of functional monomer into poly(ether ether ketone) film and structure-property analysis of the grafted membrane

Shin Hasegawa [a], Shuichi Takahashi [a], Hiroki Iwase [b], Satoshi Koizumi [b], Norio Morishita [a], Ken Sato [c], Tadashi Narita [c], Masato Ohnuma [d], Yasunari Maekawa [a,*]

[a] Environment and Industrial Materials Research Division, Quantum Beam Science Directorate, Japan Atomic Energy Agency (JAEA), 1233 Watanuki, Takasaki, Gunma 370-1292, Japan
[b] The Advanced Science Research Center, Japan Atomic Energy Agency (JAEA), Tokai, Ibaraki 319-1195, Japan
[c] Graduate School of Engineering, Saitama Institute of Technology, 1690 Fusaiji, Fukaya, Saitama 369-0203, Japan
[d] Quantum Beam Center, National Institute for Materials Science (NIMS), 1-2-1 Sengen, Tsukuba, Ibaraki 305-0047, Japan

ARTICLE INFO

Article history:
Received 29 July 2010
Received in revised form
21 October 2010
Accepted 6 November 2010
Available online 13 November 2010

Keywords:
Graft polymerization
Radiation
Fuel cell

ABSTRACT

Radiation-induced graft polymerization of sulfo-containing styrene derivatives into crystalline poly(ether ether ketone) (PEEK) substrates was carried out to prepare thermally and mechanically stable polymer electrolyte membranes based on an aromatic hydrocarbon polymer, so-called "super-engineering plastics". Graft polymerization of the sulfo-containing styrene, ethyl 4-styrenesulfonate (E4S) into a high crystalline PEEK substrate (degree of crystallinity: 32%) hardly progressed, whereas graft polymerization into a low crystalline PEEK substrate (degree of crystallinity: 11%) gradually progressed, achieving a grafting degree of more than 50% after 72 h. Oxygen radicals appeared in the ESR spectra of irradiated PEEK films, indicating that graft polymerization initiates from the phenoxy radicals generated by scission of PEEK main chains and proceeds so as to yield block type grafts. The PEEK-based polymer electrolyte membrane (PEM) converted by aqueous hydrolysis of grafted films exhibited mechanical strength (100 MPa), being 88% of the original PEEK substrates. These mechanical properties of PEEK-based PEM are much higher than those of graft-type fluorinated PEM reported previously and almost three times higher than that of Nafion (35 MPa). Wide- and small-angle X-ray scattering (WAXS and SAXS) indicated that the graft polymerization was accompanied with recrystallization of the amorphous phase of PEEK substrate, the well known solvent-induced recrystallization of amorphous PEEK solids, to form a weak lamellar structure with 8 nm spacing. Complementary SAXS and small-angle neutron scattering (SANS) observations clearly showed that the graft-type PEEK membranes possessed ion channel domains with the average distance of 13 nm, being larger than that of Nafion. Furthermore, there was a micro-structure in the ion channels with the average distance of 1.8 nm.

1. Introduction

A pre-irradiation grafting method, in which polymer substrates are first irradiated under inert gas and then immersed in a monomer solution to commence graft polymerization of the monomer into the substrates, is a fascinating technique for direct introduction of a new functional polymer phase as a grafting chain (grafts) into polymer films serving as a substrate which allows those films to retain their characteristics such as thermal stability, mechanical strength, electronic properties, and crystallinity[1–4]. One of the unique characteristics of the pre-irradiation grafting method is the graft polymerization of solid polymer films, i.e. "solid state polymerization". Whereas in general, a radical in a solution has a short lifetime, the polymerization initiating and propagating species in solid films are long lived radicals (occasionally, days and weeks), owing to suppression of termination reactions in the polymer matrix, resulting in the formation of large numbers of functional polymer chains in the solid polymer films. It is widely accepted that in graft polymerization into polyethylene (PE) [5,6], polypropylene (PP), poly(tetrafluoroethylene) (PTFE) [2,7], poly(tetrafluoroethylene-co-hexafluoropropylene) (FEP) [1,8], and poly(vinylidene fluoride) (PVDF) [9,10], long lived free radicals in crystalline phases meet monomers, which have diffused through amorphous phases, at crystalline/amorphous interfaces of the solid films to initiate radical graft polymerization in an amorphous phase or at interfaces.

* Corresponding author.
E-mail address: maekawa.yasunari@jaea.go.jp (Y. Maekawa).

0032-3861/$ – see front matter © 2010 Elsevier Ltd. All rights reserved.
doi:10.1016/j.polymer.2010.11.009

The radiation technique has been widely applied to the preparation of a high performance fuel cell PEM for mobile electricity, vehicles, and a domestic co-generation system, in which grafts containing an ion conducting (electrolyte) group such as sulfonic acid are introduced into fluorinated polymer films such as FEP, PTFE, ETFE, and PVDF, which act as hydrophobic matrix in PEM [2–4,11–15]. This graft-type PEM has the advantages of resistance to methanol and low production costs, which are the most severe problems for fully fluorinated PEMs such as Nafion. However, even when grafted, the fluorinated PEM have drawbacks such as less mechanical strength at higher operating temperatures and unsatisfactory gas barrier properties. In this connection, a sulfonated form of aromatic hydrocarbon polymers, so-called "super-engineering plastics" including poly(ether ether ketone) (PEEK), polyimide (PI), and poly(sulfone) (PSU) have been attracting attention owing to their excellent mechanical properties at elevated temperatures as well as excellent barrier properties against fuels (methanol, H_2) and oxygen [16–20].

However, these super engineering plastic films also have high chemical resistance; thus, it is difficult to introduce grafting monomers into the films. Accordingly, as far as we know, there have been very few examples of radiation grafting into these super engineering plastic films [21]. Recently, we succeeded in radiation-induced grafting of styrene into a crystalline PEEK film with grafting degrees of more than 60%, and found that the graft polymerization of styrene proceeds in the amorphous region of PEEK without destroying the crystalline region because polystyrene grafts have similar hydrocarbon structures to the PEEK substrate, so that these grafts are compatible to the amorphous phase of the PEEK films [22,23]. However, the sulfonation of the polystyrene grafts with chlorosulfonic acid in a dichloroethane solution proceeded not only at the graft layers but also at the crystalline and amorphous phases of PEEK, making PEEK-based electrolyte membranes with conductivity of more than 0.01 S/cm subject to severe deformation due to higher water uptake.

In this paper, to prevent the damage to PEEK substrate during the sulfonation process, graft polymerization of the sulfo-containing styrene, ethyl 4-styrenesulfonate (E4S) into two PEEK substrates with different crystallinity (degree of crystallinity: 32 and 11%) by the pre-irradiation grafting method was examined, because with E4S the grafted PEEK films could be converted to PEEK-based PEM merely by hydrolysis of the sulfonic acid ester in the precursor grafts. The radical polymerization of E4S proceeds with faster polymerization kinetics than that of styrene [24]. Since this is the first clearly successful radiation-induced graft polymerization into a "super-engineering plastic", we investigated the detailed mechanisms of this graft polymerization, including the morphological changes (crystallinity and phase separation) of crystalline PEEK using differential scanning calorimetry (DSC), thermogravimetry (TGA), wide angle X-ray scattering (WAXS), and the initiation species using electron spin resonance (ESR). Furthermore, small-angle X-ray and neutron scattering experiments (SAXS and SANS) with PEEK substrates, grafted PEEK, and PEEK-based PEM were carried out, since the obtained PEM must have nano- to meso-scale hierarchical structures.

2. Experimental section

2.1. Materials

PEEK films of 25 μm in thickness with 11% and 32% crystallinity (VICTREX PEEK amorphous (2000-25, density: 1.26 g/cm^3) and crystalline (1000-25, density: 1.32 g/cm^3)) were purchased from Victrex plc, Japan and used as a substrate. Ethyl 4-styrenesulfonate (E4S) was purchased from Tosoh Co., Japan (>95%) and used without further purification. Acetone and 1, 4-dioxane (dioxane) were purchased from Wako Pure Chemical Industries, Ltd., Japan. Sodium chloride (NaCl), sodium hydroxide (NaOH), and hydrochloric acid (HCl) used for titrimetric analysis were purchased from Wako Pure Chemical Industries, Ltd, Japan.

2.2. Graft polymerization

PEEK films were cut into 2 × 3 cm rectangles and wiped with acetone to remove impurities on the film surface. The PEEK films were irradiated in a glass ampoule in an argon atmosphere at room temperature using ^{60}Co γ-rays with doses ranging from 30 to 200 kGy (dose rate: 10 kGy/h). Then, the sample was immersed in 15 ml of an E4S solution of dioxane (1/1 v/v) at 80 °C under an argon atmosphere for graft polymerization. After graft polymerization, the grafted PEEK films were taken out and washed with acetone. Then, the samples were immersed in a large amount of acetone at room temperature overnight to remove the homo-polymers and residual monomers. We calculated the grafting degree from the following equation, [GD (%)] = 100 × (W_g–W_0)/W_0, where W_0 and W_g are the film weights before and after graft polymerization, respectively. Finally, the grafted films were hydrolyzed by immersing in water at 95 °C for 24 h to prepare hydrolyzed PEEK membranes (PEEK-based PEM).

2.3. Electrolyte properties of PEEK-based PEM

The degree of hydrolysis and ion exchange capacity (IEC) of the samples were determined by titrimetric analysis. Dry hydrolyzed membranes containing a protonic form of sulfonic acid were immersed in 20 ml of an aqueous 3 M NaCl solution and equilibrated for 24 h. The remaining solutions were titrated with a 0.02 M NaOH solution using an automatic titrator, HIRANUMA COM-555. The IEC of the membrane was calculated using titration result with the following equation:

$$\mathrm{IEC} = \frac{0.02 \times \mathrm{V_{NaOH}}}{\mathrm{W}_d} \tag{1}$$

where V_{NaOH} (ml) is the titer of a 0.02 M NaOH solution and W_d is the dry weight of a hydrolyzed membrane in a protonic form. The degree of hydrolysis (%) is defined as the molar ratio of sulfonic acid to monomer units of the grafted polymer chain. The sulfonation degree (SD) is calculated by the following equation:

$$\mathrm{SD}(\%) = \frac{0.02 \times \mathrm{V_{NaOH}}}{\mathrm{W}_g \times \frac{\mathrm{GD}}{(100+\mathrm{GD})}/\mathrm{M}} \times 100 \tag{2}$$

where GD is the grafting degree and M is the molecular weight of E4S (212.3).

The proton conductivity of hydrated membranes was measured by impedance spectroscopy at room temperature using a Solartron 1269 analyzer. The hydrolyzed samples were hydrated in water at room temperature for 24 h, and clamped between two platinum-plate electrodes after wiping off excess water on the membrane surface. The proton conductivity, σ along the perpendicular direction of membranes is calculated from the obtained impedance, R (Ω) by the following equation:

$$\sigma = \frac{d}{\mathrm{RS}} \tag{3}$$

where d (cm) is the membrane thickness and S (cm^2) is the contact area of two electrodes.

The water uptake of hydrolyzed membranes was calculated from the following equation, [water uptake (%)] = 100 × (W_w–W_d)/W_d, where W_w is the weight of a membrane after immersing the dry

membrane in deionized water at room temperature for 24 h and W_d is the weight of the dried membrane.

2.4. Characterization of E4S-grafted PEEK and PEEK-based PEM

The membranes were embedded in epoxy resin, polished using microtome, and coated with carbon. The cross-section of the samples was measured by a JEOL JSM-5600 scanning electron microscope (SEM). The depth profiles of sulfur atoms of the sulfonic acid group in the membrane perpendicular direction were measured by SEM connected with an energy distribution X-ray spectroscopy (EDS) and operated at a voltage of 15 kV. Differential scanning calorimetry (DSC) was performed using Thermo Plus2/DSC8230 with the specimen of ca. 5 mg at a heating rate of 10 °C/min. Thermo gravimetric analysis (TGA) was performed using a Thermo Plus2/TG-DTA (Rigaku, Japan). In TGA measurement, the specimen of ca. 5 mg was initially heated at a heating rate of 10 °C/min to the temperature of 200 °C. After cooling down, they were reheated at a rate of 10 °C/min to eliminate absorbed water and the data from the second scan were used. The nitrogen flow rates through the specimen were 100 ml/min for the DSC and TG analysis. Wide angle X-ray scattering (WAXS) experiment was undertaken with a Rigaku CN 2013 spectrometer (*Cu-Kα*). The degree of crystallinity (DC) of PEEK substrates was calculated using the following equation: $DC\ (\%) = \Delta H_m \times (100 + GD)/(100 \times \Delta H_{m,100})$, where, ΔHm is the heat of melting of PEEK films which is proportional to the area under the melting peak and $\Delta H_{m,100}$ is the heat of melting of 100% crystalline PEEK, 130 J/g [25]. The mechanical properties were determined using an STA-1150 universal testing instrument (A&D Co., Ltd, Japan) at a constant crosshead speed of 50 mm/min. Five specimens with a dumbbells shape were prepared according to ASTM D 1882-L and were used for the measurement.

2.5. ESR measurement of original and irradiated PEEK substrates

ESR spectra were measured under Ar atmosphere at room temperature with a JEOL ESR spectrometer, JES-FSE60 with a modulation frequency of 9.2 GHz and a power of 1 mW. PEEK, Kapton (DuPont, PI, 25 μm in thickness), polyethersulfone (Sumitomo Bakelite, PES, 25 μm), and polyphenylenesulfide (TORAY, PPS, 50 μm) films were set in the ESR quartz tube connected to a long glass tube. The samples were degassed before sealing off and irradiated with 55 kGy at room temperature. The irradiated films were moved to upper part of the glass tube and the irradiated quartz tube was annealed with flame to quench the ESR signal of quartz (SiO_2).

Then, the irradiated films were moved back to the original position to measure ESR spectrum at room temperature. The amount of radicals was obtained by integration of the ESR spectra on the basis of standard DPPH (1, 1-diphenyl-2-picrylhydrazyl) intensity.

2.6. SANS and SAXS measurements

SANS measurements were performed on focusing and polarized neutron small-angle scattering spectrometer (SANS-J-II) at the research reactor JRR-3 in Japan Atomic Energy Agency (JAEA) at Tokai, Japan [26]. The wavelength (λ) of the incident neutron was $\lambda = 0.65$ nm with a wavelength resolution $\Delta\lambda/\lambda = 13\%$. The SANS profiles were obtained with a sample-to-detector distances of 10 and 2.5 m, covering from $Q = 0.04–1\ nm^{-1}$, where Q is a magnitude of scattering vector given by $Q = (4\pi/\lambda)\sin(\theta/2)$ with θ being scattering angle. The scattering profiles were detected with a two-dimensional position sensitive detector. The exposure time for an original PEEK, a grafted PEEK, and PEEK-based PEM were 4, 1, 1 h, respectively. The two-dimensional data was corrected for detector efficiency, instrumental background on a pixel-to-pixel basis. After circular averaging, we converted scattering intensity to the absolute intensity per a sample volume by secondary standard of irradiated aluminum. All SANS measurements were performed at ambient temperature (25 ± 0.5 °C).

SAXS experiments were carried out on two in-house SAXS spectrometers (NIMS-SAXS-II and NIMS-SAXS-III) in the National Institute of Materials Science (NIMS), Tsukuba, Japan [27], in order to cover wide Q range from 0.07 to 12 nm^{-1}. The NIMS-SAXS-II consists of 18-kW rotating-anode X-ray generator with a conformal mirror system to obtain Mo–Kα beam ($\lambda = 0.07$ nm) (Nanoviewer, RIGAKU, Tokyo, Japan), vacuum flight path, and multi-wire two-dimensional position sensitive proportional counter with active area of 23 × 23 cm^2 (Hi-Star, Bruker Optik GmbH, Germany), respectively. A sample-to-detector distances was 30 cm, covering Q range of $0.7 < Q < 12\ nm^{-1}$. NIMS-SAXS-III is NanoSTAR SAXS system (Bruker Optik GmbH, Germany), which is set up to obtain Cr-Kα beam ($\lambda = 0.23$ nm). A sample-to-detector distance was 100 cm covering Q range of $0.07 < Q < 1.5\ nm^{-1}$. The SAXS measurements were conducted with varying exposure time in the range of 0.5–12 h. The SAXS profiles were circularly averaged, and then were corrected for the absorption of the sample, instrumental background. The absolute SAXS intensity was obtained by using the secondary standard of glassy carbon [27].

3. Results and discussion

3.1. Graft polymerization of E4S into crystalline and amorphous PEEK substrates

Graft polymerization of pre-irradiated polymer substrates is made possible by using grafting solvents; empirically, aromatic hydrocarbons such as toluene and xylene and alcohols such as 1- and 2-propanols have been found to be effective solvents for a graft polymerization of styrene and acrylate monomers [1–4]. However, E4S is insoluble in toluene and other hydrophobic solvents, and yields white precipitates in protic solvents such as 1-propanol. Thus, dioxane was used to dilute E4S for the graft polymerization because E4S dissolves in dioxane at moderate concentrations and does not yield precipitants even at the boiling point (100 °C). When highly crystalline PEEK substrates (degree of crystallinity: 32%) irradiated in the range of 30–200 kGy at room temperature were immersed in E4S/dioxane solution (1/1 v/v) at 80 °C, the graft polymerization of E4S hardly progressed at all, with grafting degrees lower than 5% after 72 h (Fig. 1). In contrast, the graft polymerization of E4S into a low crystalline PEEK substrate (degree of crystallinity: 11%) irradiated with 60 kGy gradually proceeded under the same conditions, and the grafting degree reached around 50% after 72 h (Scheme 1). With doses of less than 100 kGy for grafting in this experiment, the cross-linking of PEEK film should not be taken in account, because the cross-linking reaction of the PEEK film requires the irradiation with doses of higher than several MGy [19]. Surprisingly, the graft polymerization of E4S into the non-irradiated low crystalline PEEK, i.e. the original PEEK substrate, also proceeded at a relatively low grafting rate, resulting in E4S-grafted PEEK films with grafting degrees of about 30% even though it is well accepted that graft polymerizations into most common polymer substrates such as PE, PP, PMMA, PTFE, and PET do not progress without irradiation [1–4]. This means that a low crystalline PEEK substrate is amenable to thermal graft polymerization of monomers.

3.2. Initial species of graft polymerization of E4S into PEEK substrates

ESR spectra of the original PEEK substrate with 11% crystallinity and the film irradiated with 90 kGy in vacuo at room temperature

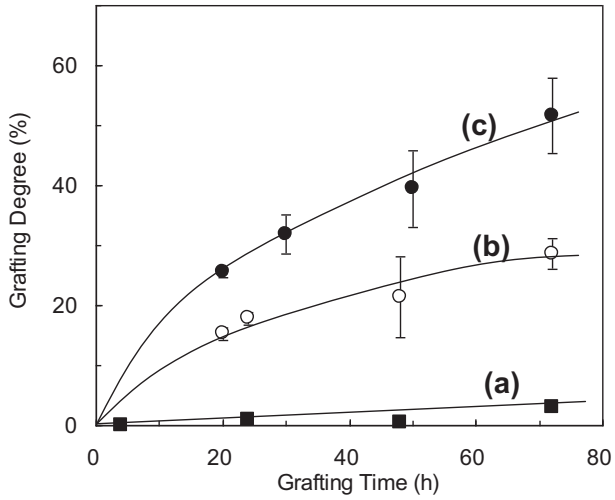

Fig. 1. Plots of grafting degrees of E4S into h-PEEK (degree of crystallinity = 32%) (a) and l-PEEK (degree of crystallinity = 11%) pre-irradiated with 0 (b) and 60 kGy (c).

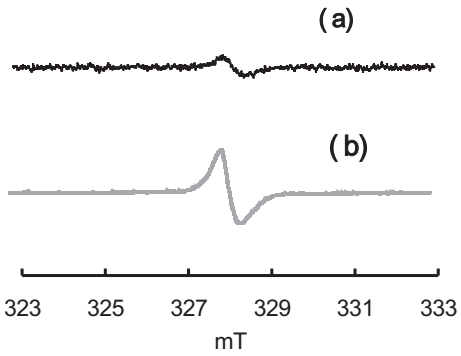

Fig. 2. ESR spectra of the original PEEK film (a) and the film irradiated with 90 kGy in vacuo at room temperature (b).

were measured at room temperature (Fig. 2). Clearly, the original PEEK exhibited a very weak peak ($g = 2.0074$), corresponding to a radical density of 1.0×10^{16}/g even without irradiation (Fig. 2a). It had already been reported that PEEK films contain a small amount of radicals, and that the intensity of the ESR signal increases by about 4 times upon UV irradiation but gradually decreases to the original value when the irradiated films are kept at room temperature. However, there is no information about the structure or origin of the ESR signal [28].

An intensive signal was observed at a similar position ($g = 2.0077$) in the irradiated film with density of 7.4×10^{16}/g, seven times larger than that of the original film (Fig. 2b). These spectral changes in ESR were almost the same as that observed in highly crystalline PEEK (h-PEEK: degree of crystallinity = 32%) upon irradiation [23]. The broad signal without any fine structure in the PEEK films with and without irradiation seemed to be a phenoxy radical, which is well known as a stable radical species in polymer resins [29,30]. The phenoxy radical has even been used as an index (for sensors) of anti-weather resistance of polymer resin films owing to its long life time. The neat phenoxy radical exhibits a g-value of 2.0043; however, the p-chlorophenoxy radical, a phenoxy radical with an electron-withdrawing group, exhibits a g-value upward shift ($g = 2.0063$) [31]. In our case, the expected phenoxy radical should have a benzoyl (carbonyl) group at the para position, and the higher g-value (2.0075) should have electron-withdrawing effects. It had been reported that the ESR signal of the PEEK films irradiated at 77 K using electron beam was stable at low temperatures and was quenched by illumination with visible light with wavelengths above 520 nm. Judging from this relatively low thermal stability and this photo-bleaching with visible light, the ESR signal in the PEEK films irradiated at lower temperatures has been assigned to radical anions [32]. However, this signal gradually decayed at room temperature and was not observed in the PEEK films irradiated at room temperature. In this study, the irradiation of PEEK substrates and subsequent graft polymerization were carried out at room temperature and at 80 °C, and thus, it is clear that the initiation species of the graft polymerization of styrene on PEEK substrates are not radical anions.

Fig. 3 shows the ESR spectra of aromatic polyimide (PI, Kapton), polyethersulfone (PES), and polyphenylenesulfide (PPS) films irradiated with 90 kGy at room temperature and measured at room temperature. The PI and PES, which have the same diphenyl ether moiety as PEEK, exhibited exactly the same broad signals at $g = 2.0072$ and 2.0079, with similar intensities of 1.6×10^{17}/g and 6.1×10^{16}/g, respectively. In contrast, the irradiated PPS film, which has no diphenyl ether substructure, exhibited a totally different ESR pattern. Furthermore, the scission of the ether linkage of diphenyl ether upon the radiation cross-linking of PES films has been reported [33,34]. As is well known, it is difficult to confirm the exact structure at the joint position of the polymer chains of PEEK substrates with polystyrene grafts, due to the very small number of these points in grafted films. However, the above results strongly suggest that the graft polymerization started from the phenoxy radical generated by radiation-induced scission of ether linkages, resulting in block type grafts consisting of poly(styrenesulfonic acid), not conventional T-shape grafts such as grafts of polystyrene into PE, PP, or PTFE (Scheme 2). It is surmised that the initiating species of the original PEEK (non-irradiated) are terminal phenoxy radicals, generated by the scission caused by a drawing molding process.

3.3. Morphological changes of PEEK substrates in graft polymerization of E4S

Figs. 4 and 5 show the DSC and TGA profiles of original PEEK (a), grafted PEEK with 46% GD (b), and PEEK-based PEM (sulfonated form of film (b)) with a sulfonation degree (SD) of 90% (c), (d)

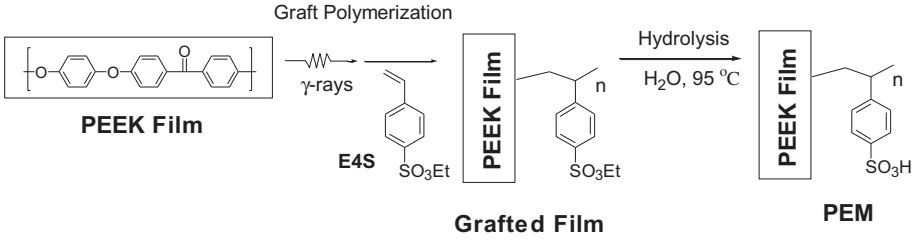

Scheme 1. Radiation-induced graft polymerization of E4S into PEEK films and subsequent hydrolysis of poly(E4S) grafts.

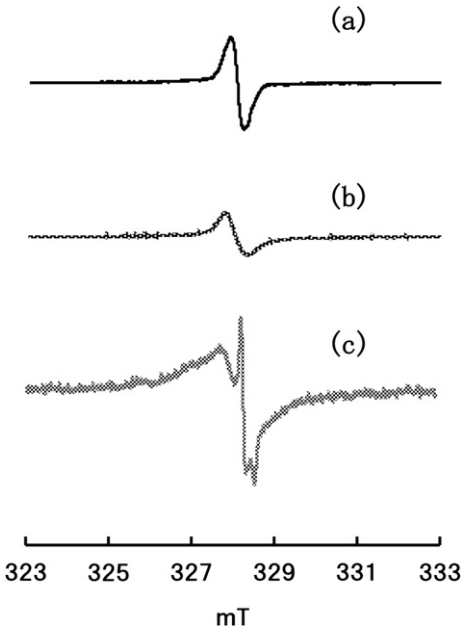

Fig. 3. ESR spectra of PES (a), PI (Kapton) (b), and PPS (c) films irradiated with 90 kGy in vacuo at room temperature.

respectively. The endothermic peaks at around 240 °C shown in Fig. 4b likely signify the elimination of the ethyl group of the sulfonic esters in the grafts because this temperature is in good agreement with the temperature at which there is weight loss of the grafted PEEK in the TGA profile (Fig. 5b). The TGA and DSC profiles of the grafted PEEK after the elimination of the ethyl group are similar to those of hydrolyzed PEEK-PEM, further indicating ethyl group elimination at around 240 °C (see also next section).

In the DSC profiles, the grafted PEEK with 46% GD did not exhibit the glass transition temperature (T_g) at 143 °C and the exothermic peak at 173 °C, which was observed in the annealing of the PEEK substrate and can be assigned to recrystallization of PEEK chains in the amorphous phase (Fig. 4a) [35]. As shown in Fig. 6, which are the WAXS profile of the original PEEK (a) and grafted PEEK with 46% GD (b), it is clear that the grafted film exhibited discernible peaks at 19 and 21°, assigned to (110) and (220) peaks [36]. The increases of

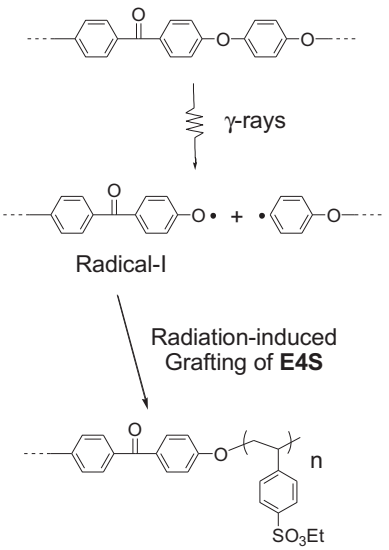

Scheme 2. Graft polymerization mechanism of E4S into PEEK films.

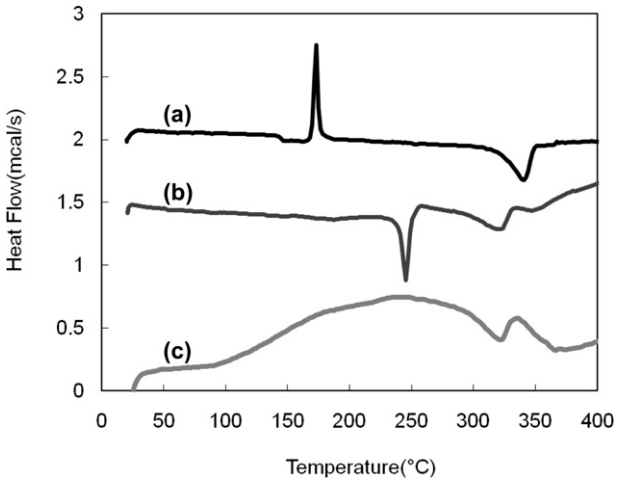

Fig. 4. DSC profiles of original l-PEEK (a), E4S-grafted PEEK with 46% GD (b), and PEEK-based PEM (sulfonated form of film b) with 90% SD (c).

these peaks indicate that the graft polymerization proceeded along with recrystallization of the amorphous phase of PEEK substrate, which is a well known solvent-induced recrystallization of amorphous PEEK solids [37–39].

During the above disappearance of T_g and the increases of crystallinity of the PEEK substrates, the grafting of E4S progressed in the amorphous phase of the PEEK substrates, probably because E4S has a hydrocarbon structure similar to the base PEEK polymer, making the E4S compatible with the amorphous phase of the PEEK films for easy grafting. Furthermore, it should be noted that this is the first instance of graft polymerization which progresses along with increase in crystallinity of the substrate, and so should be of practical advantage in obtaining mechanically stronger grafted films[5–10].

3.4. Preparation (hydrolysis) and property of PEEK-based PEM

The grafted PEEK with 25–46% GD were hydrolyzed in the yields of 84–91% after immersion in hot water (95 °C) for 24 h, to yield PEEK-based PEM with ion exchange capacities (IEC) of 0.80–1.36 mmol/g. The proton conductivity (σ, S/cm) through the

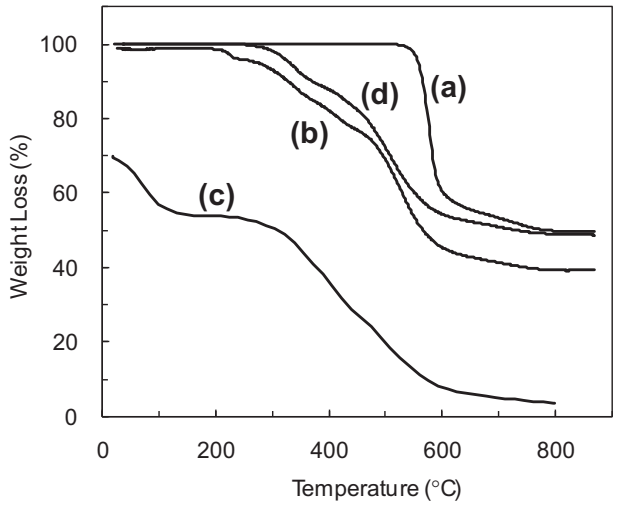

Fig. 5. TGA profiles of original l-PEEK (a), E4S-grafted PEEK with 46% GD (b), and PEEK-based PEM (sulfonated form of film b) with 90% SD at the first run (c) and second run (d). The profile (c) was shifted by −30% vertically for clarity.

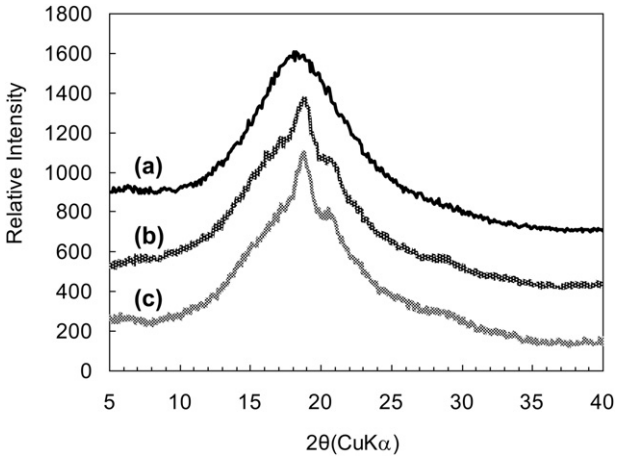

Fig. 6. WAXS of original l-PEEK (a), E4S-grafted PEEK with 46% GD (b), and PEEK-based PEM (sulfonated form of film b) with 90% SD (c).

film perpendicular to the surface of PEEK-PEM hydrated in water at room temperature for 24 h are plotted as a function of IEC in Fig. 7. Ion conductivity of the PEEK-PEM gradually increased with the increase of IEC from 0.80 to 1.36 mmol/g, reaching 0.12 S/cm with IEC of 1.36 mmol/g (GD = 46%). Accordingly, the conductivity of the membranes can be controlled by changing the IEC (grafting degree) of the membranes.

It seems that the water uptake of a membrane is constant as its IEC ranges from 0.80 to 1.36 mmol/g even though there is relatively large fluctuation among membranes (23–47%). It should be noted that the PEM here with 0.12 S/cm, which is 1.3 times higher than that of Nafion, exhibited lower water uptake (27%) than that of Nafion (35%) [40]. This is likely because in the PEEK-based PEM the hydrophobic and mechanically tough aromatic hydrocarbon polymer substrate suppressed the swelling of the hydrophilic grafts with water.

The distribution of the grafts in the PEEK-based PEM was observed with SEM-EDS. The images in Fig. 8 are SEM micrographs of cross-sections of PEEK-PEMs with 25 and 46% GD, together with the EDS of sulfur in the perpendicular direction. It is clear that E4S

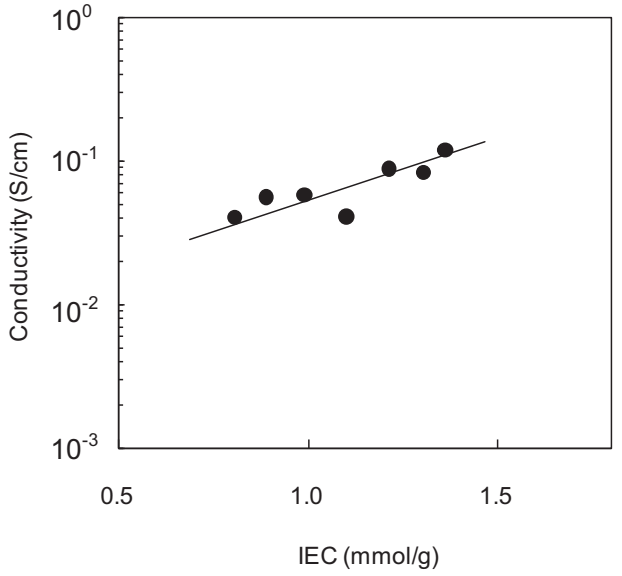

Fig. 7. Plots of proton conductivity (σ, S/cm) of PEEK-based PEM with various grafting degrees as a function of IEC in the range of 0.5 and 1.8 mmol/g.

monomers grafted homogeneously into PEEK substrates even when the IEC of the PEM was as low as 0.80 (GD = 25%). Homogeneous grafting in the perpendicular direction to the film surface is essential for the grafted films to be usable as a fuel cell electrolyte membrane, which needs high proton conductance in the perpendicular direction.

The DSC and TGA profiles of PEEK-based PEM with 90% SD are shown with those of original PEEK and grafted PEEK in the same figures (Figs. 4c and 5d). In Fig. 5d, the gradual weight losses in two regions, 290–380 °C and 380–480 °C, can be attributed to the degradations of sulfonic acid and polystyrene grafts, respectively [41]. There is continuing weight loss above 480 °C, attributed to the degradation of PEEK main chains, which is much lower than the decomposition temperature (ca. 550 °C) of the original PEEK substrate. In Fig. 4c, the broad peak at 100–350 °C in the DSC profile of PEEK-based PEM corresponded to the continuous weight losses of water and decomposition of sulfonic acid, judging from the result of TGA. Fig. 6c shows the WAXS profile of PEEK-based PEM with 90% *SD*. Since the PEEK-based PEM exhibits clear (110) and (220) peaks, which also are observed in the grafted PEEK, it seems that the hydrolysis of poly(E4S) grafts proceeds without decrease in the crystallinity of the grafted films. It should be noted that the radiation-induced graft polymerization of a functional monomer (E4S) followed by hydrolysis is superior to conventional styrene grafting and subsequent sulfonation using chlorosulfonic acid, in which the sulfonation intended only for the polystyrene grafts proceeds not only at the graft layers but also at the crystalline and amorphous phases of PEEK.

The tensile strength and elongation at break in the mold direction of the original PEEK substrate, the PEEK substrate irradiated with a dose of 30 kGy, the grafted PEEK with 46% GD, and the PEEK-PEM with 90% SD are listed in Table 1. The pre-irradiation with a dose of 30 kGy does not affect both tensile strength (113 MPa) and elongation at break of ETFE film (96 and 93%), respectively. The grafted PEEK has about 70% of the original elongation at break (67%); however, it maintains tensile strength at 110 MPa. The mechanical properties of PEEK-PEM with 90% SD were quite similar to those of the grafted PEEK. The tensile strength slightly reduced (100 MPa) but the elongation at break became even larger (86%) with the hydrolysis of the E4S grafts of the film. In considering the mechanical property measurements of these films, it should be noted that the tensile strength of the PEEK-PEM is almost three times higher than that of Nafion (35 MPa), because mechanical properties after the grafting of the functional monomers and subsequent hydrolysis procedure are maintained at 88% and 90% of the original PEEK substrate levels in tensile strength and elongation at break (100/113 MPa and 86/96%) [40].

3.5. SANS analysis of original PEEK, grafted PEEK, and PEEK-based PEM

SANS profiles of the original PEEK substrate, grafted PEEK, and PEEK-PEM were obtained to elucidate morphological change during the preparation procedure. The SANS analysis of each sample specimen was expected to reveal the mechanism of how grafting chains are introduced into PEEK substrate via radiation-induced solid state polymerization as well as precise structures such as the size of ion channels formed by the PSSA grafts and the phase separation of the grafts and substrate PEEK chains, which are important factors influencing the conductivity of the membranes. The SANS profiles in the Q range from 0.04 to 1 nm^{-1} of the original PEEK substrate, grafted PEEK, and PEEK-PEM are shown in Fig. 9a.

SANS profiles of the original PEEK substrate showed no clear scattering while the grafted PEEK (line (ii) in Fig. 9a) exhibited much stronger scattering over the whole Q range and a new shoulder-like

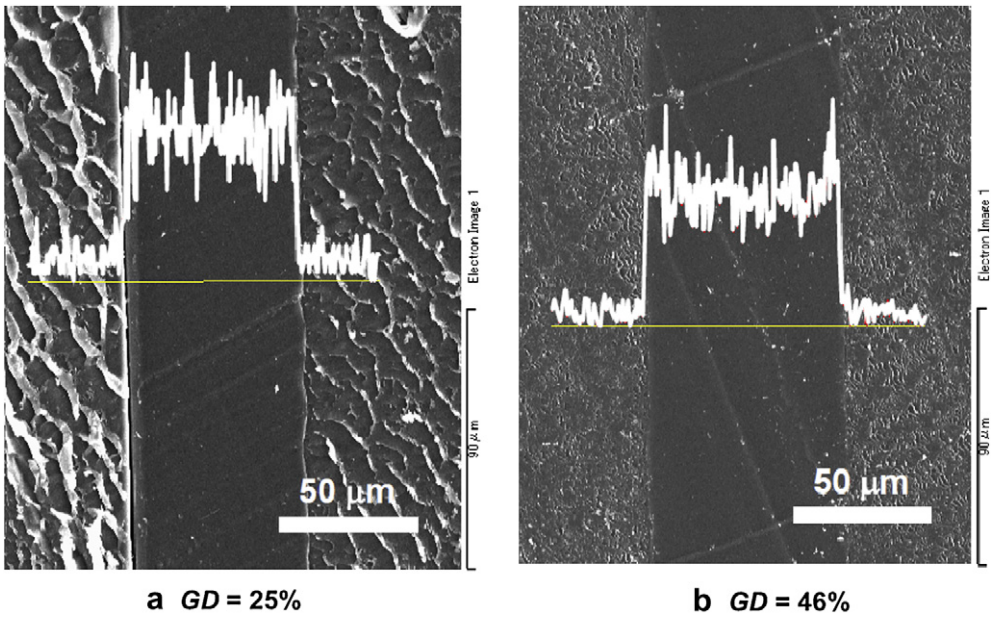

Fig. 8. SEM micrograph of cross-section of PEEK-based PEM with the EDS of sulfur in the perpendicular direction: (a) GD = 25%, *SD* = 85%, IEC = 0.80 mmol/g (b) GD = 46%, SD = 90%, IEC = 1.38 mmol/g.

peak at Q = 0.49 nm^{-1} ($d = 2\pi/Q = 13$ nm). The SANS profile of the PEEK-PEM (line (iii) in Fig. 9a) had a similar profile with a shoulder-like peak at Q = 0.50 nm^{-1}, which was slightly stronger than that of the grafted PEEK; i.e., *d* (= 12.6 nm) was smaller. The decrease in *d*-spacing was in good agreement with the decrease of the volume of the grafts due to the elimination of the ethyl group by hydrolysis. Since the slight decrease of the Q-value via hydrolysis also supports the assignment of the shoulder-like peak to a poly (E4S) graft domain, the above SANS results clearly show that the size of ion channels (13 nm) formed by PSSA grafts is 2.5 times larger than that in Nafion [36,42,43]. Furthermore, the nano- to meso-scale structures of PEEK-based PEM greatly differ from those of other graft-type fluorinated polymer membranes. In a report of SANS measurement of styrene grafted poly(tetrafluoroethylene-*co*-hexafluoropropylene) (FEP) [44], the domain size of the polystyrene grafts was estimated to be from 35 to 43 nm, depending on the grafting degree. The author of this report surmised that these domain sizes are related to the lamellar period of the original FEP substrate (31 nm).

The grafted FEP exhibited Q^{-4} power law behavior, which is well explained by Porod's Law as being due to the sharp interface between the graft domains and the FEP substrates [44,45]. In contrast, the asymptotic Q-behavior of Q^{-2} at the higher Q-region of Q > 0.49 nm^{-1} indicates that there was no sharp interface between the grafts and PEEK substrate. Since both FEP and PEEK-based grafted films possess the polystyrene derivatives consisting of only hydrocarbons but not fluorine atoms, the different interfacial structures, clear and unclear boundaries, should result from different solubility of the graft polymers with perfluorinated or aromatic hydrocarbon polymer substrates; namely, the graft polymers are miscible with the PEEK chains but not miscible with the FEP chains [46]. It was surprising to observe the Q^{-2} behavior in the *Q*-region of Q > 0.50 nm^{-1}, which also indicated that there was no sharp interface between the grafts and PEEK substrate, which in

Table 1
Tensile strength and elongation at break of the original PEEK substrate, the PEEK substrate irradiated with a dose of 30 kGy, the grafted PEEK with 46% GD, and the PEEK-PEM with 90% SD.

Films	Tensile strength (MPa)	Elongation (%)
PEEK	113	96
Irradiated PEEK	113	93
Grafted PEEK (GD = 46%)	110	67
PEEK-PEM (IEC = 1.38 mmol/g)	100	86

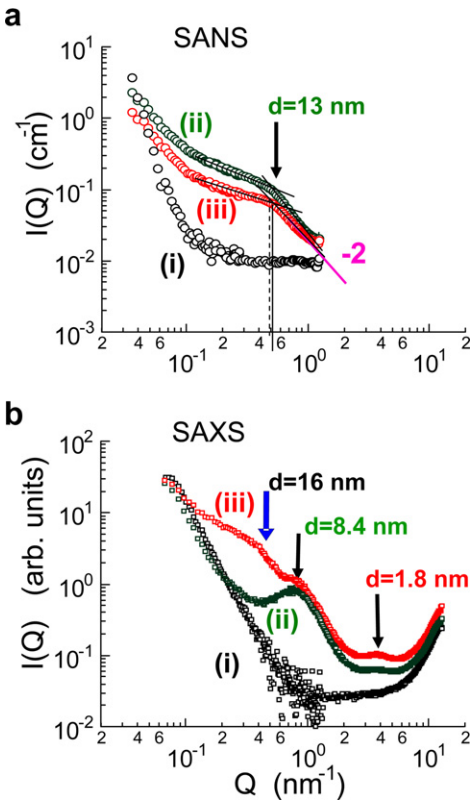

Fig. 9. SANS profiles in the Q range from 0.04 to 1 nm^{-1} (a) and SAXS profiles in the Q range from 0.07 to 12 nm^{-1} (b): (i) original PEEK substrate, (ii) E4S-grafted PEEK with 46% GD, and (iii) PEEK-PEM with 90% SD.

turn indicated that the E4S grafts are miscible with the substrate PEEK chains, even though the hydrolyzed PSSA grafts should be more hydrophilic than the E4S grafts and substrate PEEK chains. Since the graft domain is miscible with the amorphous phase of PEEK substrates, ion channel domains formed in sulfo group-containing grafts which exhibited smaller correlation period (13 nm) than in grafted FEP membranes.

3.6. SAXS analysis of original PEEK, grafted PEEK, and PEEK-based PEM

The SAXS of the original PEEK substrate, grafted PEEK, and PEEK-PEM are shown in Fig. 9b in the Q range from 0.07 to 12 nm^{-1} ($d = 0.5–90$ nm), which covers a range one order shorter than the SANS measurement. The same samples used for the SANS were concurrently used for the SAXS. The SAXS profile of the PEEK substrate was almost the same as the SANS profile, though the SAXS profile of the grafted PEEK exhibited a clear peak at $Q = 0.75$ nm^{-1} ($d = 8.4$ nm), which did not appear in the SANS profile.

We surmised that the SAXS peak at $Q = 0.75$ nm^{-1} originates from the PEEK crystallite structure, the crystallinity of which increases during the graft polymerization observed in the WAXS experiment, and therefore we measured the contrasts between amorphous and crystalline phases in the PEEK substrate observed in SANS and in SAXS, as shown in Fig. 10. In the case of SANS, the scattering contrasts between PEEK crystal and amorphous regions ($\Delta\rho_1 = \rho_c - \rho_a$), and between grafts and PEEK amorphous region ($\Delta\rho_2 = \rho_g - \rho_a$) were estimated to be 0.29 and −1.21 ($\times 10^{10}$ cm^{-2}), respectively. This means that the SANS intensity from the PEEK-PEM is dominated by that from the grafts, and that the PEEK crystal region, a lamellar structure, is not detected by SANS because scattering intensity is proportional to the square of scattering contrast. The situation is different for SAXS; the $\Delta\rho_1$ and $\Delta\rho_2$ for X-rays are estimated to be 1.22 and −0.12 ($\times 10^{10}$ cm^{-2}), respectively.

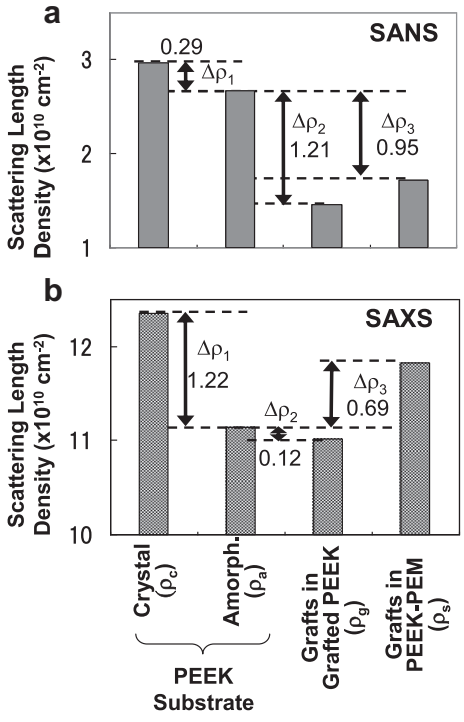

Fig. 10. Variation of scattering length densities among crystalline and amorphous phases of PEEK substrates, polystyrene grafts in grafted PEEK, and PSSA grafts in PEEK-based PEM: (a) SANS and (b) SAXS.

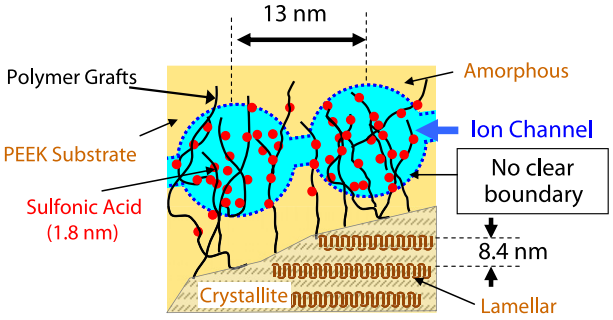

Fig. 11. Schematic illustration of the morphology of PEEK-based PEM.

Therefore, SAXS is more sensitive to crystallites in the amorphous phase in PEEK substrates than SANS. Specifically, the peak-profile observed in SAXS but not in SANS likely originated from the crystalline/amorphous interfaces in the PEEK substrate [10,47]. As described in Section 3.3, the graft polymerization proceeds along with recrystallization in the amorphous phase of PEEK substrate, which is a well known solvent-induced recrystallization of amorphous PEEK films [37–39]. Accordingly, the new peak implies that a lamellar structure with $d = 8.4$ nm grows with increase in crystallinity during the graft polymerization. However, this lamellar structure is indistinct compared with those generated by heat annealing because of lower scattering intensity as well as the smaller spatial distance, which is in good agreement with the previous reports of solvent-induced recrystallization [48].

SAXS profiles of the PEEK-based PEM (line (iii) in Fig. 9b) exhibited a similar peak at $Q = 0.75$ nm^{-1} ($d = 8.4$ nm), together with increase of intensity at the Q-region between 0.2 and 0.6 nm^{-1} ($d = 10–30$ nm) including a shoulder-like peak profile appearing at $Q = 0.38$ nm^{-1} which was slightly higher than that observed in the SANS profile and is attributed to PSSA grafts. Furthermore, a small peak can be seen at $Q = 3.5$ nm^{-1} ($d = 1.8$ nm). This peak was only observed in PEM, and we hypothesize that it reflects the statistical mean distance among sulfonic acids directly attached to grafting polystyrene chains.

Judging from the above complementary observations, we illustrate the PEEK-based PEM as shown in Fig. 11: (1) The hydrophobic matrix in the PEM chiefly consists of the original PEEK substrate including crystalline phases. (2) PSSA grafts are not phase-separated from the PEEK amorphous region, and form ion channel domains with the average distance of 13 nm (3) There are microstructures in the ion channels, which correspond to the average distance of 1.8 nm between sulfonic acids in the grafts.

4. Conclusions

We can prepare thermally and mechanically stable polymer electrolyte membranes based on an aromatic hydrocarbon polymer, a so-called “super-engineering plastic,” by radiation-induced graft polymerization of sulfo-containing styrene derivatives into crystalline PEEK substrates. Graft polymerization of a sulfo-containing styrene, E4S, hardly proceeded at all into a high crystalline PEEK substrate, whereas it gradually proceeded into a low crystalline PEEK substrate, achieving a grafting degree of more than 50%. This is the first graft polymerization that has been accompanied with increase in the crystallinity of the substrate, which should be of practical advantage in obtaining mechanically stronger grafted films. The graft polymerization started from the phenoxy radical, and formed ether linkages at the starting points of grafts, resulting in block type grafts consisting of PSSA, not conventional T-shape grafts such as polystyrene grafts into PE, PP, and PTFE. The PEEK-based PEM converted

by aqueous hydrolysis of grafted films maintained the mechanical strength (95 MPa) with 62% of the original PEEK substrates. Wide and small-angle X-ray scattering (WAXS and SAXS) revealed that the graft polymerization proceeded along with recrystallization in the amorphous phase of PEEK substrate, which is a well known solvent-induced recrystallization of amorphous PEEK film, to form a weak lamellar structure with 8 nm spacing. Furthermore, through complementary SAXS and SANS observation, it was revealed that the grafted PEEK-based PEM possesses ion channel domains with the average distance of 13 nm, in which there are micro-structures of sulfonic acid with the average distance of 1.8 nm.

Acknowledgments

This work was partially supported by Grant-in-Aid for Scientific Research of Japan Society for the Promotion of Science (Grant number 19550213 and 20760479). This work was performed under the NIMS - RIKEN - JAEA Cooperative Research Program on Quantum Beam Science and Technology.

References

[1] Chapiro A. Radiation Chemistry of Polymeric System. Chap. XII. New York: Interscience Publishers, John Wiley & Sons; 1962.
[2] Dargaville TR, George GA, Hill DJT, Whittaker AK. Prog Polym Sci 2003;28:1355–76.
[3] Nasef MM, Hegazy E. Prog Polym Sci 2004;29:499–561.
[4] Gursel SA, Gubler L, Gupta B, Shcerer GG. Adv Polym Sci 2008;215:157–217.
[5] Smit I, Bezjak A. Polymer 1981;22:590–6.
[6] Seguchi T, Tamura NJ. Phys Chem 1973;77:40–4.
[7] Chapiro AJ. Polym Sci 1959;34:481–501.
[8] Bozzi A, Chapiro A. J Radiat Phys Chem 1988;32:193–6.
[9] Gebel G, Ottomani E, Allegraud JJ, Betz N, Moël AL. Nucl Instrum Meth B 1995;105:145–9.
[10] Jokela K, Serimaa R, Torkkeli M, Sundholm F, Kallio T, Sundholm GJ. Polym Sci Polym Phys 2002;40:1539–55.
[11] Yamaki T, Asano M, Maekawa Y, Morita Y, Suwa T, Chen J, et al. Radiat Phys Chem 2003;67:403–7.
[12] Chen J, Asano M, Yamaki T, Yoshida MJ. Power Sources 2006;158:69–77.
[13] Sato R, Ikeda S, Iida M, Oshima A, Tabata Y, Washio M. Nucl Instrum Meth B 2003;208:424–8.
[14] Schmidt TJ, Simbeck K, Scherer GG. J Electrochem Soc 2005;152:A93–7.
[15] Takahashi S, Okonogi H, Hagiwara T, Maekawa YJ. Membr Sci 2008;324:173–80.
[16] Rikukawa M, Sanui K. Prog Polym Sci 2000;25:1463–502.
[17] Hickner MA, Ghassemi H, Kim YS, Einsla BR, McGrath JE. Chem Rev 2004;104:4587–612.
[18] Miyatake K, Chikashige Y, Higuchi E, Watanabe MJ. J Am Chem Soc 2007;129:3879–87.
[19] Chen J, Maekawa Y, Asano M, Yoshida M. Polymer 2007;48:6002–9.
[20] Hu Z, Yin Y, Kita H, Okamoto K, Suto Y, Wang H, et al. Polymer 2007;48:1962–71.
[21] Furtado Filho AAM, Gomes AS. Polym Bull 2006;57:415–21.
[22] Hasegawa S, Suzuki Y, Maekawa Y. J Radiat Phys Chem 2008;77:617–21.
[23] Hasegawa S, Sato K, Narita T, Suzuki Y, Takahashi S, Morishita N, et al. J Membr Sci 2009;345:74–80.
[24] Kienkamp K, Schnell I, Groehn F, Wegner G. Macromol Chem Phys 2006;207:2066–73.
[25] Blundell DJ, Osborn BN. Polymer 1983;24:953–8.
[26] Koizumi S, Iwase H, Suzuki J, Oku T, Motokawa R, Sasao H, et al. Appl Cryst 2007;40:s474–9.
[27] Ohnuma M, Suzuki J, Ohtsuka S, Kim SW, Kaito T, Inoue M, et al. Acta Mater 2009;57:5571–81.
[28] Li HM, Fouracre RA, Given MJ, Banford HM, Wysocki S, Karolczak S. IEEE Trans Dielect Electr Ins 1999;6:295–303.
[29] Potter WD, Scott G. Eur Polym J 1971;7:489–97.
[30] Okamoto S, Hikita K, Ohya-Nishiguchi H. Polym Paint Colour J 1987;177:683–5.
[31] Khachatryan L, Adounkpe J, Dellinger BJ. Phys Chem A 2008;112:481–7.
[32] Heiland K, Hill DJT, O'Donnell JH, Pomery PJ. Polym Adv Tech 1994;5:116–21.
[33] Ohshima A, Miura T, Washio M. Polym Deg Stabi 2006;91:2867–73.
[34] Heiland K, Hill DJT, Hopewell JH, Lewis DA, O'Donnell JH, Pomery PJ, et al. Adv Chem 1996;249:637–49.
[35] Fougnies C, Dosie` re M, Koch Roovers MHJ. Macromolecules 1999;32:8133–8.
[36] Fougnies C, Dosie` re M, Koch Roovers MHJ. Macromolecules 1998;31:6266–74.
[37] Stober EJ, Seferis JC, Keenan JD. Polymer 1984;25:1845–52.
[38] Grayson MA, Wolf CJJ. Polym Sci Pol Phys 1988;26:2145–67.
[39] Wolf CJ, Bornmann JA, Grayson MA, Anderson DP. J Polym Sci Pol Phys 1992;306:251–7.
[40] Mauritz KA, Moore RB. Chem Rev 2004;104:4535–85.
[41] Nasef MM. Polym Degrad Stabil 2000;68:231–8.
[42] Page KA, Landis FA, Phillips AK, Moore RB. Macromolecules 2006;39:3939–46.
[43] Shcmidt-Rohr K, Chen Q. Nat Mater 2008;7:75–83.
[44] Mortensen K, Gasser U, Gürsel SA, Scherer GG. J Polym Sci Polym Phys 2008;46:1660–8.
[45] Porod G, Kolloid-Z 1951;124:83–114.
[46] Motokawa R, Iida Y, Zhao Y, Hashimoto T, Koizumi S. Polym J 2007;39:1312–8.
[47] Hietala S, Holmberg S, Nasman J, Ostrovskii D, Paronen M, Serimaa R, et al. Angew Makromol Chem 1997;253:151–67.
[48] Cornélis H, Kander RG, Martin JP. Polymer 1996;37:4573–8.

Polymer 52 (2011) 107–115

Contents lists available at ScienceDirect

Polymer

journal homepage: www.elsevier.com/locate/polymer

Emulsion templated bicontinuous hydrophobic-hydrophilic polymers: Loading and release

Tamar Gitli, Michael S. Silverstein*

Department of Materials Engineering, Technion – Israel Institute of Technology, Haifa 32000, Israel

ARTICLE INFO

Article history:
Received 14 September 2010
Received in revised form
3 November 2010
Accepted 6 November 2010
Available online 13 November 2010

Keywords:
Bicontinuous
High internal phase emulsion
Release

ABSTRACT

Water absorption is often poor in hydrophobic polyHIPEs, porous polymers synthesized within high internal phase emulsions (HIPEs). This paper describes bicontinuous polyHIPEs, the simultaneous polymerization of hydrophobic monomers (external phase) and hydrophilic monomers (internal phase). Integrating hydrogels within polyHIPEs extended the release of water-soluble dye from 10 h to more than 10 days. PolyHIPE capillary action promoted the rapid distribution of water throughout the hydrogel. The diffusion pathway in this bicontinuous system was similar to diffusion through an assembly of polydisperse spheres. The copolymerization of the hydrophilic monomers with the monomers in the external phase enhanced the hydrophilicity of the scaffold, reduced the modulus of the hydrated polyHIPE, and reduced the tortuosity of the diffusion path. Pre-polymerization of the external phase reduced the extent of copolymerization, enhanced the modulus, sealed the interconnecting holes, reduced the capillary action, increased the tortuosity, and extended the release time to 3 weeks.

1. Introduction

A high internal phase emulsion (HIPE) is an emulsion in which the droplets of the internal, dispersed, phase are the major phase (more than 74 vol %). PolyHIPEs are porous polymers with highly interconnected porosities that result from polymerizing monomers within the external phases of HIPEs [1–7]. The droplets of the internal phase, which can become interconnected during the polymerization in the external phase, are then removed, leaving voids in place of the droplets. A variety of polyHIPEs and polyHIPE-based materials have been synthesized, such as copolymers [8,9], interpenetrating polymer networks (IPN) [10], crystallizable side chain polymers [11], biocompatible polymers [12–16], functional surfaces [17,18], organic–inorganic hybrids [19,20], and composites [21–26]. As water-in-oil (W/O) HIPEs with hydrophobic monomers in the external phase were employed for most of these systems, the resulting polyHIPEs were usually hydrophobic and exhibited poor water absorption [6].

There are three routes that are commonly used to synthesize water-absorbent polyHIPE. In one route, hydrophobic polyHIPEs, synthesized within W/O HIPEs, are modified to enhance their hydrophilicity using a second synthesis stage [2,27]. In another route, hydrophilic polyHIPEs are directly synthesized from hydrophilic monomers within oil-in-water (O/W) HIPEs [28–30]. Such hydrophilic polyHIPEs have demonstrated potential for controlled release applications [31]. Unfortunately, O/W HIPEs are often more difficult to stabilize than W/O HIPEs [6]. In addition, it can be more difficult to remove and to dispose of the organic internal phase in O/W HIPEs compared to the aqueous internal phase in W/O HIPEs. In a third route, water-absorbing polyHIPEs can be synthesized within W/O HIPEs using a single synthesis stage. In this route, hydrophobic and hydrophilic monomers are simultaneously polymerized within the external phase and the internal phase, respectively, of W/O HIPEs [32–35]. Ideally, the structure is bicontinuous, consisting of a hydrophobic scaffold filled with an interconnected hydrogel [36].

Water absorption is often a critical requirement for various biomedical applications. Hydrogels are potentially useful as controlled drug delivery systems since the rate of drug diffusion can be controlled through copolymerization and crosslinking [37]. Drug release from dried hydrogels follows the absorption of water from the environment, making the absorption of water a controlling step. Placing the hydrogel within a hydrophobic scaffold whose porous structure can affect water absorption and drug diffusion provides another way to control drug release. In principle, bicontinuous hydrogel-filled polyHIPEs could offer a unique mechanism to influence the release of drugs from the hydrogel phase.

* Corresponding author. Tel./fax: +972 4 829 4582.
E-mail address: michaels@tx.technion.ac.il (M.S. Silverstein).

0032-3861/$ – see front matter © 2010 Elsevier Ltd. All rights reserved.
doi:10.1016/j.polymer.2010.11.006

Previous work investigated a HIPE containing styrene (S) and divinylbenzene (DVB, crosslinking comonomer) in the external phase (around 11 wt %) and acrylamide (AAm) and N,N-methylenebisacrylamide (MBAM, crosslinking comonomer) in the external phase [36]. The unexpected and significant reduction in the hydrated polyHIPE modulus with increasing acrylamide content indicated that the polymerizations were not mutually exclusive and that the acrylamide affected the molecular structure of the hydrophobic polymer synthesized in the external phase. The polymer in the external phase became more hydrophilic and more hygroscopic on incorporation of acrylamide, reducing the stiffness of the hydrated polyHIPE and enhancing its tendency to collapse on drying. Unfortunately, the mechanical properties of these bicontinuous, hydrogel-filled polyHIPEs were not suitable for uptake and release experiments that involved multiple drying cycles.

In this paper, bicontinuous, hydrogel-filled polyHIPEs based on S, DVB, AAm, and MBAM that contain around 20 wt % external phase and exhibit significantly enhanced mechanical properties are investigated. The effects of the synthesis parameters on the molecular structure, porous structure, and mechanical properties are described and discussed in detail. The main thrust of this manuscript is the unique behavior of these bicontinuous polyHIPEs in the uptake and release of a water-soluble dye molecule as well as the dependence of this behavior on the structure and properties. The results indicate that the synergistic combination of polyHIPE capillary action and hydrogel swelling and diffusion can be used to enhance uptake and release properties.

2. Experimental

2.1. Materials

The hydrophobic monomer in the external phase of the HIPEs was S (Fluka Chemie) and the hydrophobic crosslinking comonomer was DVB (containing 20% ethylstyrene, Aldrich). The hydrophilic monomer in the internal phase of the HIPEs was AAm (Fluka) and the hydrophilic crosslinking comonomer was MBAM (Aldrich). The hydrophobic monomers were washed to remove the inhibitor (three times with an aqueous 5 wt % sodium hydroxide (NaOH, Carlo Erba) solution followed by three times with deionized water). The hydrophilic monomers were used as received. The emulsifier was sorbitan monooleate (SMO, Span 80, Fluka Chemie). The water-soluble initiator was potassium persulfate (KPS, Riedel-de-Haen). Benzoyl peroxide (BPO, Fluka), an oil-soluble initiator, was used in some specific samples, as will be described. Potassium sulfate (K_2SO_4, Frutarom, Israel) was used to stabilize the HIPEs. The water-soluble dye used for the uptake and release experiments was Eosin Y ($C_{20}H_6Br_4Na_2O_5$, Aldrich).

2.2. Standard polyHIPE synthesis

In most of the HIPEs formed, the organic phase contained the hydrophobic comonomers and the emulsifier, while the aqueous phase contained deionized water, the hydrophilic comonomers, the initiator, and the stabilizer. The volume fraction of the aqueous phase in the HIPEs was approximately 0.8. The HIPEs were produced by adding the aqueous phase dropwise to the organic phase while stirring vigorously. The resulting HIPEs were covered by plastic film and aluminum foil. Polymerization took place in a convection oven at 65 °C for 24 h. The resulting polyHIPEs were then placed in a Soxhlet extraction apparatus. The extraction procedure was 24 h in methanol followed by 24 h in water. The samples were dried in a vacuum oven at room temperature for between 48 and 72 h, until a constant weight was achieved.

2.3. HIPE compositions

The amount of DVB with respect to the hydrophobic monomer content (S and DVB) was held constant at 44.0 mol %. The amount of MBAM with respect to the hydrophilic monomer content (AAm and MBAM) was held constant at 9.1 mol %. The concentration of the hydrophilic comonomers (AAm and MBAM) in the aqueous phase, c_{AAm}, was varied from 0 to 0.092 g/cm^3. The mass fraction of the hydrophilic comonomers (AAm and MBAM) with respect to all the monomers (S, DVB, AAm, and MBAM), w_{AAm}, was varied from 0 to 29 wt %. Typical HIPE recipes are listed in Table 1. The c_{AAm} and w_{AAm} for the various samples are listed in Table 2.

2.4. Pre-polymerization

In a pre-polymerized HIPE, the monomers in the organic phase underwent partial polymerization prior to HIPE formation. To this end, BPO was added to the organic phase (Table 1). The organic phase was placed in a convection oven at 80 °C for 15 min. Following this pre-polymerization, the aqueous phase was added and the polyHIPE was synthesized in the usual manner.

2.5. Hydrogel synthesis

Hydrogels were synthesized using solution polymerization of AAm and MBAM (9.1 mol % MBAM) and c_{AAm} of 0.043 and 0.063 g/cm^3 (Tables 1 and 2). The water, AAm, MBAM, and KPS ratios were the same as those used in the respective HIPEs (Table 1). The components were mixed and polymerized in a convection oven at 65 °C for 24 h. The hydrogel was cooled to 4 °C for 1.5 h and then freeze dried.

2.6. Characterization

The polymer mass was calculated by subtracting the masses of emulsifier, initiator, and stabilizer in the feed from the mass of the dried polyHIPE. The yield was the ratio of the polymer mass to the mass of the monomers. The density, ρ_m, was determined using gravimetric analysis. A predictive estimate for the density based on the compositions of the HIPEs, ρ_c, used the following assumptions: 100% conversion during polymerization; no shrinkage during polymerization and drying; and all the water was removed during drying. The specific surface area, A, was determined using the single-point BET (Brunauer, Emmett, Teller) method, with nitrogen adsorption at 77 K (Quantachrome).

The porous morphologies of the polyHIPEs were described using high resolution scanning electron microscopy of uncoated fracture surfaces of dried specimens at accelerating voltages between 3 and 4 kV (HR-SEM, Zeiss LEO 982). Compressive stress–strain

Table 1
Typical HIPE and hydrogel recipes (S3, HG3, P4).

Content, wt %				
Phase	Component	S3	HG3	P4
External (organic)	S	9.3	–	9.0
	DVB	9.3	–	9.0
	SMO	1.6	–	1.6
	BPO	0.0	–	0.2
	Total	20.2	–	19.8
Internal (aqueous)	Water	74.0	93.0	63.0
	AAm	4.3	5.3	6.3
	MBAM	0.6	0.7	0.9
	K_2SO_4	0.7	0.8	0.4
	KPS	0.2	0.2	0.2
	Total	79.8	100	80.2

Table 2
AAm contents in the polyHIPEs and in the control hydrogels.

Sample	c_{AAm}, g/ml	w_{AAm}
S0	0.00	0.00
S1	0.022	0.08
S2	0.043	0.15
HG2	0.043	–
S3	0.063	0.21
HG3	0.063	–
S4, P4	0.092	0.28

measurements were carried out at room temperature on 0.5 cm × 0.7 cm × 0.7 cm polyHIPE cubes which were hydrated after Soxhlet extraction (Lloyd-Single Column Bench Mounted). The stress–strain experiments continued until equipment-related force or displacement limitations were reached. The compressive modulus, E, was determined from the slope of the compressive stress–strain curves at low strains.

2.7. Loading and release

Eosin Y was loaded into the polyHIPEs by immersing dried polyHIPE slabs (0.3 cm × 1 cm × 1 cm) into an aqueous Eosin Y solution (40 mg/ml). The loading was characterized by monitoring the sample's weight. Loading was conducted until the sample's mass remained constant. The uptake, u_s, the ratio of the mass of Eosin Y solution absorbed per mass polyHIPE sample, was calculated using Equation (1). The normalized uptake, u_{AAm}, the ratio of the mass of Eosin Y solution absorbed per mass AAm, was calculated using Equation (2). The volumetric uptake, u_v, the ratio between the volume of Eosin Y solution absorbed and the pore volume in the polyHIPE was calculated using Equation (3). The amount of Eosin Y loaded into the polyHIPE, m_d, was calculated using Equation (4).

$$u_s = \frac{m_t - m_0}{m_0} \tag{1}$$

$$u_{AAm} = u_s \cdot \frac{1}{w_{AAm}} \tag{2}$$

$$u_{vol} = \frac{(m_t - m_0)/\rho_l}{V_0 - \left(m_0/\rho_p\right)} \tag{3}$$

$$m_d = (m_t - m_0) \cdot w_d \tag{4}$$

where m_0 is the mass of the dry specimen, m_t is the sample mass at time t, V_0 is the initial volume of the polyHIPE, ρ_l is the density of the aqueous solution, ρ_p is the density of the polymers, and w_d is the mass fraction of the drug in the aqueous solution, 0.038. The density of the aqueous solution was 1.03 g/ml. The average density of the polymers in the polyHIPE was assumed to be 1.1 g/cm^3 [38].

The polyHIPEs loaded with Eosin Y solution were then dried in a vacuum oven at room temperature for 48 h. For the release experiments, individual, dried, loaded polyHIPEs were each immersed in 250 ml of deionized water. Aliquots of 2 ml were withdrawn at predetermined time intervals. The concentration of Eosin Y was determined using absorbance measurements at 517 nm. The linear absorption range for Eosin Y at 517 nm was between 10^{-6} mg/ml and 10^{-3} mg/ml. The release is defined as the mass of Eosin Y released into the deionized water normalized by the initial mass of Eosin Y in the immersed polyHIPE. The loading and release experiments for the hydrogels were similar except that the hydrogels were freeze dried following loading in order to prevent their collapse.

3. Results and discussion

3.1. PolyHIPE and hydrogel synthesis

Unfortunately, for this HIPE system, increasing the surfactant concentration beyond 8% produced polyHIPEs that tended to collapse during drying. Previous work on a similar system has shown that the hydrophobic monomers in the external phase undergo copolymerization with the hydrophilic monomers from the internal phase, yielding a significant reduction in the modulus of the hydrated polyHIPEs and reducing their resistance to collapse during drying [36]. Increasing the surfactant concentration reduces the size of the internal phase droplets and increases the amount of interfacial area. Such an increase in interfacial area would enhance copolymerization, reduce the modulus, and reduce the resistance to collapse during drying, leading to an optimum in surfactant concentration that is smaller than that typically found in HIPEs.

Solution polymerization of AAm/MBAM in water with a c_{AAm} of 0.043 g/ml produced a hydrogel surrounded by free water, not all the water was incorporated into the hydrogel. The solution polymerization of AAm/MBAM with a c_{AAm} of 0.063 g/ml produced a hydrogel that incorporated all of the feed water.

3.2. Porous structure

The densities predicted from the compositions of the HIPEs, ρ_c, and the measured densities, ρ_m, are presented as a function of c_{AAm} in Fig. 1. The density increases with increasing AAm concentration as the voids of the polyHIPE become filled with increasing amounts of hydrogel. At low c_{AAm} the ρ_m are quite similar to the ρ_c. The disparity between ρ_m and ρ_c increases with increasing c_{AAm}, with ρ_m becoming significantly greater than ρ_c for a c_{AAm} of 0.063 g/ml. The large disparity in densities for a c_{AAm} of 0.092 g/ml reflects the partial collapse of the polyHIPE during drying.

The morphologies of the dried polyHIPEs are presented in Fig. 2. The polyHIPE with no AAm exhibits interconnected, empty voids (Fig. 2a and b) [6]. The interconnecting holes can be clearly seen at

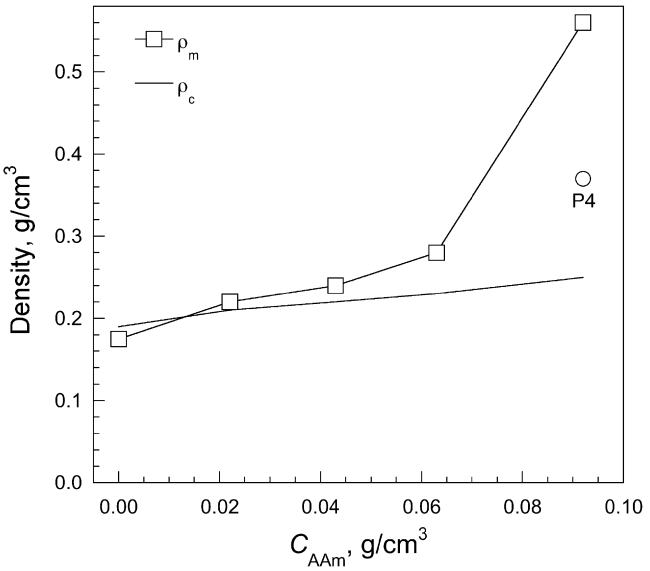

Fig. 1. Densities of the dried polyHIPEs as a function of c_{AAm}.

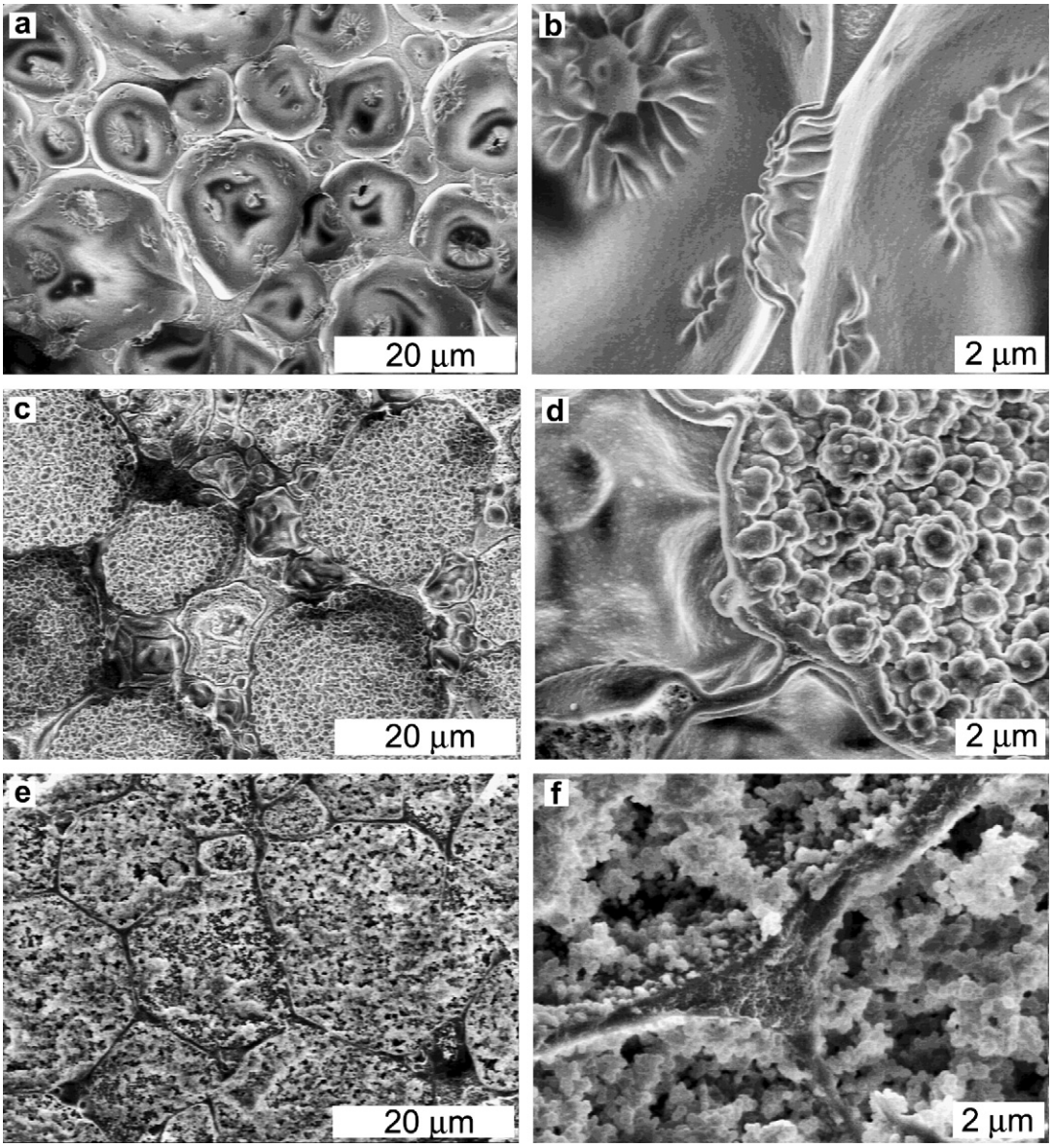

Fig. 2. SEM micrographs of various dried polyHIPEs: (a,b) S0; (c,d) S1; (e,f) S2; (g,h) S3; (i,j) S4; (k,l) P4.

a higher magnification (Fig. 2b). The degree of interconnectivity is smaller than that in typical polystyrene-based polyHIPEs [2]. This low degree of interconnectivity results from the relatively low surfactant concentration, 8% of the organic phase instead of the 20% commonly used for similar HIPEs [5]. The reduction of the surfactant concentration to 5% has been shown to yield a closed-cell structure for some polyHIPEs, even at external phase contents of less than 10% [5].

There are two types of voids seen for S1, the polyHIPE with the lowest c_{AAm}, in Fig. 2c and d. The larger voids (around 15–20 μm in diameter) are usually filled with the nodular structure typical of dried hydrogels, while the smaller voids (around 3–5 μm in diameter) usually seem to be empty. Since for S1 the hydrogel seems to collapse onto the walls during drying, the hydrogel would be more predominant in the larger voids since the volume to area ratio increases proportionately with void diameter. At higher c_{AAm} all the voids are filled with the nodular structure typical of dried hydrogels (Fig. 2e–h). The dried hydrogel conceals the interconnecting holes typical of the bicontinuous structure of polyHIPEs. Nonetheless, the reversible dehydration and rehydration of these polyHIPEs proves that such interconnecting holes exist and that the hydrogel phase is continuous.

The void diameters increase with c_{AAm}, from between 5 and 17 μm for S0 to between 40 and 50 μm for S3. The increase in c_{AAm} seems to reduce HIPE stability, leading to droplet coalescence and/or Ostwald ripening. The presence of increasing amounts of the surface active AAm at the interface can enhance the solubility of the surfactant within the aqueous phase and interfere with the formation of a stable interfacial film [39,40]. At a c_{AAm} of 0.063 g/ml the dried hydrogel is detached from the walls of the polyHIPE (Fig. 2g and h). For S3 the c_{AAm} is high enough for the hydrogel to maintain its shape and it collapses towards the center during drying, detaching from the wall. At even higher c_{AAm}, S4 in Fig. 2i and j, the hydrogel dominates the cross-section and it becomes difficult to distinguish individual voids.

The specific surface area increases with c_{AAm} up to a c_{AAm} of 0.063 g/ml (Fig. 3). The increase in surface area reflects the addition of the nodular dried hydrogel surface area to the typical polyHIPE surface area. Since S4 underwent partial collapse during drying its

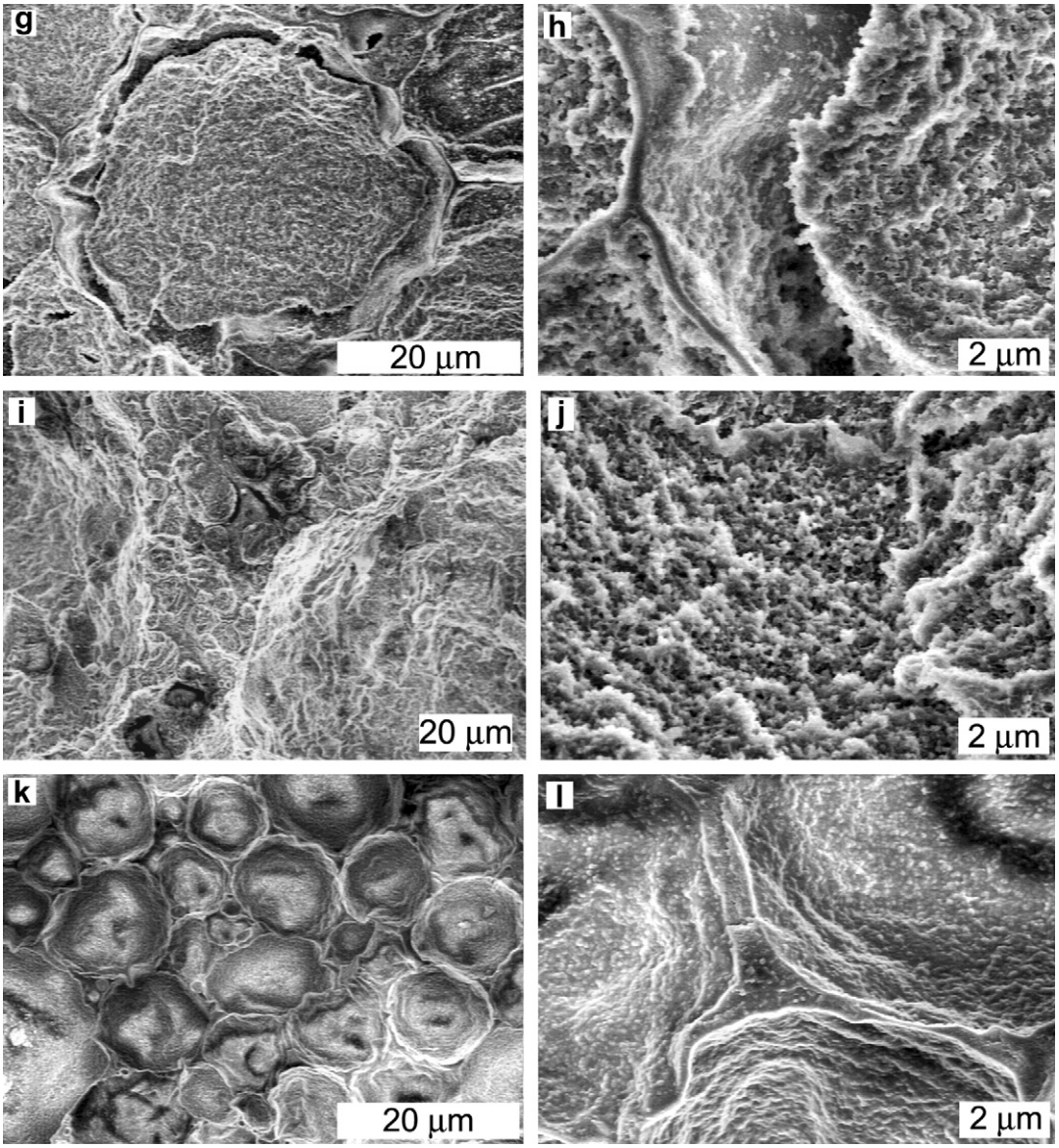

Fig. 2. (*continued*).

specific surface area is smaller than that of S3. The specific surface area thus reflects the complex two-phase structures of the hydrogel-filled polyHIPEs.

3.3. Mechanical properties

Representative compressive stress–strain curves from the hydrated polyHIPEs are presented in Fig. 4. The variation of the hydrated polyHIPE moduli with c_{AAm} is presented in Fig. 5. The decrease in modulus with increasing c_{AAm} is consistent with the results in a previous work [36]. Copolymerization of the hydrophobic monomers in the external phase with the hydrophilic monomers from the internal phase enhances the hydrophilicity of the scaffold. Water that is absorbed by the hydrophilic monomers that have copolymerized with the hydrophobic monomers plasticizes the polymer framework synthesized in the external phase and reduces the modulus of the hydrated polyHIPE. The moduli of the hydrated polyHIPEs in this work are higher than those of similar polyHIPEs in a previous work. This increase in modulus reflects the higher external phase content used in this work. The 20% external phase in this work, as opposed to the 10% in a previous work, results in a significant increase in wall thickness which enhances polyHIPE stiffness and resistance to collapse.

3.4. Loading

The Eosin Y solution loading curves are presented in Fig. 6. The loading plateau values, $u_{s\infty}$, are listed in Table 3. The amount of Eosin Y loaded is, of course, directly proportional to the amount of Eosin Y solution loaded. HG3 exhibits the highest loading plateau of all the materials studied. The ratio of the absorbed volume to the available empty volume, u_v, is also listed in Table 3. The u_v of 1.5 for HG3 reflects its swelling during absorption which increases the volume available for absorption.

The absorption plateaus for the polyHIPEs are substantially less than that for HG3. S0 did not absorb the Eosin Y solution at all. The P(S-*co*-DVB) polyHIPE is highly hydrophobic and poorly wetted by water. The Eosin Y solution absorption plateau increases with increasing c_{AAm} (Table 3) until a maximum is reached for S2. The absorption plateau then decreases with further increases in c_{AAm}.

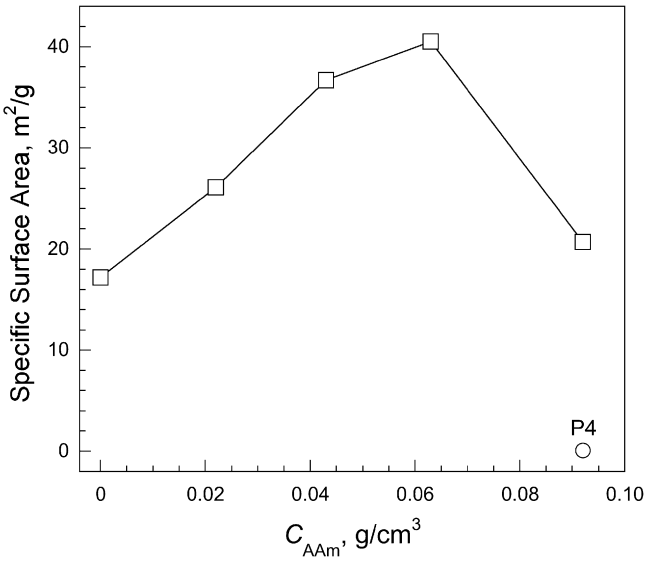

Fig. 3. Specific surface areas of the dried polyHIPEs as a function of c_{AAm}.

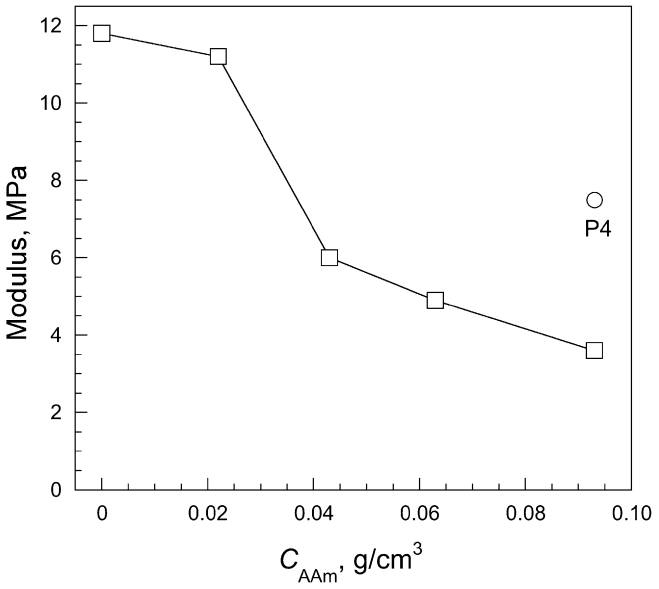

Fig. 5. Variation of hydrated polyHIPE moduli with c_{AAm}.

S1 is only partially filled with hydrogel, as seen in Fig. 2c. S2 is filled with hydrogel, enhancing absorption, and did not undergo significant collapse. While both S3 and S4 are completely filled with hydrogel, they also underwent partial collapse, with their absorption ability reduced by the increase in density and reduction of porosity. The partial collapse is more significant for S4 and, therefore, the absorption plateau is lower. Only 26% of the empty volume was filled for S1, reflecting its low hydrogel content. Around 85% of the empty volume is filled for S2 and S3. Therefore, the differences in plateau values for S2 and S3 reflect their different empty volume contents. Interestingly, the maximum absorption of 85% indicates that 15% of the empty space is inaccessible. The u_v of 1.5 for S4 reflects its swelling during absorption which increases the volume available for absorption. The ability of S4 to swell confirms that its framework from polymerization in the external phase is not a copolymer of S and DVB, but rather a copolymer of S, DVB, AAm, and MBAM.

The absorption of the solution is associated with the presence of AAm in the polyHIPE. $u_{s\infty}$ was normalized by the AAm content to yield the u_{AAm} listed in Table 3. Surprisingly, u_{AAm} for S1 is similar to that of HG3. This seems to indicate that the hydrogel within the polyHIPE has absorbed its equilibrium amount. Unexpectedly, the u_{AAm} for S2 is higher than that of HG3. This indicates that the amount absorbed is greater than the equilibrium absorption of the hydrogel. Not all the water was incorporated into the solution polymerized hydrogel synthesized using a c_{AAm} of 0.043 g/ml. Similarly, in S2, with a c_{AAm} of 0.043 g/ml, the swollen hydrogel may not fill the entire void volume, leaving additional volume in the void for absorption. This type of structure is illustrated schematically in Fig. 7.

The hydrogel in S3, polymerized with a c_{AAm} of 0.063 g/ml, is expected to fill the entire porous structure. The u_{AAm} for S3 is somewhat less than that of HG3. However, if only 85% of the porosity in S3 is available for absorption owing to the presence of some closed porosity (as indicated by the u_v), then the u_{AAm} of 11.1 for the 85% of available hydrogel within the polyHIPE corresponds

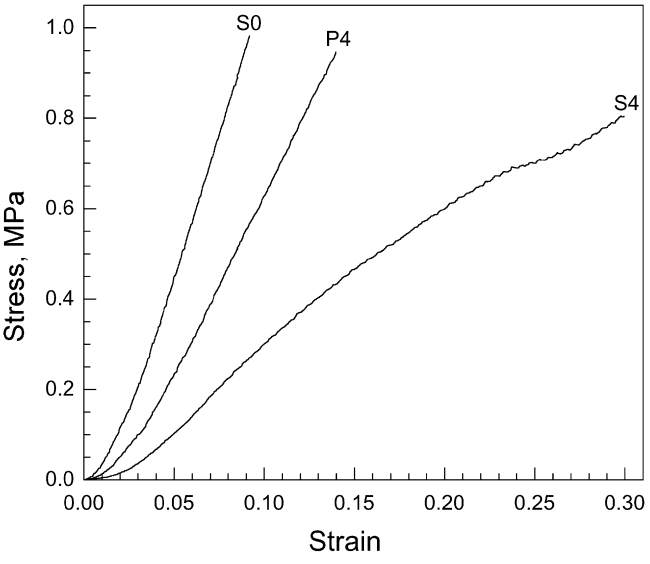

Fig. 4. Compressive stress–strain curves for selected hydrated polyHIPEs.

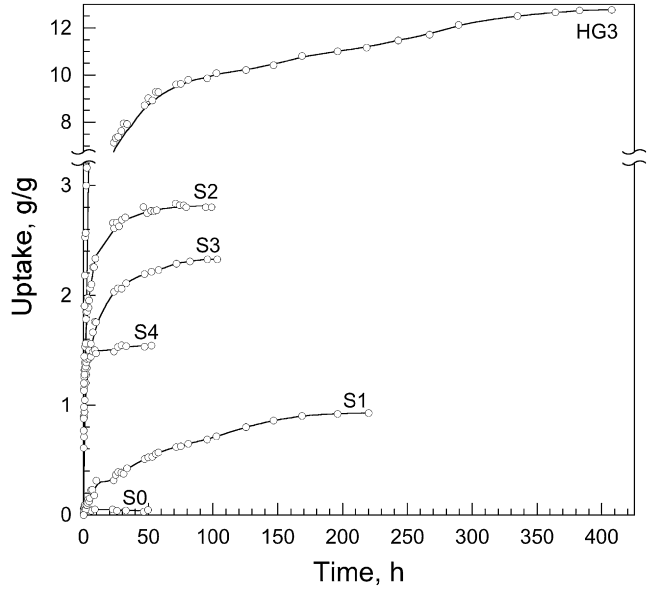

Fig. 6. Eosin Y solution loading curves for various dried polyHIPEs and dried HG3.

Table 3
Plateau values from loading curves (Fig. 6).

Sample	$u_{s\infty}$	u_v	u_{AAm}	Comments
S1	0.9	0.26	11.1	
S2	2.7	0.86	18.1	
S3	2.2	0.85	11.2	
S4	1.5	1.50	5.5	Swells
HG3	13.0	1.50	13.0	Swells
P4	2.1	1.15	7.2	Swells

well with the u_{AAm} of 13.0 for the neat hydrogel. This type of structure is also illustrated schematically in Fig. 7. The porous volume in S4 is not sufficient for the hydrogel polymerized with a c_{AAm} of 0.092 g/ml to reach equilibrium swelling, as illustrated schematically in Fig. 7. The u_{AAm} for S4 of 5.5, which is significantly smaller than that for HG3 in spite of its swelling, indicates that the hydrogel did not reach its equilibrium swelling.

The relative uptake, $u_s/u_{s\infty}$, is presented on a log–log scale in Fig. 8. All the curves exhibit a power-law relationship at short times, described by a power-law exponent, n_1, and a coefficient, k_1, listed in Table 4. The relative uptake at 1 h is reflected by k_1. For HG3, n_1 is 0.44, close to the value of 0.5 that is associated with the diffusion-controlled absorption mechanism in slabs [41]. The relative uptake at 1 h is comparatively small for HG3. S1, with its small hydrogel content and incomplete continuity of the hydrogel-filled structure, does not absorb a great deal of the Eosin Y solution. The n_1 for S1 of 0.55 indicates that the absorption mechanism is similar to the diffusion-controlled absorption mechanism in slabs. S1 does not exhibit the rapid uptake typical of capillary action and has a relatively low k_1.

Most hydrogel-filled polyHIPEs (S2, S3, and S4) exhibit a relatively high uptake at short times. In fact, the relative uptake was greater than 20% before the first point could be measured. This rapid uptake results from the capillary action within the porous polyHIPE structure. The time scale for capillary action can vary from seconds to minutes, depending upon the wetting angle and the capillary diameter [42,43]. The absorption of water within a hydrophilic polyHIPE scaffold based on poly(2-hydroxyethyl methacrylate) exhibited capillary action and reached equilibrium swelling in less than 10 min [28]. The voids, filled with dried hydrogel, are rapidly filled through capillary action. The rate of uptake for these polyHIPE decreases following the rapid initial uptake through capillary action. Following capillary action, the diffusion pathway is analogous to diffusion through an assembly of polydisperse spheres [41]. The n_1 of around 0.24 for these polyHIPEs is relatively low, as was found for diffusion through polydisperse spheres [41].

3.5. Release

The release curves for Eosin Y are presented in Fig. 9 HG3 exhibits a relatively rapid and complete release of Eosin Y. S1

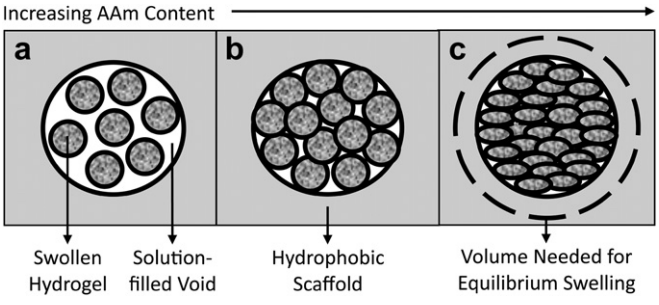

Fig. 7. Schematic illustration of hydrogel swelling in the polyHIPE voids for different c_{AAm}: (a) the swollen hydrogel does not fill the void volume; (b) the swollen hydrogel fills the void volume; (c) the equilibrium swelling volume of the hydrogel is larger than the void volume.

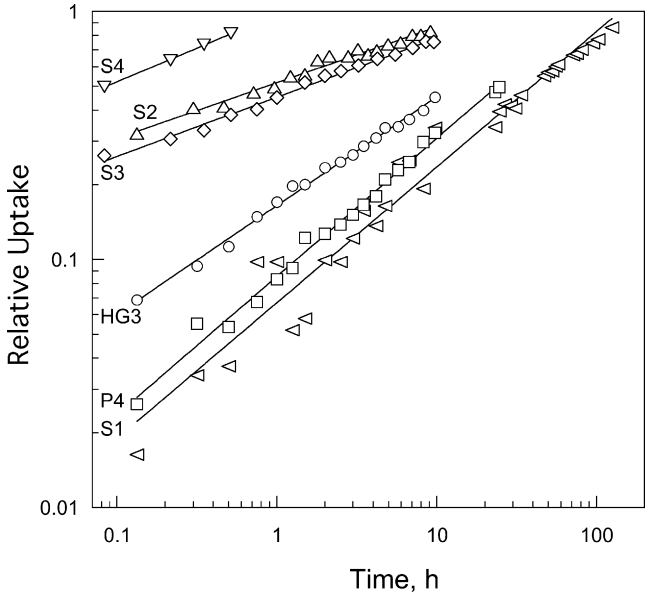

Fig. 8. Eosin Y solution loading curves for various dried polyHIPEs and dried HG3 (log–log).

exhibits a relatively low release plateau. The relatively low uptake in S1 was ascribed to its incompletely interconnected hydrogel phase and the release is relatively low for the same reason. The release curves from S2 and S3 exhibit a more sustained release when compared to the release from HG3. HG3 reaches a release plateau within 10 h, while S2 and S3 only reach plateaus after periods of around 250 h (10.4 days). The release curve for S4, with the highest hydrogel concentration, is similar to that for HG3. As discussed previously, in S2 and S3 the PS-based walls are more hydrophobic than for S4. Therefore, in S2 and S3 the diffusion path is through the interconnected hydrogel phase and highly tortuous, yielding a more sustained release [44]. The walls are significantly more hydrophilic for the more extensive copolymerization in S4 and diffusion via the walls offers a less tortuous alternative. The reduction in tortuosity makes diffusion through the bicontinuous polymer system in S4 similar to diffusion through the neat hydrogel HG3.

The Eosin Y release curves are presented on a log–log scale in Fig. 10. All the materials in Fig. 10 exhibit a power-law relationship over an extended time. The coefficients n_2 and k_2 from the power-law fit to the data are listed in Table 4. The n_2 for HG3 is consistent with diffusion through a slab, as was the n_1. S1 reaches a release plateau so rapidly that it does not exhibit a power-law relationship over an extended time.

The release of Eosin Y from a dried polyHIPE consists of two stages: (1) the absorption of water through capillary action and swelling of the gel; (2) the diffusion of Eosin Y through the hydrated polyHIPE. Eosin Y has a relatively high water solubility and, therefore, it can be considered to dissolve immediately. The measurement of the Eosin concentration outside the polyHIPE is, in

Table 4
Kinetic parameters from loading curves (Fig. 8) and release curves (Fig. 10).

	Loading		Release	
Sample	k_1	n_1	k_2	n_2
S1	0.07	0.55	–	–
S2	0.52	0.22	0.15	0.27
S3	0.45	0.24	0.14	0.34
S4	0.97	0.27	0.33	0.46
HG3	0.17	0.44	0.47	0.46
P4	0.09	0.56	0.06	0.41

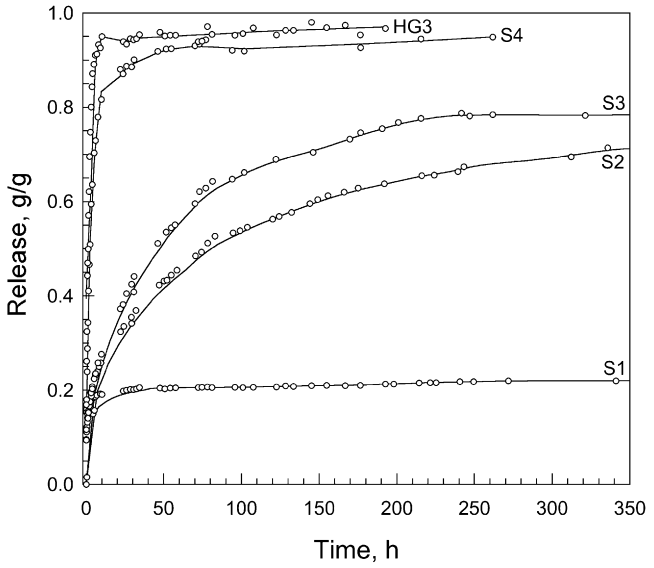

Fig. 9. Eosin Y release curves for various dried polyHIPEs and dried HG3.

essence, a measurement of the second process. The rapid absorption of water through capillary action seen in the loading experiments will not necessarily produce the rapid release of Eosin Y since the release is also dependent on the diffusion of Eosin Y out of the polyHIPE. The n_2 for S2 and S3 are significantly smaller than 0.5, as the case for their n_1. This indicates that the diffusion pathway is equivalent to diffusion through an assembly of polydisperse spheres, as discussed previously [41]. S4 exhibits an n_2 of 0.46, similar to that of the hydrogel. This is another indication that copolymerization of the AAm in the external phase enhanced the hydrophilicity of the scaffold, making the diffusion similar to diffusion through a slab, making the diffusion through S4 similar to diffusion through HG3.

3.6. Pre-polymerization

Pre-polymerization of the S4 HIPE, polymerization of the external phase prior to HIPE formation, limited the amount of AAm incorporated into the polymer walls through copolymerization, enhanced the hydrophobicity of the walls, and increased the tortuosity of the diffusion path. The HIPE recipe for P4 is identical to that for S4, except that the external phase underwent pre-polymerization. As a result of the pre-polymerization, which limited the AAm incorporation into the walls, the density of P4 is significantly lower than that of S4 (Fig. 1) and is closer to the predicted density. The lower density indicates that P4 is better able to resist the capillary forces generated during drying and does not collapse to the same extent as S4. While the copolymerization with AAm is more limited in P4 than in S4, it does occur to some extent, as reflected in the partial collapse that produces a density that is greater than expected (Fig. 1). This is also reflected in the mechanical properties. The stress–strain curve of P4 (Fig. 4) falls between that of S4 and that of S0, the control polyHIPE containing no AAm. The modulus of P4, while less than that of S1, is greater than that of S2 (Fig. 5).

Pre-polymerization seems to enhance HIPE stability. The void dimensions of P4 (Fig. 2k and l) are significantly smaller than the void dimensions of S4 (Fig. 2i and j). The void dimensions of P4 are, in fact, similar to those of S0 (Fig. 2a and b). The reduction in void dimensions and the increase in porosity combine to yield a higher surface area to volume ratio for P4 than is found for S4. The volume of hydrogel distributed over the greater surface area caused the formation of a hydrogel coating on the void walls (Fig. 2l) when the polyHIPE is dried. This coating seems to block the interconnecting holes and makes the porous structure inaccessible to the surface area measurement, yielding an extremely low surface area for the dried polyHIPE (Fig. 3).

The Eosin Y solution loading curve and the Eosin Y release curve for P4 are presented in Fig. 11 and Fig. 12, respectively. The power-law parameters from Figs. 11 and 12 are listed in Table 4. The sealing of the interconnecting holes by a hydrogel coating (Fig. 2l) prevents the rapid capillary action seen during uptake for S2, S3, and S4. The Eosin solution diffuses through the hydrogel coating on the walls and this diffusion process yields the n_1 of 0.56 for P4. The release from P4 is less affected by the lack of capillary action since the hydrogel is already partially swollen once release begins, producing an n_2 of 0.41. The n_2 for P4 is less than that of S4, reflecting the more hydrophobic wall in P4 which prevents slab-like diffusion.

The reduction in the extent of copolymerization with AAm through pre-polymerization, reduced the permeability of the walls to Eosin Y, and resulted in a significant reduction in release rate.

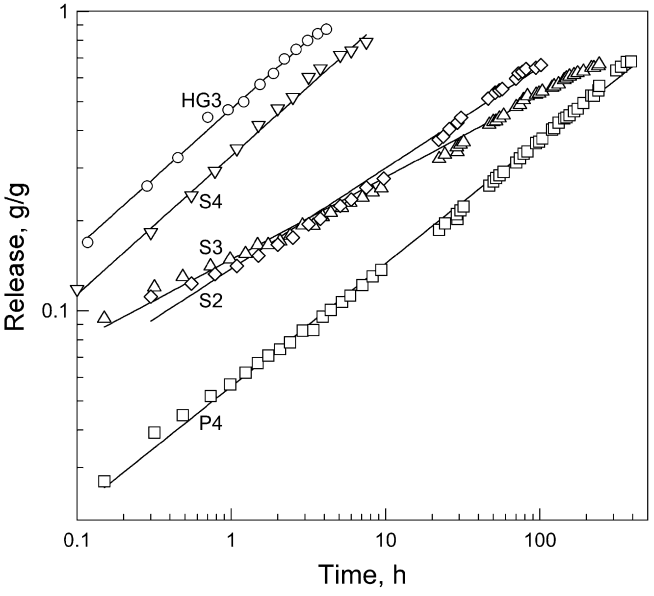

Fig. 10. Eosin Y release curves for various dried polyHIPEs and dried HG3 (log–log).

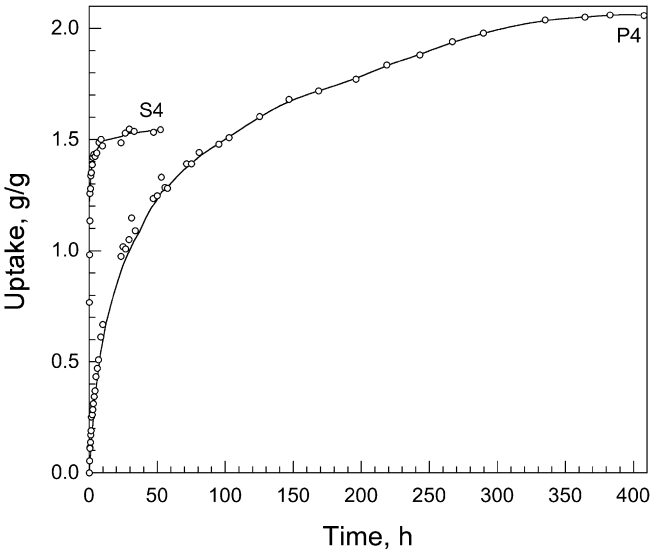

Fig. 11. The effect of pre-polymerization on the Eosin Y solution loading curve.

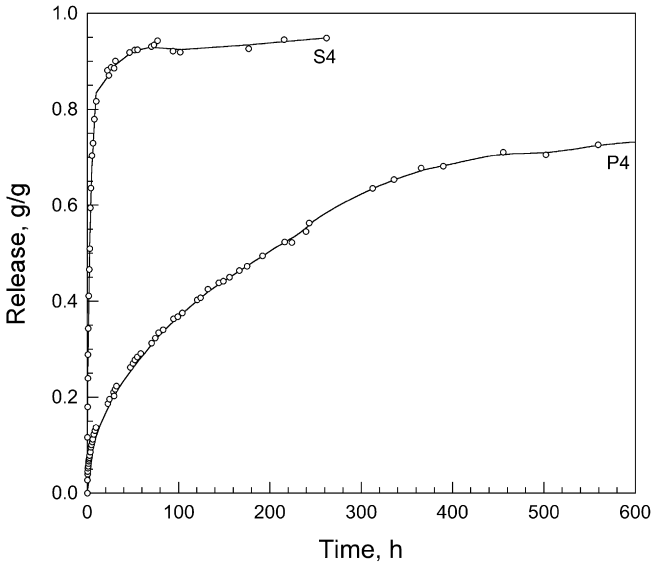

Fig. 12. The effect of pre-polymerization on the Eosin Y release curve.

While S4 reached a release plateau in 10 h, it took 450 h for P4 to reach its release plateau, longer than the times exhibited by S2 and S3. Pre-polymerization affected the molecular structure of the walls which, in turn, affected the porous structure tortuosity, the bicontinuous structure, the porosity, and, finally, the release mechanism. By sealing the interconnecting holes in the dried polyHIPE, pre-polymerization reduced the contribution of capillary action, made the diffusion pathway more tortuous, and, thus, extended the time needed for uptake and release.

4. Conclusions

Simultaneous polymerizations within both phases of W/O HIPEs were used to synthesize a synergistic bicontinuous material consisting of hydrogel-filled hydrophobic polymer scaffolds. The PS-based scaffold that contained no hydrogel could not absorb the aqueous Eosin Y solution. The PAAm-based hydrogels, on the other hand, reached release plateaus after 10 h. By integrating hydrogels within polyHIPEs, the release continued for more than 10 days. The pre-polymerized hydrogel-containing polyHIPE continued to exhibit release for up to 3 weeks.

The bicontinuous polyHIPEs combine capillary action with more typical hydrogel behavior. The capillary action, enhanced by the hydrophilicity of the hydrogel-coated surfaces, caused the water to be rapidly distributed throughout the hydrogel. This is quite different from the transport of water through a moving front of swelling hydrogel. The diffusion pathway was analogous to diffusion through an assembly of polydisperse spheres and produced the relatively low power-law exponents of around 0.24 during uptake and of around 0.30 during release. The copolymerization of AAm in the external phase enhanced the hydrophilicities of the scaffolds, reduced the moduli of the hydrated polyHIPEs, reduced the tortuosities of the diffusion paths, and increased the power-law exponent. Pre-polymerization reduced the extent of copolymerization, enhanced the modulus of the hydrated polyHIPE, sealed the interconnected structure in the dried polyHIPE, reduced the contribution of capillary action, increased the tortuosity, and, thus, extended the time needed for uptake and release.

Acknowledgements

The partial support of the Israel Science Foundation and of the Technion VPR Fund is gratefully acknowledged.

References

[1] Barby D, Haq Z. US Pat 4552953;1985.
[2] Cameron NR. Polymer 2005;46:1439–49.
[3] Williams JM, Wrobleski DA. Langmuir 1988;4:656–62.
[4] Williams JM, Gray AJ, Wilkerson MH. Langmuir 1990;6:437–44.
[5] Cameron NR, Sherrington DC. Advances in Polymer Science 1996; 126:163–214.
[6] Cameron NR, Krajnc P, Silverstein MS. In: Silverstein MS, Cameron NR, Hillmyer MA, editors. Porous polymers. Hoboken NJ: Wiley; 2011 [Chapter 4].
[7] Silverstein MS, Cameron NR. PolyHIPEs – Porous polymers from high internal phase emulsions. In: Encyclopedia of polymer science and technology. Online: John Wiley & Sons, Inc; New York, doi:10.1002/0471440264.pst571, 2010.
[8] Sergienko A, Tai H, Narkis M, Silverstein MS. Journal of Applied Polymer Science 2004;94:2233–9.
[9] Leber N, Fay JDB, Cameron NR, Krajnc P. Journal of Polymer Science Part A: Polymer Chemistry 2007;45:4043–53.
[10] Tai H, Sergienko A, Silverstein MS. Polymer Engineering & Science 2001;41:1540–52.
[11] Livshin S, Silverstein MS. Macromolecules 2007;40:6349–54.
[12] Busby W, Cameron NR, Jahoda CAB. Biomacromolecules 2001;2:154–64.
[13] Hayman MW, Smith KH, Cameron NR, Przyborski SA. Biochemical and Biophysical Methods 2005;62:231–40.
[14] Akay G, Birch MA, Bokhari MA. Biomaterials 2004;25:3991–4000.
[15] Stefanec D, Krajnc P. Reactive and Functional Polymers 2005;65:37–45.
[16] Lumelsky Y, Lalush-Michael I, Levenberg S, Silverstein MS. Journal of Polymer Science Part A: Polymer Chemistry 2009;47:7043–53.
[17] Mercier A, Deleuze H, Maillard B, Mondain-Monval O. Advanced Synthesis & Catalysis 2002;344:33–6.
[18] Moine L, Deleuze H, Maillard B. Tetrahedron Letters 2003;44:7813–6.
[19] Tai H, Sergienko A, Silverstein MS. Polymer 2001;42:4473–82.
[20] Silverstein MS, Tai H, Sergienko A, Lumelsky Y, Pavlovsky S. Polymer 2005;46:6682–94.
[21] Normatov J, Silverstein MS. Macromolecules 2007;40:8329–35.
[22] Normatov J, Silverstein MS. Chemistry of Materials 2008;20:1571–7.
[23] Menner A, Powell R, Bismarck A. Soft Matter 2006;4:337–42.
[24] Haibach K, Menner A, Powell R, Bismarck A. Polymer 2006;47:4513–9.
[25] Menner A, Haibach K, Powell R, Bismarck A. Polymer 2006;47:7628–35.
[26] Desforges A, Backov R, Deleuze H, Mondain-Monval O. Advanced Functional Materials 2005;15:1689–95.
[27] Livshin S, Silverstein MS. Journal of Polymer Science Part A-Polymer Chemistry 2009;47:4840–5.
[28] Kulygin O, Silverstein MS. Soft Matter 2007;2:1525–9.
[29] Butler R, Davies CM, Cooper AI. Advanced Materials 2001;13:1459–63.
[30] Butler Hopkinson R, Hopkinson I, Cooper AI. Journal of the American Chemical Society 2003;125:14473–81.
[31] Zhang H, Cooper AI. Advanced Materials 2007;19:2439–44.
[32] Ruckenstein E, Sun F. Journal of Membrane Science 1993;81:191–201.
[33] Ruckenstein JS, Park S. Journal of Polymer Science Part C: Polymer Letters 1988;26:529–36.
[34] Park JS, Ruckenstein E. Journal of Applied Polymer Science 1989;38:453–61.
[35] Ruckenstein E, Park JS. Journal of Applied Polymer Science 1990;40:213–20.
[36] Gitli T, Silverstein MS. Soft Matter 2008;4:2475–85.
[37] Saltzman WM. Drug delivery. New York: Oxford University Press; 2001. pp 259–262.
[38] Welsh WJ. In: Mark JE, editor. Pysical properties of polymers handbook. New York: American Institute of Physics; 1996. p. 401–9.
[39] Zhu JH, Shao F, Zhan YH, Yan XL, Zhang B. Colloids and Surfaces A 2006; 290:19–24.
[40] Carnachan RJ, Bokhari M, Przyborski SA, Cameron NR. Soft Matter 2006;2:608–16.
[41] Ritger PL, Peppas NA. Journal of Controlled Release 1987;5:37–42.
[42] Lavi B, Marmur A, Bachmann J. Langmuir 2008;24:1918–23.
[43] Van-Oss CJ, Giese RF, Li Z, Murphy K, Norris J, Chaudhury MK, et al. Journal of Adhesion Science and Technology 1992;6:413–28.
[44] Saltzman WM. Drug delivery. New York: Oxford University Press; 2001. p. 79–82.

Polymer 52 (2011) 116–121

Contents lists available at ScienceDirect

Polymer

journal homepage: www.elsevier.com/locate/polymer

Polyvinylbutyral assisted synthesis and characterization of chalcopyrite quaternary semiconductor Cu(In_xGa_{1-x})Se_2 nanofibers by electrospinning route

Lin-Jer Chen [a], Jiunn-Der Liao [a,*], Yu-Ju Chuang [a], Yaw-Shyan Fu [b]

[a] Department of Materials Science and Engineering, National Cheng Kung University, Tainan 701, Taiwan, ROC
[b] Department of Greenergy Technology, National University of Tainan, 701, Taiwan

ARTICLE INFO

Article history:
Received 28 August 2010
Received in revised form
20 October 2010
Accepted 31 October 2010
Available online 11 November 2010

Keywords:
CIGS
Electrospinning
Polyvinylbutyral

ABSTRACT

Chalcopyrite quaternary semiconductor Cu (In_xGa_{1-x}) Se_2 nanocrystals were successfully prepared via a relatively simple electrospinning route and characterized using X-ray powder diffraction (XRD), scanning electron microscopy (SEM), thermogravimetric analysis (TGA) and transmission electron microscopy (TEM). Semiconductor Cu(In_xGa_{1-x})Se_2 nanofibers were obtained for PVB/Cu(In_xGa_{1-x})Se_2 precursor at an applied voltage of 20 kV after annealing treatment at 400 °C for 6 h. The optical property of Cu (In_xGa_{1-x}) Se_2 nanocrystals was also recorded by means of UV–vis absorption spectroscopy. We also report the first electrospinning synthesis of uniform chalcopyrite crystals Cu (In_xGa_{1-x})Se_2 nanofibers and demonstrate can be used to create simple thin film solar cells, with our first cells exhibiting an efficiency of 1.96% under AM1.5 illumination.

1. Introduction

I–III–VI_2 chalcopyrite compounds are some of the most promising candidates for thin film photovoltaic applications, such as Cu (In_xGa_{1-x})Se_2 (CIGS), have been regarded as one of the most promising materials for photovoltaic because of their low toxicity and high conversion efficiency [1–5]. An attractive alternative is the synthesis of nontoxic I–III–VI_2 family. Crystalline CIGS films offer an alternative solar energy conversion material, providing both efficiencies up to 19.2% [6] and excellent longevity [7]. However, the widespread utilization of I–III–VI_2 based solar cells has been hindered by the high costs vacuum deposition techniques. Various wet-chemical have been explored to reduce the processing cost [8–10].

The I–III–VI_2 quaternary alloy system can be synthesized by a variety of ways such as solvothermal techniques [11], hydrothermal techniques [12], single-source decomposition [13,14], and hot-injection technique [15,16]. It has been known that crystal structure, composition, and size of the nanocrystals may significantly affect their optoelectronic property and device performance [17]. As composition and structural control becomes difficult for ternary and quaternary compounds. Solution-based approach alleviates the need for a high temperature annealing step under selenium atmosphere and avoiding Se loss [18]. Semiconductor nanocrystals have also been combined with polymers to produce solution-processed photovoltaics, such as hybrid CdSe nanocrystal/poly-3(hexylthiophene) solar cells, which yield reported efficiencies of up to 1.7% [19].

The electrospinning technique is one of the most promising methods for the fabrication of 1D nanostructure materials [20]. Research on the synthesis of various inorganic and metal-oxide nanowires via electrospinning has recently increased [21,22]. The electrospinning route is a simple, versatile, and relatively inexpensive technique for the synthesis of a broad range of hybrid nanocomposites. Unlike other methods that produce short nanorods or nanotubes, electrospinning produces continuous nanofibers and nanotubes. Although electrospinning has been used mainly for the fabrication of organic polymeric nanofibers, ceramic metal-oxide nanofibers has also received considerable interest due to their potential applications in areas including photovoltaic devices, piezoelectric materials, gas sensors, and solar cells [23–26]. Polyvinylbutyral (PVB) has been commonly used as capping agent. PVB is a nontoxic, odorless, and environmentally friendly polymer that is widely used as a functional material in various fields [27]. Due to its good compatibility with inorganic materials, PVB is an excellent organic component for the fabrication of organic/inorganic hybrid composites. To the best of our knowledge, Cu (In_xGa_{1-x})Se_2 nanofibers synthesis using electrospinning routes has not been reported previously. Our synthesis marks an advance for chalcopyrite quaternary semiconductor nanofibers and offers a possible template by electrospinning. This method is attractive due to simplicity, low cost of manufacture, and scalability of the synthesis.

* Corresponding author. Tel.: +886 6 2757575x62971; fax: +886 6 2346290.
E-mail address: jdliao@mail.ncku.edu.tw (J.-D. Liao).

0032-3861/$ – see front matter © 2010 Elsevier Ltd. All rights reserved.
doi:10.1016/j.polymer.2010.10.058

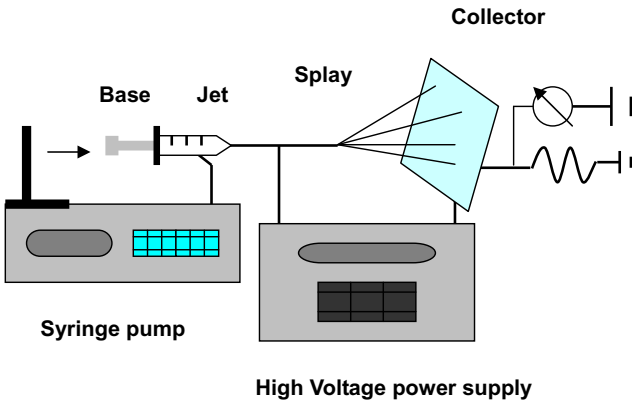

Fig. 1. Schematic diagram of electrospinning device.

2. Experimental section

2.1. Materials

All chemicals were used as received without further purification. Copper(I) chloride (CuCl; 99.99%), indium(III) chloride ($InCl_3$; 99.99%) from Aldrich Chemical Co.; elemental selenium (99.99%) and gallium (III) chloride ($GaCl_3$; 99.9999%) from Strem Chemicals; ethanol absolute and hydrochloric acid were from PA Panreac; Polyvinylbutyral (PVB) (average $M_v \sim 40$ kDa) was obtained from ChangChun Group Company.

2.2. Preparation of electrospinning solution and Cu (In_xGa_{1-x})Se_2 nanofibers

In a nitrogen-filled glovebox, a typical reaction is carried about by adding 1 mmol of CuCl, 2 mmol of elemental Se, 1 mmol total of $InCl_3$ and $GaCl_3$, 30 wt. % PVB (PVB/ethanol content ratio = 3:7), 20 ml ethanol absolute and 1 ml hydrochloric acid to a 30-ml three-neck flask with attached condenser and stopcock valve in a nitrogen-filled glovebox, while magnetically stirred at room temperature for 2 h, followed by N_2 bubbling at 80 °C for 2 h while stirring to obtain a homogenous precursor of PVB/Cu(In_xGa_{1-x})Se_2 composites.

A schematic setup of the electrospinning route used in this study is shown in Fig. 1. In the electrospinning of polymer solutions, the fiber formation process is characterized by the formation and thinning of the liquid jet and the solidification and deposition of fibers on the collection target. A stainless steel electrode was connected to a high voltage power supply (You-Shang Technical Corp.), which can generate a DC voltage of up to 30 kV. The applied voltage between the tip and collector were set at 20 kV with a tip-to-collector distance of 18 cm. The applied voltage overcomes the liquid surface tension to form a jet, which then bends and spirals into a large looping path as it thins into fine fibers and solidifies. Homogeneous precursor solutions of PVB/Cu (In_xGa_{1-x})Se_2 composites were prepared and used immediately for electrospinning. Finally PVB/Cu (In_xGa_{1-x})Se_2 nanofibers were obtained. The applied voltage, tip-to-collector distance, viscosity, and concentration were varied.

2.3. Morphologies of PVB/Cu (In_xGa_{1-x})Se_2 nanofibers

The as-prepared samples were characterized by X-ray powder diffraction (XRD), scanning electron microscopy (SEM), a thermogravimetric analysis (TGA), and transmission electron microscopy (TEM), respectively. XRD was carried out on a D/MAX-500 X-ray powder diffraction system with Cu Ka radiation (λ = 1.5418 Å). A scanning rate of 0.02 s^{-1} was applied to record the patterns in the 2 Theta range of 15–80°. TEM characterization was conducted on a JEM-2000EX system using an acceleration voltage of 160 kV.

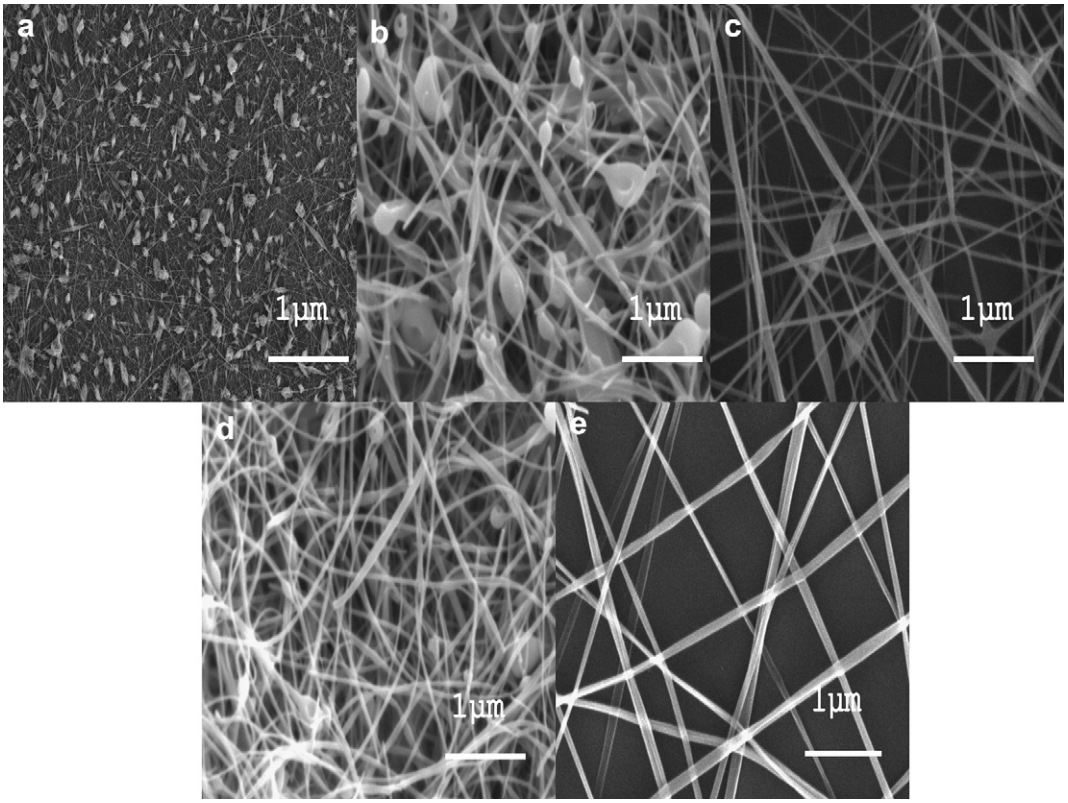

Fig. 2. SEM images of PVB/Cu (In_xGa_{1-x})Se_2 composite nanofibers electrospinning from (a) 10 wt.%, (b) 20 wt.%, (c) 30 wt.%, and (d) 40 wt.% aqueous solutions at 20 kV; (e) pure PVB fibers.

A Hitachi S-4200A scanning electron microscopy (SEM) with at an acceleration voltage of 5 kV was employed to characterize the morphologies.

3. Results and discussion

3.1. Morphologies of electrospinning PVB/Cu (In_xGa_{1-x})Se_2 composite fibers formation

Fig. 2 shows a series of SEM images of PVB/Cu (In_xGa_{1-x})Se_2 nanofibers obtained from precursor solutions with concentration ratios of 10 wt.%, 20 wt.%, 30 wt.%, and 40 wt.%(PVB/ethanol content ratio = 1:9, 2:8, 3:7 and 4:6). As can be seen in Fig. 2(a), fewer fibers were obtained when the ratio was 10 wt.%. Because of the ratio decreased, the conductivity of fibers increased, the viscosity of fibers decreased, and bead-on-string structures appeared. When the ratio further increased, the beads on fibers decreased. The results showed that high concentration preferred generated fibers ratios increased. The high conductivity solvent is helpful to the ion diffusion and reduces resistance. The high viscosity solvent can cause the diffusion of ions not to be easy, to reduce the conductivity [28].

When the concentration of PVB was increased, bead-on-string structures were observed, as shown in Fig. 2(b)–(d), and the bead density decreased. PVB/Cu (In_xGa_{1-x})Se_2 nanofibers with smooth surfaces were obtained when the PVB/ethanol ratio was 30 wt.%. The concentration of PVB is thus a key factor in the preparation of smooth PVB/Cu (In_xGa_{1-x})Se_2 nanofibers. PVB acted as the capping agent, which in the PVB/Cu(In_xGa_{1-x})Se_2 composite nanofibers exist states is adsorbed polymer chains induce not only steric repulsion but also bridging attraction. Pure PVB fibers are shown in Fig. 2(e); their morphology is smooth than those of PVB/Cu (In_xGa_{1-x})Se_2 fibers.

The effect of the parameters of the solution on the morphology of nanofibers was investigated. The diameter of PVB/Cu (In_xGa_{1-x})Se_2 composite fibers obtained at various work distances and concentrations are shown in Fig. 3. With increasing concentration ratio, the diameter of PVB/Cu (In_xGa_{1-x})Se_2 composite fibers decreased and bead-on-string structures appeared. When the concentration ratio was further increased, the beads on fibers decreased, as shown in Fig. 3 (blue line). Compared with various concentrations, the capping agent forms stable complexes with the precursor, which the rapid formation of small nanoparticles as the crystal nuclei and slow crystal growth to form nanofibers from the crystal nuclei according to the inherent crystal structure. In this instance, the work distance from the tip of the needle to the collector is enough long for the elongation and solidification of the jet to form fibers, as shown in Fig. 3 (black line). However, when the work distance was shortened, the fiber diameter increased. That is, the morphology of the electrospinning structure transformed quickly and one was the evaporation of solvent in the jet was partly suppressed. The whipping instability, which facilitated the diffusion of the jet, was greatly suppressed [29]. The results show that a large work distance is preferred for electrospinning.

Fig. 4 shows fiber diameters of PVB/Cu (In_xGa_{1-x})Se_2 composite fibers for various viscosities and applied voltages (10 kV, 15 kV, 20 kV, and 22 kV). The fiber diameter decreased with increasing viscosity, as expected (Fig. 4, black line). One hundred PVB/Cu (In_xGa_{1-x})Se_2 composite fibers were selected from ten spots of $60 \times 60\ \mu m^2$ to measure the distribution of the diameters. This may be due to the greater expanded conformation of PVB/Cu (In_xGa_{1-x})Se_2 in the solution caused by the electrostatic repulsion between PVB/Cu (In_xGa_{1-x})Se_2 mixture molecules. The molecular entanglement of PVB/Cu (In_xGa_{1-x})Se_2 in solution is thus expected to be higher. It was observed that the diameter distribution of the PVB/Cu (In_xGa_{1-x})Se_2 composite fibers decreased with increasing applied voltage (Fig. 4, blue line). The jet is driven by a high electrical potential applied between the collector and the solution. The electrical forces which stretch the wires are resisted by the elongation viscosity of the jet. A reduction in size with the applied voltage has been reported for various electrospinning organic fibers [30].

3.2. Thermal behavior of electrospinning PVB/Cu (In_xGa_{1-x})Se_2 composite fibers formation

Fig. 5 shows TGA thermogram of the PVB/Cu (In_xGa_{1-x})Se_2 nanofibers. It was observed that the weight substantially decreases in the low temperature region. PVB/Cu (In_xGa_{1-x})Se_2 nanofibers (Fig. 5(a)) exhibited three steps and a total loss of ca. 47.2%. The first step of ca. 7.7%, from 100 to 320 °C, can be attributed to the loss of volatile water and ethanol solution. The higher thermal stability of PVB/Cu (In_xGa_{1-x})Se_2 fiber might be attributed to its higher chain compactness due to the interaction between the PVB and the Cu (In_xGa_{1-x})Se_2 materials [31]. The second significant weight loss of ca. 27.7%, between 330 and 480 °C, can be attributed to the loss of crystal water and the decomposition of acetate along with the degradation of PVB by dehydration on the polymer side chain [32]. The third step, which started at about 450 °C and ended at about

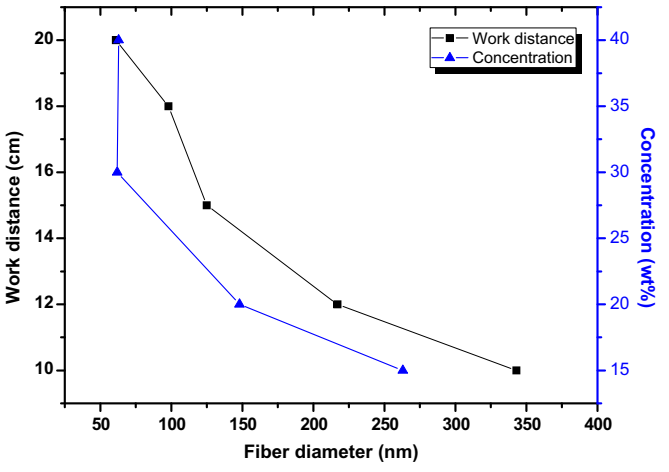

Fig. 3. Diameters of PVB/Cu (In_xGa_{1-x})Se_2 composite fibers for various work distances and concentration ratios.

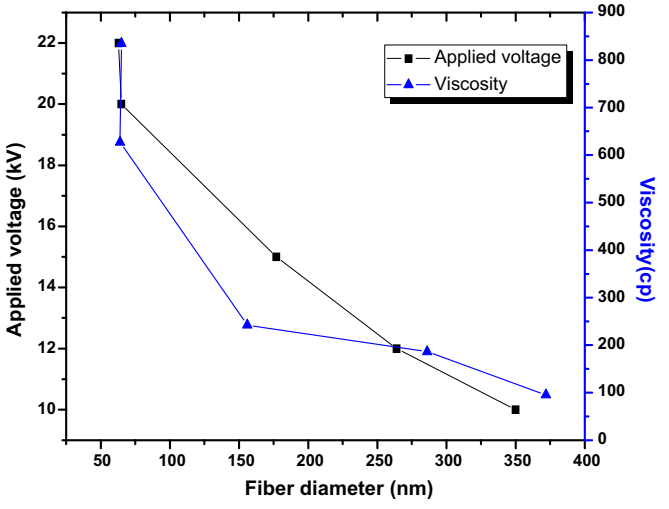

Fig. 4. Diameters of PVB/Cu (In_xGa_{1-x})Se_2 composite fibers for various viscosities and applied voltages.

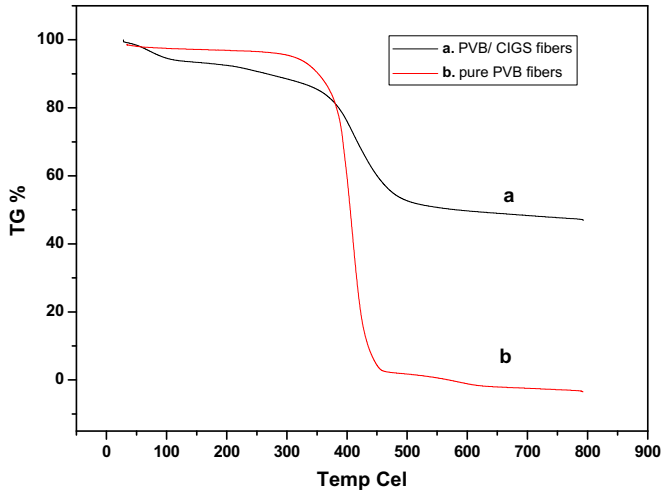

Fig. 5. Thermogravimetric analysis (TGA) curves of PVB/Cu $(In_xGa_{1-x})Se_2$ nanofibers. (a) 30 wt % PVB/Cu $(In_xGa_{1-x})Se_2$ fiber and (b) pure PVB fiber.

580 °C was a weight loss of ca.11.8%, which was assigned to the release of water formed from the condensation of carbonyl groups in the PVB/Cu $(In_xGa_{1-x})Se_2$ framework and the decomposition of the excess chalcogen species [33–35]. It is clear from the TG curve that all the PVB and the organic group were removed completely at 680 °C, resulting in a metal oxide composite phase [36–39]. The weight loss of PVB fibers (Fig. 5(b)) began to occur at approximately 320 °C and was complete at about 560 °C. The temperatures corresponding to the peak maxima were near 400 °C for ions representing aliphatic species and near 410 °C for alkyl aromatics.

3.3. *Structures of tetragonal chalcopyrite Cu $(In_xGa_{1-x})Se_2$ nanocrystals formation*

Fig. 6 shows the XRD patterns of Cu $(In_xGa_{1-x})Se_2$ fibers obtained (a) before annealing, and (b–e) after annealing at 400 °C for 3 h, 6 h and (f) after annealing at 600 °C for 6 h. Fig. 6 shows the XRD spectra of Cu $(In_xGa_{1-x})Se_2$ nanofibers were used; five peaks corresponding to (112), (204)/(220), (116)/(312), (008)/(400), and (316)/(332) of the Cu $(In_xGa_{1-x})Se_2$ crystal structure, respectively, can be observed. All of the diffraction peaks can be indexed as the tetragonal chalcopyrite phase of CIGS (JCPDS 80–0075), which implies that pure Cu $(In_xGa_{1-x})Se_2$ was synthesized. Thus, in order to determine that the nanocrystals are chalcopyrite, it is crucial to be able to observe the

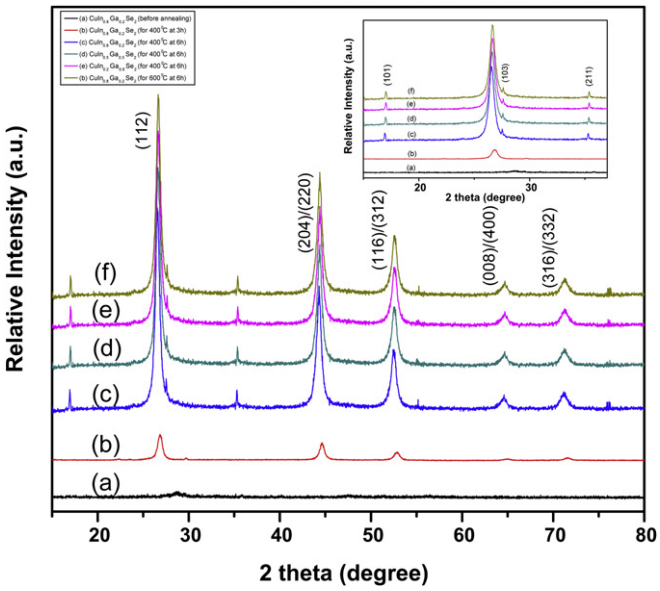

Fig. 6. XRD patterns of quaternary Cu (In_xGa_{1-x}) Se_2 nanocrystals synthesized by the electrospinning process obtained (a) before annealing, (b–e) after annealing by 400 °C for 3 h, 6 h, and (f) after annealing by 600 °C for 6 h.

minor peaks that are unique to the chalcopyrite structure. For instance, the minor peaks at 17.14°, 27.74°, and 35.55° corresponding to the (101), (103), and (211) peaks, respectively, are unique to the chalcopyrite structure and are shown as an inset of Fig. 6. The diffraction peaks also show patterns gradually shifting toward the higher angle with increasing gallium content, due to the decreased lattice spacing with smaller gallium atoms substituting for larger indium atoms. However, after annealing at 400 °C for 6 h and 600 °C for 6 h, a single phase of well-crystallized Cu $(In_{0.8}Ga_{0.2})Se_2$ with a tetragonal chalcopyrite structure was obtained. A completely crystalline structure formed in the Cu $(In_{0.8}Ga_{0.2})Se_2$ nanofibers with the addition of PVB to the electrospinning step after annealing. The FWHM (full width at half-maximum) values of the CIGS nanofibers were similar to those calculated using the Scherrer equation ($D = K\lambda/(\beta \cos\theta)$; $K = 0.89$, $\lambda = 0.15418$ nm, $\beta =$ FWHM, $\theta =$ diffraction angle). According to the Vegard's law, the lattice constants measured for the Cu $(In_{0.8}Ga_{0.2})$ Se_2 samples were $a = 5.583 \pm 0.002$ Å and $c = 11.203 \pm 0.002$ Å, with the $c/2a$ ratio of 1.003 ± 0.002. The observed lattice parameters and $c/2a$ ratio agree very well with the reported values for the chalcopyrite phase [2].

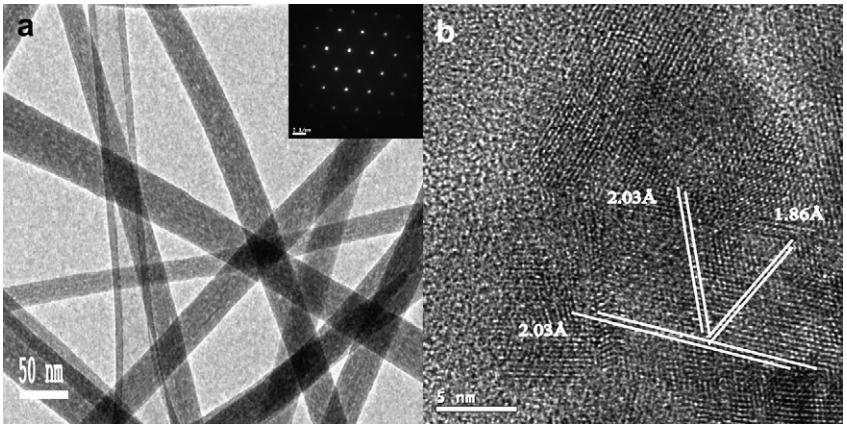

Fig. 7. TEM images of (a) as-synthesized Cu $(In_xGa_{1-x})Se_2$ nanostructures and SAED pattern (inset) and (b) high-resolution TEM of fiber-like Cu $(In_xGa_{1-x})Se_2$ nanostructures recorded along [221].

Table 1
Measured CIGS Nanocrystal Composition.

Precursor atomic ratio Cu:In:Ga:Se	Measured by EDS[a] Cu:In:Ga:Se	Measured by ICPMS[b] Cu:In:Ga:Se
1:0.8:0.2:2	1:0.76:0.18:1.98	1.02:0.74:0.23:2.01
1:0.5:0.5:2	1.04:0.52:0.47:2.02	1:0.51:0.48:1.97
1:0.2:0.8:2	0.99:0.18:0.77:1.96	1.03:0.21:0.82:2.03

[a] EDS measurements have an error of ca. ±2 atom %.
[b] ICPMS measurement have an error of ±0.2 atom % for In, ±0.1 atom % for Ga, ±0.5 atom % for Se.

The morphologies of the Cu $(In_xGa_{1-x})Se_2$ nanofibers were characterized using a transmission electron microscope (H-800) with an acceleration voltage of 160 kV Fig. 7(a) shows TEM micrographs of Cu $(In_xGa_{1-x})Se_2$ nanofibers by electrospinning at 20 kV. The fiber-like morphology of Cu $(In_xGa_{1-x})Se_2$ can be seen. The fiber-like nanostructures have diameters from 60 to 80 nm and lengths from hundreds of nanometers to several micrometers. By changing the reaction concentration, tip-to-collector distance, viscosity, and applied voltage, the nanofiber size can be easily controlled. When the PVB/ethanol ratio was increased from 10 wt. % to 40 wt. % with a tip-to-collector distance of 18 cm, the diameters decreased to about 70 nm. The growth directions for the nanofibers were determined from the selected area electron diffraction (SAED) patterns shown in the inset in Fig. 7 (a). A high-resolution bright field TEM image of characteristic nanofibers (65 nm) from the chalcopyrite synthesis is shown in Fig. 7(b). The image is taken along the [221] zone axis with the $(2\bar{2}0)$, $(\bar{2}04)$, and $(0\bar{2}4)$ crystallographic planes indicated by white lines. Spacing measurements based on 6 planes indicated *d*-spacings of 1.86 ± 0.02 Å for the $(2\bar{2}0)$ and 2.03 ± 0.02 Å for the $(\bar{2}04)$ and $(0\bar{2}4)$. The measured angle between the $(2\bar{2}0)$ and $(0\bar{2}4)$ planes is 63 ± 0.5° and is 58.5 ± 0.5° between $(\bar{2}04)$ and $(0\bar{2}4)$ planes. If the structure were sphalerite, the measured angles should be 60° between all three planes, and the measured *d*-spacings should be 1.98Å. These observed differences provide additional evidence of lattice distortion that result from cation ordering and the chalcopyrite crystal structure. The zone axis of the SAED pattern was determined to be [221], and the pattern is typical for nanocrystals from this same synthesis procedure. These extra spots correspond to 2/3 the distance of the $(\bar{1}\bar{1}4)$ or $(1\bar{2}2)$ fundamental reflections and have a *d*-spacing of 3.1 Å. Both high-resolution TEM (Fig. 7) and XRD (Fig. 6) confirmed that the nanocrystals are crystalline with tetragonal chalcopyrite structure. No other crystal phases were observed in the XRD patterns of the product. Compositional analysis by ICPMS showed that the average composition of the nanocrystals in the sample has a molar Cu/(In + Ga)/Se ratio of 1:1:2 and the composition of individual particles measured by EDS were 1:1:2 with a variation from particle to particle less than the experimental error of ca. ±2 atom % (see Table 1).

A potential mechanism was derived based on the above results. In the interaction of Cu $(In_xGa_{1-x})Se_2$ and PVB as the capping agent, the PVB molecules assembled on the surface of Cu $(In_xGa_{1-x})Se_2$, making the Cu $(In_xGa_{1-x})Se_2$ nanoparticles are partly covered by PVB long chains. There was also an interaction between Cu $(In_xGa_{1-x})Se_2$ nanoparticles due to the high Gibbs' surface free energy of Cu $(In_xGa_{1-x})Se_2$. The two competing interactions induced larger Cu $(In_xGa_{1-x})Se_2$ and PVB clusters with various diameters. The surface defects were partly passivated by PVB. With an increase of the PVB concentration, more Cu $(In_xGa_{1-x})Se_2$ nanoparticles with low aggregation were extracted. The dispersion of the Cu $(In_xGa_{1-x})Se_2$ and PVB clusters decreased, and the passivation became more effective.

3.4. Optical and electrical of tetragonal chalcopyrite Cu $(In_xGa_{1-x})Se_2$ nanocrystals formation

Fig. 8 shows UV/vis absorption spectra and optical micrographs of the chalcopyrite quaternary Cu $(In_{0.8}Ga_{0.2})Se_2$ nanocrystals synthesized by an electrospinning process and annealing at 400 °C for 6 h. The band gap energy determined from absorbance spectra (Fig. 8) of optically clear dispersions of nanocrystals was found to be 1.12 eV (1107 nm), which is in good agreement with the reported in literature [40]. The absorber layer may be formed simply by drop-casting on molybdenum coated soda-lime glass substrate. The films are annealed under flow of Ar at 500 °C for 3 h to remove the organic capping molecules. We fabricated the first batch of thin film solar cells in our laboratory using these films following chemical bath deposition of CdS layer, and RF sputtering of 60 nm intrinsic zinc oxide and 200 nm of ITO layers. The corresponding *I–V* characteristics of the solar cell are shown in Fig. 9. The final devices are

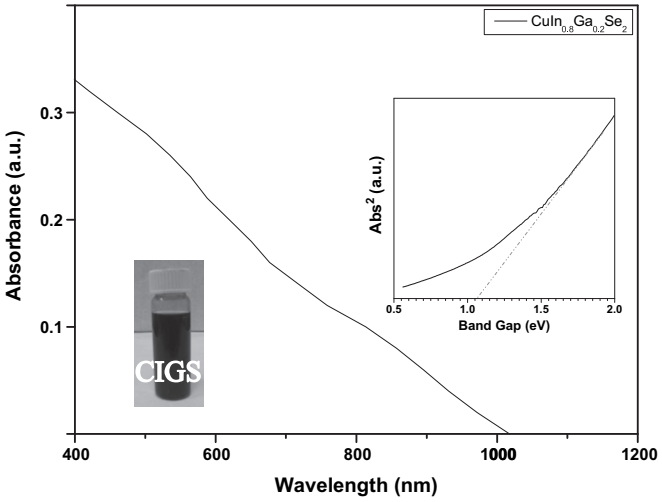

Fig. 8. UV–vis absorption spectrum of the as-synthesized Cu $(In_{0.8}Ga_{0.2})Se_2$ nanocrystals. Inset of Fig. 7 shows the abs^2 vs eV for the Cu $(In_{0.8}Ga_{0.2})Se_2$ nanocrystals; the estimated band gap energy is 1.12 eV.

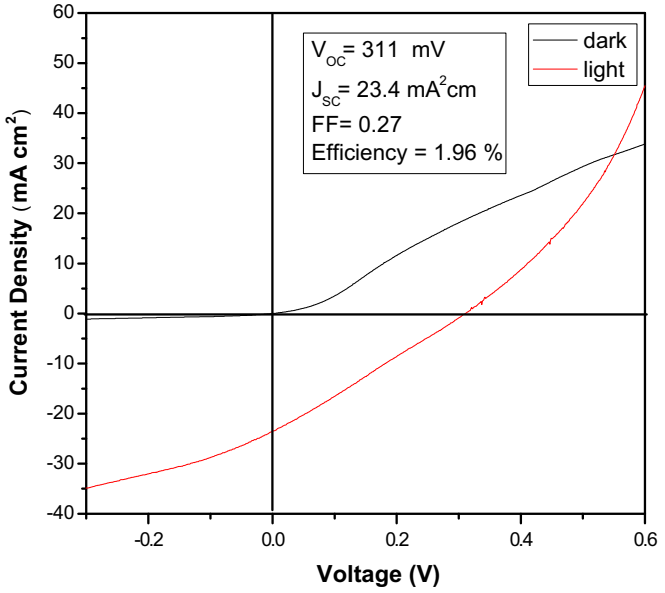

Fig. 9. Current–voltage characteristics by the AM1.5 irradiation (100 mW/cm^2). The nanocrystal absorber layer was 800 nm thick, consisting of diethylenetriamine capped Cu $(In_{0.8}Ga_{0.2})Se_2$ nanocrystals with an average diameter of 70 nm.

scribed into small areas of 0.124 cm^2 with a small dap of silver paint applied to form the top contact. The device parameters for a single junction Cu $(In_{0.8}Ga_{0.2})Se_2$ solar cell under AM1.5G are as follows: open circuit voltage of 311 mV, short-circuit current of 23.4 mA/cm^2, fill factor of 27%, and a power conversion efficiency of 1.96%.

4. Conclusion

Cu $(In_xGa_{1-x})Se_2$ nanofibers were successfully fabricated via electrospinning. The continuous PVB/Cu $(In_xGa_{1-x})Se_2$ organized fibers can be transformed to the Cu $(In_xGa_{1-x})Se_2$ nanofibers via annealing. The fibers are comprised of compact Cu $(In_xGa_{1-x})Se_2$ nanocrystals, maintaining their 1D identity. Tetragonal chalcopyrite nanofibers with a diameter of 70 nm can be produced and which is a single crystal with a growth direction of [221]. Active area cell efficiencies up to 1.96% (V_{oc} = 311 mV, J_{sc} = 23.4 mA/cm^2, FF = 0.27%) have been demonstrated using the I–III–VI_2 based absorber layer fabricated. These compositional, structural, and mechanistic findings provide valuable insight in the development of thin film solar cells using quaternary I–III–VI_2 semiconductors.

Acknowledgments

This present study has been supported in part by National Science Council of Taiwan and Solar Technology Laboratory, Department of Greenergy Technology, National University of Tainan, Taiwan (project number NSC 99-2113-M-024-002) Top 100 University Advancement and the collaboration of Center for Micro/Nano Science and Technology of National Cheng Kung University, under grant numbers D98-2740 and D98- 2700.

References

[1] Guillemoles J, Rau U, Kronik L, Schock H, Cahen D. Adv Mater 1999;11(11):957.
[2] Stanbery BJ. Crit Rev Solid State Mater Sci 2002;27(2):73–117.
[3] Paulson PD, Haimbodi MW, Marsillac S, Birkmire RW, Shafarmana WNJ. Appl Phys 2002;91:10153.
[4] Marsillac S, Paulson PD, Haimbodi MW, Birkmire RW, Shafarman WN. Appl Phys Lett 2002;81:1350.
[5] Repins I, Contreras MA, Egaas B, DeHart C, Scharf J, Perkins CL, et al. Prog PhotoVolt Res Appl 2008;16:235.
[6] Ramanathan K, Contreras MA, Perkins CL, Asher S, Hasoon FS, Keane J, et al. Prog PhotoVolt Res Appl 2003;11:225–30.
[7] Guillemoles JF, Kronik L, Rau DCU, Jasenek A, Schock HW. J Phys Chem B 2000;104:4849–62.
[8] Mitzi DB, Yuan M, Liu W, Kellock AJ, Chey SJ, Deline V, et al. Adv Mater 2008;20:3657.
[9] Luther JM, Law M, Beard MC, Song Q, Reese MO, Ellingson RJ, et al. Nano Lett 2008;8:3488.
[10] Panthani MG, Akhavan V, Goodfellow B, Schmidtke JP, Dunn L, Dodabalapur A, et al. J Am Chem Soc 2008;130:16770.
[11] Pan DC, An LJ, Sun ZM, Hou W, Yang Y, Yang ZZ, et al. J Am Chem Soc 2008;130:5620–1.
[12] Xiao JP, Xie Y, Tang R, Qian YT. J Solid State Chem 2001;161:179–83.
[13] Castro SL, Bailey SG, Raffaelle RP, Banger KK, Hepp AF. J Phys Chem B 2004;108:12429–35.
[14] Nairn JJ, Shapiro PJ, Twamley B, Pounds T, von Wandruszka R, Fletcher TR, et al. Nano Lett 2006;6:1218–23.
[15] Malik MA, O'Brien P, Revaprasadu N. Adv Mater 1999;11:1441.
[16] Zhong HZ, Li YC, Ye MF, Zhu ZZ, Zhou Y, Yang CH, et al. Nanotechnology 2007;18. 025602.
[17] Qiu JJ, Jin ZG, Wu WB, Xiao L. Thin Solid Films 2006;510:1.
[18] Kumar AP, Reddy KV. Thin Solid Films 1997;304:365–70.
[19] Huynh WU, Dittmer JJ, Alivisatos AP. Science 2002;295:2425–7.
[20] Chen LJ, Liao JD, Lin SJ, Chuang YJ, Fu YS. Polymer 2009;50:3516–21.
[21] Shao C, Guan H, Liu Y, Mu R. J Mater Sci 2006;41:3821–4.
[22] Wu H, Pan W. J Am Ceram Soc 2006;89:699–701.
[23] Zhmayev E, Cho D, Joo YL. Polymer 2010;51:274–90.
[24] Wang M, Vail SA, Keirstead AE, Marquez M, Gust D, Garcia AA. Polymer 2009;50:3974–80.
[25] Ding B, Kimura E, Sato T, Fujita S, Shiratori S. Polymer 2004;45:1895–902.
[26] Yang A, Tao X, Pang GKH, Siu KGG. J Am Ceram Soc 2008;91:257–62.
[27] Feller RL, Curran M, Colaluca V, Bogaard J, Bailie C. Polym Degrad Stab 2007;92:920–31.
[28] Ruenraroengsak P, Florence AT. Int J Pharm 2005;298:361.
[29] Reneker DH, Chun I. Nanotechnology 1996;7:216.
[30] Lee SG, Choi SS, Joo CW. J Korean Fiber Soc 2002;39:1.
[31] Karim MR, Lee HW, Kim R, Ji BC, Cho JW, Son TW, et al. Carbohydr Polym 2009;78:336–42.
[32] Chen YY, Wei WCJ. J Eur Ceram Soc 2001;21:2535–40.
[33] Zhang H, Song H, Dong B, Han L, Pan G, Bai X, et al. J Phys Chem C 2008;112:25.
[34] Liu W, Mitzi DB, Yuan M, Kellock AJ, Jay Chey S, Gunawan O. Chem Mater 2010;22:3.
[35] Lotus AF, Feaver RK, Britton LA, Bender ET, Perhay DA, Stojilovic N, et al. Mater Sci Eng B 2010;167:55–9.
[36] Stejskal J, Kratochvil P. Langmuir 1996;12:3389.
[37] Riede A, Helmstedt M, Riede V, Stejskal J. Langmuir 1998;14:6767.
[38] Beaman M, Armes SP. Colloid Polym Sci 1993;271:70.
[39] Kim SM, Kim GS, Lee SY. Mater Lett 2008;62:4354.
[40] Wei SH, Zunger A. J Appl Phys 1995;78:3846–56.

Polymer 52 (2011) 122–129

Contents lists available at ScienceDirect

Polymer

journal homepage: www.elsevier.com/locate/polymer

Preparation and properties of transparent PMMA/ZrO_2 nanocomposites using 2-hydroxyethyl methacrylate as a coupling agent

Yiqing Hu, Guangxin Gu, Shuxue Zhou*, Limin Wu

Department of Materials Science and Advanced Coatings Research Center of Educational Ministry of China, Fudan University, Shanghai 200433, PR China

ARTICLE INFO

Article history:
Received 4 May 2010
Received in revised form
6 November 2010
Accepted 12 November 2010
Available online 19 November 2010

Keywords:
PMMA
Zirconia nanocrystal
2-Hydroxyethyl methacrylate

ABSTRACT

Transparent PMMA/ZrO_2 nanocomposites were prepared by *in-situ* bulk polymerization of methyl methacrylate (MMA)/ZrO_2 dispersions that were firstly synthesized using nonaqueous synthesized ZrO_2 nanocrystals and the function monomer, 2-hydroxyethyl methacrylate (HEMA), as the ligand. The dispersion behavior of ZrO_2 nanoparticles in MMA, structure, mechanical and thermal properties of the PMMA/ZrO_2 nanocomposites were investigated comprehensively. It was found that ZrO_2 nanoparticles were well dispersed in MMA with HEMA ligand, but the MMA/ZrO_2 dispersions easily destabilized in air as well as at elevated temperatures. The destabilization temperature of the dispersion is raised by increasing the molar ratio of HEMA/ZrO_2 to match the bulk polymerization temperature. The PMMA/ZrO_2 nanocomposites showed an interesting chemical structure (namely, highly cross-linked structure even at ZrO_2 content as low as 0.8 wt% and hydrogen bonding interaction between polymer matrix and ZrO_2 nanoparticles), with enhanced rigidity without loss of the toughness and improved thermal stability. The relationship between the structure and the properties of the PMMA/ZrO_2 nanocomposites based on the HEMA coupling agent was discussed.

1. Introduction

In the past decades, incorporation of inorganic nanoparticles into polymer matrix received tremendous interests, since it can obviously improve the properties of polymers and/or render polymers with novel functions. Among all these studies, special attentions have been focused on polymethyl methylacrylate (PMMA)-based nanocomposites, because the small size effect of nanoparticles could retain the original transparency of PMMA. Fe-oxides [1], Ag [2], TiO_2 [3,4], ZnS:Mn [5], ZnO [6], and $LaPO_4:Ce^{3+}$, Tb^{3+} [7] nanoparticles have been introduced into PMMA, providing the optical plastics with magnetic, nonlinear optical, luminescent, or UV-blocking properties. Generally, four routes for fabrication of PMMA-based nanocomposites were applied: (1) *in-situ* generation of nanoparticles in PMMA solution, (2) *in-situ* generation of nanoparticles in methyl methacrylate (MMA) monomer and following radical polymerization, (3) blending *ex-situ* preformed nanoparticles with PMMA solution, and (4) *in-situ* bulk polymerization of MMA/nanoparticles dispersion. The route of *in-situ* generation of nanoparticles suffers from the drawback of the introduction of byproducts in the nanocomposites. As for the latter two processes with preformed inorganic nanoparticles, the big challenge is encountered to assure the homogeneous dispersion of nanoparticles in the nanocomposites. Since the blending method using PMMA solution is confronted with the serious environment problem due to the organic solvents employed, *in-situ* polymerization of MMA/nanoparticles dispersion would be more desirable especially for the production of bulk sheets. For this approach, the surface character of nanoparticles is extremely paramount to the dispersion of nanoparticles in PMMA and the properties of the resulted nanocomposites. A lot of surface modifiers have been chemically attached to the nanoparticles to improve the compatibility of nanoparticles with MMA and further PMMA. Successful examples include *tert*-butylphosphonic acid for ZnO nanoparticles [8], octylphosphonic acid for ZrO_2 and TiO_2 nanoparticles [9], stearic acid for calcium carbonate nanopowder [10], and 3-glycidoxypropyltrimethoxysilane for alumina nanoparticles [11], just to name a few. These ligands, however, are inert in radical polymerization. The surface-treated nanoparticles during polymerization tend to aggregate due to depletion force, reducing the transparency of PMMA-based nanocomposites especially at high nanoparticle load [8,9]. To overcome this problem, vinyl group-containing ligands were used as alternatives. For instances, γ-methacryloxypropyltrimethoxysilane (MPS) was employed for functionalization of SiO_2 nanoparticles [12] and ZrO_2 nanoparticles [13], and oleic acid for modification of ZnO nanoparticles [14] and $NaYF_4:Yb^{3+},Er^{3+}(Tm^{3+})$ nanoparticles [15]. With these

* Corresponding author. Tel.: +86 21 65643417.
E-mail address: zhoushuxue@fudan.edu.cn (S. Zhou).

0032-3861/$ – see front matter © 2010 Elsevier Ltd. All rights reserved.
doi:10.1016/j.polymer.2010.11.020

surface-treated nanoparticles, chemical bonding between PMMA matrix and nanoparticles was usually established. However, other types of vinyl group-containing ligands that provide new interaction mode (i.e. hydrogen bonding) between PMMA matrix and nanoparticles are seldom reported so far.

On the other hand, 2-hydroxyethyl methacrylate (HEMA), one of the common function acrylate monomers, has the ability to interact with inorganic moieties via its hydroxyl group and participate in radical polymerization via its vinyl group. It has been successfully used in the preparation of PHEMA/SiO_2 hybrids via versatile approaches, i.e. *in-situ* bulk polymerization of HEMA-modified SiO_2 nanoparticles/HEMA dispersion [16–18], blending PHEMA with colloidal SiO_2 or tetraethoxysilane (TEOS) [19], blending HEMA with TEOS and then undergoing an acid-catalyzed sol–gel process and radical polymerization [20], blending HEMA with fumed SiO_2 and subsequently following polymerization [21], and etc. Fabrication of PMMA/TiO_2 hybrid has also been reported by blending P(MMA-co-HEMA) with titanium butoxide [22]. In these cases, HEMA acted not only as a polymer matrix but also as a coupling agent for the interaction between polymer and inorganic moieties. Although the bridging role of HEMA was well demonstrated in SiO_2 and TiO_2-based hybrids, other successful preparation of nanocomposites based on HEMA as a coupling agent was still very limited.

Recently, we found that the ZrO_2 nanocrystals, synthesized from a solvothermal reaction of zirconium isopropoxide isopropanol complex in anhydrous benzyl alcohol, are highly dispersible in various organic media with the help of ligands [23,24]. It was proved that these nonaqueous synthesized ZrO_2 nanoparticles are very promising for the preparation of transparent polymer/ZrO_2 nanocomposites with high refractive index [25–27] and enhanced mechanical properties [13,25–27]. In this work, ZrO_2 nanocrystals were dispersed in MMA using HEMA as a coupling agent, accompanying with *in-situ* bulk polymerization to get PMMA/ZrO_2 nanocomposites. It is expected that hydrogen bonding interaction was formed in the MMA/ZrO_2 dispersion as well as in the resulted nanocomposites. Although hydrogen bonding has been frequently employed to construct supramolecular materials [28,29] and 3D elastic network with high stiffness [30], as well as to enhance the mechanical properties of polymer [31], few researches explored the preparation of nanocomposites based on hydrogen bonding. Until recently, hydrogen bonding was found in poly(D,L-lactide)/hydroxyapatite (HA) nanocomposites [32] and polyamide/HA nanocomposites [33], which was responsible for the better properties of the nanocomposites relative to the neat polymers. Therefore, this work will favor understanding the influence of hydrogen bonding on the dispersion behavior of nanoparticles and the properties of the nanocomposites, and meanwhile, provide a new preparation approach of transparent PMMA-based nanocomposites with improved properties using nonaqueous synthesized ZrO_2 nanoparticles.

2. Experimental section

2.1. Materials

Zirconia nanoparticles (size: 3.8 nm, cubic crystal) were obtained from a solvothermal reaction of zirconium(IV) isopropoxide isopropanol complex (99.9%, Aldrich) in anhydrous benzyl alcohol (≥99%, Aldrich), as described in detail elsewhere [34]. HEMA was purchased from Acros Organics (Belgium). MMA was the products of Sinopharm Chemical Reagent Co. Azo-bisisobutyronitrile (AIBN) was purchased from Shanghai Guanghua Chemical Reagent Co. (China), and re-crystallized in ethanol before use.

2.2. Preparation of ZrO_2 nanoparticle dispersion in MMA

The as-synthesized ZrO_2 nanoparticles suspended in benzyl alcohol were centrifuged and washed by two repeated cycles of sonification in xylene for 3 min and centrifugation at 1500 rpm for 3 min. The as-obtained wet ZrO_2 nanoparticles contained 49 wt% of xylene. They were directly dispersed in the pre-made MMA/HEMA monomer mixture by sonication, in which the amount of HEMA was generally designed based on the HEMA-to-ZrO_2 molar ratio of 0.8/1. For example, an MMA/ZrO_2 dispersion with 3 wt% of concentration means that the dispersion contains 2.54 g of HEMA, 94.46 g of MMA, and 5.88 g of wet ZrO_2 nanoparticles (namely, 3.0 g ZrO_2 nanoparticles and 2.88 g of residual xylene). It should be noted that if the ZrO_2 nanoparticles were dried first, they cannot be de-agglomerated in any media with the help of ligands.

2.3. In-situ polymerization of MMA/ZrO_2 dispersion

A certain amount of MMA/ZrO_2 dispersion was added into a three-necked flask, following charge of an initiator, AIBN (0.1 wt% based on the weight of ZrO_2/MMA dispersion). The polymerization reaction was conducted at 75 ± 2 °C under mechanical stirring until the reactants attained a desired viscosity. Then, the viscous prepolymer was transferred into a glass mold and kept at 40 °C for 24 h and 100 °C for 1 h to finish the polymerization. PMMA/ZrO_2 nanocomposite slices were obtained by disassembling the mold. The sample slices for mechanical tests were dried overnight at 60 °C and stored at room temperature for more than one month before testing, in order to remove the xylene and the residual monomers.

2.4. Characterization

The gel fraction (G) and the polymerization conversion (C) of the nanocomposites were determined by Soxhlet extracting experiments using THF as the solvent with 48 h of reflux. The mass of the nanocomposite remained after extraction (M_1) and the mass of the free PMMA chains dissolved in THF (M_2) were weighed. The gel fraction and the polymer conversion (C) were calculated according to the following equations:

$$G = (1.04 + C_{ZrO_2})M_1/1.04M_0 \quad (1)$$

$$C = (1.04 + C_{ZrO_2})(M_1 + M_2)/1.04M_0 \quad (2)$$

where C_{ZrO_2} is the designed weight percentage of ZrO_2 nanoparticles and M_0 is the mass of the as-synthesized nanocomposite before extraction.

FTIR spectra were recorded using a Nicolet Nexus 470 spectrometer (USA) in the wavenumber range of 400–4000 cm^{-1} with a resolution of 2 cm^{-1} and accumulation of 32 scans. Liquid samples were sandwiched between two KBr plates. PMMA nanocomposites were crashed into small powders and blended with KBr to form sample plates. A variable temperature cell equipped with a temperature control unit was used for the temperature-dependent IR transmission measurements. The spectra were recorded after equilibrating for 10 min at the desired temperature.

The UV/vis transmission spectra were obtained with a UV-1800PC spectrophotometer (Shanghai Mapada Instrument Co., Ltd., China).

Transmission electron microscope (TEM, Hitachi H-600 instrument, Hitachi Co., Japan) was used to observe the morphology of nanocomposites. The specimens were prepared using an ultramicrotome. Thin sections of about 50 nm were cut from the nanocomposite slices without further staining.

Tensile tests were performed on a CMT4104 universal testing instruments with a crosshead speed of 1.0 mm/min. The samples were cut into dumbbell shape with a punch according to GBT 1040.2–2006. The width of the narrow section is 4 mm, and the gage length is 20 mm.

Dynamic mechanical analysis was performed on a DMA2980 instrument (TA Instruments, USA) operated at a frequency of 11 Hz. Temperature sweeps from 25 to 200 °C at a heating rate of 2 °C/min.

Thermogravimetric analysis (TGA) was carried out using a Perkin Elmer TGA-7 instrument (USA) at a heating rate of 10 °C/min in air.

3. Results and discussion

3.1. Dispersion behavior of ZrO_2 nanoparticles in MMA

Our researches [23,24] have demonstrated that nonaqueous synthesized ZrO_2 nanoparticles are highly dispersible in many organic solvents (i.e. THF, butyl acetate, toluene, *N*,*N*-dimethylformamide, and etc.) with appropriate ligands. Dispersion of ZrO_2 nanoparticles in MMA was also investigated in our previous publications [13,23]. Highly transparent MMA/ZrO_2 dispersion at primary particle size level has been achieved for the cases with the ligands such as MPS [13], ethyl 3,4-dihydroxycinnamate [23], allylmalonic acid [23], or acrylic acid [23], but not for the case with the hydroxyl group-containing ligand, trimethylolpropane mono allyl ether (TMPMA) [23]. In the present article, another hydroxyl group-containing ligand, HEMA, was tried to help the dispersion of ZrO_2 nanoparticles in MMA. HEMA was adopted because of its general application as the functional comonomer for synthesis of polyacrylates, which makes the removal of free ligands unnecessary. On the other hand, the bifunctionality (hydroxyl and vinyl groups) of HEMA molecules may act as bridges between PMMA matrix and ZrO_2 nanoparticles, avoiding the depletion force-induced phase separation [35] during *in-situ* polymerization.

Experiments showed that the turbid MMA/ZrO_2 dispersion quickly turned into transparent "solution" after sonication under the existence of HEMA, even the molar ratio of HEMA/ZrO_2 down to 0.05/1. This phenomenon indicated that HEMA worked well for the dispersion of ZrO_2 nanoparticles in MMA. However, the MMA/ZrO_2 dispersions with HEMA ligand were easily destabilized during storing in air, being similar to the THF/ZrO_2 dispersion with TMPMA ligand [23]. This destabilization may be attributed to the desorption of HEMA, resulted from the competitive adsorption of water from the air. Therefore, the pre-made MMA/ZrO_2 dispersions have to be kept in a sealed container prior to polymerization. In addition, it was found that the MMA/ZrO_2 dispersions with HEMA ligand were easily destabilized at high temperatures and cannot be re-stabilized again even it was cooled down and sonified. For example, the transparent MMA/ZrO_2 dispersion with 2 wt% of ZrO_2 concentration and HEMA/ZrO_2 molar ratio of 0.6/1 became cloudy after heating at 70 °C for 10 min, as shown in Fig. 1. Further investigation revealed that the destabilizing temperature of MMA/ZrO_2 dispersion depended on the molar ratio of HEMA/ZrO_2, as summarized in Table 1. The higher the molar ratio of HEMA/ZrO_2 is, the higher the destabilized temperature is. Since the polymerization was carried out at 75 °C, HEMA/ZrO_2 molar ratio of 0.8/1 was thus employed to avoid destabilization.

The destabilization behavior of the MMA/ZrO_2 dispersions stored in air or at elevated temperatures indirectly suggested the physical adsorption of HEMA on the surface of ZrO_2 nanoparticles. Unlike the chemically-bonded ligands, the physically-bonded ligands are actually in the state of dynamic adsorption/desorption equilibrium, and are easily replaced by other molecules (for example, water molecules herein) with stronger affinity to the nonaqueous synthesized ZrO_2 nanoparticles. At elevated temperatures, the dynamic adsorption/desorption equilibrium generally tends to cause more serious disassociation of HEMA molecule, resulting in a reduced coverage of ZrO_2 nanoparticles with HEMA molecules. Meanwhile, Brownian motion of nanoparticles in the dispersion becomes stronger at higher temperature, resulting in higher probability of collision between ZrO_2 nanoparticles. Both of these two aspects lead to aggregation of ZrO_2 nanoparticles and ultimately the destabilization of the dispersion. Due to the highly-active surface of nonaqueous synthesized ZrO_2 nanoparticles, the aggregation may produce hard aggregates rather than soft agglomerates. As a consequence, the dispersion cannot become transparent any more once it was destabilized. At a higher molar ratio of HEMA/ZrO_2, more HEMA molecules are physically attached to the surface of ZrO_2 nanoparticles, which provides better protection of ZrO_2 nanoparticles from aggregation and thus better high-temperature stability of MMA/ZrO_2 dispersion.

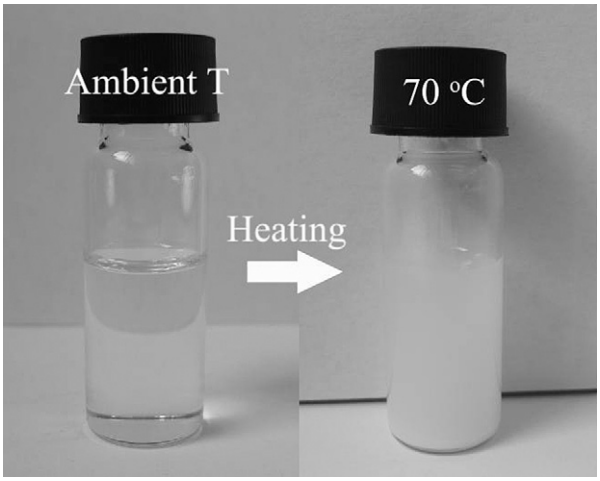

Fig. 1. Change of the appearance of MMA/ZrO_2 dispersion after keeping at 70 °C for 10 min (ZrO_2 concentration: 2 wt%, HEMA/ZrO_2 molar ratio: 0.6/1).

The HEMA on the surface of ZrO_2 nanoparticles should be attached via hydrogen bonding according to the possible fashions as presented in Scheme 1. Unfortunately, the hydrogen bonding in the MMA/ZrO_2 dispersion would additionally exist between hydroxyl and hydroxyl/carbonyl groups, and/or come from the adsorbed water molecules. It causes difficulty in confirming a low quantity of hydrogen bonds between the physisorbed HEMA molecules and ZrO_2 nanoparticles. We ever tried to identify the hydrogen bond by comparing the FTIR spectrum of MMA/HEMA solution with that of MMA/ZrO_2 dispersion, but no obvious difference was observed on the band of hydroxyl group at the wavenumber range of 3100–3650 cm^{-1}.

Table 1
Influence of HEMA content on the destabilizing temperature of the ZrO_2/MMA dispersions.

HEMA/ZrO_2 (mol/mol)	Destabilizing temperature (°C)
0.05/1	40
0.1/1	40
0.2/1	45
0.4/1	60
0.6/1	70
0.8/1	100
1/1	>110

Note: ZrO_2 concentration: 2 wt%.

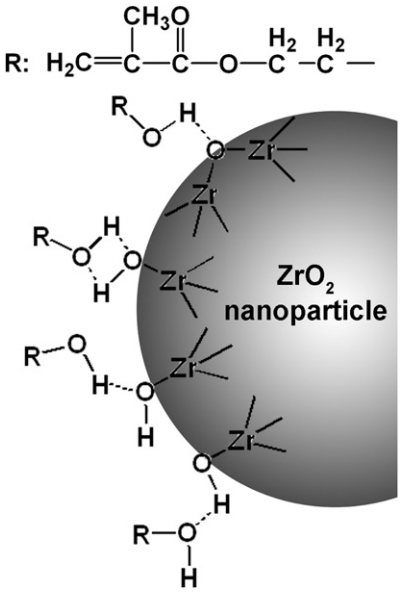

Scheme 1. Possible fashion of hydrogen bond between HEMA and ZrO_2 nanoparticles.

3.2. Bulk polymerization of MMA/ZrO_2 dispersions

Similar to the common bulk polymerization of MMA, bulk polymerization of MMA/ZrO_2 dispersion was conducted by two steps: pre-polymerization under stirring and subsequent polymerization in a glass mold. As we knew, a proper viscosity attained by pre-polymerization step is paramount for a bulk polymerization process. Table 2 summarizes the pre-polymerization time to reach a desired viscosity (~0.9 Pa s) for the MMA/ZrO_2 dispersions containing various ZrO_2 contents and MMA/HEMA mixtures. As the ZrO_2 content increases, the pre-polymerization time increases at a ZrO_2 content up to 3 wt%, and then quickly shortens at high ZrO_2 load level. This polymerization behavior is the same as that of MMA/MPS-modified ZrO_2 dispersion reported previously [13]. It may be interpreted as follows. In MMA/ZrO_2 dispersion, there are two kinds of comonomer, free HEMA molecules and those HEMA molecules associated with ZrO_2 nanoparticles via hydrogen bonds. Table 1 shows that the pre-polymerization time for copolymerization of MMA/HEMA mixture (see samples PMMA-H1 and PMMA-H7) prolongs as the amount of HEMA in the monomer mixture increases. This implies that the free HEMA molecules will decrease the polymerization rate of MMA/ZrO_2 dispersion. On the other hands, these associated HEMA molecules and the corresponding HEMA radicals (initiated or transferred) were less active both in propagation and in termination reaction due to the restricted diffusion. Since pre-polymerization was conducted before the gel effect of polymerization occurs, the polymerization rate is dominated by the propagation rate at that stage. The reduction of propagation rate due to the HEMA-associated ZrO_2 nanoparticles will ultimately decrease polymerization rate. Therefore, both the free HEMA molecules and associated HEMA molecules will reduce the polymerization rate of MMA, which well be responsible for the extended pre-polymerization time at low ZrO_2 concentration. However, at high ZrO_2 load, the desired viscosity can be reached at low monomer conversion because ZrO_2 nanoparticles play physical cross-linking role in the system. As a result, the pre-polymerization time shortens at high ZrO_2 load, despite of the reduced polymerization rate.

The gel fraction of the nanocomposites is also listed in Table 2. Surprisingly, the gel fraction reaches as high as 96.0% even with only 0.8 wt% nanoparticles. This result indicates that the HEMA-adsorbed ZrO_2 nanoparticles took part in the polymerization, and as a matter of fact, acted as a highly efficient cross-linking monomer during the polymerization of MMA. On the other hand, the high gel fraction means that the PMMA/ZrO_2 nanocomposites possess a good solvent resistance. To further understand the solvent resistance, the obtained nanocomposite slices were immersed into other solvents, i.e. xylene (at temperature of 20–130 °C) and ethyl benzoate (at temperature of 150 and 200 °C). Similarly, only swelling phenomena were observed even for the sample with extremely low ZrO_2 content (i.e. PMMA08). Therefore, copolymerization of MMA with HEMA-functionalized ZrO_2 nanoparticles can really improve the solvent resistance of PMMA.

3.3. Hydrogen bonding between polymer and ZrO_2 nanoparticles

As discussed above, HEMA molecules were attached to ZrO_2 nanoparticles possibly via hydrogen bond. It can be inferred that the hydrogen bonding interaction between polymer matrix and ZrO_2 nanoparticles would also possibly exist in PMMA/ZrO_2 nanocomposites. Since hydrogen bond is thermoreversible, variable temperature FTIR analysis was usually employed to probe the hydrogen bond in materials [36,37]. Herein, variable temperature FTIR characterization was conducted for PMMA/ZrO_2 nanocomposites using PMMA7 as an example and PMMA-H6 (corresponding to the polymer composition of PMMA7) as a control sample. As demonstrated in Fig. 2, a broad and strong absorption band attributing to the stretching vibration of hydroxyl groups is observed at the wavenumber range of 3100–3700 cm^{-1} for both PMMA7 and PMMA-HEMA. However, besides of the peak at 3444 cm^{-1} that is assigned to the hydrogen bonded hydroxyls of polymer matrix, a new shoulder peak occurs at 3522 cm^{-1} for PMMA7 and shifts to 3544, 3559 and 3568 cm^{-1} as the sample was heated to 75, 150 and 200 °C, respectively. This shifting peak returned to its origin position after the sample was cooled down and stored in air for 24 h. Interestingly, the peak at the wavenumber of 3568 cm^{-1} just corresponds to the stretching vibration of hydroxyl groups of ZrO_2 nanoparticles (see the two peaks at wavenumber of 3498 and 3568 cm^{-1} in the inserted figure of Fig. 2a). These facts indicate that the hydrogen bonding between polymer matrix and ZrO_2 nanoparticles actually exists. The new peak in PMMA7 can be assigned to the stretching vibration of the hydrogen bonded Zr–OH groups. The shift of this peak to high wavenumber under heating may be caused by the weakened

Table 2
Polymerization results of MMA/ZrO_2 dispersions using HEMA as a coupling agent.

Sample	PMMA0	PMMA08	PMMA1.6	PMMA3	PMMA5	PMMA7	PMMA-H1[b]	PMMA-H6[b]
ZrO_2 concentration (wt%)	0	0.8	1.6	3	5	7	0	0
Conversion (%)	98	99.2	99.3	98.9	99.0	99.9	99.1	98.6
Pre-polymerization time[a] (min)	45	55	58	60	30	25	60	90
Gel fraction, %	0	96.0	96.9	95.3	99.0	99.8	0	0

[a] Note: The time to reach a viscosity of ~0.9 Pa s at reaction temperature of 75 °C.
[b] Note: PMMA-H1 and PMMA-H6 represent the copolymers prepared at MMA-to-HEMA weight ratios of 99/1 and 94/6, respectively.

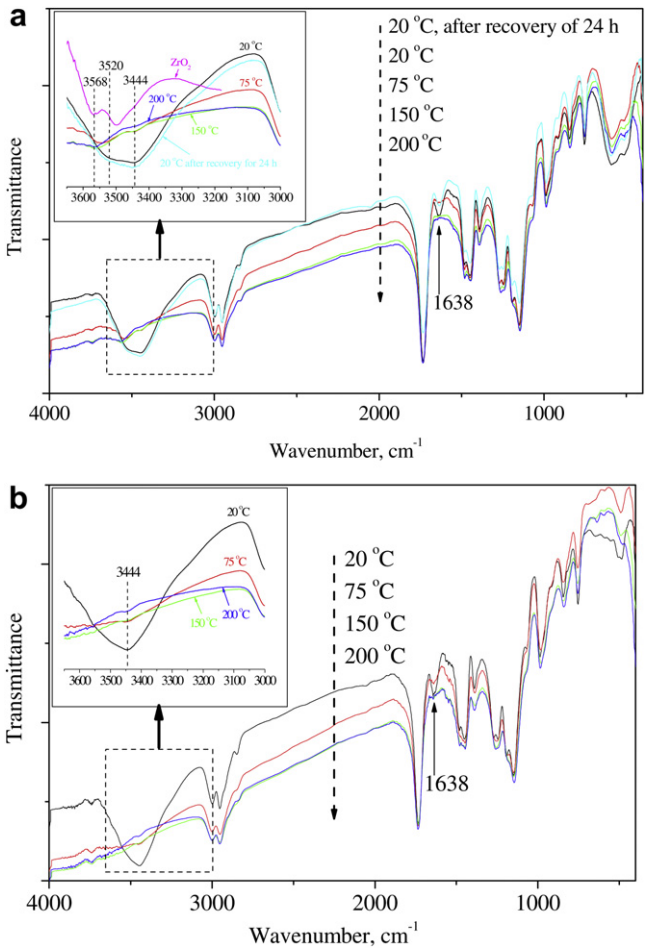

Fig. 2. Variable temperature FTIR spectra of (a) PMMA7 and (b) PMMA-H6. The ambient-temperature FTIR spectrum of ZrO_2/THF dispersion (ZrO_2 content: 1 wt%) was presented in the inserted figure of Fig. 2a.

hydrogen bonds at elevated temperatures. Fig. 2 also shows that the intensity of the absorption band at 3100–3700 cm^{-1} decreases considerably for both PMMA7 and PMMA-H6 when they were heated. The intensity reduction is mainly owed to the desorption of water, which can be evidenced from the disappearing of the peak at the wavenumber of 1638 cm^{-1} due to the bending vibration of water. The water most likely comes from KBr. In addition, another new peak at 591 cm^{-1} is exhibited in the spectrum of PMMA7, which was attributed to the stretching vibration of Zr–O. No discernible difference was found between PMMA7 and PMMA-H6 for the other main peaks, including the peaks at 2998 and 2953 cm^{-1} due to stretching vibration of CH_2 and CH_3, the peak at 1732 cm^{-1} due to stretching vibration of C=O, the peak at 1450 cm^{-1} due to stretching vibration of C(=O)–O, the peaks at 1270, 1245, 1193 and 1149 cm^{-1} due to stretching vibration of C–O–C. At temperature of 200 °C, the positions of the characteristic peaks of CH_2 and CH_3 do not have any changes. Nevertheless, the peak at 1732 cm^{-1} shift to high wavenumber (1734 and 1736 cm^{-1} for PMMA7 and PMMA-H6, respectively) and the other peaks shift to low wavenumber (namely, 1446, 1261, 1241, 1187 and 1146 cm^{-1} for both two samples). The shifts of these peaks at high temperature suggest the redistribution of hydrogen bond in the materials. Unfortunately, however, they cannot provide another evidences for the hydrogen bonding interaction between PMMA and ZrO_2 nanoparticles.

3.4. Optical clarity of the PMMA/ZrO_2 nanocomposites

Fig. 3 displays the photos of dumbbell-shaped PMMA and PMMA/ZrO_2 nanocomposite slices with various ZrO_2 contents. All slices are highly transparent and their optical differences cannot be distinguished with naked eyes. Fig. 4 shows the UV–vis spectra of PMMA/ZrO_2 nanocomposite sheets as a function of ZrO_2 content. Even for the sheet with 7 wt% of ZrO_2 content (sample PMMA7), its transmittance at wavelength of 550 nm is still beyond 80%. Nevertheless, slight reduction of transparency is exhibited with increasing ZrO_2 content, which can be attributed to the existence of a few of ZrO_2 agglomerates. An obvious reduction of the transmittance in the UV region is observed for the sheets with high ZrO_2 contents (samples PMMA5 and PMMA7), suggesting a good UV-shielding property of the nanocomposites. Fig. 5 presents the typical TEM images of PMMA/ZrO_2 nanocomposites. It can be seen that ZrO_2 nanoparticles (about 4 nm in diameter) are homogeneously dispersed in PMMA matrix at primary particle size level, which is responsible for the high transparency of the nanocomposites.

3.5. Tensile properties of PMMA/ZrO_2 nanocomposites

Tensile tests were conducted for PMMA/ZrO_2 nanocomposites using HEMA as a coupling agent as well as for neat PMMA, PMMA-H6 and PMMA/ZrO_2 nanocomposite using MPS as a coupling agent (named as PMMA2-M, 2 wt% of ZrO_2 content, prepared according to the method in reference [13]) for comparison. Only one stress–strain curve for each sample is typically plotted in Fig. 6. Nevertheless, the strength and elongation-at-break for all tensile tests are given in Table 3. Because of lacking of sufficient samples, no more than 3 parallel tensile tests were carried out for each sample, which inevitably decreases the credibility of the tensile results. However, some interesting information still can be revealed from these stress–strain curves if PMMA/ZrO_2 nanocomposites are holistically considered. First, all HEMA-based nanocomposites with various ZrO_2 contents have tensile behavior being analogous to neat PMMA or PMMA-H6. That is, the stress of the specimen

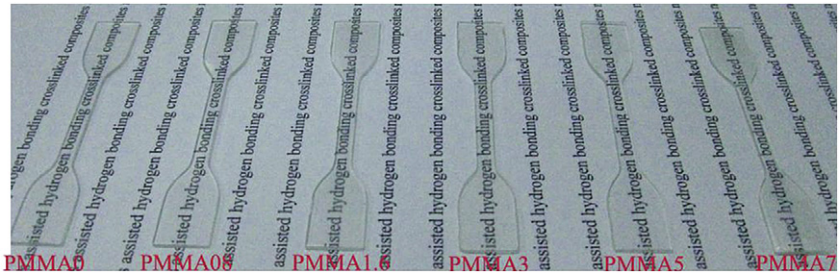

Fig. 3. Photos of neat PMMA and PMMA/ZrO_2 nanocomposites with different ZrO_2 contents.

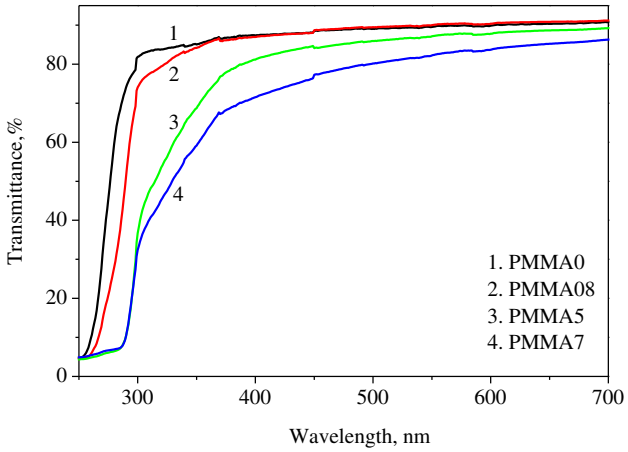

Fig. 4. UV–Vis spectra of neat PMMA and PMMA/ZrO_2 nanocomposites slices (thickness of slices:1.0 mm).

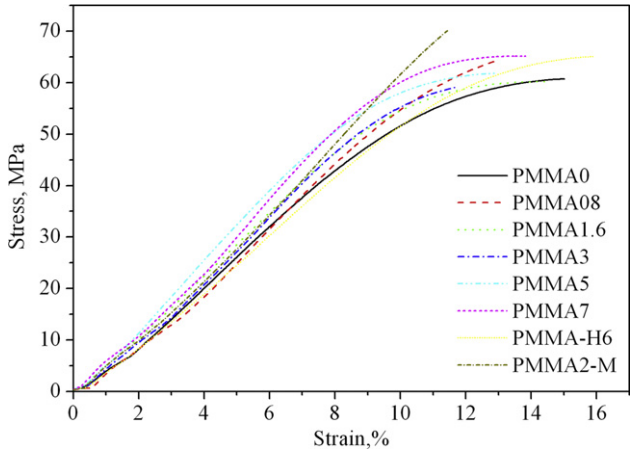

Fig. 6. Stress–Strain curves of neat PMMA, PMMA-H6 and PMMA/ZrO_2 nanocomposites using HEMA or MPS as a coupling agent (PMMA2-M: 2 wt% ZrO_2 content).

increases with increasing strain and approaches a plateau before breaking. However, no plateau is exhibited in the stress–strain curves of PMMA2-M. Additionally, Table 3 shows that all elongations-at-break of HEMA-based nanocomposites are higher than those of PMMA2-M. These results suggest that the hydrogen bond between polymer matrix and ZrO_2 nanoparticles can be easily destroyed under high stress, and the hydrogen bonding-based nanocomposite seems more ductile than chemical bonding-based nanocomposite. Second, higher slope of the stress–strain curves is found for the nanocomposites especially with higher content of ZrO_2 (PMMA5 and PMMA7) in comparison with neat PMMA and PMMA-H6, indicating increased rigidity of the nanocomposites. As for PMMA2-M, it has the highest average strength-at-break (68.9 MPa) among all the samples in Table 3. It illustrates that the external force may be efficiently delivered to ZrO_2 nanoparticles via chemical bonding interaction. As a whole, the reinforcing role, though not remarkable (possibly due to low ZrO_2 content in the nanocomposite and the trade-off effect by the flexible HEMA unit), of ZrO_2 nanoparticles for polymer can be realized via hydrogen bonding interaction between polymer matrix and nanoparticles.

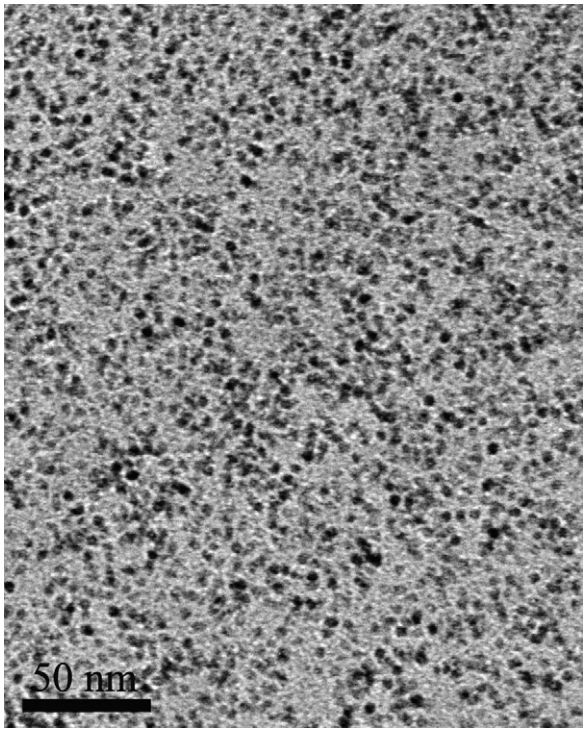

Fig. 5. Typical TEM images of PMMA/ZrO_2 nanocomposites (ZrO_2 content: 7 wt%).

3.6. DMA property of PMMA/ZrO_2 nanocomposites

The storage modulus and the damping (tan δ) as a function of temperature for PMMA/ZrO_2 nanocomposites with different ZrO_2 contents are shown in Fig. 7. The storage modulus and tan δ of the neat PMMA and PMMA-H1 are also displayed in Fig. 7 for comparison. In glassy state, the storage modulus of PMMA/ZrO_2 nanocomposites is obviously higher than those of PMMA and PMMA-H1, demonstrating the reinforcing role of ZrO_2 nanoparticles. In rubbery state, however, the storage modulus of PMMA is independent of ZrO_2 nanoparticle content. It may be due to the weak interaction between polymer matrix and ZrO_2 nanoparticles at high temperatures, as evidenced from the variable temperature FTIR spectra described above. In addition, Fig. 7a unveils the inconspicuous change of the storage modulus of the nanocomposites with ZrO_2 content. This may be due to the counteracting effect of the flexible HEMA unit in polymer matrix for the reinforced role of ZrO_2 nanoparticles, as discussed above for tensile results.

Table 3
The strength and elongation-at-break for neat PMMA, PMMA-HEMA and PMMA/ZrO_2 nanocomposites.

Sample name[a]	Strength-at-break, MPa	Elongation-at-break, %
PMMA0	60.7	15.0
PMMA08	64.2	12.9
PMMA1.6(1)	60.3	14.5
PMMA1.6(2)	60.2	14.6
PMMA3	59.1	11.7
PMMA5(1)	68.5	11.6
PMMA5(2)	61.7	12.9
PMMA7	65.1	13.8
PMMA-H6	65.1	16.0
PMMA2-M (1)	70.1	11.5
PMMA2-M(2)	60.7	10.2
PMMA2-M(3)	75.8	10.8

[a] Note: The digital in bracket represents the serial number in parallel tensile tests for the same sample.

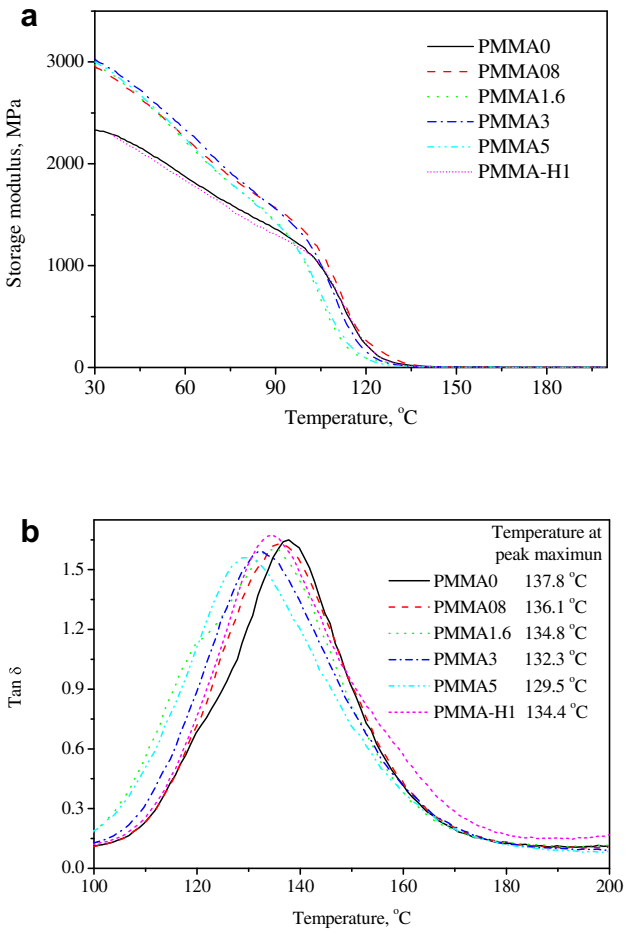

Fig. 7. Storage modulus (a) and tan δ (b) of PMMA/ZrO_2 nanocomposites with different ZrO_2 contents and PMMA-H1.

Fig. 7b shows that the damping peak unexpectedly shifts to lower temperature, being contrary to those conventional nanocomposites based on chemical bond [38,39]. The temperature at peak maximum, defined as the glass transition temperature (T_g), changes from 137.8, 136.1, 134.8, 132.3 and 129.5 °C for PMMA0, PMMA08, PMMA1.6, PMMA3 and PMMA5, respectively. The introduction of flexible HEMA units into polymer matrix is expected to be responsible for the decreased T_g, which can be confirmed from the lower T_g (134.4 °C) of PMMA-H1 relative to PMMA0. Interestingly, PMMA1.6 has a T_g slightly higher than PMMA-H1 despite of the higher HEMA content (1.4 wt%). This implies that the hydrogen bonding interaction between polymer and ZrO_2 nanoparticles can restrict the mobility of polymer chains. On the other hand, the damping peak slightly declines to low intensity and become broad as ZrO_2 content increases, which also suggests the slight restriction of the mobility of polymer chains by ZrO_2 nanoparticles.

3.7. Thermal stability of PMMA/ZrO_2 nanocomposites

TGA curves and their differential curves (DTG) for neat PMMA and PMMA/ZrO_2 nanocomposites with various ZrO_2 contents are presented in Fig. 8. It is well known that the degradation of radically polymerized PMMA in nitrogen displays three stages: cleavage of the head-to-head linkages at around 160 °C (the first stage) and end-initiated vinyl-terminated PMMA at around 270 °C (the second stage), and random scission of polymer backbone at around 360 °C (the third stage) [40]. But differential analysis of the TGA curves in Fig. 8 shows that the first and the second degradation stages are not easily to be identified, possibly being caused by instrumental error and air atmosphere. Only the third degradation stage corresponding to the scission of PMMA main chains is relatively clear. Its temperature steadily increases from 312, 324, 343 and 369 °C when ZrO_2 nanoparticles content increases from 0, 0.8, 3, and 7 wt%, respectively, indicating an improved thermal stability of PMMA main chain by ZrO_2 nanoparticles. The enhanced thermal stability of PMMA was ever observed for PMMA/SiO_2/ZrO_2 nanocomposites reported by Wang et al. [41]. They attributed the better thermal stability of the nanocomposites to the formation of networks between polymer and inorganic moieties, which led to the restrained movement of free radicals generated by thermal decomposition of PMMA matrix. Demir et al. [9] reported that those nanocomposites with weak interaction between PMMA and nanoparticles (unmodified SiO_2, AlN nanoparticles, or inert surfactant modified ZnO, TiO_2 and ZrO_2 nanoparticles) possessed improved thermal stability. But this improvement merely lied in the reduced fraction of the second degradation stage and the increased fraction of the third degradation stage of PMMA, not in the enhanced degradation temperature. Degradation temperature was also not raised for PMMA/SiO_2 nanocomposite prepared using methyl-functionalized SiO_2 nanoparticles [42]. In our cases, FTIR spectra, tensile test as well as DMA tests demonstrated that the hydrogen bonding, rather than the chemical bonding, between PMMA and ZrO_2 nanoparticles was formed. Since the hydrogen bonding interaction weakens at high temperature, it is not possible to play positive role on the thermal stability of PMMA backbone. Hence, we suggest that the enhanced thermal property of PMMA/ZrO_2 nanocomposites is probably due to the formation of chemical bond between polymer and ZrO_2 nanoparticles at high temperature during TGA testing or the trapping of the generated free radicals by ZrO_2 nanoparticles. The formation of chemical bond between hydroxyl groups-containing polymer and SiO_2 nanoparticles was ever reported for poly(2-hydroxyethyl acrylate)-co-MMA/SiO_2 nanohybrids [43].

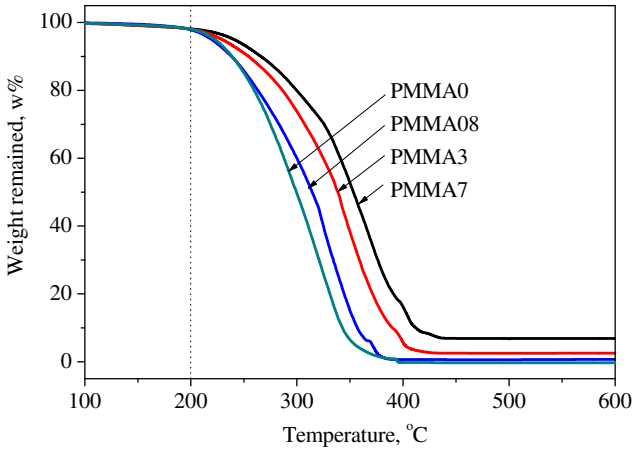

Fig. 8. TGA curves of neat PMMA and PMMA/ZrO_2 nanocomposites with various ZrO_2 contents.

4. Conclusions

Nonaqueous synthesized ZrO_2 nanocrystals can be well dispersed in MMA using the functional monomer HEMA as a ligand, forming a transparent MMA/ZrO_2 dispersion. Destabilization of the dispersion takes place in air as well as at elevated temperatures, implying the hydrogen bonding interaction between HEMA molecules and ZrO_2 nanoparticles. Higher molar ratio of HEMA/ZrO_2 benefited the

better stability of the dispersion and thus led to a higher destabilization temperature. Transparent PMMA/ZrO_2 nanocomposites with ZrO_2 content of as high as 7 wt% were prepared by *in-situ* bulk polymerization from the as-obtained MMA/ZrO_2 dispersions. Soxhlet extracting experiments indicated that the cross-linking network was formed even for the nanocomposite with ZrO_2 content of as low as 0.8 wt%. Nevertheless, variable temperature FTIR spectra revealed that hydrogen bonding rather than chemical bonding was established between PMMA and ZrO_2 nanoparticles. Tensile tests and DMA tests illustrated that PMMA can be reinforced by ZrO_2 nanoparticles. Moreover, the PMMA/ZrO_2 nanocomposites based on hydrogen bonding were more ductile than that those based on chemical bonding. TGA analysis showed the enhanced thermal stability of PMMA via addition ZrO_2 nanoparticles.

Acknowledgements

We are grateful for the financial supports from the New Century Excellent Talent Foundation of the Ministry of Education of China (NCET-07-0210), National Nature Science Foundation (No.50703005) of China, Shanghai Nano Project (0852nm00800), Shanghai Rising-Star Program (08QA1401100), Shanghai Leading Academic Discipline Project (No. B113), and Program for Changjiang Scholars and Innovative Research Team in University (IRT0911).

References

[1] Li SH, Qin J, Fornara A, Toprak M, Muhammed M, Kim DK. Nanotechnology 2009;18(20).
[2] Torres-Cisneros M, Yanagihara N, Gonzalez-Rolon B, Meneses-Nava MA, Ibarra-Manzano OG, May-Arrioja DA, et al. Microelectron J 2009;40(3):621–3.
[3] Yuwono AH, Liu BH, Xue JM, Wang J, Elim HI, Ji W, et al. J Mater Chem 2004;14 (20):2978–87.
[4] Yuwono AH, Xue JM, Wang J, Elim HI, Ji W, Li Y, et al. J Mater Chem 2003;13 (6):1475–9.
[5] Althues H, Palkovits R, Rumplecker A, Simon P, Sigle W, Bredol M, et al. Chem Mater 2006;18(4):1068–72.
[6] Li S, Toprak MS, Jo YS, Dobson J, Kim DK, Muhammed M. Adv Mater 2007;19 (24):4347–52.
[7] Chai RT, Lian HZ, Yang PAP, Fan Y, Hou ZY, Kang XJ, et al. J Colloid Interface Sci 2009;336(1):46–50.
[8] Demir MM, Koynov K, Akbey U, Bubeck C, Park I, Lieberwirth I, et al. Macromolecules 2007;40(4):1089–100.
[9] Demir MM, Castignolles P, Akbey U, Wegner G. Macromolecules 2007;40 (12):4190–8.
[10] Avella M, Errico ME, Martuscelli E. Nano Lett 2001;1(4):213–7.
[11] Ash BJ, Siegel RW, Schadler LS. Macromolecules 2004;37(4):1358–69.
[12] Chau JLH, Hsieh CC, Lin YM, Li AK. Prog Org Coat 2008;62(4):436–9.
[13] Hu YQ, Zhou SX, Wu LM. Polymer 2009;50(15):3609–16.
[14] Liu P, Su ZX. J Macromol Sci Part B-Phys 2006;B45(1):131–8.
[15] Chai RT, Lian HZ, Hou ZY, Zhang CM, Peng C, Lin J. J Phys Chem C 2010;114 (1):610–616.
[16] Hajji P, David L, Gerard JF, Pascault JP, Vigier G. J Polym Sci Part B-Polym Phys 1999;37(22):3172–87.
[17] Kaddami H, Gerard JF, Hajji P, Pascault JP. J Appl Polym Sci 1999;73 (13):2701–13.
[18] Kaddami H, Pascault JP, Gerard JF. Polym Eng Sci 2004;44(7):1231–9.
[19] Huang SL, Chin WK, Yang WP. Polymer 2005;46(6):1865–77.
[20] Li S, Shah A, Hsieh AJ, Haghighat R, Praveen SS, Mukherjee I, et al. Polymer 2007;48(14):3982–9.
[21] D'Agostino A, Colella M, De Rosa M, De Rosa A, Lanza A, Schiraldi C. J Polym Res 2009;16(5):561–7.
[22] Yeh JM, Weng CJ, Huang KY, Huang HY, Yu YH, Yin CH. J Appl Polym Sci 2004;94(1):400–5.
[23] Zhou SX, Garnweitner G, Niederberger M, Antonietti M. Langmuir 2007;23 (18):9178–87.
[24] Luo KQ, Zhou SX, Wu LM, Gu GX. Langmuir 2008;24(20):11497–505.
[25] Zhou SX, Wu LM. Macromol Chem Phys 2008;209(11):1170–81.
[26] Xu K, Zhou SX, Wu LM. J Mater Sci 2009;44(6):1613–21.
[27] Xu K, Zhou SX, Wu LM. Prog Org Coat 2010;67(3):302–10.
[28] Sivakova S, Bohnsack DA, Mackay ME, Suwanmala P, Rowan SJ. J Am Chem Soc 2005;127(51):18202–11.
[29] Cordier P, Tournilhac F, Soulie-Ziakovic C, Leibler L. Nature 2008;451 (7181):977–80.
[30] Kushner AM, Gabuchian V, Johnson EG, Guan ZB. J Am Chem Soc 2007;129 (46):14110–1.
[31] Liu XY, Gao GQ, Dong L, Ye GD, Polym Gu Y. Adv Technol 2009;20(4):362–6.
[32] Zhou SB, Zheng XT, Yu XJ, Wang JX, Weng J, Li XH, et al. Chem Mater 2007;19 (2):247–53.
[33] Li LJ, Yang GS. Polym Int 2009;58(4):380–7.
[34] Garnweitner G, Goldenberg LM, Sakhno OV, Antonietti M, Niederberger M, Stumpe J. Small 2007;3:1626–32.
[35] Piech M, Weronski P, Xu X, Walz JY. J Colloid Interface Sci 2002;247:327–41.
[36] Mikhaylova Y, Adam G, Haussler L, Eichhorn KJ, Voit B. J Mol Struct 2006;788 (1–3):80–8.
[37] Sun CX, Van der Mee MAJ, Goossens JGP, Van Duin M. Macromolecules 2006;39(9):3441–9.
[38] Xiong MN, Zhou SX, You B, Gu GX, Wu LM. J Polym Sci.-Part B Polym Phys 2004;42(20):3682–94.
[39] Xiong MN, You B, Zhou SX, Wu LM. Polymer 2004;45(9):2967–76.
[40] Kashiwagi T, Inaba A, Brown JE, Hatada K, Kitayama T, Masuda E. Macromolecules 1986;19(8):2160–8.
[41] Wang HT, Xu P, Zhong W, Shen L, Du QG. Polym Degrad Stab 2005;87 (2):319–27.
[42] Kashiwagi T, Morgan AB, Antonucci JM, VanLandingham MR, Harris RH, Awad WH, et al. J Appl Polym Sci 2003;89(8):2072–8.
[43] Xu P, Wang HT, Tong R, Iv R, Shen Y, Du QG, et al. Polym Degrad Stab 2006;91 (7):1522–9.

Polymer 52 (2011) 130–137

Contents lists available at ScienceDirect

Polymer

journal homepage: www.elsevier.com/locate/polymer

Polymerization of 4-methyl-1-pentene catalyzed by α-diimine nickel catalysts: Living/controlled behavior, branch structure, and mechanism

Haiyang Gao [a,b,*], Jin Pan [a], Lihua Guo [a], Dongjie Xiao [a], Qing Wu [a,b,*]

[a] DSAPM Lab, Institute of Polymer Science, School of Chemistry and Chemical Engineering, Sun Yat-sen University, Guangzhou 510275, China
[b] PCFM Lab, OFCM Institute, Sun Yat-sen University, Guangzhou 510275, China

ARTICLE INFO

Article history:
Received 24 July 2010
Received in revised form
11 October 2010
Accepted 7 November 2010
Available online 19 November 2010

Keywords:
4-Methyl-1-pentene
α-Diimine nickel
Living/controlled polymerization

ABSTRACT

Branched α-olefin, 4-methyl-1-pentene (4 MP), was polymerized with classical α-diimine nickel complexes in the presence of MAO. Influences of structure of α-diimine nickel catalysts and polymerization parameters including temperature and [Al]/[Ni] mole ratio were evaluated. At 0 °C, 4-methyl-1-pentene can be polymerized in a living/controlled manner. The obtained poly(4-methyl-1-pentene)s are amorphous elastomers with low glass transition temperature (T_g). Nuclear magnetic resonance (NMR) and distortionless enhancement by polarization transfer (DEPT) analyses show that various types of branches and microstructural units are present in the polymers. On the basis of assignment of microstructures, mechanistic models that involves the 1,2- and 2,1-insertion, and chain walking were constructed. The influences of temperature and [Al]/[Ni] mole ratio on branching degree, branch type, and insertion pathways were also discussed in detail.

1. Introduction

The potential applications of polyolefin are determined by its physical and mechanical properties, which largely depend on its composition (molecular weight, dispersity, and stereochemistry), branch and topology structure [1,2]. Type and distribution of branches have important influences on the properties of polyolefin. Generally, short chain branches (SCBs) are mainly related to morphology and solid-state properties while long-chain branches (LCBs) are related to viscoelastic and rheological properties. Hyperbranch and dendritic structure can lead to some unique chemical and physical properties [3–7]. Nowadays, low-density polyethylene (LDPE) is industrially synthesized at high pressure and high temperature by free radical polymerization of ethylene. However, branches of LDPE are mainly composed of short chain branches (ethyl and butyl), and are hardly controlled in the polymerization process [8,9]. Hence, search for mild polymerization conditions and fine control of branch structure to give branched polymers are important goals in polyolefin field.

Currently, branches can be produced by three pathways in insertion/coordination polymerization of ethylene. The first one is copolymerization of ethylene and α-olefin (including incorporation of an olefin-terminated polymer chain). Branch structure and incorporation can be fairly controlled by this approach [10,11]. Another pathway is *intra-* or intermolecular C–H activation. This mechanism which involves C–H bond breaking on a polymer backbone suggests that the catalyst can break C–H bonds on growing polymer chains (intramolecular C–H bond activation) or on alkanes (intermolecular C–H bond activation) [12–14]. The polymer with much longer-chain branches ($C > 6$) can be produced. The third one is chain walking. Mohring and Fink first presented the concept of chain walking during olefin polymerization with a late transition nickel catalyst [15]. α-Diimine nickel and palladium catalysts reported by Brookhart show a distinguishing chain walking mechanistic feature involving β-hydride elimination and readdition process [16–19].

Utilizing chain walking approach, linear branched (various types of branch, *e.g.* methyl, ethyl, propyl, butyl, pentyl, and long-chain branches), hyperbranched, and dendrimeric polyolefins have also been synthesized by α-diimine nickel or palladium catalysts [20–25]. In addition to ethylene polymerization, many researches have also been concentrated on polymerization of linear α-olefins such as propylene, 1-hexene, and 1-octene [16,17,26–34]. When employed in the homopolymerization of α-olefins, α-diimine nickel or palladium catalysts generally lead to unique chain-straightened poly(α-olefin)s because of the chain straightening processes (1,ω-enchainment or 2,ω-enchainment) [27,33]. Polymerization of branched α-olefins with late transition metal catalysts have been scarcely reported to date, and one noteworthy

* Corresponding authors. Institute of Polymer Science, Sun Yat-sen University, Guangzhou 510275, China. Tel.: +86 20 84113250; fax: +86 20 84114033.
E-mail addresses: gaohy@mail.sysu.edu.cn (H. Gao), ceswuq@mail.sysu.edu.cn (Q. Wu).

0032-3861/$ – see front matter © 2010 Elsevier Ltd. All rights reserved.
doi:10.1016/j.polymer.2010.11.008

example is copolymerization of ethylene and 3,3-dimethyl-1-butene reported by Ye's group with Pd-diimine catalyst [35]. Comparing to polyolefin generated from linear α-olefin, the polymer generated from branched α-olefin is anticipated to exhibit more complex branch structure.

In this paper, a branched α-olefin, 4-methyl-1-pentene (4 MP), was selected as a monomer to study its polymerization behavior and branch structure of the products using α-diimine nickel catalysts. Influences of structure of catalysts and polymerization parameters were evaluated. It was found that the polyolefin with complex branches including branch-on-branch was generated by living/controlled 4 MP polymerization using α-diimine nickel catalysts. Additionally, the NMR analyses were performed on the poly(4-methyl-1-pentene)s to gain a better understanding of polymer microstructures and the mechanisms.

2. Experimental

All manipulations involving air- and moisture sensitive compounds were carried out under an atmosphere of dried and purified nitrogen with standard vacuum-line, Schlenk, or glovebox techniques.

2.1. Materials

Toluene was dried over sodium metal and distilled under nitrogen. 4-methyl-1-pentene (4 MP) was purchased from Acros, dried over CaH_2, and distilled under nitrogen before storing over molecular sieves. Methylaluminoxane (MAO) was prepared by partial hydrolysis of trimethylaluminum(TMA) in toluene at 0–60 °C with $Al_2(SO_4)_3 \cdot 18H_2O$ as water source. The initial $[H_2O]$/[TMA] molar ratio was 1.3. The Ni(II) α-diimine complexes were prepared according to the literature [16,17], and characterized by elemental analysis. Other commercially available reagents were purchased and used without purification.

2.2. Polymerization

In a typical procedure, the appropriate MAO solid was introduced into the round-bottom glass flask, and then 4 MP monomer was added via a syringe. Toluene and a nickel complex solution were syringed into the well-stirred solution in order, and the total reaction volume was kept at 10 mL. The polymerization reaction was continuously stirred for an appropriate period at the polymerization temperature. Except for 0 °C maintained with ice-water bath, the other reaction temperatures were controlled with an external oil bath in polymerization experiments. The polymerizations were terminated by the addition of 200 mL of acidic ethanol (95:5 ethanol/HCl). The resulting precipitated polymers were collected and treated by filtration, washing with ethanol several times, and drying in vacuum at 40 °C to a constant weight. All polymerizations were reproduced, and yield and catalytic activity are average value within 10% experimental error.

2.3. Characterization

Elemental analyses were performed on a Vario EL microanalyzer. Nuclear magnetic resonance (NMR) and distortionless enhancement by polarization transfer (DEPT) spectra were carried out on a Varian Mercury-puls 500 MHz spectrometer at 120 °C. Sample solutions of the polymer were prepared in *o*-$C_6D_4Cl_2$ and *o*-$C_6H_4Cl_2$ mixture solvent (volume ratio: 20/80) in a 10 mm tube. The spectra of the quantitative ^{13}C NMR were taken with a 74° flip angle, an acquisition time of 1.5 s, and a delay of 4.0 s. The molecular weight distributions (M_w/M_n) of the poly(4 MP)s were determined on Waters GPC2000 at 135 °C with standard polystyrene as the reference, and 1,2,4-trichlorobenzene was employed as the eluent with a flow rate of 1.0 mL/min. DSC analysis was conducted with a Perkin Elmer DCS-7 system. The DSC curves were recorded at second heating curves from −100 °C to 150 °C at a heating rate of 10 °C/min and a cooling rate of 10 °C/min.

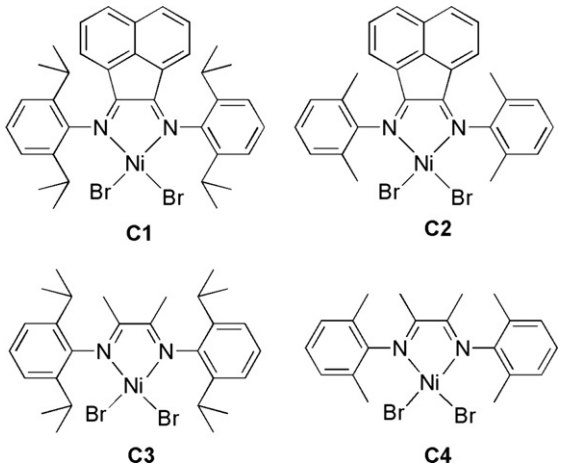

Scheme 1. Four α-diimine nickel complexes.

3. Results and discussion

3.1. Influence of structure of α-diimine nickel complexes

Four classical α-diimine nickel complexes [(ArN=C(An)–(An)C=NAr)$NiBr_2$ **C1**, An = acenaphthene, Ar = 2,6-(^{i}Pr)$_2C_6H_3$; **C2**, An = acenaphthene, Ar = 2,6-(Me)$_2C_6H_3$; **C3**, An = Me, Ar = 2,6-(^{i}Pr)$_2C_6H_3$; **C4**, An = Me, Ar = 2,6-(Me)$_2C_6H_3$)] (see Scheme 1) were used as precursors for 4 MP polymerization. With MAO as cocatalyst, the influence of structure of α-diimine nickel complexes on catalytic activity was evaluated. Table 1 summarizes the results of the initial screening study. As expected, four nickel catalysts show moderate catalytic activity for 4 MP polymerization. Comparisons of entry 1 *vs* 3, and entry 2 *vs* 4 demonstrate that complexes with the acenaphthene backbone (An = acenaphthene) show the higher activity for 4 MP polymerization, but those with the methyl backbone (An = Me) produce the higher-molecular-weight polymers. Steric effect of complexes is also illustrated by comparing entry 1 with entry 2, and entry 3 with entry 4. Bulky steric hindrance of nickel complex decreases its catalytic activity for 4 MP polymerization, but increases the molecular weight of the product markedly. This result clearly indicates that *ortho* substituent bulkiness of complex not only decreases the 4 MP insertion rate, but also decreases the rate of chain transfer reaction.

Table 1
4 MP Polymerizations catalyzed by **C1**-**4**/MAO.[a]

Entry	Catalyst	Yield (g)	Activity (kg (mol Ni·h)$^{-1}$)	M_n[b] (kg mol^{-1})	M_w/M_n[b]	T_g[c] (°C)
1	**C1**	1.04	104	217	1.64	−22
2	**C2**	1.34	134	58	1.78	−32
3	**C3**	0.42	42	238	1.72	−21
4	**C4**	0.57	57	73	1.71	−27

[a] Polymerization conditions: 10 μmol of complex; temperature, $T = 40$ °C; [Al]/[Ni] = 500; reaction time, $t = 1$ h; monomer addition, 4 MP = 2 g; solvent, toluene; total volume, 10 mL.
[b] Determined by GPC relative to polystyrene standards.
[c] Determined by DSC.

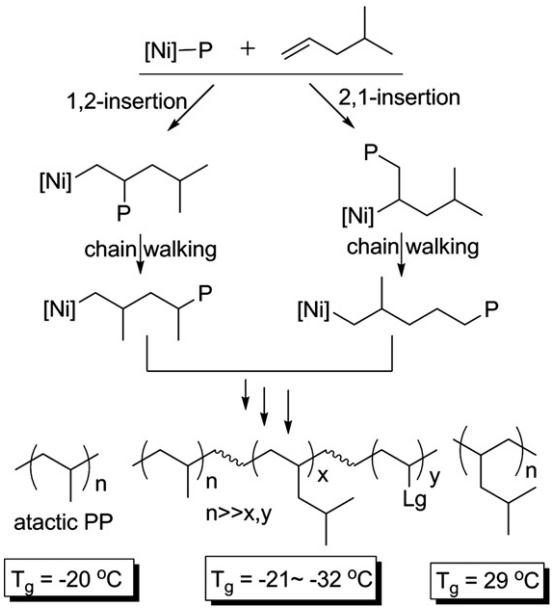

Scheme 2. Dependence of T_g of the product on chain walking.

No melting point (T_m) of poly(4 MP)s by DSC analysis was detected, indicating that the obtained polymers are amorphous elastomers. Glass transition temperatures (T_g) of the polymers are in the range from −21 to −32 °C, which are far lower than T_g of poly (4-methyl-1-1-pentene) produced by Ziegler–Natta catalyst(29 °C) but are close to T_g of atactic polypropylene (−20 °C) [36]. This result suggests that the chain walking occurs during 4 MP polymerization (see Scheme 2), and the detailed chain walking process is discussed below mechanistic model part. Considering the good catalytic activity and high molecular weight of the product, **C1** was chosen to further investigate the influences of polymerization parameters such as temperature, and [Al]/[Ni] ratio in detail.

3.2. Influences of temperature and [Al]/[Ni] mole ratio

Table 2 lists the polymerization results of 4 MP with **C1**/MAO catalytic system under various temperatures and [Al]/[Ni] mole ratios. With an increase in the reaction temperature, the catalytic activity for 4 MP polymerization increased, and then decreased. The highest activity was observed at 40 °C. Besides, raising temperature also affects molecular weight of the produced polymer. When polymerization was carried out at 0 °C, poly(4 MP) with

Table 2
4 MP Polymerization results catalyzed by **C1**/MAO under various conditions.[a]

Entry	T (°C)	[Al]/[Ni] (mol/mol)	Yield (g)	Activity [b]	M_n [c] (kg mol^{-1})	M_w/M_n [c]	T_g [d] (°C)	BD [e]
5	0	250	0.16	16	43	1.09	−17	292
6	20	250	0.73	73	191	1.31	−19	286
7	40	250	0.86	86	182	1.83	−21	270
8	60	250	0.51	51	135	1.81	−22	259
9	40	100	0.67	67	152	1.97	−24	250
1	40	500	1.04	104	217	1.64	−22	264
10	40	1000	0.94	94	180	1.79	−23	262

[a] Polymerization conditions: 10 μmol of complex; reaction time, t = 1 h; monomer addition, 4 MP = 2 g; solvent, toluene; total volume, 10 mL.
[b] In unit of kg (mol Ni·h)$^{-1}$.
[c] Determined by GPC relative to polystyrene standards.
[d] Determined by DSC.
[e] *BD*: branching degree, the number of methyl carbon in each 1000 carbons, determined by ^{1}H NMR.

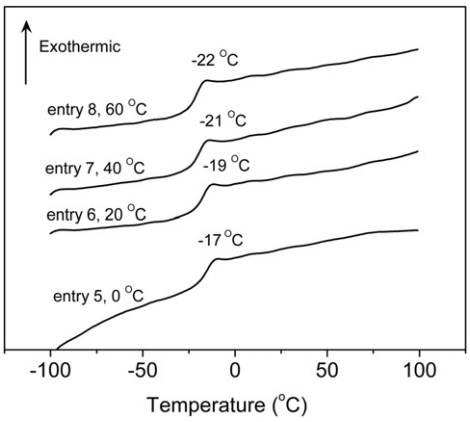

Fig. 1. DSC thermograms of poly(4 MP) prepared at different temperatures with C1/MAO.

relatively low molecular weight (M_n = 43,000) was obtained. At 20 °C, the highest molecular weight (M_n = 191,000) was produced. Higher temperatures caused a decrease in the molecular weight of the product. We note here that low temperature leads to a narrowing of the molecular weight distribution (1.09 at 0 °C, and 1.31 at 20 °C), as determined by gel permeation chromatography (GPC) calibrated against polystytene standards.

The branching degrees and T_g values were observed to decrease obviously with increasing temperature, which results from "chain strengthening" because nickel migration is favored at high temperature. For example, the branching degree decreases from 292 per 1000 carbons at 0 °C to 259 per 1000 carbons at 60 °C, and corresponding T_g value reduces from −17 to −22 °C (DSC thermograms are shown in Fig. 1). At low temperature, higher branched polymer with more bulky and rigid isobutyl side groups was produced. These bulky and rigid isobutyl side groups lead to an increase in T_g of the obtained polymer [36].

The influence of [Al]/[Ni] mole ratio was also investigated at 40 °C. With an increase in [Al]/[Ni] ratio, both the catalytic activity for 4 MP polymerization and the molecular weight of the product increased, and then decreased. When [Al]/[Ni] ratio is 500, the highest catalytic activity and the highest molecular weight of the product were observed. However, the influence of [Al]/[Ni] ratio on branching degree of the poly(4 MP)s is very slight, and all T_g of the polymers are observed around −22 °C, corresponding to ~260 per 1000 carbons branching degree.

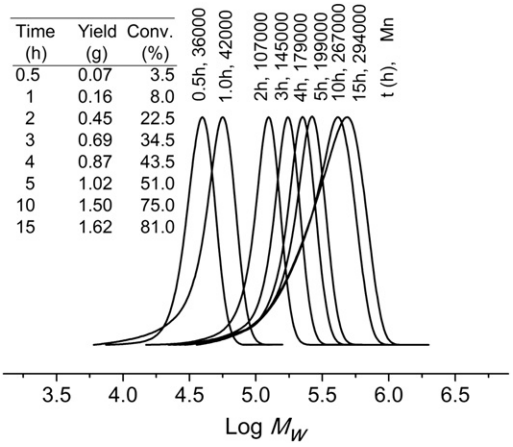

Fig. 2. GPC traces of poly(4 MP)s prepared at different polymerization time.

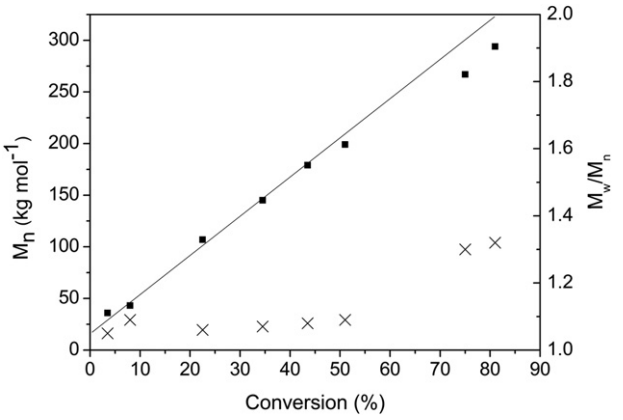

Fig. 3. Plots of M_n (■) and M_w/M_n (×) as a function of conversion for the polymerization of 4 MP (0 °C, 10 μmol catalyst, [Al]/[Ni] = 250, 4 MP = 2 g; solvent, toluene; total volume, 10 mL).

Table 3
4 MP Polymerizations with **C1**/MAO at different monomer concentrations.[a]

Entry	[4 MP] (mol L^{-1})	Yield (g)	Activity[b]	M_n[c] (kg mol^{-1})	M_w/M_n[c]	Tg[d] (°C)
11	3.6	0.18	18	48	1.10	−16
5	2.4	0.16	16	43	1.09	−17
12	1.2	0.13	13	35	1.08	−17
13	0.8	0.11	11	28	1.06	−17
14	0.6	0.08	8	24	1.07	−18

[a] Polymerization conditions: 10 μmol of complex; reaction time, t = 1 h; temperature: T = 0 °C; [Al]/[Ni] = 250; solvent, toluene; total volume, 10 mL.
[b] In unit of kg (mol Ni·h)$^{-1}$.
[c] Determined by GPC relative to polystyrene standards.
[d] Determined by DSC.

3.3. Living polymerization

Note that a narrow distribution of the polymer can be observed at 0 °C, thus 4 MP polymerizations with **C1**/MAO were carried out under 0 °C and 250 [Al]/[Ni] mole ratio. Fig. 2 shows the GPC curves of the polymers obtained at different polymerization time, which shifts to the higher-molecular-weight region with the increasing polymerization time. The M_n and M_w/M_n values are plotted against the conversion in Fig. 3. M_n grows linearly with the conversion in the early stages of polymerization (~5 h), but then the slope begins to decrease slightly. The M_w/M_n values remain very low (<1.10) through 5 h and then begin to increase slightly, reaching 1.30 at 10 h. Broadening molecular weight distribution after 10 h may arise from polymer gel and embedment of nickel species due to high conversion. Therefore, it is no doubt that the living/controlled polymerization of 4 MP can proceed with the **C1**/MAO catalyst at 0 °C within 5 h.

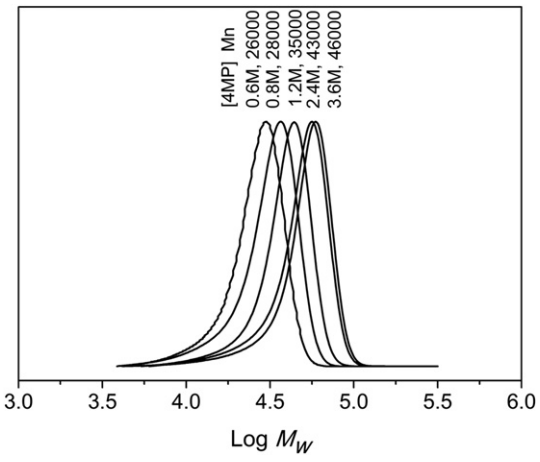

Fig. 4. GPC traces of the poly(4 MP)s obtained at different monomer concentrations.

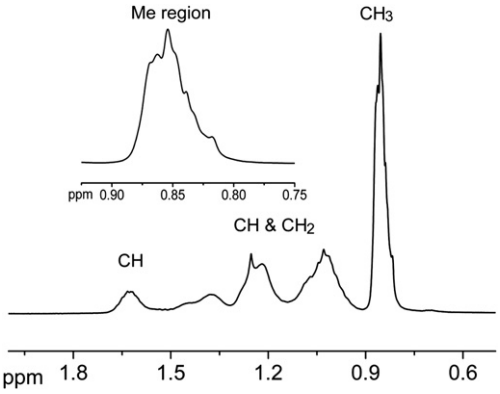

Fig. 5. ^{1}H NMR spectrum of poly(4 MP) prepared by C1/MAO at 0 °C.

It was already shown that α-olefin polymerizations such as 1-hexene with **C1**/MAO catalyst proceeded in a living/controlled manner at low monomer concentration ([M_0] < 1 mol L^{-1}). When initial [1-hexene]/[Ni] ratio is higher than 1500, the molecular weight distribution (M_w/M_n) increases sharply because noticeable chain transfer takes place at high initial monomer concentration [30–32]. However, our results in Table 3 show that the produced poly(4 MP)s exhibit narrow molecular weight distribution even at high monomer concentration ([4 MP] = 3.6 mol L^{-1} corresponding to 3600 [4 MP]/[Ni] ratio). GPC traces (Fig. 4) of the obtained polymers at different monomer concentrations are narrow and unimodal and do not contain small shoulder peaks. Also M_n of the products grows linearly with the yield at different monomer concentrations. Reasonable explanations for living/controlled 4 MP polymerizations with **C1**/MAO catalyst at high monomer concentration is that bulkiness of 4 MP monomer not only decreases the propagation rate, but also slows down chain transfer reaction [31].

3.4. Microstructure analysis of poly(4-methyl-1-pentene)

The precise microstructure analysis of poly(4-methyl-1-pentene)s synthesized by **C1**/MAO was studied by NMR spectroscopy using ^{1}H, ^{13}C, and DEPT experiments.

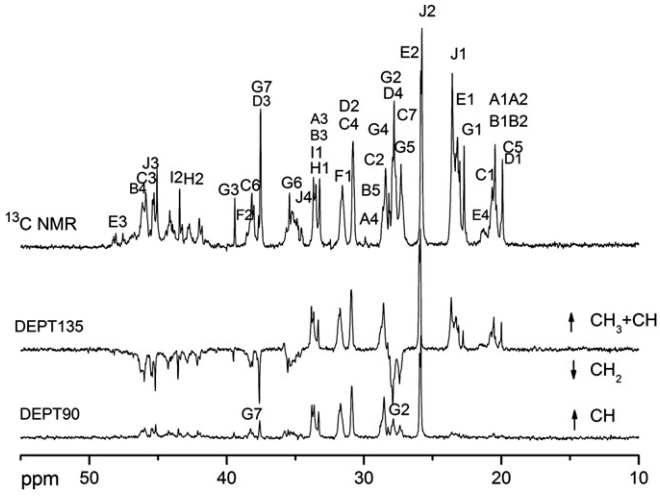

Fig. 6. ^{13}C NMR and DEPT spectra of poly(4 MP) prepared by C1/MAO (entry 7).

Table 4
^{13}C NMR chemical shifts of poly(4 MP) and assignments.

Branched units	Assignment	Chemical shift (ppm)		Ref.
		This work	Literature	
C, D	C5, D1	19.9	19.70,19.9	[42], [43]
A, B	A1, A2, B1, B2	20.5	19.5–20.07	[44]
C	C1	20.7	20.1, 20.2–20.6	[42], [44]
E	E4	21.4		
G	G1	22.7	22.4	[42]
E	E1	23.0–23.2	23.5	[42]
J	J1	23.6	23.21, 25.65, 23.5	[21], [42], [44]
J	J2	25.8	26.75, 25.8	[21], [42]
E	E2	25.9	25.8	[42]
C, G	C7, G5,	27.3	27.0, 27.24	[42], [44]
D, G	D4, G2	27.8	28.0, 27.2	[42–44]
			27.52, 27.79	
G	G4	28.2	28.1	[42]
B, C	B5, C2	28.4	27.97	[44]
A	A4	28.6	27.97	[44]
C, D	C4, D2	30.8	30.6, 30.38	[21], [42]
F	F1	31.6	31.29	[44]
A, B	A3, B3	33.2	33.38	[44]
H, I	I1, H1	33.5	31.5	[42], [45–47]
			31.29–33.62	
J	J4	33.7	33.62	[45]
G	G6	35.7	34.7	[42]
D, G	D3, G7	37.5	37.5, 37.6, 37.45, 37.47	[42–44]
C	C6	38.2	37.77	[44]
F	F2	38.5	38.87	[45–47]
G	G3	39.4	39.2	[42]
H	H2	41.8–42.7	39–42	[41]
I	I2	43.4–44.1	42–44	[41]
J	J3	45.1	45.5	[42]
C	C3	45.3–45.4	46.2	[42]
A, B	A4, B4	45.9–46.1	45.0–47.5	[44]
E	E3	46.7–48.2	47.0–48.0	[42]

No accurate chemical shift values are provided in the ref. 42, the values in ref. 42 are estimated according to the spectrum.

3.4.1. ^{1}H NMR

^{1}H NMR spectrum of poly(4 MP) prepared by **C1**/MAO at 0 °C is shown in Fig. 5. Methyl signals are observed in the region from 0.80 to 0.90 ppm. The peaks at ~0.82 ppm is short methyl branch signals, and the peaks at ~0.88 ppm can be assigned to the methyl branches in isobutyl or longer 2-methylalkyl branches [37]. Besides, a broad peak at 1.62 ppm can be unambiguously attributed to methine group attached two terminal methyl groups ($CH(Me)_2$). Therefore, it is safely concluded that the obtained poly(4 MP)s contain branch-on-branch structure such as 2-methylalkyl branches.

3.4.2. ^{13}C NMR

To have an insight into microstructure of the poly(4 MP), further investigations using ^{13}C NMR spectroscopy were undertaken. ^{13}C NMR of spectrum of poly(4 MP) is shown in Fig. 6, which is much more complex than that of catalyzed by metallocene titanium catalysts [38–40]. Two significant differences between poly(4 MP) and other poly(linear α-olefin)s such as poly(1-hexene) catalyzed by α-diimine nickel catalysts are the occurrence of more intense methyl signals at around 20 ppm, and the absence of runs of successive methylenes $-(CH_2)_n-$ ($n > 6$) at 30 ppm, indicating the presence of the complex branches. Therefore, ^{13}C NMR assignments were made by combining the result of DEPT experiments, chemical shift calculations using empirical tables of substituent effects, and reference to model compound data found in the NMR literatures [21,41–47]. The detailed peak assignments are shown in Table 4.

According to DEPT spectra, primary carbons (methyl) lie in the region from 19 to 25 ppm. Methyl groups in backbone are present in the region from 19 to 22 ppm, and methyl in isobutyl group or long 2-methylalkyl branches can be safely indentified by resonances in the region from 22 to 24 ppm. There are no detectable ethyl, propyl, and butyl branches as evidenced by lack of a terminal methyl resonance at the higher field ($\delta < 20$ ppm).

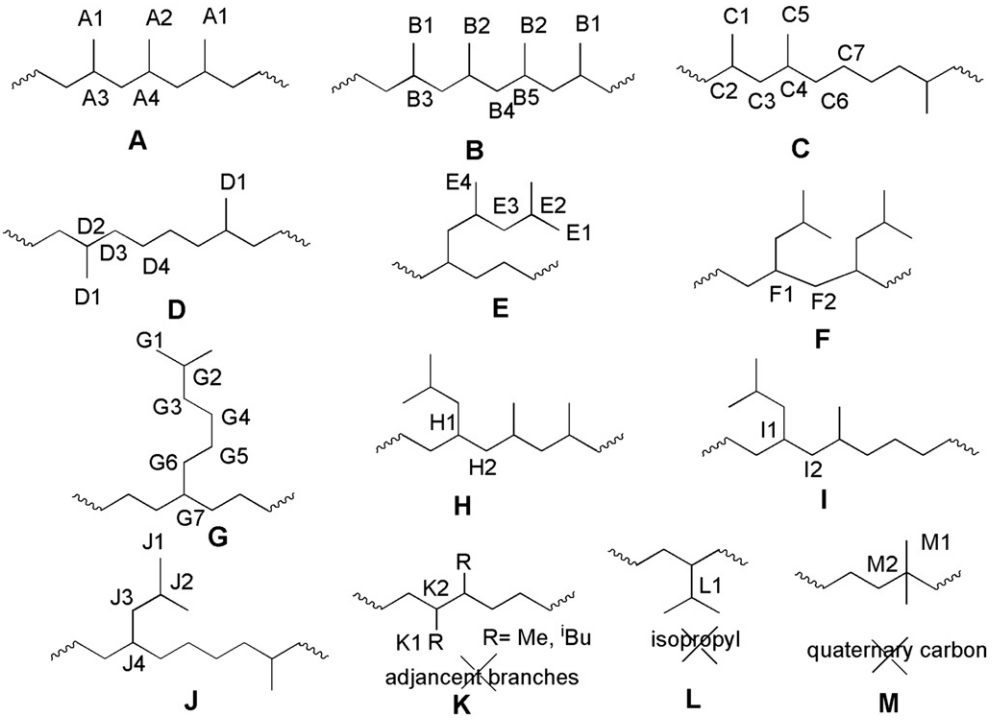

Scheme 3. Branched units in poly(4 MP).

From NMR spectrum of poly(4 MP), branched structure shown in Scheme 3 can be indentified including isolated methyl branches (unit **J**), paired methyl branches (unit **C** and **D**), successive methyl branches (1,3-B_1) (unit **A** and **B**). Also one observes runs of methylenes $(CH_2)_n$ (where $n = 2$) between branches and the corresponding methine (brB_1) can also be found at 30.8 ppm [43].

Multiple peaks in the region from 22 to 24 ppm suggest presence of complex 2-methylalkyl branches with different structure. According to reference [42], isolated isobutyl paired with methyl (unit **H**, **I**, and **J**) can be assigned. Besides, a successive isobutyl structure (unit **F**) can also be traced out according to methylene (Sαα) between two isobutyl groups at 38.6 ppm, but longer

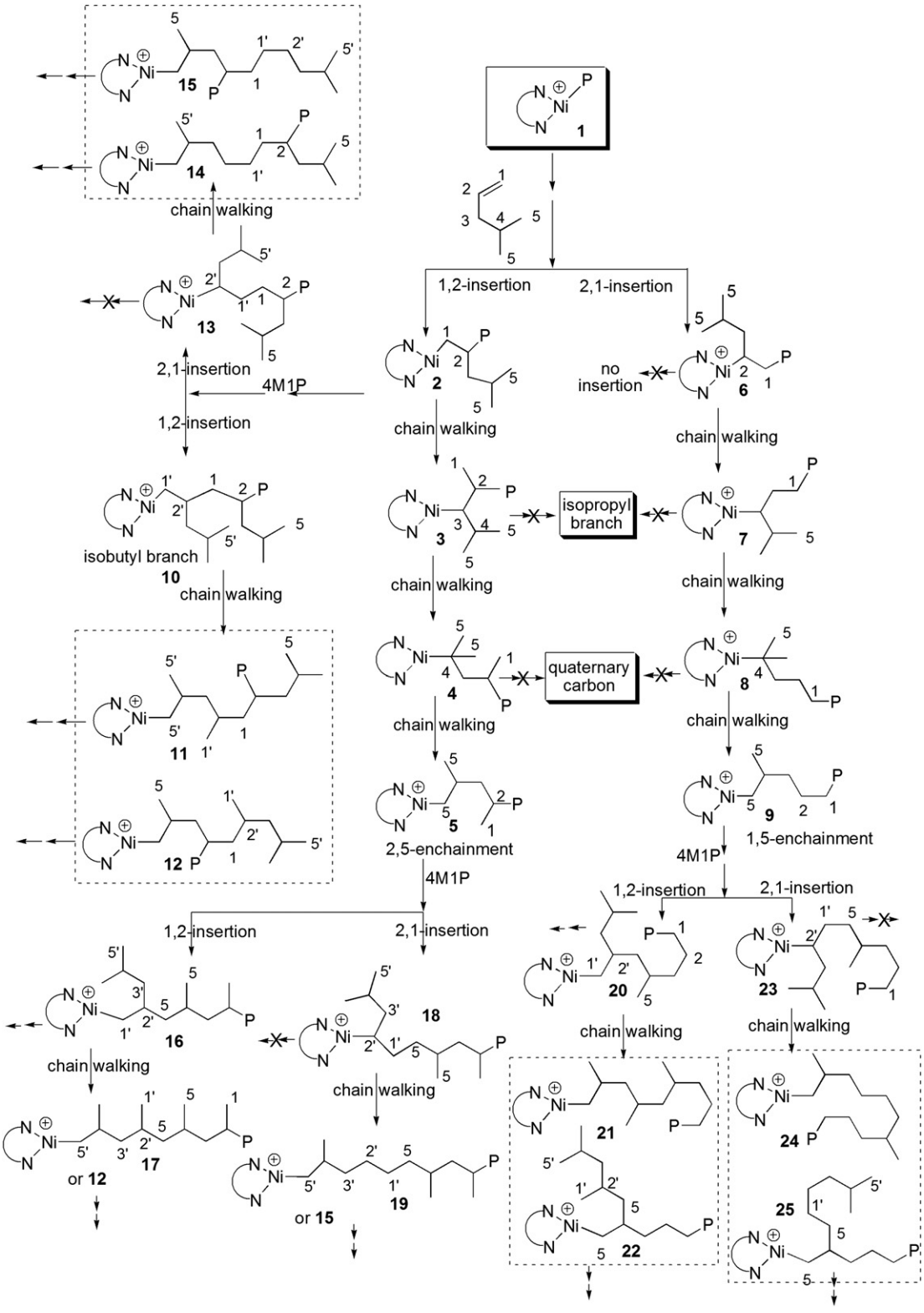

Scheme 4. Insertion pathways of 4 MP and chain walking.

successive isobutyl runs ((^{i}Bu)$_n$, $n > 3$) are not observed [40,45–47].Besides, the existence of several types of long branches in the poly(4 MP) have also been determined according to chemical shift values referred to literatures [42,48]. 2,4-Dimethylpentyl (unit **E**) branch can be confirmed by the presence of peak E3 at 48.1 and E4 at 21.3 ppm, and 2-methylhexyl (unit **G**) branch can be indentified by peak G7 at 37.6 ppm.

Brookhart previously reported unique adjacent methyl branches structure for α-olefin polymerization with α-diimine nickel catalyst [41]. The existences of adjacent branches unit must arise from a small fraction of 1,2-insertion of monomer into secondary Ni-alkyl bond with α-methyl. No signals appear below 20 ppm (K1 for methyl, R = methyl) and at ~ 41 ppm (K2 for methine, R = isobutyl) in the spectroscopy (Fig. 5), indicating that there is no adjacent branches structure (unit **K**) in the poly(4 MP). Additionally, isopropyl (unit **L**) cannot be observed, whose methine (L1) appears 29.1 ppm [48]. The methyl on quaternary carbon at 27.3 ppm and quaternary carbon at 33.0 ppm (unit **M**) are not present in the spectrum referring to assignment of the poly(4 MP) prepared by cation polymerization [48], so there is no existence of quaternary carbon in the poly(4 MP).

3.5. Mechanistic model

A particular set of branching types are expected to arise from the mechanistic model. Thus, characterization of microstructure allows further studying of polymerization mechanism. In principle, 4 MP can insert into nickel-alkyl bond (**1**) either in 1,2- (**2**) or 2,1-fashion (**6**) (see Scheme 4). Like to linear α-olefins polymerization with α-diimine nickel catalysts, 1,2-insertion of 4 MP and subsequent β-hydride elimination followed by nickel migration up to the primary carbon atom can result in 2,5-enchainment to give two short chain methyl branches in the polymer chain (**5**), while the 2,1-insertion of 4 MP can result in 1,5-enchainment to give one short chain methyl branch in the polymer chain (**9**).

There are no existences of adjacent branches (unit **K**), isopropyl group (unit **L**), and quaternary carbon (unit **M**) in the poly(4 MP), which strongly suggests that 4 MP monomer cannot insert into secondary nickel-alkyl bonds including nickel species **3**, **4**, **6**, **7** and **8**. Previously, a small fraction of 1,2-insertion into secondary carbon can be found in propylene and 1-hexene polymerization with α-diimine nickel catalyst [41,44]. However, no 4 MP monomer insertion into secondary Ni-alkyl bonds is observed, which possibly arises from crowd steric space for bulky 4 MP monomer [41]. Thus insertion of 4 MP occurs only into primary Ni−alkyl bond, and 2,1-insertion always results in chain walking to form 1,5-enchainment.

When 1,2-insertion of 4 MP follows a primary insertion, a successive isobutyl unit (**10**, (^{i}Bu)$_n$, $n = 2$, unit **F**) can be formed without occurrence of chain walking. However, longer successive isobutyl runs ((^{i}Bu)$_n$, $n > 3$) are not observed, which suggests that the rate of chain walking is generally greater than the rate of 4 MP insertion.

The nickel active species can migrate backward along the polymer or forward along the newly added monomer because of fast chain walking process [42]. When nickel metal migrates forward along the newly added 4 MP monomer, short chain methyl can be produced. When nickel metal migrates backward along the polymer, long branch such as 2-methylhexyl (**15**), and 2,4-dimethylpentyl (**12**) can be formed. 2-methylhexyl (unit **G**) and 2,4-dimethylpentyl (unit **E**) branches can be identified by ^{13}C NMR spectroscopy of poly(4 MP), while longer or more complicated branches may also exist in polymer, whose resonances cannot be distinguished from others. On the whole, units in poly(4 MP) shown in Scheme 3 can be reasonably explained by 1,2- or 2,1-insertion, and chain walking mechanism shown in Scheme 4.

On the basis of the above results, the fraction of 1,2-insertions can be predicted from ^{1}H to ^{13}C NMR spectroscopy. In the initial mechanism, every 1,2-insertion of 4-methyl-1-pentene including 2,5-enchainment gives rise to two methyl groups, while every 2,1-insertion of 4-methyl-1-pentene results in 1,5-enchainment and produces one methyl group. The total methyl branches including short chain methyl in the backbone and methyl in 2-methylalkyl can be calculated by the ^{1}H NMR. Thus the fraction of 1,2-insertions and initial 2,1-insertion can be calculated by equations (1) and (2), respectively.

$$1,2\% = \frac{BD - 167}{167} \times 100\% \tag{1}$$

$$2,1\% = \frac{333 - BD}{167} \times 100\% \tag{2}$$

where, *BD* refers to branching degree, methyl groups per 1000 carbons, which was determined from the ^{1}H NMR. 2,1% means 1,5-enchainment%.

Besides, the ratio of short chain methyl in backbone to methyl in 2-methylalkyl ((CH)Me_2) group can be easily determined by the quantitative ^{13}C NMR, thus the content of short chain methyl branch and 2-methylalkyl ((CH)Me_2) branch can be calculated by equations (3) and (4), respectively.

$$CH(Me)_2/1000\text{C} = \frac{r}{2(r+1)} \times BD \tag{3}$$

$$Me/1000\text{C} = \frac{1}{r+1} \times BD \tag{4}$$

where, r is the ratio of methyl in 2-methylalkyl (CH)Me_2 to short chain methyl integrals.

Table 5 summarizes microstructure data of poly(4 MP) prepared under different reaction conditions with **C1**/MAO. The data clearly show that as the polymerization temperature increases, initial 2,1-insertion (1,5-enchainment through chain walking) as minor insertion pathway increases from 25% at 0 °C to 45% at 60 °C, which causes a decrease in total branching degree from 292/1000C to 259/1000C (see Table 2). However, 2-methylalkyl branches increases, and then decreases with an increase in temperature. The highest content of 2-methylalkyl branches can be observed at 20 °C. This can be reasonably explained by insertion pathways and ratio of insertion rate (R_i) to chain walking rate (R_w), which are affected by polymerization temperature.

[Al]/[Ni] ratio also has a slight influence on insertion pathways and branching degree. At low [Al]/[Ni] ratio ([Al]/[Ni] = 100), initial 2,1-insertion (1,5-enchainment) reaches 50%, and relatively low content of 2-methylalkyl branches is observed. Raising [Al]/[Ni]

Table 5
Microstructure data of poly(4 MP)s and insertion pathways under different reaction conditions.

Entry	T (°C)	[Al]/[Ni]	r[a]	2-methylalkyl branches[b]	Methyl branch[c]	1,2-ins. (%)	2,1-ins.[d] (%)
5	0	250	1.42	86	121	75	25
6	20	250	2.82	106	75	71	29
7	40	250	2.02	91	89	62	38
8	60	250	1.43	76	107	55	45
9	40	100	1.69	78	93	50	50
1	40	500	2.09	90	85	58	42
10	40	1000	1.83	85	93	57	43

[a] r is the ratio of methyl in 2-methyalkyl (CH)Me_2 to short chain methyl integrals.
[b] 2-Methylalkyl branches per 1000 carbons, calculated by equation (3).
[c] Me branch per 1000 carbons, calculated by equation (4).
[d] Initial 2,1-insertion means 1,5-enchainment.

ratio to 250 leads to a 38% 2,1-insertion (1,5-enchainment) and 91/1000C of 2-methylalkyl branches. The higher [Al]/[Ni] ratios hardly have an influence on microstructure of the obtained polymers.

4. Conclusions

α-Diimine nickel catalysts show moderate catalytic activity and high yield for 4-methyl-1-pentene polymerization. Catalysts with the acenaphthene backbone show the higher activity for 4 MP polymerization, but those with the methyl backbone produce the higher-molecular-weight polymers. Bulky steric hindrance of catalysts decreases the catalytic activity for 4 MP polymerization, but increases the molecular weight of the product markedly. For **C1**/MAO, further optimization of reaction conditions ($T = 40\ ^\circ C$ and [Al]/[Ni] = 500) is likely to lead to improvements in the activity of the polymerization and the molecular weight of the polymer. At low temperature (0 °C), 4 MP polymerizations can proceed in a living/controlled manner even at high monomer concentration. The obtained poly(4-methyl-1-pentene)s are amorphous elastomers with various types of branches including 2,4-dimethylpentyl and 2-methylhexyl. The types of branch can be reasonably explained by insertion fashions and chain walking mechanism. The polymerization temperature has an important influence on insertion pathways, and total number and distribution of branches.

Acknowledgments

The financial supports by NSFC (Projects 20974125 and 20734004), the Science Foundation of Guangdong Province (Project 8251027501000018), and the Ministry of Education of China (Foundation for Ph. D. Training) are gratefully acknowledged.

References

[1] Ferry JD. Viscoelastic properties of polymers. New York: John Wiley and Sons; 1986.
[2] Doi M, Edwards SF. The theory of polymer dynamics. Oxford: Oxford University Press; 1986.
[3] Gao C, Yan D. Prog Polym Sci 2004;29:183–275.
[4] Yates CR, Hayes W. Eur Polym J 2004;40:1257–81.
[5] Patil R, Colby RH, Read DJ, Chen G, Guan Z. Macromolecules 2005;38:10571–9.
[6] Ye Z, Zhu S. Macromolecules 2003;36:2194–7.
[7] Wang L, Ye Z, Zhu S. Ind Eng Chem Res 2007;46:1174–8.
[8] Dorman DE, Otocka EP, Bovey FA. Macromolecules 1972;5:574–7.
[9] Usami T, Takayama S. Macromolecules 1984;17:1756–61.
[10] Kaminsky W, Arndt M. Adv Polym Sci 1997;127:143–87.
[11] McKnight AL, Waymouth RM. Chem Rev 1998;98:2587–98.
[12] Reinking MK, Orf G, Mcfaddin D. J Polym Sci Part A Polym Chem 1998;36:2889–98.
[13] Resconi L, Piemontesi F, Franciscono G, Abis L, Fiorani T. J Am Chem Soc 1992;114:1025–32.
[14] Stapleton RL, Chai J, Nuanthanom A, Flisak Z, Flisak Z, Nele M, et al. Macromolecules 2007;40:2993–3004.
[15] Mohring VM, Fink G. Angew Chem Int Ed Engl 1985;24:1001–3.
[16] Johnson LK, Brookhart M. J Am Chem Soc 1995;117:6414–5.
[17] Johnson LK, Mecking S, Brookhart M. J Am Chem Soc 1996;118:267–8.
[18] Mecking S, Johnson LK, Wang L, Brookhart M. J Am Chem Soc 1998;120:888–99.
[19] Leatherman MD, Svejda SA, Johnson LK, Brookhart M. J Am Chem Soc 2003;125:3068–81.
[20] Gates DP, Svejda SA, Onate E, Killian CM, Johnson LK, White PS, et al. Macromolecules 2000;33:2320–34.
[21] Kunrath FA, Mota FF, Casagrande OL, Mauler RS, de Souza RF. Macromol Chem Phys 2002;203:2407–11.
[22] Jiang H, Wu Q, Zhu F, Wang H. J Appl Polym Sci 2007;103:1483–9.
[23] Liu F, Hu H, Xu Y, Guo L, Zai S, Song K, et al. Macromolecules 2009;42:7789–96.
[24] Guan Z, Cotts PM, McCord EF, McLain SJ. Science 1999;283:2059–62.
[25] Guan Z. J Polym Sci Part A Polym Chem 2003;41:3680–92.
[26] Cherian AE, Rose JM, Lobkovsky EB, Coates GW. J Am Chem Soc 2005;127:13770–1.
[27] Yuan J, Silva LC, Gomes PT, Valerga P, Campos JM, Ribeiro MR, et al. Polymer 2005;46:2122–32.
[28] Camacho DH, Guan Z. Macromolecules 2005;38:2544–6.
[29] Rose JM, Cherian AE, Coates GW. J Am Chem Soc 2006;128:4186–7.
[30] Merna J, Cihlar J, Kucera M, Deffieux A, Cramail H. Eur Polym J 2005;41:303–12.
[31] Merna J, Hostalek Z, Peleska J, Roda J. Polymer 2009;50:5016–23.
[32] Peruch F, Cramail H, Dffieux A. Macromolecules 1999;32:7977–83.
[33] Gottfried AC, Brookart M. Macromecules 2003;36:3085–100.
[34] Ye Z, Feng W, Zhu S, Yu Q. Macromol Rapid Commun 2006;27:871–6.
[35] Xiang P, Ye Z. Macromol Rapid Commun 2010;3:1083–9.
[36] Fu R, Li G, Feng K. Polymer physics. Beijing: Chemistry Industry Press; 2005.
[37] Subramanyam U, Rajamohanan PR, Sivaram S. Polymer 2004;45:4063–76.
[38] Xu G, Cheng D. Macromolecules 2001;34:2040–7.
[39] Xu G, Cheng D. Macromolecules 2000;33:2825–31.
[40] Losio S, Tritto I, Zannoni G, Sacchi MC. Macromolecules 2006;39:8920–7.
[41] McCord EF, McLain SJ, Nelson LTJ, Ittel SD, Tempel D, Killian CM, et al. Macromolecules 2007;40:410–20.
[42] McCord EF, McLain SJ, Nelson LTJ, Arthur SD, Coughlin EB, Ittel SD, et al. Macromolecules 2001;34:362–71.
[43] Galland GB, de Souza RF, Mauler RS, Nunes FF. Macromolecules 1999;32:1620–5.
[44] Galland GB, Da Silava LP, Dias ML, Crossetti GL, Ziglio CM, Filgueiras CAL. J Polym Sci Part A Polym Chem 2004;42:2171–8.
[45] Losio S, Boccia AC, Boggioni L, Sacchi MC, Ferro DR. Macromolecules 2009;42:6964–71.
[46] Losio S, Boccia AC, Sacchi MC. Macromol Chem Phys 2008;209:1115–28.
[47] Losio S, Stagnaro P, Motta T, Sacchi MC, Piemontesi F, Galimberti M. Macromolecules 2008;41:1104–11.
[48] Ferraris G, Corno C, Priola A, Cesca S. Mocromolecules 1977;10:188–97.

Polymer 52 (2011) 138–148

Contents lists available at ScienceDirect

Polymer

journal homepage: www.elsevier.com/locate/polymer

Fluorinated phenylethynyl-terminated imide oligomers with reduced melt viscosity and enhanced melt stability

Yang Yang [a,b], Lin Fan [a], Ximing Qu [a,b], Mian Ji [a,*], Shiyong Yang [a,b,*]

[a] Laboratory of Advanced Polymer Materials, Institute of Chemistry, Chinese Academy of Sciences, Zhongguancun, Beijing 100190, PR China
[b] Graduate School of Chinese Academy of Sciences, Beijing 100049, PR China

ARTICLE INFO

Article history:
Received 25 March 2010
Received in revised form
20 October 2010
Accepted 7 November 2010
Available online 13 November 2010

Keywords:
Imide oligomer
Melt processability
Thermal-cured polyimides

ABSTRACT

Two novel fluorinated phenyethynyl-contained endcapping agents, 4-(3-trifluoromethyl-1-phenylethynyl)phthalic anhydride (3F-PEPA) and 4-(3,5-bistrifluoromethyl-1-phenylethynyl)phthalic anhydride (6F-PEPA) were synthesized, which were employed to synthesize two fluorinated model compounds, *N*-phenyl-4(3-trifluoromethyl)-phenylethynylphthalimide (3F-M) and *N*-phenyl-4(3,5-bitrifluoromethyl)-phenylethynyl phthalimide (6F-M). The thermal cure kinetics of 3F-M and 6F-M were analyzed using DSC and compared to the unfluorinated derivative, *N*-phenyl-4-phenylethynylphthalimide (PEPA-M). The thermal cure temperatures of 3F-M and 6F-M were 399 and 412 °C, which were 22 and 35 °C higher than that of PEPA-M, respectively. The thermal cure kinetics of 3F-M and 6F-M best fit a first-order rate law, although 3F-M and 6F-M reacted slower than PEPA-M. However, the exothermic enthalpy of 3F-M and 6F-M were only half of PEPA-M. Based on the model compounds study, a series of fluorinated phenylethynyl-terminated imide oligomers (F-PETIs) with different calculated molecular weights (Calc'd M_n) were synthesized by thermal polycondensation of 2,3,3′,4′-biphenyltetracarboxylic acid dianhydride (a-BPDA) and 3,4′-oxydianiline (3,4′-ODA) using 3F-PEPA or 6F-PEPA as the endcapping agent. The substituent effects of the trifluoromethyl ($-CF_3$) groups on the thermal cure behavior and melt processability of F-PETIs were systematically investigated. Experimental results reveal that the melt processability of F-PETI was apparently improved by the reduced resin melt viscosities and the enhanced melt stability due to the incorporation of the $-CF_3$ groups in the imide backbone. All of those F-PETIs exhibit outstanding thermal and mechanical properties.

1. Introduction

In recent years, significant efforts have been attempted in improving the melt processability of aromatic polyimides [1–8]. Introduction of phenylethynyl-endcapping groups into the low-molecular-weight imide oligomers was confirmed to be an effective approach [9,10]. Phenylethynyl-terminated imide oligomers (PETIs), due to its good melt processability and the great combination of thermal and mechanical properties etc., have been extensively employed as the matrices of carbon fiber-reinforced polyimide composites for high temperature applications [11–33]. Compared with nadic- or maleic-endcapped resins, phenylethynyl-endcapped imides could be thermally cured by much preferred chain extension than crosslinking, affording thermoset resins with better impact strength [34–36].

The polyimide composites derived from PETI could be produced either by autoclave [11–27] or by resin transfer molding (RTM) [28–33], resulting in composite materials with high strength and modulus as well as excellent thermal stability. PETI-5, the representative PETI with Calc'd M_n of 5000 g/mol could be melt processed by autoclave at 360–370 °C [16,18]. By reducing Calc'd M_n of PETI-5 to 1000 g/mol, imide oligomers with much lower melt viscosity and suitable for RTM have been successfully developed. The representative RTM imide resins (such as PETI-298, PETI-330 and PETI-375) could be melt at 260–280 °C and completed the thermal curing at 360–370 °C [29,30,32,33]. In the case of RTM application, the melt processability of PETI was endorsed by its low molecular weights as well as its flexible chemical backbone. However, the very low molecular weights of PETI usually result in the thermal-cured materials with poor impact toughness and the flexible oligomer backbone leads to the low glass transition temperatures (T_g) for the thermal-cured resins. Hence, to improve the RTM processability of PETI by reducing the melt viscosity and enhancing the melt stability is still of great concern to high temperature polyimide composites. Moreover, many other efforts

* Corresponding authors. Laboratory of Advanced Polymer Materials, Institute of Chemistry, Chinese Academy of Sciences, Zhongguancun, Beijing 100190, PR China. Tel.: +86 10 6256 4819; fax: +86 10 6256 9562.
E-mail address: shiyang@iccas.ac.cn (S. Yang).

0032-3861/$ – see front matter © 2010 Elsevier Ltd. All rights reserved.
doi:10.1016/j.polymer.2010.11.007

have been made to improve the RTM melt processability of PETI such as (1) by introducing comonomers for copolycondensation; (2) by mixing of low-viscous reactive diluents, or (3) by introducing asymmetric aromatic structures into the resin chemical backbone etc. [29–31,37–39].

Meanwhile, it was also found that by replacing the phenylethynyl-endcapping groups in the imide oligomers with naphthyl or anthracenyl-endcapping groups could decrease the cure temperature by 30–80 °C and accelerate the thermal cure reaction [40–43]. It was reported that the imide oligomers endcapped with 4-(2-phenylethynyl)-1,8-naphthalic anhydride (PENA), or 4-(1-naphethlethynyl)-1,8-naphthalic anhydride (NENA) cure at faster rate at a temperature nearly 30 °C lower [44], attributed by the electron-withdrawing effects of the multi-aromatic structures on the electron density and distribution of the ethynyl group in the imide oligomers. Researchers also noted that imide oligomers derived from 4-phenylethynyl phthalic anhydride (4-PEPA) with different substituted groups and 3-phenylethynyl phthalic anhydride (3-PEPA) exhibit different thermal curing behaviors [21,45].

Usually the endcapping agent could affect the properties of the imide oligomers and their final cured polyimides profoundly for the extra-high density of endcapping groups in imide oligomers. Although many researchers have designed novel endcapping agents to develop new imide resins, few studies on the imide oligomers derived from fluorinated phenyethynyl-contained endcapping agents could be found in the literature. In efforts to enhance the melt processability (including the melt viscosity and melt stability) of imide oligomers with high molecular weights, it is reasoned that introduction of the bulky trifluoromethyl in phenylethynyl-endcapping group to lower the interchain interaction or reduce the stiffness of polymer backbone, this should make it possible to maintain higher-molecular weights for oligomers to enhance the mechanical/thermal properties for their corresponding thermal-cured resins. Meanwhile fluoro-containing substituents with outstanding thermal stability could also affect the properties of the cured polyimide.

In the present research, two novel fluorinated phenyethynyl-contained endcapping agents were synthesized. The work reported herein was performed primarily to determine whether substituting fluorinated groups (e.g. $-CF_3$) in the phenylethynyl group of PEPA offered any distinct advantages in the physical and/or thermal cure properties and also to determine the melt processability, the thermal curing and mechanical properties of the fluorinated PETI and their thermal-cured polyimides.

2. Experimental

2.1. Materials

2,3′,3,4′-biphenyltetracarboxylic acid dianhydride (*a*-BPDA, mp: 196–197 °C) and 4-phenylethynyl phthalic anhydride (4-PEPA, mp: 151–152 °C) were synthesized in this laboratory according to the reported methods [46,47]. 3,4′-oxydianiline (3,4′-ODA, mp: 84–85 °C) was purchased from Shanghai Baicheng Chemicals Corp., China and recrystallized from ethanol/water (1:1) prior to use. 4-bromophthalic anhydride was purchased from Beijing Bomi Chemicals Corp., China and recrystallized from acetic acid/acetic anhydride prior to use. *N*-methyl-2-pyrrolidinone (NMP) was purchased from Beijing Beihua Fine Chemicals, China and purified by vacuum distillation over P_2O_5. Triethylamine was used after vacuum distillation in the presence of calcium hydride. 1-bromo-3-(trifluoromethyl)benzene and 1-bromo-3,5-bis(trifluoromethyl) benzene were purchased from Liaoning Fuxin Sanbao Chemicals Corp., China and used as received. 2-methyl-3-butyn-2ol was purchased from Beijing Beihua Hengyuan Chemicals Corp., China and used as received. All other reagents were commercially obtained from China National Medicines Corp., China and used as received.

2.2. Measurements

Infrared spectra (IR) were measured on a Perkin–Elmer 782 Fourier transform infrared (FTIR) spectrometer. ^1H and ^{13}C NMR spectra were obtained on a Bruker AVANCE 400 spectrometer at frequencies of 400 MHz using chloroform-*d* or DMSO-d_6 as solvents. Differential scanning calorimetry (DSC) analysis was performed on a TA-Q100 analyzer at a heating rate of 10 °C/min in nitrogen atmosphere. Thermogravimetric analysis (TGA) was accomplished on a TA-Q50 series thermal analysis system at a heating rate of 20 °C/min in nitrogen atmosphere. Complex viscosity was performed on a TA-AR 2000 rheometer using the test specimen disks with diameter of 25 mm and thickness of 1.2 mm, which were prepared by compression molding of the imide oligomer powders at room temperature. The test disks were loaded in the rheometer fixture equipped with 25 mm diameter parallel plates, in which the top plate was oscillated at a fixed strain of 5% and a fixed angular frequency of 10 rad/s whereas the lower plate was attached to a transducer for detecting the resultant torque. For the tests of dynamic thermal melt complex viscosity, the test specimens were scanned from 200 °C at a heating rate of 4 °C/min, in which the melt viscosity (η^*, complex viscosity as a function of time) was determined. Gel permeation chromatography (GPC) was performed on Waters system that was equipped with a model 1515 pump, a 2414 refractive index detector using NMP as the eluant at a flowing rate of 1.0 ml/min. The sample concentration was 1 mmol/ml and monodisperse polystyrene was employed as the standard sample. Matrix-assisted laser desorption/ionization time-of-flight (MALDI-TOF) mass spectra were carried out with a Biflex IIIMALDI-TOF mass spectrometer (Bruker, Billerica, Germany) equipped with delayed extraction, a multisample probe, a time-of-flight reflection analyzer, a nitrogen laser with a wavelength of 337 nm and a pulse width of 3 ns, and a linear flight path length of 100 cm, in which the flight tube was evacuated to 1027 Pa. Mechanical properties were obtained with an Instron model 3365 universal tester at room temperature. The tensile strength, modulus, and the elongation at breakage were measured in accordance with GB/T 16421-1996 at a strain rate of 2 mm/min.

2.3. Synthesis of 3-trifluoromethyl-1-ethynylbenzene (3F-EB)

1-bromo-3-(trifluoromethyl)benzene (22.50 g, 0.1 mol), 2-methyl-3-butyn-2-ol (10.09 g, 0.12 mol), cuprous iodide (0.95 g, 5 mmol), triphenylphosphine (0.65 g, 2.5 mmol), bis (triphenylphosphine)palladium dichloride (1.40 g, 2.0 mmol) and triethylamine (200 ml) were added into a 500 ml three-necked flask equipped with a water condenser, a mechanical stirrer and nitrogen inlet/outlet. The reaction mixture was heated to reflux for 8 h, and cooled to room temperature. The catalyst and produced salt were separated by filtration to give a filtrate, which was then performed on a rotary evaporator to remove the solvent and yield a white solid. The crude product was washed twice with hot water and transferred into a 250 ml flask equipped with Dean–Stark trap containing 100 ml cyclohexane and sodium hydroxide (0.50 g, 12.5 mmol). The resulting solution was heated to reflux for 2 h and then hot filtrated. After cooled to ambient temperature, the filtrate was vacuum distillated (5 mmHg) to give a colorless liquid with boiling point of 87–88 °C (11.74 g, yield: 69.0%). ^1H NMR (chloroform-*d*, δ ppm): 7.65 (s, 1H), 7.55–7.50 (t, 2H), 7.41–7.36 (t, 1H), 2.57 (s, 1H). Anal. calcd for $C_9H_5F_3$: C, 63.54%; H, 2.96%. Found: C, 63.57%; H, 2.93%.

2.4. Synthesis of 3,5-bitrifluoromethyl-1-ethynylbenzene (6F-EB)

This intermediate compound was obtained by the similar method as described above except that 1-bromo-3-(trifluoromethyl)benzene was replaced by 1-bromo-3,5-(bitrifluoromethyl)benzene. The product was colorless liquid with boiling point of 61–62 °C (15.24 g, yield: 64.0%). ^{1}H NMR (chloroform-*d*, δ ppm): 7.91 (s, 2H), 7.84 (s, 1H), 3.25 (s, 1H). Anal. calcd for $C_{10}H_4F_6$: C, 50.44%; H, 1.69%. Found: C, 50.47%; H, 1.72%.

2.5. Synthesis of 4-(3-trifluoromethyl-1-phenylethynyl)phthalic anhydride (3F-PEPA)

A mixture of 4-bromophthalic anhydride (22.70 g, 0.10 mol), 3F-EB (18.70 g, 0.11 mol) and triethylamine (250 ml) were added into a 500 ml flask equipped with a mechanical stirrer, a water condenser and a nitrogen inlet. The reaction mixture was stirred at room temperature until a homogeneous solution was obtained. Cuprous iodide (0.95 g, 5.0 mmol), triphenylphosphine (0.66 g, 2.5 mmol), bis (triphenylphosphine)palladium dichloride (1.40 g, 2.0 mmol) were then added. After refluxed under nitrogen atmosphere for 6 h, the reaction mixture was cooled to room temperature and then filtrated to remove the catalyst and salt generated in the reaction. The filtrate was poured into 800 ml of water, and then acidified to pH = 2 with concentrated hydrochloric acid (35–38%). The precipitate was collected and vacuum dried at 120 °C for 5 h to give a yellow powder. The obtained solid was dissolved in 200 ml of toluene in a 500 ml flask equipped with mechanical stirrer, a water condenser, a Dean–Stark trap and a nitrogen inlet. The solution was heated to reflux for 8 h under nitrogen atmosphere, in which the water generated in the reaction was simultaneously removed by azeotropic distillation. And the solution was then concentrated by partly removal of toluene. The concentrated solution was cooled to room temperature and yielded yellow solid. After filtrated and rinsed with acetic acid, the crude product was purified by recrystallization in acetic acid/acetic anhydride (2:1 v/v) to afford 23.10 g of yellow crystal (yield: 73.0%). mp: 162–163 °C [determined by DSC]. ^{1}H NMR (chloroform-*d*, δ ppm): 8.14 (s, 1H), 8.01 (s, 2H), 7.84 (s, 1H), 7.76–7.74 (d, 1H), 7.69–7.67 (d, 1H), 7.57–7.53 (t, 1H). ^{13}C NMR (chloroform-*d*, δ ppm): 162.9, 139.3, 136.0, 132.7, 131.4, 131.3, 131.1, 131.0, 129.1, 129.0, 128.5, 126.7, 126.6, 125.8, 123.6, 123.1121.3, 93.2, and 89.0. FTIR (KBr cm^{-1}): 2207 (–C≡C–), 1840 (asym C=O str), 1782 (sym C=O str), 1146 (C–F). Anal. calcd for $C_{18}H_6F_6O_3$: C, 64.57%; H, 2.23%. Found: C, 64.36%; H, 2.08%.

2.6. Synthesis of 4-(3,5-bistrifluoromethyl-1-phenylethynyl) phthalic anhydride (6F-PEPA)

6F-PEPA (yellow crystal, 26.88 g, yield: 70.0%) was obtained by the similar method as described above except that 3F-EB was replaced by 6F-EB. mp: 196–197 °C ^{1}H NMR (DMSO-d_6, δ ppm): 8.41 (s, 1H), 8.35 (s, 1H), 8.25 (s, 1H), 8.17 (s, 2H), 3.32 (s, 1H). ^{13}C NMR (chloroform-*d*, δ ppm): 162.9, 139.5, 133.0, 132.8, 132.7, 132.3, 132.0, 131.9, 130.4, 128.8, 127.8, 126.4, 125.3, 125.1, 123.5, 122.4, 119.5, 93.2, and 89.0. FTIR (KBr cm^{-1}): 2187 (–C≡C–), 1837 (asym C=O str), 1795 (sym C=O str), 1136 (C–F). Anal. calcd for $C_{17}H_7F_3O_3$: C, 56.27%; H, 1.57%. Found: C, 56.10%; H, 1.65%.

2.7. Synthesis of model compounds

Model compounds including N-phenyl-4-(3-trifluoromethyl-1-phenylethynyl)phthalimide (3F-M), N-phenyl-4-(3,5-bitrifluoromethyl-1-phenylethynyl)phthalimide (6F-M) and N-phenyl-4-(1-phenylethynyl)phthalimide (PEPA-M) were prepared by chemical cyclodehydration. In a typical experiment, 3F-M was prepared in the following procedure: 4-(3-trifluoromethyl-1-phenylethynyl) phthalic anhydride (31.60 g, 0.1 mol), aniline (9.31 g, 0.1 mol) and 150 ml DMAc were placed in a 500 ml flask equipped with a water condenser and a mechanical stirrer. The reaction solution was stirred at room temperature for 4 h. The solution was then chemically cyclodehydrated with acetic anhydride and pyridine (2:1 v/v) after stirring for 6 h. The resultant mixture was then poured into 300 ml of ethanol to yield precipitate. The solid was collected by filtration, and then dried at 100 °C in vacuum for 5 h to afford an off-white solid (36.50 g, yield: 93.3%). mp: 240–241 °C ^{1}H NMR (chloroform-*d*, δ ppm): 8.10 (s, 1H), 7.97–7.91 (m, 2H), 7.84 (s, 1H), 7.75–7.74 (d, 1H), 7.66–7.65 (d, 1H), 7.55–7.50 (m, 3H), 7.46–7.40 (m, 3H). FTIR (KBr cm^{-1}): 2205 (–C≡C–), 1843 (asym C=O str), 1811 (sym C=O str), 1383 (imide C–N str), 1141 (C–F). Anal. calcd for $C_{23}H_{12}F_3NO_2$: C, 70.59%; H, 3.09%, N 3.58%. Found: C, 70.42%; H, 3.15%; N, 3.44%.

The model compound 6F-M was prepared according to above method except that 3F-PEPA was replaced with 6F-PEPA to afford off-white solid (43.51 g, yield: 94.7%). mp: 240–241 °C by DSC. ^{1}H NMR (chloroform-*d*, δ ppm): 8.12 (s, 1H), 8.01 (s, 2H), 8.00–7.93 (m, 2H), 7.89 (s, 1H), 7.54–7.50 (m, 2H), 7.45–7.41 (m, 3H). FTIR (KBr cm^{-1}): 2117 (–C≡C–), 1853 (asym C=O str), 1820 (sym C=O str), 1392 (imide C–N str), 1147 (C–F). Anal. calcd for $C_{24}H_{11}F_6NO_2$: C, 62.75%; H, 2.41%; N 3.05%. Found: C, 62.77%; H, 2.42%; N, 3.05%.

The model compound PEPA-M as a comparative was prepared according to the method as described above except that 3F-PEPA was replaced with 4-PEPA to afford off-white solid (30.98 g, yield: 95.8%). mp: 203–204 °C. ^{1}H NMR (chloroform-*d*, δ ppm): 8.12 (s, 1H), 8.01 (s, 2H), 8.00–7.93 (m, 2H), 7.89 (s, 1H), 7.54–7.50 (m, 2H), 7.45–7.41 (m, 3H). FTIR (KBr cm^{-1}): 2117 (–C≡C–), 1853 (asym C=O str), 1820 (sym C=O str), 1392 (imide C–N str), 1147 (C–F). Anal. calcd for $C_{24}H_{11}F_6NO_2$: C, 81.72%; H, 4.05%; N 4.33%. Found: C, 81.84%; H, 4.13%; N, 4.21%.

2.8. Synthesis of the fluorinated imide oligomers (F-PETIs)

F-PETIs were prepared by the conventional two-stage polymerization and imidization process. In a typical experiment, 3,4′-ODA (10.01g, 0.050 mol) and NMP (60 ml) were placed in a flask equipped with a water condenser, a mechanical stirrer, a Dean–Stark trap, a thermometer and a nitrogen inlet/outlet. After stirred for 30 min at room temperature to give a homogeneous solution, a slurry of *a*-BPDA (7.35 g, 0.025 mol), 3F-PEPA (15.81 g, 0.050 mol) and NMP (51 ml) was added. The reaction mixture, with 30% of solids (w/w), was stirred at 80 °C for 8 h and 150 ml toluene was then added. The resultant solution was heated to reflux at 185 °C for 10 h, in which the water evolved in the thermal imidization was simultaneously removed from the reaction system by azeotropic distillation. After cooled down to about 120 °C, the hot solution was poured slowly into 1000 ml of water. The solid was collected by filtration and washed with hot water three times, and then dried at 205 °C in vacuum for 10 h to give O1-1 as yellow powder (30.28 g, 96.6%).

Other F-PETIs including O1-2, O2-1, O2-2, O10-1, O10-2 as well as the unfluorinated derivatives including O1-*comp*, O2-*comp* and

Table 1
Thermal data and kinetic parameters of the model compounds.

Sample	Endothermal temperature (°C)	Exothermal temperature (°C)			ΔH (J/g)	E (kJ/mol)	*n*	*A*
	Peak	Onset	Peak	End				
PEPA-M	202	320	377	434	516	152.9	0.94	8.1×10^{11}
3F-M	240	343	399	432	270	168.9	1.05	5.0×10^{12}
6F-M	241	350	412	–	218	187.4	1.09	8.2×10^{11}

Table 2
Chemical compositions and molecular weights of F-PETIs and the unfluorinated derivatives.

Sample	Chemical composition[a]	Calc'd P_n[b]	Calc'd M_n (g/mol)[c]	M_n (g/mol)	M_w (g/mol)	M_w/M_n
O1–1	3,4′-ODA/a-BPDA/ 3F-PEPA = 2/1/2	1	1254	2555	4957	1.94
O1–2	3,4′-ODA/a-BPDA/ 6F-PEPA = 2/1/2	1	1392	2854	4881	1.71
O1–*comp*	3,4′-ODA/a-BPDA/ 4-PEPA = 2/1/2	1	1118	2253	5691	2.52
O2–1	3,4′-ODA/a-BPDA/ 3F-PEPA = 3/2/2	2	1712	3410	5564	1.63
O2–2	3,4′-ODA/a-BPDA/ 6F-PEPA = 3/2/2	2	1850	3521	8373	2.37
O2-*comp*	3,4′-ODA/a-BPDA/ 4-PEPA = 3/2/2	2	1576	3248	4661	1.49
O10–1	3,4′-ODA/a-BPDA/ 3F-PEPA = 11/10/2	10	5376	8197	16,172	1.97
O10–2	3,4′-ODA/a-BPDA/ 6F-PEPA = 11/10/2	10	5514	10,826	20,943	1.93
O10-*comp*	3,4′-ODA/a-BPDA/ 4-PEPA = 11/10/2	10	5238	10,027	22,947	2.29

[a] Molar ratios of the reactants.
[b] Calculated polymerization degree.
[c] Calculated molecular weight.

O10-*comp* were prepared according to the similar procedure, in which the molar ratios of 3,4′-ODA, *a*-BPDA and 3F-PEPA, 6F-PEPA, or 4-PEPA were listed in Table 2.

2.9. Preparation of the thermal-cured polyimides

The imide oligomer resin powders were placed in a die, which was then placed in a hot press preheated at 200 °C. The die temperature was increased gradually to 370 °C at a rate of 4 °C/min. After it was kept there for 10–25 min, the die was applied with a pressure of 1.0–3.5 MPa. After it was kept for 1h at 370 °C, the die was then cooled with the applied pressure to less than 200 °C. The thermally cured polyimide sheet was removed from the die at room temperature and then cut to the desired sizes for thermal and mechanical testing.

3. Results and discussion

3.1. Monomers

3F-EB and 6F-EB were successfully synthesized *via* a two-step procedure of coupling and cleavage reaction in the total yield of 69.0% and 64.0%, respectively. The first step was the coupling reaction of 2-methyl-3-butyn-2-ol with 1-bromo-3-(trifluoro methyl) benzene or 1-bromo-3,5-(bitrifluoromethyl)benzene in the presence of palladium catalyst to yield the intermediates 1-(2-methyl-3-butyn-2-ol)-3-(trifluoromethyl)benzene or 1-(2-methyl-3 -butyn-2-ol)-3,5-(bistrifluoromethyl)benzene, which was then treated with NaOH to give the intermediate compounds. 3F-PEPA and 6F-PEPA were prepared *via* the palladium-catalyzed coupling reaction of 4-bromophthalic anhydride with 3F-EB or 6F-EB as showed in Scheme 1. The resultant products were recrystallized in acetic acid/acetic anhydride (2:1 v/v) in the total yield of 73.0% and 70.0%, respectively. The molecular structures of 3F-PEPA and 6F-PEPA were confirmed by means of FTIR, ^{1}H and ^{13}C NMR and elemental analysis.

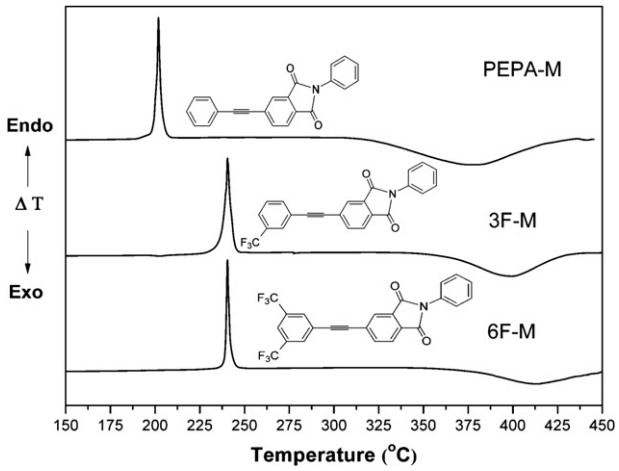

Fig. 1. DSC curves of the model compounds at 20 °C/min.

3.2. Thermal curing properties of model compounds

Prior to imide oligomers and the thermal-cured polyimide studies, model compounds (3F-M, 6F-M and PEPA-M) were synthesized by the chemical cyclodehydration in good yield and characterized. The thermal behaviors of the model compounds were investigated by DSC to determine the effect of the molecular structures on their thermal curing behaviors. Fig. 1 shows the DSC curves of the model compounds (3F-M and 6F-M) compared with PEPA-M and Table 1 lists the DSC data. The sharp endothermic peaks in the range of 202–241 °C were assigned as the melt points

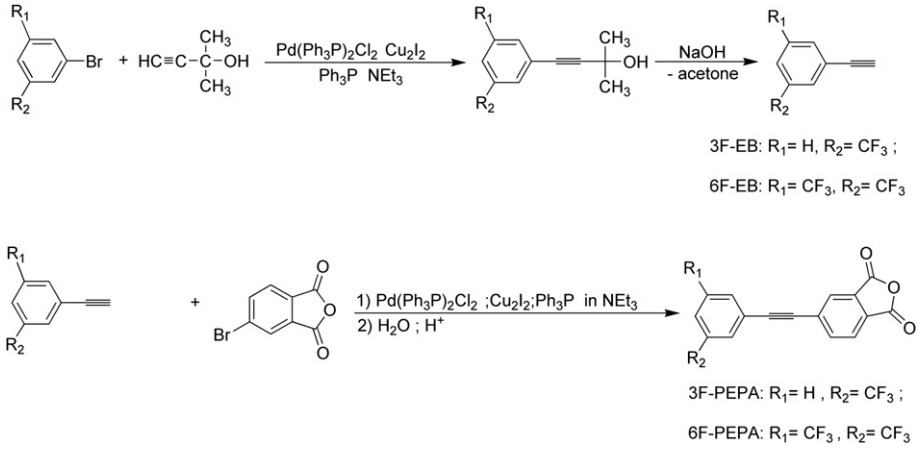

Scheme 1. Synthesis of the $-CF_3$ substituted phenylethynyl phthalic anhydrides.

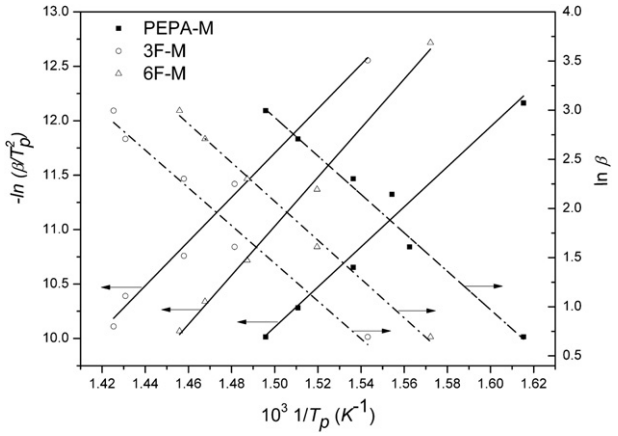

Fig. 2. Curing kinetic analysis and calculation of the thermal curing activation energy of the model compounds.

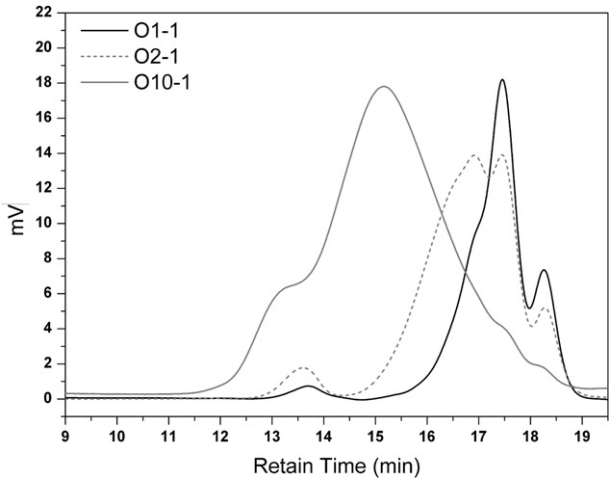

Fig. 3. Representative GPC curves of F-PETIs with different Calc'd M_n.

(T_ms) and the wide exothermic peaks in the range of 377–412 °C were attributed to the thermal curing reactions of the phenylethynyl groups in the model compounds.

The $-CF_3$ groups had pronounced impacts on the T_ms values and the thermal curing reaction of the phenylethynyl groups. The fluorinated model compounds (3F-M and 6F-M) showed the identical melting points (240 and 241 °C), 38–39 °C higher than PEPA-M (202 °C). 3F-M and 6F-M had the onset temperatures (343 and 350 °C, respectively), 23–30 °C higher than PEPA-M (320 °C). Meanwhile, the exothermal peak temperatures of 3F-M and 6F-M were 399 °C and 412 °C, respectively, 22–35 °C higher than PEPA-M (377 °C), indicating that the fluorinated phenylethynyl groups would undergo thermal curing at higher temperatures than the unfluorinated analogue. In comparing the reaction exothermal data, 3F-M ($\Delta H = 270$ J/g) and 6F-M ($\Delta H = 218$ J/g) had much lower exothermic enthalpies than PEPA-M ($\Delta H = 516$ J/g), implying that the fluorinated phenyethynyl group would undergo the thermal curing with much lower exotherm.

In order to extensively understand the thermal curing reaction of the phenylethynyl-endcapped imide oligomers, the nonisothermal DSC method was employed to study the curing kinetics of the model compounds and the resultant data are also tabulated in Table 1. In the experiments, temperatures of the model compounds (3F-M, 6F-M and PEPA-M) were scanned by DSC at different heating rates (2, 5, 10, 15 and 20 °C/min, respectively). The exothermic peak temperatures (T_p) in DSC curves were shifted into higher temperatures with increasing of the heating rate (β). Kissinger's method is based on the fact that T_p varies with β and assumes that the maximum reaction rate ($d\alpha/dt$) occurs at peak temperatures [48]. Thus, the equation can be expressed as follows (Equation (1)):

$$-\ln\left(\beta/T_p^2\right) = \ln(E/R) - \ln(An) - (n-1)\ln(1-x)_p + E/RT_p \qquad (1)$$

where E is the activation energy; R is the gas constant; A, n and x are the pre-exponential factor, the order of the cure action, and the extent of the cure action, respectively. Fig. 2 shows the scatter graphs of $-\ln(\beta/T_p^2)$ against $1/T_p$. The calculated values of Es for PEPA-M, 3F-M and 6F-M were 152.9, 168.9, and 187.4 kJ/mol, respectively.

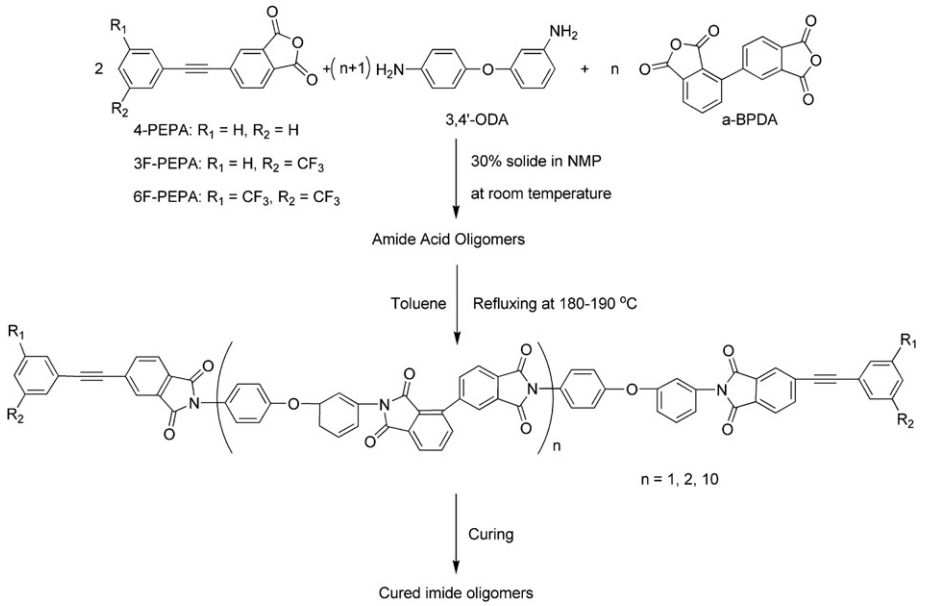

Scheme 2. Synthesis of F-PETIs and the thermal-cured polyimides.

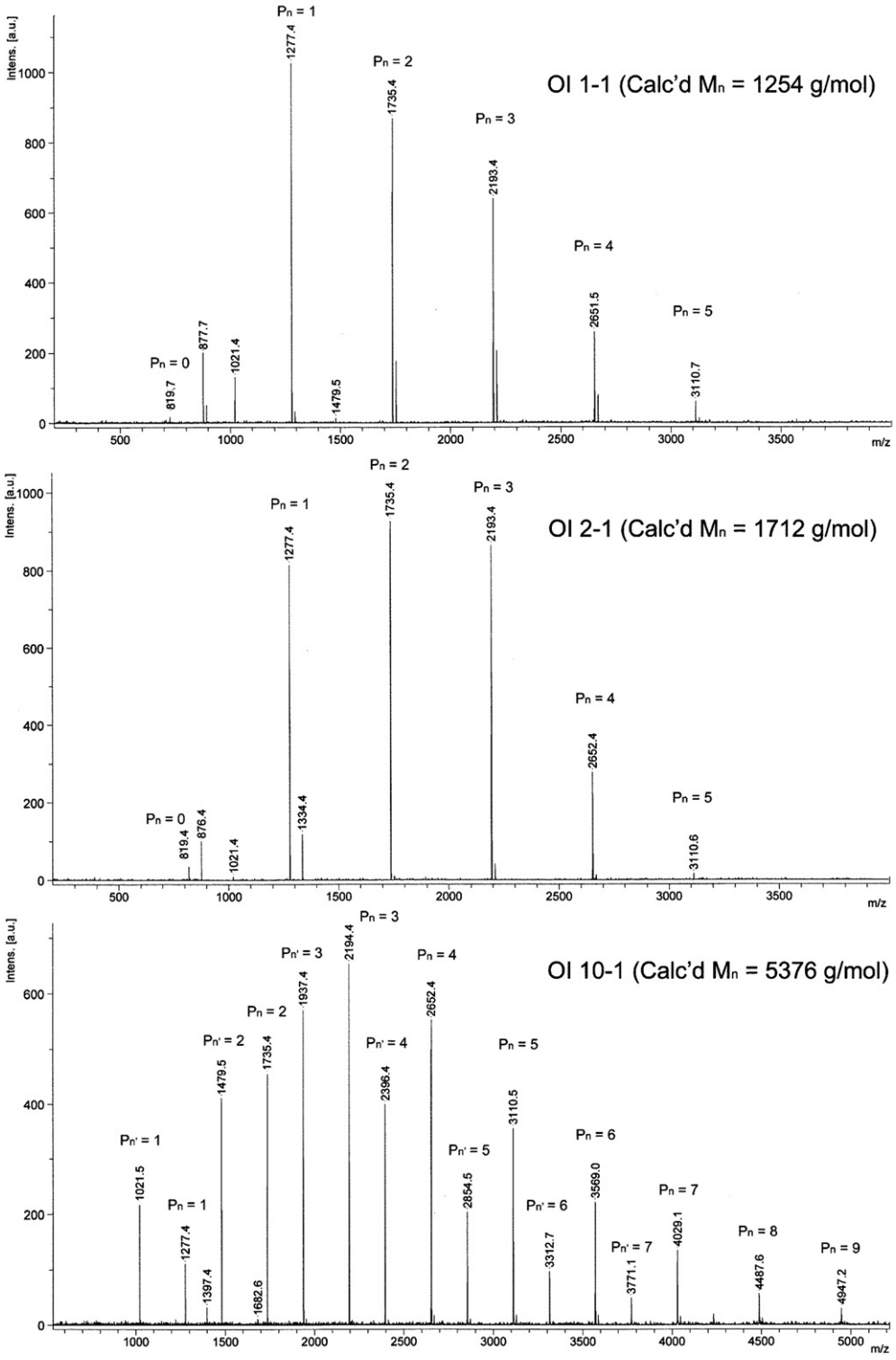

Fig. 4. MOLDI-TOF mass spectra of F-PETIs with different Calc'd M_n.

Obviously, 3F-M and 6F-M, the fluorinated phenylethynyl-endcapped imide compounds, have higher *E*s than PEPA-M. Meanwhile, 6F-M, with two $-CF_3$ groups in the phenylethynyl group, has higher *E* value (187.4 kJ/mol) than 3F-M (168.9 kJ/mol). This could be interpreted by the stronger electron-withdrawing effect and steric hindrance of the $-CF_3$ in the phenylethynyl group. If the *E* value was introduced into the Crane's equation (2):

$$d(\ln\beta)/d(1/T_p) \approx -E/nR \tag{2}$$

The scatter plot of $\ln(\beta)$ as a function of $1/T_p$ can be obtained as shown in Fig. 2, in which the *n* values were obtained as 0.94 for PEPA-M, 1.05 for 3F-M, and 1.09 for 6F-M, respectively, demonstrating that the thermal curing reaction of the model compounds fit the first-order kinetics reaction rate law, similar to other electron-

Table 3
Molecular structures of the chemical species detected by MOLDI-TOF mass spectra for F-PETIs with different Calc'd M_n

Chemical structures of the resin species	n	Mass (m/z)	Intensity %
O1-1 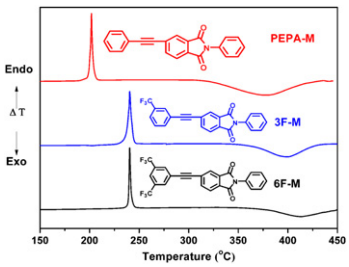	0	819.7	1.5
	1	1277.4	100.0
	2	1735.4	84.7
	3	2193.4	62.2
	4	2651.5	25.5
	5	3110.7	6.1
O1-2 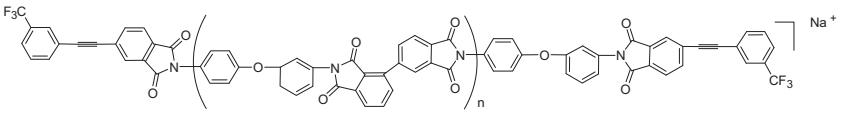 double-endcapping species	0	819.4	3.6
	1	1277.4	87.8
	2	1735.4	100.0
	3	2193.4	92.9
	4	2652.4	29.6
	5	3110.6	2.0
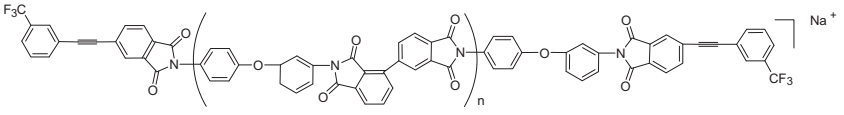 double-endcapping species	1	1277.4	16.3
	2	1735.4	69.4
	3	2194.4	100.0
	4	2652.4	84.7
	5	3110.5	54.1
	6	3569.0	33.7
	7	4029.1	20.4
	8	4487.6	8.2
	9	4947.2	4.1
O1-10 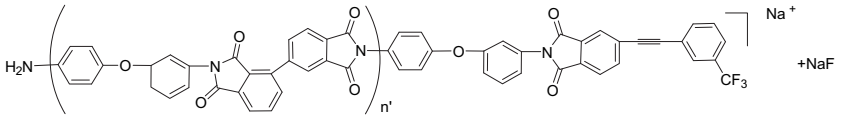 mono-endcapping species	1	1021.5	32.7
	2	1479.5	62.2
	3	1937.4	86.7
	4	2396.4	61.2
	5	2854.5	31.6
	6	3312.7	15.3
	7	3771.1	7.1

withdrawing arylethynyl-endcapped imide oligomers [40–43]. Moreover, the pre-exponential factors (A) in the range of 8.2×10^{11} to 5.0×10^{12} for the fluorinated model compounds could also be obtained according to the Kissinger's equation as shown in Table 1.

Besides the electronic effects, the trifluoromethyl group might have some steric hindrance to retard the thermal curing reaction of the phenylethynyl group, which resulted in the elevated thermal curing temperatures.

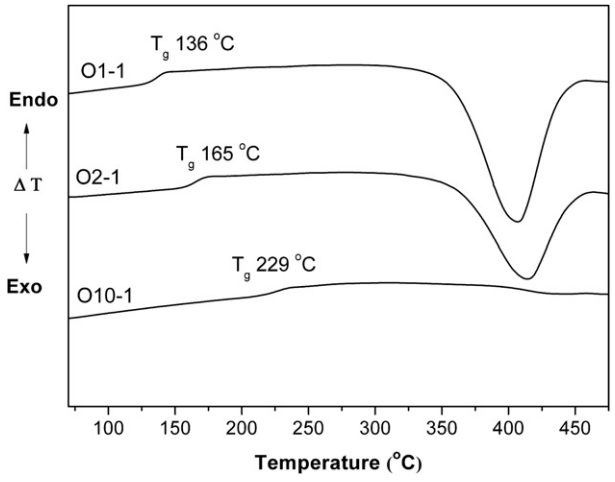

Fig. 5. DSC curves of the representative F-PETIs with different Calc'd P_n.

3.3. Molecular structures of F-PETIs

A series of F-PETIs with various Calc'd P_n (calculated polymerization degree) and different endcapping agents including 3F-PEPA, 6F-PEPA or 4-PEPA were prepared by the synthetic pathway as shown in Scheme 2 and their chemical compositions are summarized in Table 2.

The stoichiometric compositions of the monomers including aromatic dianhydride (i.e. α-BPDA) and aromatic diamine (i.e. 3,4′-ODA) and the endcapping agents were changed systematically in order to explore the influence of the oligomer molecular weights

Table 4
Thermal curing behaviors of F-PETIs with different Calc'd M_n determined by DSC.

Sample	T_g (°C)	T_{onset} (°C)	T_{exo} (°C)	ΔH (J/g)
O1-1	136	312	406	192.6
O1-2	143	325	421	174.7
O1-*comp*	137	293	397	240.1
O2-1	165	323	413	139.1
O2-2	170	334	424	109.6
O2-*comp*	168	315	392	178.5
O10-1	229	388	435	7.81
O10-2	217	398	441	5.67
O10-*comp*	218	379	422	9.64

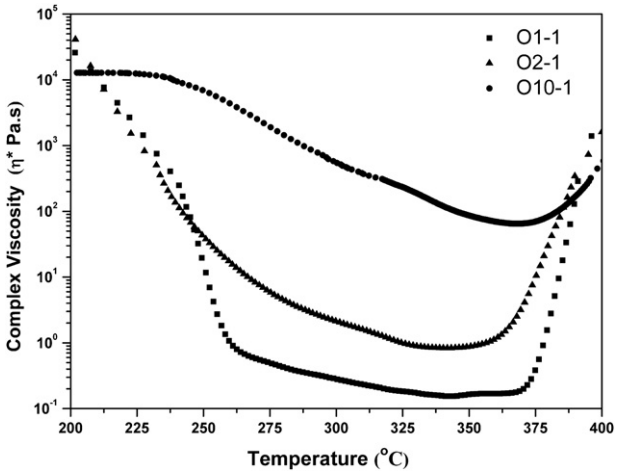

Fig. 6. Dynamic rheological behaviors of representative F-PETIs with different Calc'd M_n.

and $-CF_3$ groups on the imide oligomer properties. The Calc'd P_n of the imide oligomers were designed to be 1, 2 and 10, respectively, by controlling the molar ratios of *a*-BPDA to 3,4′-ODA along with the endcapping agents including 3F-PEPA, 6F-PEPA or 4-PEPA (Table 2), resulting in a series of F-PETIs with different Calc'd M_n in the range of 1254–5514 g/mol.

Table 2 also shows the molecular weights of the synthesized imide oligomers determined by GPC using NMP as solvent, including the number average molecular weight (M_n), weight average molecular weight (M_w), and the molecular weight distribution (M_w/M_n). The measured molecular weights are much higher than the calculated ones due to the polarity difference of the testing samples compared to the GPC standard sample (polystyrene) [30]. For instance, O1-1 has the measured M_n of 2555 g/mol, almost doubled the Calc'd M_n (1254). The molecular weight distributions of F-PETIs were in the range of 1.63–2.37.

Fig. 3 depicts the representative GPC curves of F-PETIs with different Calc'd P_n (1, 2 and 10), in which it can be seen that each imide oligomer was composed of several chemical species with different molecular weights in a broad elution time range. The major molecular weight peaks of F-PETIs were increased with increasing of the Calc'd M_n values. For instance, O10-1 (Calc'd M_n = 5376) showed a major elution time peak at 15.1 min, compared with 16.8 min for O2-1 (Calc'd M_n = 1712) and 18.2 min for O1-1 (Calc'd M_n = 1254), respectively. Moreover, the relative peak intensities in GPC curves were also obviously changed with Calc'd M_n. The higher the Calc'd M_n, the more intensified the peak intensity. For instance, O10-1 showed an intense and broad peak located at 18.8–11.6 min along with several trace peaks, while O1-1 and O2-1 had the major peaks in the relative sharp ranges, implying that O10-1 was mainly consisted of the high-molecular-weight resin species. In quantities, O10-1 has four peaks with different relative intensities: i.e. 34% at 13.1 min, 100% at 15.1 min, 17.5% at 17.5 min, and 10% at 18.3 min respectively, compared with O2-1, which also has four peaks in the elution time range of 12.7–19.1 min: 12% at 13.5 min, 99% at 16.8 min, 100% at 17.5 min and 37% at 18.3 min respectively. Obviously, the major peak intensity was intensified in the higher-molecular weight oligomer. For the oligomers with higher Calc'd M_n (O10-1), the major peak at 15.1 min (100%) was new resin species which was not detected in the lower Calc'd M_n oligomers (O1-1 and O2-1), implying that this new species was coupled by the different lower-molecular molecular resin species. It is obviously that, the molecular weights and molecular weight distributions of F-PETIs were closely related to their designed molecular weights.

Fig. 4 shows the MALDI-TOF mass spectra of the representative imide oligomers with different Calc'd P_n (O1-1, O2-1 and O10-1) and Table 3 summarizes the molecular structures of the resin species detected. The imide oligomers are resin mixtures with different molecular weights. O1-1 and O2-1 showed the same chemical species with identical P_n (0–5) and molecular weights (m/z of 796.7–3087.7), but different 100% peak intensities (O1-1: $P_n = 1$, O2-1: $P_n = 2$). For instance, O1-1, which has the lowest Calc'd P_n (=1), contains 6 resin species with molecular weights (M_n = 796.7 to 3087.7) and P_n (0–5): 796.7 ($P_n = 0$, m/z: 819.7–23.0 = 796.7, 1.5%), 1254.4 ($P_n = 1$, m/z: 1277.4–23.0 = 1254.4, 100%), 1712.4 ($P_n = 2$, m/z: 1735.4–23.0 = 1712.4, 84.7%), 2170.4 (P_n = 3, m/z: 2193.4–23.0 = 2170.4, 62.2%), 2628.5($P_n = 4$, m/z: 2651.5–23.0 = 2628.5, 25.5%) and 3087.7 ($P_n = 5$, m/z: 3110.7–23.0 = 3087.7, 6.1%), respectively, in which the species with $P_n = 1$ showed the 100% peak intensity. In comparison, O10-1, which has the highest Calc'd P_n (=10), was composed with as many as 16 chemical species with molecular weights of 965.5–4924.2, in which the 100% peak intensity was detected in the species with $P_n = 3$ ($m/z = 2194.4$).

Apparently, the major chemical species were polycondensed by the aromatic dianhydride and aromatic diamine along with the endcapping agents. It was also found that double-endcapped chemical species were primarily produced for the lower Calc'd M_n oligomers such as O1-1 and O2-1, and double- and mono-endcapped species were simultaneously formed in the case of the higher Calc'd M_n oligomer (O10-1). In comparing of the effect of Calc'd P_n on the measured molecular weights, it can be concluded that the higher-molecular-weight chemical species were produced with increasing of Calc'd P_n.

3.4. Thermal curing of F-PETIs

Fig. 5 compares the DSC curves of F-PETIs with different Calc'd M_n (O1-1, O2-1 and O10-1) and Table 4 summarizes the DSC data of

Table 5
Complex melt viscosity of F-PETIs and the unfluorinated derivatives.

Sample	Complex melt viscosity (Pa s) at different temperature (°C)					Minimum melt viscosity (Pa s/°C)	Melt viscosity variation at 280 °C for 2 h	Melt viscosity variation at 310 °C for 2 h
	250 °C	280 °C	310 °C	340 °C	370 °C			
O1–1	15.2	0.4	0.2	0.1	0.2	0.1 at 341 °C	0.46–0.51	0.29–85.7
O1–2	83.2	0.9	0.5	0.4	0.7	0.4 at 338 °C	0.65–0.93	0.50–9.75
O1–*comp*	1.9	0.9	0.8	0.8	10.7	0.8 at 320 °C	1.27–2.73	0.88–452
O2–1	40.5	4.5	1.6	0.8	3.6	0.8 at 347 °C	3.47–7.25	1.71–134.1
O2–2	25.8	4.8	2.4	2.2	31.9	2.3 at 342 °C	4.95–6.44	1.51–87.14
O2–*comp*	52.1	6.2	3.0	3.1	32.3	2.9 at 324 °C	6.19–7.37	2.93–176.5
O10–1	6952	1438	368.7	120.2	65.2	64.8 at 369 °C	–	–
O10–2	5498	1213	254.6	55.94	21.6	22.9 at 367 °C	–	–
O10–*comp*	6803	4684	1204	75.6	83.8	41.7 at 355 °C	–	–

the imide oligomers. The T_gs of the imide oligomers determined by DSC were in the range of 136 °C–229 °C. The higher Calc'd M_n oligomers showed higher T_g values. The strong curing exothermal peaks were observed for the lower Calc'd M_n oligomers (O1-1 and O2-1), in which the curing onset temperatures (T_{onset}) were measured at 312–323 °C, and the exothermic peaks (T_{exo}) at 406–413 °C, respectively. The normalized heat enthalpy (ΔH) was calculated at 139.1–192.6 J/g. However, the higher Calc'd P_n oligomer (O10-1) did not show apparently thermal curing exothermal peak, probably due to the low endcapping group density in the long imide chains.

The exothermic peaks of the thermal curing reactions for F-PETIs appeared at 406–441 °C, approximately 10–23 °C higher than the corresponding unfluorinated ones (392–422 °C). This was well accordance with the model compounds, implying that the bulky $-CF_3$ substituent leaded to steric barrier and resulted in the phenylethynyl group being much difficulty in thermal curing. In addition, the exothermic enthalpy (ΔH) decreased with increasing of the Calc'd P_n. For instance, O10-1 has ΔH of 7.81 J/g, only 5.6% of O2-1 (139.1 J/g) and 4.1% of O1-1 (192.6), respectively. This could be interpreted by the contribution of the low endcapping group density in the higher-molecular weight oligomers.

3.5. Melt processability of F-PETIs

The melt processability of F-PETIs was investigated by the dynamic rheological method. Fig. 6 depicts the typical melt viscosity–temperature curves of the imide oligomers, in which it can be seen that the melt viscosities were decreased gradually with increasing of the scanned temperatures started at 200 °C, then down to a valley stage where the melt viscosity reached the minimum point, and then went up with further increasing of the temperature due to the thermal curing of the fluorinated phenylethynyl groups. Compared with the higher Calc'd M_n oligomers (O2-1 and O10-1), O1-1 showed much broad low viscosity range started from 260 °C to 370 °C, indicating that this oligomer has the widest melt processing window.

The complex melt viscosities at different scanned temperatures and the minimum melt viscosities were summarized in Table 5. Obviously, minimum melt viscosity temperatures were increased with increasing of the molecular weights. For instance, the minimum melt viscosity temperatures were increased from 341 °C (0.1 Pa s) for O1-1–347 °C (0.8 Pa s) for O2-1 and 369 °C (64.8 Pa s) for O10-1. The minimum melt viscosities were also increased gradually with increasing of the molecular weights. Hence, reducing the resin molecular weights could result in sharp decrease in the minimum melt viscosity and widen the processing temperature window. In comparison, O2-1 (Calc'd $P_n = 2$) has the melt viscosity of 0.8 Pa s at 340 °C, the same with O1-*comp* (Calc'd $P_n = 1$), indicating that the higher-molecular-weight F-PETI could give the same low melt viscosity as the low-molecular-weight unfluorinated derivative.

Figs. 7 and 8 show the melt viscosity stabilities of the imide oligomers against the isothermal standing time at 280 °C and 310 °C, respectively. The melt viscosity variations were depended on the resin molecular weights as well as their chemical structures. O1-1 showed the lowest melt viscosity variation of 0.46–0.51 Pa s after isothermal standing at 280 °C for 2 h (Fig. 7), compared with O1-2 (0.65–0.93 Pa s) and O1-*comp* (1.27–2.73 Pa s), implying that the melt stability of the imide oligomers were closely related to their molecular weights as well as the chemical structures derived from the different endcapping agents. At higher isothermal standing temperature (310 °C), the bitrifluoromethyl phenylethynyl-endcapped oligomer (O1-2) showed the best melt viscosity stability than the monotrifluoromethyl phenylethynyl-endcapped one (O1-1) as well as the unfluorinated phenylethynyl-endcapped one (O1-*comp*). The isothermal standing time (Fig. 8) at which the oligomer melt viscosity abruptly increased was 116 min for O1-2, compared to 89 min for O1-1 and 70 min for O1-*comp*, indicating that the fluorinated phenylethynyl groups showed obvious stabilizing impacts on the oligomer melt viscosity, which is good beneficial to the oligomer melt processability. Overall, the fluorinated phenylethynyl groups would not only contribute to reduce the imide oligomer melt viscosity, but also be beneficial in improving the stability of melt viscosity. These are due to the introduction of the bulky trifluoromethyl in phenylethynyl endcapping groups reduce the interchain interaction and the stiffness of polymer backbone.

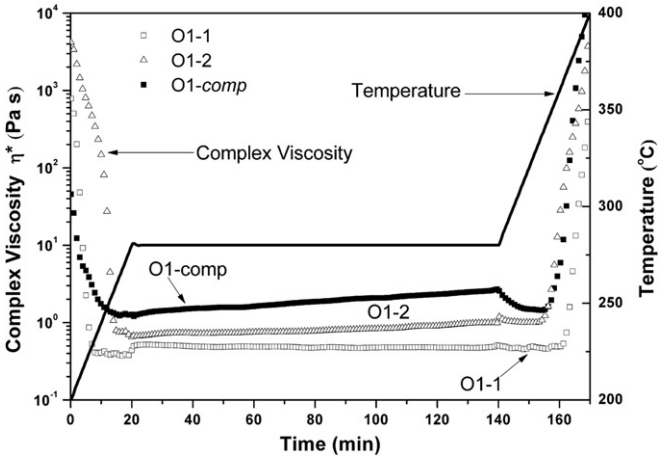

Fig. 7. Isothermal melt viscosity at 280 °C of the representative F-PETIs and the unfluorinated derivative.

3.6. Thermal properties of the thermal-cured polyimides

F-PETIs could be thermally cured at 370 °C for 1 h into the thermoset polyimides. Table 6 summarizes the thermal properties of all cured polyimides determined by DSC and TGA. The T_gs of the thermal-cured polyimides are closely related to the oligomer molecular weights. The lower the un-cured oligomer molecular weights, the higher the T_gs of the thermal-cured polyimides. For instance, O1-1, with the lowest molecular weight, has the highest T_g

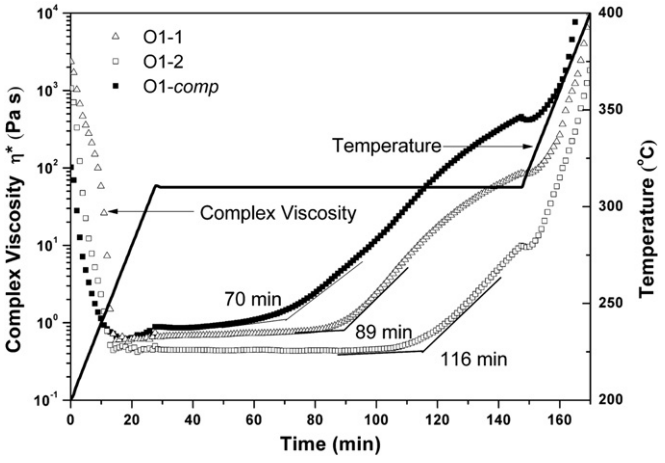

Fig. 8. Isothermal melt viscosity at 310 °C of the representative F-PETIs and the unfluorinated derivative.

Table 6
Thermal properties of the thermal-cured polyimides cured at 370 °C for 1 h

Sample	T_g (°C)	T_{onset} (°C)	T_5 (°C)	T_{10} (°C)
O1-1	332	580	559	598
O1-2	321	583	559	598
O1-*comp*	329	546	555	578
O2-1	306	583	561	603
O2-2	300	570	546	590
O2-*comp*	301	552	560	581
O10-1	269	578	573	601
O10-2	261	577	572	598
O10-*comp*	263	550	560	575

of 332 °C, 26 °C higher than O2-1 (306 °C), and 63 °C higher than O10-1 (269 °C). Additionally, the monotrifluoromethylphenylethynylendcapped oligomers (O1-1, O2-1 and O10-1) showed a little higher T_gs than the bitrifluoromethylphenyl-ethynylendcapped ones (O1-2, O2-2 and O10-2). For instance, the thermal-cured O2-1 has T_g of 306 °C, 6 °C higher than the thermal-cured O2-2 (300 °C).

The thermal-cured polyimides provided with the onset decomposition temperatures (T_{onset}) in the range of 570–583 °C, 5% loss temperatures (T_5) of 546–573 °C and 10% loss temperatures (T_{10}) of 578–603 °C (Table 6). No obvious difference in thermal stability in nitrogen was observed for the thermal-cured polyimides. In addition, the thermal-cured fluorinated polyimides exhibited little better thermal stability than the unfluorinated ones. For instance, the thermal-cured O1-1 resin has T_{onset} of 580 °C (34 °C higher than O1-*comp* (546 °C)), and T_{10} of 598 °C (20 °C higher than O1-*comp* (578 °C).

The thermal curing kinetic analysis of the imide oligomers (O1-1, O1-2 and O1-*comp*) were performed using DSC by monitoring of the changes in T_g values as a function of the thermal curing temperatures (360 °C/1 h, 370 °C/1 h, 380 °C/1 h and 390 °C/1 h, respectively). The curing degree (x) was calculated by DiBenedetto equation modified for highly crosslinked networks according to the literatures [36,40–43,49]. Applying for the first-order data analysis ($-\ln(1-x) = K_t$), the rate constant (K) at certain temperature was obtained from the very good line fit. As shown in Fig. 9 in Arrhenius relationship $K = Ae^{-Ea/RT}$ between rate constant and temperature, an activation energy (E_a) of 160.0 kJ/mol for O1-1 and 210.8 kJ/mol for O1-2 were obtained, compared to 141.5 kJ/mol for O1-*comp*. Due to the higher activation energy, O1-2 would have the higher rate

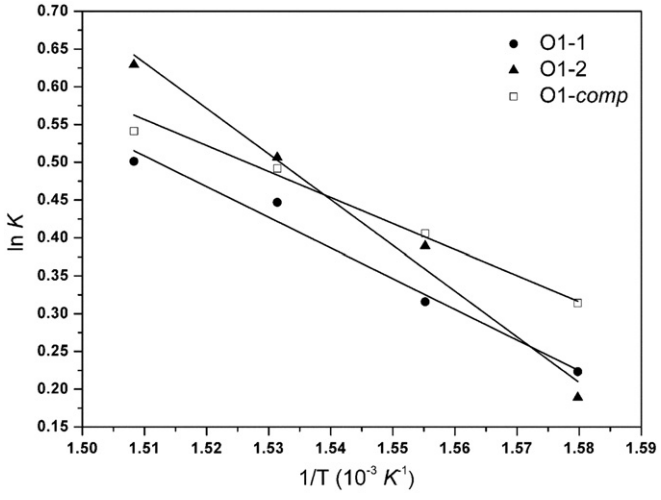

Fig. 9. Arrhenius plots of the thermal curing kinetics of the representative F-PETIs and the unfluorinated derivative.

Table 7
Mechanical properties of the thermal-cured polyimides at 370 °C/1 h.

Sample	Tensile strength (MPa)	Tensile modulus (GPa)	Elongation at break (%)
O1–1	41.7	1.2	6.2
O1–2	39.0	1.4	5.8
O1–*comp*	47.5	1.3	6.0
O10–1	112.2	1.1	18.6
O10–2	101.8	1.2	21.2
O10–*comp*	121.5	1.3	23.5

acceleration trend in the thermal curing reaction than O1-1. And the monotrifluoromethyl phenylethynyl-endcapped oligomer (O1-1) expressed similar thermal curing behavior with the unfluorinated derivative (O1-*comp*).

3.7. Mechanical properties of the thermal-cured polyimides

Table 7 summarizes the mechanical properties of the thermal-cured polyimides. After thermally cured at 370 °C for 1 h, the resulted thermoset polyimides with Calc'd $P_n = 1$ (O1-1 and O1-2) exhibited good combined mechanical properties, including tensile strength of 39.0–41.7 MPa, tensile modulus of 1.2–1.4 GPa, elongation at breakage of 5.8–6.2%. The tensile strength and elongation at breakage of the thermal-cured polyimides were greatly improved when the oligomer molecular weights were increased. For instance, the thermal-cured polyimides with Calc'd $P_n = 10$ (O10-1, O10-2) showed tensile strength of 101.8–112.2 MPa and elongation at breakage of 18–21%, much better than O1-1 and O1-2. In addition, F-PETIs could produce the thermal-cured polyimides with mechanical properties comparable to the unfluorinated derivatives, revealing that no obvious negative impacts on mechanical properties of the thermal-cured polyimides were observed due to the fluorination of the phenyethynyl groups.

4. Conclusion

Novel fluorinated phenylethynyl-contained endcapping agents, 4-(3-trifluoromethyl-1-phenylethynyl)phthalic anhydride (3F-PEPA) and 4-(3,5-bistrifluoromethyl-1-phenylethynyl)phthalic anhydride (6F-PEPA) have been synthesized, which were employed to synthesize a series of F-PETIs. The experiments on the model compounds indicated that the fluorinated model compounds exhibited 22–35 °C higher in thermal cure temperatures and 42–52% lower in exotherms than the unfluorinated derivative. F-PETIs also holded the thermal curing temperatures of 20–30 °C higher than the corresponding unfluorinated analogues. The melt processability of F-PETIs was apparently improved by the melt viscosities decreased and the melt viscosity stability enhanced due to the $-CF_3$ groups in the imide oligomers. F-PETIs could be thermally cured at 370 °C to afford the thermal-cured polyimides, which denoted thermal properties with T_g of as high as 332 °C, T_5 of >570 °C, and mechanical properties with tensile strength of as high as 122 MPa, and elongation at breakage of >18%.

References

[1] Serafini T, Delvig P, Lightsey G. J. Appl Polym Sci 1972;16:905–15.
[2] Landis AL, Bilow N, Boschan RH, Lawrence RE, Aponyi TJ. Polym Prepr 1974;15:537–41.
[3] Harris K, Sridhar K. Polym Prepr 1985;26:142–3.
[4] Chaudhari MA. 32nd Int SAMPE Symp 1987;32:597–601.
[5] Waters JF, Sutter JK, Meador MAB, Baldwin LJ, Meador MA. J Polym Sci Part A Polym Chem 1991;29:1917–24.
[6] Baldwin LJ, Meador MAB, Meador MA. Polym Prepr 1988;29:263–4.
[7] Vaucraeynest W, Stille JK. Macromolecules 1980;13:1361–7.

[8] Bisshop KC. Chem Rev 1976;76:461–86.
[9] Connell JW, Smith Jr JG, Hergenrother PM. J Macromol Sci Rev Macromol Chem Phys 2000;C40(2–3):207–30.
[10] Hergenrother PM. High Perform Polym 2003;15:3–45.
[11] Harris FW, Padaki SM, Vavaprath S. Polym Prepr 1980;21(1):3.
[12] Harris FW, Pamidimukkala A, Gupta R, Das S, Wu T, Mock G. Polym Prepr 1983;24(2):324–5.
[13] Harris FW, Sridhar K, Das S. Polym Prepr 1984;25(1):110–1.
[14] Harris FW, Pamidimukkala A, Gupta R, Das S, Wu T, Mock G. J Macromol Sci Chem 1984;A21(8–9):1117–35.
[15] Meyer GW, Jayaraman S, McGrath JE. Polym Prepr 1993;34:540–1.
[16] Paul CW, Schultz R, Fennelli SP. In: Feger C, Khoyasteh MM, Htoo MS, editors. Advances in polyimide science and technology. Lancaster, PA: Technomic; 1993. p. 220–354.
[17] Hergenrother PM, Bryant RG, Jensen BJ, Havens SJ. J Polym Sci Part A Polym Chem 1994;32:3061–7.
[18] Meyer GW, Glass TE, Grubbs HJ, McGrath JE. Polym Prepr 1994;35:549–50.
[19] Takekoshi T, Terry JM. Polymer 1994;35:4874–80.
[20] Hergenrother PM, Smith Jr JG. Polymer 1994;35:4857–64.
[21] Johnston JA, Li FM, Harris FW. Polymer 1994;35:4865–73.
[22] Hinkley JA. J Adv Mater 1994;27:55–9.
[23] Preston CML, Jill DJT, Pomery PJ, Whittaker AK, Jensen BJ. High Perform Polym 1999;11:453–65.
[24] Connell JW, Smith Jr JG, Hergenrother PM. High Perform Polym 1998; 10:273–83.
[25] Hou T, Jensen BJ, Hergenrother PM. J Comp Matls 1996;30(1):109–22.
[26] Hergenrother PM. Sampe J. 2000; 36(1): 30–41.
[27] Hergenrother PM, Conell JW, Smith Jr JG. Polymer 2000;41:5073–81.
[28] Smith Jr JG, Connell JW, Hergenrother PM. J Comp Matls 2000;34:614–28.
[29] Smith Jr JG, Connell JW, Hergenrother PM. J Comp Matls 2002;36:2255–65.
[30] Simone CD, Scola DA. High Perform Polym 2003;15:473–501.
[31] Zhou HW, Chen CH, Kanbara R, Sasaki T, Yokota R. High Perform Polym 2005;17:193–212.
[32] Connell JW, Smith Jr JG, Hergenrother PM. High Perform Polym 2003;15: 375–94.
[33] Connell JW, Smith JG Jr., Hergenrother PM. Proceedings of 48th Int SAMPE sym May; Long Beach CA (2003), CD Version.
[34] Cho D, Drzal LT. J Appl Polym Sci 2000;76:190–200.
[35] Fang X, Xie XQ, Simone CD, Stevens MP, Scola DA. Macromolecules 2000;33:1671–81.
[36] Fang X, Rogers DF, Scola DA, Stevens MP. J Polym Sci Part A Polym Chem 1998;36:461–70.
[37] Knudsen RL, Jensen BJ. High Perform Polym 1996;8:57–66.
[38] Smith Jr JG, Connell JW. High Perform Polym 2000;12:213–23.
[39] Ding MX. Prog Polym Sci 2007;32:623–68.
[40] Wright ME, Schorzman DA. Macromolecules 1999;32:8693–4.
[41] Wright ME, Schorzman DA, Pence LE. Macromolecules 2000;33:8611–7.
[42] Wright ME, Schorzman DA. Macromolecules 2001;34:4768–73.
[43] Wright ME, Schorzman DA, Berman AM. Macromolecules 2002;35:6550–6.
[44] Thompson CM, Hergenrother PM. Macromolecules 2002;35:5835–9.
[45] Liu YF, Wang ZH, Yang HL. J Polym Sci Part A Polym Chem 2008;46:4227–35.
[46] Mengxian D, Wang Z, Yang Z, Zhang J. U.S. Patent, 5, 081, 281, 1992.
[47] Zhen W, Gao L, Mengxian Ding. Chinese Patent Z. L. 2003; 10115829.8.
[48] Kissinger HE. Anal Chem 1957;29:1702–6.
[49] Ayambem SJ, Mecham SJ, Sun Y, Glass TE, McGrath JE. Polymer 2000;41: 5109–24.

Polymer 52 (2011) 149–156

Contents lists available at ScienceDirect

Polymer

journal homepage: www.elsevier.com/locate/polymer

Polymer blend emulsion stabilization using carbon nanotubes interfacial confinement

Anne-Christine Baudouin, Dietmar Auhl, FangFang Tao, Jacques Devaux, Christian Bailly*

Bio- and Soft Matter, Institute of Condensed Matter and Nanosciences, Université catholique de Louvain, Louvain-la-Neuve, Belgium

ARTICLE INFO

Article history:
Received 1 July 2010
Received in revised form
27 October 2010
Accepted 4 November 2010
Available online 3 December 2010

Keywords:
Polymer blends
Carbon nanotubes
Pickering emulsion

ABSTRACT

The present study demonstrates the effect of unfunctionalized MultiWalled Carbon Nanotubes (MWNTs) interfacial confinement on coalescence suppression in an immiscible polymer blend exhibiting a sea-island morphology. The effect of carbon nanotubes on morphological stabilization in polyamide (PA)/ethylene–methyl acrylate random copolymer (EA) blends is studied using electronic microscopy techniques. Owing to their interfacial localization, MWNTs are shown to enhance both phase dispersion and stability of the dispersed phase for long mixing time (at least 60 min) and very low filler content (0.5 wt.-% MWNTs) compared to what was previously observed in literature. MWNTs also produce a more uniform distribution of droplets size. The main stabilization mechanism proposed is the formation of a deformable barrier network providing a mechanical barrier against coalescence. Blends stabilized by solid anisotropic nanoparticles, like MWNTs, could therefore offer an interesting alternative to blends compatibilized by block-copolymers.

1. Introduction

Multiphase polymer blends have attracted tremendous attention to achieve valuable properties materials by taking advantage of the attractive features of each component. However, binary blends of immiscible polymers generally exhibit poor properties due to their coarse and unstable morphology [1]. To generate a material exhibiting the desired properties, it is therefore essential to produce a blend with fine and stable dispersed droplets.

Coalescence can be reduced by the use of interfacial block copolymers, which act as surfactants stabilizing emulsions [2]. Compatibilization can also be achieved with the help of nanoparticles (carbon black, clay, silica, metal oxides, polymer latex etc.), as it has been reported for a few decades [3–13]. The particles can be trapped at the interface between polymers to minimize the total interfacial energy of the system. These stabilized emulsions are called Ramdsen–Pickering emulsions, as a reference to Ramsden [14] and Pickering [15] studies on the stabilization of low viscosity fluids emulsions by a small proportion of insoluble particles. The effectiveness of emulsion stabilization depends on various parameters such as the concentration, the size, the shape, the wettability and the level of interparticle interactions of the particles [16]. Recently, Madivala et al. [17] demonstrated that sufficiently elongated particles can be effective coalescence suppressors of immiscible fluid phases, even when spherical or lower aspect ratio particles presenting the same wetting properties are inefficient. Thus anisotropic particles at low volume fraction lead to improved stabilization compared to spherical particles. Moreover, morphology stabilization by nanoparticles presents further advantages, compared to other methods, by adding interesting properties such as improved thermal or electrical conductivity.

Among nanofillers, carbon nanotubes have attracted tremendous attention since their discovery in 1991 [18]. They combine a high aspect ratio with exceptional electrical, mechanical and thermal properties [19].

Carbon nanotubes have already shown their ability to refine the morphology of immiscible polymer blends [20,21]. However, only few authors have focused on the stabilization of polymer blends by carbon nanotubes. Recently, Bose et al. [22] used amine functionalized multiwall carbon nanotubes (NH_2-MWCNTs) to stabilize poly(methyl methacrylate) (PMMA) phase in poly[(α-methyl styrene)-co-acrylonitrile] (PαMSAN)/PMMA blends. NH_2-MWCNTs were randomly dispersed in the homogeneous blends. Due to thermodynamic considerations, the NH_2-MWCNTs were localized only in the PαMSAN after phase separation. It was observed that a typical loading of 1.25 wt.-% NH_2-MWCNTs totally suppresses the coalescence on a practical time scale (at least 2500 s).

* Corresponding author. Tel.: +32 10 478412; fax: +32 10 451593.
E-mail address: christian.bailly@uclouvain.be (C. Bailly).

0032-3861/$ – see front matter © 2010 Elsevier Ltd. All rights reserved.
doi:10.1016/j.polymer.2010.11.004

Due to their excellent electrical properties, carbon nanotubes have often been used for the preparation of conductive materials for electrostatic dissipative or electromagnetic interference shielding applications. For the elaboration of such materials there must be a conductive path through the material. The selective localization of the conductive filler inside immiscible polymer blends allows the formation of such a path with a reduced content of carbon nanotubes. More precisely, the formation of a triple percolating structure, i.e. two immiscible polymers forming a continuous structure and the percolation of their interface where the filler is located, seems particularly efficient to produce highly conductive materials at low filler contents.

In this context, we explore the morphology of blends of polyamide (PA), ethylene methyl acrylate copolymer (EA) and carbon nanotubes (MWNTs). In previous works [23,24], we have demonstrated the interfacial localization of unfunctionalized MWNTs in immiscible polymer blends. Here we study the stabilization of a simple sea-island morphology by unfunctionalized carbon nanotubes localized at the interface, with the intention to extrapolate these results to triply percolating structures in the future. The implication of MWNTs interfacial confinement on the stabilization of blend morphology is investigated in the present paper by a combination of TEM and SEM techniques. The overall objective is to demonstrate that unfunctionalized carbon nanotubes, if localized at the interface, produce stabilized morphologies at lower filler content than was previously reported in literature.

2. Experimental

2.1. Materials

The blends under study are composed of two immiscible polymers: a polyamide and an ethylene–acrylate copolymer. The polyamide (PA) is a copolyamide 6/12 (Grilon® CF6S, EMS Grivory) with a low melting point of 130 °C. The ethylene-acrylate copolymer (EA) used is a random copolymer of ethylene and 26–30 wt% methyl acrylate (Lotryl® 28MA07, Arkema).

The MWNTs are Nanocyl®-7000 (Nanocyl S.A., Belgium), produced via a catalytic carbon vapour deposition (CCVD) process. They present 7 graphene shells, their average diameter is of 9.5 nm and their average length is of 1.5 μm. The carbon purity is 90% and the surface area is around 250–300 m^2g^{-1}.

2.2. Compounding procedure

Blends of 90 wt.-% EA and 10 wt.-% PA with and without carbon nanotubes were prepared in a co-rotating twin-screw mini-compounder (DSM Microcompounder 15 cm^3). The compounder was filled with 12 g material. The mixing temperature was 180 °C, the screw speed was 250 rpm and the mixing time was either 10 or 30 or 60 min. The polymers were dried overnight at 50 °C prior to compounding.

Two kinds of blends were prepared by simultaneous mixing: binary blends of EA and PA without MWNTs and ternary blends of EA and PA with various amounts of MWNTs. The torque was measured during the compounding of neat polymers and composites to follow their evolution with extrusion time.

3. Characterization

3.1. Scanning electron microscope (SEM)

Scanning electron microscopy was performed on cryofractured surfaces using a LEO 982 (Zeiss) operating at 1 kV.

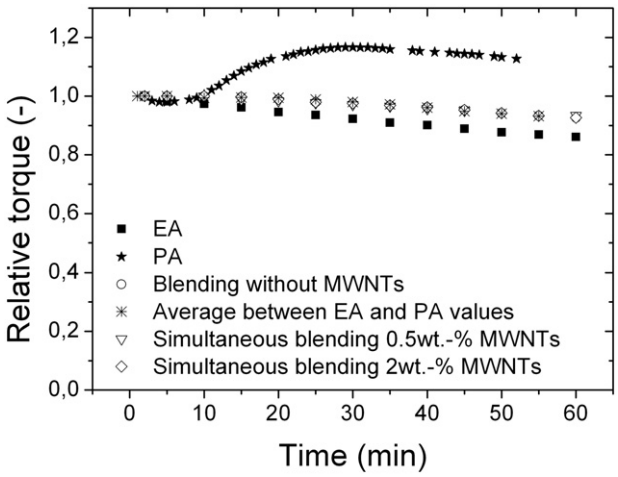

Fig. 1. Relative torque versus compounding time for pure polymers as well as unfilled and filled blends at 180 °C and 250 rpm.

3.2. Transmission electron microscope (TEM)

Transmission electron microscopy was performed using a LEO 922 microscope operating at 200 kV. The specimens were cut perpendicularly to the axes of the extruded samples using a Reichert Microtome. Ultrathin sections of approximately 95 nm in thickness were cut using a cryo-diamond knife with a cut angle of 35° (Diatome, Switzerland) and collected in a blend of 60 vol% dimethylsulfoxide (DMSO)/40 vol% demineralised water on copper grids (Diatome).

The droplets diameter was evaluated on TEM micrographs using the iTEM software (Olympus Soft Imaging System). Although the measured diameter is not the actual diameter of the droplets, this measurement allows to follow the morphology evolution with time.

3.3. Rheology

The samples were analyzed using a stress-controlled Bohlin (now Malvern) Gemini rheometer with 25 mm parallel plates. All the measurements were performed under nitrogen, to avoid thermo-oxidative degradation, at the compounding temperature, i.e. 180 °C. The samples were measured in the linear range of deformation.

The thermal stability of both polymers was analyzed using the multiwave-frequency option. For the EA copolymer, the

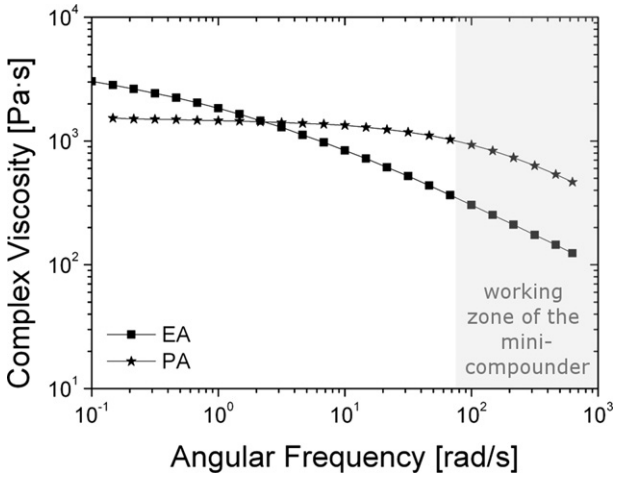

Fig. 2. Complex viscosity of EA and PA versus angular frequency. The approximate shear rate range in the minicompounder is indicated by the grey tint area.

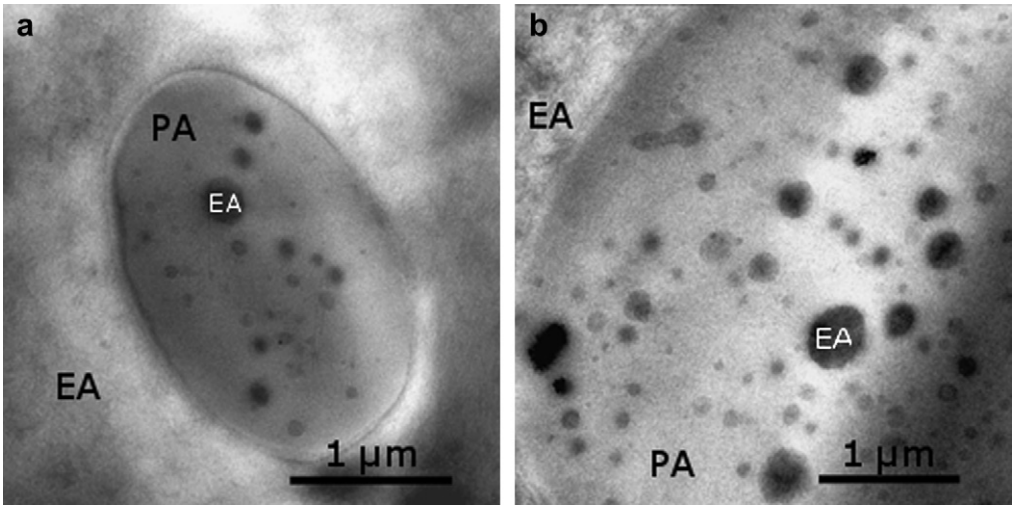

Fig. 3. (a, b) TEM micrographs of a blend of EA and PA without MWNTs, (a) 10 min mixing, (b) 60 min mixing.

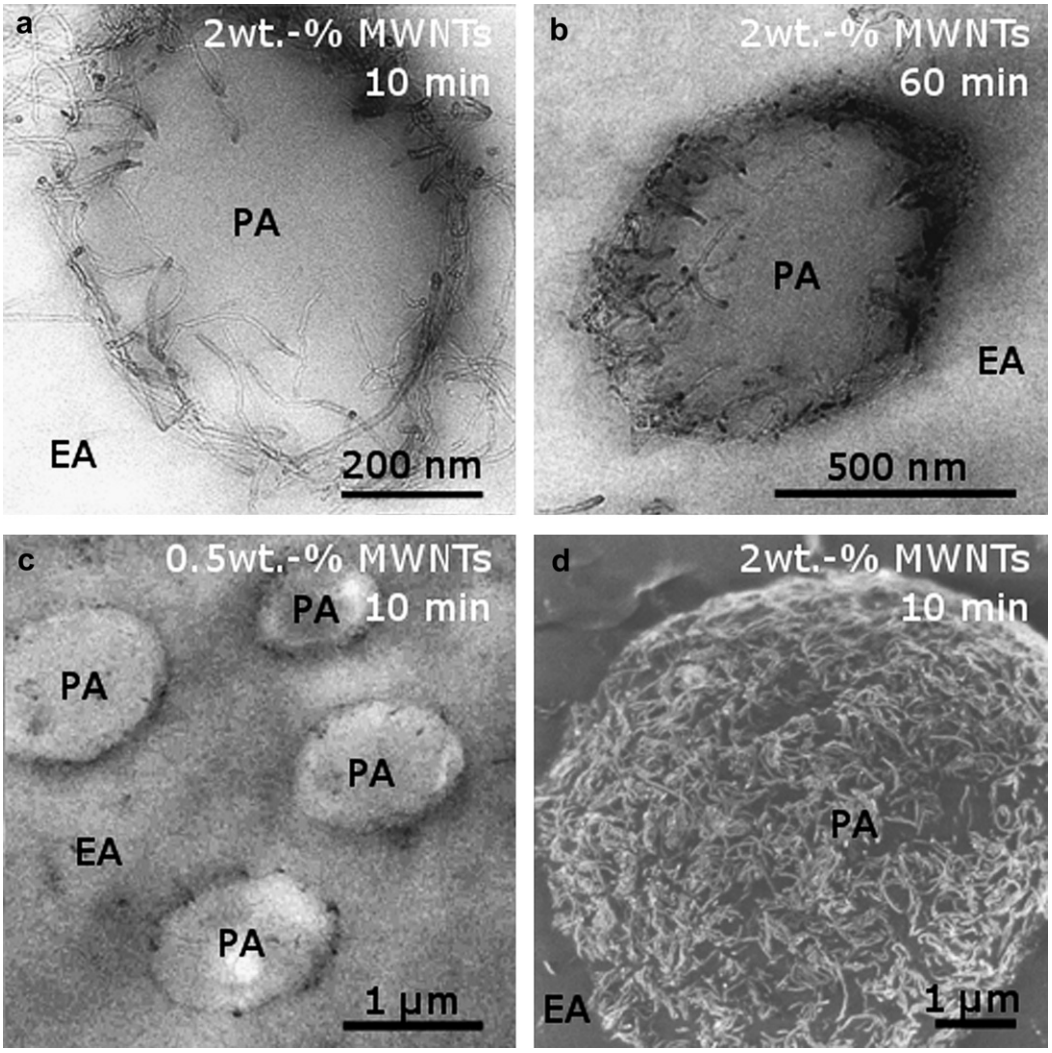

Fig. 4. (a–c) TEM micrographs of a blend of EA, PA and MWNTs: (a) 2 wt.-% MWNTs, 10 min mixing; (b) 2 wt.-% MWNTs, 60 min mixing; (c) 0.5 wt.-% MWNTs, 10 min mixing; and (d) SEM micrograph of a cryofractured blend of EA, PA and 2 wt.-% MWNTs, 10 min mixing.

fundamental frequency was 0.1 rad/s with 5% deformation plus two additional waveforms at 1 rad/s with 1.5% and 10 rad/s with 0.5% respectively. For PA, a higher deformation was applied to minimize noise at low frequency. The fundamental frequency was therefore 0.1 rad/s with 10% deformation and two other frequencies of 1 rad/s with 3% and 10 rad/s with 1%.

The frequency sweep experiments were conducted in the frequency range of 0.1–100 rad/s.

4. Results and discussion

4.1. Rheological behavior of EA and PA

The viscosity ratio is one of the most critical variables controlling blend morphology. Torque was monitored during compounding and rheological experiments performed in order to assess the possible influence of chemical changes during processing on this parameter.

The evolution of the torque in the extruder was followed during compounding (Fig. 1). The initial values are around 2500 N and 4800 N for EA and PA respectively. This is a good hint that PA is more viscous than EA under these flow conditions.

The torque of EA is slightly decreasing with compounding time, indicating the polymer is slowly degrading over long processing times.

For PA, a torque increase of about 15% is observed during the first 20 min. This increase is probably related to condensation reactions occurring in the compounder. At later times, the PA torque is decreasing, reflecting a slow degradation.

The torque behavior of the blend (circle symbol) is very similar to the data obtained by averaging the EA and PA values (cross symbol). Most probably, the two polymers behave in the blend approximately the same as when compounded alone.

A frequency sweep at compounding temperature (Fig. 2) confirms the higher viscosity of the minor phase by comparison with the continuous one. In the shear rate range of the compounder, the PA viscosity is 2–3 times higher than the viscosity of EA (assessed from Cox-Merz equivalence). This is consistent with the torque ratio observed in the compounder.

In order to assess the thermal stability of both polymers at high temperature, we have also performed a multiwave frequency time sweep of the pure polymers at compounding temperature. From this test (data not shown), we observe essentially no evolution of the dynamic moduli up to 4000 s at the tested frequencies and we can conclude that there is very little thermal degradation during the experimental time. The torque data in the extruder and the dynamic moduli in the rheometer show different trends but those differences can be understood. The torque decrease in the extruder highlights a shear-induced degradation, while in the rheometer, the pure thermal degradation appears very limited in the same time

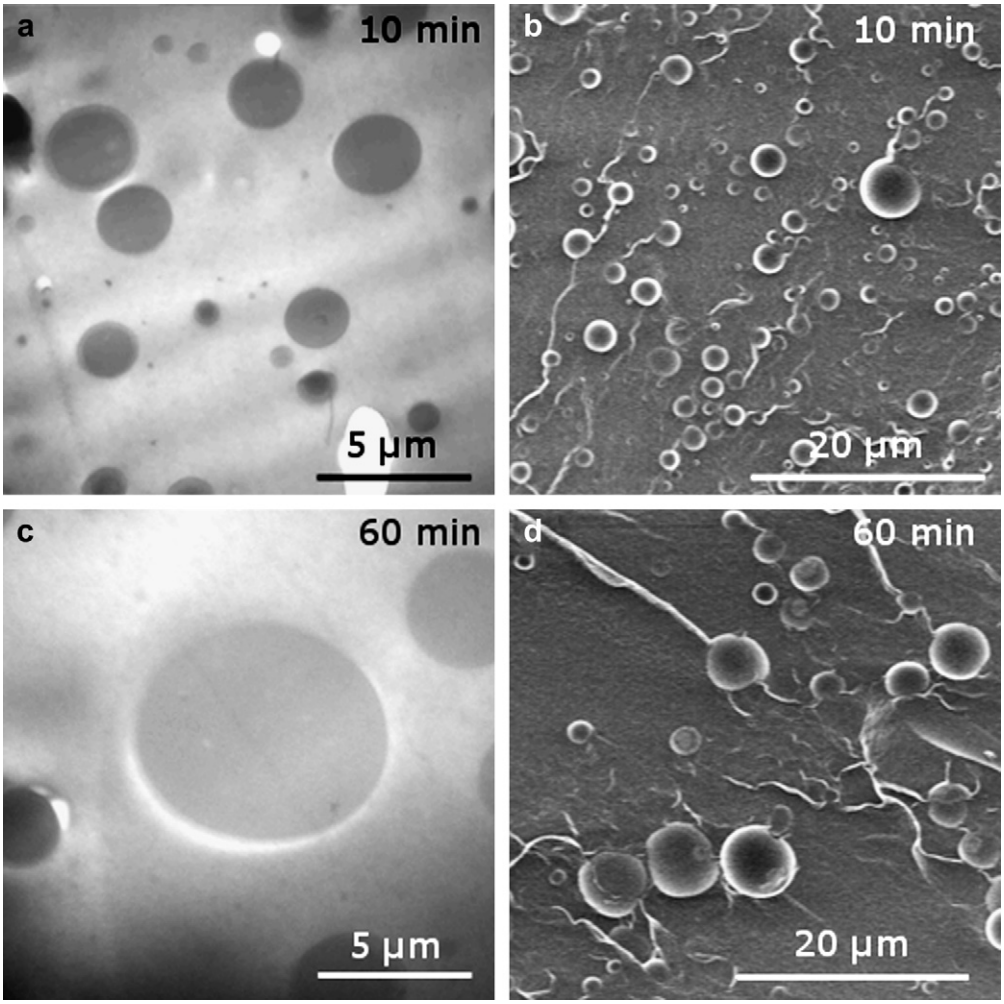

Fig. 5. TEM (a, c) and SEM (b, d) micrographs presenting the evolution of the morphology with compounding time in the absence of MWNTs (a, b) 10 min compounding and (c, d) 60 min compounding.

and temperature window. The torque increase observed for PA at short times in the extruder is not paralleled by a viscosity increase in the rheometer and must be due to a condensation reaction that is enhanced by mixing.

4.2. Blend morphology of EA/PA/MWNTs nanocomposites

The morphology of the blends without MWNTs is shown on Fig. 3. TEM micrographs show that in absence of MWNTs, many EA sub-inclusions are present in the PA dispersed phase. Fig. 3a shows a droplet of PA dispersed in the EA matrix after 10 min of mixing. Fig. 3b presents a droplet after 60 min of mixing with a very high number of EA sub-inclusions.

In the presence of MWNTs, there are nearly no EA sub-inclusions, even after 60 min of mixing (Fig. 4a–c). The MWNTs are mainly localized at the interface, whatever the amount used, after 10 min or 60 min mixing. The interfacial localization is also clear from the SEM micrograph after cryofracture (Fig. 4d), which presents a PA droplet covered with MWNTs. The observed confinement can be rationalized by thermodynamics and irreversible polymer adsorption on MWNTs [22,23].

Sub-inclusions of the matrix phase are spontaneously formed by coalescence of poorly stabilized dispersed phase during the later stage of mixing, i.e. when coalescence dominates over the melting or softening process [25,26]. The high amount of sub-inclusions observed after 60 min mixing hence witnesses the dispersed phase coalescence during mixing. On the contrary, the very low amount of sub-inclusions in presence of MWNTs highlights a strong reduction and/or slowing down of coalescence mechanisms.

4.3. Morphology evolution with time

The evolution of the morphology with increasing compounding time is shown in Fig. 5. In the absence of MWNTs, the morphology coarsens with increasing mixing time (Fig. 5a–d). This increase can be explained by the rheological behavior of both polymers. In the approximate deformation rate range of the minicompounder (assuming Cox-Merz equivalence and predominant shear deformation), the viscosity ratio is high, of the order of 3, with the dispersed phase being the more viscous (see Fig. 2). In this situation, the Grace plot (critical capillary number $C_a = \frac{\eta_c r_d \dot{\nu}}{\gamma}$, where η_c is the continuous phase viscosity, r_d is the radius of the dispersed phase, $\dot{\nu}$ is the shear rate, and γ is the interfacial tension, vs. viscosity ratio $p = \frac{\eta_d}{\eta_c}$, where η_c is the continuous phase viscosity and η_d is the dispersed phase viscosity) [27] predicts a less than optimal dispersion, moreover strongly negatively affected by the viscosity ratio. It has of course to be kept in mind that the Grace plot can only be applied very qualitatively as the deformation field in the extruder is complex rather than pure shear and the phases are viscoelastic rather than purely viscous. However, rough trends should be respected. The average particle size of the unmodified EA–PA blend (Fig. 5) increases approximately by a factor 3 between 10 and 60 min. This result is compatible with a slight increase of the viscosity ratio, which should strongly negatively affect dispersion,

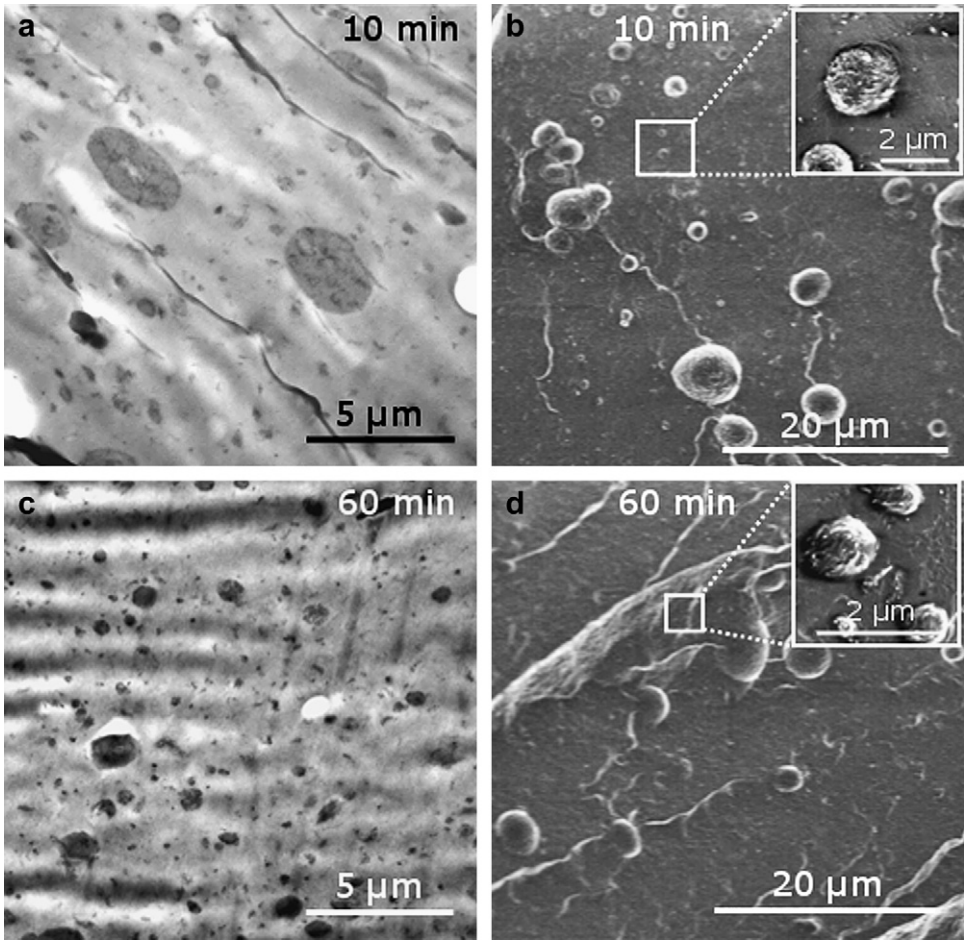

Fig. 6. TEM (a, c) and SEM (b, d) micrographs presenting the evolution of the morphology with compounding time in the presence of 2 wt.-% MWNTs (a, b) 10 min compounding and (c, d) 60 min compounding.

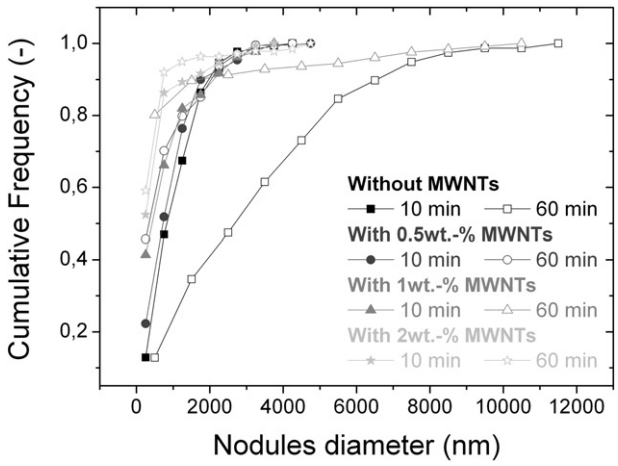

Fig. 7. Cumulative frequency versus droplet diameter for unfilled and filled blends (0.5 wt.-%–2 wt.-%MWNTs) for 10 and 60 min blending (measured on TEM micrographs).

as confirmed by the simultaneous torque increase of 15% observed for PA and slow decrease observed for EA (see Fig. 1).

On the contrary, in the presence of MWNTs, the morphology is stabilized against coalescence. TEM and SEM micrographs (Fig. 6a–d) show that when EA and PA are simultaneously mixed with 2 wt.-% MWNTs, the droplet size remains stable during mixing. No increase of the diameter is observed and small PA droplets with MWNTs at the interface are still present even after 60 min compounding (inserts Fig. 6b and d). This suggests that the distribution generated during the first moments of mixing is "frozen" and not further affected by the change in viscosity of the phases.

4.4. Quantitative image analysis

The size of the PA droplets was measured on the TEM micrographs. The cumulative frequency versus the measured droplet diameter is shown on Fig. 7 and Fig. 8.

Two effects are clearly highlighted on these graphs. First, at equivalent compounding time, the droplets are smaller when MWNTs are simultaneously mixed with the polymers even at only 0.5 wt.-% MWNTs (Fig. 7). Thus, unpurified and unfunctionalized MWNTs enhance phase dispersion. Indeed, the as-produced MWNTs exhibit a length comparable or higher than the diameter of the dispersed phase (average length 1.5 μm). They are therefore able to enhance phase dispersion during processing by splitting the polymer droplets into smaller particles, leading to finer dispersion as already been observed by Li et al. [28]

Second, due to the interfacial localization of the MWNTs, the blends behave like Pickering emulsions. The droplets of the dispersed phase are stabilized against coalescence by the MWNTs adsorbed at the interface. Moreover, this stabilization is effective even at very long mixing times (at least 60 min) and low MWNTs contents (0.5 wt% MWNTs) (Fig. 8).

The mechanisms of stabilization by nanoparticles are however not yet fully understood. Different mechanisms probably involved

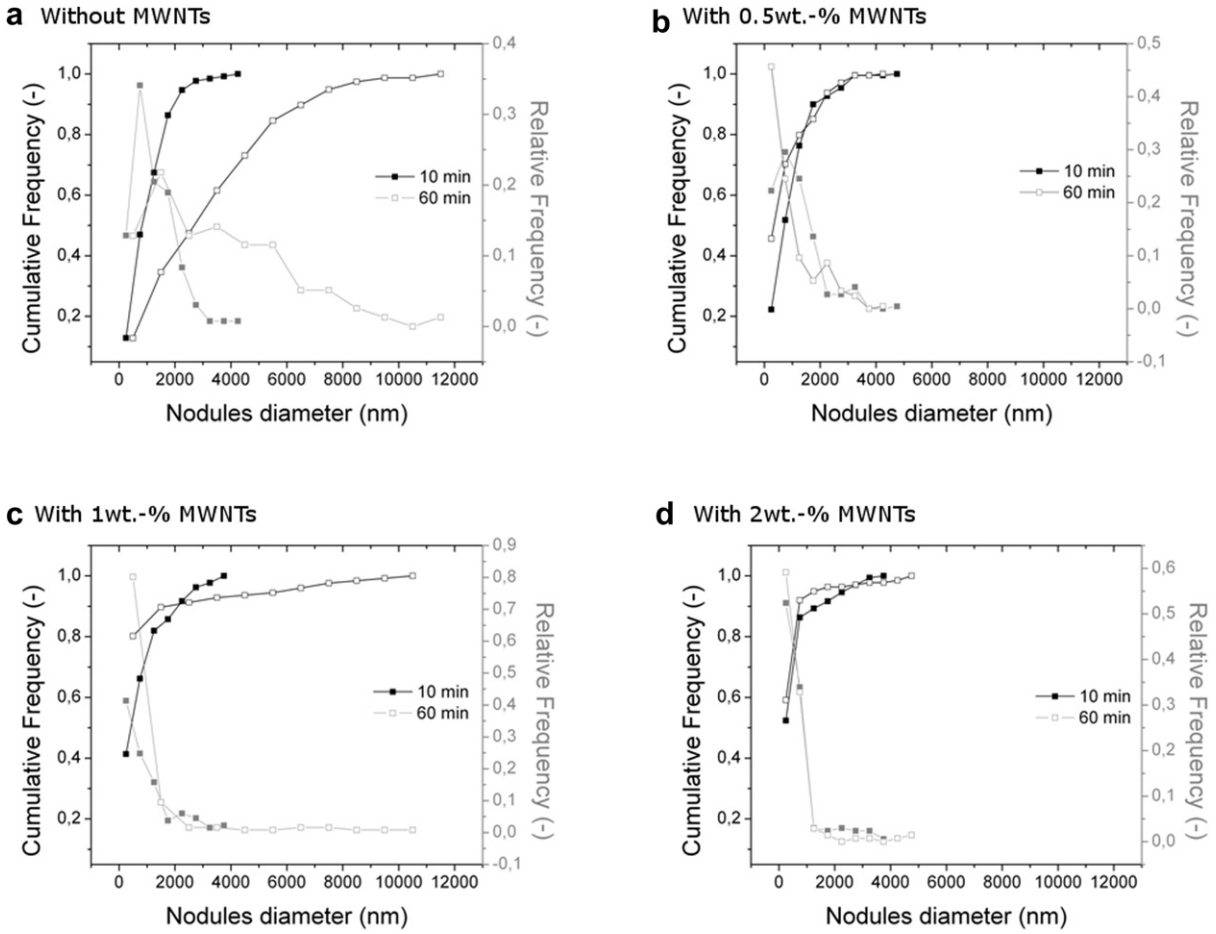

Fig. 8. (a–d) Cumulative and relative frequencies versus the droplet diameter (a) without MWNTs; (b) with 0.5 wt.-% MWNTs; (c) with 1 wt.-%MWNTs; (d) with 2 wt.-% MWNTs (measured on TEM micrographs).

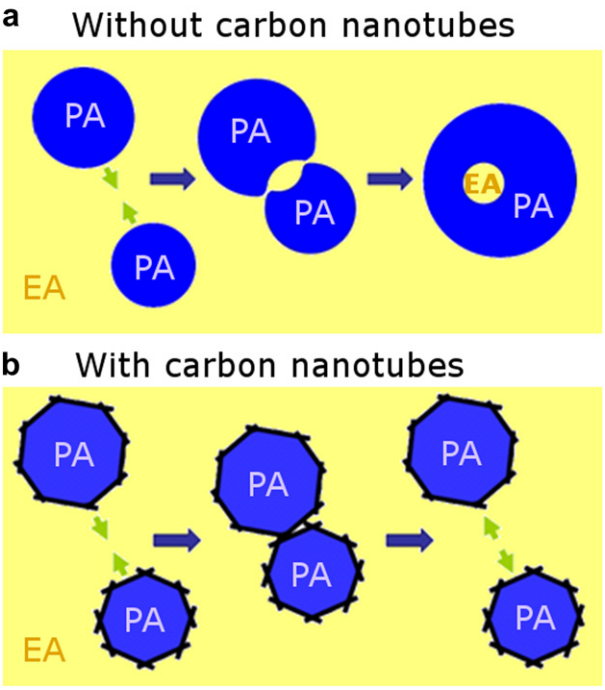

Fig. 9. Morphology development due to dispersed phase polymer droplets collision (a) in the absence and (b) in the presence of MWNTs.

in the emulsion stabilization are described in literature. A first mechanism is the reduction of the interfacial energy per unit area. Many authors [6,29–33] have measured a decrease of the interfacial tension when organomodified clay is located at the interface between immiscible polymers. However, as the clay is modified by surfactants, it is not clear if the interfacial energy reduction is due to the nanoparticles themselves or to contamination by surfactant. It is thus not clear yet if unmodified particles would significantly modify the interfacial energy per unit area. A second mechanism is an increase of the major phase viscosity due to particle localization in the matrix. This viscosity increase is responsible for a slowing down of the matrix phase drainage, thus reducing coalescence [34]. This mechanism can not be active here since the MWNTs are mainly located at the interface and the overall MWNTs concentration is too low (well below the percolation threshold) to significantly affect viscosity. Moreover, the torque measured for both polymers does not change dramatically with increasing mixing time. A third mechanism is the formation of a dense layer at the interface between phases due to the selective localization of particles at the interface. This dense layer can form a mechanical barrier preventing the coalescence of the dispersed phase [10,16,35]. Finally, the presence of particle-bridged domains can also produce morphology stabilization [36]. However, this last mechanism is considered as less important and was not observed here.

Overall, the formation of a dense interfacial layer is the most likely explanation for the observed morphology stabilization. In the absence of MWNTs, when a collision occurs between two droplets of the dispersed phase, they coalesce and sometimes, a part of the matrix material is not drained and forms a sub-inclusion (Fig. 9a). In the presence of MWNTs, when two dispersed polymer droplets collide, the deformable network formed by the MWNTs at the interface prevents them from coalescing (Fig. 9b).

It is also worth noting that MWNTs are efficient at producing a relatively narrow distribution of droplet sizes. Indeed, the cumulative frequency curve is sharper in presence of MWNTs, indicating a narrower distribution of sizes. Silica particles localized at the interface have already shown this kind of uniform morphology [37,38].

5. Conclusions

For the first time, the influence of unfunctionalized MWNTs interfacial confinement on the stability of a polymer blend morphology has been demonstrated. The effect of particle concentration on the morphology and its evolution with increasing compounding time has been studied.

MWNTs enhance both phase dispersion and stability of the dispersed phase, even at long mixing time (60 min) and low nanofiller content (0.5 wt.-%MWNTs). They also produce a more uniform distribution of droplet sizes.

Taking advantage of the MWNT interfacial localization should enable the development of stable binary blends at lower filler content than previously published in literature. In the present study, the minimum MWNTs content was 0.5 wt.-% but this concentration can probably still be reduced.

The main mechanism involved most probably is the formation of a deformable barrier network at the interface, due to MWNTs selective interfacial confinement, providing a mechanical barrier against coalescence of the droplets. Blends stabilized by solid particles, like MWNTs, could therefore offer an interesting alternative to blends compatibilized by block-copolymers.

Acknowledgements

The authors thank the EU for the financial support in the frame of the 7th Framework Program research project “HARCANA” (Grant Agreement No: NMP3-LA-2008-213277). D.A. thank the Communauté française de Belgique for financial support in the frame of the ARC SUPRATUNE. The authors thank Nanocyl S.A. for providing the Nanocyl®-7000 and Arkema for providing Lotryl®28MA07.

References

[1] Tucker CL, Moldenaers P. Annu Rev Fluid Mech 2002;34:177–210.
[2] Van Puyvelde P, Velankar S, Moldenaers P. Curr Opin Colloid Interface Sci 2001;6(5–6):457–63.
[3] Fang Z, Harrats C, Moussaif N, Groeninckx GJ. Appl Polym Sci 2007;106 (5):3125–35.
[4] Fang Z, Xu Y, Tong L. Polym Eng Sci 2007;47(5):551–9.
[5] Khatua BB, Lee DJ, Kim HY, Kim JK. Macromolecules 2004;37(7):2454–9.
[6] Wang Y, Zhang Q, Fu Q. Macromol Rapid Commun 2003;24(3):231–5.
[7] Hong JS, Kim YK, Ahn KH, Lee SJ, Kim C. Rheol Acta 2007;46(4):469–78.
[8] Ray SS, Pouliot S, Bousmina M, Utracki LA. Polymer 2004;45(25):8403–13.
[9] Ray SS, Bousmina M. Macromol Rapid Commun 2005;26(20):1639–46.
[10] Ray SS, Bousmina M, Maazouz A. Polym Eng Sci 2006;46(8):1121–9.
[11] Fenouillot F, Cassagnau P, Majeste JC. Polymer 2009;50(6):1333–50.
[12] Binks BP. Curr Opin Colloid Interface Sci 2002;7(1–2):21–41.
[13] Elias L, Fenouillot F, Majesté JC, Alcouffe P, Cassagnau P. Polymer 2008;49 (20):4378–85.
[14] Ramsden W. Proc R Soc London Ser A 1903;72:156–64.
[15] Pickering SU. J Chem Soc Abstr 1908;91-92:2001–21.
[16] Tambe DE, Sharma MM. Adv Colloid Interface Sci 1994;52:1–63.
[17] Madivala B, Vandebril S, Fransaer J, Vermant J. Soft Matter 2009;5(8):1717–27.
[18] Iijima S. Nature 1991;354(6348):56–8.
[19] Harris PJF. Int Mater Rev 2004;49(1):31–43.
[20] Bose S, Bhattacharyya AR, Bondre AP, Kulkarni AR, Pötschke P. J Polym Sci B Polym Phys 2008;46(15):1619–31.
[21] Bose S, Bhattacharyya AR, Kulkarnia AR, Pötschke P. Compos Sci Technol 2009;69(3–4):365–72.
[22] Bose S, Ozdilek C, Leys J, Seo JW, Wubbenhorst M, Vermant J, et al. ACS Appl Mater Interfaces 2010;2(3):800–7.
[23] Baudouin A-C, Devaux J, Bailly C. Polymer 2010;51(6):1341–54.
[24] Baudouin A-C, Bailly C, Devaux J. Polym Degrad Stab 2010;95(3):389–98.
[25] Pagnoulle C, Jerome R. Polymer 2001;42(5):1893–906.
[26] Martin P, Maquet C, Legras R, Bailly C, Leemans L, van Gurp M, et al. Polymer 2004;45(10):3277–84.
[27] Grace HP. Chem Eng Commun 1982;14:225–77.
[28] Li Z-M, Li S-N, Xu X-B, Lu A. Polym Plastic Tech Eng 2007;46(2):129–34.
[29] Ali Z, Le HH, Illisch S, Radusch H-J. J Mater Sci 2008;44(3):443–50.

[30] Filippi S, Dintcheva NT, Scaffaro R, La Mantia FP, Polacco G, Magagnini P. Polym Eng Sci 2009;4(6):1187–97.
[31] Huitric J, Ville J, Médéric P, Moan M, Aubry T. J Rheol 2009;53(5):1101–19.
[32] Si M, Araki T, Ade H, Kilcoyne ALD, Fisher R, Sokolov JC, et al. Macromolecules 2006;39(14):4793–801.
[33] Yoo Y, Park C, Lee S-G, Choi K-Y, Kim DS, Lee J-H. Macromol Chem Phys 2005;206(8):878–84.
[34] Kontopoulou M, Liu Y, Austin JR, Parent JS. Polymer 2007;48(15):4520–8.
[35] Horozov TS, Binks BP. Angew Chem Int Ed 2006;45:773–6.
[36] Vermant J, Cioccolo G, Golapan KN, Moldenaers P. Rheol Acta 2004;43 (5):529–38.
[37] Elias L, Fenouillot F, Majesté JC, Martin G, Cassagnau P. Polymer 2007;48 (20):6029–40.
[38] Zhang Q, Yang H, Fu Q. Polymer 2004;45(6):1913–22.

Polymer 52 (2011) 157–163

Contents lists available at ScienceDirect

Polymer

journal homepage: www.elsevier.com/locate/polymer

Bacterial cellulose–laponite clay nanocomposites

Gustavo F. Perotti [a], Hernane S. Barud [b], Younes Messaddeq [b], Sidney J.L. Ribeiro [b], Vera R.L. Constantino [a,*]

[a] Instituto de Química da USP, Av. Prof. Lineu Prestes 748, CEP 05508-000, São Paulo, SP, Brazil
[b] Instituto de Química de Araraquara–UNESP, Rua Professor Francisco Degni s/n, CEP 14806-108, Araraquara, SP, Brazil

ARTICLE INFO

Article history:
Received 28 July 2010
Received in revised form
26 October 2010
Accepted 30 October 2010
Available online 4 November 2010

Keywords:
Bacterial cellulose
Clay
Nanocomposites

ABSTRACT

A novel material comprised of bacterial cellulose (BC) and Laponite clay with different inorganic–organic ratios (m/m) was prepared by the contact of never-dried membranes of BC with a previous dispersion of clay particles in water. Field emission scanning electron microscopy (FE-SEM) data of composite materials revealed an effective adhesion of clay over the surface of BC membrane; inorganic particles also penetrate into the polymer bulk, with a significant change of the surface topography even at 5% of clay loading. As a consequence, the mechanical properties are deeply affected by the presence of clay, increasing the values of the Young modulus and the tensile strength. However the maximum strain is decreased when the clay content is increased in the composite in comparison to pristine BC. The main weight loss step of the composites is shifted towards higher temperatures compared to BC, indicating that the clay particles slightly protect the polymer from thermal and oxidative decomposition.

1. Introduction

Polymer-clay nanocomposites (PCN) have attracted much attention in the materials science field, since the nanodispersion of clays in a polymeric matrix has proved to be a successful strategy to improve certain properties such as mechanical, thermal and gas barrier, in comparison to the unmodified matrix [1–5]. The behavior PCN materials depend on the interactions between the clay and the polymeric structure and also the intimate contact of both phases.

Several polymers have been used in the clay nanocomposites preparation such as poly(methyl methacrylate) (PMMA), poly (ethylene terephthalate) (PET), polypropylene (PP), epoxy resin, polyimide, ethylene vinyl acetate (EVA) and many others [6–11]. The use of biodegradable specimens as polymeric source for nanocomposite preparation was also reported. Poly(ε-caprolactone), poly(lactic acid), cellulose and its derivatives, starch and poly(hydroxybutyrate) are the main representative polymers of biodegradable group [12–17].

Clays can also be combined with conducting polymers, such as poly(aniline) in order to enhance its electronic properties [18]. Such improvements are often associated to a distinct mode of organization assumed by the polymeric chains when intercalated into the clay galleries [19]. Spectroscopic tools as Raman spectroscopy and electron paramagnetic resonance allied to X-ray diffraction are usually employed to characterize these novel materials [19,20].

Smectite, the most common kind of clay applied to develop nanocomposite materials, is a layered silicate group primarily constituted of Si and Al and/or Mg hydrates. It presents a central octahedral sheet containing commonly Al^{3+}, Fe^{3+}, Mg^{2+} and Fe^{2+} sites coordinated to either oxygen anions and hydroxyl groups and two tetrahedral sheets at the top and below, constituted of commonly Si^{4+}, Al^{3+} and Fe^{3+} coordinated to oxygen anions arranged in a hexagonal fashion [21], as shown in Fig. 1. The isomorphic substitution in octahedral sites by less charged specimens, such as Al^{3+} by Mg^{2+}, and also in the tetrahedral sites, such as Si^{4+} for Al^{3+}, is responsible for generating an excess of negative charge in the layer The electric charge is counterbalanced by the presence of cationic species, commonly Na^{+}, K^{+} and Ca^{2+}, in a region between subsequent layers called interlayer domain [21–23].

Laponite, a synthetic smectite clay produced by Laporte Industries [24], presents Mg^{2+} ions in the octahedral sites and also Li^{+} ions in minor amount; Na^{+} ions are in the interlayer domain. The chemical formula $Na_{0.7}[Mg_{5.5}Li_{0.4}\ Si_8O_{20}(OH)_4]$ is proposed to Laponite synthetic clay. This material shows plate-like particles with dimensions typically around 20–30 nm in length and 0.92 nm in width [25,26]. Besides its well-defined chemical composition and dimensions, the inexistence of common inorganic components generally carried in natural clays, such as silica and iron oxides, allows the production of clear and transparent colloidal suspensions of clay particles in water [24]. For this reason, Laponite is suitable for example in the preparation of new materials by casting

* Corresponding author. Tel.: +55 11 3091 2151.
E-mail address: vrlconst@iq.usp.br (V.R.L. Constantino).

0032-3861/$ – see front matter © 2010 Elsevier Ltd. All rights reserved.
doi:10.1016/j.polymer.2010.10.062

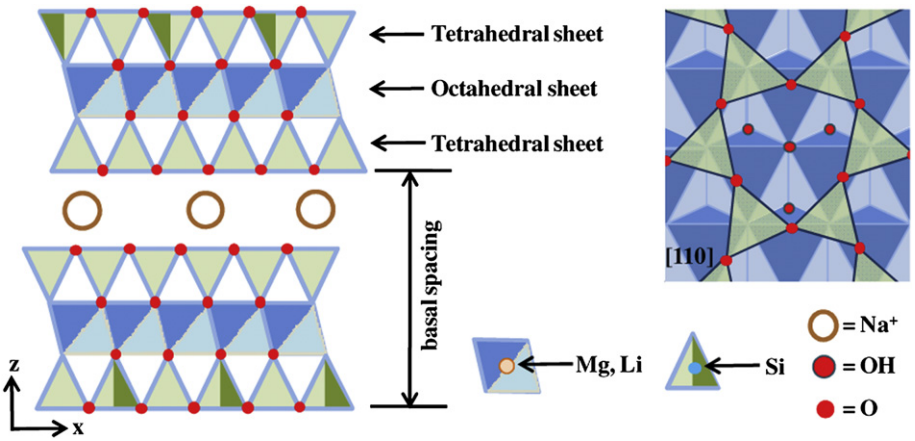

Fig. 1. Representative structure of Laponite synthetic clay (2:1 smectite).

method with potential active applications as host for rare earth ions [27] and also in the investigation of dye-clay systems through spectroscopic techniques [28]. Laponite properties have allowed its commercial application in household products, personal care items, horticulture and preparation of paper and polymer films [29].

Several applications of Laponite have been reported in the materials science field; among them, its combination with organic polymers of distinct natures. For highly hydrophobic polymers, such as polyethylene, an exchange of Na^+ ions for alkylammonium cations is generally required in order to increase the compatibility of both materials and guarantee a good dispersion of the inorganic filler in the polymeric matrix [30]. For hydrophilic polymers, such as poly(vinyl alcohol), usually the clay particles are used without further replacement of Na^+ ions in the interlayer domain. The water-based route to obtain nanocomposites in the cases where the polymer is soluble seems to be the most reasonable and viable method when the polymer processing by drastic methods, such as melt intercalation, could affect deeply in a disfavored way the properties of the organic counterpart.

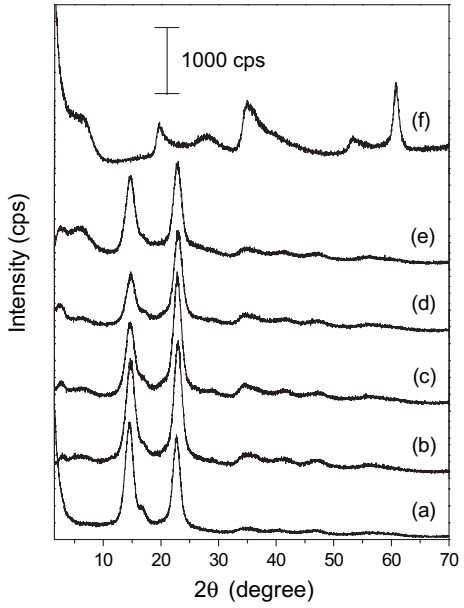

Fig. 2. XRD patterns of bacterial cellulose (a) BC-LP 5% (b) BC-LP 15% (c) BC-LP 30% (d) BC-LP 40% (e) Laponite (f).

Bacterial cellulose (BC), obtained by Gram-negative acetic acid bacteria *Acetobacter xylinum* (reclassified *Gluconacetobacter xylinus*), is a biopolymer with a great potential for development of new nanocomposite materials. The microorganism has the ability to secrete cellulose as part of its metabolism when submitted to a proper culture medium containing carbon and nitrogen sources. BC is produced as highly hydrated membranes (up to 99% water in mass), free of lignin and hemicelluloses, presenting higher crystallinity and degree of polymerization than vegetal cellulose, great elasticity, high wet strength and conformability [31–33].

The jelly-like membrane formed in static culture is characterized by a 3-D structure consisting of an ultrafine network of cellulose nanofibers ("nanocelluloses"), generating a greatly porous matrix capable of stabilizing inorganic particles and reinforce organic polymers [34,35].

Pristine BC membrane presents itself several applications, such as diaphragms for loudspeakers and headphones, commercially available by Sony Corp. [36], and also as support for Organic Light-Emitting Diodes (OLED) devices [37]. However the most promising application of BC is in the medical area for the treatment of burn injuries, due to its elevated water holding capacity, great air diffusion through the membrane, high Young modulus and also fully biocompatibility [38,39]. Bacterial cellulose can also be used in materials science, usually combined with inorganic particles. Organic–inorganic hybrids based on BC and silica have been prepared by sol-gel method [40,41]. The silica incorporated to the bacterial cellulose was able to increase the mechanical properties of

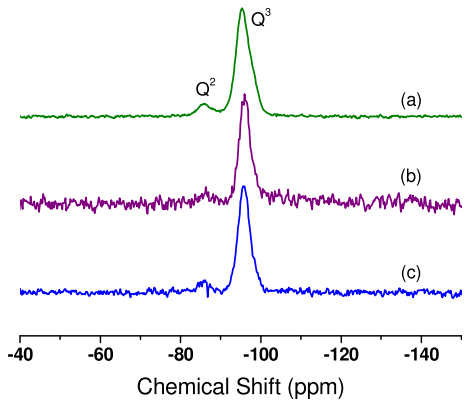

Fig. 3. ^{29}Si MAS-NMR spectra of Laponite (a) and the nanocomposites BC-LP 15% (b) and BC-LP 30% (c).

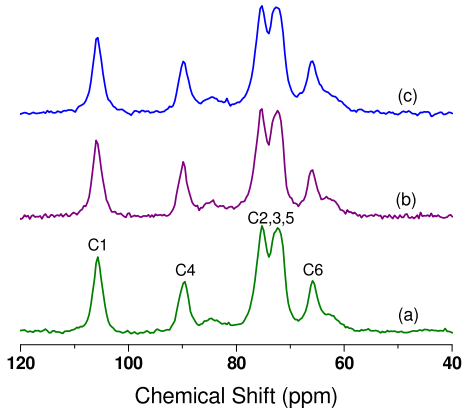

Fig. 4. ^{13}C MAS-NMR spectra of bacterial cellulose (a) and the nanocomposites BC-LP 15% (b) and BC-LP 30% (c).

the biopolymer [40]. Electron microscopies showed that BC membrane is an interesting template to control and stabilize silica nanoparticles [41].

PCN materials comprised of bacterial cellulose and Laponite clay can be interesting to produce high-technology devices. As it was mentioned above, BC membrane can be used as a flexible substrate to develop OLED devices for several applications (as for example the production of adhesives or stripes for usage in photodynamic therapy, PDT) [42]. In order to improve the performance of flexible OLED containing BC, it is necessary to reduce the water vapor and molecular oxygen transmission into the polymeric substrate [37]. PCN have recognized gas barrier property that is related to the morphology of the clay platelets, whose large aspect ratio increases the effective path length for gases diffusion [43]. Barrier properties are also important when considering the usage of biodegradable polymers (such as bacterial cellulose) for food packaging materials [44]. Taking into account the medical application of BC, Laponite particles containing cationic therapeutic species (antibiotics for example) can be dispersed into the biopolymer membrane and used for the topical drug delivery [45]. Nanocomposites of BC and Laponite can be modified and explored to produce ion-conducting membranes. PCN have been evaluated as solid electrolyte in batteries or electrochemical sensors for example [46].

The key point for an intimate contact between Laponite and BC lies on the dimensions of the employed precursors and the degree of inorganic particles delamination. Bacterial cellulose presents interconnected bundles of cellulose ribbons that produce a porous structure with average pore size of 200 nm [47]. On the other side, clay platelets of Laponite usually present the biggest dimension up to 30 nm [26], allowing it to cover virtually the whole exposed surface of the polymer. It is expected, as result of the large interface contact, an increase in the thermal and mechanical properties of the nanocomposites in comparison to pristine bacterial cellulose.

This work focuses on the preparation and characterization of hybrid bio-nanocomposites based on bacterial cellulose and Laponite clay in order to evaluate possible modifications in the structural, thermal and mechanical properties of BC after clay incorporation. BC-LP materials were characterized by X-ray diffractometry, mass coupled thermogravimetric analyses (TGA-MS), ^{29}Si and ^{13}C magic-angle spinning nuclear magnetic resonance (MAS-NMR) spectroscopy, field emission scanning electron microscopy (FE-SEM), and tensile measurements. To the best of our knowledge, studies involving the preparation of materials constituted of BC and clays were not reported before.

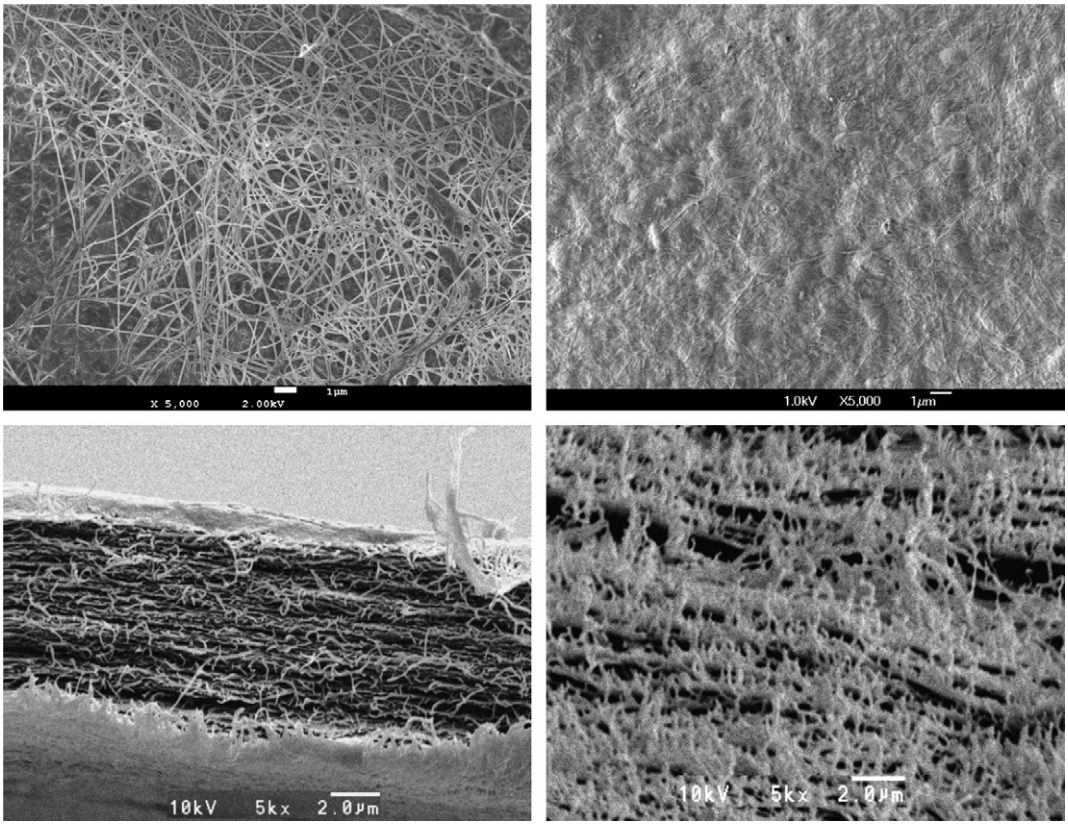

Fig. 5. FEG-SEM front images of bacterial cellulose (upper left) and BC-LP 5% (upper right) and cross section images of bacterial cellulose (lower left) and BC-LP 15% (lower right) (magnification = 5000×).

2. Experimental

2.1. Materials

Never-dried bacterial cellulose membranes were supplied by Fibrocel–Produtos Biotecnológicos LTDA (Brazil) and used as received. Laponite RD® was obtained from Bentonit União Nordeste (Brazil) and also used as received.

2.2. Preparation of BC-Laponite nanocomposites

Five never-dried stripes of bacterial cellulose (2 × 2 cm^2) weighting approximately 3.5 g were poured one by one into a 250 mL polypropylene beaker containing 200 mL of deionized water and the previously dispersed Laponite. The amount of clay added to each beaker was calculated after weigh each moist stripe. The used bacterial cellulose–clay (m/m) ratio was calculated by taking into account the mass of the wet stripe and the mass of Laponite. The clay proportions in BC-Laponite composites were 0, 5, 15, 30 and 40%; the samples were labeled as bacterial cellulose (sample without clay), BC-LP 5%, BC-LP 15%, BC-LP 30% and BC-LP 40% respectively. The mixtures of BC and Laponite in water were shaken in a mechanical shaker at 160 rpm for 3 days. After this time the stripes were removed from the beakers, washed with deionized water and dried at room temperature for 5 days.

2.3. Materials characterization

X-ray diffraction (XRD) patterns were collected on a Rigaku Miniflex diffractometer using Cu K_α radiation (λ = 1.5451 Å) equipped with Ni filter and operating at 30 kV and 15 mA. The utilized step size was 0.03° and the angular domain analyzed was comprised between 1.5 and 70°. Mass coupled thermogravimetric analyses (TGA-MS) were carried out on STA 490 PC Luxx equipment coupled to Aëolos 403C mass spectrometer at heating rate of 10 °C min^{-1}, using alumina crucible loaded with 15 mg of sample under 50 mL min^{-1} synthetic air flow. ^{29}Si and ^{13}C Magic-Angle Spinning Nuclear Magnetic Resonance (MAS-NMR) spectra were recorded in a Varian INOVA 300 (59.5 MHz for ^{29}Si and 75.4 MHz for ^{13}C) spectrometer using a silicon nitride rotor with 5 kHz spinning rate and sampling time of 0.050 s for a period of 12 h. The morphological changes caused by the presence of Laponite in the polymeric matrix were evaluated by field emission scanning electron microscopy (FE-SEM) on a JEOL JSM-7000F microscope using uncoated samples attached to a Cu ribbon.

2.4. Tensile properties

The tensile measurements were performed with a Dynamic Mechanical Analyzer 2980 (TA Instruments) equipped with a film tension clamp at 27 °C. The specimens dimensions were 18.00 mm × 1.800 mm × 0.03 mm (length × width × thickness). It was used a preload force of 0.01 N and the force ramp 8 N m^{-1} until the rupture of sample. The device was previously calibrated and a total of 5 measurements for each sample were made in order to ensure the reproducibility of the results.

3. Results and discussion

The XRD patterns of dried bacterial cellulose, Laponite and all prepared BC-LP nanocomposite films are shown in Fig. 2.

Pristine bacterial cellulose film shows the presence of two main diffraction peaks in the analyzed region, specifically in the 15–22° (2θ) range, assigned to the distinct phases known as 1α and 1β. The phase 1 is related to the uniaxial arrangement of the linear β-1,4 glucan chains while the α and β index are associated to the crystalline structure of these linear chains: triclinic and monoclinic, respectively [48–50]. For all composite samples, there is a change on the relative intensity of these two diffraction peaks after Laponite loading, suggesting a rearrangement of the polymer chains. Considering only XRD patterns, it is not possible to confirm which crystalline structure (1α or 1β) is mainly affected by the presence of Laponite since both peaks present contribution of the polymorphs [51].

To confirm the close interaction between the clay platelets and cellulose chains it is noticeable for all samples a small peak around 2.5–3.0° (2θ) associated to a Laponite basal spacing ranging from 3.0 to 3.5 nm. XRD pattern of Laponite in the sodium cation form has a broad peak at about 5–6° (2θ) associated to the (001) basal spacing of about 1.3 nm. The increase in the basal spacing after contact with BC polymer suggests the polymer chains intercalation. Considering the clay layer thickness as 0.92 nm [22,26], an interlayer space of about 2.1–2.6 nm is resulted as the presence of guest species with considerable dimensions. Probably, several glucose chains are confined between adjacent clay platelets.

^{29}Si solid-state NMR spectra of Laponite and two representative BC-LP nanocomposites are shown in Fig. 3. The NMR spectrum of Laponite shows a large peak at −95 ppm assigned to the Q^3 units, interpreted as SiO_4 group connected by three oxygen atoms to three other SiO_4 groups in the same sheet and linked to the octahedral

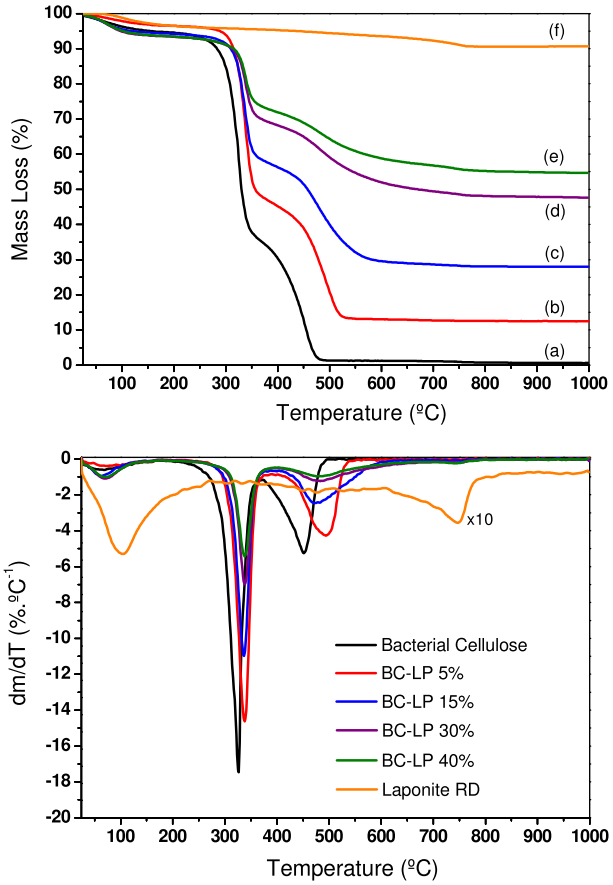

Fig. 6. TG curves (upper graphic) of bacterial cellulose (a); BC-LP 5% (b); BC-LP 15% (c); BC-LP 30% (d); BC-LP 40% (e); Laponite (f). DTG curves (lower graphic) of bacterial cellulose (black); BC-LP 5% (red); BC-LP 15% (blue); BC-LP 30% (purple); BC-LP 40% (green); Laponite (orange). (For interpretation of the references to colour in this figure legend, the reader is referred to the web version of this article).

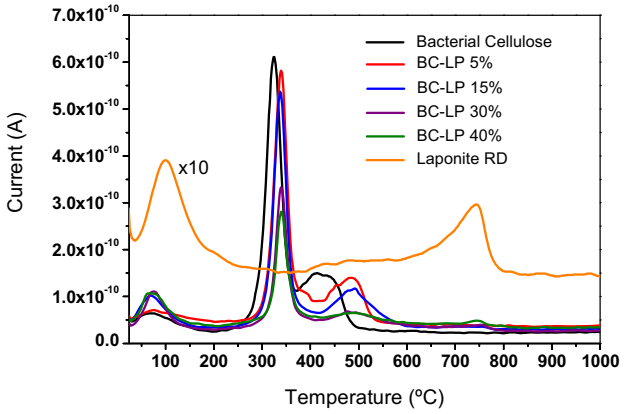

Fig. 7. MS curves related to fragment $m/z = 18$ of bacterial cellulose (black); BC-LP 5% (red); BC-LP 15% (blue); BC-LP 30% (purple); BC-LP 40% (green); Laponite (orange). (For interpretation of the references to colour in this figure legend, the reader is referred to the web version of this article).

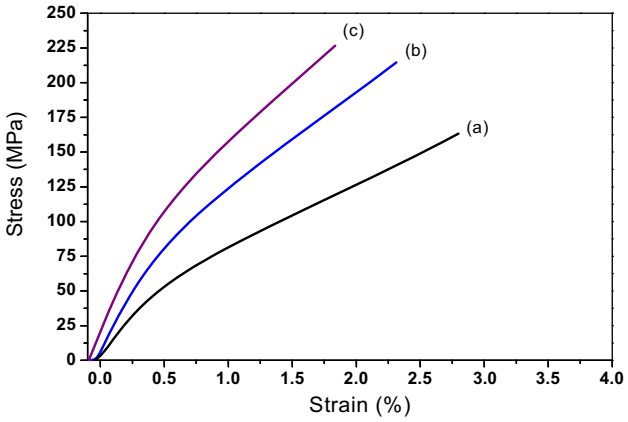

Fig. 9. Stress–strain curves of bacterial cellulose (a) and the nanocomposites reinforced with 15% (b) and 30% (c) of Laponite.

sheet by one oxygen atom (*i.e.*, $Si(OMg)(OSi)_3$ units) [52–54], as shown in Fig. 1. Another signal, around −85 ppm and assigned to Q^2 sites, arises from the SiO_4 groups at the layer edges having terminal silanol groups (*i.e.*, $Si(OMg)(OSi)_2(OH)$ units).

The NMR spectra of BC-Laponite nanocomposites reveal that the signal of Q^3 sites is substantially similar to the Laponite signal, suggesting that the abundant Q^3 silicon nuclei were almost unaffected in the nanocomposite formation. In other words, BC microfibril was able to preserve the Laponite layer structure. The ^{13}C MAS-NMR spectra of BC and BC-Laponite nanocomposites (Fig. 4) show the expected peaks for the carbon atoms of polymer chain: 105.7 ppm (C_1), 89.8 ppm (C_4), 75.2–72.3 ppm (C_2, C_3, C_5) and 65.9 ppm (C_6) [55,56]. The sharp peak in the 89.8 ppm is associated to crystalline regions of the polymer while the broad signal centered at 84 ppm is related to disordered domains and crystalline surfaces [56]. Broad peak observed at about 62 ppm as a shoulder in the C_6 peak is also attributed to amorphous regions. The ^{13}C MAS-NMR spectral profiles of BC-Laponite nanocomposites reveal no significant modifications in comparison to the pristine BC. It is possible to infer that conformation modifications are not occurring. ^{13}C MAS-NMR technique seems insensitive to hydrogen interactions between the cellulose carbon chain and the inorganic hydrophilic surface.

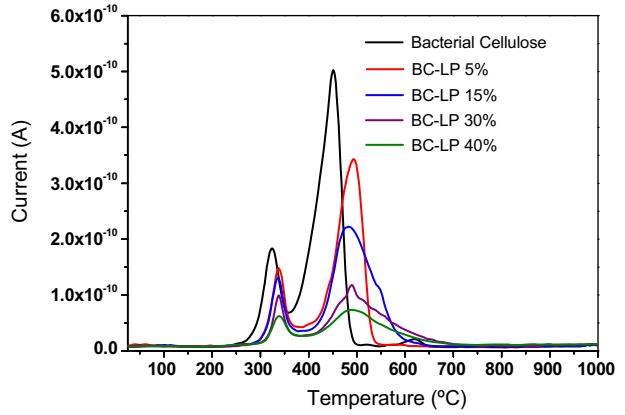

Fig. 8. MS curves related to fragment $m/z = 44$ of bacterial cellulose (black); BC-LP 5% (red); BC-LP 15% (blue); BC-LP 30% (purple); BC-LP 40% (green). (For interpretation of the references to colour in this figure legend, the reader is referred to the web version of this article).

The morphological modifications of bacterial cellulose structure promoted by the presence of clay were investigated by FE-SEM technique, as shown in Fig. 5. Bacterial cellulose itself presents a fibrilar organization where each fibril is comprised about a thousand of single linear glucan chains [32], forming a net-like structure with large holes. On the other hand, Laponite particles are well known by its plate-like shape, around 30 nm in diameter [26] and, due to its small size, clay particles can easily penetrate inside the cellulose matrix, keeping a close interaction with the polymer. Even at 5% (m/m) of clay loading, it is noticed a large deposition over the BC surface; for the material loaded with 15% of clay, its cross section image also shows a close interaction with bulk microfibrils, evidencing that the Laponite can also penetrate through the surface pores of BC (Fig. 5). It is believed that some particles are able to penetrate over the fibrils in a deeper interaction with glucan chains (as also evidenced by the presence of intercalation peaks in the XRD data). It was observed drastic change in the materials when the clay content in the composite is increased. For example, the material having 40% of Laponite presents a sandy aspect and is not possible even to distinguish the bacterial cellulose surface (FE-SEM image not shown), evidencing a high extension of interactions between the inorganic filler and the hydrophilic organic polymer.

The TGA-MS and DTG data of bacterial cellulose, Laponite and BC-LP nanocomposites are shown in Fig. 6. As it is expected, the increase of the clay content in the hybrid materials results in an increase of residual mass (comprised practically of clay thermal decomposition by-products). All the BC-LP materials present the first weight loss step associated to the water release (dehydration process occurring up to about 150 °C), noticed in TGA curves but better visualized in DTG curves (Fig. 6). The estimated water content for each BC-LP sample ranges from 3.5 to 7%. Laponite clay releases about 6% of interparticle and intercalated water up to 300 °C.

Table 1
Values of tensile strength, strain at rupture and Young modulus of bacterial cellulose and the nanocomposites BC-LP 15% and BC-LP 30%.

Samples	Tensile strength/ MPa	Strain at rupture/ MPa	Young modulus/ GPa
Bacterial Cellulose	164	2.80	11.6
BC-LP 15%	215	2.31	16.9
BC-LP 30%	227	1.83	21.0

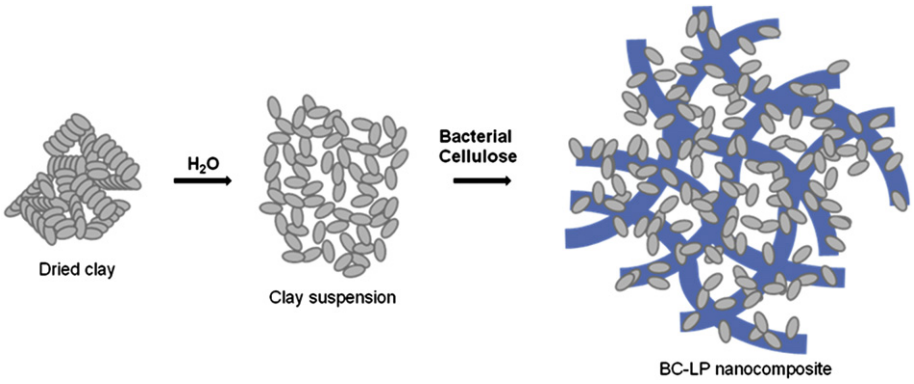

Scheme 1. Representative process of clay exfoliation and subsequent nanocomposite formation after interaction with bacterial cellulose.

The second weight loss step shows a small shift towards higher temperatures when clay content is increased, beginning at 228 °C for bacterial cellulose and at 268 °C for the BC-LP 40% sample, according to DTG data (Fig. 6). The clay presence in the polymeric matrix should act as a protective barrier against the decomposition of the carbon chain, shifting the beginning of the decomposition process. Clay particles can make difficult the polymer contact with molecular oxygen; the establishment of hydrogen bonds between organic and inorganic parts can also cause difficulties to the release of water molecules produced by the condensation of hydroxyl groups of cellulose. Considering that water is the main volatile species released in the second event, char can be formed. Usually the presence of clay makes the formed char a better insulator and barrier to the generated gases [2]. A third weight loss step related to the organic phase is observed above 350 °C. Laponite clay is thermal stable up to about 650 °C; the clay layers dehydroxylation process is observed above this temperature.

Another collected data from TGA curves are the real composition of each nanocomposite prepared. Considering that the weight loss up to 650 °C is only associated to the adsorbed water release and the BC decomposition, it is possible to estimate the mass of clay incorporated within each obtained hybrid material. Hence, considering that the weight of the residue obtained at 650 °C is the Laponite content, BC-LP X % samples (where $X = 5$, 15, 30 and 40%) have about 13, 29, 50 and 58% (m/m) of the synthetic clay, respectively. This increment in the Laponite content in the BC-LP nanocomposite occurs due to the final drying process to obtain the hybrid materials, which elevates considerably the percentage of the inorganic phase in the dried product. Before the drying step, the BC-LP materials contain a large content of water and a small amount of polymer and clay. However after drying the opposite takes place (Fig. 6 shows that the water amount in BC-LP materials is really low).

The MS curves associated to the fragments $m/z = 18$ and $m/z = 44$ (assigned to the release of water and carbon dioxide molecules, respectively) are shown in Fig. 7 and Fig. 8. It is noticed that the second weight loss step is mainly comprised of water loss associated with a small release of CO_2 (due to the beginning of the organic chain oxidation). It is relevant to notify that pristine BC decomposition at about 320 °C (second event) is sensitive to the atmosphere, as shown in Supplementary data. Also it was noticed that the event is endothermic under nitrogen flow and exothermic under synthetic air (DTA data not show). These data corroborate the partial oxidative nature of the process. On the other hand, pristine bacterial cellulose produces more CO_2 than water in the third weight loss event, but the relative intensity of the two gases release seems to change appreciably when the Laponite content is increased in the composite samples (Figs. 7 and 8).

It is also observed that the third mass loss step starts at 358 °C for pristine BC and at 402 °C for the BC-LP 40% nanocomposite. For this sample a weight loss event at higher temperature (around 650–700 °C) is related to water release from clay dehydroxylation, detected only in high-content clay materials due to the small extension of this phenomenon. Higher quantities of clay in the BC-LP nanocomposites also make wider the third event of mass loss. No other gaseous fragments were detected in appreciable quantities under the experimental conditions used in the present work.

The stress–strain curves of the bacterial cellulose and the BC-LP composites containing 15% and 30% of inorganic filler are shown in Fig. 9. All curves presented two typical distinct regions: the first one, from the beginning to low values of strain with linear shape, is related to an elastic deformation of the material, whereas the second part of the curve is associated to a plastic deformation of the material after reaching the yield point until the rupture. The increase of Laponite content in the nanocomposites tends to increase the values of the yield strength and the elastic modulus, as summarized in Table 1.

By increasing the clay content, the values of tensile strength and modulus raise, in comparison to pristine BC. It can be proposed that the occurrence of strong hydrogen bond interactions between both inorganic and organic parts hinders the slippage of the fibrils in a large extension, causing either an increase of the necessary force to disrupt the structure and also reducing the maximum strain.

The proposed schematic representation of the nanocomposite formation is shown in Scheme 1.

At first, the disk-like Laponite particles exfoliate in the presence of water at room temperature due to an osmotic swelling mechanism [57]. After mixing the polymer and the exfoliated suspension of clay occurs a strong interaction between the inorganic platelets and the hydroxyl groups of bacterial cellulose causing the formation of homogeneous thin film after dryness.

4. Conclusion

Bacterial Cellulose and Laponite nanocomposites were successfully prepared using increasing amounts of the inorganic modifier in the polymeric matrix. According to XRD data, the presence of clay affects directly the ratio of the crystalline structures presented in the BC. A small diffraction peak observed in the low angle region for all prepared materials suggests the production of both intercalated and exfoliated nanocomposites.

^{29}Si and ^{13}C MAS-NMR data were not able to show any significant change due to the established interaction between organic and inorganic parts. TGA data showed a shift to higher temperature of the beginning of decomposition process of the nanocomposites in comparison to the pristine BC. MS curves also reveal that the

profiles of water and carbon dioxide liberation were changed as well, increasing the decomposition onset temperature.

The pristine bacterial cellulose morphology was deeply affected by the clay content, showing the strong interaction involving organic–inorganic phases, and also the Laponite ability, regarding its small dimension, to penetrate into the polymer cavities originated by its net-like structure. Mechanical properties of the nanocomposites also vary as function of clay content. Rising the clay content in the BC-LP films, it is observed an increase in the tensile strength. On the other hand, it causes a decrease in the final strain of the films.

BC-LP nanocomposites can be explored in the medical field for topical drug delivery, for example, remembering that both organic and inorganic counterparts present high purities and Laponite has a high cation exchange capacity. The inorganic filler can improve the mechanical properties of BC matrix opening also opportunities to build new OLED devices.

Acknowledgements

The authors acknowledge the Brazilian agencies FAPESP (Fundação de Amparo à Pesquisa do Estado de São Paulo), CNPq (Conselho Nacional de Desenvolvimento Científico e Tecnológico) and CAPES (Coordenação de Aperfeiçoamento de Pessoal de Nível Superior) for the financial support and fellowships.

Appendix. Supplementary data

Supplementary data related to this article can be found online version at doi:10.1016/j.polymer.2010.10.062.

References

[1] Alexandre M, Dubois P. Mater Sci Eng R Rep 2000;28(1–2):1–63.
[2] Ray SS, Bousmina M. Prog Mater Sci 2005;50(8):962–1079.
[3] Pandey JK, Kumar AP, Misra M, Mohanty AK, Drzal LT, Singh RP. J Nanosci Nanotechnol 2005;5(4):497–526.
[4] Ray SS, Okamoto M. Prog Polym Sci 2003;28(11):1539–641.
[5] Paul DR, Robeson LM. Polymer 2008;49(15):3187–204.
[6] Calcagno CIW, Mariani CM, Teixeira SR, Mauler RS. Polymer 2007;48(4): 966–74.
[7] Salahuddin N, Shehata M. Polymer 2001;42(20):8379–85.
[8] Kornmann X, Lindberg H, Berglund LA. Polymer 2001;41(10):4493–9.
[9] Rohlmann CO, Failla MD, Quinzani LM. Polymer 2006;47(22):3442–7.
[10] Duquesne S, Jama C, Le Bras M, Delobel R, Recourt P, Gloaguen JM. Compos Sci Technol 2003;63(8):1141–8.
[11] Magaraphan R, Lilayuthalert W, Sirivat A, Schwank JW. Compos Sci Tech 2001;61(9):1253–64.
[12] Chivrac F, Pollet E. Averous Mater Sci Eng R 2009;67(1):1–17.
[13] Lepoittevin B, Devalckenaere M, Pantoustier N, Alexandre M, Kubies D, Calberg C, et al. Polymer 2002;43(14):4017–23.
[14] Ray SS, Maiti P, Okamoto M, Yamada K, Ueda K. Macromolecules 2002;35(8): 3104–10.
[15] Park HM, Misra M, Drzal LT, Mohanty AK. Biomacromolecules 2004;5(6): 2281–8.
[16] Choi WM, Kim TW, Park OO, Chang YK, Lee JW. J Appl Polym Sci 2003;90(2): 525–9.
[17] Romero RB, Leite CAP, Gonçalves MD. Polymer 2009;50(1):161–70.
[18] do Nascimento GM, Constantino VRL, Temperini MLA. Macromolecules 2002; 35(20):7535–7.
[19] do Nascimento GM, Constantino VRL, Landers R, Temperini MLA. Polymer 2006;47(17):6131–9.
[20] do Nascimento GM, Constantino VRL, Landers R, Temperini MLA. Macromolecules 2004;37(25):9373–85.
[21] Brigatti MF, Galan E, Theng BKG. Structures and mineralogy of clay minerals. In: Bergaya F, Theng BKG, Lagaly G, editors. Handbook of clay science, vol. 1. Amsterdam: Elsevier; 2006. p. 35–43.
[22] Brindley GW. Order–disorder in clay mineral structure. In: Brindley GW, Brown G, editors. Crystal structures of clay minerals and their x-ray identification, vol. 1. London: Mineralogical Society; 1980. p. 2–3.
[23] Powell CE, Beall GW. Curr Opin Solid State Mater Sci 2006;10(2):73–80.
[24] Laponite–Structure, chemistry and relationship to natural clays, Technical Bulletin Laponite L104/90/A, Laporte Absorbents, Cherise, United Kingdom.
[25] Kaviratna PD, Pinnavaia TJ, Schroeder PA. J Phys Chem Solids 1996;57(12): 1897–906.
[26] Mourchid A, Lécolier E, Van Damme H, Levitz P. Langmuir 1998;14(17): 4718–23.
[27] Tronto J, Ribeiro SJL, Valim JB, Gonçalves RR. Mater Chem Phys 2009;113(1): 71–7.
[28] Dias PM, de Faria DLA, Constantino VRL. Clays Clay Miner 2005;53(4): 361–71.
[29] Laponite: performance additives, Brochure produced by Rockwood Additives Limited, Cheshire, United Kingdom (available in http://www.laponite.com).
[30] Wang KH, Xu M, Choi YS, Chung IJ. Polym Bull 2001;46:499–505.
[31] Klemm D, Heublein B, Fink HP, Bohn A. Angew Chem Int Edit 2005;44(22): 3358–93.
[32] Czaja W, Krystynowicz A, Bielecki S, Brown Jr RM. Biomaterials 2006;27(2): 145–51.
[33] Putra A, Kakugo A, Furukawa H, Gong JP, Osada Y. Polymer 2008;49(7): 1885–91.
[34] Yano H, Sugiyama J, Nakagaito AN, Nogi M, Matsuura T, Hikita M, et al. Adv Mater 2005;17(2):153–5.
[35] Maneerung T, Tokura S, Rujiravanit R. Carbohydr Polym 2007;72(1):43–51.
[36] Iguchi M, Yamanaka S, Budhiono A. J Mater Sci 2000;35(2):261–70.
[37] Legnani C, Vilani C, Calil VL, Barud HS, Quirino W, Achete CA, et al. Thin Solid Films 2008;517(3):1016–20.
[38] Czaja WK, Young DJ, Kaweck M, Brown Jr RM. Biomacromolecules 2007;8(1): 1–12.
[39] Gatenholm P, Klemm D. Mater Res Soc Bull 2010;35(3):208–13.
[40] Maeda H, Nakajima M, Hagiwara T, Sawaguchi T, Yano S. J Mater Sci 2006; 41(17):5646–56.
[41] Barud HS, Assunção RMN, Martines MAU, Dexpert-Ghys J, Marques RFC, Messaddeq Y, et al. J Sol-Gel Sci Technol 2007;46(3):363–7.
[42] Attili SK, Lesar A, McNeill A, Camacho-Lopez M, Moseley H, Ibbotson S, et al. Br J Dermatol 2009;161(1):170–3.
[43] Thostenson ET, Li C, Chou T. Compos Sci Technol 2005;65(3–4):491–516.
[44] de Azeredo HMC. Food Res Int 2009;42(9):1240–53.
[45] Viseras C, Aguzzi C, Cerezo P, Bedmar MC. Mater Sci Technol 2008;24(9): 1020–6.
[46] Aranda P, Darder M, Fernandez-Saavedra R, Lopez-Blanco M, Ruiz-Hitzky E. Thin Solid Films 2006;495(1–2):104–12.
[47] Sanchavanakit N, Sangrungraungroj W, Kaomongkolgit R, Banaprasert T, Pavasant P, Phisalaphong M. Biotechnol Prog 2006;22(4):1194–9.
[48] Atalla RH, Vanderhart DL. Science 1984;223(4633):283–5.
[49] Czaja W, Romanovicz D, Brown Jr M. Cellulose 2004;11(3(4)):403–11.
[50] Koyama M, Helbert W, Imai T, Sugiyama J, Henrissat B. Proc Natl Acad Sci USA 1997;94(17):9091–5.
[51] Barud HS, Ribeiro CA, Crespi MS, Martines MAU, Dexpert-Ghys J, Marques RFC, et al. J Therm Anal Calorim 2007;87(3):815–8.
[52] Mandair APS, Michael PJ, McWhinnie WR. Polyhedron 1990;9(4):517–25.
[53] Borsacchi S, Geppi M, Ricci L, Ruggeri G, Veracini CA. Langmuir 2007;23(7): 3953–60.
[54] Daniel LM, Frost RL, Zhu HY. J Colloid Interface Sci 2008;321(2):302–9.
[55] VanderHart DL, Atalla RH. Macromolecules 1984;17(8):1465–72.
[56] Shezad O, Khan S, Khan T, Park JK. Carbohydr Polym 2010;82(1):173–80.
[57] Mongondry P, Tassin JF, Nicolai T. J Colloid Interface Sci 2005;283:397–405.

Polymer 52 (2011) 164–171

Contents lists available at ScienceDirect

Polymer

journal homepage: www.elsevier.com/locate/polymer

Monomer sequence of partially hydrolyzed poly(4-*tert*-butoxystyrene) and morphology of diblock copolymers composing this polymer sequence as one block

Siti Sarah Abdul Rahman, Daisuke Kawaguchi, Yushu Matsushita*

Department of Applied Chemistry, Graduate School of Engineering, Nagoya University, Furo-cho, Chikusa-ku, Nagoya 464-8603, Japan

ARTICLE INFO

Article history:
Received 2 September 2010
Received in revised form
1 November 2010
Accepted 7 November 2010
Available online 13 November 2010

Keywords:
Hydrolysis
Poly(4-hydroxystyrene)
Monomer sequence

ABSTRACT

The molecular characteristics of poly(4-*tert*-butoxystyrene) (O) upon hydrolysis reaction were investigated. It is known that O can be converted into poly(4-hydroxystyrene) (H) through hydrolysis reaction using strong acid. In this study, a set of poly(4-*tert*-butoxystyrene-*co*-4-hydroxystyrene)s (O/H copolymers) having various conversion rates, f_Hs, were prepared. Hydrolysis reaction is found to occur uniformly by matrix-assisted laser desorption ionization time-of-flight mass spectrometry (MALDI-TOF MS) where the average f_H obtained was consistent with that from ^{1}H NMR though a certain distribution in the number of hydrolyzed units was conceived. Monomer sequence of O/H copolymers was determined by ^{13}C NMR and the changes in triad concentration were obtained by spectra subtraction method. As a result, ^{13}C NMR reveals that O and H are statistically distributed. To evaluate the effect of hydrolysis on microphase-separated structure, we observed the morphology of partially hydrolyzed poly(4-*tert*-butylstyrene-*block*-4-*tert*-butoxystyrene) (BO) by transmission electron microscopy (TEM) and small-angle X-ray scattering (SAXS). Samples with f_H from 0.21 to 0.67 form both lamellar (major component) and cylindrical (minor component) structures reflecting both the statistical manner of hydrolysis reaction and the possible localized distribution of H sequence.

1. Introduction

To polymerize two or more monomers having inherently different properties is one of the supreme goals to control the structure and physical properties of copolymers. Although the technology is not complete yet at the stage, monomer sequence is one of the responsible factors determining the structures and properties of copolymers. Many reports have shown that the morphology [1–6] and surface and interfacial [7–13], thermal [14–16], and mechanical [5,6,17–22] properties, etc. are not a simple function of copolymer compositions but significantly depend on their monomer sequence. Although the common method in preparing copolymers is copolymerization, chemical modification of polymers having reactive functional group is another suitable method. For examples, polydiene, polyester and polyamine, etc. can be converted into copolymers easily through hydrolyzation [3,23–35], hydrogenation [35–37], sulfonation [3,38,39] or fluorination [40–43], etc. In these cases, understanding how a polymer undergoes a chemical reaction is important to clarify the relation between molecular structures of the copolymers and their properties.

One well-studied polymer reaction is hydrolysis. The reaction is easily performed by using either acid or base and easily controlled by the reaction time and acid or base concentration. The kinetics of hydrolysis reaction of polymers has been evaluated in the studies for acrylate, methacrylate and acrylamide polymers [27–29,31–34]. In these reports, it is believed that the neighboring component governs the reaction path, resulting in the formation of blocky sequence. However, the other paper reported that poly(*tert*-butyl acrylate) can be hydrolyzed statistically since the effect of neighboring components is reduced because of steric hindrance of bulky side chain [32]. Hence, monomer sequence may be determined not only by the reaction mechanism but also by the chemical structure or the stiffness of the chain.

In this work, the characterization of poly(4-*tert*-butoxystyrene) (O) upon hydrolysis reaction was conducted. O can be easily converted into poly(4-hydroxystyrene) (H) through hydrolysis reaction using a strong acid. Due to the bulky structure of O, the effect of microstructure on hydrolysis reaction is focused. Besides, since O is a hydrophobic polymer but H is a hydrophilic one [44], degree of hydrolysis makes it possible to produce a set of copolymers, which

* Corresponding author. Tel.: +81 52 789 4604; fax: +81 52 789 3210.
E-mail addresses: sitisarah@nagoya-u.jp (S.S.A. Rahman), daisuke@apchem.nagoya-u.ac.jp (D. Kawaguchi), yushu@apchem.nagoya-u.ac.jp (Y. Matsushita).

0032-3861/$ – see front matter © 2010 Elsevier Ltd. All rights reserved.
doi:10.1016/j.polymer.2010.11.010

have various interactions with other polymers depending on the extent. Therefore, we studied the morphologies of the block copolymers having partially hydrolyzed O chains as one block component at various conversion rates. Here, we employed poly(4-*tert*-butylstyrene-*block*-4-*tert*-butoxystyrene) (BO) where the relation between monomer sequence and microphase-separated structure was investigated.

2. Experimental section

2.1. Preparation of polymers

The syntheses of O homopolymer and BO were conducted by living anionic polymerizations in THF at −78 °C under vacuum using *sec*-BuLi and methanol as an initiator and a terminator, respectively. For BO, 4-*tert*-butylstyrene and 4-*tert*-butoxystyrene were added sequentially. Number-average molecular weights, M_ns, were determined by matrix-assisted laser desorption ionization time-of-flight mass spectrometry (MALDI-TOF MS) (AXIMA-CFR Plus Kratos-Shimadzu) and membrane osmometry (OSMOMAT090, Gonotec GmbH). Molecular weight distribution, M_w/M_n, was obtained from gel permeation chromatography (GPC) (HLC-8020, Tosoh Corp.). Volume fraction of B, φ_B, in BO was estimated from ^{1}H NMR (Varian INOVA, Varian). Table 1 represents the molecular characteristics of the polymers.

2.2. Hydrolysis reaction

Hydrolysis reaction was conducted by heating 5 wt.% of 1,4-dioxane solutions of O and BO under the presence of concentrated hydrochloric acid (HCl). The conversion from O into H, f_H, was controlled by reaction time, temperature, and HCl concentration; and was measured by ^{1}H NMR at 500 MHz.

2.3. Characterization of O/H copolymers

To investigate how hydrolysis reaction proceeded, the characterization of partially hydrolyzed O homopolymers was carried out. The uniformity of hydrolysis reaction was analyzed by MALDI-TOF MS. The matrix and ionization agent used were 2,5-dihydroxyl benzoic acid (DHBA) and sodium trifluoroacetate, respectively. Matrix (3 wt.% THF solution), ionization agent (0.1 wt.% methanol solution) and O/H copolymer (0.1 wt.% THF solution) were mixed at the ratio of 10:2:3. Nitrogen laser of 337 nm was used and measurement was conducted using reflection mode. Monomer sequence distribution in O/H copolymers was examined by ^{13}C NMR at 125 MHz. Samples were dissolved in THF-*d8* at 10 wt.%. THF signal was used as a reference peak. The Varian-based data were imported into personal computer using Mestre-C [45]. The aggregation states of O/H copolymers were investigated by differential scanning calorimetry (DSC) (EXTAR 6100, Seiko Instruments) at a heating rate of 10 °C/min under nitrogen atmosphere.

Table 1
Molecular characteristics of samples.

	M_n	M_w/M_n	φ_B	N^c
O	4k[a]	1.05	–	23
BO	67k[b]	1.02	0.45	399

[a] Determined by MALDI-TOF MS.
[b] Determined by membrane osmometry.
[c] Degree of polymerization, *N*.

2.4. Morphological observation

The effect of hydrolysis on the morphology of BO was evaluated. Microphase-separated structures of hydrolyzed BOs were examined by transmission electron microscopy (TEM) (H-7100, Hitachi) and small-angle X-ray scattering (SAXS). Film samples were prepared by casting the hydrolyzed BOs from their THF solutions. Films were then vacuumed dry for a day at 50 °C to remove the remaining solvent and finally annealed at 190 °C under vacuum for 3 days. Because H is prone to cross-linking, the annealed samples were checked by GPC. Even though the samples were annealed at a high temperature, only a small part of the samples could be cross-linked, whereas most of them were still in their original state. Therefore, the formation of microphase-separated structure were not affected by the cross-linking of H. For TEM observation, films were cut into ultrathin film of 50 nm thickness and stained with ruthenium tetroxide (RuO_4). TEM was conducted at 100 kV. SAXS measurement was carried out at BL-15A, Photon Factory, High Energy Accelerator Research Organization, Japan. Camera length was 2.3 m and the X-ray wavelength was 0.15 nm.

3. Results and discussion

The conversion rates of hydrolysis reaction for O homopolymer and BO are shown in Fig. 1. Three different reaction conditions were employed by varying the reaction temperature and HCl concentration. Throughout the experiments, the f_H values were found to increase linearly with an increase in reaction time. Evidently, hydrolysis reaction rate becomes higher at high temperature and high HCl concentration conditions. Hence, samples having f_H ranging from 0 to 1 were managed to be prepared by controlling the time, temperature and HCl concentration of the hydrolysis reaction.

To investigate the uniformity of hydrolysis reaction, MALDI-TOF MS measurements of O/H copolymers were conducted. Measurements for O and H homopolymers were conducted before analyzing O/H copolymers to confirm the good combination among matrix, ionization agent and polymer in order to obtain homogenously dispersed samples [46,47]. Fig. 2a represents MALDI-TOF MS spectrum for O homopolymer. The peaks in the spectrum are regularly spaced by *m*/*z* 176, which equals to the molecular weight of 4-*tert*-butoxystyrene. A representative peak at *m*/*z* 3955.7 indicates an O homopolymer having a degree of polymerization, *N*, equals to 22. This can be calculated as, $[C_4H_9\text{-}(C_{12}H_{16}O)_{22}\text{-}H\ Na^+] = 57.07 + (22 \times 176.12) + 1.01 + 22.99 = 3955.7$. Based on this, each peak can be assigned to a specific *N*. The MALDI-TOS MS spectrum of H homopolymer measured with the same manner as O homopolymer is

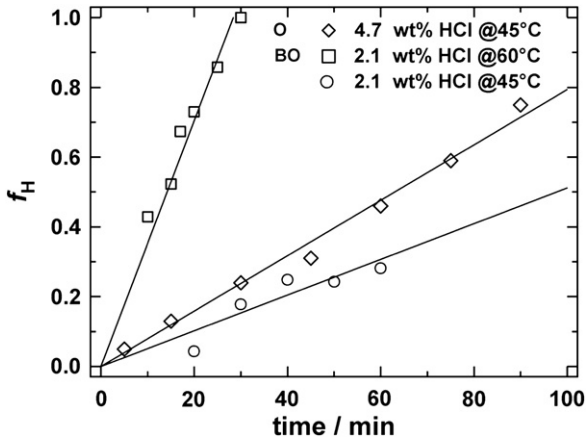

Fig. 1. Relation between conversion rate, f_H, and reaction time for O homopolymer and BO block copolymer. Solid lines are for eye guide.

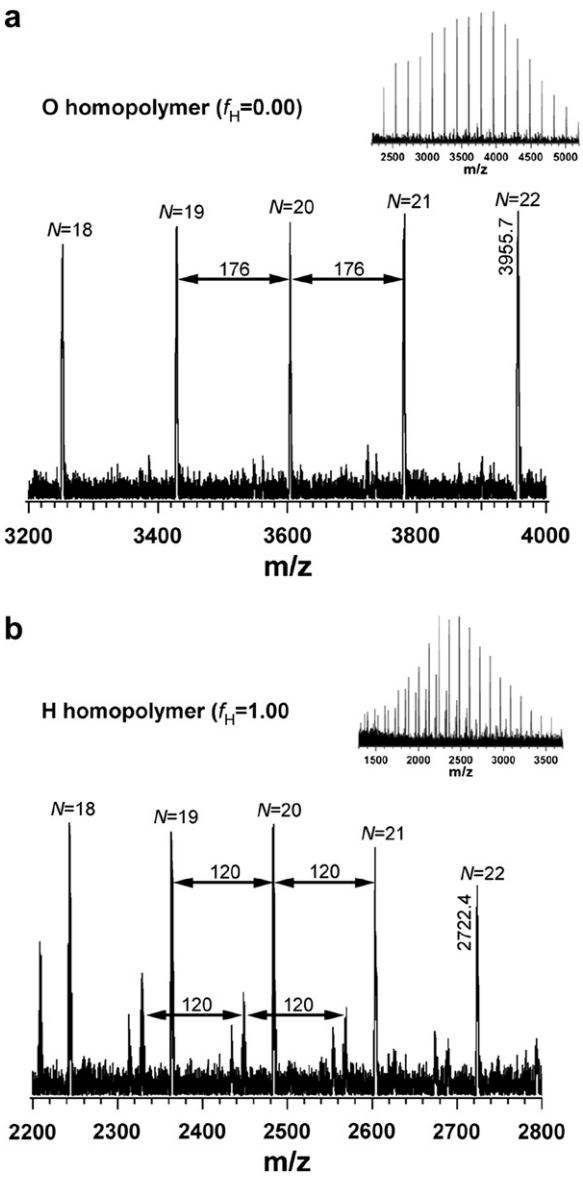

Fig. 2. MALDI-TOF MS spectra of (a) O ($f_H = 0.00$) and (b) H ($f_H = 1.00$) homopolymers at expanded scale. Inset figures show the full spectra.

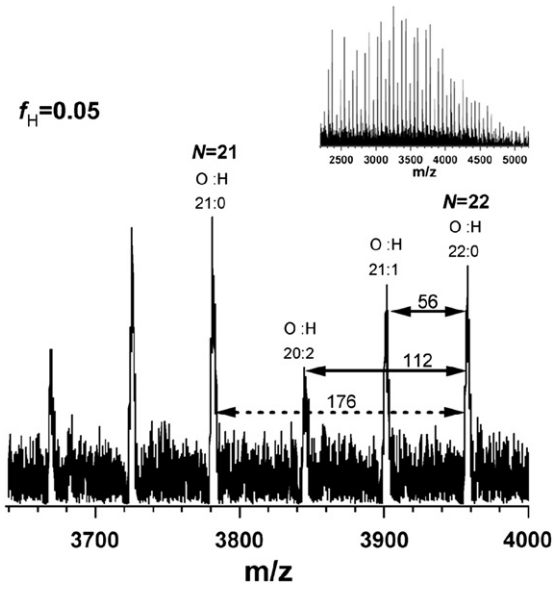

Fig. 3. MALDI-TOF MS spectrum of O/H copolymer having f_H equals to 0.05 at expended scale. Inset figure at upper-right hand represents the full spectrum.

shown in Fig. 2b. H homopolymer was prepared by 100% hydrolyzation of the parent O homopolymer that was confirmed beforehand by ^{1}H NMR and IR measurements (supporting information). Each signal is separated by *m*/*z* 120, which is the molecular weight of 4-hydroxystyrene. A signal at *m*/*z* 2722.4 corresponds to H homopolymer with *N* of 22 calculated as $[C_4H_9\text{-}(C_8H_8O)_{22}\text{-}H\cdot Na^+] = 57.07+(22 \times 120.06)+1.01 + 22.99 = 2722.4$. All main peaks in the H homopolymer spectrum show the same *N* series as the parent O homopolymer. On the other hand, small peaks appear between the peaks associated with H monomeric repeating unit. Because they are also equally spaced out by *m*/*z* 120, they may probably be due to fragmentation caused by low proton affinity of the matrix compared to H homopolymer [48–50]. Nevertheless, a suitable measurement condition for both O and H homopolymers was managed to be optimized.

Fig. 3 displays the full and expanded MALDI-TOF MS spectra of the O/H copolymer with f_H of 0.05. The full spectrum is more complicated than the homopolymer ones indicating that O homopolymer is hydrolyzed at various fractions locally. Between two O homopolymer peaks at *N* of 21 and 22 exhibited in the expanded spectrum, there are two other small peaks with *m*/*z* difference of 56 and 112 from the peak of *N* equals 22. Considering the molecular weight difference of O and H monomeric units is 56, these peaks imply that 1 and 2 monomer units of O homopolymer have been converted into H monomeric unit. Fig. 4a–c shows the histograms of H fraction in O/H copolymers with f_H ranging from 0.05 to 0.24. All samples show a distribution in the number of H monomeric units. Non-hydrolyzed O homopolymer is found in the samples with f_H of 0.05 and 0.13. However, this fraction decreases as f_H increases and it vanishes at f_H of 0.24 where O homopolymer was all converted into O/H copolymer composing of 2–8 units of H monomeric unit. On the other hand, the average number of H unit in each sample increases with an increase in f_H, which is reasonably in good agreement with that estimated from ^{1}H NMR as shown in Fig. 4d. Hence, from MALDI-TOF MS and ^{1}H NMR, it is found that the hydrolysis reaction goes uniformly according to the conversion rate with some distribution in f_H locally.

To examine the sequence distribution of monomers in O/H copolymers, ^{13}C NMR measurements were performed. Fig. 5 shows the full ^{13}C NMR spectra of O and H homopolymers in THF-*d8*. All large signals are assigned to each carbon in O and H. ^{13}C NMR also verifies the full conversion from O into H where the signals from carbons on *tert*-butoxy group (resonance peaks of g and h) of O disappear in H spectrum. The expanded view of the benzene ring carbon nearest to the backbone, which is called as aromatic C1 for O homopolymer, within the field range of 140–144 ppm is presented in Fig. 6. Since aromatic C1 resonance provides information on backbone configuration, the stereoregularity of O homopolymer was determined by using the relative magnitude of the three main peaks which is 0.32:0.47:0.21 towards high field. Because *mm* is most likely to be detected at either ends of the resonance, this data implies that the fraction of *mm* triad could be either 0.32 or 0.21. Then, statistical analysis using Bernoullian model was applied to assign these peaks to triad sequence, *mm*, *mr* + *rm* and *rr*, where *m* is meso and *r* is racemic [51–53] according to eq. (1),

$$\begin{aligned} [mm] &= P_m^2 \\ [mr] + [rm] &= 2(1 - P_m)P_m \\ [rr] &= (1 - P_m)^2 \end{aligned} \quad (1)$$

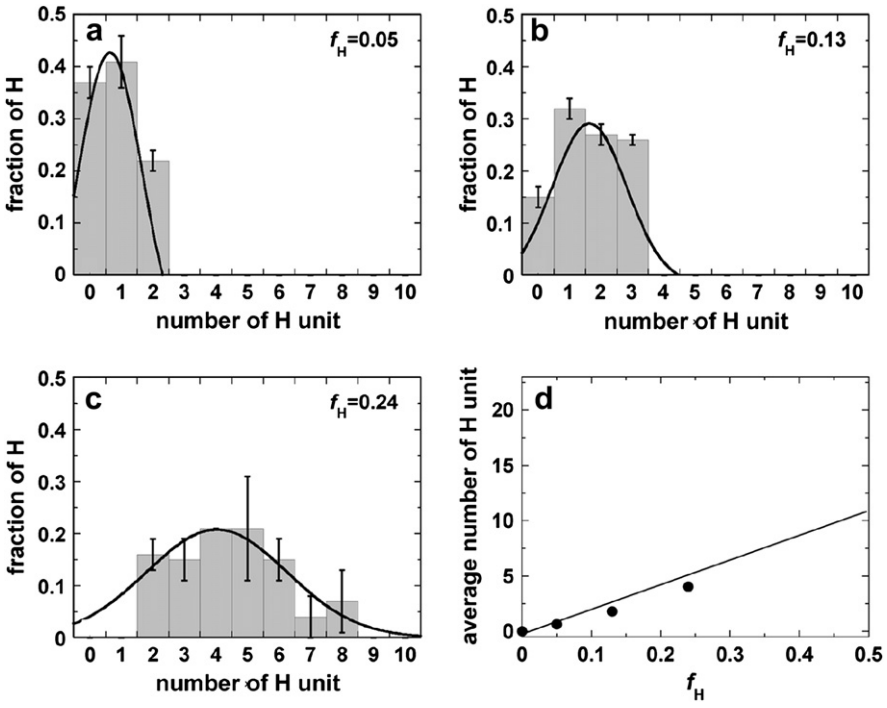

Fig. 4. Histograms of fraction of H in O/H copolymer having f_H of (a) 0.05, (b) 0.13 and (c) 0.24; and (d) average number of H unit in each sample.

where P_m is the probability of *m* configuration and [*mm*], [*mr*], [*rm*] and [*rr*] denote the fraction of *mm*, *mr*, *rm* and *rr* triad, respectively.

If we assume 0.32 for [*mm*], it gives 0.57 for P_m and; 0.49 and 0.19 for [*mr*] + [*rm*] and [*rr*], respectively. These values are comparable to the experimental 0.32:0.47:0.21. Therefore, the assignment for aromatic C1 of O homopolymer from low to high field is determined to be *mm*, *mr* + *rm* and *rr*. This order in triad assignment is consistent with other reported polystyrene derivatives [51,54–57]. Furthermore, this result implies that living anionic polymerization of 4-*tert*-butoxystyrene using *sec*-BuLi in THF gives atactic O homopolymer.

Fig. 7 compares the aromatic C1 resonances of O/H copolymers (solid lines in Fig. 7). For spectra analysis, the intensity was normalized by the intensity of methylene carbon and the total peak area for all samples was confirmed to be constant. O/H copolymers show two aromatic C1 peaks, which correspond to O component (lower field at 141.0–143.8 ppm) and H component (higher field at 137.8–139.5 ppm), respectively. As f_H increases, the peak intensity for O component decreases, while that for H component increases indicating the causal relation between O and H homopolymers. In addition, the shapes of the peaks and the chemical shift also change with f_H, implying that the chemical environment of aromatic C1 of O/H copolymers is different from their homopolymers due to monomer distribution.

Further analysis on aromatic C1 resonances of O/H copolymers provides details on monomer sequence distribution. Though we observed no explicit new peaks that could be detected to assist the assignment of monomer sequence due to the weak influence of *tert*-butoxy and hydroxyl groups on the resonance of aromatic C1 because they are situated at the outermost part of the polymer chain, we still can estimate whether the hydrolysis reaction goes on block-likely or statistically, by applying spectra subtraction method. The spectra of O and H homopolymers were reduced to each f_H (dotted lines in Fig. 7b–g) and compared to O/H copolymer ones. If the hydrolysis reaction proceeds from one end of O homopolymer,

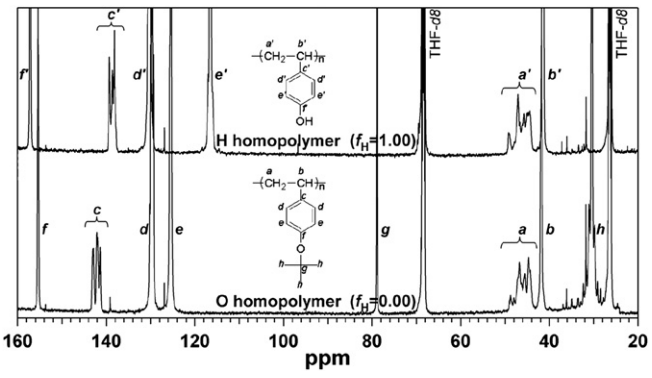

Fig. 5. ^{13}C NMR spectra of O (lower) and H (upper) homopolymers in THF-*d8*.

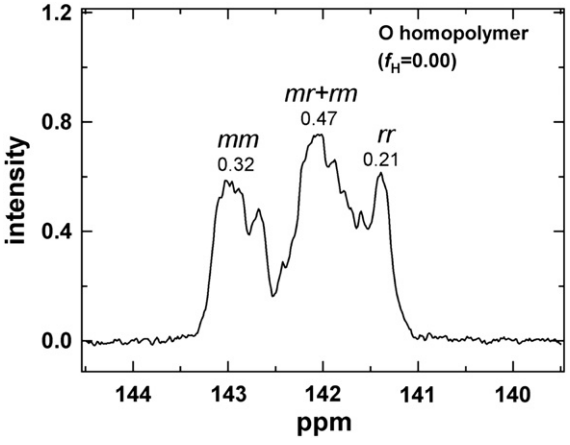

Fig. 6. Expanded view of aromatic C1 resonance of O homopolymer.

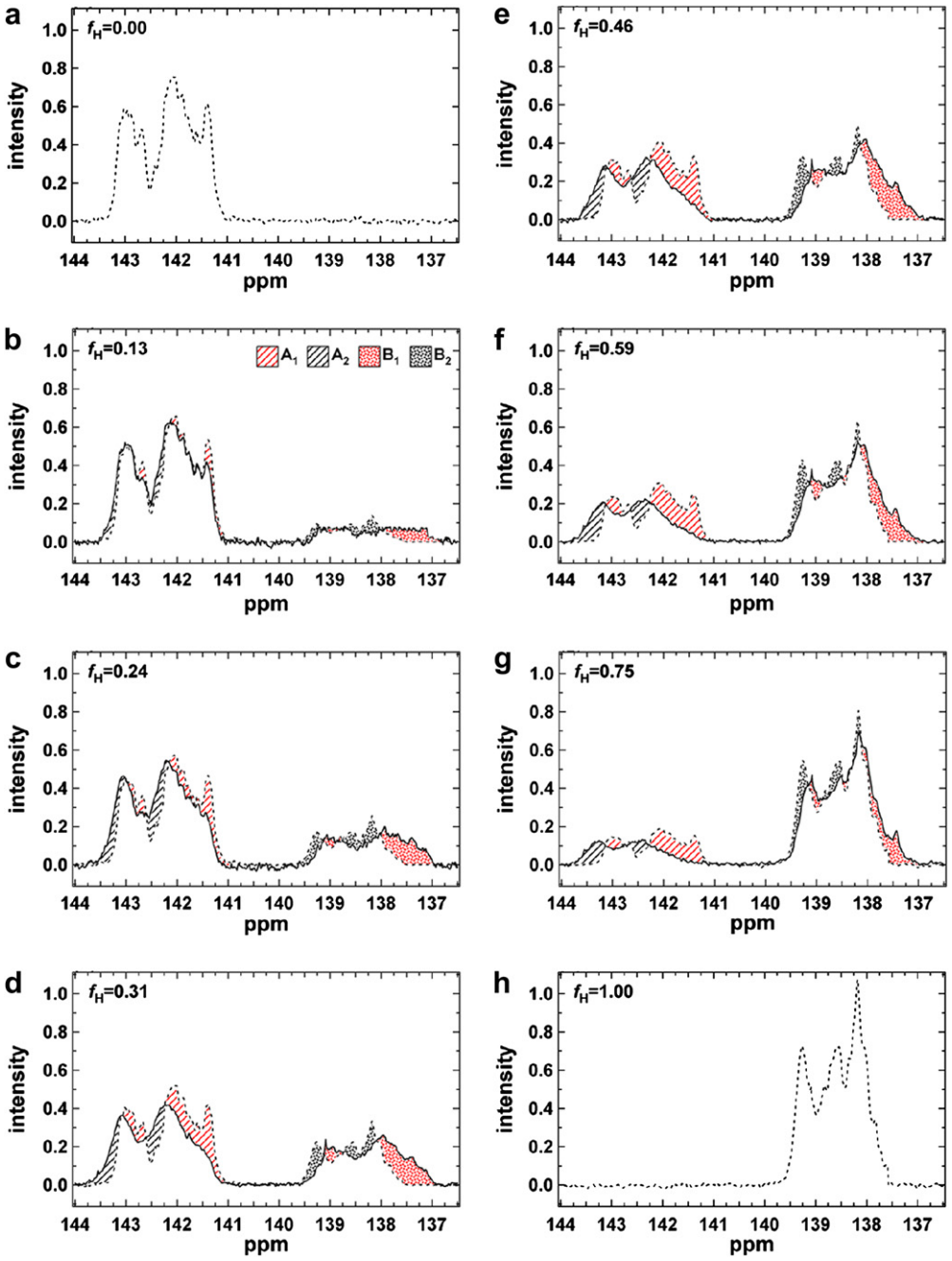

Fig. 7. Aromatic C1 resonance of O/H copolymers (solid lines) compared to O and H homopolymer (dotted lines). Shaded area represents the portion of the peak that changes upon hydrolysis reaction. Red region is the amount of H-centered triad sequence where A_1 consumes HHH, HHO and OHO; and B_1 consumes a part of HHO and OHO. Grey region is the amount of O-centered triad sequence where A_2 composes of a part of OOH and HOH; and B_2 composes of OOO, OOH and HOH (For interpretation of the references to colour in this figure legend, the reader is referred to the web version of this article).

the O/H copolymer is actually an O–H diblock copolymer. In this case, the ^{13}C NMR spectrum of the partially hydrolyzed O/H copolymer should be consistent with the reduced homopolymer's spectrum assuming that the effect of the junction point is negligible. On the other hand, if the hydrolysis reaction proceeds statistically, the difference between a hydrolyzed sample and the reduced homopolymers spectra can be observed.

The shaded regions in Fig. 7 exhibit the difference between the O/H copolymer and the homopolymer peaks which represent the portions of monomer sequence that change upon hydrolysis. There are two areas in the aromatic C1 resonance of O component. A_1 where the dotted line is above the solid one is the lost O homopolymer region due to the production of H component. It represents H-centered triad sequence of OHO, HHO and HHH. On the other hand, A_2 where the solid line of O/H copolymer exceeds the dotted one for O homopolymer is the newly detected region compared to that of O homopolymer composed of O-centered triad sequence of OOH and HOH. The same idea can also be applied to the aromatic C1 of H component. B_1 indicates the H-centered triad sequence of HHO and OHO which are formed by hydrolysis reaction, while B_2 corresponds to the overestimated amount of HHH triad sequence and therefore, includes HOH, OOH and OOO.

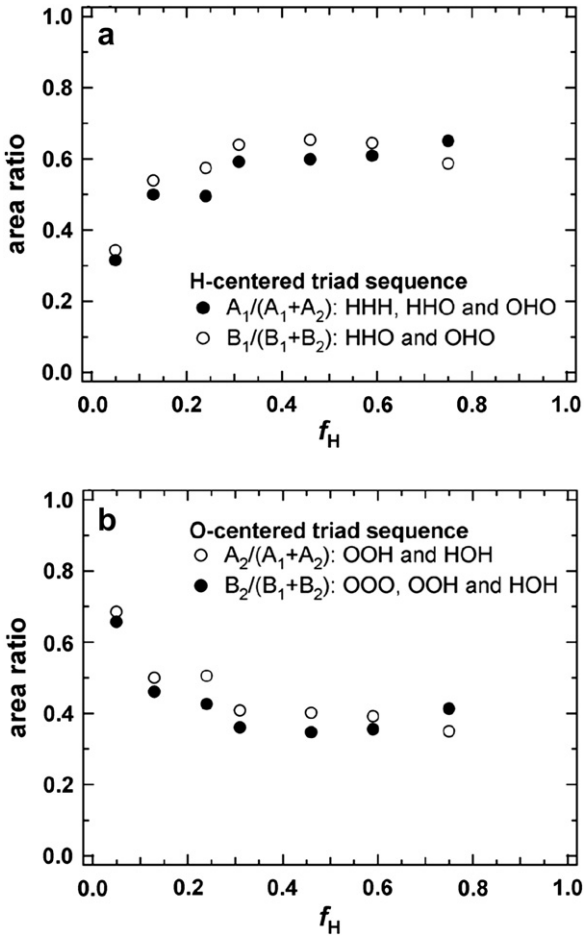

Fig. 8. Relation between the area ratios of aromatic C1 resonance and f_H. (a) exhibits changes in H-centered triad sequence, while (b) shows changes in O-centered triad sequence.

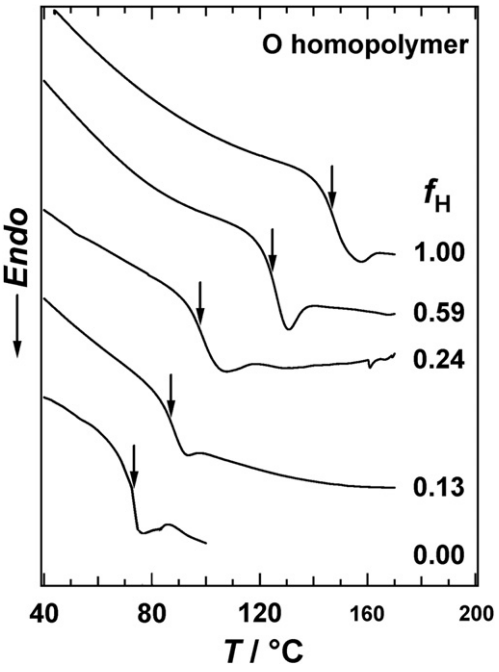

Fig. 9. DSC traces of O homopolymer having various f_H. The T_gs of the samples are shown with arrows.

By comparing the shaded areas having triad sequence of the same center as a function of f_H, we can estimate how the hydrolysis reaction occurs. Fig. 8 exhibits the relation between shaded area ratio and f_H. Here, area ratios of A_1, A_2, B_1 and B_2 to the total area of shaded regions, i.e., (A_1+A_2) and (B_1+B_2), in each aromatic C1 resonance were used. It is evident that the area fraction of A_1 is comparable to that of B_1 at any f_H meaning that the lost of O-centered triad sequence by hydrolysis is converted into the H-centered triad sequence of HHO and/or OHO. Similarly, the area fraction of A_2 is also similar to that of B_2 at any f_H, indicating the overestimated amount of HHH triad sequence corresponds to the O-centered sequence of OOH and/or HOH. These results clearly point out that the conversion from O into H by hydrolysis reaction occurs statistically rather than block-likely.

Hydrolysis reactions of acrylate polymers have been well-studied [29,32]. It has been recognized that the hydrolysis reaction of poly(methyl acrylate) is strongly influenced by the calatytic effect of neighboring group, resulting in forming blocky sequence. The effect of neighbors forms so-called a six-membered cyclic intermediate which is the postulated structure taken when a carboxylate ion attacks on the neighboring ester group [34]. However, this effect becomes small for such a polymer having bulky substituent as poly (*tert*-butyl acrylate) due to steric hindrance [32]. Poly(4-*tert*-butoxystyrene) also has a more bulky substituent. Since segment lengths of poly(methyl acrylate), poly(*tert*-butyl acrylate) and poly (4-*tert*-butoxystyrene) are 0.61, 0.69 and 0.78 nm [58–62], respectively, the effect of the substituent on steric hindrance is the strongest for poly(4-*tert*-butoxystyrene) and the catalytic effect could be the smallest among these three polymers. Hence, it is reasonable to consider that the hydrolysis reaction of poly(4-*tert*-butoxystyrene) to occur statistically.

Aggregation states of O/H copolymers were evaluated by DSC measurements prior to the morphological observation of hydrolyzed BO. DSC traces of O/H copolymers are represented in Fig. 9. For comparison, those for O and H homopolymers are also included. The glass transition temperatures, T_gs, of the polymers are pointed with arrows in Fig. 9. Both O and H homopolymers showed a single T_g at 73 and 147 °C, respectively, while all O/H copolymers exhibited a single T_g appearing between the two values for the homopolymers depending on conversion rate. This means that partially hydrolyzed O homopolymers do not phase-separate, which also supports the statistical behavior of the hydrolysis reaction confirmed by ^{13}C NMR.

Fig. 10a shows TEM images of symmetric BOs with f_H ranging from 0.21 to 1.00. B phase appears dark, while O/H phase appears bright since the samples were stained with RuO_4. Original BO sample shows no phase-separated structure. Samples with f_H from 0.21 to 0.61 exhibited two structures, lamellar structure as the major component and cylindrical structure as the minor one. On the other hand, only lamellar structure was found for samples with f_H larger than 0.61. The corresponding SAXS profiles are displayed in Fig. 10b. A broad correlation hole peak is observed for BO suggesting that it is in a disordered state. Integer order peaks indicating lamellar structure are strongly detected in all samples, while weak additional 1, $\sqrt{3}$, $\sqrt{4}$, $\sqrt{7}$, $\sqrt{9}$ and $\sqrt{12}$ peaks are detected in samples with f_H from 0.21 to 0.61, implying the coexistence of cylindrical structure in a small fraction. Hence, the morphologies observed by TEM are in good agreement with SAXS. Furthermore, O/H mixed block of the partially hydrolyzed BOs showed a single T_g, which is consistent with that observed for partially hydrolyzed O homopolymer, indicating the major component of partially hydrolyzed BO is the lamellar structure (supporting information).

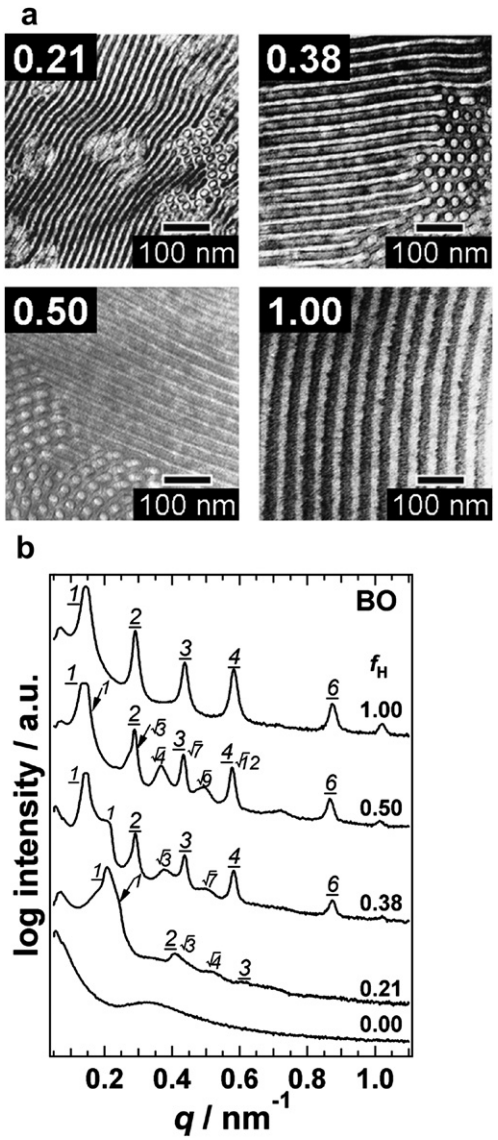

Fig. 10. (a) TEM images and (b) SAXS profiles of hydrolyzed BO with f_H of 0.21, 0.38, 0.50 and 1.00. Underlined integer order numbers in the SAXS profiles indicates the diffraction peaks from lamellar structures, while the square-root ones represent those from cylindrical structures.

Considering that the hydrolysis reaction in BO proceeds in the similar way as O homopolymer does, the observed lamellar structure can be explained by the statistical occurrence of the hydrolysis reaction. Meanwhile, cylindrical structure is formed probably due to the distribution in hydrolyzed sites that may induce some block sequence of H locally. Considering that BO is a weakly segregated pair due to their disordered state, this small clustered H can form an isolated minority domain leaving O to exist in B phase to increase the total volume of the mixed phase as matrix, which leads to produce cylindrical structure. In order to confirm this, the diameter of the cylindrical structure, d_{cyl}, was estimated based on TEM images and compared with the thickness of H domains in the lamellar structure of the fully hydrolyzed sample, d_{lam} (22 nm). d_{cyl} values obtained are 11, 14, 16 nm for samples with f_H of 0.21, 0.38 and 0.58, respectively. It is evident that the d_{cyl} values increase with increasing f_H and are smaller than the d_{lam} value. These results imply that H block sequence is formed more or less but its characteristic length is smaller than the fully hydrolyzed O block, supporting the hypothesis. Thus, this shows that the morphology of hydrolyzed BO is evidently consistent with molecular characteristic analysis of O/H copolymer.

4. Conclusions

In this study, the characterization of O/H copolymers obtained from hydrolysis reaction of O was conducted by MALDI-TOF MS and ^{13}C NMR. It was found that the reaction uniformly occurs, though a certain distribution in the number of hydrolyzed site was detected. ^{13}C NMR reveals that O and H are statistically distributed in O/H copolymers. To evaluate the effect of monomer sequence in O/H chain on the bulk structures, we studied the morphology of partially hydrolyzed BO. Samples with intermediate f_H show multiple structures, i.e. lamellar (major component) and cylindrical (minor component) structures. This observation can be explained by considering both the statistical manner of the hydrolysis reaction and the distribution of hydrolyzed sites.

Acknowledgement

This research was in part supported by the Grant-in-Aids for Scientific Research (A) (No. 22245038), for Young Scientists (A) (No. 22685013), the Priority Area “Soft Matter Physics” (No. 863), the Global COE program “Elucidation and Design of Materials and Molecular Functions” from the Ministry of Education, Culture, Sports, Science, and Technology (MEXT), Japan and the aid fund for doctoral students’ research of Nagoya University, Japan. This work was performed using BL-15A of Photon Factory, Institute of Materials Structure Science, High Energy Accelerator Research Organization, Japan under the programme number of 2008G701. The authors acknowledge the Division for Medical Research Engineering, Nagoya University Graduate School of Medicine, for technical support of TEM observation.

Appendix. Supplementary material

Supplementary data associated with this article can be found in the online version, at doi:10.1016/j.polymer.2010.11.010.

References

[1] Michell RM, Muller AJ, Castelletto V, Hamley I, Deshayes G, Dubois P. Macromolecules 2009;42(17):6671–81.
[2] Wang R, Li W, Luo Y, Li BG, Shi AC, Zhu S. Macromolecules 2009;42(6):2275–85.
[3] Quinn JD, Register RA. J Polym Sci Part B Polym Phys 2009;47(21):2106–13.
[4] Park MJ, Balsara NP. Macromolecules 2008;41(10):3678–87.
[5] Phan TNT, Maiez-Tribut S, Pascault JP, Bonnet A, Gerard P, Guerret O, et al. Macromolecules 2007;40(13):4516–23.
[6] Wu L, Cochran EW, Lodge TP, Bates FS. Macromolecules 2004;37(9):3360–8.
[7] Kim J, Sandoval RW, Dettmer CM, Nguyen ST, Torkelson JM. Polymer 2008;49(11):2686–97.
[8] Joseph S, Laupretre F, Negrell C, Thomas S. Polymer 2005;46(22):9385–95.
[9] Kim J, Gray MK, Zhou H, Nguyen ST, Torkelson JM. Macromolecules 2005;38(4):1037–40.
[10] Lefebvre MD, Dettmer CM, McSwain RL, Xu C, Davila JR, Composto RJ, et al. Macromolecules 2005;38(25):10494–502.
[11] Harrats C, Fayt R, Jerome R, Blacher S. J Polym Sci Part B Polym Phys 2003;41(2):202–16.
[12] Eastwood EA, Dadmun MD. Macromolecules 2002;35(13):5069–77.
[13] Lee MS, Lodge TP, Macosko CW. J Polym Sci Part B Polym Phys 1997;35(17):2835–42.
[14] Mok MM, Kim J, Marrou SR, Torkelson JM. Eur Phys J E 2010;31(3):239–52.
[15] Gray MK, Zhou H, Nguyen ST, Torkelson JM. Macromolecules 2004;37(15):5586–95.
[16] Gray MK, Zhou H, Nguyen ST, Torkelson JM. Polymer 2004;45(14):4777–86.
[17] Jakubowski W, Juhari A, Best A, Koynov K, Pakula T, Matyjaszewski K. Polymer 2008;49(6):1567–78.
[18] Mok MM, Kim J, Torkelson JM. J Polym Sci Part B Polym Phys 2008;46(1):48–58.

[19] Denizli BK, Lutz JF, Okrasa L, Pakula T, Guner A, Matyjaszewski K. J Polym Sci Part A Polym Chem 2005;43(15):3440–6.
[20] Shinoda H, Matyjaszewski K, Okrasa L, Mierzwa M, Pakula T. Macromolecules 2003;36(13):4772–8.
[21] Cho K, Ahn TO, Ryu HS, Seo KH. Polymer 1996;37(21):4849–52.
[22] Chakraborty AK, Fredrickson GH. Macromolecules 1994;27(24):7079–84.
[23] Budhlall BM, Landfester K, Sudol ED, Dimonie VL, Klein A, El-Aasser MS. Macromolecules 2003;36(25):9477–84.
[24] Halverson F, Lancaster JE, O'Connor MN. Macromolecules 1985;18(6): 1139–44.
[25] Merle L, Merle Y. Macromolecules 1982;15(2):360–6.
[26] Moritani T, Fujiwara Y. Macromolecules 1977;10(3):532–5.
[27] Johnsen A, Klesper E, Wirthlin T. Makromol Chem 1976;177(8):2397–429.
[28] Klesper E, Gronski W, Barth V. Makromol Chem 1970;139(3461):1–16.
[29] Matsuzaki K, Okada M, Hosonuma K. J Polym Sci Part A-1 1972;10(4):1179–86.
[30] Tubbs RK. J Polym Sci Part A-1 1966;4(3PA1):623–9.
[31] Nagase K, Sakaguchi K. J Polym Sci Part A 1965;3(7PA):2475–82.
[32] Smets G, van Humbeeck W. J Polym Sci Part A 1963;1(4):1227–38.
[33] De Loecker W, Smets G. J. Polym Sci 1959;40(136):203–16.
[34] Morawetz H, Zimmering PE. J Phys Chem 1954;58(9):753–6.
[35] Adams JL, Quiram DJ, Graessley WW, Register RA, Marchand GR. Macromolecules 1998;31(1):201–4.
[36] Hahn SF. J Polym Sci Part A Polym Chem 1992;30(3):397–408.
[37] Gehlsen MD, Bates FS. Macromolecules 1993;26(16):4122–7.
[38] Xu K, Li K, Khanchaitit P, Wang Q. Chem Mater 2007;19(24):5937–45.
[39] Mokrini A, Acosta JL. Polymer 2001;42(1):9–15.
[40] Zhang W, Dubois M, Guerin K, Hamwi A. Polymer 2007;48(14):3961–73.
[41] Dubois M, Guerin K, Giraudet J, Pilichowski JF, Thomas P, Delbe K, et al. Polymer 2005;46(18):6736–45.
[42] Davidock DA, Hillmyer MA, Lodge TP. Macromolecules 2004;37(2):397–407.
[43] Reisinger JJ, Hillmyer MA. Prog Polym Sci 2002;27(5):971–1005.
[44] Kawaguchi D, Nomura H, Rahman SSA, Nakayama M, Matsushita Y. Macromolecules 2009;42(22):8992–7.
[45] Cobas C, Cruces J, Sardina J. Mestre-C 2.3a. Spain: University of Santiago de Compostela; 1995.
[46] Thomson B, Suddaby K, Rudin A, Lajoie G. Eur Polym J 1996;32(2):239–56.
[47] Macha SF, Limbach PA. Curr Opin Solid State Mater Sci 2002;6(3):213–20.
[48] Zhu L, Parr GR, Fitzgerald MC, Nelson CM, Smith LM. J Am Chem Soc 1995;117 (22):6048–56.
[49] Karas M, Bahr U, Strupat K, Hillenkamp F, Tsarbopoulos A, Pramanik BN. Anal Chem 1995;67(3):675–9.
[50] Zenobi R, Knochenmuss R. Mass Spectrom Rev 1998;17(5):337–66.
[51] Randall JC. Polymer sequence determination: carbon-13 NMR method. New York: Acedemic Press; 1977 [chapters 1, 4 and 6].
[52] Price FP. J Chem Phys 1962;36(1):209–18.
[53] Bovey FA. Acct Chem Res 1968;1(6):175–85.
[54] Matsuzaki K, Uryu T, Asakura T. NMR spectrometry and stereoregularity of polymer. Tokyo: Japan Scientific Societies Press; 1996 [chapters 12, 13 and 14].
[55] Matsuzaki K, Uryu T, Osada K, Kawamura T. Macromolecules 1972;5(6): 816–8.
[56] Inoue Y, Nishioka A, Chujo R. Makromol Chem 1972;156(NFEB):207–23.
[57] Randall JC. J Polym Sci Polym Phys Ed 1975;13(5):889–99.
[58] Matsuda H, Yamano K, Inagaki H. J Polym Sci. Part A-2 1969;7(4PA2):609–33.
[59] Cole DH, Shull KR, Baldo P, Rehn L. Macromolecules 1999;32(3):771–9.
[60] Jerome R, Desreux V. Eur Polym J 1970;6(2):411–21.
[61] Brandrup J, Immergut EH. Polymer handbook. 3rd ed. New York: Wiley; 1988 [chapter 7].
[62] Iwatsuki R, Kawaguchi D, Matsushita Y. Unpublished results; 2006.

Polymer 52 (2011) 172–179

Contents lists available at ScienceDirect

Polymer

journal homepage: www.elsevier.com/locate/polymer

Preparation and characterization of thermosensitive organic–inorganic hybrid microgels with functional Fe_3O_4 nanoparticles as crosslinker

Tianyou Chen [a], Zheng Cao [a], Xiaolei Guo [a], Jingjing Nie [b], Junting Xu [a], Zhiqiang Fan [a], Binyang Du [a,*]

[a] MOE Key Laboratory of Macromolecular Synthesis and Functionalization, Department of Polymer Science & Engineering, Zhejiang University, Hangzhou 310027, China
[b] Department of Chemistry, Zhejiang University, Hangzhou 310027, China

ARTICLE INFO

Article history:
Received 4 September 2010
Received in revised form
30 October 2010
Accepted 7 November 2010
Available online 13 November 2010

Keywords:
Organic–inorganic hybrid microgels
Thermosensitive
Superparamagnetic

ABSTRACT

A methodology is described for the preparation of thermosensitive organic–inorganic hybrid microgels with functional Fe_3O_4 nanoparticles as the crosslinker and *N*-isopropylacrylamide (NIPAm) as the monomer. Magnetic Fe_3O_4 nanoparticles were first prepared via a redox reaction in aqueous solution and then modified with 3-(trimethoxysilyl)propylmethacrylate (TMSPMA) via the silanization. The bonding of multiple TMSPMA monomers on the surface of Fe_3O_4 nanoparticles renders them as crosslinker. Surfactant-free emulsion polymerization (SFEP) of NIPAm was then carried out with the presence of TMSPMA-modified Fe_3O_4 nanoparticles at 70 °C in aqueous solution, leading to the formation of thermosensitive PNIPAm-Fe_3O_4 hybrid microgels crosslinked with Fe_3O_4 nanoparticles. Transmission electron microscopy (TEM), scanning electron microscopy (SEM), energy dispersive X-ray analysis (EDX), thermogravimetric analysis (TGA), dynamic light scattering (DLS) and physical properties measurement system (PPMS) were then used to characterize the resultant hybrid microgels. The experimental results show that the PNIPAm-Fe_3O_4 hybrid microgels were spherical in shape with a large size distribution and the Fe_3O_4 nanoparticles were randomly distributed inside the microgels. The PNIPAm-Fe_3O_4 hybrid microgels were thermosensitive, exhibiting a reversible swelling and deswelling behavior as a function of temperature. The PNIPAm-Fe_3O_4 hybrid microgels also show superparamagnetic behavior at room temperature (300 K).

1. Introduction

Since Pelton and Chibante [1] first reported the preparation and characterization of thermosensitive poly(*N*-isopropylacrylamide) (PNIPAm) microgels via surfactant-free emulsion polymerization (SFEP) in 1986, microgels have attracted extensive interests due to their potential applications in many diverse fields, specially such as drug delivery, biosensor, templates for nanoparticle synthesis and catalyst [2–6]. It is thus greatly significant to tailor the properties and functionalities of the microgels. Conventional methods mainly involve the introduction of the second or third monomer during the SFEP of *N*-isopropylacrylamide (NIPAm), which will lead to the microgels with various functionalities, like response to pH value, UV irradiation of the environments, etc. [7–10].

In recent decades, a new type of materials, namely organic–inorganic hybrid materials, has emerged [11–16]. These organic–inorganic hybrid materials possess and combine at the same time the properties of organic components and inorganic components, which render them more superior microstructures and properties. Many researchers have devoted their numerous efforts to the fabrication and characterization of organic–inorganic hybrid materials [3,4,6,11–14,17–28]. Concerning the research field of microgels, the organic–inorganic hybrid microgels have been reported in recent years [11,24,26,27,29–35]. In a recent review, Karg and Hellweg have classified the types of hybrid microgels reported in literature [11]. Three typical classes of organic–inorganic hybrid microgels were discussed. They are: (1) Core-shell microgels with inorganic nanoparticles as cores, of which the gel shells are formed on the surface of inorganic nanoparticles; (2) Microgels filled with inorganic nanoparticles, of which the inorganic nanoparticles are in-situ synthesized inside the microgels; (3) Microgels covered with nanoparticles, of which the microgels are first prepared and the inorganic nanoparticles are coated onto the microgels in the following step. Various inorganic nanoparticles, such as Au, Ag, Fe_3O_4, SiO_2 and TiO_2, etc., have been incorporated into the microgels, forming the hybrid systems [17,19,20,22,23,28–35]. Depending on the inorganic nanoparticles used, the resultant hybrid microgels can have various special properties, such as local surface plasmon, magnetic and

* Corresponding author. Tel.: +86 571 87953164; fax: +86 571 87952400.
E-mail address: duby@zju.edu.cn (B. Du).

0032-3861/$ – see front matter © 2010 Elsevier Ltd. All rights reserved.
doi:10.1016/j.polymer.2010.11.014

fluorescence properties, etc. [19,20,28–36] However, most of the hybrid microgels reported in recent years have microgel-shells or microgels prepared with the presence of conventional chemical crosslinker, *N,N′*-methylene-bisacrylamide (BIS).

The fourth possible class of organic–inorganic hybrid microgels is that the hybrid microgels are in-situ formed via covalent crosslinking with functional inorganic nanoparticles without adding any conventional chemical crosslinker. In other word, the functional inorganic nanoparticles act as chemical crosslinkers. Currently, reports about such fourth class of organic–inorganic hybrid microgels are still rare. Clay nanoparticles were first successfully used as crosslinking agent for the preparation of organic–inorganic hybrid hydrogels [37–40] and microgels [41] in the absence of conventional chemical crosslinker. However, the crosslinking mechanism of the clay particles is not well-defined and still unclear [37–41]. It remains unknown whether there are covalent bonds between the clay particles and the network chains. For organic–inorganic hybrid solid nanoparticles, modified clay nanoparticles were successfully encapsulated inside latex particles via covalent bonds [42]. In another report, magneto-responsive polystyrene (PS) gels were fabricated by using functional Fe nanoparticles as crosslinking agent via the surface-initiated atomic transfer radical polymerization (SI-ATRP) without adding any conventional chemical crosslinker [43]. However, the mechanism of crosslinking and network formation was not well-established as well and still under debate for such Fe–PS hybrid gels. The authors argued that the crosslinking points were formed via the interparticle termination of propagating radicals on the Fe nanoparticles [43]. Here, we reported the successful preparation of thermosensitive organic–inorganic PNIPAm-Fe_3O_4 hybrid microgels with functional Fe_3O_4 nanoparticles as the crosslinker and NIPAm as the monomer. The PNIPAm chains were covalently crosslinked with surface-functional Fe_3O_4 nanoparticles. The crosslinking mechanism was well-defined in the present work, which involved the radical crosslinking polymerization of multiple carbon–carbon double bonds grafted on the surface of Fe_3O_4 nanoparticles and the formation of covalent bonds between Fe_3O_4 nanoparticles and network chains. No conventional chemical crosslinker was used. Transmission electron microscopy (TEM), scanning electron microscopy (SEM), energy dispersive X-ray analysis (EDX), thermogravimetric analysis (TGA), dynamic light scattering (DLS), and physical properties measurement system (PPMS) were then used to characterize the functional Fe_3O_4 nanoparticles and resultant hybrid microgels. We demonstrated that the thermosensitive and magnetic PNIPAm-Fe_3O_4 hybrid microgels were indeed obtained, which were spherical in shape with a relatively large size distribution. The Fe_3O_4 nanoparticles were randomly distributed inside the hybrid microgels.

2. Experimental

2.1. Chemical and materials

N-isopropylacrylamide (NIPAm: 99%) and 3-(trimethoxysilyl) propylmethacrylate (TMSPMA: 98%) were purchased from Acros Organics. Ferrous chloride tetrahydrate ($FeCl_2 \cdot 4H_2O$), anhydrous ferric chloride ($FeCl_3$), potassium peroxydisulfate ($K_2S_2O_8$) (Sinopharm Chemical Reagent Co. LTD) and ammonia solution (25%, Hangzhou Changzheng Chemical Reagent Co. LTD) were used without further treatment. All other reagents were of analytical grade and used as received. Deionized water was used.

2.2. Preparation and surface modification of Fe_3O_4 magnetic nanoparticles

The preparation of Fe_3O_4 magnetic nanoparticles was adapted from a literature method [18,44,45]. First, ferric chloride ($FeCl_3$, 820.2 mg) was dissolved in 30 ml deionized water under mechanical stirring and nitrogen atmosphere at 25 °C in a three-neck flask. 10 ml of ferrous chloride tetrahydrate ($FeCl_2 \cdot 4H_2O$, 52.94 mg/ml) aqueous solution was then added into the flask under stirring. After 10 min, ammonia aqueous solution (~4.5 g, 25%) was slowly injected into the flask. The reacting solution turned into black with the injection of ammonia solution. The total amount of the reacting solution was about 45 ml. The reaction was maintained for 2 h. When the reaction was complete, the Fe_3O_4 nanoparticles were separated and washed with deionized water several times with the help of a magnet until the deionized water was neutral. (Fig. S1a in Supplementary Material) The purified Fe_3O_4 nanoparticles were redispersed into 45 ml deionized water. Afterward, 0.30 ml of 3-(trimethoxysilyl)propylmethacrylate (TMSPMA) was injected into the Fe_3O_4 nanoparticles solution under mechanical stirring at 25 °C. The surface silanization of Fe_3O_4 magnetic nanoparticles was allowed to proceed for 24 h. Surface modified Fe_3O_4 magnetic nanoparticles were then collected and washed with deionized water for several times with the help of a magnet. (Fig. S1b in Supplementary Material).

2.3. Synthesis of PNIPAm-Fe_3O_4 hybrid microgels via surfactant-free emulsion polymerization (SFEP)

The thermosensitive organic–inorganic PNIPAm-Fe_3O_4 hybrid microgels were synthesized via SFEP. Surface modified Fe_3O_4 magnetic nanoparticles (2.05 mg/ml) were first well dispersed in 10 ml deionized water by sonication for about 1.5 h, and then transferred into a three-neck flask. The temperature of the solution was increased to 70 °C under mechanical stirring with a polytetrafluoroethene (PTFE) stirrer. Oxygen was eliminated by bubbling nitrogen through the solution. After 15 min, 20 ml of $K_2S_2O_8$ aqueous solution (ca.1.09 mg/ml) was added into the flask. After another 15 min, 10 ml of NIPAm aqueous solution (NIPAm, 30.52 mg/ml) was injected into the reacting solution. The reaction was continued at 70 °C for 12 h. The obtained brown PNIPAm-Fe_3O_4 hybrid microgels were purified by several centrifugation and redispersion cycles with the supernatant replaced by deionized water during each cycle.

2.4. Instrumental and characterization

2.4.1. Fourier transform infrared spectrum (FT-IR)

Fourier Transform Infrared (FT-IR) spectra were recorded by a Vector 22 Bruker spectrometer in the transmission mode using potassium bromide (KBr) pellets of the sample. The dried powders of the pure and TMSPMA-modified Fe_3O_4 nanoparticles as well as the PNIPAm-Fe_3O_4 hybrid microgels were mixed with KBr and pressed to a plate for the FT-IR measurements, respectively.

2.4.2. Transmission electron microscopy (TEM)

The morphologies of the pure and TMSPMA-modified Fe_3O_4 nanoparticles as well as the PNIPAm-Fe_3O_4 hybrid microgels were observed by transmission electron microscopy (TEM) on a JEOL JEM-1200 electron microscope operating at an acceleration voltage of 60 kV. The TEM samples were prepared by dip-coating with carbon-coated copper grids into the corresponding solutions. The solvent was gently absorbed away by a filter paper. The grids were then allowed to dry in air at room temperature before observation.

2.4.3. Scanning electron microscope (SEM) and energy dispersive X-ray analysis (EDX)

The morphologies of the PNIPAm-Fe_3O_4 hybrid microgels were also observed by scanning electron microscope (SEM) on a Hitachi S4800 electron microscope. A droplet of the microgels solution was

cast onto the aluminum foil at room temperature. After about 15 min, the excess solution was gently absorbed away by a filter paper and the aluminum foil was then allowed to dry in air at room temperature. Before SEM observation, the microgel samples were coated with platinum vapors. Several positions of the samples were imaged and energy dispersive X-ray analysis (EDX) of the PNIPAm-Fe_3O_4 hybrid microgels was also carried out.

2.4.4. Thermogravimetric analyses (TGA)

Thermogravimetric analyses (TGA) of TMSPMA-modified Fe_3O_4 nanoparticles and PNIPAm-Fe_3O_4 hybrid microgels were performed by a NETZSCH STA 409 PC/PG instrument from 30 to 600 °C under a nitrogen atmosphere with a heating rate of 20 °C/min.

2.4.5. Dynamic light scattering (DLS)

The hydrodynamic diameter, size distribution, and thermosensitive behavior of the PNIPAm-Fe_3O_4 hybrid microgels were investigated by dynamic light scattering (DLS) as a function of measuring temperature at a scattering angle θ of 90° on a 90 Plus Particle Size Analyzer (Brookhaven Instruments Corporation). The hybrid microgels were diluted in deionized water to give a concentration of 0.35 g/L. For each measuring temperature, the microgel solution was equilibrated for 10 min and measured for four times with each run of 1 min. The hydrodynamic diameter and size distribution of the pure and TMSPMA-modified Fe_3O_4 nanoparticles were also characterized by DLS.

2.4.6. Physical properties measurement system (PPMS)

Magnetic properties of the TMSPMA-modified Fe_3O_4 nanoparticles and PNIPAm-Fe_3O_4 hybrid microgels were measured by using a physical properties measurement system (PPMS-9, Quantum Design). The magnetization hysteresis loops were measured at 10 and 300 K, respectively.

3. Results and discussion

The synthesis procedure for the thermosensitve PNIPAm-Fe_3O_4 hybrid microgels consists of the following three steps as shown schematically in Scheme 1: (1) the preparation of magnetic Fe_3O_4 nanoparticles via redox reaction; (2) the surface modification of magnetic Fe_3O_4 nanoparticles by using TMSPMA; (3) the synthesis of thermosensitive PNIPAm-Fe_3O_4 hybrid microgels via SFEP by using TMSPMA-modified Fe_3O_4 nanoparticles as the crosslinker and NIPAm as the monomer.

Fig. 1 shows the TEM morphologies of pure Fe_3O_4 nanoparticles in aqueous solution and TMSPMA-modified Fe_3O_4 nanoparticles in acetone. The pure Fe_3O_4 nanoparticles and surface modified Fe_3O_4 nanoparticles were spherical shape with slightly polydispersed size distribution. The average size of the Fe_3O_4 nanoparticles was 13 ± 2 nm. The pure Fe_3O_4 nanoparticles tended to aggregate in aqueous solution, whereas the TMSPMA-modified Fe_3O_4 nanoparticles were well dispersed in acetone. There were strong magnetic interactions among the pure Fe_3O_4 nanoparticles, which easily led to the formation of large aggregates. However, after the surface modification, TMSPMA formed a steric layer on Fe_3O_4 nanoparticles, which inhibited the formation of aggregates to certain extent. The DLS results indicated that there were large aggregates of pure Fe_3O_4 nanoparticles in aqueous and acetone solutions. (Fig. S2 in Supplementary Material) Due to the existence of large aggregates, the mean apparent sizes of the pure Fe_3O_4 nanoparticles measured by DLS were about 1178 ± 27 nm and 1715 ± 21 nm in aqueous solution and acetone, respectively. With the hydrophilic hydroxyl groups, the pure Fe_3O_4 nanoparticles had relatively better dispersity in aqueous solution. After the modification of TMSPMA, the dispersity of modified Fe_3O_4 nanoparticles in both water and acetone was strongly improved. Although the formation of aggregates can not be completely avoided due to the strong magnetic interaction, the steric TMSPMA layer indeed inhibited Fe_3O_4 nanoparticles to form big aggregates to some extent. The hydrodynamic diameters of TMSPMA-modified Fe_3O_4 nanoparticles in aqueous (333 ± 11 nm) and acetone (162 ± 2 nm) solutions were almost ten times less than the corresponding values of pure Fe_3O_4 nanoparticles (Fig. S3 in Supplementary Material). Due to the hydrophobic nature of TMSPMA, the TMSPMA-modified Fe_3O_4 nanoparticles exhibited much improved dispersity in acetone. The DLS results were coincident with those of TEM (cf. Fig. 1).

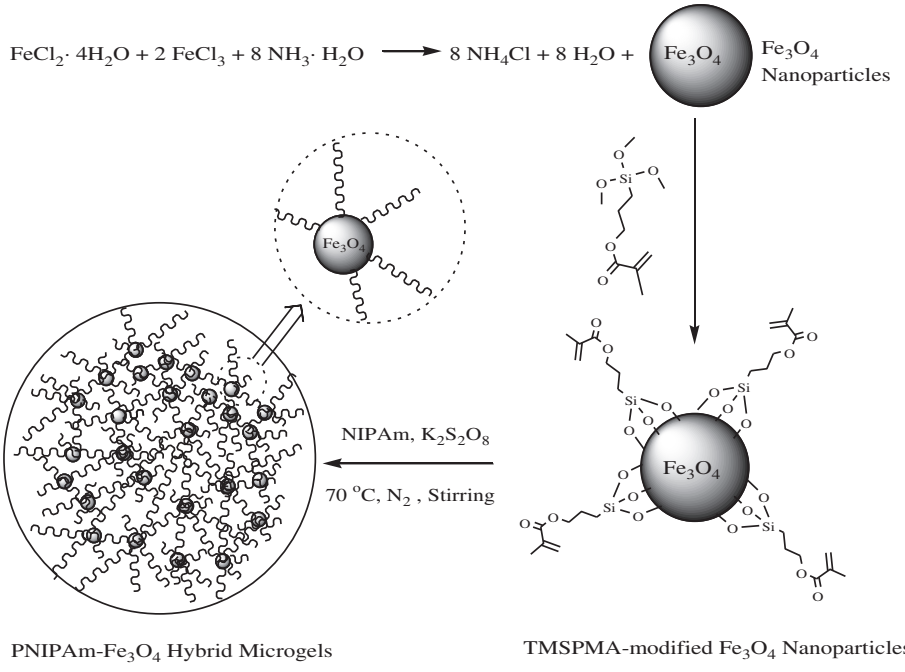

Scheme 1. The synthetic procedure of thermosensitive PNIPAm-Fe_3O_4 hybrid microgels with TMSPMA-modified Fe_3O_4 nanoparticles as the crosslinker.

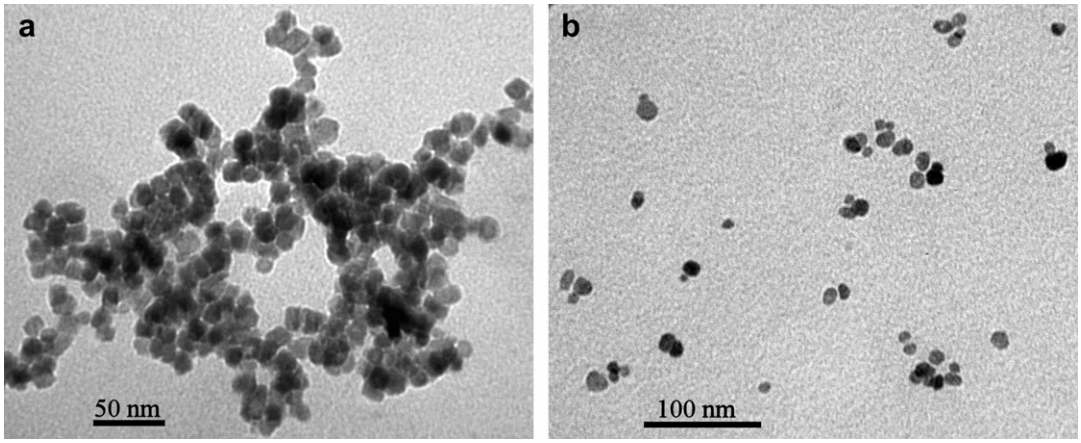

Fig. 1. (a) TEM image of pure Fe_3O_4 nanoparticles in aqueous solution and (b) TEM image of TMSPMA-modified Fe_3O_4 nanoparticles in acetone.

Fourier transform Infrared (FT-IR) spectra of pure Fe_3O_4 nanoparticles, pure TMSPMA, and TMSPMA-modified Fe_3O_4 nanoparticles are shown in Fig. 2. In the spectrum of Fe_3O_4 nanoparticles, the characteristic absorption band of Fe_3O_4 appears at 581 cm^{-1}, which also appears in the spectrum of TMSPMA-modified Fe_3O_4 nanoparticles. An intense and broad band appeared in the region 3200–3600 cm^{-1}, corresponding to the O–H stretching vibration. The surfaces of pure Fe_3O_4 nanoparticles were readily covered with hydroxyl groups in aqueous environment. In the spectrum of TMSPMA-modified Fe_3O_4 nanoparticles, there are many other peaks, most of which are the characteristic absorption bands of 3-(trimethoxysilyl)propylmethacrylate (TMSPMA). For example, bands at 2955 and 2893 cm^{-1} are attributed to stretching vibrations of $-CH_2$ group, a strong absorption band at 1719 is attributed to the stretching vibration of the –CO– groups, band at 1044 cm^{-1} is due to the stretching vibration of Si–O bond. The band at 1636 cm^{-1}, corresponding to the vinyl groups of TMSPMA units on the microspheres, indicates that the carbon–carbon double bonds (C=C) have been successfully introduced onto the surface of Fe_3O_4 nanoparticles. The absorption peaks at 818 and 1081 cm^{-1} have disappeared, indicative of decomposition of the methoxysilyl groups (Si–O–CH_3). The FT-IR results confirm that TMSPMA was successfully grafted onto the Fe_3O_4 nanoparticles via the silanization reaction [18,25,46].

The magnetic properties of Fe_3O_4 nanoparticles were previously investigated [18] and here we will focus on the utilization of TMSPMA-modified Fe_3O_4 nanoparticles as possible crosslinker for the fabrication of microgels. The amount of grafted TMSPMA was determined by TGA to be ~15.2 wt%, as shown in Fig. 3. Comparing with the feeding amount, the TGA result indicates that only part of TMSPMA successfully grafted onto the surface of Fe_3O_4 nanoparticles. It was worthy to note that only the grafted TMSPMA could be preserved after purification with a magnet. If the average size of the Fe_3O_4 nanoparticles was taken as ~13 nm, the grafted density of TMSPMA was estimated to be ~5 TMSPMAs/nm^2 and 2500 TMSPMA molecules on a single Fe_3O_4 nanoparticle [18]. (See Supplementary Material) The C=C bonds of the grafted TMSPMA on Fe_3O_4 nanoparticles can take part in the free radical polymerization. The hybrid microgels were hence prepared at 70 °C by applying the surfactant-free emulsion polymerization (SFEP) technique with TMSPMA-modified Fe_3O_4 nanoparticles as the crosslinker and NIPAm as the monomer. The initiator of $K_2S_2O_8$ was first added into the aqueous dispersion of TMSPMA-modified Fe_3O_4 nanoparticles. After 15 min, the thermosensitive monomer, NIPAm, was then added into the reaction solution and the radical copolymerization was allowed to perform at 70 °C for 12 h. Thermosensitive PNIPAm microgels crosslinked with magnetic Fe_3O_4 nanoparticles were thus obtained.

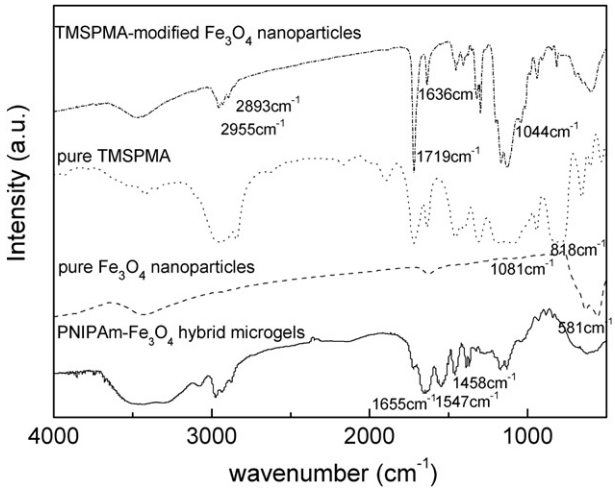

Fig. 2. FT-IR spectra of pure Fe_3O_4 nanoparticles, pure TMSPMA, TMSPMA-modified Fe_3O_4 nanoparticles, and PNIPAm-Fe_3O_4 hybrid microgels.

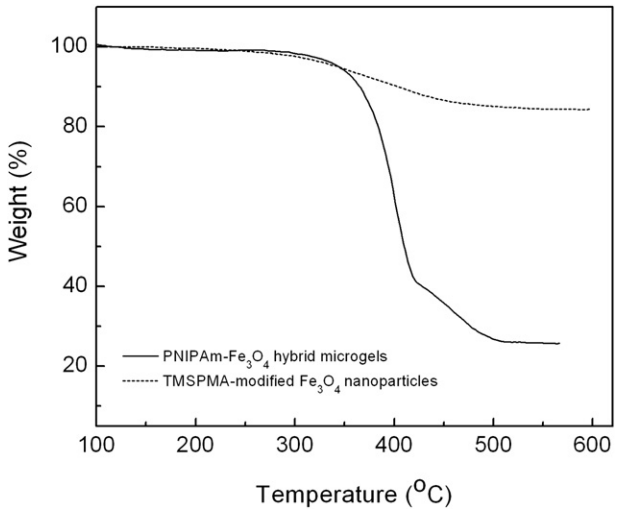

Fig. 3. Thermogravimetric analysis (TGA) curves of TMSPMA-modified Fe_3O_4 nanoparticles (dash line) and PNIPAm-Fe_3O_4 hybrid microgels (solid line).

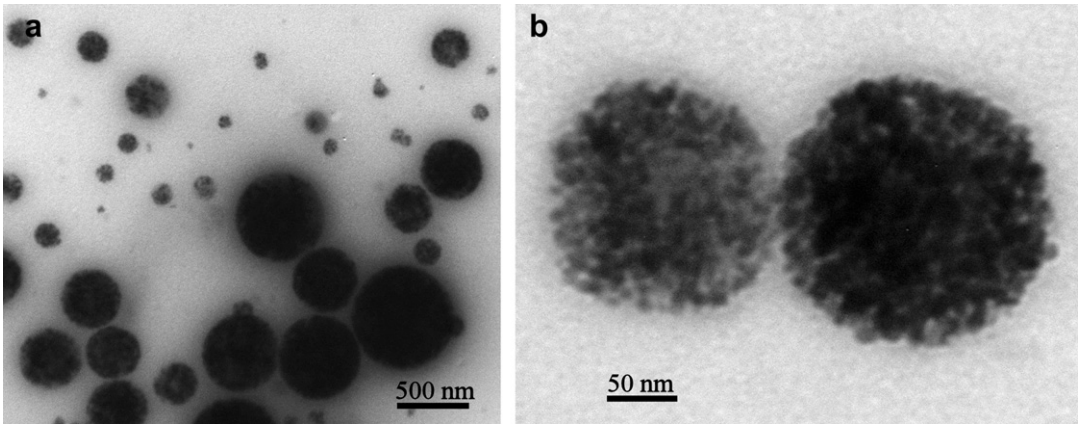

Fig. 4. Typical TEM images of the PNIPAm-Fe_3O_4 hybrid microgels crosslinked with TMSPMA-modified Fe_3O_4 nanoparticles.

The TEM observation indicates that the PNIPAm-Fe_3O_4 hybrid microgels were spherical in shape with large size distribution and contained many small black spheres, which were Fe_3O_4 nanoparticles, as shown in Fig. 4. The TEM images suggest that the TMSPMA-Fe_3O_4 nanoparticles indeed behaved as crosslinkers. The covalent bonds of TMSPMA took part in the radical polymerization of NIPAm. The bonding of multiple TMSPMA monomers on the surface of Fe_3O_4 nanoparticles hence led to the crosslinking reactions during the polymerization. In other word, the TMSPMA-modified Fe_3O_4 nanoparticles are like chemical crosslinkers with multiple function groups, leading to the successful formation of spherical microgels. From the TEM image with higher magnification (Fig. 4b), it can be seen that the Fe_3O_4 nanoparticles were randomly distributed inside the resultant PNIPAm-Fe_3O_4 hybrid microgels and the number of Fe_3O_4 nanoparticles in each hybrid microgel was different.

Fig. 5 shows the typical SEM image and the energy dispersive X-ray analysis (EDX) of the PNIPAm-Fe_3O_4 hybrid microgels. The SEM result is consistent with that of TEM. The PNIPAm-Fe_3O_4 hybrid microgel particles were rather spherical with a large size distribution (Fig. 5a). The average diameter of the hybrid microgels was 226 ± 62 nm. The elemental composition of the PNIPAm-Fe_3O_4 hybrid microgels was determined by using EDX (Fig. 5b). Elements C, O, Fe, and Si were found, which confirmed that the microgel particles indeed contain TMSPMA-modified Fe_3O_4 nanoparticles. The element aluminum (Al) was resulted from the aluminum foil substrate and the element platinum (Pt) was from the coating layer which was used to increase the surface electronic conductivity of the microgels. Note that the percentage of each element obtained by EDX can only serve as qualitative indication of the existence of the element and can not be used for quantitative calculation due to the experimental uncertainty. For example, the weight percentages of O, Si, and Fe did not fit to the formulation of the PNIPAm-Fe_3O_4 hybrid microgels. If the weight percentage of Fe was chosen as reference, the weight percentage of O was largely underestimated, while the weight percentage of Si was overestimated according to ~15.2 wt% of TMSPMA grafted onto Fe_3O_4 nanoparticles and ~25.8 wt% of Fe_3O_4 nanoparticles inside the hybrid microgels (see below).

The PNIPAm-Fe_3O_4 hybrid microgels were also characterized by FT-IR, as shown in Fig. 2. In the spectrum of PNIPAm-Fe_3O_4 hybrid microgels, bands at 1655, 1547, and 1458 cm^{-1} were attributed to the –CO–NH– group of the PNIPAm. Characteristic absorption bands of Fe_3O_4 and TMSPMA were also observed. No absorption bands of vinyl groups was observed for PNIPAm-Fe_3O_4 hybrid microgels, indicating all of the carbon–carbon double bonds (C=C) have taken part in the free radical polymerization. Furthermore, the TGA results showed that the amount of Fe_3O_4 nanoparticles inside the PNIPAm-Fe_3O_4 hybrid microgels was ca. 25.8 wt%, as shown in Fig. 3 (solid line).

The TEM, SEM, EDX, TGA, and FT-IR results confirmed that the PNIPAm-Fe_3O_4 hybrid microgels was successfully obtained with TMSPMA-modified Fe_3O_4 nanoparticles as the crosslinker and

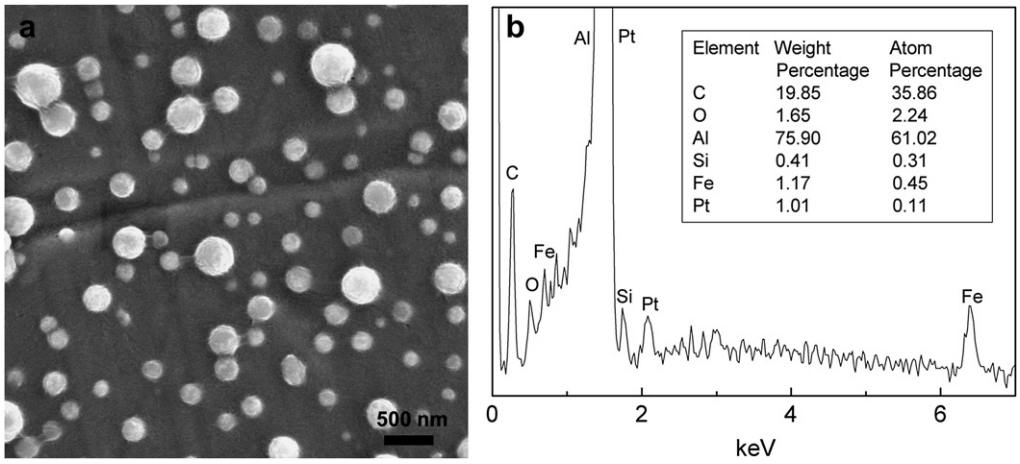

Fig. 5. (a) Scanning electron microscope (SEM) image and (b) energy dispersive X-ray analysis (EDX) of the PNIPAm-Fe_3O_4 hybrid microgels.

NIPAm as the monomer. The Fe_3O_4 nanoparticles and PNIPAm network chains were connected and crosslinked via the covalent bonds. As compared with the conventional poly(*N*-isopropylacrylamide) (PNIPAm) microgels prepared by SFEP with chemical crosslinker *N,N′*-methylene-bisacrylamide and P(NIPAm-co-TMSPMA) microgels [1,9,21], the shortcomings of the present methodology are that the size of PNIPAm-Fe_3O_4 hybrid microgels obtained was relatively polydisperse and the crosslinking density of each microgel was different. Two possible reasons may lead to the large size distribution of the PNIPAm-Fe_3O_4 hybrid microgels. First, the Fe_3O_4 nanoparticles were not uniformly modified with TMSPMA, leading to the heterogeneous crosslinking reaction. Secondly, the TMSPMA-modified Fe_3O_4 nanoparticles were hydrophobic in nature and formed aggregates with various sizes in aqueous solution even after ultrasonication. These aggregates behaved as crosslinkers, which then led to the large size variation of resultant PNIPAm-Fe_3O_4 hybrid microgels. As a consequence, the number of Fe_3O_4 nanoparticles in each hybrid microgel was different and hence the crosslinking density of each microgels was different as well. With the ongoing efforts, these shortcomings could be overcome in the near future. Nevertheless, the present work offers a new and alternative way for synthesizing organic–inorganic hybrid microgels, of which the inorganic nanoparticles have well-defined crosslinking mechanism and are covalently connected with the network chains.

It is well known that PNIPAm chains and PNIPAm microgels exhibit thermosensitive characters. PNIPAm microgels will swell in aqueous solution below it's lower critical solution temperature (LCST) and deswell upon raising the temperature above it's LCST. As expected, the PNIPAm-Fe_3O_4 hybrid microgels obtained here are also thermosensitive. Fig. 6 shows the hydrodynamic diameters of the PNIPAm-Fe_3O_4 hybrid microgels in aqueous solution as a function of temperature. The hydrodynamic diameters of the hybrid microgels decrease from ca. 1100 nm to ca. 329 nm with increasing the measuring temperature from 15 to 55 °C. When the temperature was cooled from 55 °C down to 15 °C, the hydrodynamic diameter of the PNIPAm-Fe_3O_4 hybrid microgels increase again along the similar track. There was no apparent hysteresis during the heating and cooling cycles, suggesting that the thermosensitive behavior of the PNIPAm-Fe_3O_4 hybrid microgels was reversible.

Fig. 7 shows that the PNIPAm-Fe_3O_4 hybrid microgels exhibited a relative narrow size distribution in aqueous solution at 15 °C and a double-mode size distribution at 55 °C, respectively. The PNIPAm-Fe_3O_4 hybrid microgels were fully swelled in aqueous solution at low temperature. Furthermore, DLS was more sensitive to the large particles. Therefore, the hybrid microgels exhibited a relative narrow size distribution at 15 °C as measured by DLS. However, the PNIPAm-Fe_3O_4 hybrid microgels were shrinking at high temperature. Due to the different crosslinking density, the collapsed hybrid microgels at 55 °C had various sizes and exhibited a double size distribution measured by DLS, which were consistent with the size distribution of dried hybrid microgels obtained by TEM and SEM (cf. Figs. 4 and 5). It was worthy to note that the double size distribution started to appear at ca. 35 °C.

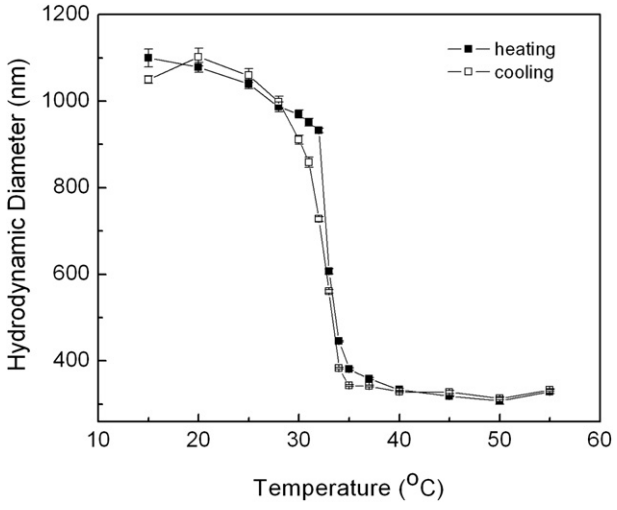

Fig. 6. The hydrodynamic diameters of the PNIPAm-Fe_3O_4 hybrid microgels as a function of measuring temperature.

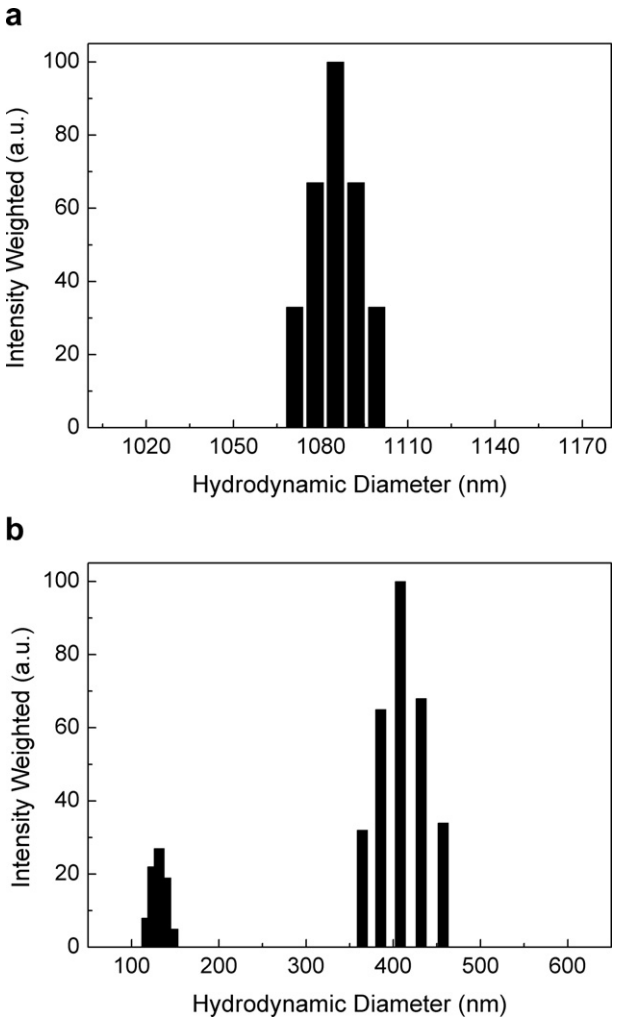

Fig. 7. Size distribution of PNIPAm-Fe_3O_4 hybrid microgels at 15 °C (a) and 55 °C (b), respectively.

The volume phase transition temperature of the PNIPAm-Fe_3O_4 hybrid microgels was determined to be ca. 33 °C via the first-derivative plot of the hydrodynamic diameter of the hybrid microgels as a function of measuring temperature, (Fig. S4 in Supplementary Material) which is similar with the P(NIPAm-co-TMSPMA) microgels (around 30–32 °C) [21] and the conventional PNIPAm microgels (32 °C) [1,9,47,48] with chemical crosslinker *N,N′*-methylene-bisacrylamide (BIS) in aqueous solution. The PNIPAm-Fe_3O_4 hybrid microgels show a steep hydrodynamic diameter change in a narrow temperature range.

The magnetic properties of the TMSPMA-modified Fe_3O_4 nanoparticles and PNIPAm-Fe_3O_4 hybrid microgels were measured at 300 and 10 K, respectively, by using a physical properties measurement system (PPMS-9, Quantum Design). Fig. 8 shows the

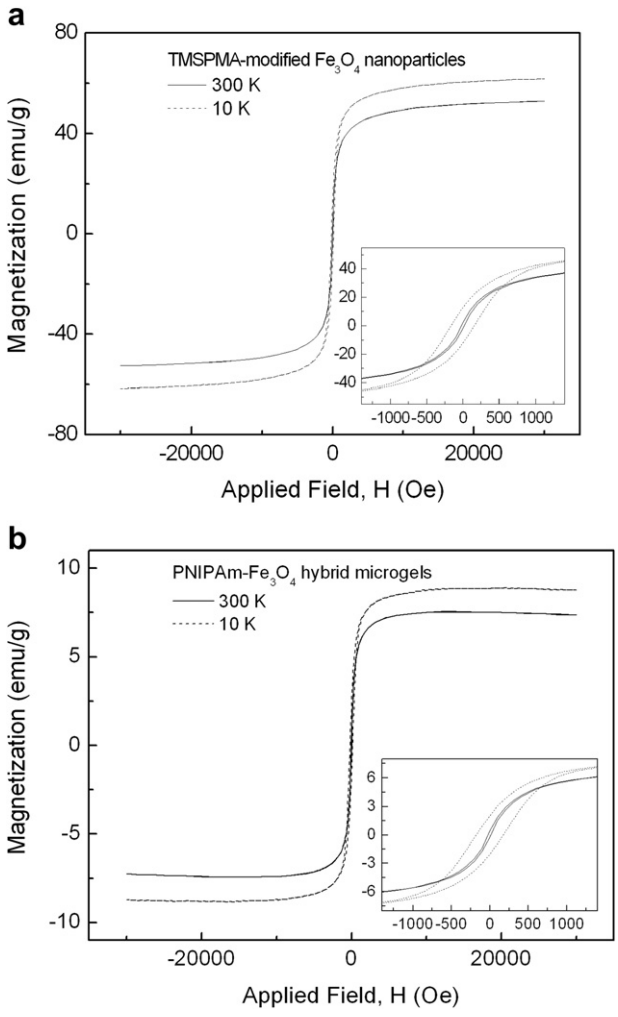

Fig. 8. (a) The magnetization hysteresis loops of the TMSPMA-modified Fe_3O_4 nanoparticles at 300 K (solid line) and 10 K (dash line), respectively. (b) The magnetization hysteresis loops of the PNIPAm-Fe_3O_4 hybrid microgels at 300 K (solid line) and 10 K (dash line), respectively. The insets of (a) and (b) show the coercivity and remanence magnetization of corresponding samples.

magnetization hysteresis loops of the TMSPMA-modified Fe_3O_4 nanoparticles and PNIPAm-Fe_3O_4 hybrid microgels at 300 and 10 K, respectively. At room temperature (300 K), the TMSPMA-modified Fe_3O_4 nanoparticles and PNIPAm-Fe_3O_4 hybrid microgels exhibited superparamagnetic behavior with negligible coercivity and remanence. The saturation magnetization M_s of the TMSPMA-modified Fe_3O_4 nanoparticles and PNIPAm-Fe_3O_4 hybrid microgels were about 52.7 and 7.5 emu/g, respectively, at 300 K. At 10 K, obvious hysteresis loops were observed for both TMSPMA-modified Fe_3O_4 nanoparticles and PNIPAm-Fe_3O_4 hybrid microgels, indicating the typical ferromagnetic behavior. The saturation magnetization M_s of the TMSPMA-modified Fe_3O_4 nanoparticles and PNIPAm-Fe_3O_4 hybrid microgels were about 61.6 emu/g and 8.8 emu/g, respectively, at 10 K. The coercivity of ca. 322 Oe and the remanence of ca. 25 emu/g were observed for TMSPMA-modified Fe_3O_4 nanoparticles at 10 K. For PNIPAm-Fe_3O_4 hybrid microgels at 10 K, the coercivity and remanence were ca. 354 Oe and ca. 4 emu/g, respectively. Because of the large amount of nonmagnetic PNIPAm component, the M_s value of PNIPAm-Fe_3O_4 hybrid microgels was much lower than that of TMSPMA-modified Fe_3O_4 nanoparticles. In our previous work [18], a linear relationship between the amount of organic polymer coating and M_s of poly [N-isopropylacrylamide-co-3-(trimethoxysilyl)-propylmethacrylate] [P (NIPAm-co-TMSPMA)] capped Fe_3O_4 nanoparticles was established (cf. Fig. 7A in Ref. 18).Since the same chemicals (NIPAm and TMSPMA) were used in the present work, the amounts of organic components could be estimated form the M_s of PNIPAm-Fe_3O_4 hybrid microgels. By using M_s of 52.7 emu/g at 300 K, the weight percent of organic polymer components in the PNIPAm-Fe_3O_4 hybrid microgels was then calculated to be ca. 76.0 wt %, which was in good agreement with the TGA result (i.e. 74.2 wt%).

4. Conclusions

The thermosensitive organic–inorganic PNIPAm-Fe_3O_4 hybrid microgels were successfully prepared via surfactant-free emulsion polymerization (SFEP) by using *N*-isopropylacrylamide (NIPAm) as the thermosensitive monomer and 3-(trimethoxysilyl)propylmethacrylate (TMSPMA)-modified magnetic Fe_3O_4 nanoparticles as the crosslinker. The TMSPMA-modified magnetic Fe_3O_4 nanoparticles were confirmed to behave as crosslinkers, leading to the formation of PNIPAm-Fe_3O_4 hybrid microgels. The resultant PNIPAm-Fe_3O_4 hybrid microgels were spherical in shape with a large size distribution and the Fe_3O_4 nanoparticles were randomly distributed inside the microgels. The PNIPAm-Fe_3O_4 hybrid microgels exhibit reversible thermosensitive swelling and deswelling properties with a volume phase transition temperature of 33 °C. At room temperature (300 K), the PNIPAm-Fe_3O_4 hybrid microgels show superparamagnetic behavior. Such method can be also adapted for other monomers and inorganic nanoparticles. Further experiments are ongoing to improve the size distribution of the resultant hybrid microgels and to control the distribution of the functional inorganic nanoparticles inside the hybrid microgels as well as the crosslinking density of the hybrid microgels.

Acknowledgments

The authors thank the National Natural Science Foundation of China (No. 20604022, 20874087) and 863 project (No. 2009AA04Z125) for financial supports.

Appendix. Supplementary data

Supplementary data related to this article can be found online at doi:10.1016/j.polymer.2010.11.014.

References

[1] Pelton RH, Chibante P. Colloids Surf 1986;20(3):247–56.
[2] Oh JK, Drumright R, Siegwart DJ, Matyjaszewski K. Prog Polym Sci 2008;33 (4):448–77.
[3] Palioura D, Armes SP, Anastasiadis SH, Vamvakaki M. Langmuir 2007;23 (10):5761–8.
[4] Pich A, Karak A, Lu Y, Ghosh AK, Adler HJP. J Nanosci Nanotechnol 2006;6 (12):3763–9.
[5] Lopez VC, Hadgraft J, Snowden MJ. Int J Pharm 2005;292(1–2):137–47.
[6] Zhang JG, Xu SQ, Kumacheva E. J Am Chem Soc 2004;126(25):7908–14.
[7] Garcia A, Marquez M, Cai T, Rosario R, Hu ZB, Gust D, et al. Langmuir 2007; 23(1):224–9.
[8] Bradley M, Ramos J, Vincent B. Langmuir 2005;21(4):1209–15.
[9] Saunders BR, Vincent B. Adv Colloid Interface Sci 1999;80(1):1–25.
[10] Snowden MJ, Chowdhry BZ, Vincent B, Morris GE. J Chem Soc, Faraday Trans 1996;92(24):5013–6.
[11] Karg M, Hellweg T. J Mater Chem 2009;19(46):8714–27.
[12] Hoffmann F, Cornelius M, Morell J, Froba M. Angew Chem Int Ed 2006;45 (20):3216–51.
[13] Sanchez C, Lebeau B, Chaput F, Boilot JP. Adv Mater 2003;15(23):1969–94.
[14] Sanchez C, Soler-Illia G, Ribot F, Lalot T, Mayer CR, Cabuil V. Chem Mater 2001;13(10):3061–83.
[15] Wen JY, Wilkes GL. Chem Mater 1996;8(8):1667–81.
[16] Judeinstein P, Sanchez C. J Mater Chem 1996;6(4):511–25.
[17] Lu Y, Proch S, Schrinner M, Drechsler M, Kempe R, Ballauff M. J Mater Chem 2009;19(23):3955–61.

[18] Du BY, Mei AX, Tao PJ, Zhao B, Cao Z, Nie JJ, et al. J Phys Chem C 2009;113 (23):10090–6.
[19] Wong JE, Gaharwar AK, Muller-Schulte D, Bahadur D, Richtering W. J Colloid Interface Sci 2008;324(1–2):47–54.
[20] Contreras-Caceres R, Sanchez-Iglesias A, Karg M, Pastoriza-Santos I, Perez-Juste J, Pacifico J, et al. Adv Mater 2008;20(9):1666–70.
[21] Cao Z, Du BY, Chen TY, Nie JJ, Xu JT, Fan ZQ. Langmuir 2008;24(22):12771–8.
[22] Wang XJ, Hu DD, Yang JX. Chem Mater 2007;19(10):2610–21.
[23] Wang GZ, Zhang Y, Fang Y, Gu ZZ. J Am Ceram Soc 2007;90(7):2067–72.
[24] Pich AZ, Adler HJP. Polym Int 2007;56(3):291–307.
[25] Narain R, Gonzales M, Hoffman AS, Stayton PS, Krishnan KM. Langmuir 2007;23(11):6299–304.
[26] Ballauff M, Lu Y. Polymer 2007;48(7):1815–23.
[27] Das M, Zhang H, Kumacheva E. Annu Rev Mater Res 2006;36:117–42.
[28] Zhang JG, Xu SQ, Kumacheva E. Adv Mater 2005;17(19):2336–40.
[29] Nayak S, Lyon LA. Angew Chem Int Ed 2005;44(47):7686–708.
[30] Agrawal M, Rubio-Retama J, Zafeiropoulos NE, Gaponik N, Gupta S, Cimrova V, et al. Langmuir 2008;24(17):9820–4.
[31] Gong YJ, Gao MY, Wang DY, Mohwald H. Chem Mater 2005;17(10):2648–53.
[32] Rubio-Retama J, Zafeiropoulos NE, Frick B, Seydel T, Lopez-Cabarcos E. Langmuir 2010;26(10):7101–6.
[33] Rubio-Retama J, Zafeiropoulos NE, Serafinelli C, Rojas-Reyna R, Voit B, Cabarcos EL, et al. Langmuir 2007;23(20):10280–5.
[34] Zhang F, Wang CC. Langmuir 2009;25(14):8255–62.
[35] Lian XM, Jin J, Tian J, Zhao HY. ACS Appl Mater Interfaces 2010;2(8):2261–8.
[36] Pich A, Zhang FB, Shen L, Berger S, Ornatsky O, Baranov V, et al. Small 2008;4:2171–5.
[37] Haraguchi K, Takeshita T. Adv Mater 2002;14:1121.
[38] Haraguchi K, Takeshita T, Fan S. Macromolecules 2002;35:10162–71.
[39] Nie JJ, Du BY, Oppermann WJ. Macromolecules 2005;38:5729–36.
[40] Nie JJ, Du BY, Oppermann WJ. Phys Chem B 2006;110:11167–75.
[41] Zhang QS, Zha LS, Ma JH, Liang BR. Macromol Rapid Commun 2007;28:116–20.
[42] Voorn DJ, Ming W, van Herk AM. Macromolecules 2006;39:4654–6.
[43] Czaun M, Hevesi L, Takafuji M, Ihara H. Chem Commun 2008;18:2124–46.
[44] Ghosh M, Lawes G, Gayen A, Subbanna GN, Reiff WM, Subramanian MA, et al. Chem Mater 2004;16(1):118–24.
[45] Kang YS, Risbud S, Rabolt JF, Stroeve P. Chem Mater 1996;8(9):2209–11.
[46] De Palma R, Peeters S, Van Bael MJ, Van den Rul H, Bonroy K, Laureyn W, et al. Chem Mater 2007;19(7):1821–31.
[47] Pinkrah VT, Beezer AE, Chowdhry BZ, Gracia LH, Mitchell JC, Snowden MJ. Langmuir 2004;20:8531–6.
[48] Kawaguchi H, Fujimoto K, Mizuhara Y. Colloid Polym Sci 1992;270(1):53–7.

Polymer 52 (2011) 180–190

Contents lists available at ScienceDirect

Polymer

journal homepage: www.elsevier.com/locate/polymer

Morphology and mechanical properties of glass fiber reinforced Nylon 6 nanocomposites

Youngjae Yoo [1], M.W. Spencer, D.R. Paul*

Department of Chemical Engineering and Texas Materials Institute, The University of Texas at Austin, Austin, TX 78712, USA

ARTICLE INFO

Article history:
Received 25 August 2010
Received in revised form
27 October 2010
Accepted 30 October 2010
Available online 5 November 2010

Keywords:
Nanocomposite
Glass fibers
Nylon 6

ABSTRACT

Nylon 6 composites containing both an organoclay and glass fibers as fillers were prepared by melt processing. The aspect ratios of the glass fibers and the clay platelets were determined by electron microscopy techniques. The aspect ratio of each type of filler decreased as filler loading increased. A two particle population model for the tensile modulus was constructed based on the Mori–Tanaka composite theory. The experimental levels of reinforcement appear to be reasonably consistent with model predictions when changes in particle aspect ratios are accounted for. The tensile strength increases and elongation at break decreases as the content of either filler increases according to expected trends. Izod impact strength increased with glass fiber content but decreased with clay content.

1. Introduction

Fiber reinforced polymer composites have been widely used for applications requiring high stiffness and strength, e.g., aerospace, automotive, marine, and sporting goods [1–3]. In most cases, rather high loadings of glass fibers are required to achieve the desired performance; this leads to an undesirable increase in specific gravity, decreased melt flow, and increased brittleness [4].

In recent years, polymer nanocomposites have attracted great interest due to the considerable enhancement in stiffness realized at very low filler loadings [5–12]. Substantial improvements in mechanical [13,14], barrier [15,16], thermal [17,18], and flammability [19,20] properties have been reported while maintaining similar density and optical properties to those of the neat polymer matrix. Among these, nanocomposites based on polyamides have received attention due to their excellent compatibility with specific organoclays [13,21–23].

Although polymer nanocomposites reinforced by montmorillonite (MMT) have exhibited improved thermal and mechanical properties at very low filler contents; loadings of more than 10 wt% MMT lead to poor dispersion and processing characteristics [9,10,12]. On the other hand, glass fiber loadings of 30 to 50 wt% are quite common [4]. It is of interest to explore whether combining these two fillers would give the desired performance at low to intermediate filler loadings. Such materials could be viewed as a polymer matrix containing two different types of fillers of rather different size scales. Alternatively, one might view these materials as a nanocomposite matrix filled with glass fibers because the clay platelets are so much smaller than the glass fibers. Although there have been extensive reports on polymer nanocomposites and micro-composites, only a few preliminary studies have been reported on the structure and properties of glass fiber reinforced polymer composites where the nanocomposite plays the role of the matrix as illustrated by the conceptual vision shown in Fig. 1.

Recently, several efforts have been made to investigate the combined effects of fillers at two different size scales, i.e., micro and nano. Akkapeddi [4] reported that the nature of the increase in properties of polyamide 6 composites reinforced by MMT and short glass fibers is not completely additive, but there is clearly an increase over single filler based composites. Similar enhanced mechanical properties are reported for the composites based on polyamide 6 [24–28], and some thermosetting polymers [29–32]. The slight enhancement of tensile properties by two fillers were reported for glass fiber reinforced polypropylene nanocomposites using glass fiber mat [33,34]. More recently, Isitman et al. [35] observed a synergistic flame retardancy effect of organoclays for glass fiber reinforced nylon 6 with conventional flame retardants.

Because of our experience with nylon 6 nanocomposites [13,21,22,36–41] and glass fiber composites [42–46], nylon 6 was chosen as the polymer for this study. The purpose of this work is to explore the morphology and mechanical property changes upon the incorporation of short glass fibers into nylon 6/MMT

* Corresponding author. Tel.: +1 512 471 5392; fax: +1 512 471 0542.
E-mail address: drp@che.utexas.edu (D.R. Paul).
[1] Current address: Information & Electronics Polymer Research Center, Korea Research Institute of Chemical Technology, Daejeon 305-600, Korea

0032-3861/$ – see front matter © 2010 Elsevier Ltd. All rights reserved.
doi:10.1016/j.polymer.2010.10.059

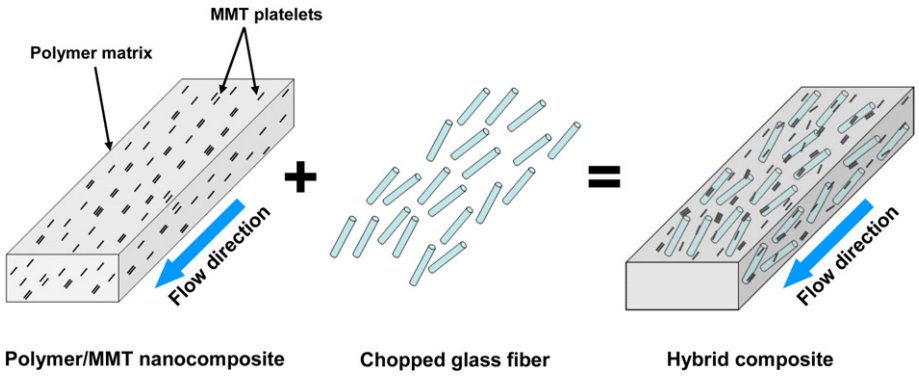

Fig. 1. Hybrid composites based on a polymer/MMT nanocomposite and short glass fibers.

nanocomposites. In other words, this study investigates the reinforcement from two fillers of very different size scales: glass fibers with diameters on the order of 10 μm and MMT platelets with thickness of 1 nm.

2. Experimental section

2.1. Materials

Table 1 summarizes the materials used in this study. A commercial grade of nylon 6 was chosen that is commonly used for injection molding and extrusion applications. The organoclay was formed by cation exchange reaction between sodium montmorillonite and trimethyl hydrogenated-tallow ammonium chloride, designated here as $M_3(HT)_1$, and was obtained from Southern Clay Products. The data below are reported in terms of weight percent montmorillonite, wt% MMT, in the composite rather than the amount of organoclay, since the silicate is the reinforcing component. The chopped strand glass fibers (fiber diameter = 13 μm, length = 4 mm) with a proprietary surface treatment intended for use in polyamide matrices was provided by Owens Corning. Prior to melt processing, all materials employed were dried for a minimum of 24 h in a vacuum oven at 80 °C.

Table 1
Materials used in this study.

Material (designation in this paper)	Commercial designation	Specifications	Supplier
Polymer			
Nylon 6[a]	Aegis® H73WP	$[COOH]/[NH_2] = 0.9$ $T_g = 55$ °C, $\overline{M}_n = 22{,}000$ Brabender torque = 6.37 N·m[b]	Honeywell
Fillers			
Organoclay	$M_3(HT)_1$,[c] Trimethyl hydrogenated-tallow ammonium montmorillonite	Organic loading = 95 mequiv/100 g clay Organic content = 29.6 wt % d_{001} spacing = 18.0 Å[d]	Southern clay products
Glass fiber	CS 995-13P, 4 mm	Chopped strand glass fiber with unknown sizing[e] $D = 13$ μm $L = 4$ mm	Owens Corning

[a] Referred to as a medium molecular weight grade in prior studies from this laboratory [39,47,48].
[b] Data from reference [48].
[c] The selected organoclay is designated as $M_3(HT)_1$ in this study, where M = methyl and HT = hydrogenated tallow. Tallow is a natural product composed predominantly (63%) of saturated and unsaturated C18 chains. HT is the saturated form yet still contains a small fraction of double bonds.
[d] The basal spacing corresponds to the characteristic Bragg reflection peak d_{001} obtained from a powder WAXS scan of the organoclay.
[e] Chopped strand glass fiber coated with a proprietary sizing intended for use in polyamide matrices.

2.2. Melt processing

The nanocomposites of nylon 6 and the organoclay were made in a Haake co-rotating, intermeshing twin-screw extruder (diameter = 30 mm, $L/D = 10$) operating at a barrel temperature of 235–240 °C, a feed rate of ~1 kg/h, and a screw speed of 280 rpm. Extruded nanocomposite pellets were dry mixed with various amounts of glass fiber and injection molded to prepare standard 3.18 mm thick tensile (ASTM D638) and Izod bars (ASTM D256) using an Arburg All-rounder 305-210-700 injection molding machine with an injection pressure of 70 bar and a holding pressure of 35 bar. The temperature of the feed zone of the injection molder was set at 240 °C and was ramped up to 270 °C at the nozzle. The mold temperature was held at 80 °C. After molding, the specimens were immediately sealed in a polyethylene bag and placed in a vacuum desiccator for a minimum of 24 h prior to mechanical testing.

In the early stages of this work, another processing procedure was considered where the nanocomposite was formed as described above, but the glass fibers were compounded into the nanocomposite using a single screw extruder. This single screw extruder causes far less fiber breakage than would have been the case if the glass fibers were compounded into the material using the twin screw extruder. The resulting glass fiber reinforced nanocomposite was injection molded into test bars. However, the resulting mechanical properties obtained by this method were, within the margin of error, the same as obtained in the first described method. Thus, this simpler processing method was used for the remainder of this work because it facilitated sample preparation and minimized, but did not eliminate, glass fiber attrition.

2.3. Morphology characterization

Fracture surfaces of the composites were examined with a LEO 1530 Scanning Electron Microscope (SEM) operating at an accelerating voltage of 10 kV. SEM specimens were sputter-coated with gold prior to observation. For analysis of the glass fiber length, the polymer was burned off from the injection molded samples in a furnace at 500 °C for 4 h to isolate the short glass fibers. The glass fibers obtained were dispersed in water with a small amount of detergent to reduce surface tension. Using a pipette, a small amount of solution with fibers was placed on a glass slide and then observed by SEM. The morphology of MMT particles was

determined by a JEOL 2010F transmission electron microscope (TEM) operating at an accelerating voltage of 120 kV. TEM samples were cryogenically microtomed into ultra-thin sections of approximately 50 nm with a diamond knife at a temperature of −40 °C using an RMC PowerTome XL microtome. These microtoming procedures have been fully described elsewhere [49–51].

2.4. Mechanical testing

Tensile tests were performed according to ASTM D638 using an Instron model 1137 testing machine upgraded for computerized data acquisition. Tensile modulus, tensile strength and elongation at break results were determined at a crosshead rate of 0.51 cm/min. For accurate analysis, values of the tensile modulus were determined using an extensometer. Notched Izod impact tests were performed at room temperature using a TMI Impact tester (model 43-02) with a 6.8 J hammer and 3.5 m/s impact velocity.

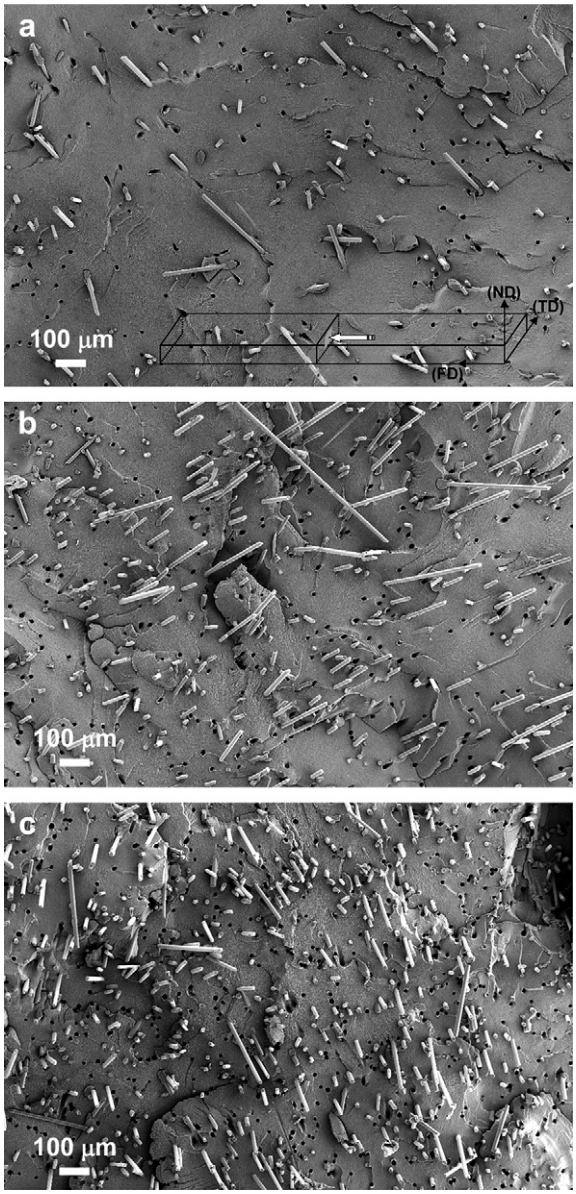

Fig. 2. SEM micrographs of fractured surfaces of glass fiber reinforced nylon 6 nanocomposites based on 5 wt% MMT with the following glass fiber contents: (a) 5 wt% (b) 10 wt%, and (c) 15 wt%. The micrographs are viewed parallel to mold fill direction, showing dark voids where fiber pull-out occurred during Izod impact testing.

3. Results and discussion

3.1. Morphology

SEM micrographs of fracture surfaces for nylon 6 nanocomposites with 5, 10 and 15 wt% glass fiber are shown in Fig. 2. Over the entire range of glass fiber contents, the glass fibers are generally well dispersed in the nylon 6 matrix, and many fibers are pulled out from the matrix. In order to fabricate effective composites, it is necessary to minimize the attrition of fiber length and to have excellent interfacial strength. Fiber length has an important effect on the mechanical properties of the resulting composites, and glass fibers can be broken by melt processing steps [52].

According to the theory of Kelly and Tyson [53], the minimum fiber length that allows the ultimate strength of the fiber to be reached is called the critical fiber length, l_c, and is given by

$$\frac{l_c}{d} = \frac{\sigma_{fu}}{2\tau_y} \tag{1}$$

where d is the mean fiber diameter, σ_{fu} is the ultimate fiber strength, and τ_y is the fiber-matrix interfacial shear strength. The critical fiber length represents the minimum fiber length that can be fractured by stress transfer; below l_c, the fiber will be pulled out of the matrix polymer before fiber failure. For perfectly bonded glass fibers, the interfacial shear strength, τ_y, becomes the shear strength of the polymer matrix, which is 59 MPa for nylon 6 [43]. Using the ultimate fiber strength of 3450 MPa and a fiber diameter of 13 μm as reported by the manufacturer, a critical fiber length of 380 μm is calculated from equation (1). Because the calculated critical fiber length is larger than the average fiber lengths determined from image analysis as will be discussed later, many glass fibers are expected to be pulled out instead of fracturing during loading of the composite as shown in Fig. 2.

Fig. 3 shows a representative SEM micrograph of the dispersed glass fibers extracted from the composites. The measurement of fiber length distribution was completed by image analysis of the glass fibers taken from such micrographs. Quantitative particle analysis was performed by opening a digital image file in Adobe Photoshop where the dispersed glass fibers are traced over an overlapped blank layer. To ensure accurate measurements of the

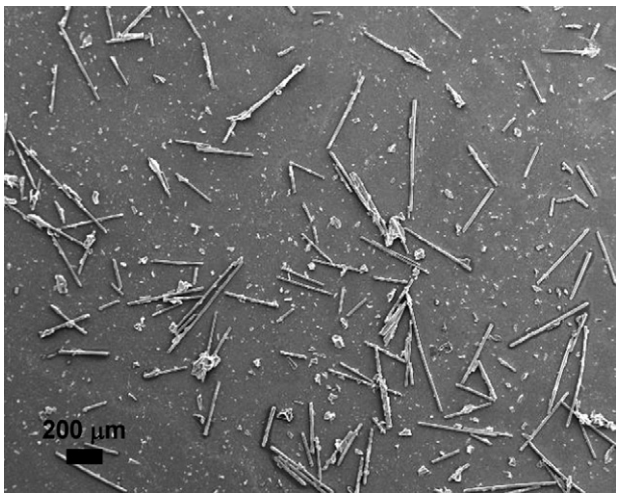

Fig. 3. SEM micrograph of glass fibers extracted from glass fiber reinforced nanocomposites with 5 wt% MMT and 10 wt% GF.

glass fiber length, the image is sufficiently magnified so that most of the fibers are counted. The resulting black/white layer file is imported into the image analysis program, SigmaScan Pro, used to analyze the traced fiber lengths. Using the software, each fiber was assigned a numerical label, and exported to separate files [54,55].

From the distribution of glass fiber particle sizes, the number ($\bar{l}_n$) and weight ($\bar{l}_w$) average fiber length are calculated by [56]

$$\bar{l}_n = \frac{\sum n_i l_i}{\sum n_i} \quad (2)$$

$$\bar{l}_w = \frac{\sum n_i l_i^2}{\sum n_i l_i} \quad (3)$$

where n_i is the number of glass fibers within a specified range about the value l_i; the number average fiber length is always smaller than the weight average value. Fig. 4 shows representative histograms for glass fiber length obtained from SEM analyses of the glass fiber reinforced nanocomposites. The weight average fiber length for the composite with 20 wt% GF without MMT is 581 μm; however, when a composite with the same glass fiber content is made from a nylon 6 nanocomposites containing 7.0 wt% of MMT, the weight average fiber length is reduced to 299 μm.

The measured average glass fiber lengths are divided by the fiber diameter of 13 μm specified by the supplier to compute the aspect ratios for the composites. Fig. 5 shows the aspect ratio changes for the composites versus wt% GF for a fixed MMT content of 0 and 5 wt%. For both series of composites, there is a substantial decrease in the length or aspect ratio of the glass fibers as the content of either filler increases. The decrease for the composites with 5 wt% MMT is gradual up to 20 wt% GF and then levels off with further addition of GF, while the lengths and the aspect ratios of GF for the composites without MMT remain the same up to 20 wt% GF loading. Glass fiber attrition is frequently observed due to the high stresses generated during melt processing owing to the high viscosity of the polymer melt. When MMT is added, the matrix viscosity increases and higher shear stresses are expected. In addition, particle impingement during melt processing can be another reason for glass fiber attrition and this has increased importance at high filler concentrations.

TEM observations allow similar analysis of the MMT particles in the glass fiber reinforced nylon 6 nanocomposites to assess the degree of exfoliation in the polymer matrix. Fig. 6 shows typical TEM micrographs at both low and high magnifications of a composite containing 5 wt% MMT and 30 wt% GF. The low magnification micrograph shows a few glass fibers for one of the materials formulated as described above; the glass fibers were shattered by the microtoming process and parts fell out of the thin

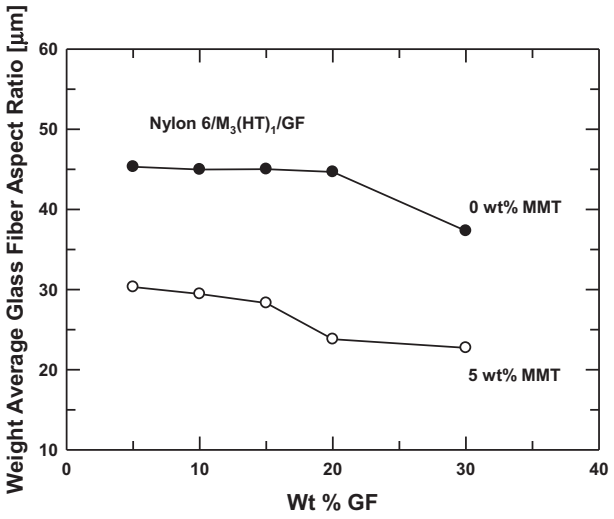

Fig. 5. Aspect ratio changes for fiber reinforced nanocomposites with 0 or 5 wt% MMT and 0–30 wt% GF.

section. Examination of a number of TEM images revealed that the MMT composition is approximately the same everywhere in the nanocomposites, regardless of proximity to glass fibers. The high magnification TEM micrograph reveals well-exfoliated structures containing dispersed layers of MMT, in which individual platelets are easily observed.

Visual assessments from images like those in Fig. 6 were also quantified by MMT particle analysis. Fig. 7 shows a series of representative histograms for MMT particle length, thickness, and aspect ratio obtained from the analysis of the TEM images. The histogram for MMT thickness reveals that most of MMT particles are single platelets, while the particle length and the aspect ratio have a broad distribution as expected.

The average lengths, thicknesses, and aspect ratios from MMT particle analysis are plotted in Fig. 8 versus the MMT content of the composites with/without GF. Without GF, the average MMT particle length, thickness, and aspect ratio show little change with increasing MMT content. With GF, however, the average MMT particle length appears to decrease as MMT content increases while the average MMT particle thickness decreases only slightly. As a result, the average MMT aspect ratio generally decreases for composites with a fixed GF content of 20 wt% as MMT content increases as shown in Fig. 8(c).

As the content of glass fiber increases, higher stresses are generated during melt processing owing to the increased viscosity

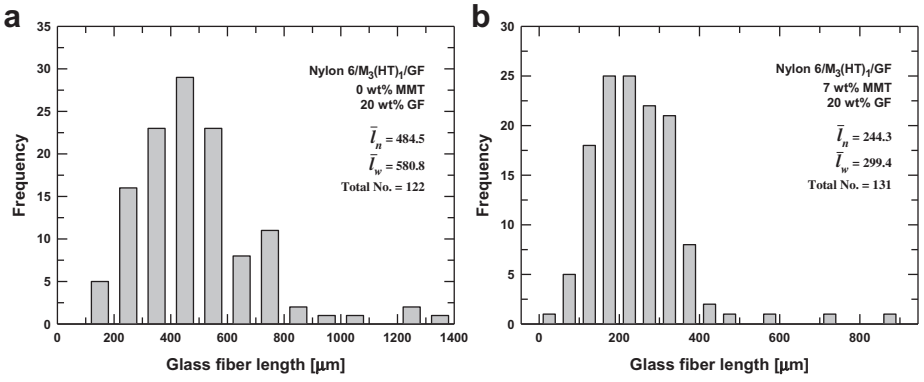

Fig. 4. Glass fiber length distribution for composites with (a) 20 wt% GF and (b) 7 wt% MMT and 20 wt% GF.

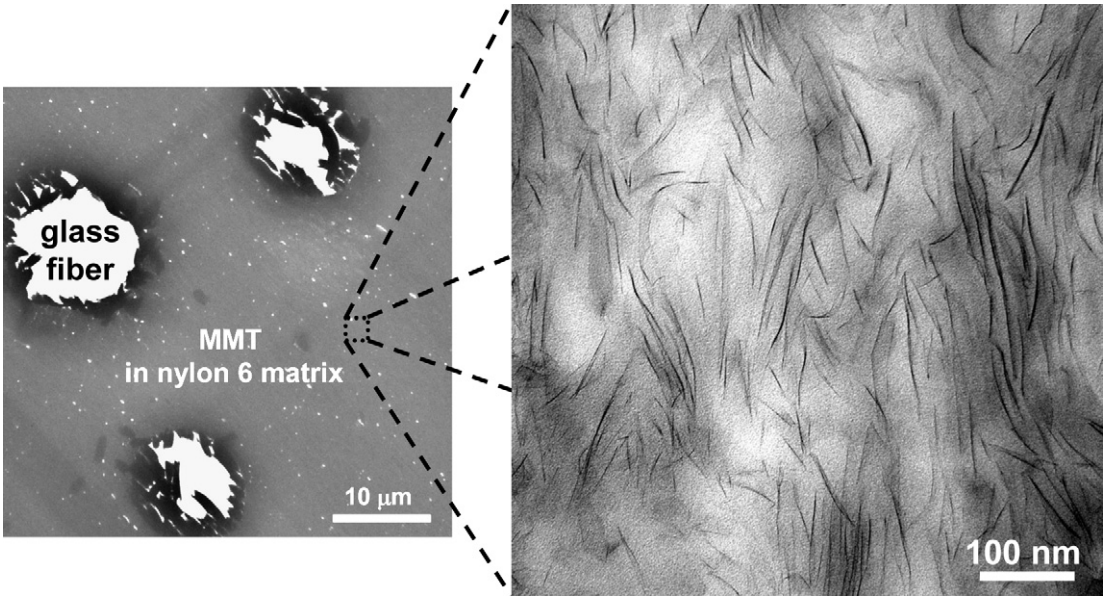

Fig. 6. TEM micrographs of a glass fiber reinforced nanocomposite with 5 wt% MMT and 30 wt% GF showing glass fibers at low magnification and MMT platelets dispersed in the polymer matrix at high magnification.

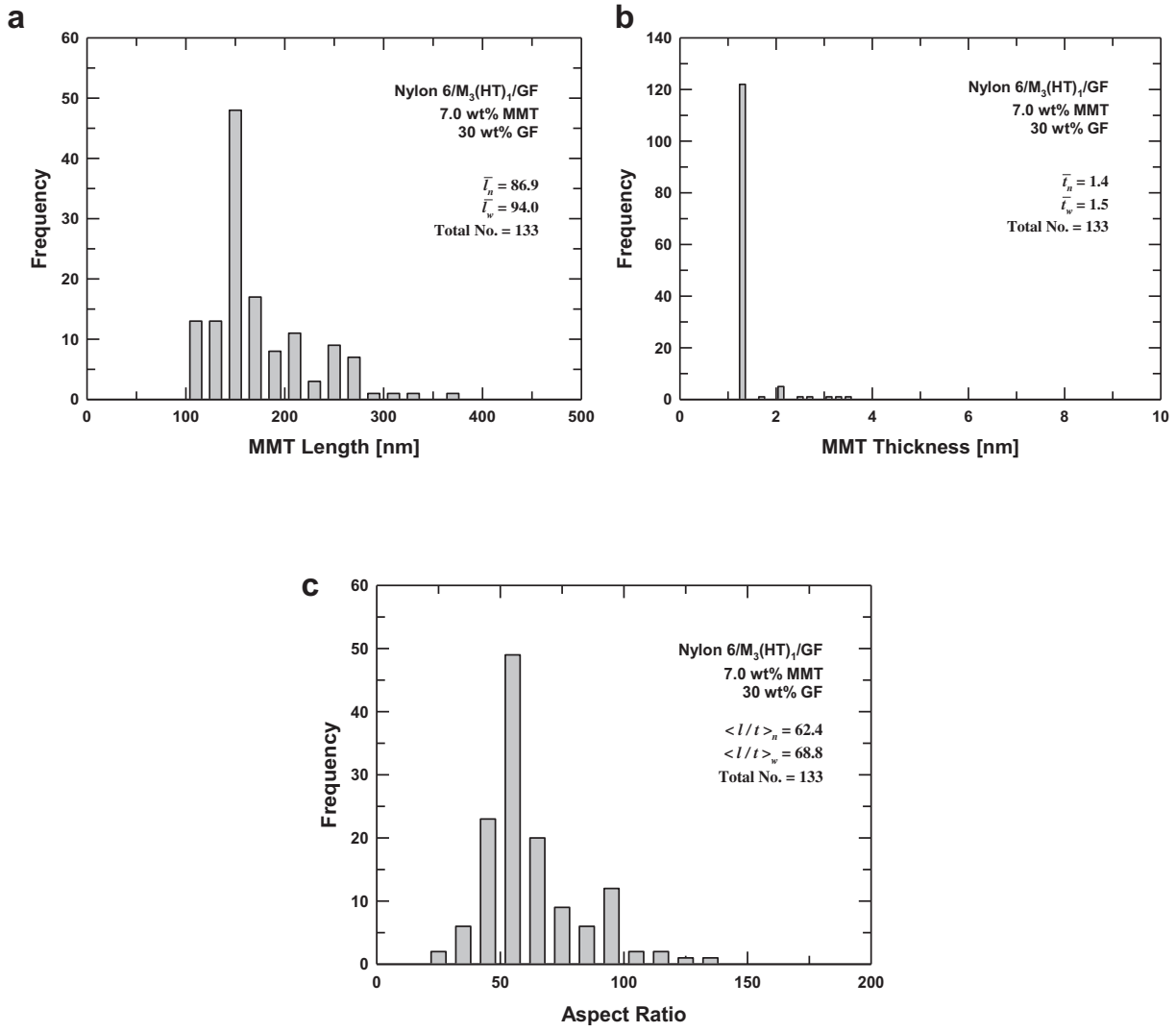

Fig. 7. Histograms of MMT particle length (a), thickness (b), and aspect ratio (c) from a glass fiber reinforced nanocomposite containing 7 wt% MMT and 30 wt% GF.

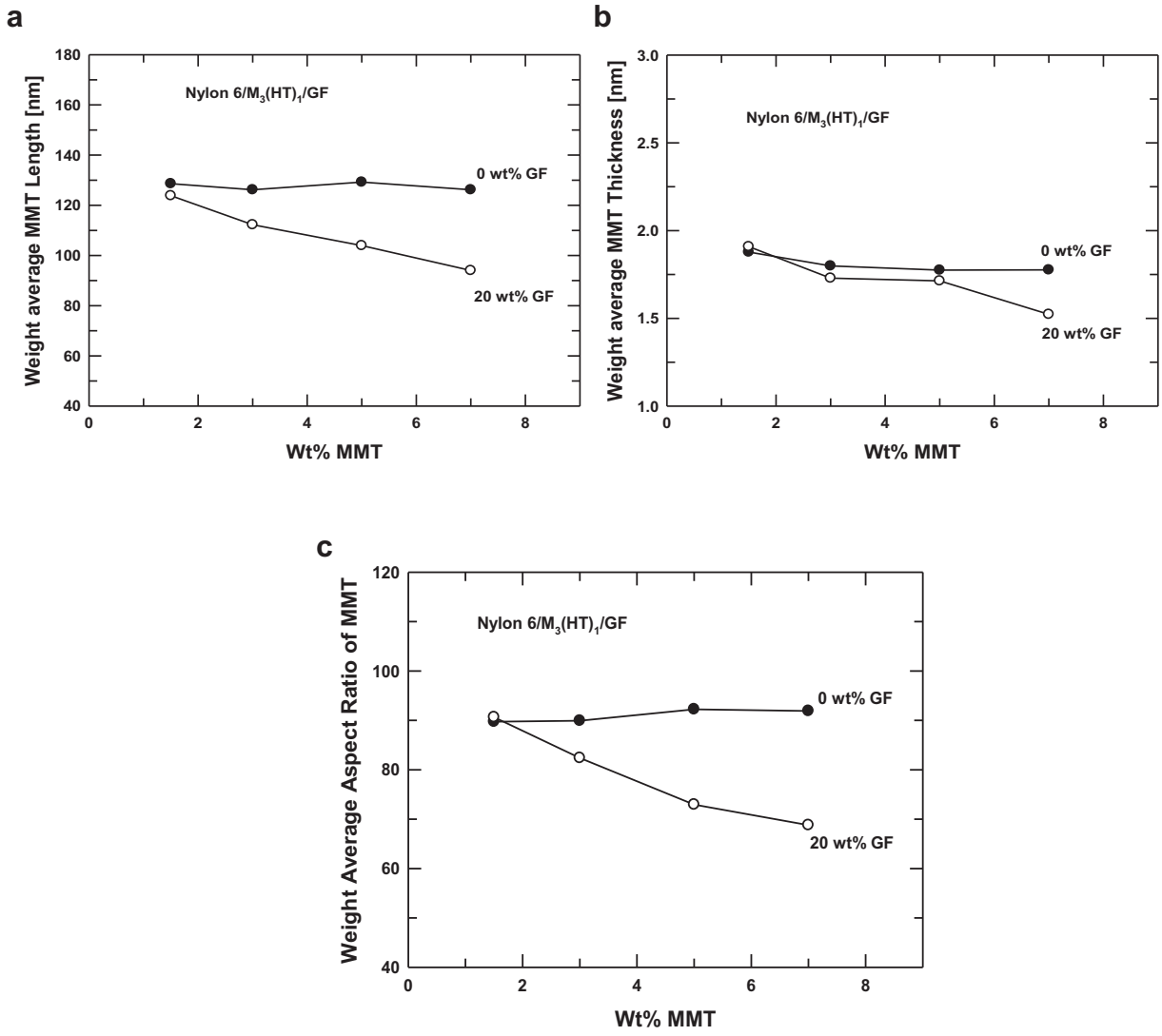

Fig. 8. Weight average MMT particle length (a), thickness (b), and aspect ratio (c) from a glass fiber reinforced nanocomposite containing 0 or 20 wt% GF and 0–7 wt% MMT.

of the polymer melt. This could promote the delamination and exfoliation of partially overlapped MMT platelets as shown in Fig. 9. Thus, the effective MMT particle length would decrease with the addition of glass fibers, while the MMT particle thickness remains mostly unchanged. This mechanism, however, is not well understood at this time. It is not clear yet whether this simply involves the deaggregation of bundles of platelets into smaller particles or whether the platelets of MMT are actually broken or attrited during melt processing. It is unlikely that MMT platelets are broken by particle impingement with glass fibers due to their very different size scales. Whatever the mechanistic details may be, the net effect of melt processing with glass fibers is a decrease in aspect ratio that becomes more significant at higher clay loadings as shown in Fig. 8(c). As a result, the stiffness enhancements are not as large at high loadings because of the decreased aspect ratio. It would be useful to better understand this behavior and to find ways to increase the aspect ratio, especially at higher clay loadings.

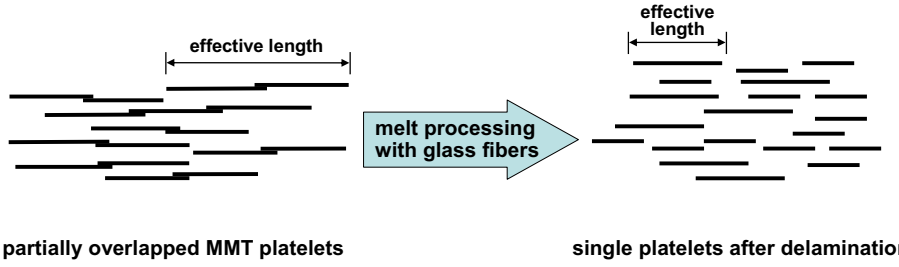

Fig. 9. Schematic illustration of a proposed mechanism for the change in effective MMT particle length when processed with glass fibers.

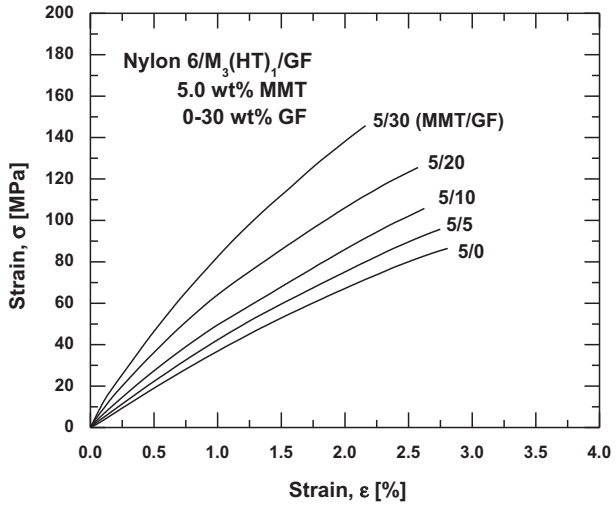

Fig. 10. Stress-strain diagram determined at a crosshead speed of 0.51 cm/min for glass fiber reinforced nanocomposites containing 5 wt% MMT and 0–30 wt% GF.

4. Mechanical properties

Fig. 10 shows representative stress-strain curves for glass fiber reinforced nanocomposites that fracture prior to yielding. The break stress increases while the break strain decreases as the glass fiber content increases. This trend is consistent with observations for adding fillers to a brittle matrix [50,57].

The moduli of glass fiber reinforced nylon 6 nanocomposites are shown in Fig. 11 versus the glass fiber content for a fixed MMT contents of 0 and 5 wt% and versus the MMT content for a fixed glass fiber content of 0 and 20 wt%. For both series of nanocomposites, there is a substantial increase in stiffness over the range of the filler contents examined. However, there are notable differences between the effects of the two fillers. At low filler contents (0–10 wt%), the improvement in tensile modulus with increased MMT loading is significantly higher than that with increased glass fiber loading due to the high modulus of MMT. The morphological results indicate excellent dispersion of both MMT and glass fibers; thus, effective filler reinforcement is expected. However, the decreased aspect ratio of each filler during melt processing reduces the reinforcing efficiency from each filler. Other factors, such as incomplete particle orientation and incomplete bonding between the particles and the matrix, may also reduce the reinforcement.

Similar trends with respect to the content of each filler are evident in the tensile strength results. Fig. 12 shows the tensile strength of glass fiber reinforced nylon 6 nanocomposites versus filler content. Tensile strength increases upon addition of each filler. As with modulus improvement at low filler contents (0–10 wt%), the improvement in tensile strength with increased MMT loading is significantly higher than that caused by an equal loading of glass fibers.

The relationship between filler content and elongation at break for either filler is shown in Fig. 13. Nylon 6 and its nanocomposites, without glass fibers, have large elongation at break values when the MMT loading is below 3.0 wt%. However, the addition of glass fibers to these composites significantly lowers the elongation at break. The elongation at break of the composites reinforced by glass fiber decreases rapidly at low glass fiber concentrations of 5 wt% GF. Even larger reductions were observed for composites containing both fillers.

The notched Izod impact results for the glass fiber reinforced nylon 6 nanocomposites are shown in Fig. 14. In Fig. 14(a), the Izod impact strength is plotted as a function of glass fiber content, while in Fig. 14(b), impact strength is shown as a function of MMT content. The impact strength of the composites with and without MMT increases gradually with increasing glass fiber contents. The increased impact strength observed here reflects the increased stiffness and strength that overshadows the loss in ductility resulting in a larger area under the force-deflection curve. Fig. 10 shows that the maximum stress experienced by the composite samples with 5 wt% MMT and 0–30 wt% glass fiber increases with glass fiber content. The impact strength of the composites with and without glass fiber decreases gradually with increasing MMT contents.

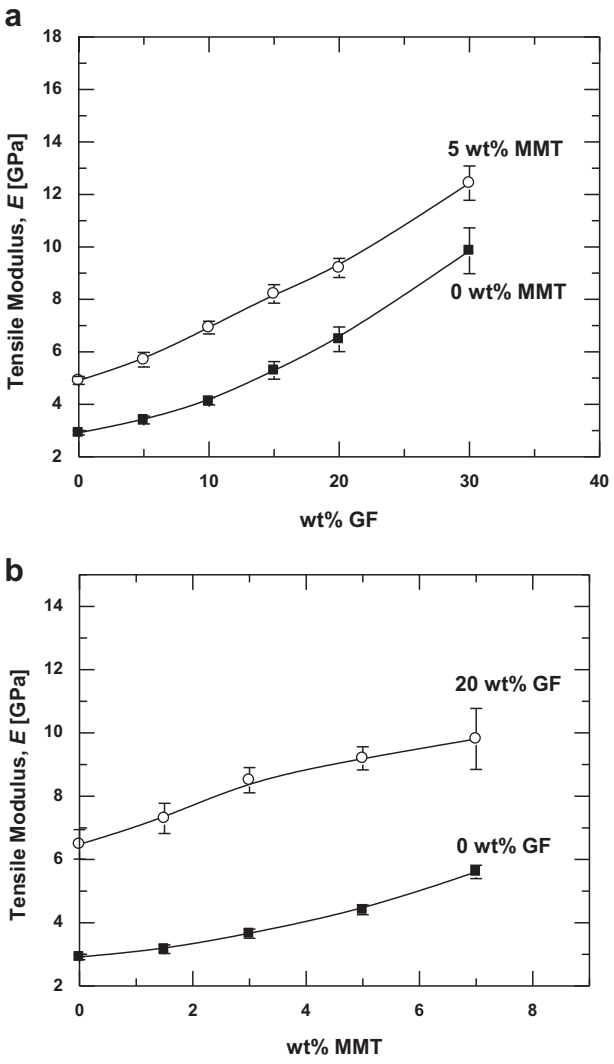

Fig. 11. Tensile modulus of the glass fiber reinforced nanocomposites as a function of (a) glass fiber content with 0 or 5 wt% MMT and (b) MMT content with 0 or 20 wt% GF.

5. Model predictions of modulus

There have been numerous attempts to model the properties of nanocomposites and to correlate the experimental data with composite models [21,24,37,49,55,58–63]. The assumptions typically made include the following: the polymer matrix is not affected by the presence of the filler, e.g., no change in crystallinity, the filler is perfectly aligned, there is good bonding between the matrix and the filler, the matrix and the filler are isotropic, and there are no filler particle-particle interactions or agglomerations

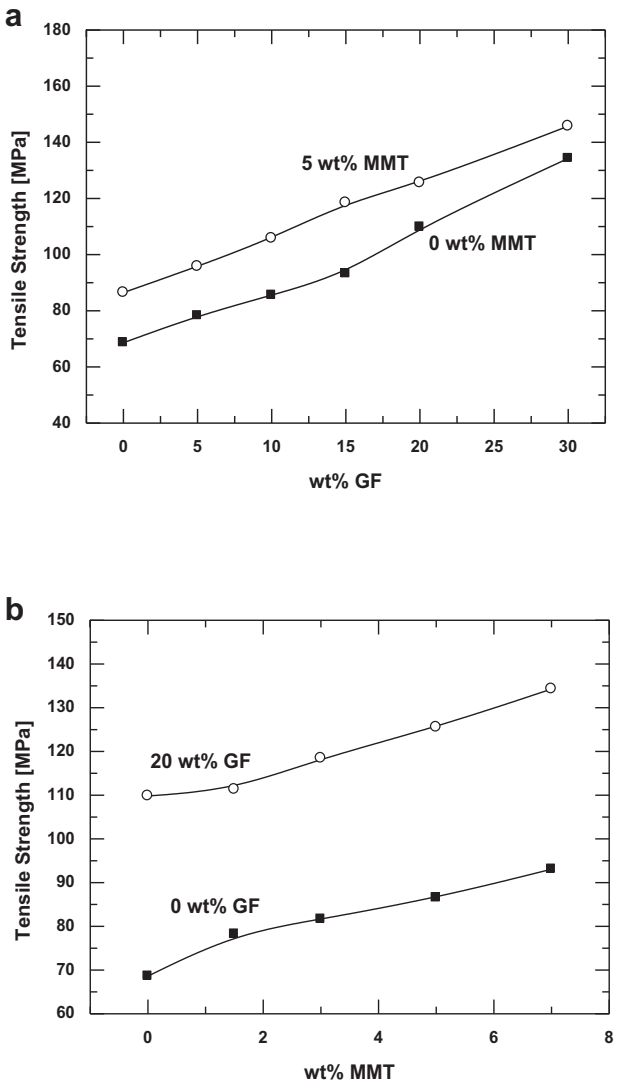

Fig. 12. Tensile strength of glass fiber reinforced nanocomposites as a function of (a) glass fiber content with 0 or 5 wt% MMT and (b) MMT content with 0 or 20 wt% GF.

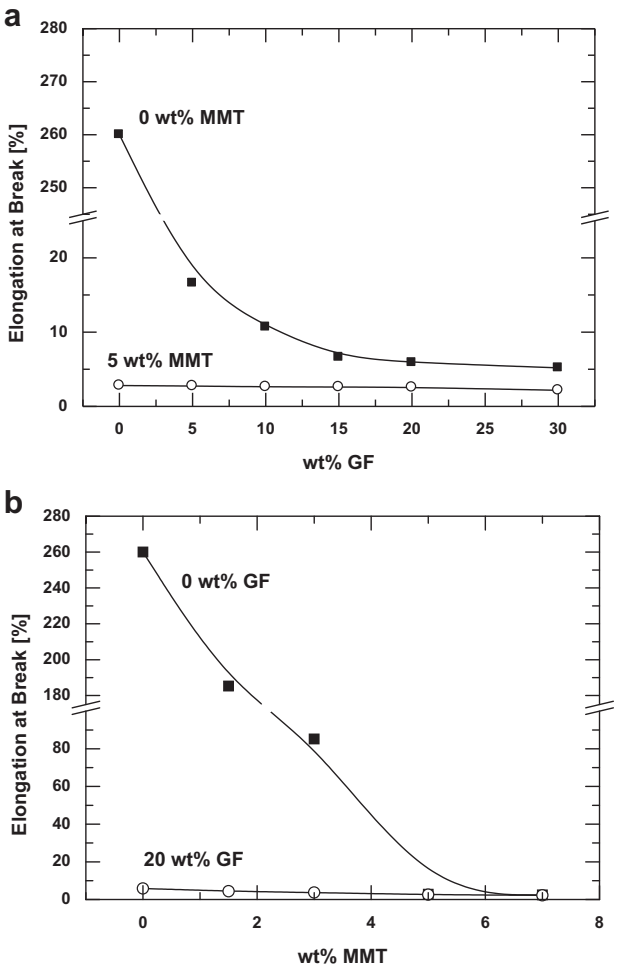

Fig. 13. Elongation at break of glass fiber reinforced nanocomposites as a function of (a) glass fiber content with 0 or 5 wt% MMT and (b) MMT content with 0 or 20 wt% GF.

[37]. Of course, the morphology of real composites is far more complex than this and injection molded specimens usually have a skin-core structure. However, the simplified model does allow one to predict the behavior of an ideal structure and estimate the effects of filler attrition as shown below.

Halpin–Tsai [64,65] and Mori–Tanaka [66,67] composite theories are widely used to predict the tensile modulus of composites. These two theories differ in how they approximate the filler and its effect on the composite; however, both theories clearly show that higher levels of reinforcement are achieved by larger aspect ratios, improved orientation, etc. Previous work in this laboratory and others have shown that both theories predict the modulus trends for polymer nanocomposites to an acceptable extent [21,37,54,58,59]. Specific details of these two theories and their application for predicting the stiffness behavior of nanocomposites are given elsewhere [21,37].

For simplicity, only the Mori–Tanaka theory was employed in this work to relate the tensile modulus of the composites prepared in this study to the particle morphology determined by TEM and SEM. A more complete discussion of the Mori–Tanaka theory and other related issues has been given previously [37,60]. From the Mori–Tanaka theory, the relative modulus parallel to either major axis of the disk-like spheroids for a composite with disk-shaped inclusions is

$$\frac{E^{(M-T)}}{E_m} = \frac{2A}{2A + \phi_p[-2\nu_m A_3 + (1-\nu_m)A_4 + (1+\nu_m)A_5 A]} \quad (4)$$

and for a fiber-based composite, the relative modulus parallel to the fiber length is

$$\frac{E^{(M-T)}}{E_m} = \frac{A}{A + \phi_p[A_1 + 2\nu_m A_2]} \quad (5)$$

where ϕ_p is the volume fraction of filler, ν_m is Poisson's ratio of the matrix, and A_1, A_2, A_3, A_4, A_5, and A are functions of Eshelby's tensor and the properties of the filler and the matrix, specifically Young's modulus, Poisson's ratio, filler concentration, and filler aspect ratio; complete details of these equations are given elsewhere [60,66,67]. Poisson's ratios of the nylon 6 matrix (ν_m), of the glass fiber (ν_{gf}), and of the organoclay (ν_{MMT}) are assumed to be 0.35, 0.20, and 0.20, respectively [37,68–70].

The Mori–Tanaka theory as generally used is a model for a single-filler population in a matrix. However, the composites of interest here consist of both organoclay and glass fiber fillers. These fillers have different effects on the mechanical properties of the composites, and separate methods are needed to predict their

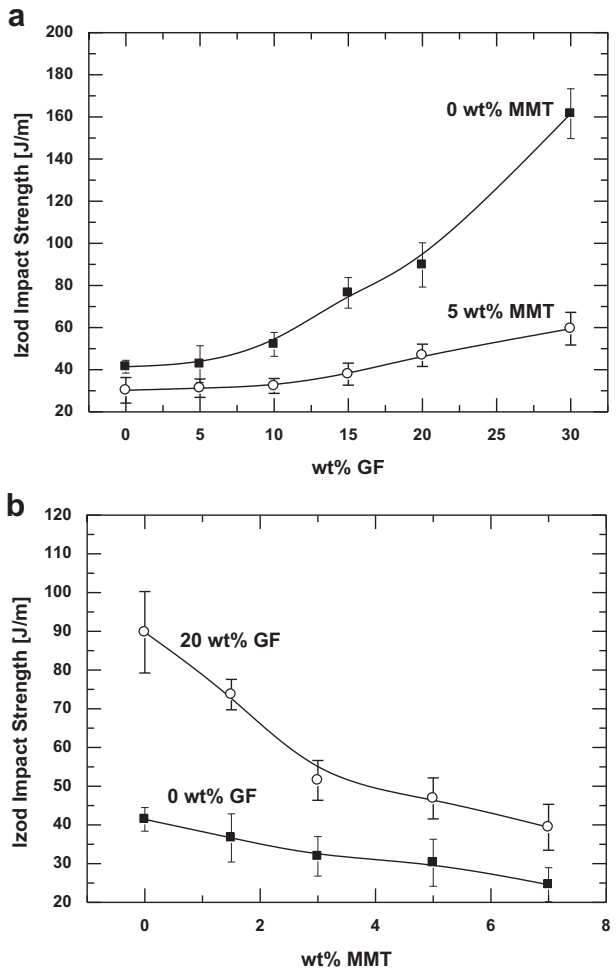

Fig. 14. Izod impact strength of glass fiber reinforced nanocomposites as a function of (a) glass fiber content with 0 or 5 wt% MMT and (b) MMT content with 0 or 20 wt% GF.

properties. When both fillers exist in a single nanocomposite, they should be considered separately to more accurately predict the experimental modulus. Recently, Spencer et al. [60] reported a similar approach based on these concepts that treats exfoliated single MMT platelets and intercalated tactoids as separate populations. A similar two-population approach was used here to model the combined effects of the glass fibers and the clay platelets in these composites.

A two-population model can be thought of in terms of an *additive* approach or a *multiplicative* approach. In the *additive* approach, the contributions of each filler are calculated separately and summed together without double counting the matrix contribution as follows

$$\frac{E_{\mathrm{add}}}{E_{\mathrm{m}}} = \frac{E_{\mathrm{gf}}}{E_{\mathrm{m}}} + \frac{E_{\mathrm{cl}}}{E_{\mathrm{m}}} - 1 \tag{6}$$

where E_{gf} and E_{cl} are the moduli calculated for the composites based on the glass fiber or the clay, respectively. Specific details of this approach and its application for predicting the stiffness behavior of nanocomposites containing a mixture of single platelets and tactoids are given in a prior publication [60].

On the other hand, in the *multiplicative* approach, the contribution of the clay is calculated first and the nanocomposite is then considered to be the matrix for the glass fiber reinforcement. The contribution of the glass fibers is calculated using the calculated modulus of the clay nanocomposite (E_{cl}) as the matrix rather than that of the neat polymer matrix (E_{m}). The contributions of the fillers are multiplied as follows

$$\frac{E_{\mathrm{mult}}}{E_{\mathrm{m}}} = \frac{E_{\mathrm{gf}}}{E_{\mathrm{cl}}}\frac{E_{\mathrm{cl}}}{E_{\mathrm{m}}} \tag{7}$$

Table 2
Component property data used in composite modeling.

Components	Modulus (GPa)	Density (g/cm^3)	Poisson's ratio
Neat nylon 6	2.92	1.14	0.35
Glass Fiber	72.4	2.54	0.20
MMT	178	2.83	0.20

Table 2 lists pertinent physical property data for the components of the composites investigated in this work [37,68,70].

Fig. 15 shows modulus predictions for fiber reinforced nylon 6 nanocomposites by the Mori–Tanaka theory using the *additive* and *multiplicative* two- population methods. Comparisons for fiber reinforced nanocomposites with 0 and 5 wt% MMT and 0–30 wt% GF and those with 0 and 20 wt% GF and 0–7 wt% MMT are shown in Fig. 15(a) and (b), respectively. The aspect ratios used in these calculations were 100 for MMT and 45 for GF. Based on Figs. 5 and 8 (c), aspect ratios on this order could reasonably be achieved with

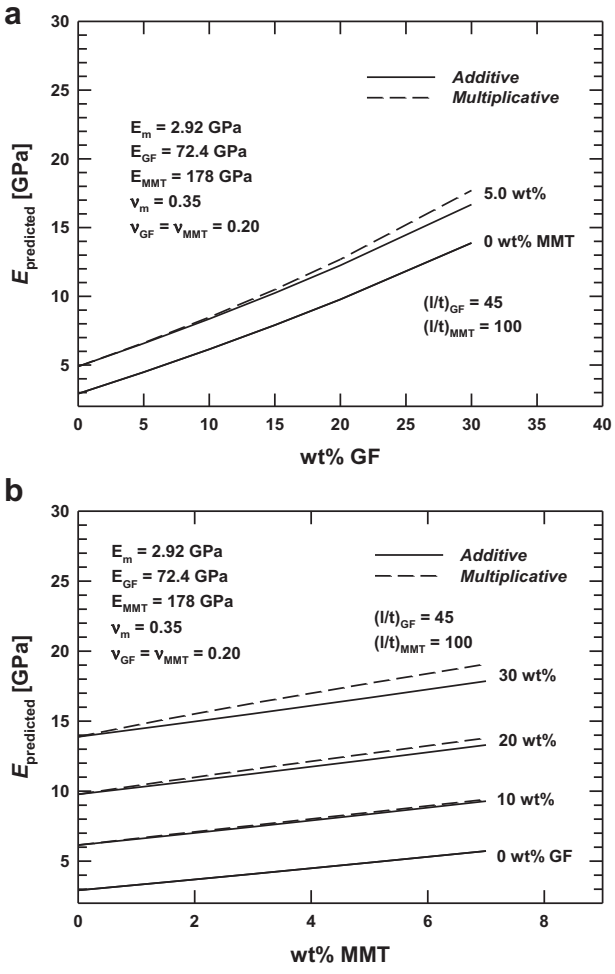

Fig. 15. Comparison of predictions from the Mori–Tanaka theory using the *additive* and *multiplicative* two-population model approaches for glass fiber reinforced nanocomposites containing (a) 0 and 5 wt% MMT and 0–30 wt% GF and (b) 0, 10, 20, and 30 wt% GF and 0–7 wt% MMT.

optimized processing conditions where filler attrition and breakage are minimized. These calculations assume each filler is perfectly oriented and well dispersed.

Both the *additive* and *multiplicative* two-population methods predict similar modulus improvements, though the *multiplicative* approach predicts a slightly larger modulus improvement with increased filler content than the *additive* approach for both cases. Recall that the *multiplicative* approach treats the nanocomposite as the matrix for the glass fiber reinforcement.

Fig. 15(a) shows nearly parallel curves for composites containing 0 and 5 wt% MMT as the GF content is increased from 0 to 30 wt%. These trends are similar to those of the experimental data in Fig. 11 (a). Fig. 15(b) shows the predicted increase in reinforcement as the MMT content is increased in composites containing 0, 10, 20, and 30 wt% GF. The experimental trends shown in Fig. 11(b) are similar except that the predicted modulus values are somewhat higher as might be expected owing to differences in assumed and actual aspect ratios and particle orientations. The effect of filler type on reinforcement can be seen by comparing Fig. 15(a) and (b). At low filler contents (0-10 wt%), the improvement in tensile modulus by MMT is significantly higher than that by glass fiber due to the higher modulus and aspect ratio of MMT than those of GF.

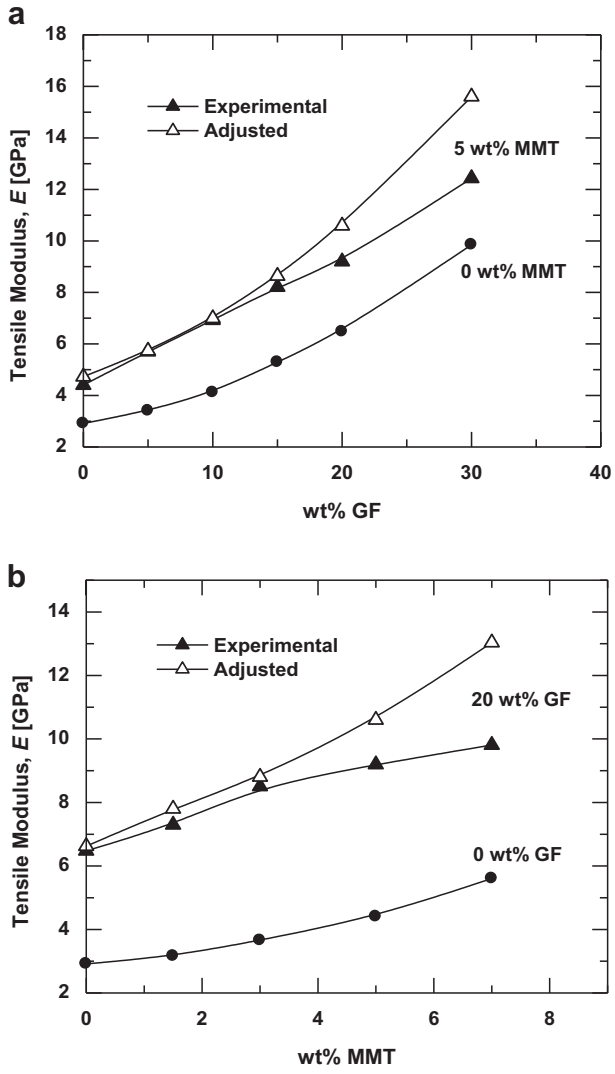

Fig. 16. Comparison of experimental tensile modulus and the adjusted modulus for glass fiber reinforced nanocomposites containing (a) 0 and 5 wt% MMT and 0–30 wt% GF and (b) 0 and 20 wt% GF and 0–7 wt% MMT.

As seen in Figs. 5 and 8, the average experimentally determined aspect ratios of MMT and GF are significantly decreased as filler content is increased; this leads to a reduction in the extent of modulus improvement that is actually realized. With ideal optimized processing conditions, however, filler attrition could be minimized or perhaps prevented. The experimental values of modulus can be adjusted to predict the modulus that could be achieved without filler attrition using the following expression:

$$E_{adj} = E_{cl\ exp}\left\{\frac{(E_{cl}/E_m)_{ideal}}{(E_{cl}/E_m)_{exp}}\right\} + E_{gf,\ exp}\left\{\frac{\left(E_{gf}/E_m\right)_{ideal}}{\left(E_{gf}/E_m\right)_{exp}}\right\} - E_m \tag{8}$$

where E_{adj} is the adjusted modulus, E_m is the matrix modulus and $E_{cl,\ exp}$ and $E_{gf,\ exp}$ are the experimental moduli of composites based on clay and glass fiber for a given content of filler. The ratios $(E_{cl}/E_m)_{ideal}$ and $(E_{gf}/E_m)_{ideal}$ are the ideal relative moduli predicted by the *additive* Mori–Tanaka model for clay and glass fiber composites calculated using the aspect ratios on which the predictions in Fig. 15 were based (100 for MMT and 45 for glass fiber) and that might be achieved with optimized processing condition, while $(E_{cl}/E_m)_{exp}$ and $(E_{gf}/E_m)_{exp}$ are the predicted relative moduli calculated from the experimentally measured aspect ratios. Fig. 16 compares the observed (or experimental) and the adjusted tensile modulus values for glass fiber reinforced nanocomposites. The adjusted modulus values for glass fiber reinforced nanocomposites shown in Fig. 16 are rather similar to the model predictions shown in Fig. 15. Thus, if filler attrition during melt processing could be prevented by well-designed processing conditions, these composites would approach the predictions given by the Mori–Tanaka theory.

6. Conclusions

The structure and property relationships of glass fiber reinforced nylon 6 nanocomposites prepared by melt processing have been investigated to explore the reinforcing effects from two fillers of very different size scales (micro- and nano-). The micro- and nano-structures of the two fillers in the composites were assessed by SEM and TEM and quantified by detailed particle analyses. These analyses showed a reduction in glass fiber length as fiber loading increased, as expected, and a quite significant further reduction as clay was added. These effects stem, no doubt, from the increased stresses these particles generate during melt processing. The apparent aspect ratio of the clay platelets also appeared to similarly decrease. It is suggested that to some degree this observation may stem from the delamination of partially overlapped MMT platelets as the processing stresses are increased. Breakage of clay platelets cannot be ruled out.

Theoretical predictions of the reinforcement or modulus enhancements caused by the combination of these nano- and micro-fillers were made using the Mori–Tanaka composite theory by considering their contributions to be additive and by considering the nanocomposite as the matrix and the glass fiber as the filler, i.e., a so-called ‘multiplicative” approach. The latter gave slightly higher predictions, but the differences are not regarded as very significant. The experimentally observed values of the tensile modulus approach the predictions of the model when adjustments for the reductions in particle aspect ratio are taken into account. It appears that the reinforcement observed is about what is expected from an appropriate theory that accounts for two types of fillers.

The tensile strength of these composites increased and the elongation at break decreased as the content of either filler

increased in ways that are expected. Interestingly, the Izod impact strength increased with glass fiber content but decreased with increased clay content.

Acknowledgements

This work was supported in part by a grant from General Motors Global Research and Development; the authors would like to thank William R. Rodgers for his continued interest. The authors express their appreciation to Honeywell and Southern Clay Products, Inc. for providing the polymers and the organoclays and to Don Sage of Owens Corning for helpful discussions and for providing the glass fibers that made this investigation possible.

References

[1] Agarwal BD, Broutman LJ. Analysis and performance of fiber composites. New York: Wiley and Sons; 1980.
[2] Chu PF. Glass fiber-reinforced polypropylene. In: Karian HG, editor. Handbook of polypropylene and polypropylene composites. New York: Marcel Dekker; 1999. p. 263–334.
[3] von Turkovich R, Erwin L. Polym Eng Sci 1983;23:743–9.
[4] Akkapeddi MK. Polym Compos 2000;21(4):576–85.
[5] Usuki A, Kojima Y, Kawasumi M, Okada A, Fukushima Y, Kurauchi T, et al. J Mater Res 1993;8(5):1185–9.
[6] Usuki A, Kojima Y, Kawasumi M, Okada A, Fukushima Y, Kurauchi T, et al. J Mater Res 1993;8(5):1179–84.
[7] Giannelis EP. Adv Mater 1996;8:28–35.
[8] Vaia RA, Jandt KD, Kramer EJ, Giannelis EP. Chem Mater 1996;8(11):2628–35.
[9] Krishnamoorti R, Vaia RA. J Polym Sci Part B Polym Phys 2007;45(24):3252–6.
[10] Vaia RA, Maguire JF. Chem Mater 2007;19(11):2736–51.
[11] Paul DR, Robeson LM. Polymer 2008;49(15):3187–207.
[12] Zeng QH, Yu AB, Lu GQ, Paul DR. J Nanosci Nanotechnol 2005;5(10):1574–92.
[13] Fornes TD, Hunter DL, Paul DR. Macromolecules 2004;37(5):1793–8.
[14] Yoo Y, Kim S-S, Won JC, Choi K-Y, Lee JH. Polym Bull 2004;52(5):373–80.
[15] Bharadwaj RK. Macromolecules 2001;2001(34):26.
[16] Messersmith PB, Giannelis EP. J Polym Sci Part A Polym Chem 1995;33 (7):1047–57.
[17] Kim DH, Fasulo PD, Rodgers WR, Paul DR. Polymer 2008;49(10):2492–506.
[18] Lee H-S, Fasulo PD, Rodgers WR, Paul DR. Polymer 2006;47(10):3528–39.
[19] Gilman JW, Jackson CL, Morgan AB, Harris Jr RH. Chem Mater 2000;12 (7):1866–73.
[20] Kashiwagi T, Harris Jr RH, Zhang X, Briber RM, Cipriano BH, Raghavan SR, et al. Polymer 2004;45(3):881–91.
[21] Chavarria F, Paul DR. Polymer 2004;45(25):8501–15.
[22] Fornes TD, Paul DR. Macromolecules 2004;37(20):7698–709.
[23] Yoo Y, Paul DR. Polymer 2008;49:3795–804.
[24] Clifford MJ, Wan T. Polymer 2010;51(2):535–9.
[25] Daud W, Bersee HEN, Picken SJ, Beukers A. Compos Sci Technol 2009;69 (14):2285–92.
[26] Isitman NA, Aykol M, Kaynak C. Compos Struct 2010;92(9):2181–6.
[27] Vlasveld DPN, Parlevliet PP, Bersee HEN, Picken SJ. Composites 2004;36A (1):1–11.
[28] Wu S-H, Wang F-Y, Ma C-CM, Chang W-C, Kuo C-T, Kuan H-C, et al. Mater Lett 2001;49(6):327–33.
[29] Chandradass J, Kumar MR, Velmurugan R. Mater Lett 2007;61(22):4385–8.
[30] Kornmann X, Rees M, Thomann Y, Necola A, Barbezat M, Thomann R. Compos Sci Technol 2005;65(14):2259–68.
[31] Norkhairunnisa M, Azhar AB, Shyang CW. Polym Int 2007;56(4):512–7.
[32] Zhou G, Movva S, Lee LJ. J Appl Polym Sci 2008;108(6):3720–6.
[33] Houphouët-Boigny C, Plummer CJG, Wakeman MD, Månson J-AE. Polym Eng Sci 2007;47(7):1122–32.
[34] Plummer CJG, Vacche SD, Houphouët-Boigny C, Michaud V, Månson J-AE. Solid State Phenom 2009;151:60–6.
[35] Isitman NA, Gunduz HO, Kaynak C. Polym Degrad Stab 2009;94 (12):2241–50.
[36] Cho JW, Paul DR. Polymer 2001;42(3):1083–94.
[37] Fornes TD, Paul DR. Polymer 2003;44(17):4993–5013.
[38] Fornes TD, Yoon PJ, Hunter DL, Keskkula H, Paul DR. Polymer 2002;43 (22):5915–33.
[39] Fornes TD, Yoon PJ, Keskkula H, Paul DR. Polymer 2001;42(25):9929–40.
[40] Shah RK, Paul DR. Polymer 2004;45:2991–3000.
[41] Yoon PJ, Fornes TD, Paul DR. Polymer 2002;43(25):6727–41.
[42] Cho JW, Paul DR. J Appl Polym Sci 2001;80(3):484–97.
[43] Laura DM, Keskkula H, Barlow JW, Paul DR. Polymer 2000;41:7165–74.
[44] Laura DM, Keskkula H, Barlow JW, Paul DR. Polymer 2001;42(14):6161–72.
[45] Laura DM, Keskkula H, Barlow JW, Paul DR. Polymer 2002;43(17):4673–87.
[46] Laura DM, Keskkula H, Barlow JW, Paul DR. Polymer 2003;44(11):3347–61.
[47] Huang JJ, Keskkula H, Paul DR. Polymer 2004;45(12):4203–15.
[48] Oshinski AJ, Keskkula H, Paul DR. Polymer 1996;37(22):4891–907.
[49] Cui L, Troeltzsch C, Yoon PJ, Paul DR. Macromolecules 2009;42(7):2599–608.
[50] Yoo Y, Cui L, Yoon PJ, Paul DR. Macromolecules 2010;43(2):615–24.
[51] Yoo Y, Shah RK, Paul DR. Polymer 2007;48(16):4867–73.
[52] Bailey R, Kraft H. Int Polym Proc 1987;2(2):94–101.
[53] Kelly A, Tyson WR. J Mech Phys Solids 1965;13(6):329–50.
[54] Cui L, Ma X, Paul DR. Polymer 2007;48(21):6325–39.
[55] Kim DH, Fasulo PD, Rodgers WR, Paul DR. Polymer 2007;48(18):5308–23.
[56] Kumar KS, Ghosh AK, Bhatnagar N. Polym Compos 2007;28(2):259–66.
[57] Stretz HA, Paul DR, Li R, Keskkula H, Cassidy PE. Polymer 2005;46 (8):2621–37.
[58] Shah RK, Kim DH, Paul DR. Polymer 2007;48(4):1047–57.
[59] Sheng N, Boyce MC, Parks DM, Rutledge GC, Abes JI, Cohen RE. Polymer 2004;45(2):487–506.
[60] Spencer MW, Cui LL, Yoo Y, Paul DR. Polymer 2010;51(5):1056–70.
[61] Stretz HA, Paul DR, Cassidy PE. Polymer 2005;46(11):3818–30.
[62] Hill R. Proc Phys Soc Sect A 1952;65(5):349–54.
[63] Hill R. J Mech Phys Solids 1965;13(4):213–22.
[64] Halpin JC. J Compos Mater 1969;3(4):732–4.
[65] Halpin JC, Kardos JL. Polym Eng Sci 1976;16(5):344–52.
[66] Mori T, Tanaka K. Acta Metall Mater 1973;21(5):571–4.
[67] Tandon GP, Weng GJ. Polym Compos 1984;5(4):327–33.
[68] Hui CY, Shia D. Polym Eng Sci 1998;38(5):774–82.
[69] Mark JE. Polymer data handbook. New York: Oxford University Press; 1999.
[70] van Es M, Xiqiao F, van Turnhout J, van der Giessen E. Comparing polymer–clay nanocomposites with conventional composites using composite modeling. In: Malaika SA, Golovoy A, Wilkie CA, editors. Specialty polymer additives. London: Blackwell Science; 2001 [chapter 21].

Polymer 52 (2011) 191–200

Contents lists available at ScienceDirect

Polymer

journal homepage: www.elsevier.com/locate/polymer

Compatibilization and morphology development of immiscible ternary polymer blends

Dong Wang [1], Yan Li, Xu-Ming Xie*, Bao-Hua Guo

Advanced Materials Laboratory, Department of Chemical Engineering, Tsinghua University, Beijing 100084, China

ARTICLE INFO

Article history:
Received 23 March 2010
Received in revised form
10 November 2010
Accepted 11 November 2010
Available online 18 November 2010

Keywords:
Polymer blends
Compatibilization
Morphology

ABSTRACT

We report a novel and effective strategy that compatibilizes three immiscible polymers, polyolefins, styrene polymers, and engineering plastics, achieved by using a polyolefin-based multi-phase compatibilizer. Compatibilizing effect and morphology development are investigated in a model ternary immiscible polymer blends consisting of polypropylene (PP)/polystyrene(PS)/polyamide(PA6) and a multi-phase compatibilizer (PP-*g*-(MAH-*co*-St) as prepared by maleic anhydride (MAH) and styrene (St) dual monomers melt grafting PP. Scanning electron microscopy (SEM) results indicate that, as a multi-phase compatibilizer, PP-*g*-(MAH-*co*-St) shows effective compatibilization in the PP/PS/PA6 blends. The particle size of both PS and PA6 is greatly decreased due to the addition of multi-phase compatibilizer, while the interfacial adhesion in immiscible pairs is increased. This good compatibilizing effect is promising for developing a new, technologically attractive method for achieving compatibilization of immiscible multi-component polymer blends as well as for recycling and reusing of such blends. For phase morphology development, the morphology of PP/PS/PA6 (70/15/15) uncompatibilized blend reveals that the blend is constituted from PP matrix in which are dispersed composite droplets of PA6 core encapsulated by PS phase. Whereas, the compatibilized blend shows the three components strongly interact with each other, i.e. multi-phase compatibilizer has good compatibilization between the various immiscible pairs. For the 40/30/30 blend, the morphology changed from a three-phase co-continuous morphology (uncompatibilized) to the dispersed droplets of PA6 and PS in the PP matrix (compatibilized).

1. Introduction

Polymer blending is a convenient and attractive route for obtaining new polymeric materials. Comparing with the development of a novel homopolymer via the synthesis of a new monomer, making blends of currently available homopolymers offers significant savings in time and cost, and the blend properties may be tuned by changing the composition [1,2]. However, this approach is complicated by the fact that polymer blends are generally thermodynamically immiscible [3]. Thus, achieving compatibilization of immiscible polymer blends has been a long-standing academic and technological challenge.

In the past decades, in spite of the very large number of studies on the compatibilization of binary polymer blends, few studies have considered ternary or multi-component polymer blends [4,5]. In order to discriminate with the vocabulary used in literature, a 'ternary polymer blend' in this work consists of three immiscible components, which are non-reactive or chemical affinity towards each other. Many ternary blends reported in literature contain at least two miscible phases and/or one of the components is a compatibilizer. The received less attention on ternary or multi-component blends may arise from the difficulty of compatibilization in such systems, especially the preparation of an effective compatibilizer for such blends. Although increasing the number of polymer components does indeed lead to complications, there are several important reasons for studying the multi-component polymer blends. Besides the desire to develop new high-performance materials arising from synergistic interactions, there has also been significant interest in the recycling and reusing of plastic materials because of environmental as well as economic concerns in recent years [4,5].

It is well known that the scrap or waste plastics available for recycling often contain a number of different polymers. In such mixtures, polyolefins (PP, PE etc.), styrene polymers (PS, ABS, etc.) and engineering plastics (PA, PC etc.) occupy the largest share of the

* Corresponding author. Tel.: +86 10 6277 3607.
E-mail address: xxm-dce@mail.tsinghua.edu.cn (X.-M. Xie).
[1] Present address: WPI Advanced Institute for Materials Research, Tohoku University, 2-1-1 Katahira, Aoba, Sendai 980-8577, Japan.

0032-3861/$ – see front matter © 2010 Elsevier Ltd. All rights reserved.
doi:10.1016/j.polymer.2010.11.019

waste plastics and are the most recycled polymeric materials. Usually, it is hard to isolate or separate these plastics individually from recycled materials. Moreover, the blends of such systems are generally thermodynamically immiscible. In order to obtain useful mechanical and physical properties from such mixtures, it is necessary to compatibilize these plastics. Then, combining different plastics, with the help of a compatibilizer, become a convenient way to upgrade the properties of recycled materials.

Two main strategies are used to achieve polymer blends compatibilization. One is the addition of pre-made block or graft copolymer during melt mixing of immiscible blends [6–16]. The other is reactive compatibilization in which a block or graft copolymer is formed in situ at the interfacial regions of the immiscible blends by reaction of condensation-type functional groups [17–34]. In addition, Torkelson et al. employ a novel method, solid state shear pulverization, to compatibilize immiscible blends [35–40]. However, these approaches are mainly used to compatibilize binary blends (typical examples includes PP/PA, PS/PMMA, and PP/PS et al.), and cannot be easily carried out for ternary or multi-component blends. For polyolefins, styrene polymers and engineering plastics ternary or multi-component blends, a multi-phase compatibilizer is necessary. Among the few previous reports concerned with mixtures of three or more polymers (not including the compatibilizers), those most like the present report are Debolt and Robertson [4,5] and Omonov et al. [41]. Debolt and Robertson tried compatibilization of this ternary polymer blend using complex compatibilizers. They investigated the Izod impact strength, tensile elongation-to-break and morphology for blends of nylon 66 and polystyrene in a polypropylene matrix with and without compatibilization by an ionomer resin (for nylon 66) and a styrene-*block*-ethylene-*co*-butylene-*block*styrene copolymer (for polystyrene). However, the results show that there seem to be relatively little gross interference (or synergism) between the compatibilizers when they are used together for the ternary blend [4,5]. Only specific to understand and identify the phase morphology in a blend having three immiscible components, Omonov et al. [41] studied the phase morphology development for blends of polypropylene and polystyrene in a nylon 6 matrix with and without compatibilization by the complex compatibilizers of a maleic anhydride grafted PP (PP-*g*-MAH, for PP) and a styrene maleic anhydride copolymer (SMA, for PS).

How can we design a multi-phase compatibilizer for polyolefins (PO), styrene polymers (StP) and engineering plastics (EP) ternary blends? It would be satisfied if we could make polyolefin-based compatibilizers that performs the above two functions at the same time: one is in situ formation of block or graft copolymer at the interface by chemical reactions with reactive groups of engineering polymers, the other is intermolecular attraction or chemical affinity with styrene polymers. As known, styrene and maleic anhydride dual monomers (or glycidyl methacrylate, acrylic acid, etc.) melt grafting polypropylene (or polyethylene, etc.) have been successfully prepared [42–48]. In the presence of styrene (St), the graft degree of functional monomer on the PP backbone is increased and the degradation of PP is depressed. In the grafting process, the reactive monomer, St and its copolymer can react with the PP macroradicals producing long chain branches [45,46]. The resulting grafted PP molecular has both reactive MAH group and PS segment [49–51].

The object of this study is to present a novel and effective strategy not only for compatibilization of three immiscible polymers (polyolefins, styrene polymers, and engineering plastics), but also for recycling and reusing these three immiscible polymers from the scrap or waste plastics, by using a multi-phase compatibilizer, and further, is to understand the morphology development and interaction in a blend having three immiscible components when the multi-phase compatibilizer is added during the melt-blending operation. A scheme of the compatibilization strategy for PO/StP/EP ternary blends is shown in Fig. 1. This novel compatibilization strategy is flexible. Depending on the type of dispersion phase and matrix, the functional groups in the compatibilizer can be changed from MAH to glycidyl methacrylate(GMA), acrylic acid (AA), etc., while the matrix can be changed from PP to propylene or ethylene based polyolefins, such as PE-*g*-(MAH-*co*-St).

2. Experimental

2.1. Materials

The isotactic polypropylene is H314-02Z supplied by Dow Chemical; (T_m = 162.0 °C, T_c = 110.5 °C), a melt viscosity of 649.7 Pa s (240 °C, 150/s). The polystyrene (PS) used is 666D supplied by Yanshan Petrochemical Co.; (T_g = 98 °C), a melt viscosity of 397.7 Pa s (240 °C, 150/s). The PA6 is 1013B grade from Ube Co. having the following characteristics: T_m = 219.8 °C, T_c = 180.3 °C, and a melt viscosity of 143.3 Pa s (240 °C, 150/s). Maleic anhydride (MAH) and styrene monomer (St) are products of Beijing Chemical Co. (analytical grade) and used as received. The peroxide, dicumyl peroxide (DCP) from Beijing Xizhong Chemical Co. is adopted as initiator and used without further purification. The multi-phase compatibilizers, MAH-St melt grafted polypropylene, PP-*g*-(MAH-*co*-St) (MAH and St graft content are 1.02 and 1.65 wt.%, respectively), was prepared and characterized following the procedure given in the literature [46]. The melt-grafting reactions were carried out in a single screw extruder (Φ = 30 mm, L:D = 25:1). For a typical grafting procedure, the peroxide was added to the liquid styrene monomer. The resulting mixture was then premixed with PP pellets and MAH monomer. The whole system was charged into the extruder, which was preheated up to 170–210 °C. The screw speed was fixed at 35 rpm. Extrudates were cooled in water and then pelletized.

2.2. Blend preparation

Binary and ternary blends were prepared by melt-blending using a batch mixer of Rheocord Haake type. It has a chamber of 50 cm^3, in which two sigma rotors rotated in opposite directions to ensure mixing. The rotation speed was set at 80 rpm. Before

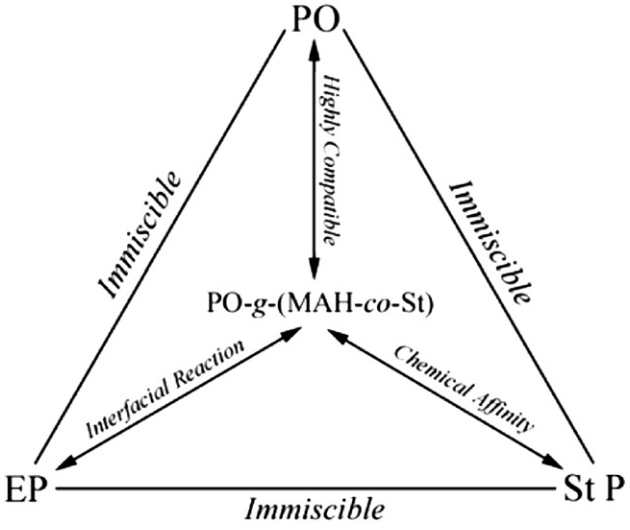

Fig. 1. Schematic representation of the compatibilization strategy used for PO/StP/EP immiscible ternary blends.

blending, the compositions were dried in a vacuum oven at 80 °C for 10 h and used immediately. A series of blends prepared were listed in Table 1.

2.3. FTIR measurements

The grafted PP samples were dissolved in refluxing xylene at a concentration of 1% (wt/vol.), and excess acetone was then added to precipitate them. Acetone could precipitate only the grafted and ungrafted PP [i.e. PP, and PP-*g*-(MAH-*co*-St)]. By this procedure any homo- and copolymer of MAH and St was separated [43–46]. The precipitated samples were filtered, washed and dried under vacuum at 80 °C for 24 h. The sample thus obtained was then hot-pressed under 210 °C into film and analyzed by a Nicolet 560 Fourier transform infrared (FT-IR) spectrometer at room temperature.

2.4. Phase morphology characterization

A Hitachi S-450 scanning electron microscopy, operating at a 20 kV accelerating voltage, was used to observe blend morphology. The surfaces taken from cryofractured samples were examined. In order to investigate the different phases present in the blends, one series of cryofractured surfaces was etched with formic acid or tetrahydrofuran (THF) for 48 h at 50 °C to remove the PA6 or PS phase, respectively. After etching and drying procedure, the samples were coated with 20 nm thick gold using a sputtering coater. The obtained digital SEM micrographs of the cryofractured surfaces were analyzed to determine average particle size. An average of 300–500 particles per sample was examined.

3. Results and discussion

3.1. FTIR spectroscopy analysis of the compatibilizers

The FTIR spectra of the prepared compatibilizers are shown in Fig. 2. Comparing with virgin PP, the observed new absorption bands at 1782 and 702 cm^{-1} can be assigned to the absorption of carbonyl groups and grafted St, respectively. Therefore, the resulted grafted PP molecular have both reactive MAH group and PS segment [49,50].

3.2. Morphology

3.2.1. PP/PS and PP/PA6 binary blends

Prior to study of the PP/PS/PA6 ternary blends, it is necessary to investigate the compatibilizing effect of the PP-*g*-(MAH-*co*-St) on individual PP/PS and PP/PA6 binary blends. Figs. 3 and 4 show the SEM micrographs of the uncompatibilized PP/PS and PP/PA6 binary blends. As expected, both PS and PA6 are immiscible with PP. The interfacial adhesion between PS particles and PP matrix in PP/PS blend (Fig. 3(A) and (A′)) or PA6 particles and PP matrix in the PP/PA6 blend (Fig. 4(A) and (A′)) is very poor. Indeed, all the particles debonded from the matrix are clearly loose on the cryofractured surfaces. The surfaces of the particles are smooth without any visible roughness (the surface roughness of particles is usually expected in case of good interfacial adhesion between the particles and the matrix). As shown in Table 2, average particle sizes of 2.2 and 3.9 μm are obtained in the absence of compatibilizer in 85PP/15PS and 70PP/30PS blends, respectively. The particle size increase upon the increase of the minor phase content is expected since the process of particle–particle coalescence is favored by increasing the minor phase concentration. Similarly, the particle size distribution of PS phase gets broader when the minor phase concentration is increased. Fig. 4 illustrates the phase morphology of 85PP/15PA6 and 70PP/30PA6 uncompatibilized blends. The former blend exhibits an average particle size of 3.5 μm. Whereas, as expected, coarser PA6 particles having an average diameter of 6.4 μm are obtained in the latter blend. For the same reasons of favored coalescence, a broader particle size distribution is observed in the blends containing 30 wt.% PA6 compared to blends containing only 15 wt.%. Note that the average particle size in PP/PS is smaller than that in PP/PA6 blend at both compositions investigated (Table 2). This picture of particle size difference is due to the significant difference in the viscosity ratio between the two pairs.

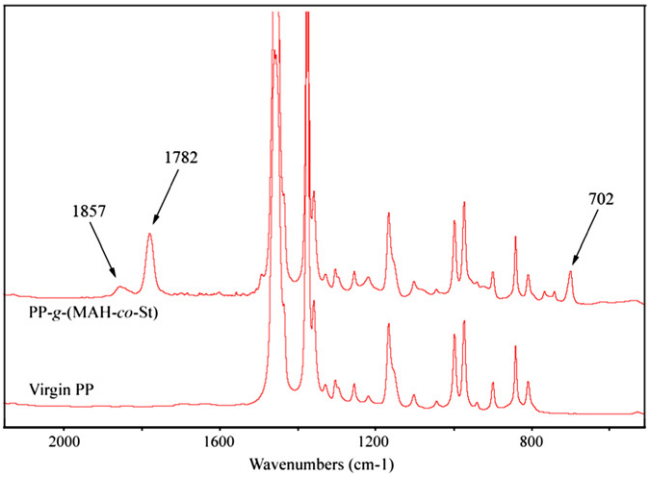

Fig. 2. FTIR spectra of virgin PP and the multi-phase compatibilizer, PP-*g*-(MAH-*co*-St).

With the addition of multi-phase compatibilizer, the particle size and interfacial adhesion are greatly changed for the PP/PS blends. As illustrated in Table 2 or Fig. 5, the addition of 5 wt.% PP-*g*-(MAH-*co*-St) to the PP/PS binary blend reduces significant the average particle size of the PS dispersed phase at both blend compositions. The sizes of the PS particles reduce from 2.2 to 0.7 μm and 3.9 to 1.6 μm in 85/15 and 70/30 compatibilized PP/PS blends, respectively. The particle size distribution gets narrower than that in uncompatibilized blends. That is a clear indication of the chemical affinity between the multi-phase compatibilizer and PS. The multi-phase compatibilizer, PP-*g*-(MAH-*co*-St), shows good compatibilization not only for the PP/PS blends but also for the PP/PA6 blends. The addition of 5 wt.% of PP-*g*-(MAH-*co*-St) results in large improvement of the state of PA6 phase dispersion and particle size (illustrated in Table 2 or Fig. 6). Comparing with the state of PA6 dispersion in uncompatibilized PP/PA6 blends (Fig. 4), the compatibilized blends show a very fine particle size and apparently good interfacial adhesion between the phases. The particle size of PA6 decreases from 3.5 to 6.4 μm for uncompatibilized 85/15 and 70/30 PP/PA6 blends to 1.0 and 1.4 μm for compatibilized 85/15 and 70/30 PP/PA6 blends, respectively. The

Table 1
Formulation of binary and ternary blends.

Blends	Composition (wt.%)
Uncompatibilized	
PP/PS	85/15; 70/30
PP/PA6	85/15; 70/30
PP/PS/PA6	70/15/15; 40/30/30
Compatibilized	
PP + PP-*g*-(MAH-*co*-St)/PS	82 + 3/15; 64 + 6/30
PP + PP-*g*-(MAH-*co*-St)/PA6	82 + 3/15; 64 + 6/30
PP + PP-*g*-(MAH-*co*-St)/PS/PA6	(67 + 3)/15/15; (34 + 6)/30/30

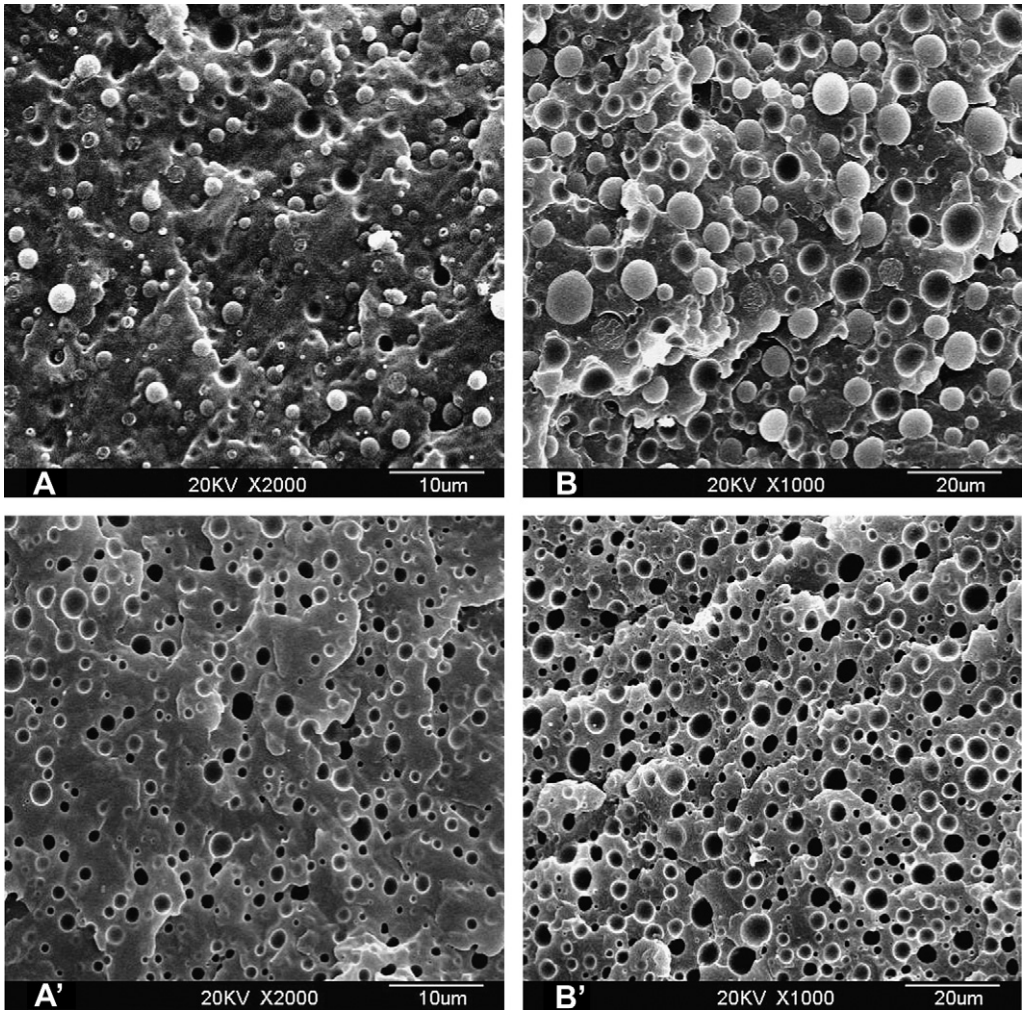

Fig. 3. Morphology of the uncompatibilized 85PP/15PS (A, A′) and 70PP/30PS (B, B′) blends: (A, B) cryofractured surface, (A′, B′) cryofractured and PS phase extracted using THF.

increased PA6 dispersion and enhancement of interfacial adhesion between PA6 and PP domains are due to the in situ generation of the grafted copolymer during melt-blending. It's well known that a maleic anhydride (MAH) functional group can easily react with an amine end group of a polyamide. The reaction between MAH and polyamide to form a copolymer is well known and verified [1,52].

3.2.2. PP/PS/PA6 ternary blends

For compatibilized blends, domain size and interfacial adhesion are the two most important characteristics. Fig. 7 shows the effect of multi-phase compatibilizers on the morphologies of the PP/PS/PA6 (70/15/15) ternary blends. As expected, for the uncompatibilized blend, both PS and PA6 are immiscible with PP. The blends show large discrete domains of PS and PA6 dispersed in the PP matrix. The interfacial adhesion between PS or PA6 particles and PP matrix is very poor (Fig. 7(A)), which is evident from the "ball-and-socket" topography. However, the addition of compatibilizers induces relative uniformly sized PA6 or PS domains. Due to the characteristics of in situ formation of copolymer at the PP/PA6 interface and chemical affinity with PP/PS homopolymers of PP-*g*-(MAH-*co*-St), the blend with PP-*g*-(MAH-*co*-St) as compatibilizers displays a very fine dispersion of disperse phase and strong interfacial adhesion with PP matrix (Fig. 7 (B)). The good compatibilizing effect of PP-*g*-(MAH-*co*-St) can be explained by two mechanisms. First, the MAH groups in compatibilizer react with amine groups in PA6 to form copolymer, leading to good adhesion at interface between PP and PA6. In addition, hydrogen bonding may also exist between MAH and amine groups, further increasing compatibility. Second, since the compatibilizer also contains styrene blocks, resulting in good compatibility with PS. Consequently, the remarkable compatibilizing effect of PP-*g*-(MAH-*co*-St) induced a drastic decrease in interfacial tension and suppression of coalescence between the originally immiscible polymer phases.

For the micro-structure of the uncompatibilized ternary blends, Fig. 7(A′) reveals the existence of encapsulated droplets dispersed in PP matrix. Somewhat surprisingly, the PS has encapsulated every PA6 particle (see white ellipse). Most of the PA6 articles are between 1 and 6 μm in diameter, and the average PS shell thickness is less than 1 μm. A close observation of the SEM micrograph shows that, besides encapsulating the PA6, the PS also exists as discrete particles dispersed in the PP (see white square), most of which are smaller than 2 μm in diameter. To further confirm this micro-structure, the cryofractured surface of the uncompatibilized blends is etched using formic acid to remove the PA6 phase. As shown in Fig. 7(A″), this test further evidences that PS constitutes the shell of the encapsulated structures and the core is the PA6 phase. However, for the blends with PP-*g*-(MAH-*co*-St) as compatibilizer, the phase structure exhibits a significant change. The selective etching of the PS phase from the cryo-fracture surfaces using THF shows the remaining PA6 in PP matrix (Fig. 7(B′)). This picture reveals that PA6 particle is partial encapsulated by the PS phase. Comparing Fig. 7(B′) with Fig. 7(A′), an interesting result is clearly seen that PS does not encapsulate every PA6 particle anymore. PS

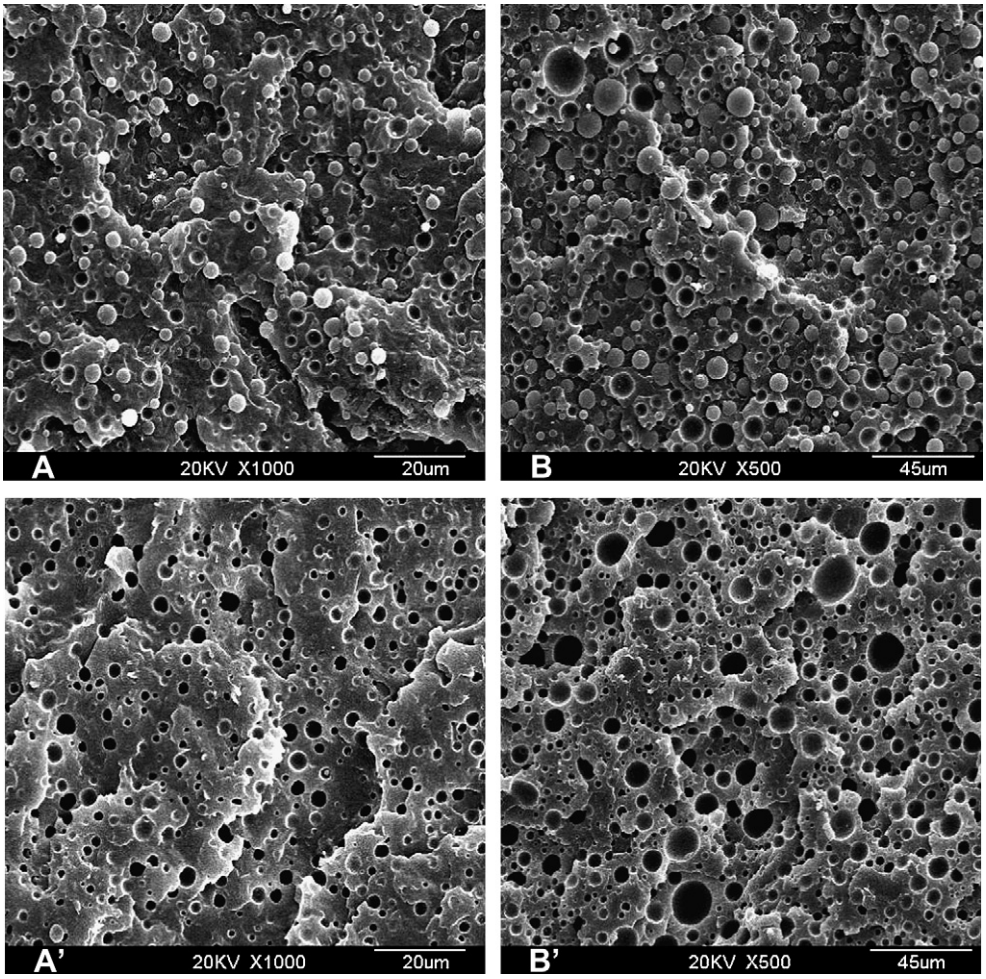

Fig. 4. Morphology of the uncompatibilized 85PP/15PA6 (A, A′) and 70PP/30PA6 (B, B′) blends: (A, B) cryofractured surface, (A′, B′) cryofractured and PA6 phase extracted using HCOOH.

partial encapsulates one, two, even three PA6 particles. Indeed, PS particles locate at the interface between the PA6 particles and the PP matrix. No visible and neat PS shells are visible around the PA6 core. Simultaneity, PA6 particles are also tightly contact with PP matrix. These results indicate the three components strongly interact with each other. Therefore, the compatibilizing effect of the multi-phase compatibilizer on the PP/PS/PA6 ternary immiscible system is very clear. The formed copolymer by in situ reaction between the MAH groups in compatibilizer and amine groups in PA6 greatly decrease the interfacial tension of PP/PA6, resulting in good adhesion at the interface regions. The compatibilizer also contains styrene blocks, leading to good compatibility with PS. Consequently, the multi-phase compatibilizer has good compatibilizating effect between the various immiscible pairs.

Table 2
The value of average particle size (μm) for the binary blends.

Blends	Composition (wt.%)	Average particle size (μm)	
		PS	PA6
Uncompatibilized blends			
PP/PS	85/15	2.2	–
PP/PS	70/30	3.9	–
PP/PA6	85/15	–	3.5
PP/PA6	70/30	–	6.4
Compatibilized blends			
PP + PP-*g*-(MAH-*co*-St)/PS	85/15	0.7	–
PP + PP-*g*-(MAH-*co*-St)/PS	70/30	1.6	–
PP + PP-*g*-(MAH-*co*-St)/PA6	85/15	–	1.0
PP + PP-*g*-(MAH-*co*-St)/PA6	70/30	–	1.4

According to Hobbs et al. [53] it is possible to predict qualitatively the type of the phase morphology developed in a ternary immiscible polymer blend by using the concept of the spreading coefficient as initially introduced by Harkin [54]. For our case, the ternary blend has PP as a matrix and two dispersed phases: PS and PA6. The spreading coefficient $\lambda_{PS/PA6}$ of PS phase on PA6 phase is:

$$\lambda_{PS/PA6} = \sigma_{PA6/PP} - \sigma_{PS/PP} - \sigma_{PA6/PS} \quad (1)$$

where the σ_{ij} are the interfacial energies between the phases i and j. If $\lambda_{PS/PA6} > 0$, then PS phase will encapsulate PA6 phase. The interfacial energy between PA6 and PP has been reported to be 13.61 mN/m at 230 °C [55]. The interfacial energy between PA6 and PS has been reported to be 20.0 [56], 10.0 [57], and 7.63 mN/m [58] at 230 °C. Averaging of the three values at 230 °C gives 12.54 mN/m. The interfacial energy between PS and PP has been reported to be 4.3 mN/m at 230 °C [59]. Using these interfacial energies, the spreading coefficient of $\lambda_{PS/PA6}$, is predicted to be −3.19 at 230 °C. Although this concept is successful to predict the phase morphologies claimed, it fails in our case because the development of the phase in polymer melt depends also on other key factors such as the viscosity and elasticity of the blend [41].

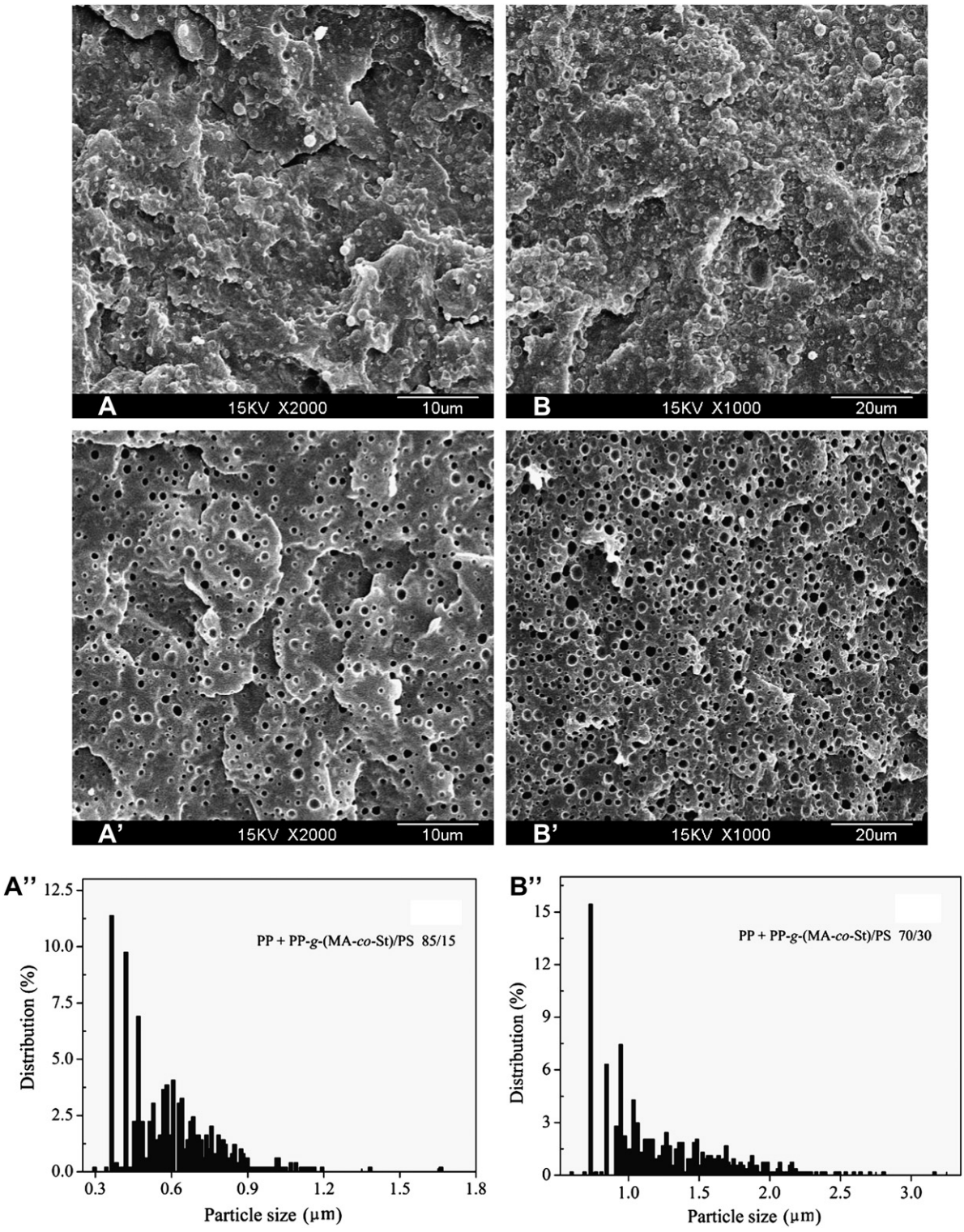

Fig. 5. Morphology of the compatibilized 85PP/15PS (A, A′) and 70PP/30PS (B, B′) blends: (A, B) cryofractured surface, (A′, B′) cryofractured and PS phase extracted using THF, (A″, B″) particle size distribution.

Fig. 8 presents the SEM micrographs of uncompatibilized 40PA6/30PP/30PS blends. The cryo-fracture surfaces (Fig. 8(A)) show complex phase morphology where it is not possible to identify which phase is located where. Fig. 8(A′) shows a SEM micrograph of the same blend in which the PS phase is extracted using THF. The result reveals that the PS phase constitutes a continuous phase as indicated by the hollow continuous space in between the PP and PA6 phase. A few percentage of the PS phase is also dispersed in PP and PA6 phase. This picture does not allow indicating 'which phase is which' and where the sub-inclusions of the PS phase are located? The SEM picture of Fig. 8(A″) is obtained from a sample where only PA6 was extracted. It reveals that the PA6 is in the form of droplets on the observed surface. Does the PA6 phase form a dispersion or is it continuous? The quantitative extraction experiments carried out on

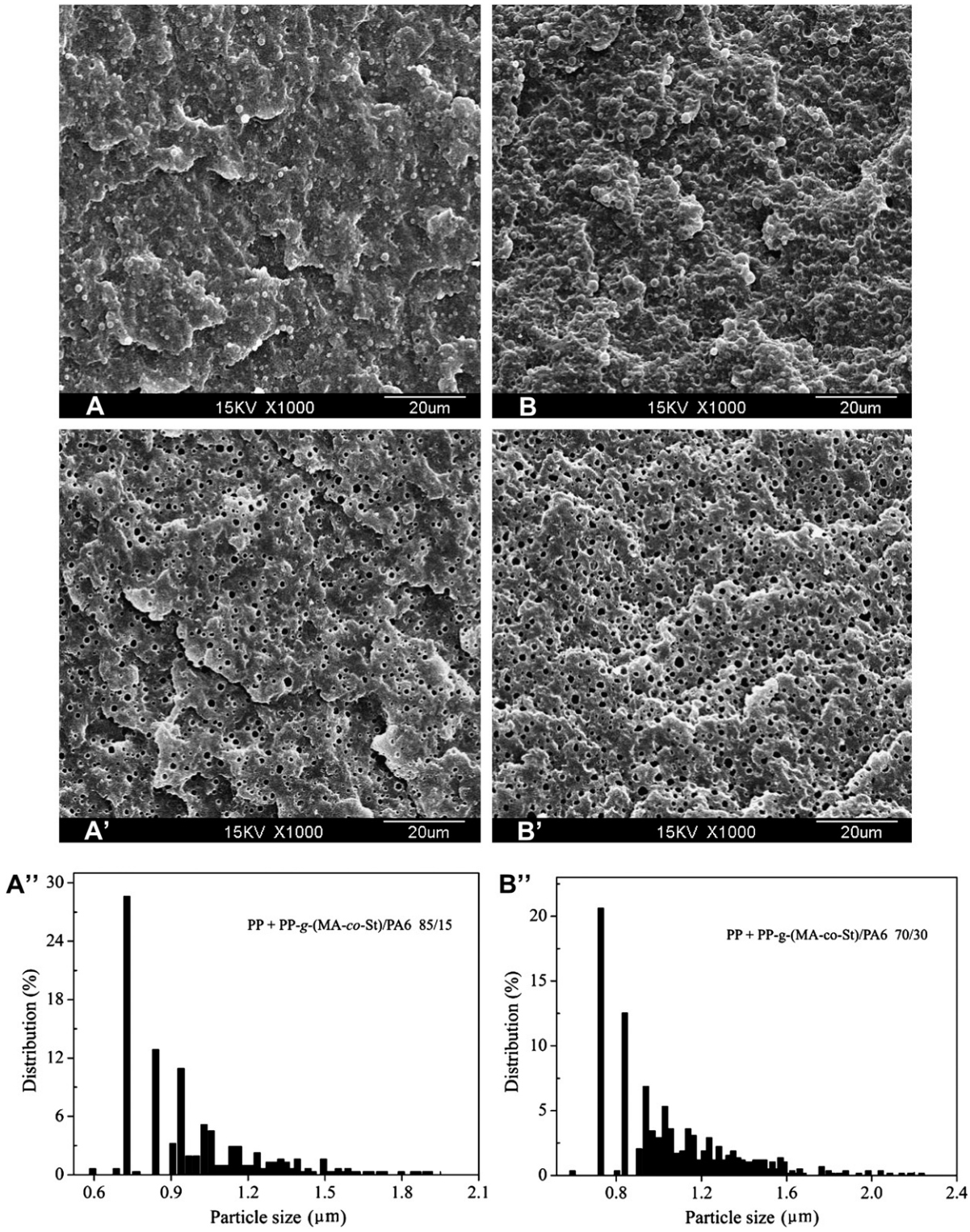

Fig. 6. Morphology of the compatibilized 85PP/15PA6 (A, A′) and 70PP/30PA6 (B, B′) blends: (A, B) cryofractured surface, (A′, B′) cryofractured and PA6 phase extracted using HCOOH, (A″, B″) particle size distribution.

the same blends using formic acid confirmed that PA6 is continuous. Almost all the PA6 phase was extracted from the blend by the formic acid solvent (86 wt.%). That means the PA6 phase is certainly elongated in a network structure in the extrusion direction as Omonov et al. have observed [41]. Thus, it is clear that the three blend components form a three-phase-co-continuous morphology. Furthermore, a close observation of the extraction data reveals that in the blends of 40PA6/30PP/30PS about 8 wt.% of PA6 is dispersed as sub-inclusions in the blends.

Upon addition of the PP-*g*-(MAH-*co*-St) multi-phase compatibilizer, the phase morphology has been changed completely (as shown in Fig. 8(B)). To identify which of the phases is where in the blend, the cryofractured surfaces of the compatibilized blend was etched with formic acid or THF to remove the PA6 or PS phase,

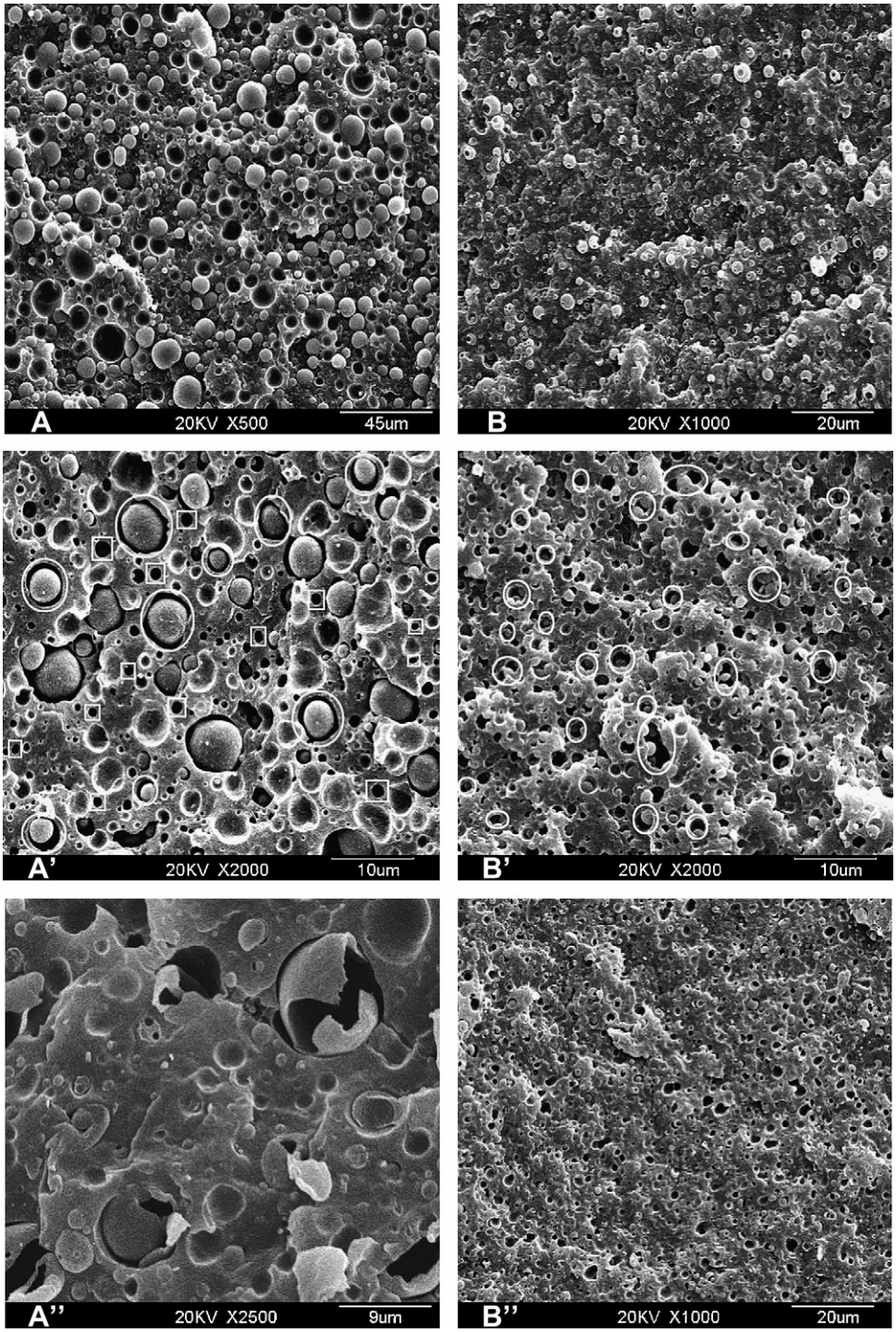

Fig. 7. Morphology of the uncompatibilized (A, A′, A″) and compatibilized (B, B′, B″) ternary PP/PS/PA6(70/15/15) blends: (A, B) cryofractured surface, (A′, B′) cryofractured and PS phase extracted using THF, (A″, B″) cryofractured and PA6 phase extracted using HCOOH.

respectively. Fig. 8(B′) shows a SEM picture of the cryofractured surfaces after extraction of the PS phase. The PS phase is in the form of droplets in the PP matrix. The two remaining phases are clearly visible but is not possible to distinguish the PP phase from PA6 phase. This question can be addressed by a further selective extraction of phase. Fig. 8(B″) illustrate a SEM micrograph of the same blend where THF-extracted sample (PS removed) has been further treated with formic acid. As it is clearly seen, the PA6 phase is included as granules particles in the PP matrix. Thus, it is clear that in the case of compatibilized 40PP/30PS/30PA6 ternary blends, both PS and PA6 phases form droplets in the PP matrix. However, detailed observation shows, besides in the PP matrix, PA6 phase is also included as granules particles in the PS phase. It indicates in compatibilized 40PP/30PS/30PA6 blends, the three components also tightly interact with each other. Such result further demonstrates the good compatibilizing effect of the multi-phase compatibilizer.

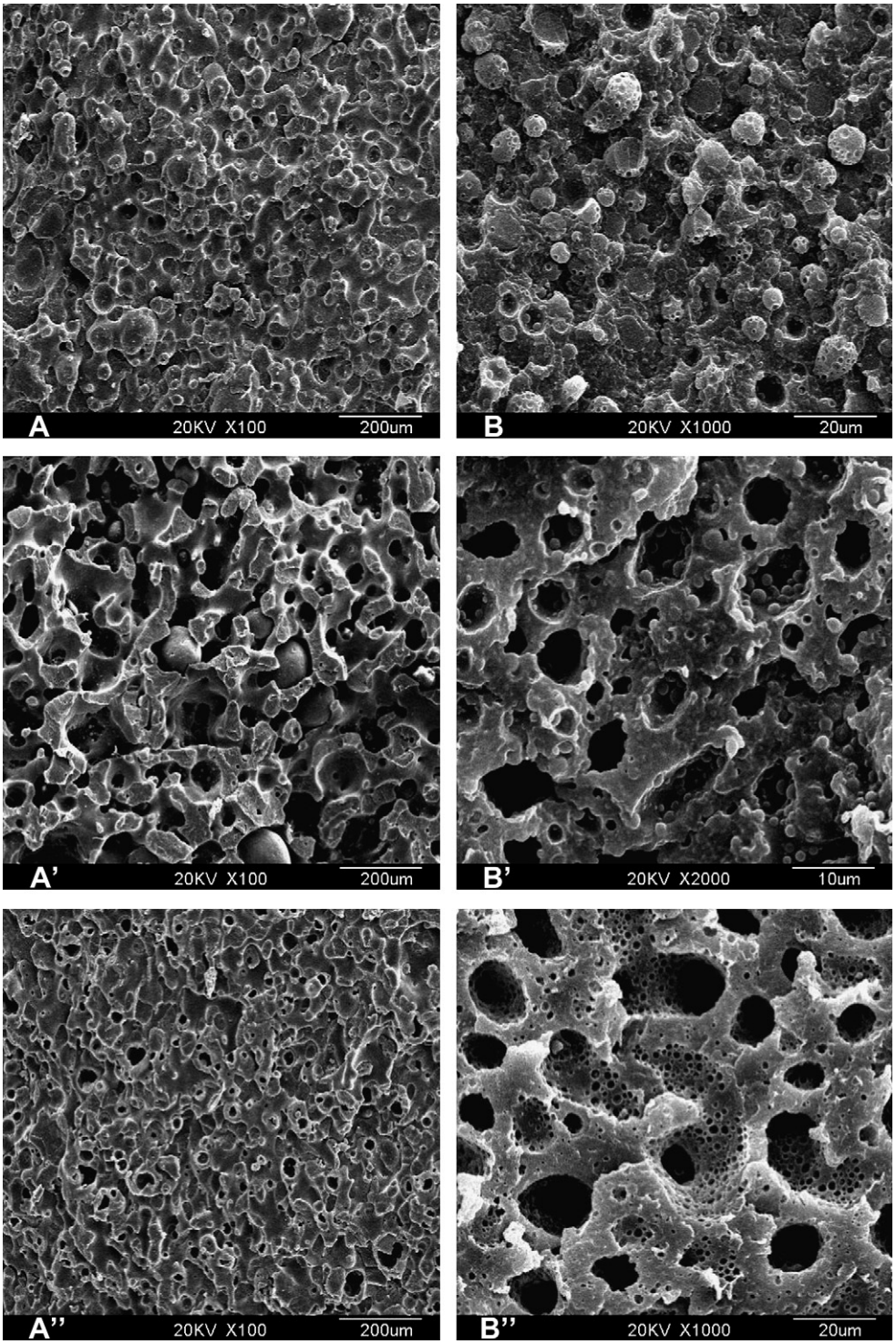

Fig. 8. Morphology of the uncompatibilized (A, A′, A″) and compatibilized (B, B′, B″) ternary PP/PS/PA6(40/30/30) blends: (A, B) cryofractured surface, (A′, B′) cryofractured and PS phase extracted using THF, (A″) cryofractured and PA6 phase extracted using HCOOH, (B″) PA6 phase extracted with formic acid after PS phase extraction with THF.

4. Conclusions

This study provides a novel and effective strategy for achieving compatibilization of ternary or multi-phase immiscible polymer blends, by using a multi-phase compatibilizer. The good compatibilization of the multi-phase compatibilizer for the PP/PS and PP/PA6 binary and PP/PS/PA6 ternary blends can be explained by synergetic compatibilization of two functional groups in the compatibilizer.

Phase morphology in uncompatibilized ternary 70PP/15PS/15PA6 blends exhibits an encapsulated phase morphology having PA6 cores and PS shells. The addition of the PP-*g*-(MAH-*co*-St) multi-phase compatibilizer greatly changes the situation that PS and PA6 particles gets finely dispersed in the PP matrix while three components interact with each other. Such morphology demonstrates the multi-phase compatibilizer has good compatibilization between the various immiscible pairs. In the ternary blends having almost equal amount of PP, PS and PA6 (composition of 40PP/30PS/30PA6) a three-

phase co-continuous morphology is developed. This morphology has been significantly changed by the compatibilization. The phase morphology is constituted from PP matrix in which are dispersed droplets of PS and PA6 phase.

In conclusion, this work is promising not only for developing ternary or multi-phase polymeric blends with unique performance, but also useful for recycling and reusing three immiscible polymers, polyolefins, styrene polymers, and engineering plastics from the waste stream.

Acknowledgments

This project was supported by a grant from the National Natural Science Foundation of China (No. 20874056), which is gratefully acknowledged.

References

[1] Paul DR, Bucknell CB. Polymer blends: formulation & performance. New York: Wiley; 2000.
[2] Koning C, Van Duin M, Pagnoulle C, Jérôme R. Prog Polym Sci 1998;23:707–57.
[3] Sperling LH. Introduction to physical polymer science. 4th ed. New York: Wiley; 2005.
[4] Debolt MA, Robertson RE. Polym Engng Sci 2006;46:385–98.
[5] Debolt MA, Robertson RE. Polym Engng Sci 2004;44:1800–9.
[6] Kim J, Sandoval RW, Dettmer CM, Nguyen ST, Torkelson JM. Polymer 2008;49:2686–97.
[7] Zhang CL, Feng LF, Zhao J, Huang H, Hoppe S, Hu GH. Polymer 2008;49:3462–9.
[8] Zhang CL, Feng LF, Gu XP, Hoppe S, Hu GH. Polymer 2007;48:5940–9.
[9] Macosko CW, Guegan P, Khandpur AK, Nakayama A, Marechal P, Inoue T. Macromolecules 1996;29:5590–8.
[10] Koulic C, Yin Z, Pagnoulle C, Gilbert B, Jérôme R. Polymer 2001;42:2947–57.
[11] Adedeji A, Lyu S, Macosko CW. Macromolecules 2001;34:8663–8.
[12] Chen B, Li XL, Xu SQ, Tang T, Zhou BL, Huang BT. Polymer 2002;43:953–61.
[13] Maric M, Macosko CW. J Polym Sci Part B Polym Phys 2002;40:346–57.
[14] Harrats C, Fayt R, Jérôme R, Blacher S. J Polym Sci Part B Polym Phys 2003;41:202–16.
[15] Chirawithayaboon A, Kiatkamjornwong S. J Appl Polym Sci 2004;91:742–55.
[16] Anderson KS, Hillmyer MA. Polymer 2004;45:8809–23.
[17] Chen JH, Rong MZ, Ruan WH, Mai YL, Zhang MQ. Macromol Chem Phys 2008;209:1826–35.
[18] Raquez JM, Nabar Y, Narayan R, Dubois P. Polym Engng Sci 2008;48:1747–54.
[19] Ide F, Hasegawa A. J Appl Polym Sci 1974;18:963–74.
[20] Plummer CJG, Kausch HH, Creton C, Kalb F, Léger L. Macromolecules 1998;31:6164–76.
[21] Wildes G, Keskkula H, Paul DR. Polymer 1999;40:7089–107.
[22] Charoensirisomboon P, Inoue T, Weber M. Polymer 2000;41:4483–90.
[23] Pagnoulle C, Koning C, Leemans L, Jérôme R. Macromolecules 2000;33:6275–83.
[24] Cartier H, Hu GH. Polymer 2001;42:8807–16.
[25] Schulze JS, Moon B, Lodge TP, Macosko CW. Macromolecules 2001;34:200–5.
[26] Kim HJ, Lee KJ, Seo YS, Kwak SJ, Koh SK. Macromolecules 2001;34:2546–58.
[27] Yin Z, Koulic C, Jeon HK, Pagnoulle C, Macosko CW, Jérôme R. Macromolecules 2002;35:8917–9.
[28] Yeung C, Herrmann KA. Macromolecules 2003;36:229–37.
[29] Kim HY, Jeong U, Kim JK. Macromolecules 2003;36:1594–602.
[30] Lu QW, Macosko CW. Polymer 2004;45:1981–91.
[31] Koulic C, Jérôme R. Macromolecules 2004;37:3459–69.
[32] Wilkinson AN, Clemens ML, Harding VM. Polymer 2004;45:5239–49.
[33] Zhang JB, Lodge TP, Macosko CW. Macromolecules 2005;38:6586–91.
[34] Harton SE, Stevie FA, Ade H. Macromolecules 2005;38:3543–6.
[35] Furgiuele N, Lebovitz AH, Khait K, Torkelson JM. Macromolecules 2000;33:225–8.
[36] Lebovitz AH, Khait K, Torkelson JM. Macromolecules 2002;35:8672–5.
[37] Lebovitz AH, Khait K, Torkelson JM. Macromolecules 2002;35:9716–22.
[38] Lebovitz AH, Khait K, Torkelson JM. Polymer 2003;44:199–206.
[39] Tao Y, Lebovitz AH, Torkelson JM. Polymer 2005;46:4753–61.
[40] Tao Y, Kim J, Torkelson JM. Polymer 2006;47:6773–81.
[41] Omonov TS, Harrats C, Groeninckx G. Polymer 2005;46:12322–36.
[42] Sun YJ, Hu GH, Lambla M. Angew Makromol Chem 1995;229:1–13.
[43] Sun YJ, Hu GH, Lambla M. J Appl Polym Sci 1995;57:1043–54.
[44] Cartier H, Hu GH. J Polym Sci Part A Polym Chem 1998;36:1053–63.
[45] Xie XM, Chen NH, Guo BH, Li S. Polym Int 2000;49:1677–83.
[46] Li Y, Xie XM, Guo BH. Polymer 2001;42:3419–25.
[47] Flores-Gallardo SG, Sánchez-Valdes S, Ramos De Valle LF. J Appl Polym Sci 2001;79:1497–505.
[48] Saelao J, Phinyocheep P. J Appl Polym Sci 2005;95:28–38.
[49] Li ZJ, Xie XM, Guo BH. Chem J Chin U 2004;25:1941–4.
[50] Li ZJ, Guo BH, Hu P, Xie XM. Chem J Chin U 2001;22:1244–8.
[51] Wang D, Xie XM. Polymer 2006;47:282–6.
[52] Macosko CW, Jeon HK, Hoye TR. Prog Polym Sci 2005;30:939–47.
[53] Hobbs SY, Dekkers ME, Watkins VH. Polymer 1988;29:1598–602.
[54] Harkin WD. The physical chemistry of surface films. New York: Reinhold; 1952.
[55] Kirjava J, Rundqvist T, Holsti-Miettinen R, Heino M, Vainio T. J Appl Polym Sci 1995;55:1069–79.
[56] Verdier C, Vinagre HTM, Piau M, Joseph DD. Polymer 2000;41:6683–9.
[57] Macaùbas PHP, Demarquette NR. Polymer 2001;42:2543–54.
[58] Cho K, Jeon HK, Park CE. Polymer 1996;37(7):1117–22.
[59] Chappelear DC. ACS Polym Prepr 1964;5:363.

Polymer 52 (2011) 201–210

Contents lists available at ScienceDirect

Polymer

journal homepage: www.elsevier.com/locate/polymer

Mesoscale modeling of the influence of morphology on the mechanical properties of proton exchange membranes

Yue Qi [a,*], Yeh-Hung Lai [b]

[a] Chemical Sciences and Materials Systems Lab, General Motors R&D Center, Warren, MI, USA
[b] Electrochemical Energy Research Lab, General Motors R&D Center, Honeoye Falls, NY, USA

ARTICLE INFO

Article history:
Received 28 June 2010
Received in revised form
3 November 2010
Accepted 5 November 2010
Available online 13 November 2010

Keywords:
Coarse graining modeling
Proton exchange membranes
Mechanical property
Polymer morphology

ABSTRACT

The nano-scale morphology of a proton exchange membrane (PEM) strongly influences its proton conductivity and mechanical performance. In this paper, a multi-scale modeling approach has been developed to obtain the morphologies of hydrated perfluorosulfonic acid (PFSA) membranes and then to predict their mechanical properties based on the simulated morphology. Two representative ionic domain morphologies were compared, spherical and cylindrical, to represent cast and extruded membranes. The calculated overall elastic Young's moduli are very close for both morphologies and agree well with experiments. The nano-scale phase segregation in hydrated PFSA induces a non-uniform distribution of local stress. The peak stress is localized at the smeared water/PFSA interface. The cylindrical morphology develops much lower peak stress than the isotropic spherical morphology under the same level of strain. These results explain why the extruded membranes show more than 10 times longer life in durability tests than recast membranes, despite having similar bulk moduli.

1. Introduction

Among many challenges that proton exchange membrane (PEM) fuel cells face is the mechanical durability of the fuel cell stack and components. Gas crossover through microscopic pinholes in the PEM resulting from hygrothermal fatigue stresses has been identified as one of the major failure modes. PEMs show complicated time, temperature, and humidity dependent mechanical behavior [1]. Thus, the experimental characterization of their mechanical properties includes many aspects. Their elastic modulus, yield strength, stress and strain at break are typically measured with uniaxial tensile tests [1–6]. Their viscoelastic properties are routinely obtained with dynamic mechanical tests (DMA) at small deformations [7–11]. Their fracture resistance is evaluated with double edge notch tension specimens or knife slit tests [12–16]. Their time- and/or cycle-dependent strength can be measured by pressure-loaded blisters tests [17–19], and the overall mechanical durability can be evaluated by relative humidity (RH) cycling tests [20–23].

Processing conditions can dramatically change the mechanical durability of PEMs. Currently, perflurosulfonic acid (PFSA) polymer membranes are still considered as the "bench mark" for PEM fuel cells. PFSA membranes are typically manufactured by melt extrusion or solution cast. Moore and Martin have demonstrated that cast PFSA film is more brittle and the melt-extruded film is more ductile [24]. Only after thermal annealing or recasting from high temperature, do solution-cast films' properties resemble those of extruded membranes [25]. To illustrate the role of processing methods on mechanical properties, previous studies have compared two commercially available 25 μm-thick PEM, Nafion® NRE-211 and N111-IP. The NRE-211 membrane is a recast homogeneous PFSA membrane by DuPont [26]. The N111-IP is an extruded version of NRE-211 by Ion Power [27]. In the in-situ wet to dry humidity cycling tests using standard fuel cell fixtures, NRE-211 had a significantly shorter RH cycling lifetime than N111-IP [20]. Similar results are observed in the ex-situ life test using pressure-loaded blister and knife-slit tests, in which NRE-211 was found to have shorter lifetime until leakage occurs with faster crack propagation rates under the same applied stress [28]. In this study, both membranes show very similar stress-strain responses and time dependent relaxation moduli in DMA tests, while N111-IP has a slightly lower coefficient of hygral expansion, which results in slightly lower hygrothermal stress from humidity cycling [28]. The combination of a lower hygrothermal fatigue stress, higher fatigue strength, and higher fracture toughness can mechanistically justify the dramatically higher RH cycling lifetime in the extruded N111-IP than the solution-cast NRE-211 membrane. However, it is still not clear how processing procedure drastically changes the mechanical durability of PEMs.

* Corresponding author.
E-mail address: yue.qi@gm.com (Y. Qi).

0032-3861/$ – see front matter © 2010 Elsevier Ltd. All rights reserved.
doi:10.1016/j.polymer.2010.11.013

The mechanical properties of PFSA result from its unique structure. PFSA consists of a highly hydrophobic polytetrafluoroethylene (PTFE) backbone with a fully perfluorinated ether side chain terminated by a strongly hydrophilic $-SO_3H$ group. This leads to spontaneous nano-phase segregation into hydrophilic and hydrophobic domains, especially in a solvent. It is well accepted that in a hydrated PFSA, the sulfonic groups and water develop an interconnected proton conducting network above a threshold of water content, while the fluorocarbon backbone forms a semi-crystalline hydrophobic phase. A detailed review by Mauritz and Moore summarizes the efforts in the last two decades toward understanding the structures of PFSA [29]. The debate over the shape and structure of the ionic clusters and semi-crystalline polymeric matrix is partly due to the lack of direct imaging methods of PFSA and partly due to the different methods used to interpret the diffraction data. Various morphological models have been proposed, such as the cluster-channel model of Gierke et al. [30], the modified core-shell model of Fujimura et al. [31], the lamellar model of Litt [32], the sandwich-like model by Haubold et al. [33], the channel model by Kreuer [34], the rod-like model by Rubatat et al. [35], and the recent "long parallel water channel" model by Schmidt-Rohr and Chen [36].

It has been recognized that the processing conditions can change the morphology in PEM. Small angle neutron scattering (SANS) data revealed that the melt-extruded membranes show an anisotropic scattering pattern, thus have partially aligned and better organized hydrophilic domains than those solution-cast [37]. The understanding of the mechanical properties of PFSA membranes progresses with the understanding of its structure. Rubatat and Diat [38] recently used SAXS and SANS to monitor the evolution of the morphology upon deformation and observed uniaxial deformation at moderate elongation extent. The morphology they proposed is elongated polymeric aggregates aligning along the stretching direction. Liu et al. also rationalized the stress–strain behavior of PFSA and sulfonated poly(arylene ether sulfone) copolymer via a three-dimensional "bundle-cluster model", considering elongated polymer aggregates, proton conduction channels, and states of water [2]. They proposed that the polymer bundles rotate and the interphase chains readjust before yielding; and the polymer aggregates disentangle and reorient after yielding.

The rather complicated morphology–property relationships have been very helpful to understand the mechanical properties of PFSA. But they have not been developed into a numerical model to predict the mechanical responses of PFSA. In contrast, many continuum models for PFSA, such as the biaxial constrain [20–22,39] model, plane strain [40–42] model and three-dimensional hygro–thermo–mechanical finite element methods (FEM) [43], have been constructed to simulate the mechanical response and model failure in PEMs. These continuum models are based on different constitutive properties and boundary conditions. However, these continuum models have not taken the unique structure of PFSA into account.

In this paper, we present a nano-structure based finite element modeling approach to reveal the influence of morphology on the average modulus and local stress under applied tensile load. As the nano-meter scale hydrophilic and hydrophobic domains in hydrated PFSA are too large for atomic simulations, a mesoscale model is required. Recently, we developed a coarse-grained mesoscale model for hydrated PFSA equivalent weight of 1100 (EW = 1100) by dividing the system into three phases, backbone, side chain, and water, then obtaining the morphologies with a dynamic self-consistent mean field theory (SC-MFT) [44–47]. The simulated hydrophilic domain size and shape are generally consistent with some experimental observations [48,49]. Based on this coarse-grain scheme, we developed two representative ionic domain morphologies, spherical and cylindrical, to represent cast and extruded membranes. Similar morphology control has been realized in mesoscale simulations for lamellar ordering [50] and hexagonal cylindrical morphology [51] in block copolymers. Both spherical and cylindrical morphologies were then analyzed by a finite element method (FEM) to compute their responses to the external deformation. Both the bulk averaged Young's modulus and the local stress distribution resulting from the hydrated PFSA under a tensile strain are computed in order to understand the morphology–property relationship.

2. Methods

2.1. Coarse-graining approach

Generating a mesoscale model requires two stages of parameterization [48]. First, PFSA molecules are mapped into a Gaussian chain comprised of coarse-grained beads as shown in Fig. 1a. To retain the branched nature and match the flexibility of the polymer chain, the backbone of the PFSA was represented by *F* beads, which represents 4 ($-CF_2-CF_2-$) monomers, the ether–sulfonic acid ($-O-CF_2-CF(CF_3)-O-CF_2-CF_2-SO_3H$) side chain was presented by an *S* bead. As a result a PFSA chain with equivalent weight of 1100 g/mol (EW = 1100), is represented by 20 repeating coarse-grained FF(S) monomers. About ten water molecules are included in a *W* bead, such that all beads have the same reference volume of 0.315 nm^3 [48]. While the Gaussian chains are ideal (no interactions), the inter-chain and intra-chain interactions in a real polymer are included via a series of effective external potentials including mean field Flory–Huggins-type interactions [44]. The mean field bead interaction energies were determined via the Flory–Huggins mixing parameters δ_I and δ_J, through the difference between their Hildebrand solubility parameters. So the second step in the coarse-graining process is to computed the solubility parameters from atomic simulations, leading to the following Flory–Huggins parameters, $\chi_{FS} = 9.8/RT$, $\chi_{FW} = 15.7/RT$ and $\chi_{SW} = 0.7/RT$. The simulations were performed on cubic grids of $32 \times 32 \times 32$ nodes, occupying $(29\ nm)^3$ volume with the grid resolution of 0.90 nm, for PFSA–water mixtures. The water volume fraction was changed to mimic different hydration levels. Starting from a homogeneous distribution of each component (bead), at each time step a density distribution is generated which minimizes the free energy within the constraints of the external field. The system is then dynamically evolved via stochastic diffusion of the density fields. This time-evolution dynamics of the associated density and potential fields of each phase was solved using a self-consistent mean field theory (SC-MFT) [44–47] implemented in Mesodyn.

The morphologies of the PSFA–water mixture, defined by the distribution of the grid-based concentration density of the three phases (*F*, *S* and *W*) in the overall simulation cell, were equilibrated in up to 5000 time steps ($\sim$150 μs) at 30 °C to simulate casting process. By applying a high shear rate of 0.001/ns, an extrusion process was simulated. After the shearing field is released, the system is allowed to reach a stable state. In hydrated membranes, the water content is usually stated in terms of the parameter, λ, defined as the number of water molecules per sulfonic group. PFSA membranes with water contents of $\lambda = 2$, 6, and 8 (water volume fractions of 6%, 16%, 20%, respectively) were simulated. These values of λ cover the range of water content accessible by membrane hydration using water vapor ($T \leq 120$ °C and RH ≤ 1) [30] and represent the 25 °C water uptake at about 20%, 80%, 100% RH, respectively.

2.2. Mechanics modeling

The distribution of the grid-based concentration density of the three phases (*F*, *S* and *W*) in the periodic simulation cell is the input

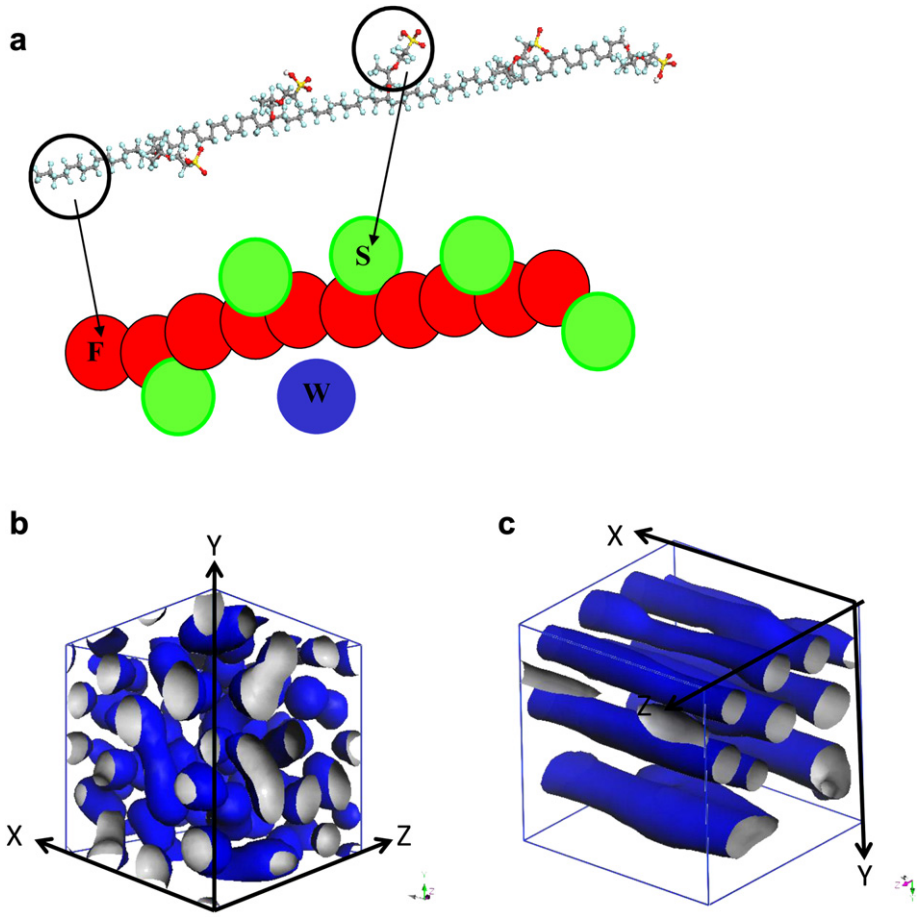

Fig. 1. (a) Sketch of the coarse graining strategy employed in the mesoscale simulation for hydrated PFSA (EW = 1100), and the morphology of water clusters formed in hydrated PFSA with 20% water ($\lambda = 8$), under (b) equilibrium condition and (c) under an applied shearing field along x direction.

morphology for FEM simulations, which computes both the overall and the local mechanical responses based on the material properties in each grid. When the cell is divided into cubic grids, each grid contains a mixture of three phases. The concentration density of each phase contained in that particular grid is specified as $\rho_{J,i}$, where J is the index of phases and i is the index of the grid. The volume fraction of each phase at the grid i is $V_{J,i} = \rho_{J,i} / \sum_j \rho_{J,i}$. Two methods can be chosen for calculating the properties of each grid element that is a combination of different phases: serial (arithmetic) averaging or parallel averaging. We compared the two representations, found no difference to our final conclusions. Therefore, in the present study, the average material properties (e.g. mass density, Young's modulus and Poisson's ratio) of the mixture within each grid is calculated based on the volume fraction and the property of each phase in the grid, as $P_i = V_{F,i}P_F + V_{S,i}P_S + V_{W,i}P_W$. Thus each grid only has one material, with the property tensor, P_i. Each cubic grid used in Mesodyn is refined into six tetrahedron meshes for FEM simulations. By applying a displacement-based FEM to these volume meshes, the response to external deformations is calculated [52,50]. Since input structure is periodic, the FEM simulations boundary condition is 3-D periodic as well. The FEM method has been implemented in MesoProp, which has largely been applied to the calculation of various properties of composite materials [52–54]. The deformation is assumed to be linear elastic in the current study, sufficient for this preliminary investigation.

The mechanical properties of the F and S beads, as an integrated part of the PFSA polymer, are difficult to separate. We thus assigned the dry PFSA properties for both phases. The average material property at each cubic grid is represented by $P_i = (V_{F,i} + V_{S,i})P_N + V_{W,i}P_W$, where N represents PFSA phase, which is the sum of the volume fraction of F and S phases. These properties include mass density, Young's modulus E, and Poisson's ratio υ, which are listed in Table 1. Note that Young's modulus for dry PFSA was derived using the DMA test in dynamic tensile mode at 1 Hz frequency and 25 °C. Following the results by Lai and Dillard [1], a relatively high Poisson's ratio of 0.495 was used for the current study, knowing the effect of Poisson's ratio is generally considered to be secondary. Material properties for dry PFSA and water are assumed to be isotropic, thus the anisotropic properties for hydrated PFSA is a direct result from the underlying structures.

3. Results and discussions

3.1. Simulated PEM morphology

Two representative ionic morphologies are shown in Fig. 1b and c. Meso-scale modeling shows that with 20% water ($\lambda = 8$), at equilibrium condition, the water clusters are ~5 nm diameter

Table 1
Material properties for dry PFSA and water phase.

	Mass density (kg/m^3)	Young's modulus E (GPa)	Poisson's ratio υ
Dry PFSA	2050	0.346	0.495
Water	998	0	0.4925

spheres, with only a few spheres connecting as shown Fig. 1b. Conducting ionic channels along the shearing direction are formed under the applied shear field, and retained their shapes even after the shear field is released, as shown in Fig. 1c. Similar morphologies are also found in hydrated PFSA at various water contents, ranging from $\lambda = 2$ to $\lambda = 8$. Comparing the simulated morphology with the SANS experimental observations, which have shown that that the melt-extruded membranes have partially aligned and better organized hydrophilic domains than solution-cast membranes [37], we believe that the spherical structure from Mesodyn simulations reasonably represent the isotropic morphology formed in PFSA in casting process and the cylindrical structure represents the anisotropic morphology structure formed in PFSA after extrusion process.

Figs. 2 and 3 show more detailed comparison of the concentration density distribution contours of water and PFSA on cross-sections in hydrated PFSA membranes with both morphologies at a water concentration of $\lambda = 2$. In previous studies, we have shown that both the *F* and *S* densities are concentrated in regions not filled by water, indicating strong phase segregation, so in the present study we can take the summation of both phases as the density of the PFSA phase. It has also been noted that the highest *S* density, overlapping with the lowest *F* density, forms thin shell around the *W* clusters, consistent with the observed reverse micelle structure. Fig. 2a shows four spherical water domains on this cross section. The density of the water phase is around 100% at the center of the water domain and almost zero outside the water domain. The PFSA phase surrounds the water domains has its density higher than 80%, while its density at the center of the water domains is zero, as shown in Fig. 2b. Fig. 3a and c shows the cross-sections perpendicular to the water channels. Fig. 3b and d shows the cross-sections at $y = 12.5$, along the water channel direction, *x*. Fig. 3b and d shows two elongated water channels along the *x* direction. This cross-section passes the center of the upper water channel, indicated by the 100% water concentration in Fig. 3b. However, it misses the center of the lower water channel where the smeared water/PFSA region shows a mixture of 80% water and 20% PFSA. With the same amount of water, the cylindrical morphology has a lower number of water domains than the spherical morphology. The diameters of the water domains are similar in the two morphologies, while it seems slightly larger in the spherical morphology. For both morphologies, the PFSA phase has a higher concentration around the water domains (Figs. 2b, 3c, and 3d). On average, the concentration density of the PFSA phase is above 80% outside the water domains, so it would be a reasonable assumption that the hydrated PFSA can be approximated by a two phase model, with a smeared interface of water and the hydrophilic phase.

3.2. Overall modulus

The elastic modulus for hydrated PFSA was computed based on the spherical and cylindrical morphologies generated from Mesodyn. Young's modulus, E, along the *x*, *y* and *z* directions were plotted in Fig. 4. Notice that *x* is parallel to the water channel direction while *y* and *z* are perpendicular to water channel direction. The results in Fig. 4 show that E decreases with increasing water content from $\lambda = 2$ to $\lambda = 12$. In Fig. 4, the E of Nafion NRE-211 membrane measured by DMA test in dynamic tensile mode at 1 Hz frequency and 25 °C are also plotted. Good agreement between the experimental measurement and model prediction is observed. As expected, the spherical morphology shows an overall isotropic behavior. It is interesting to note that the E of the spherical morphology decreases linearly with water content, basically following the rule of mixtures (the volume fraction of the PFSA phase times its modulus at dry condition), especially when $\lambda < 6$, shown as the straight line in Fig. 4. The cylindrical morphology shows slight anisotropic behavior, the modulus along the water channel direction (*x*) is slightly higher than those perpendicular to the water channel direction (*y* and *z*). The former is higher and the later is lower than the modulus in the spherical morphology. Thus, Young's modulus in the direction of aligned water domain is stiffer. The anisotropy in the cylindrical morphology increases with water content, as the difference between the modulus along *x* and *y* direction increases from 1% at $\lambda = 2$ to 6–8% at $\lambda = 8$. This small difference in Young's modulus cannot explain the significant mechanical durability difference between the cast and extruded version of PFSAs.

3.3. Local stress distribution

In a heterogeneous material, the distribution of the local stress is often non-uniform and depends on the detailed morphology. For the hydrated PFSA, the shape and size of the ionic (water) domains can greatly influence the local stress distribution. Therefore, the local stress distribution subjected to an applied mechanical strain of 1% along either the *x*, *y* or *z* direction is analyzed by the distribution of the von Mises stress, which is given by

$$\tau = \sqrt{\frac{(\sigma_{xx}-\sigma_{yy})^2+(\sigma_{yy}-\sigma_{zz})^2+(\sigma_{zz}-\sigma_{xx})^2}{2}+6\left(\sigma_{xy}^2+\sigma_{yz}^2+\sigma_{zx}^2\right)} \quad (1)$$

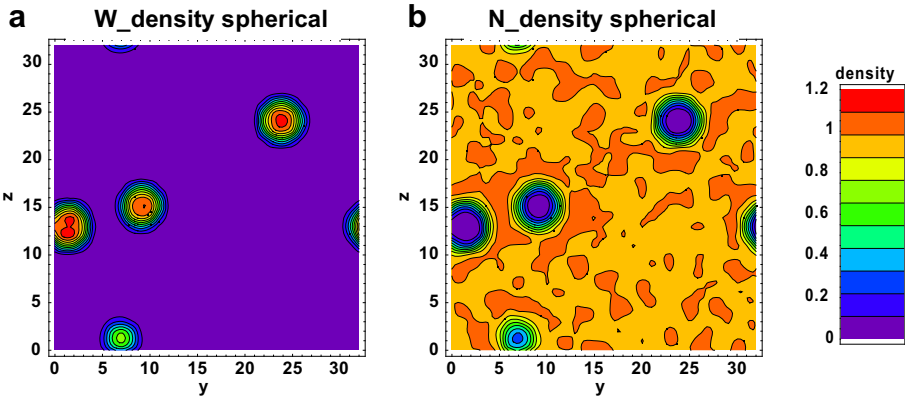

Fig. 2. Concentration density of (a) water phase (W_phase) and (b) PFSA phase (N_phase) on one cross section in the spherical morphology, at $\lambda = 2$, each contour plot has a dimension of 32×32 grids.

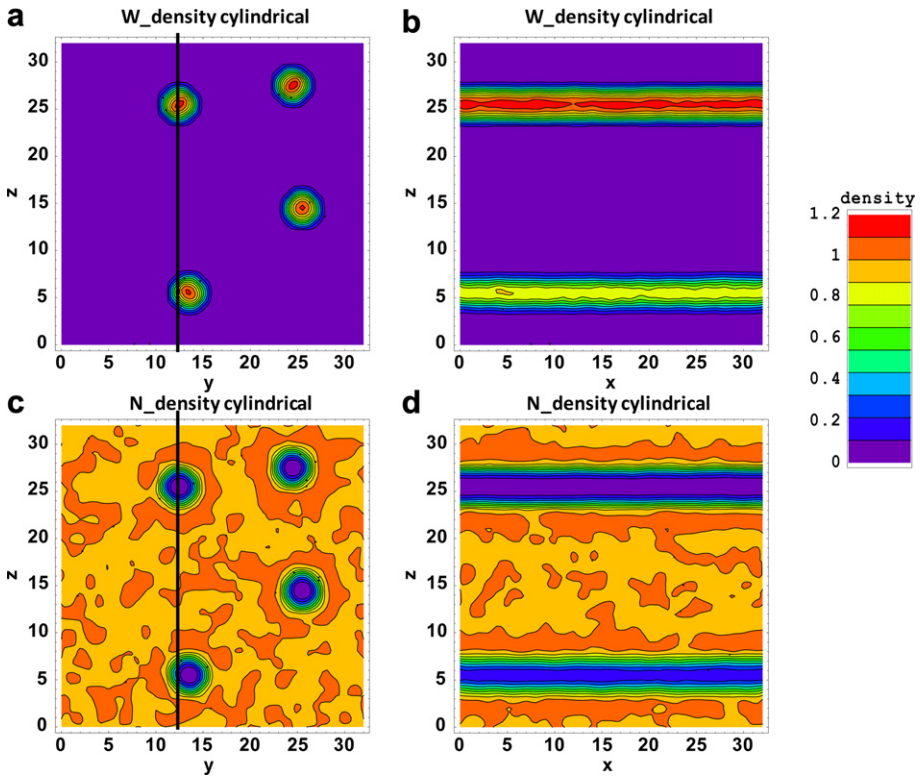

Fig. 3. Concentration density of (a) water phase (W_phase) and (b) PFSA phase (N_phase) on one cross section in the spherical morphology, at $\lambda = 2$, each contour plot has a dimension of 32 × 32 grids.

Fig. 5 illustrates the local stress distribution on a cross session from the 3-D structure of hydrated PFSA at $\lambda = 2$ under 1% tensile strain along the x direction ($\varepsilon_{xx} = 1\%$). Correlating the local stress and the distribution of water and PFSA phases on the same cross section shown in Figs. 2 and 3, it is clear that higher stresses concentrate around the water domains and zero stresses reside inside the water phase. For both the spherical and cylindrical morphologies, the peak stresses are located around the water domains in the PFSA phase. In this cross-section contour plot, the peak stress is around 12–14 MPa in the spherical morphology and 8–10 MPa in the cylindrical morphology, although both are subjected to the same strain of $\varepsilon_{xx} = 1\%$. Examining the stress distribution on the overall 3-D simulation cell, we find that the peak stress in the spherical morphology reaches 17.53 MPa, 30% higher than the peak stress of 11.93 MPa in the cylindrical morphology. When the applied stress is perpendicular to the water channel direction, e.g. along y or z directions, the peak stress reaches 13.55 MPa. As expected, the peak stress found in the spherical morphology does not show such strain orientation dependence. The observed non-isotropic strain distribution from mesoscale calculations is due to the fact that the density distribution of both water and PFSA phases is non-uniform in all three directions, as shown in Fig. 3.

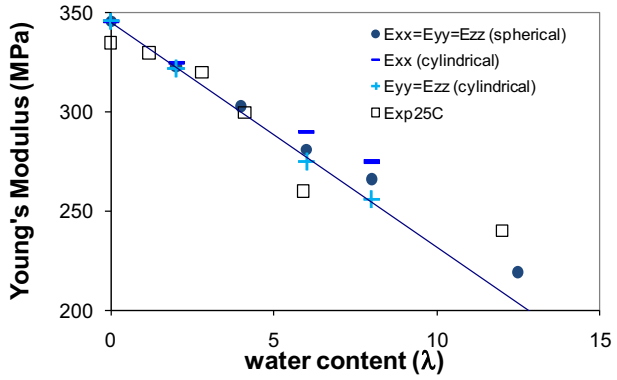

Fig. 4. Computed Young's Modulus along the three main deformation directions in comparison with experimental values. The straight line is plotted according to the rule of mixture, more specifically, as the volume fraction of PFSA phase times its Young's modulus at dry condition.

The location and the magnitude of the peak stress are important factors that relate to the failure of hydrated PFSA membranes. In Fig. 6, we analyzed the relationship between stress distribution and the density distribution of each phase around the representative water domain in both morphologies. In this analysis, we first drew a line cross the center of a water domain. The origin means the center of a water sphere in Fig. 6a and at a water channel in Fig. 6b, respectively. We then plotted the stress and the density of both PFSA and the water phases along this line, as a function of the distance to the center of the water domain, r. Fig. 6 clearly shows that the peak stress occurs right outside the water domain, where the volume fraction of water is below 0.2. In both morphologies in Figs. 5 and 6, stresses drop to about 3 MPa at $r > 5$ nm. This stress level is the same as the applied far-field stress, which equals 1% of the strain multiplied by the overall Young's modulus. This suggests that the water domains are sufficiently far away from each other and their stress fields are not affected by others, at $\lambda = 2$. The peak stress in the cylindrical morphology is about 3 times that of the far-field stress, which seems to agree with the well known stress concentration factor of 3 for an individual circular hole in an infinite 2-D solid matrix predicted from the continuum theory. However, in the spherical morphology case, the peak stress is about 4 times of the far-field stress, much larger than the stress concentration factor

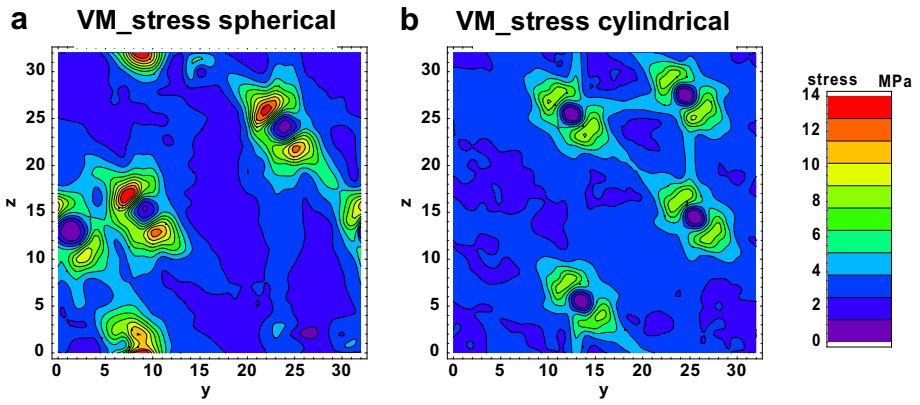

Fig. 5. Local Von Mises stress distribution on a cross section of the two membranes with (a) spherical morphology and (b) cylindrical morphology. Both membranes are subject to 1% tensile strain along *x* direction. For the cylindrical morphology, the cross section is perpendicular to the water channels and the strain is along the water channels.

of 2 for an individual spherical void in an infinite 3-D matrix. Thus, the simple geometric effect based on continuum mechanics alone cannot explain the higher stress concentration in the spherical morphology. Comparing the water and PFSA concentration density distribution between the two morphologies in Fig. 6, the volume fractions of PFSA phase increased from 5% to 95% within a 1 nm region in the spherical morphology and within a 1.5 nm region in the cylindrical morphologies. Thus, the spherical morphology has a sharper interface region. Therefore, when the material property changes from water to PFSA phase, its gradient is larger in the spherical morphology. The higher stress computed for the spherical morphology agree with what was found in other composite materials where higher stress is localized in the interface region with higher material property gradient [55].

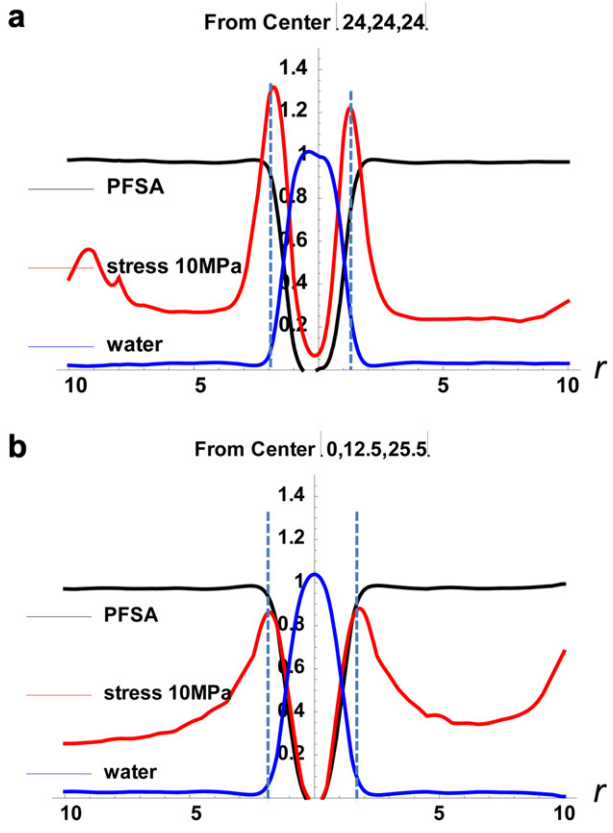

Fig. 6. Local water and PFSA volume fraction and stress distribution around a water (a) sphere along $(x_0 + r, y_0 - r, z_0 + r)$ and (b) cylinder center $(x_0, y_0 + r, z_0 - r)$, where (x_0, y_0, z_0) is the location of the center. The stress is plotted with the unit of x10 MPa.

The water/PFSA interface appears to play an important role in the mechanical strength, in addition to its known important role in influencing the proton transport in PEM. The contour plots of the density distribution in Figs. 2 and 3 are consistent with a relatively diffused water/PFSA interface over 1–2 nm. Various diffusion measurements have demonstrated that the water near the PFSA bonds tightly and the proton diffusion is much slower in this confined water shells. Our results revealed that the smeared water/PFSA interface also controls the mechanical properties of the PFSA. As shown in experiments [29] and previous Mesodyn calculations [48], the PFSA morphology contains reverse micelle structures embedded in the PTFE matrix (*F*). These reverse micelles are filled with water (*W*) and enclosed by the sulfonic side chains(*S*). The thickness of the smeared water/PFSA interface is mainly related to the thickness of the *S* phase shell around the water domains. Both simulated spherical and cylindrical morphologies had similar water domain diameters at the same water concentration. From the simulated morphologies, we found that, with the same total volume fraction of *S* phase and *W* phase, spherical morphologies will have larger surface area, and therefore a smaller shell thickness than cylindrical morphology. The thinner hydrophilic phase (*S*) around the water domains in spherical morphologies will lead to higher stress localization. However, we might have overestimated the width of the smeared interface during coarse-graining the atomic structures into larger beads. Especially, the *S* beads average the hydrophilic nature of the side chain over the entire bead, which physically differs from the molecular side chain that has a strongly hydrophilic $-SO_3H$ terminal group attached to an otherwise covalent fragment. Fully atomistic MD simulations have revealed that the average distance between sulfonate groups is around 0.6 nm, and the average distance between the first water solution shell around the sulfonate group is about 0.4 nm for PFSA 117 at $\lambda = 15$ [56]. To fully understand the role of the water/PFSA interface on the mechanical properties of hydrated PEM, more combined mesoscale and atomic simulations are required.

3.4. Peak local stress

The magnitude and the location of the peak stresses in hydrated PFSA directly relate to its failure mechanism. The peak stresses for the two morphologies are compared at different water concentrations in Fig. 7. The peak stress increases with water content for both morphologies, with a higher peak stress in the spherical

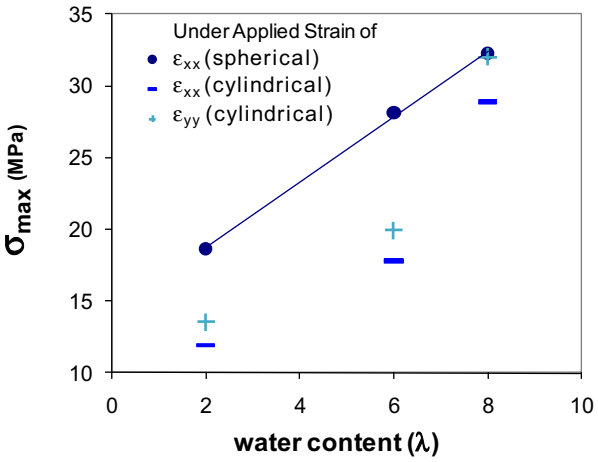

Fig. 7. The peak local stress in the 3-D morphology under applied 1% strain along *x* or *y* direction. The *x* direction is parallel and the *y* direction is perpendicular to the water channel direction in cylindrical morphology. The straight line is a linear fitting for the peak local stresses developed in spherical morphology, which are higher than the peak stresses in cylindrical morphology regardless of the straining direction.

morphology than cylindrical morphology. In the cylindrical morphology, the peak stress is higher when the 1% strain is perpendicular to the channel direction than when it is parallel to the channel direction.

The peak stresses reached in the cylindrical structure are 20%–30% lower than that in the spherical morphology, under the same tensile strains. It's important to notice that the local stress developed in the cylindrical morphology is always lower than that in the spherical morphology, independent of the relationship between the strain direction and the water channels direction. The difference between the two morphologies increases as the water content decreases. This difference is as large as 30% at $\lambda = 2$, which is a significant reduction of local stress due to the cylindrical morphology. As shown in Figs. 5 and 6, the peak stress is located around the water domains. In many organic polymers the first inelastic events such as plasticity and fracture start to occur when the von Mises stress reaches a level of ~30 MPa [13]. Because the spherical morphology develops higher local stress than cylindrical morphologies, it is more susceptible to failure; and the failure of these hydrated PFSA is likely to initiate from the water/polymeric domain interface. Further, since the hydrated PFSA develops the lowest peak stress when the applied strain is parallel to the water channels, one would expect that the membrane is stronger in the channel direction. Considering that the in-plane tensile stress from humidity cycling during fuel cell operation is the key factor in the mechanical degradation of PEM fuel cells, the cylindrical morphology with water channels aligning in the plane should be the preferred morphology in PEMs.

Based on the peak stress comparison between the cylindrical and spherical morphologies, a Nafion NRE-211 membrane, being solution cast and having a spherical morphology, is predicted to have a lower mechanical strength compared to its extruded counterpart of cylindrical morphology and identical chemistry, the Ion Power N111-IP membrane. This conclusion is in good agreement with the experimental results from the blister and knife slit test [28] in which NRE-211 has a lower burst strength, fatigue strength, and fracture toughness than N111-IP. Furthermore, coupling the lower local peak stress and the lower far-field stress resulting from its lower coefficient of hygral expansion, an N111-IP membrane is expected to have significant better humidity cycling durability than an NRE-211 membrane. Again, this prediction agrees well with the result from the in-situ RH cycling test where an N111-IP membrane lasts more than 10 times longer than an NRE-211 membrane.

Another interesting finding from this study, also seen in Fig. 7, is that the local peak stress increases as the water content increases under the applied 1% tensile strain, even though the far-field nominal stress can decrease as the bulk modulus decreases. The result suggests that the bulk mechanical strength of the PEM would decrease as the water content increases. Again, this result correlates well with the experimental results from the blister and knife slit tests [57,17], where the blister burst and fatigue strengths and fracture toughness were found to decrease with increasing water content for both NRE-211 and N111-IP membranes.

From the concentration density distribution of water and PFSA, the hydrated PFSA can be approximated into a two phase model, with a smeared interface. Since water cannot take any load during tension, one can roughly treat the two phase model as a dry PFSA with voids. We developed an analytical solution of stress concentration factor around water domains based on continuum mechanics [58] in the Appendix. Comparing the analytical solution with mesoscale results, we found the computed stress concentration factor increases much faster with water concentration than the analytical solution. So the peak stress from the normal stress concentration created by the geometric discontinuity from a two phase model alone cannot explain the relatively high peak stress in Fig. 7, especially at higher water content. This probably due to two reasons: a) the high peak stress is likely amplified further by the material composition in the interface region between the water and PFSA domains. This is probably true, since water/PFSA interface gets thinner with increasing water content; b) there exists a high disparity of local water content distribution, the stress concentration, and therefore the peak stress, in the region of highly packed water domains could be significantly higher. One would then expect that the material failure can initiate from these regions.

Fig. 7 revealed that the local stress developed in the cylindrical morphology is always lower than that in the spherical morphology, regardless the relationship between the strain direction and the water channels direction. Extrusion process tends to align water domains parallel to the membrane plane. Although this structure is mechanically more stable than the spherical morphology, it will not improve the proton conductivity through the membrane plane, because a connected network of hydrophilic domains is required to transport protons through the membrane. As we observed in experiments, both NRE-211 and N111-IP membranes show similar conductivity. Similar observations have been shown by Kim et al., the melt-extruded and solution-cast membranes with different SANS pattern have water vapor diffusion coefficient on the order of 2×10^{-7} to 4×10^{-7} cm^2/s [37]. However, if one can align the water channels perpendicular to the membrane plane, conducting water channels will form at lower water content and provide the shortest conducting path for protons passing through the PEM, thus improve the proton conductivity dramatically. In fact, like block copolymer melts with different dielectric constant for the two segments can be transformed into an ordered structure under an external electric field [59], the ionic channels in PFSA can be oriented perpendicularly to the membrane plane by an external electric field [60]. Umeda and Uchida showed that a PEM film recast from a ternary polymer blend under an electric-field exhibited 10 times higher proton conductivity than that prepared without the external electric field [61]. For these membranes, the in-plane deformation is perpendicular the water channels, and it still develops lower peak stress than the membranes with spherical water domains. Thus, in term of improving both proton conductivity and mechanical stability of PEM, we suggest aligning water domains perpendicular to the membrane plane.

3.5. Limitations

It is known that processing history plays a substantial role in the polymer morphology. Most of the previous papers have attributed the strength of PFSA to its polymeric phase. Moore has attributed the brittleness of solution-cast PFSA to the lack of semi-crystalline phase [24]. Kim indicated that the structure of the melt-extruded membrane is better arranged matrix and backbone chain [37]. The bundles of aggregates will most likely orient themselves toward the machine direction if PEMs are extruded. For solution-cast films, the orientation of bundles will be much more random. In this model, we did not explicitly change the dry PFSA input elastic properties based on the processing condition, but rather focused on the influence of the shape of the ionic domain on the mechanical response of the hydrated PFSA. To fully simulate the mechanical responses and failure of PEM, the multi-scale mechanical model should also include the property variation of the polymer phase. The processing conditions, casting, drying and shearing, can alter the local structure, such as structural ordering, of the PFSA phase. The mechanical properties, such as the modulus, of the PFSA will depend on the local ordering of the polymer.

Nano-scale phase segregation induces non-uniform nano-scale stress distribution. The cylindrical morphology develops much lower peak stress than the uniform spherical morphology under the same applied strain. No experimental work has been done to confirm this finding yet. To reveal the difference of local stress or strain, one could utilize the image correlation method. Hector and Lai have used this approach to measure the strain accumulation in PEM during a single hydration/dehydration cycle [62], however the resolution was about 1 mm^2, which is not enough to reveal the local stress concentration discovered in the current simulation work.

4. Conclusions

A multi-scale modeling approach has been developed to first obtain the morphologies of hydrated perfluorosulfonic acid (PFSA) membranes and then to predict their mechanical properties based on the simulated morphology. Two representative ionic domains morphologies were compared, namely spherical and cylindrical, to represent cast and extruded membranes. The overall elastic moduli are very close for both morphologies and agree well with experiments. The nano-scale phase segregation in hydrated PFSA induces non-uniform distribution of local stresses. The peak stress is localized at the smeared water/PFSA interface and increases with increasing water content. The cylindrical morphology develops much lower peak stress than the isotropic spherical morphology under the same level of strain. Thus, the spherical morphology (typically formed in cast membranes) is more susceptible to failure; and the failure of these hydrated PFSA is likely to initiate around the water domains, due to a more smeared interface. These results can explain the durability difference between recast and extruded PEM samples, which show similar modulus but the extruded membrane shows 10 times longer life time in in-situ fuel cell humidity cycling test and ex-situ blister and knife slit tests.

Appendix. Geometric effect on the development of peak stress

In this appendix, we describe an analytical solution for peak stress as a function of water contents based on continuum mechanics. Consider a hydrated PFSA domain with an original dry cubic domain size of $L_0 \times L_0 \times L_0$. At a hydrated state, the total volume of water V_w within the PFSA matrix can be given by:

$$V_w = \frac{18\rho\lambda}{\mathrm{EW}} L_0^3 \tag{A1}$$

where λ is the water content, ρ is the dry PFSA density, and EW is the equivalent weight of PFSA. Alternately, assuming that N spherical water domains of diameter d exist for a given λ, V_w can be given by:

$$V_w = N(\lambda)\frac{\pi d^3}{6} \tag{A2}$$

Both experiments and simulations have confirmed that the size of water domain d increases with increasing water content [48,49]. It is interesting to note that, from the Mesodyn hydration PFSA simulations [48], the number of spherical water domains also changes with λ. From Eqs. (A1) and (A2), one can find the following relationship for the number of water domains

$$N(\lambda) = \frac{108\rho\lambda}{\pi \times \mathrm{EW} \times d^3} \tag{A3}$$

Assuming that the water domains are uniformly distributed within the material and a characteristic spacing L representing the distance between the centers of the adjacent water domains, the total volume of the swollen ionomer can be given by $N(\lambda)AL^3$, where A is a geometric factor depending on the geometric arrangement of the neighboring water domains. For example, $A = 1$ when water domains are arranged in a cubic pattern with spheres occupying the vertices of the cube. Since the total volume of the swollen ionomer is also given by $(1 + 18\rho\lambda/\mathrm{EW})L_0^3$, one can easily determine the ratio between the water domain diameter d and characteristic distance L as:

$$\frac{d}{L} = \left[\frac{108A\rho\lambda}{\pi\mathrm{EW}\left(1+\frac{18\rho\lambda}{\mathrm{EW}}\right)}\right]^{1/3} \tag{A4}$$

Similarly, one can find the d to L ratio for the cylindrical morphology as

$$\frac{d}{L} = \left[\frac{72B\rho\lambda}{\pi\mathrm{EW}\left(1+\frac{18\rho\lambda}{\mathrm{EW}}\right)}\right]^{1/2} \tag{A5}$$

where B is the geometric factor representing the geometric arrangement of the neighboring water tubes in the x–y plane. B equals to one when the water tubes are arranged in a square pattern. One can find that d/L increases monotonically as water content λ increases as seen in Fig. A1, in which A and B are assumed to be one. It is also seen that the d/L ratio in the cylindrical morphology is lower than that in the spherical morphology for a given λ. Comparing the d/L ratio between the spherical and cylindrical morphologies, it is interesting to see that the spherical morphology would be more sensitive to the uniformity of the water domain distribution as its d/L ratio can approach 1 (and approaching a theoretical infinite stress concentration factor) at a much smaller λ.

Consider the case of applying a uniaxial far-field stress field σ on an infinite body containing an infinite matrix of spherical or cylindrical voids of diameter d separated by a characteristic length L. Based on a simple dimensional analysis, one can expect that the stress concentration factor k, defined as the ratio between the peak stress $\sigma_{\max}$ and the far-field stress σ, would be a function of a non-dimensional length term d/L. Based on the classical work on the mechanical stress concentration by Peterson [58], the stress concentration factor increases with increasing d/L. Fig. A2 illustrates the stress concentration factor of the cylindrical morphology with the water tubes ideally arranged in square pattern and a far-field strain applied in the y or z direction. It can be seen that the

stress concentration factor increase from with water content, especially for a hydrated PFSA under an RH less than 100%, it would have a stress concentration factor between 3 and 4 if the water domains are uniformly distributed. However we noticed that mesoscale results increases much faster with water concentration, ranging from 4 to 12 when λ increases from 2 to 8.

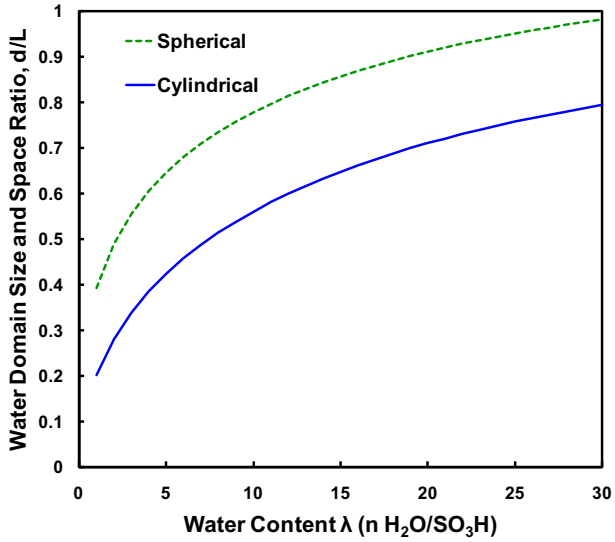

Fig. A1. The water domain size and space ratio d/L following Equation (A4) and (A5) for the spherical and cylindrical structures. The d/L ratio increases monotonically with water content. The d/L ratio is generally higher in spherical structure for all water contents

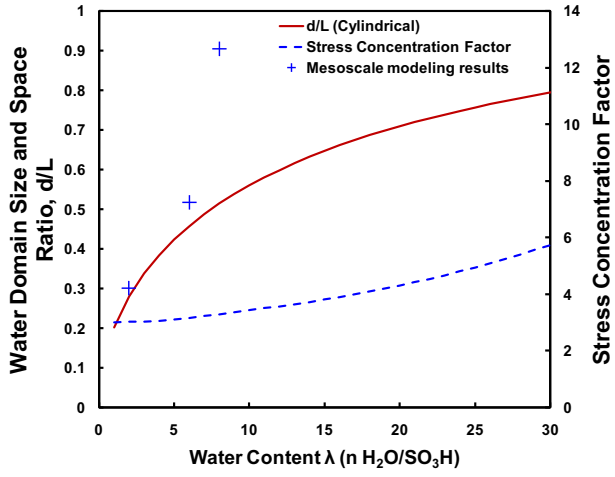

Fig. A2. The water domain size and space ratio d/L and stress concentration factor for the cylindrical structure. Both d/L and k increase monotonically with water content. The symbols are stress concentration factors computed based on mesoscale results of peak stresses, modulus at 1% strain, "+" is for the applied stress is perpendicular to the cylindrical water channels.

References

[1] Lai YH, Dillard DA. Handbook of fuel cells. In: Vielstich AW, Gasteiger H, Yokokama H, editors. Advances in electrocatalysis, materials, diagnostics and durability, vol. 5. John Wiley & Sons, Ltd.; 2009.
[2] Liu D, Kyriakides S, Case SW, Lesko JJ, Li YX, McGrath JE. Journal of Polymer Science. Part B, Polymer Physics 2006;44:453.
[3] Huang XY, Solasi R, Zou Y, Feshler M, Reifsnider K, Condit D, et al. Journal of Polymer Science. Part B, Polymer Physics 2006;44:2346.
[4] Tang Y, Karlsson AM, Santare MH, Gilbert M, Cleghorn S, Johnson WB. Materials Science and Engineering A 2006;425:297.
[5] Tang Y, Kusoglu A, Karlsson AM, Santare MH, Cleghorn S, Johnson WB. Journal of Power Sources 2008;175:817.
[6] Kusoglu A, Karlsson AM, Santare MH, Cleghorn S, Johnson WB. Journal of Power Sources 2007;170:345–58.
[7] Curtin DE, Lousenberg RD, Henry TJ, Tangeman PC, Tisack ME. Journal of Power Sources 2004;131:41.
[8] Bauer F, Denneler S, Willert-Porada M. Journal of Polymer Science. Part B, Polymer Physics 2005;43:786–95.
[9] Kundu S, Simon LC, Fowler M, Grot S. Polymer 2005;46:11707–15.
[10] Patankar K, Dillard D, Case S, Ellis M, Lai Y, Budinski M, et al. Proceedings of the SEM Annual Conference and Exposition on Experimental and Applied Mechanics; 2007.
[11] Patankar K, Dillard DA, Case SW, Ellis MW, Lai YH, Budinski MK, Gittleman CS. Mechanics of Time-Dependent Materials 2008;12:221–36.
[12] Patankar K, Dillard DA, Case SW, Ellis MW, Lai YH, Budinski MK, et al. Journal of Membrane Science, submitted for publication.
[13] Gittleman CS, Budinski MK, Lai Y, Litter B, Miller, D. AIChE Annual meeting; 2004.
[14] Dillard DA, Budinski M, Lai Y, Gittleman C. Proceedings of the 3rd International Conference on Fuel Cell Science, Engineering and Technology, 2005; pp. 153–159.
[15] Li Y, Quincy JK, Case SW, Ellis MW, Dillard DA, Lai Y, et al. Journal of Power Sources 2008;185:374–80.
[16] Patankar K, Dillard DA, Case SW, Ellis MW, Lai YH, Budinski MK, et al. Journal of Polymer Science Part B. Polymer Physics 2010;48:333–43.
[17] Dillard DA, Li Y, Grohs J, Case SW, Ellis MW, Lai YH, et al. Journal of Fuel Cell Science and Technology 2009;6:031014-1–031014-8.
[18] Li Y, Grohs J, Pestrak MT, Dillard DA, Case SW, Ellis MW, et al. Journal of Power Sources 2009;194:873–9.
[19] Grohs JR, Li Y, Dillard DA, Case SW, Ellis MW, Lai YH, Gittleman CS. Journal of Power Sources 2010;195:527–31.
[20] Gittleman CS, Lai YH, Miller DP. Extended Abstract in the AIChE 2005 Annual Meeting, Cincinnati, OH; 2005.
[21] Lai Y, Mittelsteadt CK, Gittleman CS, Dillard DA. Journal of Fuel Cell Science and Technology 2009;6:021002-2–021002-13.
[22] Lai Y, Gittleman CS, Mittelsteadt CK, Dillard DA. Proceedings of the 3rd International Conference on Fuel Cell Science. Engineering and Technology; 2005:161–7.
[23] Gittleman CS. Automotive Perspective on PEM Evaluation. DOE High Temperature Membrane Working Group, Washington, DC. http://www1.eere.energy.gov/hydrogenandfuelcells/pdfs/htmwg_may09_automotive_perspective.pdf; 2009
[24] Moore RB, Martin CR. Macromolecules 1988;21:1334–9.
[25] Hensley JE, Way JD, Decb SF, Abney KD. Journal of Membrane Science 2007;298:190–201.
[26] DuPont Fuel Cells, Dupont Nafion PFSA membranes: NRE-211 and NRE-212. Available at: http://www.fuelcell.com/techsheets/Nafion%20NRE-211%20212.pdf.
[27] Ion Power, Inc. Product information. Available at: http://www.ion-power.com/products.html#films.
[28] Gittleman CS, Coms FD, Lai YH, Modern topics in polymer electrolyte fuel cell degradation. In: Matthew M Mench, Caglan Kumbur E, Nejat Veziroglu T, editors. Elsevier, in press.
[29] Mauritz KA, Moore RB. Chemical Reviews 2004;104:4535.
[30] Gierke TD, Munn GE, Wilson FC. Journal of Polymer Science. Part B, Polymer Physics 1981;19:1687.
[31] Fujimura M, Hashimoto T, Kawai H. Macromolecules 1981;14:1309;
Fujimura M, Hashimoto T, Kawai H. Macromolecules 1982;15:136.
[32] Litt MH. Polymer Preprints 1997;38:80.
[33] Haubold HG, Vad T, Jungbluth H, Hiller P. Electrochim Acta 2001;46:1559.
[34] Kreuer KD. Journal of Membrane Science 2001;185:29.
[35] Rubatat L, Rollet A, Gebel G, Diat O. Macromolecules 2002;35:4050.
[36] Schmidt-Rohr K, Chen Q. Nature Materials 2008;7:5.
[37] Kim MH, Glinka CJ, Grot SA, Grot QG. Macromolecules 2006;39:4775–87.
[38] Rubatat L, Diat O. Macromolecules 2007;40:9455.
[39] Park SJ, Lai YH, Coupar T, Case SW, Ellis MW, Dillard DA, et al. Mechanics of Time-Dependent Materials, submitted for publication.
[40] Kusoglu A, Karlsson AM, Santare MH, Cleghorn S, Johnson WB. Journal of Power Sources 2006;161(2):987–96.
[41] Tang Y, Santare MH, Karlsson AM, Cleghorn S, Johnson WB. Journal of Fuel Cell Science and Technology 2006;3:119–24.
[42] Solasi R, Zou Y, Huang X, Reifsnider K, Condit D. Journal of Power Sources 2007;167:366–77.
[43] Al-Baghdadi MARS, Al-Janabi HAKS. Energy and Fuels 2007;21:2258–67.
[44] Fraaije CGEM, van Vlimmeren BAC, Maurits NM, Postma M, Evers OA, Hoffman C, et al. Journal of Chemical Physics 1997;106:4260.
[45] Maurits NM, van Vlimmeren BAC, Fraaije JGEM. Physical Review E 1997;56:816.
[46] Maurits NM, Zvelindovsky AV, Sevink GJA, van Vlimmeren BAC, Fraaije JGEM. Journal of Chemical Physics 1998;108:9150.
[47] Zvelindovsky AV, Sevink GJA, van Vlimmeren BAC, Maurits NM, Fraaije JGEM. Physical Review E 1998;57:4699.
[48] Wescott JT, Qi Y, Subramanian L, Capehart TW. Journal of Chemical Physics 2006;124:134702.
[49] Young K, Trevino SF, Tan NCB. Journal of Polymer Science. Part B, Polymer Physics 2002;40:387.

[50] Zvelindovsky AV, Sevink GJA, van Vlimmeren BAC, Maurits NM, Fraaije JGEM. Physical Review E 1998;57:R4879.
[51] Zvelindovsky AVM, Sevink GJA. Europhysics Letters 2003;62:370.
[52] Gusev AA. Macromolecules 2001;34:3081.
[53] Gusev AA, Lusti HR. Adv Mater. Weinheim Ger 2001;13:1641.
[54] Gusev AA. Physical Review Letters 2004;93:034302.
[55] Esmaeili N, Tomita Y. International Journal of Mechanical Sciences 2006;48:1186–95.
[56] Jang SS, Molinero V, Cagin T, Goddard WA. Journal of Physical Chemistry. B 2004;108:3149.
[57] Li Y, Grohs J, Pestrak MT, Dillard DA, Case SW, Ellis MW, Lai YH, Gittleman CS, Miller DP. Journal of Power Sources 2009;194:873–9.
[58] Peterson RE. Stress concentration factors. John Wiley & Sons; 1974.
[59] Kyrylyuk AV, Zvelindovsky AV, Sevink GJA, Fraaije JGEM. Macromolecules 2002;35:1473.
[60] Qi Y, Xie T, Fuller TJ, Enhancing proton conductivity of proton exchange membranes, USPTO Application # 20080176965; 2005.
[61] Umeda M, Uchida I. Langmuir 2006;22:4476–9.
[62] Hector LG, Lai YH, Tong W, Lukitsch MJ. Journal of Fuel Cell Science and Technology 2007;4:19–28.